ISSN 0289-842X

RIKEN Accelerator Progress Report

1986

vol. 20

理化学研究所
the Institute of Physical and Chemical Research

RIKEN Accelerator Progress Report 1986

January-December

理化学研究所
the Institute of Physical and Chemical Research
Wako-shi, Saitama, 351-01 JAPAN

Editors

This volume contains recent information of the accelerators at RIKEN (IPCR), informal reports and abstracts of papers which will be published at scientific meetings or in publications by staff members, guests, and visitors.

CONTENTS

Page

2. Atomic and Solid-State Physics

I. INTRODUCTION

H. Kamitsubo

The most remarkable achievement in this period is the commissioning of RIKEN Ring Cyclotron (RRC), the construction of which started in 1980. The main part of RRC was fabricated by Sumitomo Heavy Industries, Ltd.; the control system was made by Mitsubishi Electric Corporation. The assembly of RRC was completed in October and the acceleration test of Ar ions started at the end of November. We succeeded in the extraction of the beam on December 16, 1986.

Research work with the 160 cm cyclotron and the variable-frequency heavy-ion linac (RILAC) was extensively performed in the first half of this year. However, because of unexpected contaminations found in the hot laboratory and experimental area in the cyclotron building in August, both accelerators were stopped compulsorily for three months. RILAC was put back into operation in the middle of November.

Studies on nuclear physics have been continued mainly using 160 cm cyclotron and facilities of other institutions such as Institute for Nuclear Study (University of Tokyo), Research Center for Nuclear Physics (Osaka University), Lowrence Berkeley Laboratory, Nuclear Spectroscopy Laboratory (Strasbourg), and GANIL (Caen). The design studies on experimental equipment for RRC have extensively been performed by the nuclear physics group throughout this year.

Calculations of cross sections of heavy-ion reactions and fission process were performed on the basis of the transport theory. Theoretical research on atomic collision processes has been performed in connection with various problems such as radiative electron capture at high energy, ionization process in collision of proton with highly stripped ions, and charge exchange collision on solid surface. The structure of muonic molecular ions was also studied theoretically.

Experimental work was carried out on the atomic collision processes and on the beam foil spectroscopy by measuring the spectra of lights, X-rays and Auger electrons, charge state distribution of ions after collision, and angular distributions of X-rays and electrons as well as scattered ions. Various kinds of ions accelerated by RILAC were used for these studies. Subnanosecond measurement of the light emitted along the heavy-ion trajectory in the gaseous materials was extensively studied.

Mössbauer spectroscopy and perturbed angular correlation studies were performed using γ-rays emerging from Coulomb excitated nuclei. Mössbauer studies with short lived radioisotopes produced by the cyclotron have been continued.

Analysis of the distributions of implanted or dissolved impurities in various materials has been continued using the Rutherford back-scattering method, Rutherford forward recoil measurement, elastic recoil detection method, and nuclear reaction method. Activation analysis of light element impurities in the semiconductor materials and high purity materials were continued. PIXE analysis was applied to medical, environmental, and geological samples.

Development of new instrumentation and experimental technique has been extensively carried on in this period. Accelerator development was pursued as in preceding years.

RIKEN Accel. Prog. Rep. 20 (1986)

II. OPERATION OF ACCELERATORS

1. Cyclotron Operation

S. Fujita, K. Ikegami, T. Kageyama, S. Kohara,
K. Ogiwara, H. Takebe, and I. Kohno

The 160 cm cyclotron was operated on the 24 h a day basis during the period from Nov. 8, 1985, to Nov. 7, 1986. Statistics of the machine operation time is shown in Table 1. The total net beam-time in this period decreases drastically on account of long scheduled shutdown of 134 d.

Table 2 shows the beam-time allotment to various activities during this period. Table 3 shows the distribution of the scheduled beam-time among various particles.

Table 1. Cyclotron operation in the period XXI.

	Oscillator	Ion source	Beam
Reading of the time meter on Nov. 08 1985 (h)	90,854.9	95,638.6	57,457.6
Reading of the time meter on Nov. 07 1986 (h)	93,985.8	99,050.2	59,334.9
Difference (h)	3,130.9	3,411.6	1,877.3
Percentage of 365 d	35.7%	38.9%	21.4%
Schedule in this period:			
Beam-time		153 d	
Overhaul and installation		25	
Periodical inspection and repair		48	
Scheduled shutdown		134	
Machine troubles		5	

Table 2. Scheduled beam-time and research subjects in the period XXI.

Subject		Heavy ion	Light ion	Total
Nucl. Phys.		1,162	242	1,404
Fields other than Nucl. Phys.	Nuclear chemistry	0	518	518
	Radiation biology	59	112	171
	Radiation chemistry	372	23	395
	Radiation damage of metal	0	60	60
	Test of radiation detector	0	108	108
	Radiation damage of polymer	0	54	54
	Atomic collision	46	0	46
Outside users	Radiation damage	0	35	35
	RI production	0	50	50
	Test of track detector	0	34	34
	Radiochemical analysis	0	152	152
	Test of single event upset	251	0	251
	Proton irradiation on Si	0	53	53
Total		1,890	1,441	3,331
Percentage in total		56.7%	43.3%	100%
Maintenance, operation, and engineering:				
Exchange of ion source	64 h			
Machine inspection and repair	250 h			
Total	314 h			

Table 3. Distribution of beam-time among particles accelerated.

Particle	(h)	(%)
p	345	10.4
d	108	3.2
$^{3}He^{2+}$	271	8.1
$^{4}He^{2+}$	759	22.8
$^{12}C^{4+}$	354	10.6
$^{14}N^{4+}$	740	22.2
$^{14}N^{5+}$	50	1.5
$^{16}O^{5+}$	240	7.2
$^{18}O^{5+}$	168	5.0
Ne^{6+}	296	8.9
Total	3,331	

RIKEN Accel. Prog. Rep. 20 (1986)

II-2. Operation of TANDETRON

H. Sakairi, T. Kobayashi, E. Yagi, and T. Urai

The TANDETRON was operated for 140 d of the past year from November, 1985, during which ^{1}H, ^{3}He, ^{4}He, ^{11}B, and ^{12}C were accelerated.

A negative-ion source of a duoplasmatron type has been newly equipped to generate negative hydrogen ion beams with sufficient intensity and stability.

A charge exchanger connected to a duoplasmatron, mainly used for negative helium ion generation, had trouble frequently; therefore, a new exchanger was designed and constructed by us. It increased both beam intensity and the life of charged lithium twice compared with the former exchanger; the maintenance also became easier.

An automatic controller using a personal computer was used to trial in time-consuming channeling experiments.

Experimental studies have been carried out by Rutherford backscattering spectroscopy, channeling and nuclear reaction analysis, or by combination of these, on the following subjects:

(a) Lattice location of hydrogen atoms in metals (Metal Phys. Lab. and Beam Analysis Center),

(b) Depth profile of implanted ions in high polymers (Biopolymer Phys. Lab. and Beam Analysis Center),

(c) Depth profile and lattice location of Eu in CaF_2 (Semiconductors Lab. and Beam Analysis Center),

(d) Solubility of D in Si (Nuclear Chem. Lab.); and

(e) *In situ* observation of heavy ion-induced damage in Metals (Metal Phys. Lab. and Beam Analysis Center).

RIKEN Accel. Prog. Rep. 20 (1986)

II-3. RILAC Operation

Y. Miyazawa, M. Hemmi, T. Inoue, T. Kambara, M. Yanokura, M. Kase, T. Kubo, E. Ikezawa, T. Aihara,* T. Ohki,* Y. Chiba, and I. Tanihata

RILAC (RIKEN heavy-ion linear accelerator) continues to supply various kinds of ion beams for many fields of research. Tables 1 and 2 give statistics of operation for the period of Sep. 1, 1985–July 12, 1986.

Five new sputter PIG sources[1] have been operated since the fall of 1985. With these sources, ions of solid elements, Mg^{3+}, Al^{3+}, Si^{3+}, Ti^{5+}, Cr^{5+}, Ni^{6+}, and Cu^{6+} were delivered to various target stations.

Pulsing of a beam was tried by modulating relative RF phase between accelerating tank 1 and 2. Figure shows a pulsed beam obtained by phase modulation of 10 ms. The pulsed beam with a time range longer than 1 ms was successfully obtained in this way.

From July 14 to Sep. 16, 1986, the operation of RILAC was discontinued to construct a beam injection line to the new Ring Cyclotron.

Table 1. Statistics of operation for the period of Sep. 1, 1985–July 12, 1986.

	d	%
Beam time	173	54.9
Frequency change	19	6.0
Overhaul and improvement	11	3.5
Periodic inspection and repair	22	7.0
Machine trouble	0	0
Scheduled shutdown	90	28.6
	315	100

Table 2. Percentage of beam time for research activities.

	%
Atomic physics	35.3
Solid-state physics	20.2
Nuclear physics	9.8
Radiochemistry and nuclear chemistry	18.5
Radiation chemistry and radiation biology	5.8
Accelerator research	10.4

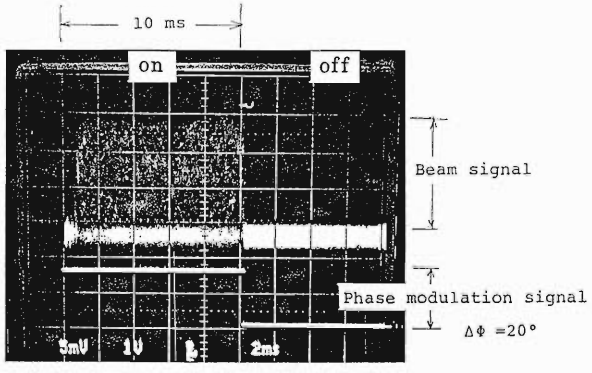

Fig. 1. A pulsed beam obtained by phase modulation of 10 ms.

The No. 2 resonator had a small vacuum leak on a cooling pipe of a shorting plate. The damaged part was replaced with a new one. To improve seasonal temperature variation in the cubicles of the RF power supply, an air conditioner was provided for them.

We had a trouble with RF phase fluctuation of about 20 to 30 ms period in each resonator; it was suspected to be due to mechanical vibration of some parts. We have confirmed that main vibrating parts were side pannels of the upper RF linear and their vibration source was a circulation pump in the Freon cooling system installed near the first tank. Remedies for them are being investigated.

The operation of RILAC was also discontinued for the period of Sep. 17–Nov. 11, 1986, when a general inspection of the attached hot laboratory was conducted.

Reference

1) Y. Miyazawa, M. Hemmi, T. Chiba, and M. Kase: p. 195 in this report.

* Sumijyu Accelerator Service, Ltd.

RIKEN Accel. Prog. Rep. 20 (1986)

III. RESEARCH ACTIVITIES

1. Nuclear Physics

1. γ-Ray Angular Distributions in the ^{98,100}Mo(^{16}O, 4nγ)^{110,112}Sn Reactions

H. Harada, J. Kasagi, T. Murakami, K. Yoshida,
T. Inamura, and T. Kubo

{NUCLEAR REACTIONS ^{98,100}Mo(^{16}O, 4nγ)^{110,112}Sn, E=76, 72 MeV; measured γ-ray angular distributions, deduced J^{π}.}

In a previous progress report,[1] the existence of deformed bands in high-spin region of ^{110}Sn and ^{112}Sn has been reported. The spins of the new members ($J \geqq 12\hbar$) of the deformed bands have been tentatively assigned. In the present work, we have measured γ-ray angular distributions for the unambiguous spin assignments of the members of the deformed bands. High spin states in ^{110}Sn and ^{112}Sn were excited by the ^{98,100}Mo(^{16}O, 4n)^{110,112}Sn reactions at $E(^{16}\mathrm{O})=76$ and 72 MeV, respectively. The angular distributions of γ-rays were measured by two sets of BGO anti-Compton spectrometer[2] in coincidence with neutrons detected by a neutron multiplicity filter.[3]

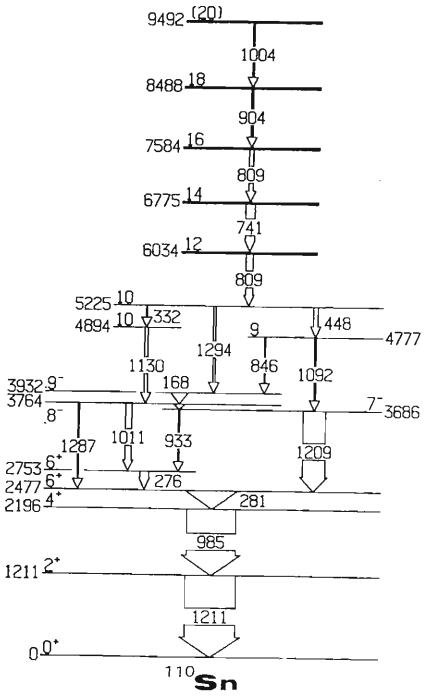

Fig. 1. Level scheme of ^{110}Sn.

Relevant parts of the decay scheme of ^{110}Sn and ^{112}Sn are shown in Figs. 1 and 2, respectively. Levels above ~ 5 MeV were established in the course of this work. Levels assigned to the members of the deformed bands are drawn by thick-heavy lines in the decay scheme. Examples of the measured angular distributions of γ-rays from the band members in ^{112}Sn are shown in Fig. 3. The solid curves in the figure are the best fit results of the function $W(\theta) = N\cdot(1 + A_2\cdot P_2(\cos\theta) + A_4\cdot P_4(\cos\theta))$. They show the characteristics of the stretched E2-type transition. The 663 and 741 keV transitions have been

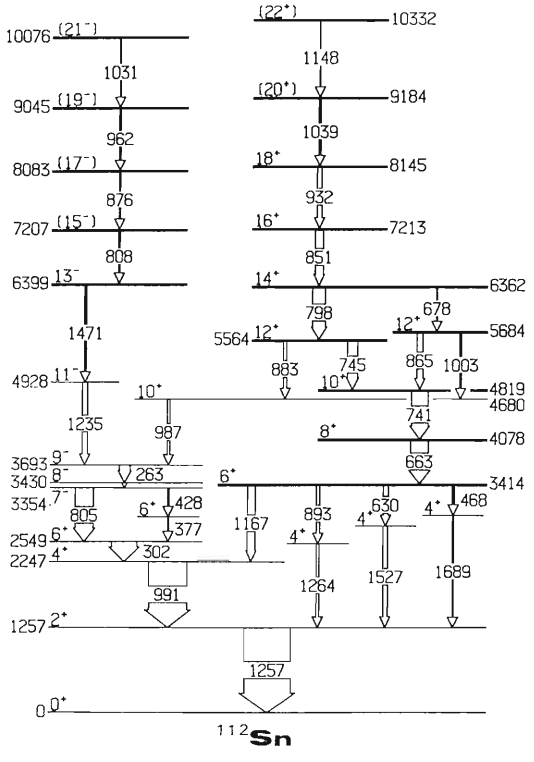

Fig. 2. Level scheme of ^{112}Sn.

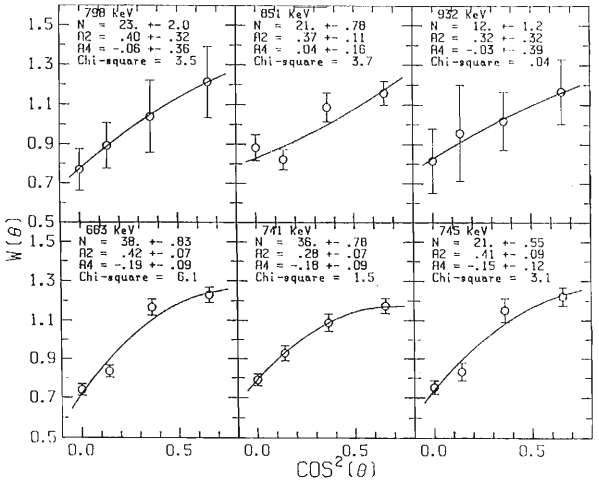

Fig. 3. Experimental angular distributions of γ-rays measured in the ^{100}Mo(^{16}O, 4n)^{112}Sn reaction at $E(^{16}O) = 72$ MeV. The solid curves are fits of the experimental data to the angular-distribution function $W(\theta)$.

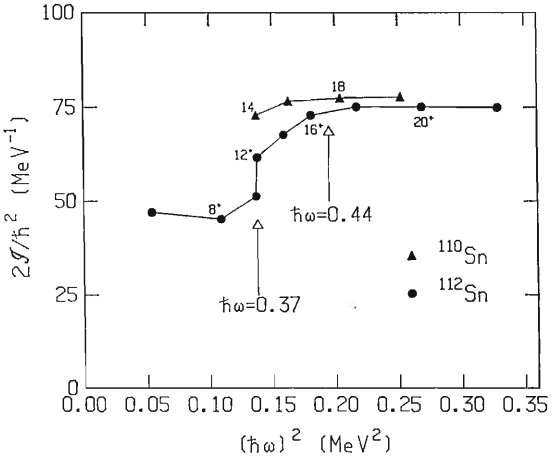

Fig. 4. Moment of inertia *vs.* squared frequency.

known as $8^+ \rightarrow 6^+$ and $10^+ \rightarrow 8^+$ transitions in Ref. 4. Therefore, the band built on the 5,564 keV state is proposed to have positive parity. The lifetime limit obtained for the 5,564, 6,362, 7,213, and 8,145 keV states from Doppler shift and the recoil distance measurement[5] also supports the positive parity assignment. For the other band in ^{112}Sn, displayed on the left side of Fig. 2, the angular distributions of the 1,471, 876 and 962 keV γ-rays also show the characteristics of the stretched E2-type transition, while that of the 808 keV γ-ray could not be measured because of the existence of an unresolved 805 keV ($7^- \rightarrow 6^+$) γ-ray. The lifetime limit for the 1,471 keV transition obtained from the recoil distance measurement also supports a negative parity assignment to the band. For the band in ^{110}Sn, the angular distributions of the 809, 741, and 904 keV γ-rays are also consistent with the stretched E2-type transitions. The positive parity assignment is suggested from the similarity of the level sequence as in ^{112}Sn.

The intra-band transitions of the deformed bands shown in Figs. 1 and 2 are the most intensive ones in high excitation energy $E_x \gtrsim 5$ MeV. Therefore, it is concluded that the deformed bands form the yrast lines at high spin region $J \gtrsim 14\,\hbar$ in both nuclei.

The moment of inertia *vs.* squared frequency plot for the positive parity bands in ^{110}Sn and ^{112}Sn is shown in Fig. 4. Upbend in ^{112}Sn occurring at $\hbar\omega \sim 0.37$ MeV corresponds to the band crossing from the previously known band[4] to the newly established band. It should be noticed that the values of the moment of inertia are almost constant in higher frequency region for both nuclei.

References

1) H. Harada, T. Murakami, H. Tachibanaki, K. Yoshida, J. Kasagi, T. Kubo, and T. Inamura: *RIKEN Accel. Prog. Rep.*, **19**, 18 (1985).
2) M. Fukuda, Y. Gono, Y. Ishikawa, M. Sugawara, T. Inamura, M. Ishihara, T. Nomura, I. Kohno, H. Kamitsubo, J. Kasagi, and T. Murakami: *RIKEN Accel. Prog. Rep.*, **18**, 152 (1984).
3) T. Murakami, J. Kasagi, H. Harada, and T. Inamura: *Nucl. Instrum. Methods A*, **241**, 172 (1985).
4) J. Bron, W. H. A. Hesselink, A. van Poelgeest, J. J. A. Zalmstra, M. J. Uitzinger, H. Verheul, K. Heyde, M. Waroquier, H. Vincx, and P. van Isacker: *Nucl. Phys. A*, **318**, 335 (1979).
5) J. Kasagi, H. Harada, T. Murakami, K. Yoshida, H. Tachibanaki, and T. Inamura: *Phys. Lett. B*, **176**, 307 (1986).

RIKEN Accel. Prog. Rep. 20 (1986)

III-1-2. Continuum γ-Ray Spectra in the ^{98,100}Mo(^{16}O, 4n)^{110,112}Sn Reactions

K. Yoshida, J. Kasagi, T. Murakami, H. Harada,
T. Kubo, and T. Inamura

[NUCLEAR REACTIONS ^{98,100}(^{16}O, 4n)^{110,112}Sn, E = 76, 72 MeV; measured continuum γ-ray spectra and anisotropy.]

In order to study the nature of γ-ray decays above the yrast line, we have measured continuum γ-rays emitted from highly excited states in the ^{98,100}Mo+^{16}O fusion reactions. Special care has been made in the present work in a treatment of the Compton process in γ-ray detectors and in the selection of a reaction channel.

γ-rays emitted from highly excited states populated by heavy-ion fusion reactions cannot be resolved individually and form continuum spectra because of the high density of states. The Compton process in a γ-ray detector always smears out the actual distribution of continuum γ-rays. Because of their high peak-to-total ratio, NaI detectors have been commonly used in previous experiments on continuum γ-rays. However, a Compton-suppressed Ge detector has a particular advantage since it has high resolution as well as a high peak-to-total ratio. The high resolution ensures the quality in subtraction of the known yrast transitions, so that one can obtain reliable continuum spectra down to the low energy region where strong discrete lines exist.

It is important to select a proper reaction channel because continuum γ-rays emitted from various residual nuclei cannot be distinguished in spectrum. We have selected the residual nuclei ^{110,112}Sn for the present purpose. From our previous studies,[1,2] a rotation-like collective band appears above $E_x >$ 3 MeV together with the neutron quasi-particle states, and two other collective bands have been identified above $E_x > 6$ MeV in ^{112}Sn. In contrast, only one collective band is observed above $E_x >$ 6 MeV in ^{110}Sn.

Experiments were performed with 76 MeV (for ^{98}Mo+^{16}O) and 72 MeV (for ^{100}Mo+^{16}O) ^{16}O beams from the RIKEN 160 cm cyclotron. Two BGOACS Ge detectors[3] were employed for γ-ray detection: one was placed at about 100° with respect to the beam axis and the other at about 140°. A neutron multiplicity filter[4] was employed to select the reaction channel. Foils of enriched molybdenum 1.0 (^{98}Mo, 96.9%) and 2.0 (^{100}Mo, 94.5%) mg/cm^2 in thickness, backed with lead, were used as targets.

Observed spectra were corrected for the detector response to obtain actual γ-ray intensity spectra. The detector response functions were calculated by a Monte Carlo simulation program[3] modified to include the pair creation process and scattering from a lead collimator. The spectra were calculated at 19 incident γ-ray energies between 50 keV and 4,500 keV and were compared with the spectra from γ-ray sources such as ^{137}Cs, ^{133}Ba, ^{22}Na, ^{60}Co, ^{152}Eu, and ^{56}Co. The experimental spectra were well reproduced by the calculation although small correction was needed in the low energy region. On the basis of these results a set of detector response functions at intervals of 4 keV γ-ray energy was obtained by interpolation.

The Compton background was removed from the observed spectra by an iterative method using the following relation

$$T^{(m+1)} = T^{(m)} + M - RT^{(m)} \qquad (1)$$

where $T^{(m)}$ is the m-th estimate of the true spectrum, M is the observed spectrum, and R is the response function. After twenty iteration processes, the Compton background was almost completely removed and

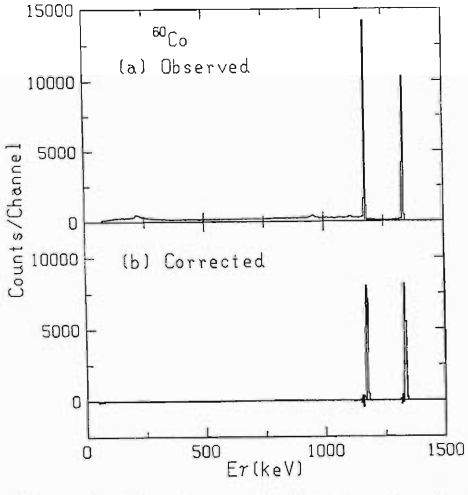

Fig. 1. Observed (a) and corrected (b) spectra for ^{60}Co.

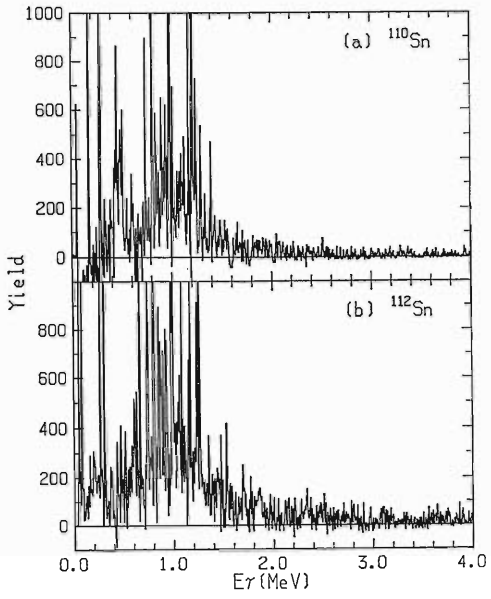

Fig. 2. Corrected spectra for ^{110}Sn (a) and ^{112}Sn (b) at 100°.

the peak-to-total ratio for the ^{60}Co spectrum was improved to 0.9, compared with the ratio of 0.4 before correction (Fig. 1).

In Fig. 2 are shown the unfolded spectra obtained for ^{110}Sn and ^{112}Sn before subtraction of discrete lines. The bumps around $E_\gamma \sim 1$ MeV are clearly seen in both ^{110}Sn and ^{112}Sn under the intensive discrete lines for the good resolution of Ge detectors. Further analysis is in progress to study the properties of these bumps.

References

1) A. van Poelgeest, J. Bron, W. H. A. Hesselink, K. Allart, J. J. A. Zalmstra, M. J. Vitzinger, and H. Verheul: *Nucl. Phys. A*, **346**, 70 (1980).
2) H. Harada, J. Kasagi, T. Murakami, K. Yoshida, T. Inamura, and T. Kubo: *RIKEN Accel. Prog. Rep.*, **19**, 19 (1985).
3) M. Fukuda, Y. Gono, Y. Ishikawa, M. Sugawara, T. Inamura, M. Ishihara, T. Nomura, I. Kohno, H. Kamitsubo, J. Kasagi, and T. Murakami: *RIKEN Accel. Prog. Rep.*, **18**, 152 (1984).
4) T. Murakami, J. Kasagi, H. Harada, and T. Inamura: *Nucl. Instrum. Methods A*, **241**, 172 (1985).

RIKEN Accel. Prog. Rep. 20 (1986)

III-1-3. Dipole Moment of ^{222}Ra as a System of Pb + ^{14}C Molecular Configuration

N. Yoshinaga and S. Yamaji

[NUCLEAR STRUCTURE two-center shell model, dipole moment, ^{222}Ra.]

Nuclei in the actinide region have characteristic features essentially different from those in the other regions: one is strong $E1$ enhancement and the other is ^{14}C decay. There are three models to explain these characteristics. The first one is the octupole deformation model,[1] which predicts that permanent octupole deformation is energetically favorable in this region. The second is the Vibron model proposed by Iachello.[2] His idea consists in that α-clustering effects are important for the actinide nuclei so that s and p bosons which simulate α-clustering effects must be added to the ordinary s and d bosons. These s and d bosons are the basic elements in the interacting boson model.[3] The third model is the octupole vibration model, which is rather traditional.

Up to now, there are no definite experimental data which selectively exclude one of these models. This is partly due to the fact that the octupole deformation model is microscopical and suitable to explain the intrinsic ground state, while the Vibron model is a macroscopic model and suitable to explain the excited states. Our original motivation is to compare these models and find out which is more suitable to describe the nuclei in this region. We analyzed ^{222}Ra using the two-center shell model, which sometimes simulates octupole deformation and sometimes molecular configuration such as Pb + ^{14}C.

In Fig. 1 the defined nuclear shape of ^{222}Ra is shown. By assuming axial symmetry, the shape is defined by

$$\rho(z)^2=(R_1^2-(z-z_1)^2) \quad \text{for } z\geqq z_m$$
$$(R_2^2-(z-z_2)^2) \quad \text{for } z\leqq z_m \tag{1}$$

where R_1 and R_2 are determined by

$$(R_1/R_2)^3=(A_1/A_2) \tag{2}$$

and volume conservation. The nuclear radius R is defined by $R=1.18\ A^{1/3}$ fm.

It is known experimentally that the electric intrinsic dipole moment in this region is at most 0.5 fm (Note we omit electric charge e). Therefore at first we try to see how large is the macroscopic dipole moment in our model. The dipole moment in the liquid drop model is calculated by Strutinsky's method[4]:

$$D_{\mathrm{LDM}}=\int_{\mathrm{Shape}} dv\, z\rho_z(z) \tag{3}$$

where $\rho_z(z)$ is the proton distribution in a nucleus. The macroscopic dipole moment as a function of a center separation Z_0 is shown in Fig. 2, which indicates that the experimental dipole moment is

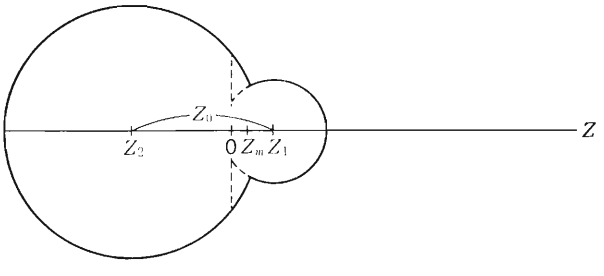

Fig. 1. Nuclear shape defined in Eq. (1) in text. Z_1 and Z_2 are the centers of Pb and C clusters; Z_0 is the center separation.

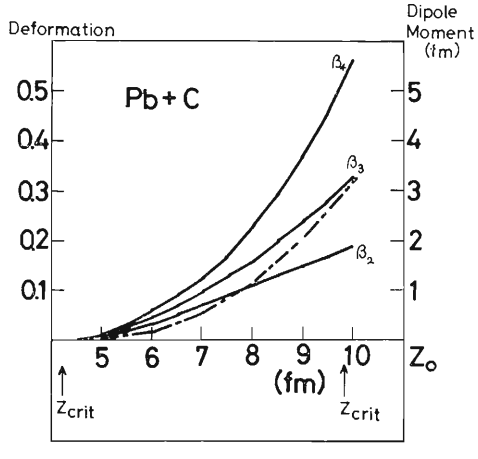

Fig. 2. Dipole moment and deformation parameters as a function of the center separation Z_0. At two Z_{crit} points, C cluster appears on the ^{222}Ra surface and Pb and C clusters separate from each other.

reproduced at the center separation $Z_0=7$ fm, provided that all contributions come from the liquid part. Figure 2 also shows the deformation parameters (β_2, β_3, β_4) as a function of the center separation.

In order to see how deep the configuration of separation $Z_0=7$ fm is in potential energy, we calculate the total energy by the micromacroscopic method. The macroscopic part is defined by Krappe *et al.*[5] as

$$E_{\mathrm{LDM}}=E_{\mathrm{surf}}+E_{\mathrm{coul}} \tag{4}$$

while the microscopic potential is defined by

$$V=V_{\mathrm{C}}+V_{\mathrm{LS}}+V_{\mathrm{coul}}+V_{\mathrm{pairing}} \tag{5}$$

where V_{C} is the folded Yukawa potential defined by[6]

$$V_{\mathrm{C}}(\vec{r})=-(V_0/4\pi a^3)\int\exp(-|\vec{r}-\vec{r}'|)/(|\vec{r}-\vec{r}'|/a) \tag{6}$$

For theoretical good reproduction of the Pb+^{14}C system a harmonic oscillator potential is inadequate. At a large center separation the nucleons must be filled in properly to reproduce the Pb+^{14}C configuration. A two-center harmonic oscillator potential does not satisfy this condition. This calculation shows that the total energy has a second minimum around $Z_0=7$ fm.

In conclusion, we obtained the total energy as a function of the center separation Z_0 and found that the local minimum exists around $Z_0=7$ fm. At that point of $Z_0=7$ fm, $D_{\mathrm{LDM}}=0.5$ fm and $\beta_2=0.07$, $\beta_3=0.10$, $\beta_4=0.13$, where β_2 and β_3 are nearly equal to $\beta_2=0.12$, $\beta_3=0.11$ obtained by Leander.[1] Using the folded Yukawa potential, we obtained the Pb+^{14}C configuration and a reasonable dipole moment: $D_{\mathrm{LDM}}=6.3$ fm and $D_{\mathrm{shell}}=6.8$ fm at $Z_0=14$ fm. This good agreement between macro- and micro-scopic calculations is due to the fact that the two microscopic levels centered $Z_0=14$ fm apart are filled in properly by ^{208}Pb and by ^{14}C, respectively.

References

1) G. A. Leander: Proc. Niels Bohr Centenial Conf. on 'Nuclear Structure 1985,' Copenhagen (eds. R. A. Broglia, G. B. Hagemann, and B. Herskind), p. 249 (1985).
2) F. Iachello: *Phys. Lett. B.*, **160**, 1 (1985).
3) A. Arima and F. Iachello: *Ann. Rev. Nucl. Part. Sci.*, **31**, 75 (1981).
4) V. Strutinsky: *J. Nucl. Energy*, **4**, 523 (1957).
5) H. J. Krappe, J. R. Nix, and A. Sierk: *Phys. Rev., C*, **20**, 992 (1979).
6) P. Möller and J. R. Nix: *Nucl. Phys. A*, **361**, 11 (1981).

III-1-4. Level Structure of ^{217}Ra

M. Sugawara, Y. Gono, T. Kohno, and M. Fukuda

{ NUCLEAR REACTIONS ^{208}Pb(^{13}C, 4n)^{217}Ra, $E=75$ MeV: measured E_γ, I_γ, γ-γ coin., $\gamma\gamma(\theta)$, oriented nuclei, ^{217}Ra deduced levels, J, π, B(E1)/B(E2). }

A level scheme for ^{217}Ra was previously reported by three groups.[1-3] Levels up to 4,186 keV (47/2) state have been studied by Roy, *et al.*[2] An in-beam γ-ray study of ^{217}Ra was performed using five sets of BGOACS (Anti-Compton Spectrometer) to extend the level scheme to higher spin states. Five detectors were placed at −135°, −45°, 30°, 90°, and 150° with respect to the beam axis. Excited states of ^{217}Ra were populated by the ^{208}Pb(^{13}C, 4n) reaction at $E=75$ MeV and γ-γ coincidence measurement was performed using this detector system. The γ-γ coincidence data also provided the information on the DCO (Directional Correlation from Oriented nuclei) of γ-transitions from which spin values were deduced.

A proposed level scheme is shown in Fig. 1. The

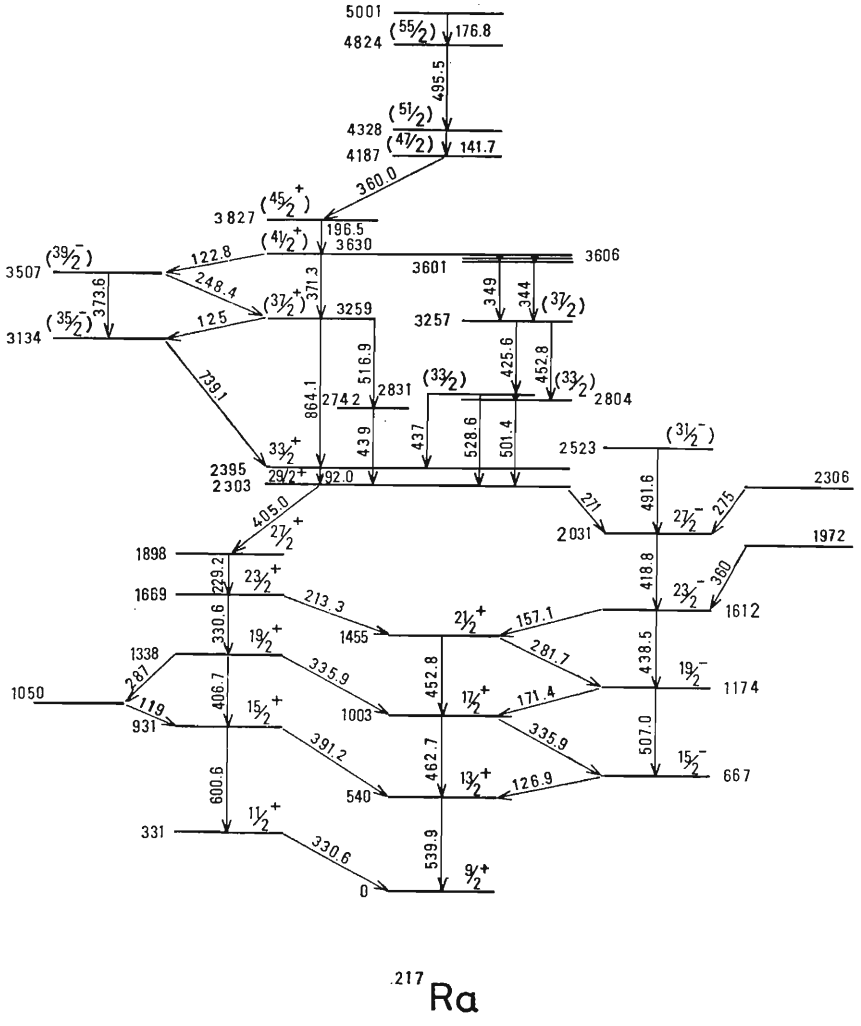

^{217}Ra

Fig. 1. A proposed level scheme of ^{217}Ra.

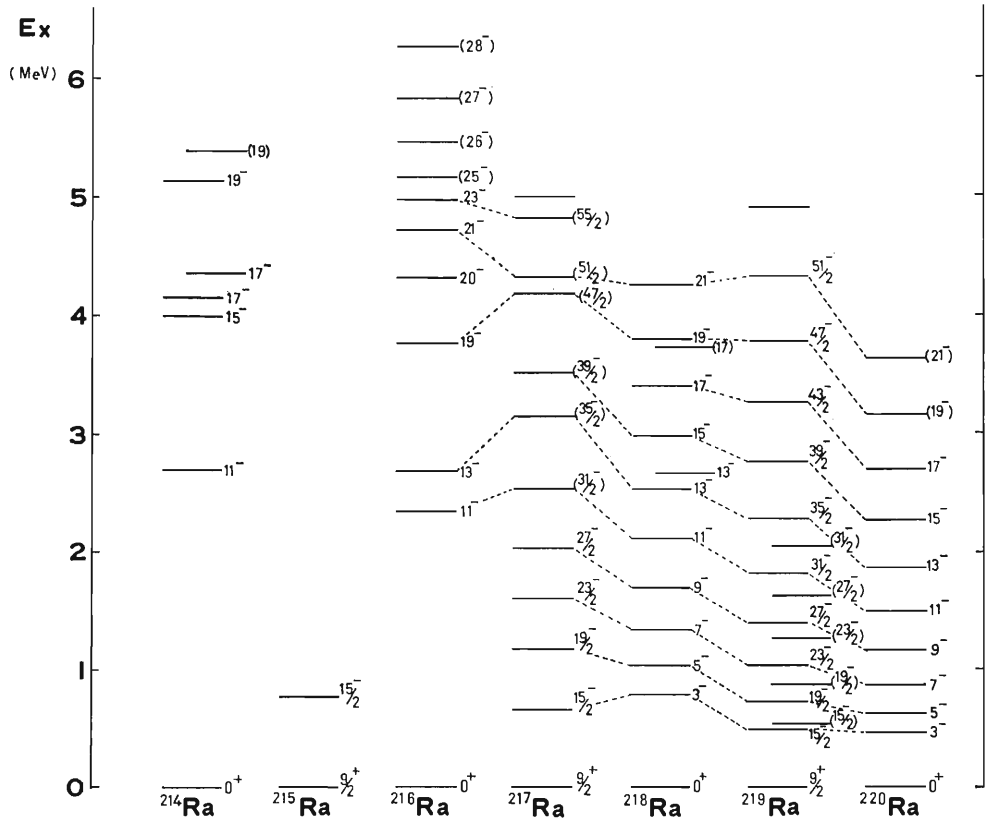

Fig. 2. Systematics of negative parity states in Ra isotopes.

level scheme could be extended to 5,001 keV state and several non-yrast states were newly found between 2,303 and 3,630 keV. The negative parity was inferred to be assigned to the states above 4,187 keV (47/2) on the basis of the systematics of negative parity states in Ra isotopes. Figure 2, which shows the systematics of negative parity states in Ra isotopes, indicates that the excitation energy is almost constant for spin states higher than 19^- for even isotopes, or $47/2^-$ for odd ones although the neutron number increases from ^{216}Ra to ^{219}Ra.

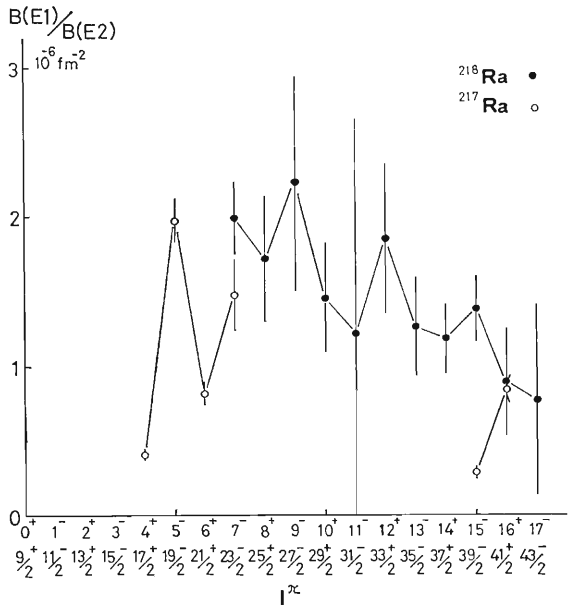

Fig. 3. B(E1)/B(E2) ratios in ^{217}Ra in comparison with those in ^{218}Ra.

B(E1)/B(E2) branching ratios were also deduced from the γ-γ coincidence data. Figure 3 shows the B(E1)/B(E2) values for several states in ^{217}Ra together with those in ^{218}Ra. The decreasing trend of the B(E1)/B(E2) ratios with increasing spin resembles the case in ^{218}Ra. This result is different from that reported by Roy, *et al.*,[2] in which staggering but almost constant B(E1)/B(E2) ratios are observed with increasing spin.

References

1) T. Lönnroth and C. Baktash: *Phys. Scr.*, **28**, 459 (1983).
2) N. Roy, D. J. Decman, H. Kluge, K. H. Maier, A. Maj, C. Mittag, J. Fernandez-Niello, H. Puchta, and F. Riess: *Nucl. Phys. A*, **426**, 379 (1984).
3) M. Sugawara, Y. Gono, and Y. Itoh: *J. Phys. Soc. Jpn.*, **53**, 2956 (1984).

RIKEN Accel. Prog. Rep. 20 (1986)

III-1-5. Spectroscopy of ^{220}Ac

M. Fukuda, Y. Gono, T. Kohno, M. Sugawara,
Y. Hatsukawa, and H. Taketani*

{NUCLEAR REACTIONS ^{208}Pb(^{15}N, 3n), $E=78$ MeV; ^{209}Bi(^{18}O, 3n), $E=88$ MeV; measured E_γ, I_γ, $\gamma(\theta)$, γ-γ coin, E_α, I_α. ^{220}Ac deduced levels, J, π, $T_{1/2}$.}

The excited states of ^{220}Ac were studied by means of in-beam γ-ray spectroscopy and α-spectroscopy with a He-jet system.

(1) γ-Spectroscopy

^{220}As was populated through the ^{208}Pb(^{15}N, 3n)-^{220}Ac reaction. An 18 mg/cm^2, 99% enriched ^{208}Pb target was bombarded with a ^{15}N beam from the RIKEN 160 cm cyclotron. Measurements were performed on the excitation functions, γ-ray anisotropies, γ-γ coincidence and lifetime. In γ-γ coincidence, five Ge-detectors with BGO anti-Compton shields were used. Coincidence data were accumulated for 41 h with an average beam current of 0.7 pnA at $E_B=78$ MeV. In the other measurements, singles spectra were taken mainly with 1 cm^3 LEPS. About 30 γ-rays were assigned to ^{220}Ac from the excitation function and the coincidence relation. A proposed level scheme of ^{220}Ac constructed from the coincidence data is shown in Fig. 1. Multi-

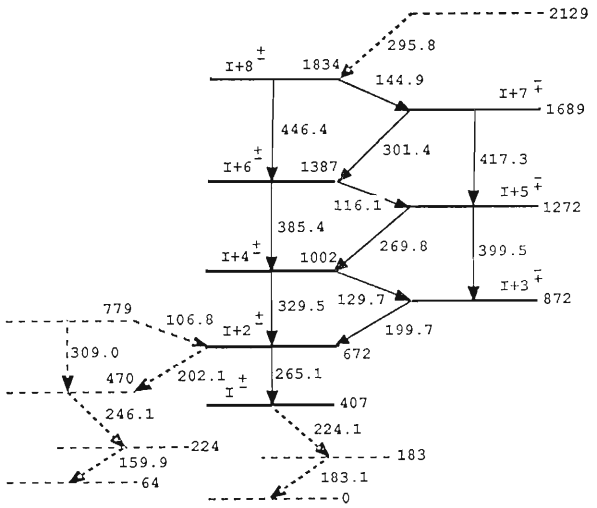

Fig. 1. Proposed level scheme of ^{220}Ac constructed from γ-ray data. Dotted lines indicate the uncertain levels.

* Department of Applied Physics, Tokyo Institute of Technology.

polarities of the transitions were deduced from γ-ray anisotropies on the assumption that the transitions are of stretched type. The types of the transitions (electric or magnetic) were determined from the intensity consideration. In the level scheme, alternating parity states connected by strong $E1$ transitions were found, similar to the other nuclei in this region. The average value of $B(E1)/B(E2)$ deduced from the branching ratio between $E1$ and $E2$ transitions is 2×10^{-6} fm^{-2}. From this, the $B(E1)$ value of $\sim10^{-2}$ w.u. was obtained for ^{220}Ac, assuming $B(E2)\sim100$ w.u. which is similar to the value in ^{218}Ra (Ref. 1). This $B(E1)$ value is similar to those in the neighbouring even-even or odd-A nuclei ($^{218-220}$Ra, $^{220-224}$Th, ^{219}Ac) (Ref. 2), but is $10^3\sim10^4$ times larger than the typical value of transitions between the single particle states in this mass region.

(2) α-Spectroscopy

We also studied the excited states of ^{220}Ac by observing the α-decay of ^{224}Pa to them. ^{224}Pa was produced by the ^{209}Bi(^{18}O, 3n)^{224}Pa reaction. Three ^{209}Bi targets of 0.5 mg/cm^2 deposited on 50 μg/cm^2 carbon foils were bombarded with an ^{18}O beam at $E_B=88$ MeV provided by the cyclotron; a typical beam current was 20 pnA. Fusion products recoiled out from the targets were transported by He-gas mixed with oil and NaCl through thin capillary to a counting room and collected on a tape. During the collection, radiated α-particles were detected with a Si-surface barrier detector of annular type faced to the tape. The tape was moved every two seconds to reflesh, because the half-life of ^{224}Pa is 1 s. Energy information of the detected α-particle was recorded on a magnetic tape with its time information by 100 Hz clock. In this experiment, 8×10^3 counts of 7.49 MeV α-group of ^{224}Pa were collected during 43-hour run. The 7.49 MeV peak is the only peak of ^{224}Pa that was previously observed (Ref. 3). In order to find α-groups of ^{224}Pa which feed to excited states of ^{220}Ac, we used the following genetic relation.

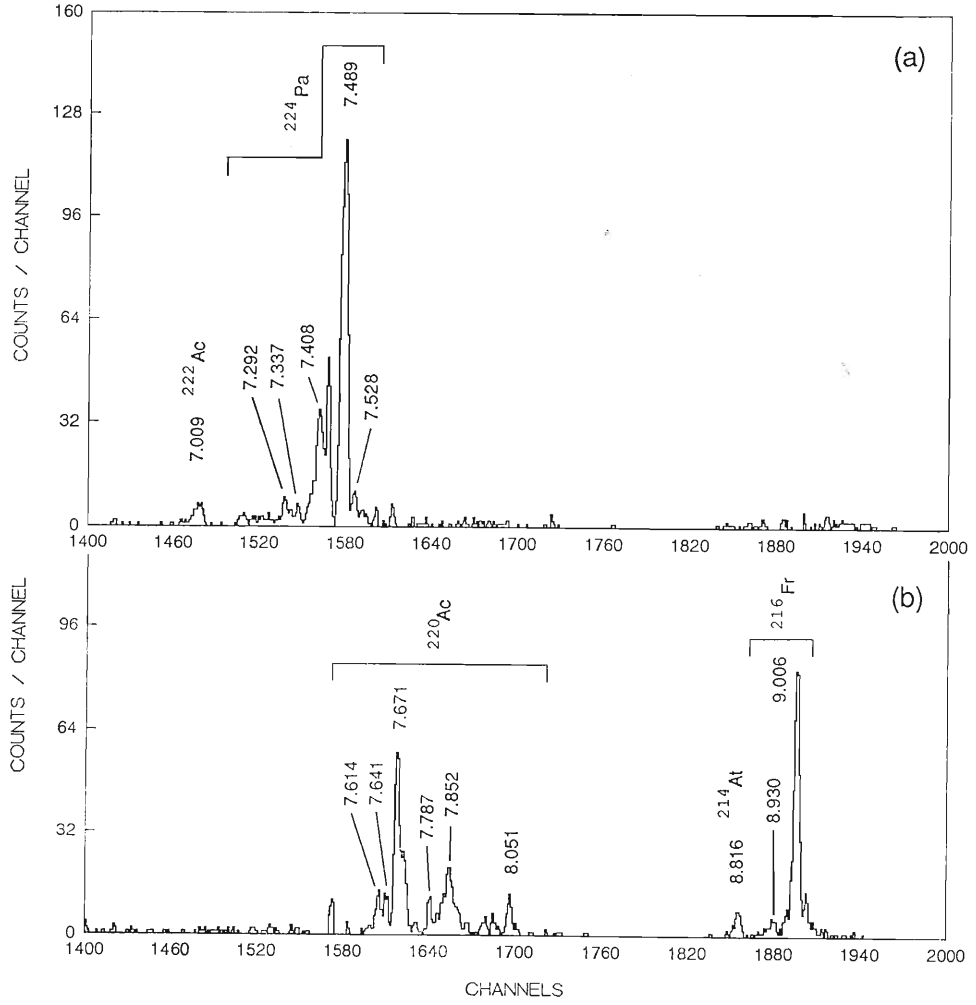

Fig. 2. Time correlation of α-particles. Two succeeding α-particles whose time interval is less than 100 ms were sorted. (a) Preceding α-particles, (b) following α-particles.

$$^{224}\mathrm{Pa} \xrightarrow[\alpha]{0.95\ \mathrm{s}} {}^{220}\mathrm{Ac} \xrightarrow[\alpha]{26\ \mathrm{ms}} {}^{216}\mathrm{Fr} \xrightarrow[\alpha]{0.7\ \mu\mathrm{s}} {}^{212}\mathrm{At} \xrightarrow[\alpha]{0.31\ \mathrm{s}} {}^{208}\mathrm{Bi}$$

In an off-line analysis, time correlated α-particles were sorted under a restriction that a time interval between two succeeding α-particles was less than 100 ms. Energy spectra of preceding and following α-particles are shown in Fig. 2 (a) and (b). By means of this kind of time correlation of α-particles, we have newly found six α-groups of ^{224}Pa. α-Energies and branching ratios of these nuclides are shown in Fig. 3.

One possible interpretation for the fact that the level scheme of ^{220}Ac from α-decay data could not be conbined to that from in-beam γ-spectroscopy is the high-Ω neutron orbit of the ground state of ^{224}Pa, because γ-rays are considered to be emitted from states along yrast line while α-transitions in this case tend to feed to those away from yrast line. This high-Ω neutron orbit also explains well the α-energy systematics of $N=133$ isotones (Ref. 3). But it is incompatible with the octupole deformation model

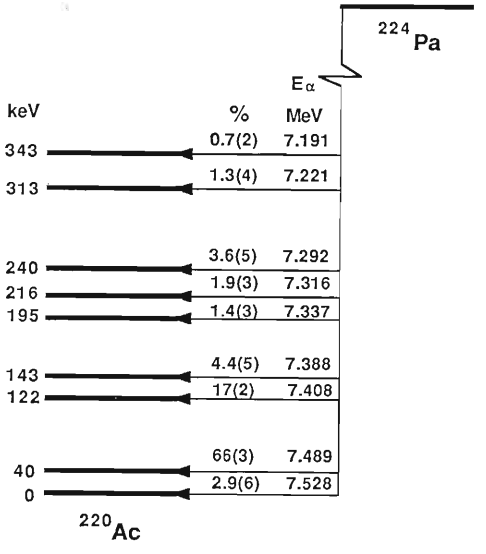

Fig. 3. α-Decay scheme of ^{224}Pa.

(Ref. 4) which was proposed to explain the features of actinide nuclei (strong $E1$ transitions, alternating parity states, parity doublets, *etc.*). Further study is necessary to make the relation of them clear.

References

1) A. Celler, Ch. Briancon, J. S. Dionisio, A. Lefebvre, Ch. Vieu, J. Zylic, R. Kulwssa, C. Mittag, J. Fernandez-Niello, Ch. Lauterbach, H. Puchta, and F. Riess: *Nucl. Phys. A*, **432**, 421 (1985).
2) Y. Gono, T. Kohno, M. Sugawara, Y. Ishikawa, and M. Fukuda: *Nucl. Phys. A*, **459**, 427 (1986) and references therein.
3) J. Borggreen, K. Valli, and E. K. Hyde: *Phys. Rev. C*, **2**, 1841 (1970).
4) G. A. Leander and R. K. Sheline: *Nucl. Phys. A*, **413**, 375 (1984) and references therein.

RIKEN Accel. Prog. Rep. 20 (1986)

III-1-6. In-Beam γ-Ray Study of ^{222}Th with BGOACS and 4π Crystal Ball

T. Kohno, Y. Gono, Ch. Briancon,* F. A. Beck,**
and Château de Cristal Collaboration

NUCLEAR REACTIONS ^{208}Pb(^{18}O, 4n), $E=95$ MeV, measured γ-γ coin., γ-multiplicity, γ-ototal energy, ^{222}Th deduced levels. 12 sets of Ge with BGOACS and BaF_2-ACS, BaF_2 crystal ball, enriched target.

Several nuclei in the Ra–Th region are expected to show a stable octupole deformation, and a characteristic feature of these nuclei is the existence of alternating parity states connected by enhanced E1 transitions. In this work the excited states of ^{222}Th were studied by means of in-beam spectroscopic techniques. Since the excited states up to $J^{\pi}=17^{-}$ are known in ^{222}Th,[1] we aimed to observe higher spin states and side bands.

An experiment was carried out using 12 sets of Ge detectors with RIKEN BGOACS[2] and BaF_2-ACS, 2 planar Ge detectors, and BaF_2 4π crystal ball (Château de Cristal)[3] set in the beam line of an MP tandem accelerator at CRN Strasbourg. γ-γ Coincidence was measured with the ^{208}Pb(^{18}O, 4n)^{222}Th reaction at 95 MeV. γ-Ray multiplicity

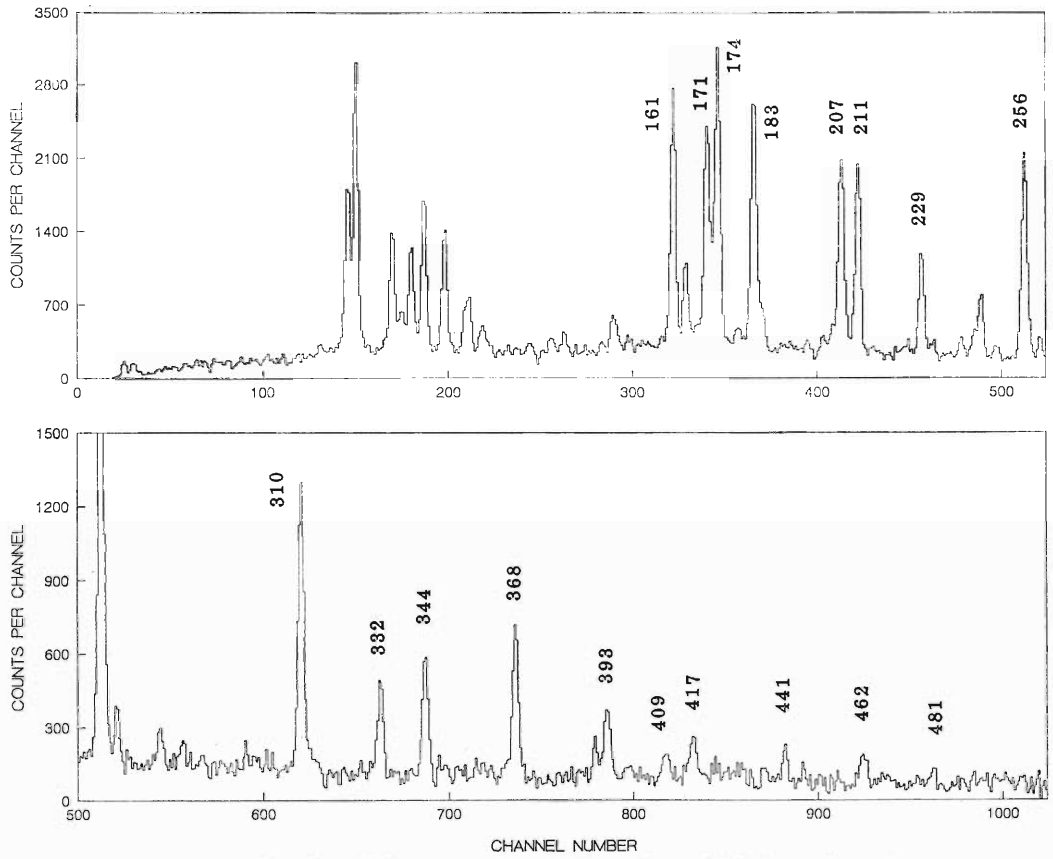

Fig. 1. An example of coincidence spectra gated on the multiplicity and total energy.

* CSNSM Orsay.
** CRN Strasbourg.

and total energy as well as γ-ray energy for coincidence events were recorded event by event on magnetic tapes for off-line analysis.

When the nuclei in this region are produced, fission events strongly compete with fusion events. An electrostatic separator was previously used[4] to discriminate evaporation residues from this strong fission background. In this work we were able to observe γ-rays from ^{222}Th in singles spectra clearly by using the ACS. Since it was shown that the S/N ratios of the γ-rays from ^{222}Th are best under the condition of low multiplicity and low total energy, the data of γ-γ coincidence measurement were analyzed by gating on the multiplicity between 2 and 8 and the lower part of the total energy spectrum. These conditions predict a disadvantage for the observation of high spin states.

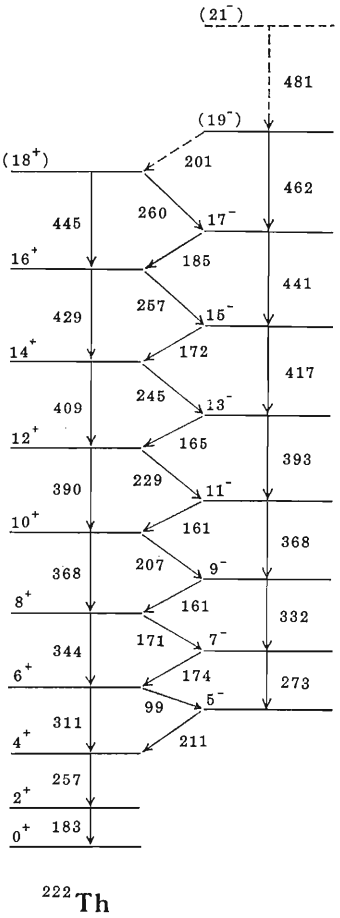

Fig. 2. A partial level scheme of ^{222}Th.

Figure 1 shows an example of gated spectra. Strong lines in the low energy region represent enhanced E1 transitions which connect positive- and negative-parity bands. The excited states up to $J^{\pi} = (21^-)$ have been assigned tentatively. Although several γ-rays were found in a side band, the relation between these lines and the ground state band has not been identified because of their low intensities. A partial level scheme is shown in Fig. 2. Analysis of data is now in progress.

References

1) D. Ward, G. D. Dracoulis, J. R. Leigh, R. J. Charity, D. J. Hinde, and J. O. Newton: *Nucl. Phys. A*, **406**, 591 (1983).
2) M. Fukuda, Y. Gono, Y. Ishikawa, M. Sugawara, T. Inamura, M. Ishihara, T. Nomura, I. Kohno, H. Kamitsubo, J. Kasagi, and T. Murakami: *RIKEN Accel. Prog. Rep.*, **18**, 152 (1984).
3) F. A. Beck: Proc. Int. Conf. on Instrumentation for Heavy Ion Nuclear Research, Oct. 22–25, p. 129 (1984).
4) W. Bonin, H. Backe, M. Dahlinger, S. Glienke, D. Habs, E. Hanelt, E. Kankeleit, and B. Schwartz: *Z. Phys. A*, **322**, 59 (1985).

RIKEN Accel. Prog. Rep. 20 (1986)

III-1-7. Spin Alignment in Projectile Fragmentation at Intermediate Energies

K. Asahi, M. Ishihara, T. Ichihara, Y. Gono, A. C. Mueller,* R. Anne, D. Bazin,* D. Guillemaud-Mueller,* R. Bimbot,** W. D. Schmidt-Ott,*** and J. Kasagi

[NUCLEAR REACTION $^{18}O + {}^{9}Be$, $E(^{18}O)/A = 65$ MeV/u; β-delayed γ-rays from ^{14}B, measured $W_\gamma(\theta)$; deduced spin alignment of ^{14}B products, $T_{1/2}(^{14}B)$.]

Recent extensive studies of the heavy ion reactions at intermediate energies[1,2] have revealed that the projectile fragmentation is the dominant process already at these energies. Isotope production using the projectile fragmentation process can be a very powerful tool to study nuclei far from the stability line, as demonstrated in the recent successive discoveries of new isotopes.[3,4] This is not only because of the high production rates available for the wide ranges of unstable nuclei but also due to the strong kinematical focusing of the product nuclei with respect to both the emission angle and the velocity, which facilitates the isotope separation by means of magnetic analysis during flight. The usefulness would be further augmented if these product nuclei are spin-oriented, since then the more detailed spectroscopic investigations such as the observation of angular distribution of radiations from oriented nuclei becomes possible. Measurement of the spin alignment in projectile fragmentations is also interesting from the view point of reaction mechanisms, since it provides a unique testing ground for models describing the reactions. We thus started an experiment to measure the alignment of the projectile fragments using intermediate-energy heavy-ion beams at GANIL.

Spin alignment in ^{14}B produced in $^{18}O + {}^{9}Be$ reaction at $E(^{18}O)/A = 65$ MeV/u is investigated. Nucleus ^{14}B is chosen because i) the short lifetime of ^{14}B allows us to get rid of the spin relaxation effect during the period until the β-ray emission, ii) the angular distribution of β-delayed γ-rays from a spin-aligned state has a large anisotropy, and iii) the high energy of the γ-ray eases background contaminations in the detection. Spectrometer LISE[5] is used for the isotope separation of the reaction products. LISE is the spectrometer consisting of two dipole magnets, with the first one providing a dispersion according to the magnetic rigidity at an intermediate focal plane (F1) whereas the second restoring the achromatism at the final focus point (F2). A wedge-shaped energy degrader is inserted at F1 to afford an additional analysis of particles according to the differences in stopping power for different Z numbers.[6] Use of the degrader indeed purified remarkably the isotope distribution observed at F2 by means of time-of-flight and ΔE measurements using a silicon detector.

We report below the preliminary results obtained up to now. ^{14}B products were stopped in a stopper foil (Pt) placed at F2. The beam was pulsed so that the γ-rays were detected during the beam-off periods. Static magnetic field $B_0 = 310$ mT parallel to the fields of the dipole magnets in LISE was applied to the stopper in order to preserve[7] the spin alignment for duration longer than the nuclear lifetime. In addition a small solenoid was installed to produce a field of about 0.5 mT in the direction parallel to the axis of the ^{14}B beam incident on the stopper. This field destroys the spin alignment when B_0 is off, and assures at that condition the equality of the γ intensities at the two detection angles mentioned below. The 6.09 MeV γ-rays emitted after the β decays of ^{14}B were detected using two NaI(Tl) scintillation counters (15 cm in diameter, 15 cm in length) placed at 0° and 90° to the direction of B_0. Angular distribution of the 6.09 MeV γ-rays in the presence of the external field B_0 perpendicular to the initial alignment axis is given by

$$W_\gamma(\theta) = 1 - (1/4)AP_2(\cos\theta)$$

where the initial alignment A is defined as $A = (2a_{+2} - a_{+1} - 2a_0 - a_{-1} + 2a_{-2})/2$ in terms of

* Grand Accelerateur National d'Ions Lourds (GANIL), Caen, France.
** Institut de Physique Nucleaire, Orsay, France.
*** Physikalisches Institut, Universität Göttingen, Göttingen, Fed. Rep. of Germany.

the population probability a_m for the magnetic sublevel m. The $0°/90°$ ratio $R = N_\gamma(0°)/N_\gamma(90°)$ of the γ-ray yield was measured both with B_0 on (*i.e.*, with the spin alignment preserved) and off (with the alignment destroyed). A was deduced from the change of R between the two conditions by

$$A = (8/3)(1 - R_{ON}/R_{OFF})$$

where ON and OFF refer to the measurements with B_0 on and off, respectively.

In Fig. 1 the result for spin alignment is shown together with the measured momentum distribution of the ^{14}B particles. For the momentum window $\Delta p/p = \pm 2.3\%$ around the peak in the fragment momentum distribution, the spin alignment of ^{14}B, $A = +(3.8 \pm 2.3)\%$, was obtained. The positive sign of the present result seems to conform the prediction from a simple model of the projectile fragmentation,[8] though a more improved statistics is required to draw any definitive conclusion. The measurements for different momentum regions are also anticipated, since the simple fragmentation argument[8] leads to negative alignments in the momentum regions corresponding to the tails of the peak in the fragment momentum distribution.

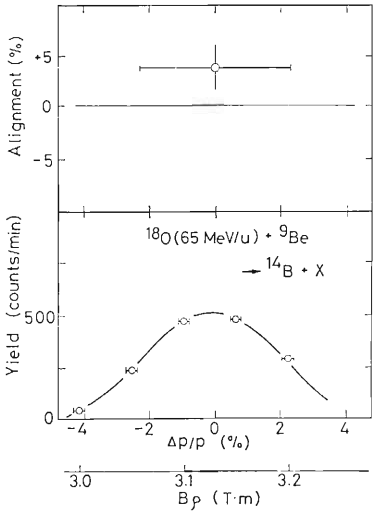

Fig. 1. Preliminary result for spin alignment of ^{14}B produced in the reaction ^{18}O (65 MeV/u) + ^{9}Be. Observed momentum distribution for ^{14}B is also shown.

The halflife of ^{14}B has been deduced from the least-squares fitting of a theoretical function to the time spectrum of the 6.09 MeV γ-rays obtained in the course of alignment measurement. The result is: $T_{1/2} = (13.7 \pm 0.6)$ ms. Two measurements are reported previously for the halflife of ^{14}B, but differ substantially from each other. The presently obtained value is considerably shorter than the value reported by Alburger *et al.*[9] and in agreement with the recent measurement by Curtin *et al.*[10] within the experimental error. Transition probability deduced from the present value is smaller than that obtained by the shell model calculation[10] by only 19%. This reduction in transition probability is much smaller compared to the commonly observed reduction of about 50% for the s-d shell nuclei.

References

1) V. Borrel, D. Guerreau, J. Galin, B. Gatty, D. Jacpuet, and X. Tarragao: *Z. Phys. A*, **314**, 191 (1983).
2) D. Guerreau: *Nucl. Phys. A*, **447**, 37c (1985).
3) M. Langevin, E. Quiniou, M. Bernas, J. Galin, J.C. Jacmart, F. Naulin, F. Pougheon, R. Anne, C. Detraz, D. Guerreau, D. Guillemaud-Mueller, and A.C. Mueller: *Phys. Lett. B*, **150**, 71 (1985).
4) D. Guillemaud-Mueller, A.C. Mueller, D. Guerreau, F. Pougheon, R. Anne, M. Bernas, J. Galin, J.C. Jacmart, M. Langevin, F. Naulin, E. Quiniou, and C. Detraz: *Z. Phys. A*, **322**, 515 (1985).
5) M. Langevin and R. Anne: Instrumentation for Heavy Ion Nuclear Research (ed. D. Shapira), Vol. 7, Harwood Academic Publishers, London, p. 191 (1985).
6) R. Bimbot, S. Della-Negra, M. Manasijevic, P. Aguer, G. Bastin, R. Anne, H. Delagrange, Y. Schutz, F. Hubert, Y. Gono, and K. Hatanaka: *J. Phys (Paris)*, **47** (Suppl. C4-8), 241 (1986).
7) K. Sugimoto, K. Nakai, K. Matuda, and T. Minamisono: *Phys. Lett. B*, **25**, 130 (1967).
8) K. Asahi and M. Ishihara: p. 21 in this report.
9) D.E. Alburger and D.R. Goosman: *Phys. Rev. C*, **10**, 912 (1974).
10) M.S. Curtin, L.H. Harwood, J.A. Nolen, B. Sherrill, Z.Q. Xie, and B.A. Brown: *Phys. Rev. Lett.*, **56**, 34 (1986).

RIKEN Accel. Prog. Rep. 20 (1986)

III-1-8. A Simple Model for Spin Alignment in Projectile Fragmentation

K. Asahi and M. Ishihara

[NUCLEAR REACTION projectile fragmentation model, Wigner distribution; spin alignment of fragments.]

The production of projectile-like fragments in heavy ion reactions at high energies has been discussed in terms of projectile fragmentation models.[1] These models well expain the widths of both the longitudinal and transverse momentum distributions for ejected fragments. Recent experimental studies[2] have shown that these models seem to hold also for the intermediate energy regions: Observed mass and charge distributions of the fragments conform well to these models, though some effects due to the final state interactions and the dissipative process manifest themselves in the momentum distribution. For better understanding, more comprehensive studies extending to other observables are awaited. In this report, we discuss what is to be expected for the spin alignment of ejectiles in the projectile fragmentation, on the basis of a simple fragmentation model.[3]

In the projectile fragmentation picture, the momentum distribution of an outgoing fragment reflects the momentum distribution of the cluster which is removed from the surface of the projectile nucleus. Although the uncertainty principle prohibits us from defining the probability of finding a particle with a definite momentum at a definite position, the quantal analogue to this quantity, represented by the Wigner transform W of the one-body density matrix $\hat{\rho}$, can be introduced:

$$W(\boldsymbol{R},\boldsymbol{k})=\int d^3\boldsymbol{x}/(2\pi)^3 \times\exp(-i\boldsymbol{k}\cdot\boldsymbol{x})<\boldsymbol{R}-\boldsymbol{x}/2|\hat{\rho}|\boldsymbol{R}+\boldsymbol{x}/2>$$

The following expression in terms of W for the momentum distribution of the fragmentation cross section at high energies is derived[3] from the Glauber theory of multiple scattering[4]:

$$d^3\sigma/dk^3=\int d^2\boldsymbol{s}D(\boldsymbol{s})\int dz\,W(\boldsymbol{s},z;\boldsymbol{k}_\perp,k_{//})$$

Here $\boldsymbol{R}=(\boldsymbol{s},z)$ and $\boldsymbol{k}=(\boldsymbol{k}_\perp,k_{//})$ denote respectively the position and momentum of a removed cluster, and z axis is taken parallel to the incident beam direction. The weighting function $D(s)$ contains the reaction dynamics and localizes the reaction to the nuclear surface.

As the simplest example we take ^{16}O for the projectile nucleus and consider the process where one nucleon is removed from the 0p orbit. We employ for simplicity the harmonic oscillator wave function ϕ_m with the oscillator parameter b to describe the orbit $(l,l_z)=(1,m)$, and neglect the intrinsic spin of the nucleon. Then the corresponding Wigner distribution is written in the form

$$W_m(\boldsymbol{R},\boldsymbol{k})=\int d^3\boldsymbol{x}/(2\pi)^3 \times\exp(-i\boldsymbol{k}\cdot\boldsymbol{x})\phi_m(\boldsymbol{R}-\boldsymbol{x}/2)\phi_m^*(\boldsymbol{R}+\boldsymbol{x}/2)$$

leading to the cross section

$$d\sigma_m/dk_{//}=\int d^2\boldsymbol{s}D(\boldsymbol{s})\int dz\int d^2\boldsymbol{k}_\perp W_m(\boldsymbol{s},z;\boldsymbol{k}_\perp,k_{//})$$

Setting $D(\boldsymbol{s})\propto\delta(s-s_0)$ and after a brief manipulation, we obtain the expressions for the longitudinal momentum distribution:

$$d\sigma/dk_{//}\equiv d\sigma_{+1}/dk_{//}+d\sigma_0/dk_{//}+d\sigma_{-1}/dk_{//} =N\cdot\exp(-b^2k_{//}^2)\cdot[1+(k_{//}/\Gamma)^2]$$

and for spin alignment:

$$A\equiv[d\sigma_{+1}/dk_{//}-2d\sigma_0/dk_{//}+d\sigma_{-1}/dk_{//}]/[2d\sigma/dk_{//}] =[(1/2)-(k_{//}/\Gamma)^2]/[1+(k_{//}/\Gamma)^2]$$

where $\Gamma=s_0/b^2$. The longitudinal momentum of the outgoing fragment is given by $p=p_0-k_{//}$, where p_0 denotes the fragment momentum corresponding to the projectile velocity.

The result is schematically displayed in Fig. 1, where $b=1.75$ fm and $s_0=3$ fm are taken. Alignment takes a positive maximum at the peak $p=p_0$, whereas it decreases as p increases or decreases from p_0, approaching a negative value in the tail regions The qualitative features observed in this result can be understood in a more intuitive way, as illustrated on the bottom of Fig. 1. The process leading to the outgoing momentum smaller than p_0 (see Fig. 1(a)) involves the removal of nucleon moving in the direction parallel to the projectile velocity $\boldsymbol{v}_0$ in the projectile nucleus. For peripheral collisions ($\boldsymbol{R}\perp$

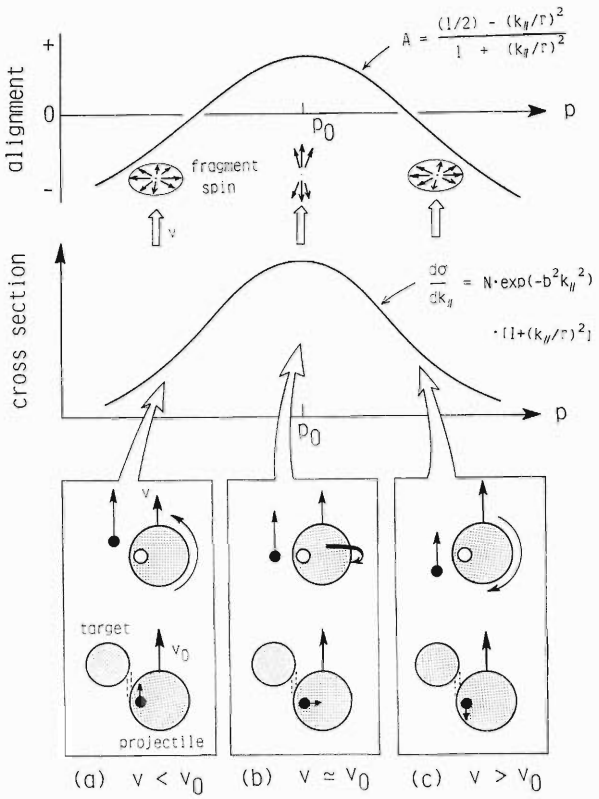

Fig. 1. Predicted behavior of fragment spin alignment based on a simple projectile fragmentation consideration. On the bottom, situations for the outgoing velocity (a) $v < v_0$, (b) $v \simeq v_0$, and (c) $v > v_0$ are intuitively illustrated, where v_0 denotes the velocity of the projectile.

$\boldsymbol{v}_0$, where $\boldsymbol{R}$ is the position of nucleon in the projectile-rest frame), this implies that nucleon with orbital angular momentum parallel to the vector $\boldsymbol{R} \times \boldsymbol{v}_0$ is removed, leaving the fragment spin in the direction perpendicular to $\boldsymbol{v}_0$ (negative alignment). A similar consideration for $p > p_0$ leads to the same result for the alignment. On the other hand for $p \simeq p_0$, motion of the removed nucleon in the projectile is perpendicular to $\boldsymbol{v}_0$, resulting in the positive spin alignment for the outgoing fragment.

The result would be modified to a certain extent if one takes into account the deexciting stage subsequent to the production of some intermediate excited nucleus in the abrasion process. The characteristic feature discussed here for spin alignment, however, is expected to persist. The present result shows that the observation of the spin alignment in the projectile fragmentation would afford an opportunity for testing models for reaction mechanisms. It also has an important implication that the projectile fragmentation might provide a promising tool to produce spin-aligned unstable nuclei which should no doubt be extremely useful for detailed spectroscopic studies of the nuclei far from stability.

References

1) A. S. Goldhaber: *Phys. Lett. B*, **53**, 306 (1974).
2) R. Dyras: *J. Phys. (Paris)*, **47** (Suppl. C4-8), 13 (1986).
3) J. Hüfner and M. C. Nemes: *Phys. Rev. C*, **23**, 2538 (1981).
4) P. J. Glauber: Lectures in Theoretical Physics (eds. W. E. Britten and L. G. Dunham), Vol. 1, Interscience, New York, p. 315 (1959).

RIKEN Accel. Prog. Rep. 20 (1986)

III-1-9. β Decay of Polarized Nucleus ^{15}C and Magnetic Moment of the $1/2^+$ Ground State

K. Asahi, M. Ishihara, T. Shimoda,* N. Ikeda,** T. Fukuda,***
N. Takahashi,* K. Katori,*** S. Shimoura,** A. Nakamura,** K. Hanakawa,***
T. Itahashi,**** Y. Nojiri,*** and T. Minamisono***

[NUCLEAR REACTION ^{232}Th(^{15}N, ^{15}C), $E=158$ Mev, β decay of ^{15}C; observed β-ray asymmetry, NMR; determined magnetic moment for the ground state.]

Measurement of magnetic moment provides useful information on nuclear structure and interaction. Moreover, the g factor for a nucleon residing in the $s_{1/2}$ orbital is of special interest since it amounts to a direct observation of the intrinsic moment of a nucleon embedded in the nucleus. Possible effects on the magnetic moment due to modification of nucleon properties in a nuclear medium have been discussed recently.[1,2] On the other hand it is only for a few nuclei that the $I=1/2$ magnetic moment is already known experimentally. This is because the $I=1/2$ states do not bear the rank-2 spin orientation (alignment) which facilitates observation of spin precession through the angular distribution of the de-excitation γ-rays. Under these circumstances the observation of asymmetry in β-ray angular distribution from polarized nucleus is the only sensitive means to determine the $I=1/2$ moment.

We have measured the magnetic moment for the ground state of a neutron-rich nucleus ^{15}C ($I^\pi=1/2^+$, $T_{1/2}=2.449$ s, $Q_\beta=9.772$ MeV). The nuclear magnetic resonance (NMR) has been observed by detecting the change in asymmetry in the angular distribution of β-rays from Gamow-Teller transition to the $1/2^+$ excited state of ^{15}N. ^{15}C decays also with a 36.8% branch to the $1/2^-$ ground state.[3] The measurement of β asymmetry for this $1/2^+ \rightarrow 1/2^-$ first-forbidden transition is by itself interesting since the role played by virtual pion in the weak axial current is predicted to enhance in this class of transition.[4] This interest affords an additional motivation to the present study of ^{15}C magnetic moment, since the spin control technique by means of NMR is indispensable for the precise measurement of β asymmetry.

* College of General Education, Osaka University.
** Faculty of Science, Kyoto University.
*** Faculty of Science, Osaka University.
**** Research Center for Nuclear Physics, Osaka University.

A 158 MeV ^{15}N beam from the AVF cyclotron at the Research Center for Nuclear Physics, Osaka University, was used to produce spin-polarized[5] ^{15}C nucleus by (^{15}N, ^{15}C) reaction. The setup used for the measurement has been reported previously.[6] A spectrometer DUMAS[7] provided a means for isotope separation of projectile-like fragments. The reaction products emitted from the target at $\theta_L=25°$ were transmitted to DUMAS, in which those with $B\rho=0.99$–1.07 Tm passed through the momentum slit in the medium focal plane and then were triple-focussed on a stopper foil placed at the second focal point. For a stopper substance we employed high-purity graphite, in which the spin-lattice relaxation time T_1 for ^{13}C has been reported[8] to be as long as 89 s at room temperature. Static magnetic field $B_0=74.5$ mT perpendicular to the reaction plane was applied on the stopper.

Beam was pulsed with a repetition period of 10 s and a beam-on period of 3 s. β-Rays emitted from the products implanted in the stopper were detected during the intervening beam-off period by using counter telescopes placed above and below the stopper. A radio-frequency (RF) field perpendicular to B_0 for NMR was applied for 20 ms duration preceding the β detection period, with the frequency swept in the specified range ν to $\nu+\Delta\nu$. Spins were thus inverted when the range of sweep was across the resonant frequency ν_0, by means of the adiabatic fast passage method of NMR. The spin inversion was detecteded as change in the measured up/down ratio of the β-ray yield.

The results of the resonance scans performed for several different values of $\Delta\nu$ are displayed in Fig. 1. From the spectrum obtained with the narrowest window ($\Delta\nu=0.075$ MHz), the g factor for the ^{15}C was found to be $|g|=2.63\pm0.14$. The overall uncertainty associated with this measurement is determined solely by the RF window width $\Delta\nu$ in which

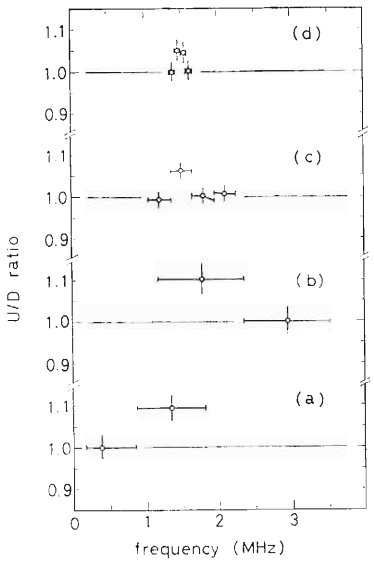

Fig. 1. Up/down ratio of β-ray yield, measured after application of the RF field with the frequency swept over the specified ranges (represented by horizontal bars). The width of the range for the frequency sweep was chosen to be (a) $\Delta\nu$=0.94 MHz; (b) $\Delta\nu$=1.17 MHz; (c) $\Delta\nu$= 0.43 MHz; and (d) $\Delta\nu$=0.075 MHz.

the resonance is located. Neither of instrumental uncertainties including that of the external field calibration procedure contribute significantly to the uncertainty in the final number.

The ^{15}C ground state wave function can be written[3,9] as $^{14}\mathrm{C}(0^+) \times \nu 1s_{1/2}$ with small admixtures of other configurations such as $^{14}\mathrm{C}(2^+) \times \nu 0d_{5/2}$ and $^{14}\mathrm{C}(2^+) \times \nu 0d_{3/2}$. In fact an experimental spectroscopic factor close to unity has been reported for $^{14}\mathrm{C}(\mathrm{d}, \mathrm{p})^{15}\mathrm{C}(1/2^+)$ reaction.[10] The observed g factor, however, deviates substantially from the Schmidt value $g_{\mathrm{Schmidt}} = g_{\mathrm{n}} = -3.83$ for the single $s_{1/2}$ neutron configuration, where g_{n} denotes the free neutron g factor. A simple estimate of correction for the first-order core polarization,[11] $\delta g^{\mathrm{1st}} = 0.23$, explains only a small part of the observed deviation $\delta g^{\mathrm{exp}} = +1.20 \pm 0.14$ from the Schmidt value (assuming a negative sign for the observed value). This is in contrast to the case for the $5/2^+$ excited state of ^{15}C, for which a $\nu d_{5/2}$ single particle model including the first-order correction well explains the observed g factor.[12] Clearly, a more elaborate theoretical treatment is needed to clarify the situation for the ^{15}C ground state.

References

1) G. Karl, G. A. Miller, and J. Rafelski: *Phys. Lett. B*, **143**, 326 (1984).
2) T. Yamazaki: *Phys. Lett. B*, **160**, 227 (1985).
3) E. K. Warburton, D. E. Alburger, and D. J. Millener: *Phys. Rev. C*, **29**, 2281 (1984).
4) K. Kubodera, J. Delorme, and M. Rho: *Phys. Rev. Lett.*, **40**, 755 (1978).
5) K. H. Tanaka, Y. Nojiri, T. Minamisono, K. Asahi, and N. Takahashi: *Phys. Rev. C*, **34**, 580 (1986).
6) K. Asahi, M. Ishihara, T. Shimoda, T. Fukuda, N. Takahashi, K. Katori, S. Shimoura, N. Ikeda, C. Konno, H. Hanakawa, A. Nakamura, T. Itahashi, Y. Nojiri, and T. Minamisono: *J. Phys. Soc. Jpn.*, **55**, Suppl., 1032 (1986).
7) T. Noro, T. Takayama, H. Ikegami, M. Nakamura, H. Sakaguchi, H. Sakamoto, H. Ogawa, M. Yosoi, T. Ichihara, N. Isshiki, M. Ieiri, Y. Takeuchi, H. Togawa, T. Tsutsumi, and S. Kobayashi: *J. Phys. Soc. Jpn.*, **55**, Suppl., 470 (1986).
8) G. P. Carver: *Phys. Rev. B*, **2**, 2284 (1970).
9) D. E. Alburger and D. J. Millener: *Phys. Rev. C*, **20**, 1891 (1979).
10) F. E. Cecil, J. R. Shepard, R. E. Anderson, R. J. Peterson, and P. Kaczkowski: *Nucl. Phys. A*, **255**, 243 (1975).
11) H. Morinaga and T. Yamazaki: Beam Gamma-Ray Spectroscopy, North-Holland Publ. Co., Chap. 3, Amsterdam (1976); H. Noya, A. Arima, and H. Horie: *Prog. Theor. Phys.*, **8**, Suppl., 33 (1958).
12) J. Asher, D. W. Bennett, B. A. Brown, H. A. Doubt, and M. A. Grace: *J. Phys. G*, **6**, 251 (1980).

RIKEN Accel. Prog. Rep. 20 (1986)

III-1-10. Measurement of Interaction Cross Sections Using He, Li, Be, B, and C Isotope Beams and Radii of Light p-Shell Nuclei

I. Tanihata, H. Hamagaki,* O. Hashimoto,* Y. Shida,* O. Yamakawa,*
T. Kobayashi,** K. Sugimoto,*** and N. Takahashi***

(Heavy-ion collisions, Radioactive beam, High-energy collisions, Interaction cross section, Nuclear radii, Isobaric dependence, p-shell nuclei.)

It has been shown that nuclear radii can be determined from a measurement of interaction cross sections of high-energy heavy-ion collisions.[1,2] In particular, the use of unstable nuclear beams provides a unique tool for determining radii of unstable nuclei.

The secondary beams of ^{4,6,8}He, $^{6-9,11}$Li, $^{7,9-12,14}$Be, $^{8,13-15}$B, and ^{10,12}C were produced through the projectile fragmentation of 800 MeV/nucleon ^{11}B and ^{20}Ne accelerated by the Bevalac at the Lawrence Berkeley Laboratory. The energy of the secondary beams was 790 MeV/nucleon at the target. The interaction cross sections (σ_I) were measured using Be, C, and Al targets by a transmission experiment with a large acceptance spectrometer. The experimental procedures were the same as those reported in the previous papers.[1,2]

The root-mean-square (*rms*) radii of nucleon matter distribution† have been determined using Glauber-type calculations.[3] The obtained *rms* radii are shown in Fig. 1 as a function of the neutron number (N). It is seen that the radii of Li and Be isotopes show similar behavior with N. The radii of nucleus with $N=6$ and 8 ($p_{3/2}$ and $p_{1/2}$ closed, respectively), except ^{8}He and ^{11}Li, are close to the prediction from a Hartree-Fock calculation based on spherical nucleus.[3] A large increase in the *rms* radius is seen at $N=7$. It is considered that the increase in radius is due to deformation of ^{11}Be (or admixture of sd-shell components).[3] The nucleus ^{11}Li, with the neutron number of p-shell closure in the naive shell model, shows a radius considerably larger than neighboring nuclei. It suggests the existence of a large deformation and/or of a long tail in the matter distribution due to weakly bound nucleons. Further increase in the radius of ^{11}Li from that of ^{11}Be may therefore suggest that $N=8$ is not a neutron magic number for Li isotopes.

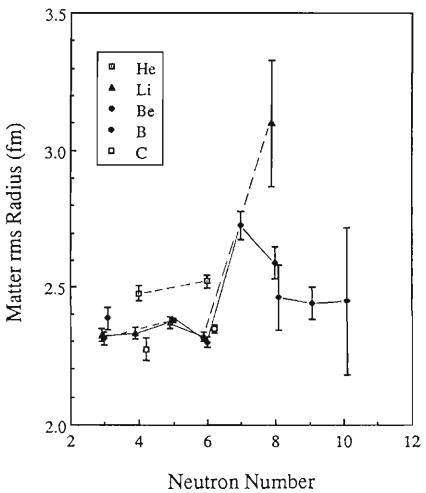

Fig. 1. Root-mean-square radii of nucleon distributions determined from the interaction cross section of 790 MeV/nucleon heavy-ion collisions. Radioactive nuclear beams were used for obtaining the radii of β-unstable nuclei. Lines in the figure are only guides for eyes.

Appreciable differences in radii are observed between pairs of isobars with different isospin, ^{6}He-^{6}Li, ^{8}He-^{8}Li, and ^{9}Li-^{9}Be. The larger radii of the neutron-rich isotopes ^{6}He and ^{8}He, which have only two protons, may suggest the existence of thick neutron skins. On the other hand, pairs of mirror nuclei (the same isospin isobars) ^{7}Li-^{7}Be, ^{8}Li-^{8}B, and ^{10}Be-^{10}C show equal radii. It indicates that the difference in the Coulomb interaction does not affect the nuclear radius in visible size for light p-shell nuclei.

References

1) I. Tanihata, H. Hamagaki, O. Hashimoto, S. Nagamiya, Y. Shida, N. Yoshikawa, O. Yamakawa, K. Sugimoto, T. Kobayashi, D. E. Greiner, N. Takahashi, and Y. Nojiri: *Phys. Lett. B*, **160**, 380 (1985).
2) I. Tanihata, H. Hamagaki, O. Hashimoto, Y. Shida, N. Yoshikawa, K. Sugimoto, O. Yamakawa, T. Kobayashi, and N. Takahashi: *Phys. Rev. Lett.*, **55**, 2676 (1985).
3) A. Brown: private communication.

* Institute for Nuclear Study, The University of Tokyo.
** National Laboratory for High Energy Physics.
*** Faculty of Science, Osaka University.

† Nuclear matter radii shown here correspond to the *rms* radii of point nucleon distribution.

RIKEN Accel. Prog. Rep. 20 (1986)

III-1-11. Fragmentation Cross Sections of ^{11}Li at 0.8 GeV/Nucleon

T. Kobayashi,* K. Omata,** K. Sugimoto,*** T. Shimoda,***
N. Takahashi,*** Y. Shida,* I. Tanihata, and O. Yamakawa*

[Heavy-ion collisions, Radioactive beam, High-energy collisions, Projectile fragmentation, Nucleon distribution, ^{11}Li.]

Recently, high-quality secondary nuclear beams were produced by the INS-LBL collaboration at the Lawrence Berkeley Laboratory, and were used for studying the matter radii of light nuclei by interaction cross section measurements.[1,2] This new technique allows us to study the various properties of β-unstable nuclei through, for example, the projectile fragmentation of exotic nuclei. We report the first measurement of projectile fragments produced by the breakup of extremely neutron-rich nuclei (^{11}Li and ^{6,8}He) at 0.79 GeV/nucleon incident energy.

The experiment was carried out at LBL Bevalac. The experimental-setup is approximately the same as that described in Ref. 1. Projectile fragments were detected inclusively by the magnetic spectrometer (HISS). Figure 1 shows production cross sections of Li and He isotopes from ^{11}Li + C reaction as a function of mass number of the fragment. One interesting speculation is that it may be possible to deduce the information on the neutron skin in these extremely neutron-rich nuclei by measuring the fragmentation cross sections into various isotopes. This kind of measurement is complementary to the interaction cross section measurement which is sensitive to the nuclear matter distribution.[2] A difference between He fragment and Li fragment in the mass dependence is what we would expect on the basis of a naive abrasion model[3] consistent with the existence of thick neutron skin: note that ^{11}Li has 3 protons and 8 neutrons. It is, however, necessary to take into account the ablation stage (slow evaporation stage) in the calculation to estimate proton and neutron radii from the experimental values.

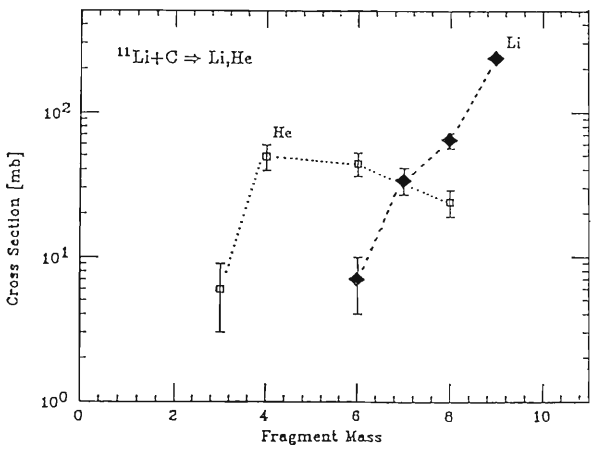

Fig. 1. Fragmentation cross sections of ^{11}Li on a carbon target.

Fragmentation cross sections of ^{11}Li into ^{9}Li and ^{6}He were also measured with a lead target. Ratios of cross sections ($\sigma(^{11}\text{Li} + \text{Pb} \rightarrow {}^{9}\text{Li})/\sigma(^{11}\text{Li} + \text{C} \rightarrow {}^{9}\text{Li}) = 9.1 \pm 1.9$ and $\sigma(^{11}\text{Li} + \text{Pb} \rightarrow {}^{6}\text{He})/\sigma(^{11}\text{Li} + \text{C} \rightarrow {}^{6}\text{He}) = 4.2 \pm 3.1$) indicates an importance of electromagnetic dissociation of ^{11}Li nucleus from a high Z target.[4]

An attempt was also made to search for ^{10}He isotope (one proton removal from ^{11}Li) from the projectile fragmentation of ^{11}Li beam on a carbon target. This seems to be a much better method to produce ^{10}He compared with a spallation method due to a kinematic focusing (100% detection efficiency) and a large one-proton removal cross section. At present, the upper limit of the production cross section is 50 μb.

* National Laboratory for High Energy Physics.
** Institute for Nuclear Study, The University of Tokyo.
*** Faculty of Science, Osaka University.

References

1) I. Tanihata, H. Hamagaki, O. Hashimoto, S. Nagamiya, Y. Shida, N. Yoshikawa, O. Yamakawa, K. Sugimoto, T. Kobayashi, D. E. Greiner, N. Takahashi, and Y. Nojiri: *Phys. Lett. B*, **160**, 380 (1985).
2) I. Tanihata, H. Hamagaki, O. Hashimoto, Y. Shida, N. Yoshikawa, K. Sugimoto, O. Yamakawa, T. Kobayashi, and N. Takahashi: *Phys. Rev. Lett.*, **55**, 2676 (1985).
3) J. Hüfner, K. Schäter, and B. Schürman: *Phys. Rev. C*, **12**, 1888 (1975).
4) D. L. Olson, B. L. Berman, D. E. Greiner, H. H. Heckman, P. J. Lindstrom, and H. J. Crawford: *Phys. Rev. C*, **28**, 1602 (1983).

RIKEN Accel. Prog. Rep. 20 (1986)

III-1-12. NMR on β-Emitting ^{39}Ca Produced through Projectile Fragmentation in High-Energy Heavy-Ion Reactions

K. Matsuta,[*1] T. Minamisono,[*1] Y. Nojiri,[*1] K. Sugimoto,[*1] K. Takeyama,[*1] K. Omata,[*2] Y. Shida,[*2] I. Tanihata, T. Kobayashi,[*3] S. Nagamiya,[*4] K. Ekuni,[*5] S. Shimoura,[*5] J. R. Alonso,[*6] G. F. Krebs,[*6] and T. J. M. Symons[*6]

{ Heavy-ion collisions, Radioactive beam, Isotope production, Projectile fragmentation, Nuclear magnetic moment, Mirror nuclei, ^{39}Ca. }

A new experimental method has been developed for the studies of magnetic moments of mirror nuclei in the $f_{7/2}$ region. As at least one partner of mirror pairs in this region is short-lived (0.1 to 1 s) β-emitter, the preparation of spin polarized separated isotope samples for NMR (nuclear magnetic resonance) studies presents a challenge. The method developed uses the Lawrence Berkeley Laboratory Bevalac to (1) produce short-lived nuclei by means of projectile fragmentation in high-energy heavy-ion reactions, (2) separate and purify the desired isotopes from other reaction products and from the primary beam by magnetic analysis and suitably-located energy degraders,[1] (3) produce nuclear spin polarization through ion interactions with tilted foils,[2] (4) implant the isotopes in a crystalline catcher, and (5) detect NMR by means of β-decay asymmetry of the polarized nuclei.[3]

The method has been developed using ^{39}Ca ($I^{\pi} = 3/2^{+}$, $T_{1/2} = 0.86$ s), for which the magnetic moment has been previously measured.[4]

A secondary beam of ^{39}Ca ion was produced by striking a 1.27 cm beryllium target with ^{40}Ca ions extracted from the Bevalac at 220 MeV/nucleon. To reduce the momentum spread inherent in the fragmentation process and due to the target thickness, a thin wedge momentum compensator was used at a momentum-dispersive focusing point in the beam transport separator line. As a result, the total energy spread at the final stopping point of the ^{39}Ca ions was reduced to 3 MeV/nucleon (HWHM). Such a low energy spread is essential for proper utilization of the tilted-foil technique. A stack of 10 foils, tilted at 60° relative to the beam axis and located in a field-free region just upstream of the catcher, was used to polarize the ions. Final implantation (stopping) of the ^{39}Ca ions occurred in a CaF_2 single crystal of 0.2 mm in thickness located in a 0.48 T magnetic field. Since the observed efficiency for producing, analyzing, and stopping of ^{39}Ca ions was 1 part in 10^5 of the primary ^{40}Ca beam, and the contamination of other short-lived ions in the stopping catcher was sufficiently low, the ^{39}Ca decay time spectrum was observed cleanly down to 1 part in 10^3 (Fig. 1).

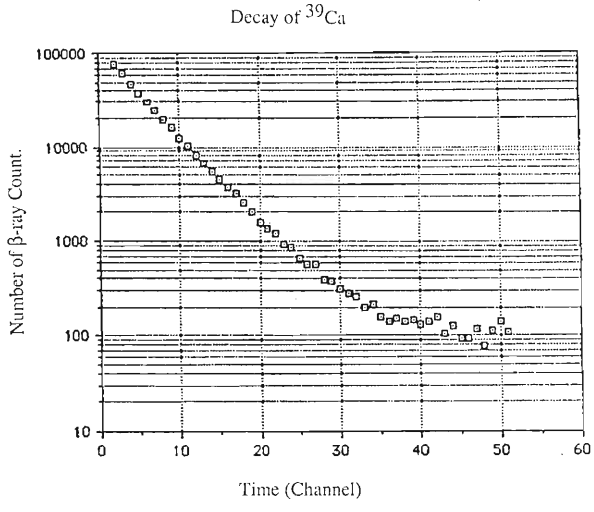

Fig. 1. The time spectrum of β-rays emitted from ^{39}Ca stopped in the CaF_2 stopper. ^{39}Ca were produced through the projectile fragmentation of ^{40}Ca and separated by a secondary beam line at the Bevalac; it shows an extremely small background.

RF was applied to induce depolarization of the stopped ^{39}Ca ions in the crystal. An asymmetry change in the β-ray distribution was successfully observed, $R = 2APf\eta = +(0.65 \pm 0.19)\%$, where the asymmetry parameter A is predicted to be $A = +0.8$, P is the polarization, and η, the correction for the

*1 Faculty of Science, Osaka University.
*2 Institute for Nuclear Study, The University of Tokyo.
*3 National Laboratory for High Energy Physics.
*4 Faculty of Science, The University of Tokyo.
*5 Department of Physics, Kyoto University.
*6 Lawrence Berkeley Laboratory, University of California.

large solid angle of the β-ray counters, is $\eta \geq 0.5$. A null calibration measurement gave $R = -(0.13 \pm 0.19)\%$.

The present work was supported in part by the Yamada Science Foundation and the Grant in Aid for Scientific Research from the Ministry of Education, Science and Culture of Japan. The study is partially supported also by the U.S. Department of Energy under contract No. DE-AC03-76SF0098, by the INS-LBL Collaboration, and by the Japan-U.S. Cooperative Research Program from the Japan Society for the Promotion of Science.

References

1) Y. Nojiri, K. Matsuta, T. Minamisono, K. Sugimoto, K. Takeyama, H. Hamagaki, S. Nagamiya, K. Omata, Y. Shida, I. Tanihata, T. Kobayashi, S. Matsuki, S. Shimoura, J. R. Alonso, G. Krebs, and T. J. M. Symons: Proc. VIIth Int. Conf. Hyp. Int., Bangalore, India, Sep. 8–12 (1986) to be published.
2) Y. Nojiri, K. Matsuta, T. Minamisono, K. Sugimoto, K. Takeyama, H. Hamagaki, S. Nagamiya, K. Omata, Y. Shida, I. Tanihata, S. Matsuki, S. Shimoura, J. R. Alonso, T. Kobayashi, G. Krebs, and T. J. M. Symons: *J. Phys. Soc. Jpn.*, **55**, Suppl., 391 (1986).
3) T. Minamisono: *J. Phys. Soc. Jpn.*, **34**, Suppl., 324 (1973); K. Sugimoto, A. Mizobuchi, K. Nakai, and K. Matuda: *Phys. Lett.*, **18**, 38 (1965).
4) T. Minamisono, J. W. Hugg, D. G. Mavis, T. K. Saylor, H. F. Glavish, and S. S. Hanna: *Phys. Lett. B*, **61**, 155 (1976).

RIKEN Accel. Prog. Rep. 20 (1986)

III-1-13. Two-Step Analysis for the $^{12}C(d, ^2He)^{12}B$ Reaction

T. Motobayashi, M. Ishihara, H. Sakai,* N. Matsuoka,* K. Hosono,* T. Saito,* A. Okihana,** S. Shimoura,*** and A. Sakaguchi****

[NUCLEAR REACTIONS $^{12}C(d, ^2He)^{12}B$, $E=70$ MeV; measured $\sigma(\theta)$, Ay(θ), DWBA and two-step analysis.]

Charge exchange reactions are suitable for studying isovector excitation modes of nuclei. To extract quantitative information about their strength, usually the DWBA (Distorted Wave Born Approximation) (or sometimes DWIA (Distorted Wave Impulse Approximation)) calculations are performed assuming a one-step reaction mechanism. Therefore, it is important to estimate the contributions of the two-step process especially at low incident energies. We report here the two-step analysis for the (d, ^{2}He) reaction on ^{12}C at $E_{in}=70$ MeV. Experimental procedures and one-step DWBA calculations have been reported elsewhere.[1]

In the present calculation, the processes *via* d-p-^{2}He and d-^{3}He-^{2}He channels were taken into account. The code TWOFNR[2] in its exact finite range option was used to calculate two-step amplitudes. Intermediate states involved in these two-step processes are $1/2^-$ ground state and $3/2^-$ excited state ($E_x=3.68$ MeV) of ^{13}C for the d-p-^{2}He process and $3/2^-$ ground state and $1/2^-$ excited state ($E_x=2.12$ MeV) for the d-^{3}He-^{2}He process. Spectroscopic amplitudes involved in the above processes were calculated by the INS shell model code[3] based on the Cohen-Kurath wave functions.[4] The optical potential parameters for incident and intermediate channels were taken from the studies of elastic scattering.[5,6] The potential of the outgoing channel was taken to be the same as that of the incident channel. Single particle wave functions were generated by the usual separation energy method. The non-orthogonality terms were wholly taken into account by the method described in Ref. 7.

The results are shown in Fig. 1 together with the experimental data. General features of the experimental angular distributions of the cross section and the vector analyzing power are reasonably described by the calculations. Although the theoretical cross section for the two-step process is smaller than that of the one-step process, inclusion of the two-step process clearly improves the fit to the data.

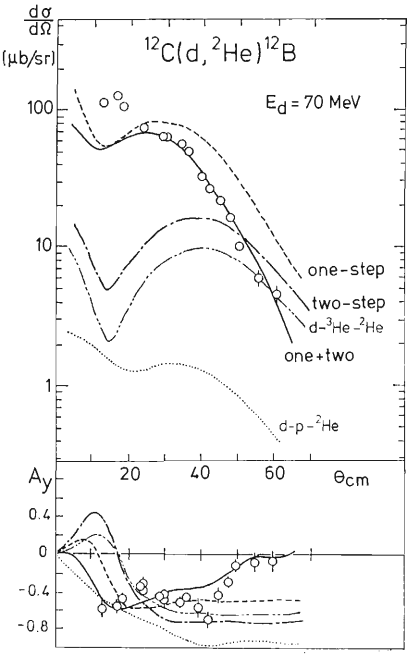

Fig. 1. Differential cross sections and vector analyzing powers of the reaction $^{12}C(d, ^2He)^{12}B$. Open circles indicate the experimental data. Dashed-dotted lines represent the theoretical two-step contributions which are coherent sums of the amplitudes of the d-^{3}He-^{2}He (double dashed-dotted lines) and d-p-^{2}He (dotted lines) processes. Broken lines represents the one-step DWBA calculation. Solid lines indicate the full calculation which is the coherent sum of one- and two-step amplitudes. Normalization of the one-step calculation is determined so that the full calculation may fit the experimental cross section.

* Research Center for Nuclear Physics, Osaka University.
** Kyoto University of Education.
*** Department of Physics, Kyoto University.
**** National Laboratory for High Energy Physics.

References

1) T. Motobayashi, M. Ishihara, N. Matsuoka, H. Sakai, T. Saito, K. Hosono, A. Sakaguchi, S. Shimoura, and A. Okihana: *RIKEN Accel. Prog. Rep.*, **19**, 7 (1986).
2) M. Igarashi: private communication.
3) K. Ogawa: private communication.
4) S. Cohen and D. Kurath: *Nucl. Phys. A*, **255**, 315 (1975).
5) K. Hatanaka, N. Matsuoka, T. Saito, K. Hosono, M. Kondo, S. Kato, T. Higo, S. Matsuki, Y. Kadota, and K. Ogino: *Nucl. Phys. A*, **419**, 530 (1984).
6) T. Tanabe, K. Koyama, M. Yasue, H. Yokomizo, K. Sato, J. Kokame, N. Koori, and S. Tanaka: *J. Phys. Soc. Jpn.*, **41**, 361 (1976).
7) M. Igarashi: *Phys. Lett. B*, **78**, 379 (1978).

RIKEN Accel. Prog. Rep. 20 (1986)

III-1-14. Mass-Number Dependence of the Hexadecapole (Y_{42}) Transition Strength to the γ-Vibrational Band in Inelastic Proton Scattering at 65 MeV

T. Ichihara, H. Sakaguchi,* M. Nakamura,* M. Yosoi,* M. Ieiri,*
Y. Takeuchi,* H. Togawa,* T. Tsutsumi,* and S. Kobayashi*

NUCLEAR REACTIONS ^{152,154}Sm, ^{160}Gd, ^{164}Dy, ^{166,168}Er, ^{176}Yb, ^{182,184}W, ^{192}Os (p, p') $E_p = 65$ MeV; measured differential cross sections and analyzing powers; coupled-channel calculation, deduced transition strength, RPA model calculation.

For the study of nuclear collective motion, it is interesting to investigate the γ-vibrational band in the $152 \leqq A \leqq 192$ region,[1-4] where the nuclei are well-deformed and the non-collective components are suppressed up to the gap energy (2Δ) owing to the superconductivity of the ground state. In particular, the hexadecapole degree of freedom in the collective motion is of renewed interest. The possible existence

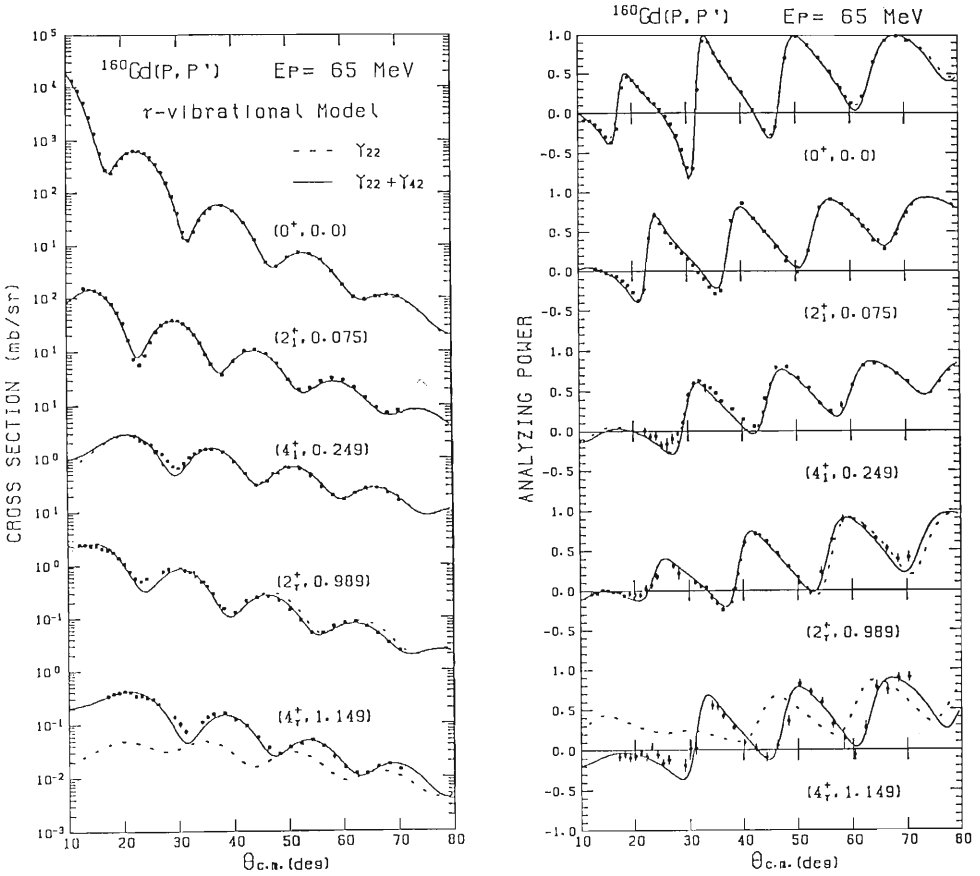

Fig. 1. Measured cross sections and analyzing powers for the ^{160}Gd (p, p') scattering at 65 MeV. The solid (dotted) curves show the best-fit result of the coupled-channel calculation assuming the Y_{22} and Y_{42} (only Y_{22}) γ-vibration.

* Department of Physics, Kyoto University.

of the hexadecapole (Y_{42}) component in the γ-vibration was reported in early works on inelastic scattering.[4-6] Experimentally, recent progress in high quality beams and high resolution spectrographs has made it possible to measure the low-lying inelastic scattering for deformed nuclei in the $152 \leqq A \leqq 192$ region. In this respect, we have recently studied the excitation to γ-vibrational states in ^{168}Er(p, p′) at 65 MeV and performed a precise measurement and analysis on the cross sections and analyzing powers.[1] The results have clearly shown the importance of the hexadecapole (Y_{42}) component. However, the systematic behavior of the Y_{42} strength with mass number, which will be the key to understanding the γ-vibration, is still an open problem.

Here we have extended the investigation over the whole range of deformed nuclei; inelastic scattering of polarized protons at 65 MeV exciting the γ-vibrational states has been studied for ^{152,154}Sm, ^{160}Gd, ^{164}Dy, ^{166,168}Er, ^{176}Yb, ^{182,184}W, and ^{192}Os. The characteristic behavior of the hexadecapole (Y_{42}) strength with mass number has been revealed; the behavior fits a simple theoretical picture relating the strength with shell filling of valence nucleons.[7]

The experiment has been performed with polarized protons from the cyclotron at the Research Center for Nuclear Physics (RCNP), Osaka University, and the data have been obtained using a high resolution spectrograph RAIDEN.[8] The overall energy resolution was 20–26 keV (FWHM). Details of the experimental method are described elsewhere.[9-11]

Coupled-channel analysis assuming the γ-vibrational model has been performed with a modified version of the code ECIS79,[12] which includes the form factors of surface vibration in deformed nuclei. The potential surface is assumed to be

$$R(\Omega') = R_0[1 + \sum_{\lambda=2,4,6} \beta_{\lambda 0} Y_{\lambda 0}(\Omega') + \alpha_{22}\{Y_{22}(\Omega') + Y_{2-2}(\Omega')\} + \alpha_{42}\{Y_{42}(\Omega') + Y_{4-2}(\Omega')\}] \quad (1)$$

where α_{22} and α_{42} are the collective coordinates corresponding to the quadrupole (Y_{22}) and hexadecapole (Y_{42}) γ-vibration. The spin-orbit deformation (full Thomas term) and Coulomb excitation were included in the calculation. The deformation parameters for each part of the optical potential were set to be identical for simplicity.

Without the hexadecapole (Y_{42}) term, the 4+ state of the γ-vibrational band cannot be reproduced for all the nuclei measured. Excellent fits have been obtained for all the states by introducing the hexadecapole (Y_{42}) γ-vibration. The solid (dashed) curves in Fig. 1 show examples of the coupled-channel calculation for ^{160}Gd assuming the Y_{22} and Y_{42} (only Y_{22}) γ-vibration. The coupled-channel

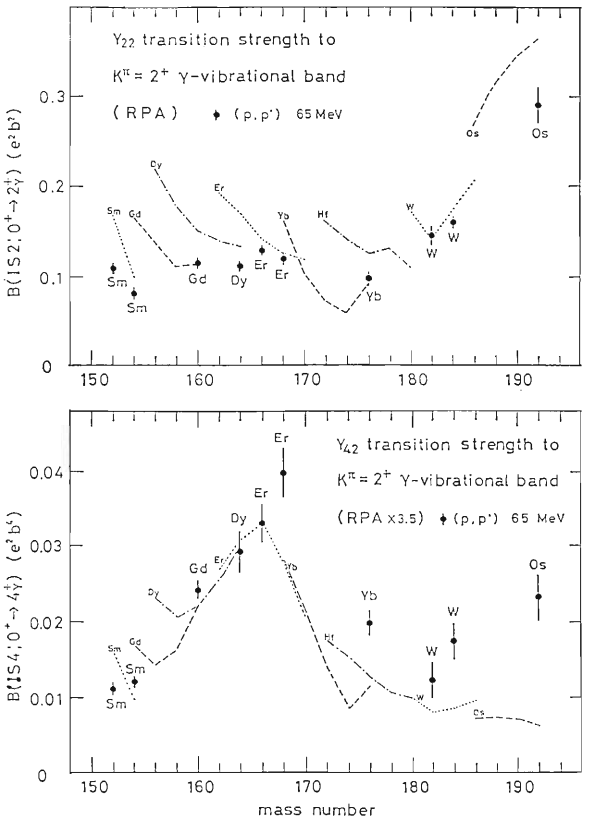

Fig. 2. The Y_{22} and Y_{42} transition strength to the γ-band obtained from the present experiments (closed circles) and from the RPA calculations (various lines).

analysis assuming an asymmetric rotor model gives similar results.[1]

The quadrupole (Y_{22}) and hexadecapole (Y_{42}) transition strengths were calculated from the best-fit optical potential parameters and they are plotted as closed circles in Fig. 2. We also show RPA calculations[13] assuming the paring plus Q–Q force in the doubly stretched coordinates in Fig. 2, where the results of the Y_{42} strength of the RPA calculations were multiplied by 3.5.

The RPA calculation reproduces the Y_{22} transition strength quantitatively well. In the region of ^{166}Er, the proton sub-shell $(N, n_z) = (4, 1)$ and the neutron sub-shell $(N, n_z) = (5, 3)$ which satisfy the selection rule of the γ-phonon excitation are half-filled and it is expected that the collectivity of the γ-vibration becomes large. This effect is known as the sub-shell structure effect.[14] The experimental Y_{22} strength has a broad local maximum near the ^{168}Er region. The RPA calculation successfully reproduces this trend.

The RPA calculation reproduces the trend of the Y_{42} strength, but fails to reproduce the absolute values by about a factor of 3. Since this RPA calculation assumes only the Q–Q force, only the Y_{22}-mode γ-vibration is induced. Therefore, it will be

necessary to introduce the Y_{42}-mode in the γ-vibration to explain the experimental Y_{22} and Y_{42} transition strengths consistently.

In conclusion, the present study has revealed the importance of the hexadecapole (Y_{42}) degree of freedom in the γ-vibration for the whole range of deformed nuclei. The quadrupole (Y_{22}) and the hexadecapole (Y_{42}) transition strengths to the γ-vibrational band show the strong mass-number dependences. A microscopic calculation assuming the random phase approximation (RPA) has been compared with the present data; this indicates the necessity of the hexadecapole degree of freedom in the γ-vibration.

References

1) T. Ichihara, H. Sakaguchi, M. Nakamura, T. Noro, F. Ohtani, H. Sakamoto, H. Ogawa, M. Yosoi, M. Ieiri, N. Isshiki, Y. Takeuchi, and S. Kobayashi: *Phys. Lett. B*, **149**, 55 (1984).
2) I. M. Govil, H. W. Fulbright, D. Cline, E. Wesolowski, B. Kotlinski, A. Backlin, and K. Gridnev: *Phys. Rev. C*, **33**, 793 (1986).
3) P. O. Tjøm and B. Elbek: *Nucl. Phys. A*, **107**, 385 (1968).
4) R. S. Mackintosh: *Phys. Lett. B*, **29**, 629 (1969).
5) L. Ray, G. S. Blanpied, and W. R. Coker: *Phys. Rev. C*, **20**, 1326 (1979).
6) K. Van der Borg, M. N. Harakeh, and B.S. Nilsson: *Nucl. Phys. A*, **325**, 31 (1979).
7) T. Ichihara, H. Sakaguchi, M. Nakamura, M. Yosoi, M. Ieiri, Y. Takeuchi, H. Togawa, T. Tsutsumi, and S. Kobayashi: *Phys. Lett. B*, **182**, 301 (1986).
8) H. Ikegami, S. Morinobu, I. Katayama, M. Fujiwara, and K. Hosono: *Nucl. Instrum. Methods*, **175**, 335 (1980).
9) T. Ichihara, H. Sakaguchi, M. Nakamura, T. Noro, F. Ohtani, H. Sakamoto, H. Ogawa, M. Yosoi, M. Ieiri, N. Isshiki, and S. Kobayashi: *Phys. Rev. C*, **29**, 1228 (1984).
10) F. Ohtani, H. Sakaguchi, M. Nakamura, T. Noro, H. Sakamoto, H. Ogawa, T. Ichihara, M. Yosoi, and S. Kobayashi: *Phys Rev. C*, **28**, 120 (1983).
11) H. Ogawa, H. Sakaguchi, M. Nakamura, T. Noro, H. Sakamoto, T. Ichihara, M. Yosoi, M. Ieiri, N. Isshiki, Y. Takeuchi, and S. Kobayashi: *Phys. Rev. C*, **33**, 834 (1986).
12) J. Raynal: code ECIS79 (unpublished).
13) M. Matsuo: private communications, submitted to *Prog. Theor. Phys.*
14) A. Bohr and B. R. Mottelson: Nuclear Structure, Vol. II, Benjamin, New York (1975).

RIKEN Accel. Prog. Rep. 20 (1986)

III-1-15. Transport Coefficients for Fission at High Excitations

S. Yamaji and H. Hofmann*

[FISSION transport equation, linear response theory, two-center shell model.]

The dynamics of fission can be viewed as a diffusion process in a phase space of collective degrees of freedom. This picture was introduced by Kramers,[1] who assumed forces local in time, and the diffusion coefficient was given by the famous Einstein relation. Such a Markoffian behavior is questionable since the timer scales for collective and intrinsic degrees of freedom, although different from each other, are not separated widely enough.

In Ref. 2 it was argued that Krammers' picture can still be retained in its essential features whose transport coefficients are calculated at a finite local frequency. The transport coefficients are determined by the response of the intrinsic system, and this response depends on the frequency of perturbation (Ω_0), however, the perturbation must be given by collective motion itself. Hence, this frequency has to be calculated by solving locally a dispersion relation (secular equation) for the collective motion. The details of the theory will be published elsewhere.[3]

An aim of this report is to study how important such a non-Markoffian effect is. We reported a microscopic computation of the transport coefficients for inertia M, friction γ, and local stiffness C both in the present self-consistent version ($\Omega_0 \neq 0$) as well as in a zero frequency limit.[4]

Our computation is similar to the one of Ref. 2 where the fission dynamic was followed up to a saddle. It is necessary to go beyond that point. But then the microscopic picture has to be based on a two-center shell model.[5] This is a new feature here. In this first computation within a two-center shell model, we restrict ourselves to a one dimensional case and take the center-separation Z as a collective coordinate.

Actual microscopic calculations were carried out for fission of ^{212}Po at temperature of about 2 MeV and above. We plot stiffness C, inertia M, and friction γ as a function of Z in Figs. 1 to 3. In each case, we show a self-consistent value as well as a zero frequency limit. We observed that this zero frequency limit is a very good approximation to the self-consistent case. The stiffness coefficient $C(0)$ in Fig. 1 is a basic ingredient in our theory. We approximate this by the second derivative of the

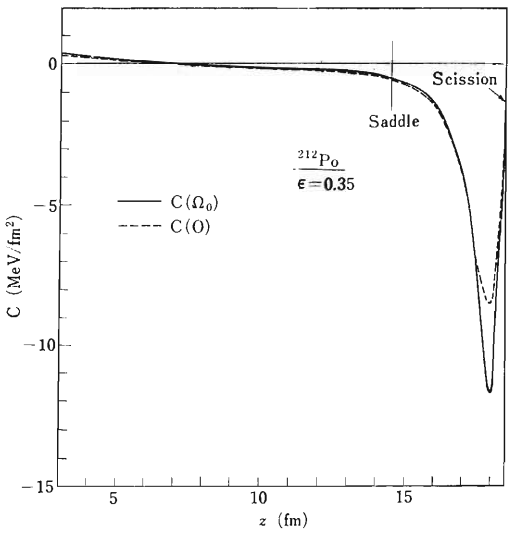

Fig. 1. The local stiffness as a function of center-separation Z. The local stiffness from the liquid drop energy is shown by the dashed curve and the self-consistent approach by fully drawn curve.

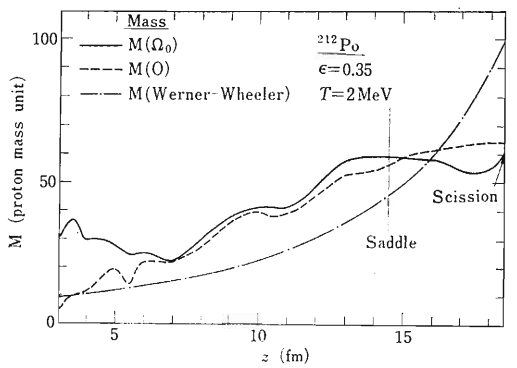

Fig. 2. The inertia M as a function of Z. We show the self-consistent value (fully drawn curve), the zero frequency limit (dashed curve) as well as the liquid drop value (dotted-dashed curve).

* Physik-Department der Technischen Universität München.

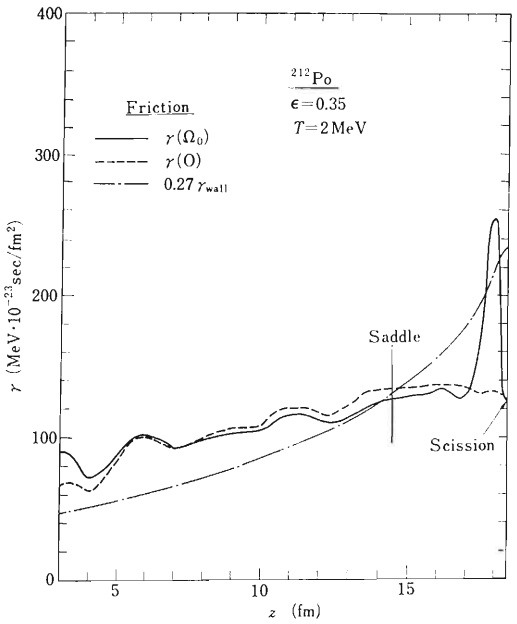

Fig. 3. The friction coefficient γ as a function of Z. The self-consistent value is given by the full curve, the zero frequency limit by the dashed one. The dotted-dashed curve represents Nix's modified formula.

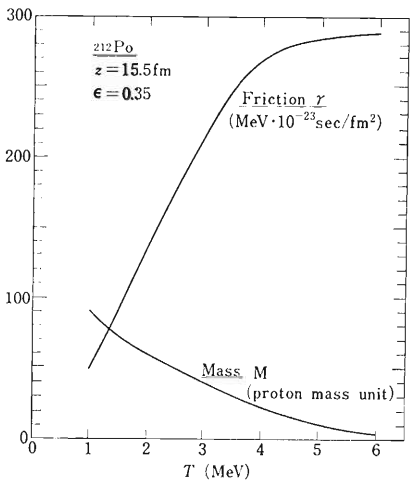

Fig. 4. The temperature dependence of friction and inertia.

liquid drop energy with respect to Z. In Fig. 2 we compare our result for inertia to a liquid drop model. We find a usual situation that the irrotational flow value underestimates the inertia. It is only in the scission region where the situation is reversed. As for friction, in Fig. 3 we have added a plot of Nix's modified version of the wall formula.[6]

Finally, we wish to draw attention to temperature dependence. We plot in Fig. 4 inertia and friction computed within the zero frequency limit as a function of T. As the most striking feature we observe strong temperature dependence of γ. This is in remarkable contrast to the wall formula.[6] As the wall formula depends on T only slightly, the agreement between the dashed curve and the dotted-dashed one in Fig. 3 is accidental to some extent and just true for $T=2$ MeV.

From our observations we deduce the following statements:

a) for a region of temperature higher than 1.5 to 2 MeV, the zero frequency limit appears to be a good approximation to the self-consistent calculation;

b) friction increases with T until a plateau is reached at about 4 MeV.

References

1) H. A. Kramers: *Physica*, **VII**, No. 4, 284 (1940).
2) H. Hofmann and A. S. Jensen: *Nucl. Phys. A*, **428**, 1c (1984).
3) H. Hofmann, R. Samhammer, and S. Yamaji: Unpublished.
4) H. Hofmann and P. J. Siemens: *Nucl. Phys. A*, **257**, 156 (1976).
5) A. Iwamoto, S. Yamaji, S. Suekane, and K. Harada: *Prog. Theor. Phys.*, **55**, 115 (1976).
6) J. R. Nix and A. J. Sierk: Preprint LA-UR-86-698 (1986).

RIKEN Accel. Prog. Rep. 20 (1986)

III-2. Atomic and Solid-State Physics

1. Cross Sections of the Relativistic Radiative Electron Capture by Use of the Strong-Potential Born Calculation

K. Hino and T. Watanabe

The relativistically extented strong-potential Born (SPB) formalism is applied to the radiative electron capture (REC) process caused by the bombardment of a heavy and highly stripped charged particle with a relativistically high velocity.[1] The results are compared with those obtained from the non-relativistic SPB calculations[2] and with those from the relativistic Born calculation (Sauter's formula);[3,4] the latter includes no distortion effects between a heavy projectile ion and an active electron. Even if the strong distortion effects are taken into consideration in the SPB approximation, the shapes of photon angular distributions in the laboratory frame still behave nearly as $\sin^2\theta_L$ (θ_L is the angle of the emitted photon) in the vicinity of the angle of 90°. This behavior is the same as the results calculated by Sauter's formula. The higher the charge of a projectile ion becomes, however, the greater the discrepancy between the angular shape of our results and that of Sauter's becomes at both angles smaller and larger than 90° (Figs. 1 and 2). As is expected, the magnitudes of the differential and the total cross sections are drastically influenced by the distortion

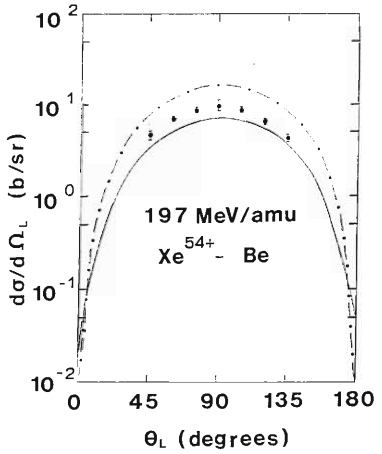

Fig. 1. Angular distributions of REC photons for 197 MeV/amu Xe^{54+}-Be collisions. Solid lines, the present calculations; Dotted chain curve, the relativistic Born calculations of Sauter (Ref. 2). Experimental results are quoted from Ref. 5.

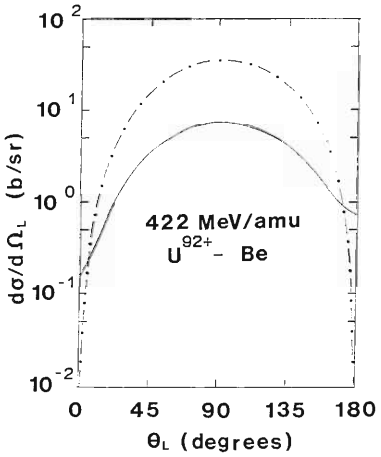

Fig. 2. The same as Fig. 3 for 422 MeV/amu U^{92+}-Be collisions.

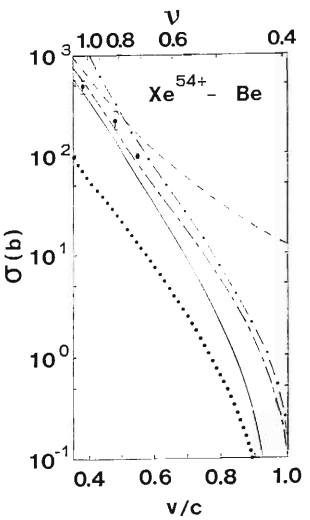

Fig. 3. Total cross sections for Xe^{54+}-Be collisions *versus* the incident velocity v/c and the Coulomb parameter between an active electron and the projectile ion ν. Solid lines (——), the present calculations (RSPB-I); Chain lines (— - —), the relativistic SPB calculations without the Lorentz contraction factor based on the motion of a target nucleus in the moving frame (RSPB-II); Dotted-chain lines (—·—), the relativistic Born calculations of Sauter (RB); Broken lines (- - - -), the non-relativistic SPB calculation of Ref. 2 (NRSPB); Dotted lines (·····), the relativistic impulse calculations (RIA); Experimental results are quoted from Ref. 5.

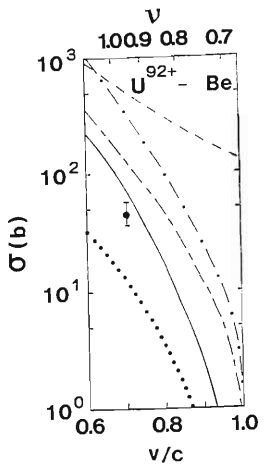

Fig. 4. The same as Fig. 5 for U^{92+}-Be collisions. The experimental result is quoted from Ref. 5.

effects ascribable to a large charge of a heavy projectile ion such as U^{92+}. Our results are in good agreement with recent experiments.[5] In addition, the Coulomb off-shell factor introduced by the SPB theory is found playing important roles in the case of the relativistic REC process because the results calculated by using the relativistic impulse approximation are too underestimated to explain the experimental ones (Figs. 3 and 4). The Coulomb off-shell factor represents the radiative transitions from the Rydberg states of the electron-projectile bound system into the final state of the K-shell. The SPB wave function includes the contributions from intermediate bound states as well as from the continuum states. The former contributions are absent in the impulse wave function.

References

1) K. Hino and T. Watanabe: *Phys. Rev. A* (in press).
2) M. Gorriz, J.S. Briggs, and S. Alston: *J. Phys. B*, **16**, L665 (1983).
3) F. Sauter: *Ann. Phys. (Leipzig)*, **9**, 217 (1931); **11**, 454 (1931).
4) E. Spindler, H.-D. Betz, and F. Bell: *Phys. Rev. Lett.*, **42**, 832 (1979).
5) R. Anholt, S.A. Andriamonje, E. Morenzoni, Ch. Stoller, J.D. Molitoris, W.E. Meyerhof, H. Bowman, J.-S. Xu, Z.-Z. Xu, J.O. Rasmussen, and D.H.H. Hoffmann: *Phys Rev. Lett.*, **53**, 234 (1984); W.E. Meyerhof, R. Anholt, J. Eichler, H. Gould, Ch. Munger, J. Alonso, P. Thieberger, and H.E. Wegner: *Phys. Rev. A*, **32**, 3291 (1985); R. Anholt, Ch. Stoller, J.D. Molitoris, D.W. Spooner, E. Morenzoni, S.A. Andriamonje, W.E. Meyerhof, H. Bowmann, J.-S. Xu, X.-Z. Xu, J.O. Rasmussen, and D.H.H. Hoffmann: *Phys. Rev. A*, **33**, 2270 (1986).

RIKEN Accel. Prog. Rep. 20 (1986)

III-2-2. Charge Exchange Collisions on the Solid Surface

K. Fujima and H. Adachi*

Recently, Ion-Neutralization-Spectroscopy (INS) has attracted a much interest as an effective tool for investigating electronic properties of the solid surface.[1] Four mechanisms *i.e.*, resonant charge transfer, Auger neutralization, inner-shell resonant charge transfer and radiative neutralization, have been proposed in which an electron is transferred from the solid surface to an ion.[2] The latter two are thought to be less important for low energy collisions.

In this report we concentrate attention on the first mechanism. When an ion comes to a certain distance from the solid surface, the orbital of ion mixes with that of solid surface. An electron can move from the solid to the ion or *vice versa* by tunneling. This mechanism is often called 'resonant charge transfer.' The possibility of charge exchange by this mechanism has so far been discussed based on the comparison between the work function of the solid and the ionization potential of the ion.

So, we feel an urgent need of a quantitative study of charge exchange cross section from the first principle and plan to apply to this process a semi-classical treatment, which is now commonly used for charge transfer collisions of ion-ion and ion-atom charge (namely diatomic system). There are three difficulties in extending this method to the collision of an ion with a solid surface. First, we have to calculate the wavefunction of the system composed of a solid and an ion and compute the coupling matrix elements. It is hard to do this even for a di-atomic system when many states are involved in the calculation. Second, we can reduce the dimension of coupled equation by introducing a polar coordinate and rotational and radial coupling between channels for the diatomic system. But, for the system of ion and solid surface, we must compute matrix elements for the operators $\partial/\partial x$, $\partial/\partial y$, and $\partial/\partial z$ in the Cartesian coords. because we can not use the rotational and the radial coupling operators *i.e.*, iL_y and $\partial/\partial R$. Third, the potential between an ion and a solid is not so easily obtained which is necessary to get a classical trajectory of the ion.

To this end, we have developed a new computer code which calculates the coupling matrix elements in the Cartesian coord. using the wavefunction obtained by the DV-Xα cluster calculation. We applied this program to Si + $He^+ \rightarrow Si^+$ + He charge transfer collision which the most simplified model of neutralization of He on the Si surface. The energy diagram for Si + He^+ is shown in Fig. 1. Figure 2 shows the impact parameter dependence of charge

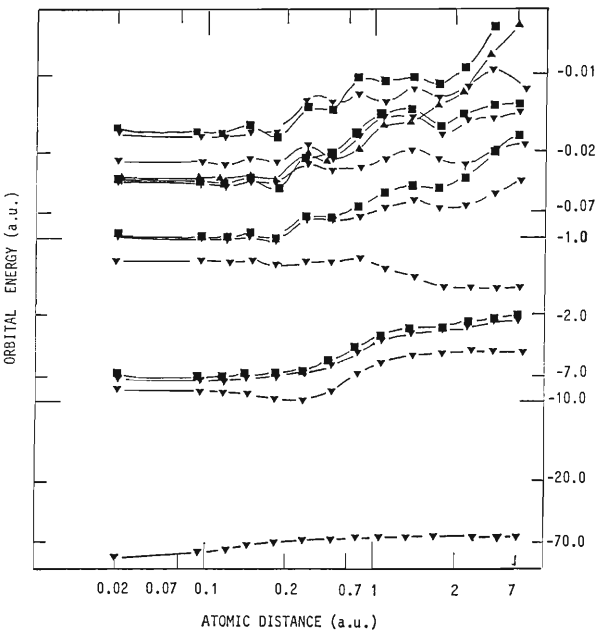

Fig. 1. Energy diagram for Si+He^+ system. Orbitals belong to σ, π, and δ irreducible representation are marked with ▼, ■, and ▲, respectively.

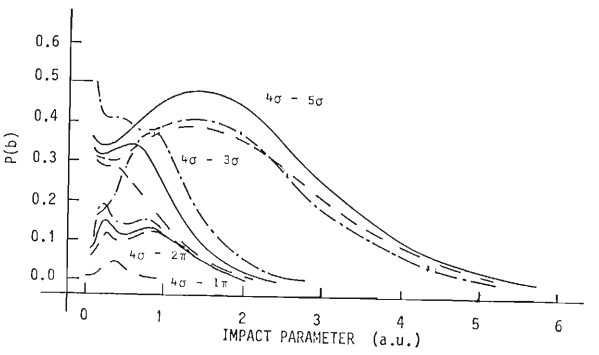

Fig. 2. Charge exchange probabilities *versus* impact parameter. Chain —·—·—, solid ——, and dushed — — curves correspond to the cases of incident energy 0.5, 1, and 2 keV, respectively.

* The Hyogo University of Teacher Education.

exchange cross sections at the incident energies 0.5, 1, and 2 keV. The integration of the coupled equation in orthogonal coordinate and computation of the charge transfer cross section in ion-surface collision are in progress.

References

1) R. Souda and M. Aono: *Butsuri*, **41**, 633 (1986) (in Japanese).
2) H. Hangstrum: *Phys. Rev.*, **96**, 336 (1954).

RIKEN Accel. Prog. Rep. 20 (1986)

III-2-3. Calculation of Ionization Cross Sections of Multi-Charged Ions in Proton Impact by TFD Method Using BEA†

S. Zhou,* X. Zhang,* Q. Ma,* J. Cheng,* Y. Liu,* and T. Watanabe

Using the binary encounter approximation (BEA), we have calculated the ionization cross sections by the Thomas-Fermi-Dirac model for the reaction

$$H^+ + {}_ZA^{q+} \rightarrow H^+ + e + {}_ZA^{(q+1)+}(\sum) \qquad (1)$$

where Z is the atomic number of A and $Z=18$ and 36 are taken in the present calculation, $q=1$–5, and ${}_ZA^{(q+1)}(\sum)$ stands for all possible electronic states of the ion. In the present approach, we aim to obtain the cross sections for relatively high Z values by taking into account the exchange effect for inner shell electrons of the target ion.

These processes are characterized by a large magnitude of momentum transferred to the electrons in the ions ${}_ZA^{(q+1)+}$ by colliding with incident protons. Such collision can be treated by the classical description and this feature supports the use of BEA.[1] In this treatment an electron in the target ion is assumed to be ejected into the continuous states when the energy transferred to the electron exceeds its binding energy.

Both the momentum distribution $f(p)dp$ for an electron having momentum between p and $p+dp$ and the probability $I_r(p)dp$ for finding an electron at a distance r from the nucleus of the target ion whose momentum is in this range are obtained from the TFD model.[2]
They are

$$I_r(p)\,dp = \begin{cases} 3p^2dp/p^3{}_{\max} & \text{for } p(r) \leqslant p_{\max}(r) \\ 0 & \text{for } p(r) > p_{\max}(r) \end{cases} \qquad (2)$$

and

$$f(p)dp = \begin{cases} 32\pi^2p^2r^3(p)dp/3(Z-q)h^3 & \text{for } p \geq p(R) \\ 32\pi^2p^2R^3dp/3(Z-q)h^3 & \text{for } p < p(R), \end{cases} \qquad (3)$$

where $p_{\max}(r) = (2me^2Z/u)^{1/2}[\varepsilon + (\psi/x)^{1/2}]$. $r(p)$ is determined from the relations $p = (2me^2Z/u)^{1/2} \cdot [\varepsilon + (\psi/x)^{1/2}]$, $x = r(p)/u$, and $u = (3/32\pi^2)^{2/3}h^2/2me^2Z^{1/3}$, where R is the radius of ${}_ZA^{q+}$, $X = R/u$, $\varepsilon = (3/32\pi^2Z^2)^{1/3}$, and ψ is the TFD function which satisfies the following equation and conditions:[3]

$$\psi'' = x[\varepsilon + (\psi/x)^{1/2}]^3$$
$$\psi|_X = \varepsilon^2X/16$$
$$x\psi'(x)|_X = -q/Z + \psi|_X\,,\ \psi(0) = 1 \qquad (4)$$

Here we define a cross section $\sigma^{(i)}(v, w)$ in the laboratory frame, where the nucleus of ${}_ZA^{q+}$ is stationary, for ionization in the collision between an electron with velocity w in ${}_ZA^{q+}$ and a proton with velocity v. The cross section $\sigma_{AV}{}^{(i)}(v)$ for the electron ejected from ${}_ZA^{q+}$ by collision with the proton is defined as[4]

$$\sigma_{AV}^{(i)}(v) = \int_0^\infty \sigma^{(i)}(v, w) f(w)\,dw \qquad (5)$$

where $f(w)$ denotes the velocity distribution function of an electron of the ion ${}_ZA^{q+}$ determined in Eq. (3). $\sigma^{(i)}(v, w)$ for projectile proton is explicitly derived from the Vriens theory,[4]

(1) $2mv^2 > U_i$

$$\sigma_{AV}^{(i)}(v) = \int_0^{v-U_i/2mv} \sigma_{A+B} f(w)\,dw + \int_{v-U_i/2mv}^\infty \sigma_B \cdot f(w)\,dw \qquad (6)$$

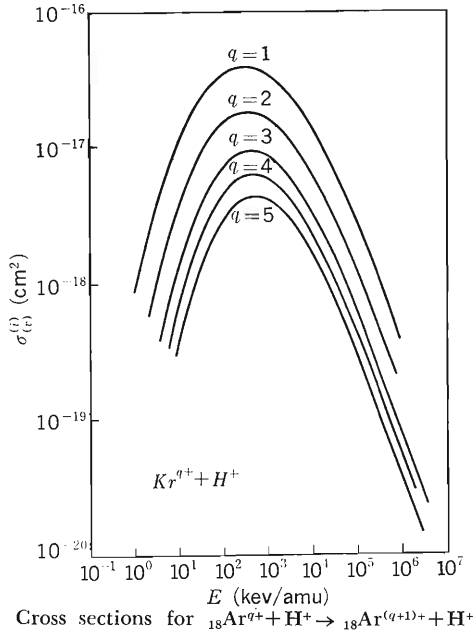

Fig. 1. Cross sections for ${}_{18}Ar^{q+} + H^+ \rightarrow {}_{18}Ar^{(q+1)+} + H^+ + e$ by the binary encounter theory with the Thomas-Fermi-Dirac approximation as a function of impact energy per nucleon.

† Presented at the Xth International Conference on Atomic Physics, 25–29th August, 1986, Tokyo.

* Dept. of Modern Physics, Univ. of Science and Technology of China (USTC), Hefei, Anhui, China.

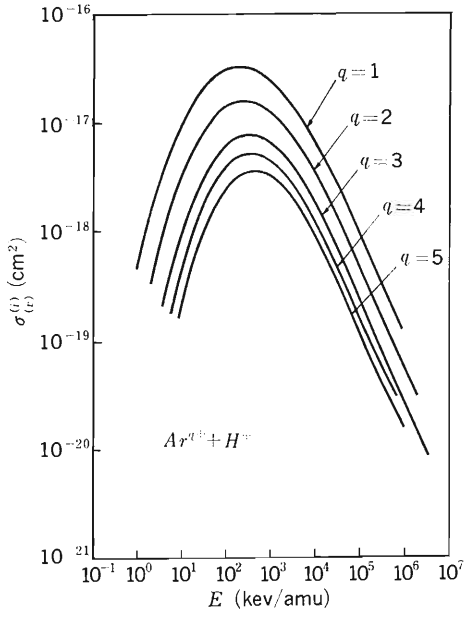

Fig. 2. Cross sections for ${}_{36}Kr^{q+}+H^+ \rightarrow {}_{36}Kr^{(q+1)+}+H^++e$ by the binary encounter theory with the Thomas-Fermi-Dirac approximation as a function of impact energy per nucleon.

(2) $2mv^2 < U_i$

$$\sigma_{AV}^{(i)}(v)=\int_{U_i/2mv-v}^{\infty}\sigma_B\cdot f(w)\,dw \tag{7}$$

where

$$\sigma_{A+B}=2\pi e^4[1/U_i+mw^2/3U_i^2-1/2m(v^2-w^2)]/mv^2$$

$$\sigma_B=\pi e^4\{1/2mw(v+w)+1/U_i+m[2v^3+w^3-(2U_i/m+w^2)^{3/2}]/3wU_i^2\}/mv^2$$

and

U_i is the ionization energy of ${}_ZA^{q+}$.

Figures 1 and 2 show the results we have obtained of $\sigma_{AV}{}^{(i)}(v)$ for ${}_{18}Ar^{q+}$ + H and ${}_{36}Kr^{q+}$ + H. They are comparable to the results of another article[5] which used the TF model instead of the TFD model.

References

1) L. Vriens: in Case Studies in Atomic Collision Physics I (eds. E. W. McDaniel and M. R. S. McDowell), North-Holland, Amsterdam, Chap. 6, p. 335 (1969).
2) C. A. Coulson and N. H. March: *Proc. Phys. Soc. A*,
3) P. Gombas: Die statistische Theorie des Atoms und ihre Anwendungen, Springer, Vienna (1948); *Ann. Phys.*, **18**, 1 (1956).
4) L. Vriens: *Proc. Phys. Soc.*, **90**, 935 (1967).
5) X. Fang: Electron Stripping Cross Sections of Charged Ions by H^+ Impact, USTC thesis (1985).

RIKEN Accel. Prog. Rep. 20 (1986)

III-2-4. Extended Bethe Surface: Behavior of the Generalized Oscillator Strength along Isoelectronic Sequence

M. Iwai, I. Shimamura, and T. Watanabe

The generalized oscillator strength (GOS), which is the generalization of the optical oscillator strength, is directly related to the differential cross section for inelastic collision of the fast charged particle with atoms and molecules.[1,2] This atomic or molecular property is important, since it reflects the detailed electronic structure of target atoms or molecules, and represents the response of the system to a sudden change of momentum of its electron.

In this report we investigate the behavior of GOS's along isoelectronic sequence using the configuration-mixing wave functions. An isoelectronic sequence consists of a neutral atom and many ions. Each member of a sequence has the same number of electrons. Effects of electron correlation are negligible for ions with sufficiently large Z due to the strong nuclear attraction potential. As Z decreases, however, the configuration-mixing effects become appreciable. Behavior of optical oscillator strengths along isoelectronic sequence has been investigated in depth so far.[3] However, the behavior of GOS's has been only partially analyzed. Such an analysis will afford the systematic understanding of electron-electron correlation effects on GOS's. In principle one has to apply the Coulomb-Born approximation rather than the plane-wave Born approximation to the scattering of a charged particle by an ion. If the incident particle is not an electron but an ion, however, the effect of Coulomb deflection must be negligible except for slow collisions. Then GOS's of ions still contain important information about inelastic scattering of a heavy particle.

In these analyses we propose to extend the Bethe surface,[1] which is a three-dimensional plot of a GOS as a function of a momentum transferred and excitation energy, by introducing an additional axis for the inverse of the (effective) nuclear charge. We shall call this new surface an "extended Bethe surface" and show the usefulness of this surface to visualize effects of electron correlation on GOS's.

The GOS for excitation of the target state from $|0>$ to $|n>$ is defined by[1]

$$F_{on}(K)=\frac{2E_{on}}{K^2}|<n|\sum_j e^{i\boldsymbol{k}\cdot\boldsymbol{r}_j}|0>|^2 \qquad (1)$$

where E_{on} is the excitation energy and K denotes the momentum transferred during the collision.

Here we define the scaled GOS as a function of the scaled momentum transfer $\tilde{K}=K/Z$ by

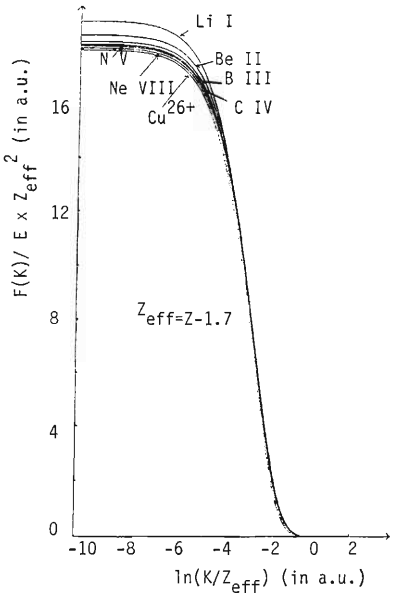

Fig. 1 (a). Scaled GOS for $1s^22s\ ^2S$–$1s^22p\ ^2P$ transition in Li-like system.

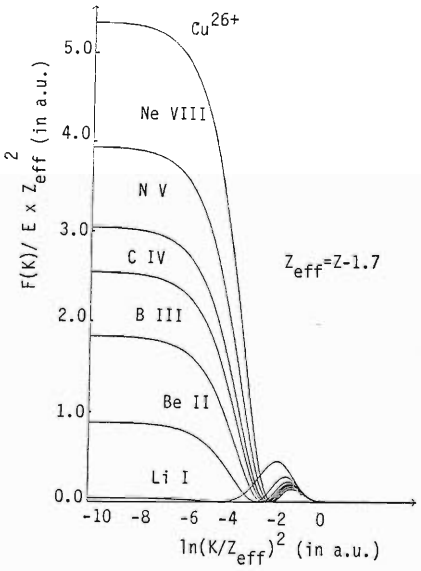

Fig. 1 (b). Scaled GOS for $1s^22s\ ^2S$–$1s^23P\ ^2P$ transition in Li-like system.

$$S_{on}(\tilde{K}) = \frac{F_{on}}{E_{on}} Z^2 \qquad (2)$$

If electron-electron interaction can be completely neglected, $S_{on}(K)$ is universal for all atoms, being independent of Z. Then we notice that the variation of the scaled GOS from the universal value is wholly due to the electron-electron interaction.

Figure 1(a) and Fig. 1(b) show the GOS's for the 2s–2p and 2s–3p transitions in the Li-like system, respectively. Note that the scaled GOS's are plotted as functions of the scaled momentum transfer. At sufficiently high Z, the shape of the scaled GOS almost coincides with that in the hydrogenic model for both transitions. We readily notice, by comparison of Fig. 1(a) and Fig. 1(b), that the behavior of the GOS's along the isoelectronic sequence is quite different between these transitions. Variations of the GOS's with Z can be almost scaled for the 2s–2p transition. However, the situation for the 2s–3p transition is totally different: The optical oscillator strength decreases rapidly with decreasing Z, and almost complete cancellation occurs in the region near Li I. As Z becomes small, the minima in the GOS along the K-axis approach the optical plane ($K=0$ plane) while the maxima become larger (Fig. 1(b)).

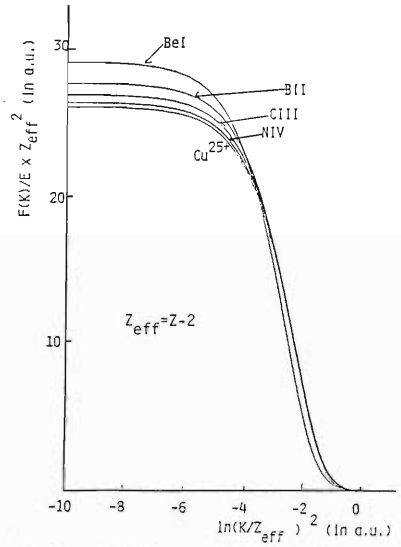

Fig. 2(a). Scaled GOS for $2s^2\ {}^1S$–$2s2p\ {}^1P$ transition in Be-like system.

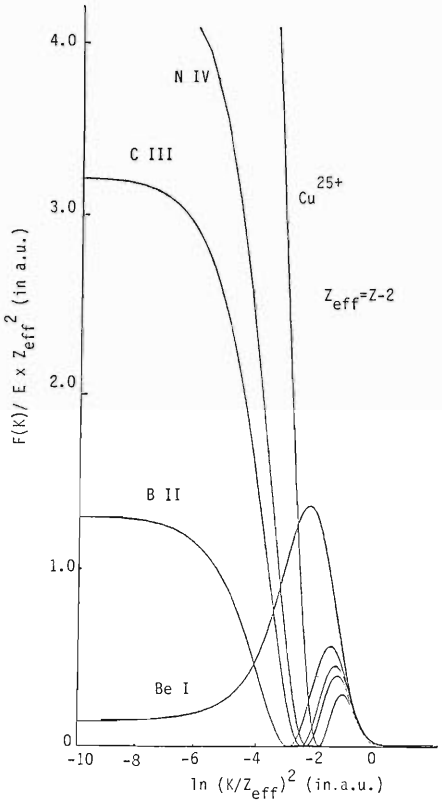

Fig. 2(b). Scaled GOS for $2s^2\ {}^1S$–$2s^23p\ {}^1P$ transition in Be-like system.

Next, we see the behavior of the GOS's for the 2s–2p and 2s–3p transitions in the Be-like system in Fig. 2(a) and Fig. 2(b). We again find the characteristic behavior of the GOS's for these transitions similar to those in the Li-like system. The two-dimensional plot of Fig. 2(b) is represented in the form of the "extended Bethe surface," *i.e.*, three-dimensional plot as a function of Z^{-1} and K in Fig. 3. Effect of electron correlation on the GOS is clearly seen from Fig. 3. The minima in the GOS look like a valley and smoothly move towards the optical plane. Almost exact cancellation of the optical oscillator strength is found at $Z=4.2$ ($Z_{eff}=2.2$). These phenomena are quite similar to Cooper minima in the optical oscillator strength which occurs

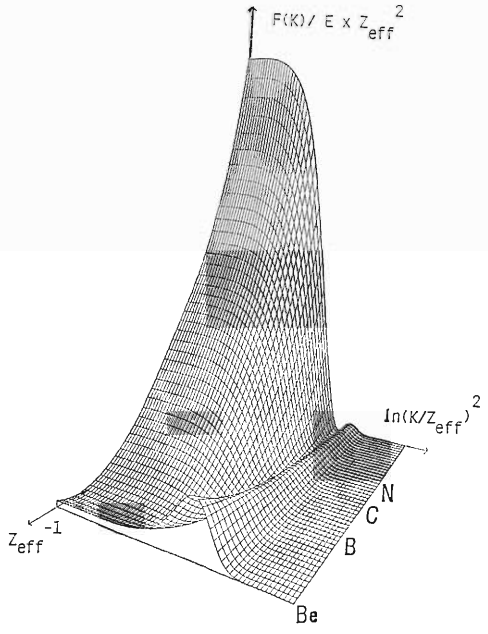

Fig. 3. Extended Bethe surface for $2s^2\ {}^1S$–$2s^23p\ {}^1P$ transition in Be-like system.

on the usual Bethe surface.[1]

It is well known that the level crossings frequently occur along the Z^{-1} axis. It often happens that, near the neutral end of a sequence, a state which is stable at large Z lies high up in a spectrum. Such a state will cross other states with which it can interact. A typical example of this is the $2s2p^2$ ^2S state in the B-like system, which has the same energy as the ground state at infinite Z and is embedded in the Rydberg series of $2s^2ns$ in B I. This state crosses $2s^23s$ ^2S in the region near G II and the conspicuous irregularity in the optical oscillator strength is found.[3] We see the GOS for the transition $2s^22p$ ^2P–$2s^23s$ ^2S in Fig. 4 as the "extended Bethe surface." The drastic irregularity of the oscillator strength is found in Fig. 4, reflecting the fact that the configuration-mixing and the change in K introduce complicated interference effects on the matrix element.

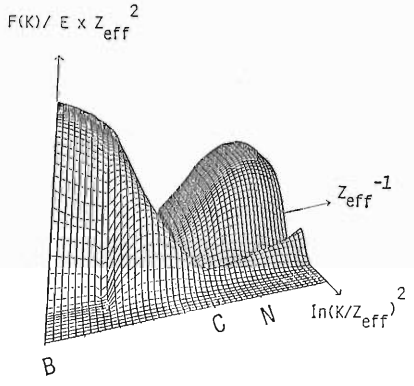

Fig. 4. Extended Bethe surface for $2s^22p$ ^2P–$2s^23s$ ^2S transition in B-like system.

Through these analyses, we found that the extension of the Bethe surface by introducing an additional axis for Z^{-1} gives new aspects of GOS's. We plan to study the behavior of GOS's for molecules in the future.

References

1) M. Inokuti: *Rev. Mod. Phys.*, **43**, 297 (1971).
2) M. Inokuti, Y. Itikawa, and J. E. Turner: *Rev. Mod. Phys.*, **50**, 23 (1978).
3) A. W. Weiss: Beam-Foil Spectroscopy, Vol. 1 (eds. Sellin and Pegg), Plenum Press, New York and London, p. 51 (1976).

RIKEN Accel. Prog. Rep. 20 (1986)

III-2-5. R-Matrix Method for Rearrangement Collisions: Dissociative Recombination $e + (AB)^+ \rightarrow A + B$

I. Shimamura

Recombination of an electron and an atomic ion in a two-body collision occurs only through emission of a photon. The rate of this process is usually very low. Molecular ions, on the other hand, can efficiently recombine with electrons. This is due to another much faster recombination called dissociative recombination, in which excess energy released from the electron is absorbed by the relative motion between dissociation fragments. For diatomic molecular ions AB^+, for example, the process is expressed as

$$e + AB^+ \rightarrow A + B$$
$$\rightarrow A^+ + B^-$$

The dissociative recombination (DR) is important in either physics or chemistry when secondary electrons play a decisive role; DR controls the number of charged particles in the medium. Radiation physics and chemistry, physics of the earth's upper atmosphere, and physics of gaseous discharge are typical research fields where the knowledge of DR is indispensable.

Theoretical treatment of the DR process is difficult. This is partly because of the rearrangement of the particles, which makes the final channel quite different from the initial channel. Another source of the difficulty lies in an infinite number of Rydberg states of the compound AB, which plays the role of intermediate states in DR.

We have started application of the R-matrix method to DR. The R-matrix method for non-rearrangement collisions divides the whole configuration space into two, namely, the inner region ($r < a$) and the outer region ($r > a$),[1),2)] where r is the distance between the collision partners. They form a complex in the inner region, and they are separate and interact through a local potential (or a potential matrix) in the outer region. The two regions are treated independently in two different approximations appropriate in the two regions, and the wave functions are smoothly connected at the boundary between the regions.

There are two different arrangement channels in DR. Therefore, each arrangement channel needs to be divided into inner and outer regions. Because the inner region of the initial arrangement channel confines all electrons in a finite region, there are no Rydberg states. We have to take into account only a finite (and hopefully, small) number of intermediate states. This simplifies the whole procedure for detailed *ab initio* calculations.

As a first example we apply the R-matrix method to DR

$$e + H_2^+ \rightarrow H(n > 1) + H(n = 1)$$
$$\rightarrow H^+ + H^-$$

The electron-molecule collision part of the calculation is nearly the same as the ordinary R-matrix calculation.[1),2)] The atom-atom (ion-ion) collision part is treated with a one-electron picture. In this picture one of the two electrons in the system is always sitting in the ground orbit of the hydrogen atom, and only the other electron is active.

Calculations are now in progress, and results will be reported soon.

References

1) I. Shimamura: Electronic and Atomic Collisions, Invited Papers at Xth Int. Conf. Phys. Elec. Atom. Coll., Paris, July 1977 (ed. G. Watel), North-Holland, Amsterdam, p. 213 (1978).
2) I. Shimamura: Electron-Molecule Collisions (eds. I. Shimamura and K. Takayanagi), Plenum, New York, Chap. 2 (1984).

RIKEN Accel. Prog. Rep. 20 (1986)

III-2-6. Classical-Trajectory Monte Carlo Calculations for Coulomb-Interacting Three-Body Systems†

K. Nakanishi, K. Iguchi,* A. Ohsaki, and T. Watanabe

Coulomb-interacting three-body problems in quantum mechanics are among the major research subjects to be studied in contemporary physics. Many problems, such as charge transfer processes between an ion and an atom, are solved in practical way by taking an approximation that nuclear masses are much heavier than electron's mass. On the other hand, three-body problems can always be solved numerically by classical mechanics. Such an approximation of classical mechanics as the classical-trajectory Monte Carlo (CTMC) method has been successfully proved to give accurate cross sections for the charge transfer process empirically.[1] In this paper, we calculate the cross sections of the following processes:

$$\begin{aligned} \mu^-+d+t &\rightarrow \mu^-+t+d \\ &\rightarrow \mu^-+t+d \qquad (1) \\ e^-+(e^+e^-)_{singlet} &\rightarrow (e^+e^-)_{triplet}+e^- \\ &\rightarrow e^-+e^++e^- \qquad (2) \end{aligned}$$

and

$$\begin{aligned} \mu^-+(\mu^+e^-) &\rightarrow (\mu^+\mu^-)+e \\ &\rightarrow \mu^++\mu^-+e \qquad (3) \end{aligned}$$

The CTMC method is based on classical Hamilton's canonical equations, which are given by

$$\dot{p}=-\partial H/\partial q\,, \quad \dot{q}=\partial H/\partial p \qquad (4)$$

where q and p are the generalized coordinate and its canonically conjugate variable (momentum) and H is the classical Hamiltonian of the three-body system. The equation can be treated to 12 coupled equations. The montion of a three-particle system can be solved numerically under the randomly-selected quantum-mechanical initial conditions. The initial quantum state of the target atom is represented by the microcanonical distribution of classical orbits; the requirement of a fixed binding energy leads to the uniform distribution of the square of the angular momentum, while the initial quantum state of the projectile is represented by an ensemble of classical trajectories distributed uniformly on the square of the impact parameter. Both uniform distributions can be generated by random sampling with respect to the corresponding ensembles of trajectories. The final states of the system can be classified according to the signs of the interaction energies between the two particles having different-sign charges when the distance between the particles having the same-signed charge becomes infinite. The cross section is given by

$$\sigma=(N_R/N)\pi b_{max}^2$$

where b_{max} is the maximum value of the impact parameter taken in the calculation, N_R and N are the number of events occuring, and the total number of trajectories, respectively,

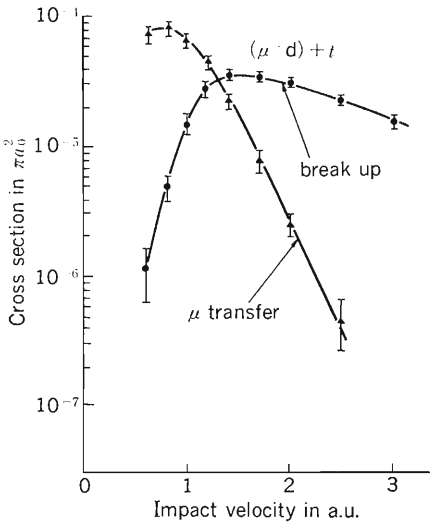

Fig. 1. Muon transfer and break-up cross sections, $t+(\mu^-d) \rightarrow (\mu^-t)+d \rightarrow \mu^-+d+t$, as a function of impact velocity.

The results for the process (1) are given in Fig. 1. In the process (1), the lowest binding energy of (μ^-d) is not different greatly from that of (μ^-t): $E_{1s}=2{,}713$ eV for (μ^-t) and $=2{,}652$ eV for (μ^-d) and the difference $E \rightarrow 61$ eV. The cross section for the inverse process of μ^--transfer, $(\mu^-t)+d \rightarrow (\mu^-d)+t$, is almost the same except for the low velocity impact (< 0.5 a.u.).

† Presented at the Xth International Conference on Atomic Physics 25–29th August, 1986, Tokyo.

* Department of Chemistry, Waseda University.

Reference

1) R. E. Olson and A. Salop: *Phys. Rev. A*, **16**, 531 (1977).

RIKEN Accel. Prog. Rep. 20 (1986)

III-2-7. Total and Differential Cross Sections for $(\mu^+\mu^-)$ Formation by Collisions of μ^+ with (μ^-p) in the Eikonal Approximation†

X. Liu,* Q. Ma,* J. Cheng,* X. Zhang,* Y. Liu,* and T. Watanabe

We have carried out the calculation for the process from the initial ground state (μ^-p) to the final ground state $(\mu^+\mu^-)$ using the eikonal approximation.[1] The differential cross section was also calculated.

We can write the total Hamiltonian in the initial coordinate system $\vec{R}$ and $\vec{r}$ or in the final coordinate system $\vec{R}'$ and $\vec{r}'$, where $\vec{R}$ and $\vec{R}'$ mean the coordinates of the relative motion, and $\vec{r}$ and $\vec{r}'$ the coordinates of the inner motion as shown in Fig. 1. The reduced masses of the system in the initial state frame, ν for the inner motion and μ for the relative motion, are given by

$$\nu=\frac{m_p m_\mu}{m_p+m_\mu},\quad \mu=\frac{m_\mu(m_p+m_\mu)}{m_p+2m_\mu} \tag{1}$$

and those in the final state frame are given by

$$\nu'=\frac{m_\mu}{2},\quad \mu'=\frac{2m_p m_\mu}{m_p+2m_\mu} \tag{2}$$

where m_μ and m_p are the masses of μ and p, respectively.

The eikonal approximation to the post form of the scattering wave function is given by

$$\phi^{(+)}(\vec{R},\vec{r})=\exp\left(i\vec{K}_i\cdot\vec{R}-\frac{i}{K_i}\int_{-\infty}^{Z}U_i(\vec{R},\vec{r})dz'\right)\phi_i(r) \tag{3}$$

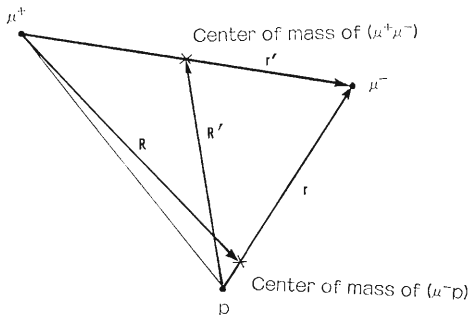

Fig. 1. Coordinate system of collision system. $\mu^+p+\mu^-\rightarrow(\mu^+\mu^-)+p$.

† Presented at the Xth International Conference on Atomic Physics, 25–29th August, 1986, Tokyo.

* Department of Modern Physics, University of Science and Technology of China, Hefei, Anhui Province, China.

where U_i is the interaction Hamiltonian in the initial state frame and is explicitly given by

$$U_i(\vec{R},\vec{r})=\frac{1}{|\vec{R}+(1-\eta)\vec{r}|}-\frac{1}{|\eta\vec{r}-\vec{R}|}$$

$$\eta=\frac{m_p}{m_p+m_\mu}$$

$\vec{K}_i$ is the wave vector of relative motion in the initial state, and $\phi_i(r)$ is the wave function of initial ground state (μ^-p).

The eikonal scattering amplitude can be reduced to a compact two-dimensional integral form

$$F_{if}(\theta)=i2^{4-i/K_i}\frac{1}{K_i}\mu'(\nu\nu')^{3/2}\int_0^\infty ds\, s^{-i/K_i-1}\times\int_0^1 dx\, x^{-1}(\nu-x^{-1}(1-x)s)\times\left(\frac{d}{d\nu^2}\right)^2\{(\beta^2+Q^2)^{i/K_i-1}(\beta-i\vec{Q}\cdot\vec{Z})^{-i/K_i}\} \tag{4}$$

where

$$\beta=[(\nu^2+K_i'^2)x-(\vec{K}_i'\cdot x+is(1-x)\hat{Z})^2]^{1/2}+\nu'$$
$$\vec{Q}=\vec{K}_f'-x\vec{K}_i'-is(1-x)\hat{Z}$$
$$\vec{K}_i'=\vec{K}_f+\eta\vec{K}_i,\quad \vec{K}_f'=-\frac{1}{2}\vec{K}_f+\vec{K}_i$$

where K_f is the wave vector of relative motion in the final state. The differential cross section in the eikonal approximation is given by

$$\frac{d\sigma}{d\Omega}=\frac{K_f}{2\eta K_i}|F_{if}(\theta)|^2 \tag{5}$$

Table 1. Cross sections calculated for $\mu^+ + (\mu^-p) \rightarrow (\mu^+\mu^-)+p$.

Impact energy (keV)	Eikonal approximation (πa_0^2)	FBA (πa_0^2)	DWBA (πa_0^2)
1.20	1.22×10^{-4}	2.44×10^{-5}	4.80×10^{-5}
1.70	2.36×10^{-4}	1.62×10^{-4}	1.79×10^{-4}
2.00	2.29×10^{-4}	1.77×10^{-4}	1.89×10^{-4}
2.40	2.01×10^{-4}	1.67×10^{-4}	1.75×10^{-4}
3.60	1.18×10^{-4}	1.05×10^{-4}	1.09×10^{-4}
7.00	2.62×10^{-5}	2.54×10^{-5}	2.79×10^{-5}
20.00	6.45×10^{-7}	7.51×10^{-7}	9.76×10^{-7}

FBA, First-order Born approximation; DWBA, First-order distorted wave Born approximation.

The total cross section is given by

$$\sigma = \frac{K_f}{2\eta K_i} \int |F_{if}(\theta)|^2 \, d\Omega \qquad (6)$$

Table 1 shows the numerically calculated total cross section. FBA[2] and DWBA[2] are also shown. Figure 2 shows the results of present calculation for the total cross section, which are compared with

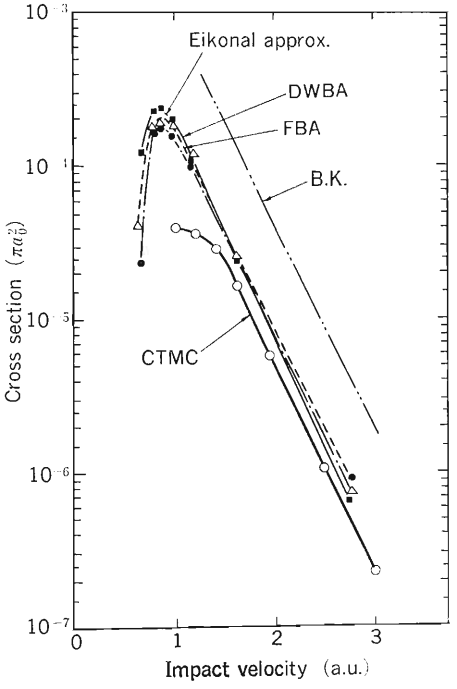

Fig. 2. $(\mu^+\mu^-)$ formation cross sections by μ' collision on (μ^-p) as a function of impact velocity. DWBA, First-order distorted wave Born approximation; FBA, First-order Born approximation; CTMC, Classical trajectory Monte Carlo calculation; B.K., Brinkman-Kramers approximation.

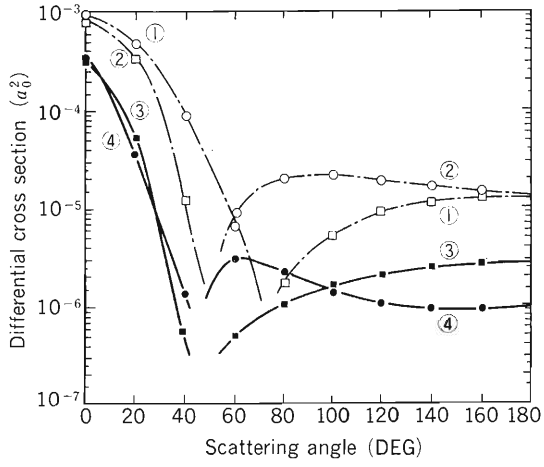

Fig. 3. $(\mu^+\mu^-)$ formation differential cross sections by μ^+ collision on (μ^-p) as a function of scattering angle. Curve ①, eikonal approximation (2.4 keV); Curve ②, FBA (2.4 keV); Curve ③, eikonal approximation (7.0 keV); Curve ④, FBA (7.0 keV).

those by other calculations *i.e.* FBA,[2] DWBA,[2] and CTMC.[3] In Fig. 3, the differential cross sections obtained by eikonal approximation are compared with those by the first-order Born approximation.

References

1) F. T. Chan, M. Leiber, G. Foster, and W. Williamson: Advances in Electronics and Electron Physics (eds. L. Marton and C. Marton), Vol. 49, Academic Press, New York, p. 134 (1979).
2) Q. Ma, X. Zhang, Z. Liu, Y. Liu, and T. Watanabe: *Phys. Rev. A*, **132**, 2645 (1985).
3) A. Ohsaki, T. Watanabe, K. Nakanishi, and K. Iguchi: *Phys. Rev. A*, **132**, 2460 (1985).

RIKEN Accel. Prog. Rep. 20 (1986)

III-2-8. Bound States of the dtμ System Formed in the Muon-Catalyzed Fusion Cycle

I. Shimamura and M. Iwai

Muon-catalyzed fusion is a kind of nuclear fusion that avoids heating plasma to very high temperature.[1] In this fusion two nuclei are brought close to each other not by thermal motion but by Coulomb binding just as in ordinary diatomic molecules. Therefore, muon-catalyzed fusion may be called the "cold" nuclear fusion.

When driven into the mixture of deuterium and tritium, muons are slowed down and eventually captured by deuterons or tritons to form muonic atoms dμ or tμ. Because the binding energy of the ground state of tμ is larger than that of dμ, the muons in the atoms dμ are transferred to tritons, resulting in tμ atoms. The tμ atoms are then captured by deuterons to form muonic molecules dtμ. This molecular system is similar to that of diatomic molecular ions, especially to H_2^+, in the sense that a negatively charged light particle orbits around two nuclei and forms a three-body bound state.

The two nuclei d and t in the muonic molecule have a finite probability of being found at the same position, this probability being proportional to the square of the vibrational wave function at $R=0$. Then the nuclear fusion reaction

$$d + t + \mu \rightarrow {}^4He + n + 17.6\ MeV + \mu$$

occurs in the muonic molecule, and the muon is released.

The released muon is again captured by either d or t and goes over into another cycle. According to experimental measurements of neutrons emitted after the d-t fusion, muons experience more than 150 cycles on the average before they decay. This is the muon-catalyzed fusion.

The muon emitted after nuclear fusion is sometimes bound by ^4He and can no more participate in the muon-catalyzed fusion cycle. The probability of this muon sticking to ^4He, the rate of formation of the dtμ molecules, and the rate of the d-t fusion in the dtμ system are the three main factors that determine the energy gain in the muon-catalyzed fusion. Knowledge of the bound-state wave functions of the dtμ molecule is crucial in theoretical understanding of the three main processes. This has motivated the present study.

Some accurate calculations of the dtμ bound states including only Coulomb interaction have been reported by other authors. It has been pointed out recently, however, that the nuclear force acting between d and t can increase the d-t fusion rate by as much as two orders of magnitude.[2] To settle this question one has to carry out detailed three-body calculations for the dtμ system taking both Coulomb and nuclear interactions into consideration at the same time.

We plan to apply a kind of R-matrix-eigenchannel theory to the bound states of the dtμ molecule. The whole configuration space of the three-body coordinates is divided into two regions, one for short distances between d and t where the nuclear force is predominant and the other for long d-t distances for which only Coulomb interaction exists. Some computational procedures have been formulated for smooth connection of bound-state wave functions in the two regions.

Before application of these procedures to detailed dtμ calculations, we have carried out model calculations to determine the best computational procedure. The model problem is a two-channel bound-state problem in which each element of the potential matrix consists of square wells and a square barrier. The procedure that appears the best for our purpose is the following.

We carry out inner-region calculations using the variational R-matrix theory to obtain the R matrix at the boundary between the inner and outer regions. Then we diagonalize the R matrix to define eigenchannels at the boundary. A trial function for the variational calculation for the outer region is constructed so that each eigenchannel function satisfies the logarithmic derivative determined from the inner-region calculation. With a small size of the inner region taken into consideration, the outer-region calculation is replaced by the whole-region calculation in which integrals are more easily obtained than in the outer region.

Success of this computational procedure for the model problem has led us to proceed to the real dtμ system.

References

1) L. I. Ponomarev: Atomic Physics X (eds. H. Narumi and Y. Shimamura), North-Holland, Amsterdam, p. 197 (1987).
2) Y. Haga, H. Kazama, Y. Akaishi, and H. Tanaka: Abstracts, Xth Int. Conf. Atom Phys., Tokyo, August 1986 (eds. H. Narumi and I. Shimamura), p. 92.

RIKEN Accel. Prog. Rep. 20 (1986)

III-2-9. Energy Levels of Muonic Molecular Ions

S. Hara

Recently, the energy levels for the bound states of muonic molecular hydrogen ion $(pp\mu)^+$ and of its isotopes attract much attention since they are related to muon-catalyzed fusion reaction.[1]

Carter[2] and Bhatia and Drachman[3] carried out variational calculations using Hylleraas type wavefunctions to describe three-body systems. Frolov and Efros[4,5] and Hu[6] adopted basis functions including exponential functions of the internuclear distance R, and showed that this type of basis functions gave rise to faster convergence. Vinitsky *et al.*[7] and Gocheva *et al.*[8] solved a set of coupled equations in the adiabatic representation of the three body problem, where the wavefunction for a muonic molecule is expanded in terms of a complete set of solutions of the adiabatic two center problem solved accurately in the spheroidal coordinate system. The spheroidal type wavefunction has once been used by Halpern[9] in variational calculations for the ground states of the homo-nuclear muonic molecules with total angular momentum $J=1$.

Here, we present the results of the variational calculations adopting the same form of the trial function as that used by Halpern[9] for the ground $(v=0)$ and the first excited $(v=1)$ states of the homo-nuclear muonic molecular hydrogen ions $(pp\mu)^+$, $(dd\mu)^+$, and $(tt\mu)^+$ with total angular momentum $J=0$ and 1. It is shown that the spheroidal-type trial function works well and, in fact, the best binding energies among those so far reported are obtained for several states.

The muon coordinates are expressed by the spheroidal variables $r(\xi, \eta, \phi)$:

$$\xi=(r_a+r_b)/R,\ \eta=(r_a-r_b)/R,$$

where r_a and r_b are the distances between the muon and the two nuclei a and b, respectively, R the distance between the nuclei, and ϕ the azimuthal angle around the internuclear vector $\boldsymbol{R}(R, \Theta, \Phi)$. Our trial function for homo-nuclear molecules is written in the form[9]

$$\Psi^{JM}=\sum_{m=-J}^{J}\sum_{i}A_i^{JM}\chi_i^m(R)\times f_i^m(\xi,\eta,\phi,R)D^J_{mM}(\Phi,\Theta,0) \quad (1)$$

where f_i^0 and f_i^{+1} are σ_g- and π_g-type molecular functions, respectively;

$$f_i^m=\{(\xi^2-1)(1-\eta^2)\}^{|m|/2}\xi^{b_i}\times\exp(-\beta_i R\xi)\eta^{c_i}\exp(im\phi) \quad (2)$$

D^J_{mM} represents the Wigner functions and $\chi_i^m(R)$ the functions of internuclear distance R:

$$\chi^{im}(R)=R^{a_i}\exp(-\alpha_i R) \quad (3)$$

Here a_i, b_i, and c_i are integers with c_i being even for the σ_g-state and odd for π_g-state; Σ_i stands for the summation over sets of parameters $(a_i, b_i, c_i, \alpha_i, \beta_i)$.

The explicit form of the matrix elements for the Hamiltonian operator of the three body system is given by Hunter *et al.*[10]

We have used following values for the physical constants; proton mass $M_p=1{,}836.151\,m_e$, deuteron mass $M_d=3{,}670.481\,m_e$, triton mass $M_t=5{,}496.899\,m_e$, and muon mass $M_\mu=206.7686\,m_e$, where m_e is the electron mass and $1\,\mathrm{Ry}=13.605804\,\mathrm{eV}$.

Two sets of orbital exponents (α_i, β_i) are taken for the σ_g-type basis function and one set for the π_g-type basis function. At first, these orbital exponents are optimized at a small number $(\leqq 120)$ of the basis set, for each (J, v) state of each isotope, by Powell's procedure.[11] The number of terms in the trial functions are then increased while checking the convergence of the results. The maximum number of terms is 380 for $(dd\mu)^+$ with $J=1$ and $v=1$, and 300 for other cases. These results, compared with other recent variational calculations in Table 1, are satisfactory even for the weakly bound state of $(dd\mu)^+$.

Table 1. Energy levels of muonic molecules in eV. A 380-term trial function is used for $(dd\mu)^+$ with $J=1$ and $v=1$, and a 300-term one for other cases. The binding energy of the former obtained by the 300-term trial function is 1.944 eV. (a), present; (b), Bhatia and Drachman[3]; (c), Frolov and Efros[4]; (d), Frolov and Efros.[5]

	(J, v)	(0,0)	(0,1)	(1,0)	(1,1)
$pp\mu^+$	(a)	−253.152		−107.203	
	(b)	−253.15		−107.26	
	(c)	−253.152		−107.266	
$dd\mu^+$	(a)	−325.073	−35.843	−226.670	−1.955
	(b)	−325.07	−35.815	−226.66	−1.862
	(c)	−325.072	−35.836	−226.682	−1.781
	(d)			−226.690	−1.971
$tt\mu^+$	(a)	−362.909	−83.770	−289.137	−45.198
	(b)	−362.90	−83.630	−289.12	−45.096
	(c)	−362.900	−83.722	−289.139	−45.194

References

1) L. Bracci and G. Fiorentini: *Phys. Rep.*, **86**, 169 (1982).
2) B. P. Carter: *Phys. Rev.*, **165**, 139 (1968).
3) A. K. Bhatia and R. J. Drachman: *Phys. Rev. A*, **30**, 2138 (1984).
4) A. M. Frolov and V. D. Efros: *Pis'ma Zh. Eksp. Teor. Fiz.*, **39**, 449 (1984).
5) A. M. Frolov and V. D. Efros: *J. Phys. B*, **18**, L265 (1985).
6) Chi-Yu Hu: *Phys. Rev. A*, **32**, 1245 (1985).
7) S. I. Vinitsky, V. S. Melezhik, L. I. Ponomarev, I. V. Puzynin, T. P. Puzynina, L. N. Somov, and N. F. Truskova: *Sov. Phys. JETP*, **52**, 353 (1980).
8) A. D. Gocheva, V. V. Gusev, V. S. Melezhik, L. I. Ponomarev, I. V. Puzynin, T. P. Puzynina, L. N. Somov, and S. I. Vinitsky: *Phys. Lett. B*, **153**, 349 (1985).
9) A. Halpern: *Phys. Rev. Lett.*, **13**, 660 (1964).
10) G. Hunter, B. F. Gray, and H. O. Prichard: *J. Chem. Phys.*, **45**, 3806 (1966).
11) M. J. D. Powell: Numerical Analysis; An Introduction (ed. J. Walsh), Academic Press, London and New York, p. 143 (1966).

RIKEN Accel. Prog. Rep. 20 (1986)

III-2-10. Measurement of Lifetimes of Highly Ionized Aluminium Atoms

S. Kohmoto, K. Ando, Y. Awaya, H. Kumagai, T. Tonuma, and S. Tsurubuchi

We have been carrying on lifetime measurements of Al-ions making use of RILAC.[1] Here, we report the preliminary results of lifetime measurements and analysis of the first excited state 2s2p ^{1}P of Be-like Al-ion. As shown in Fig. 1, there are some cascades which feed directly this state. Taking account of the effect of these direct cascades to the lifetime determination, we have measured and analyzed the decay curves of the primary decay as well as the direct cascades. Measurements were performed at an incident energy of 35.3 MeV. As for the details of the experimental procedure, see Ref. 1. Decay curves were measured for the following transitions: a) $2s^2\ ^1S$–$2s2p\ ^1P$ (332.78 Å); b) $2s2p\ ^1p$–$2s3s\ ^1S$ (63.13 Å); c) $2s2p\ ^1P$–$2p^2\ ^1D$ (670.06 Å) and d) $2s2p\ ^1P$–$2p^2\ ^1S$ (395.62 Å). The last one has a wavelength, which is very close to that (395.36 Å) of the transition between triplet states ($2s2p\ ^3P$–$2p^2\ ^3P$), and was excluded from the final analysis. The wavelength of the transition from $2s3d\ ^1D$ (59.11 Å) is slightly too short to measure with our monochromator.

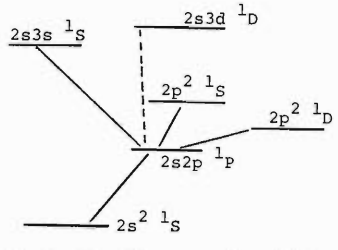

Fig. 1. Partial energy level diagram.

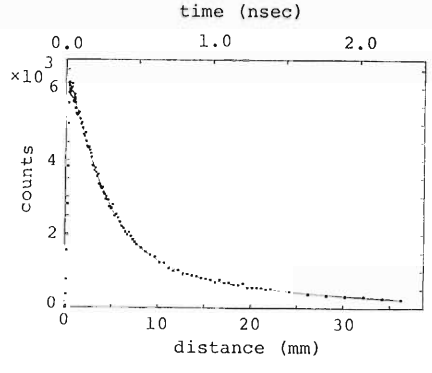

Fig. 2. Decay curves measured (dots) and calculated (line) for the transition: $2s^2\ ^1S$–$2s2p\ ^1P$ (332.78Å).

Table 1. Time constants obtained from the multi-exponential fit.

Transition	Time constant (ns^{-1})
a) $2s^2\ ^1S$–$2s2p\ ^1P$	0.84±0.04, 4.42±0.19
b) $2s2p\ ^1P$–$2s3s\ ^1S$	3.43±0.30, 42.5±4.2
c) $2s2p\ ^1P$–$2p^2\ ^1D$	0.95±0.06, 2.5±1.6
d) $2s2p\ ^1P$–$2p^2\ ^1S$ ($2s2p\ ^3P$–$2p^2\ ^3P$)	0.65±0.16, 4.43±0.05

First, measured decay curves were analyzed individually by use of the multi-exponential-fitting programme cord DISCRETE.[2] Examples of measured and calculated decay curves are shown in Fig. 2. The resultant time constants are summarized in Table 1. The primary decay curve is decomposed into three exponential terms; among them, the strongest is that with a time constant 4.42 ns^{-1} = 1/(0.226 ns).

Secondly, these time constants and intensities, as well as the experimental primary decay curve itself, were used as input data to the programme code CANDY[3] to extract the lifetime of the $2s2p\ ^1P$ state. Excluding the decay curve d) from the analysis because of the reason mentioned above, we obtain 0.192 ± 0.015 ns as the lifetime of the primary state. To see the effect of the cascades on the lifetime determination, additional calculations were performed. If we take account of only the cascading from $2s3s\ ^1S$, resulting lifetime of the primary state is larger than the quoted value by about 30%. If we consider only the cascading from $2p^2\ ^1D$, calculated lifetime is also larger by the same amount. The decay curve d) contains a strong term with a time constant 4.43 ns^{-1}, which is very close to that of the main component of the primary decay. Therefore, if we include the decay curve d) in the calculation, it gives an extremely short lifetime of about 0.05 ns.

More detailed analysis and comparison with theoretical works are now in progress.

References

1) S. Kohmoto, K. Ando, Y. Awaya, H. Kumagai, K. Sato, T. Tonuma, and S. Tsurubuchi: *RIKEN Accel. Prog. Rep.*, **19**, 65 (1985).
2) S. W. Provencher: *J. Chem. Phys.*, **64**, 2772 (1976).
3) L. Engstrom: *Nucl. Instrum. Methods*, **202**, 369 (1982).

RIKEN Accel. Prog. Rep. 20 (1986)

III-2-11. Identification of Al X 2p3d–2p4f Transition in Beam-Foil Spectrum

K. Ando, Y. Awaya, S. Kohmoto, H. Kumagai, T. Tonuma, and S. Tsurubuchi

In beam-foil spectra, spectral lines arising from the f levels are so strongly observed that the transition from other unknown f levels would be expected to appear in the spectra. In a Be-like ion of aluminum, the transitions from displaced levels of 2p4f to those of 2p3d have not yet been identified. A preliminary calculation of atomic energy levels using the Hartree-Fock approximation predicts that the transition array of 2p3d–2p4f will appear near strong lines of 2s3d–2s4f and a pattern of the array is also similar to the observed line group near 2s3d–2s4f lines.

The strongest line in the transition array comes from ^{3}G to ^{3}F levels, but the energy values for the lower states ^{3}F of this line are unknown. Therefore, energies of the ^{3}F states are estimated from an isoelectronic sequence.

Slater integrals for the upper levels of 2p4f configuration in the expressions of term energies are experimentally determined from the observed level energies by least-squares fit calculation. A pattern of the transition array with the fitted values of Slater integrals is shown in Fig. 1 together with the spectra obtained from the beam-foil experiment. The strongest line in this calculated spectrum did not fit to the experimental one, because the ^{3}F of the lower level is uncertain as mentioned before. Strong lines can be identified in the spectrum, but weak lines are not for lack of sufficient resolution.

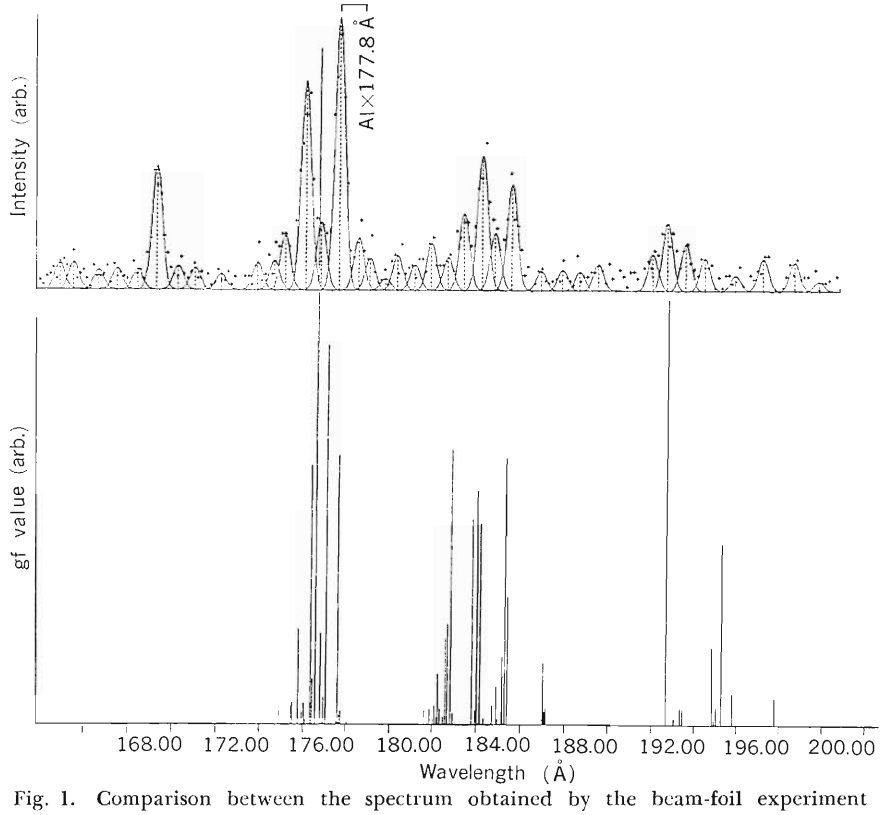

Fig. 1. Comparison between the spectrum obtained by the beam-foil experiment (upper) and the theoretically generated one of 2p3d–2p4f transition of Al X (lower).

RIKEN Accel. Prog. Rep. 20 (1986)

III-2-12. Dependence of the Effective K-Vacancy Production Cross Section on the Target Thickness and Projectile Charge State for Argon Ions Colliding with Carbon Foils

T. Mizogawa, Y. Awaya, T. Kambara, Y. Kanai, M. Kase,
H. Kumagai, P. H. Mokler, and K. Shima

Target-thickness dependent measurements of X-rays emitted in collisions between fast heavy ions and solid targets have been recognized to be an important technique for the study of the inner-shell processes of heavy ions in solids, where the relaxation times of excited states are not short enough compared with a mean collision interval.[1] Here we report our high-resolution X-ray measurements as a function of the target thickness and projectile charge state, and the importance of the effect of L-shell configuration on K-vacancy formation.

Target-thickness dependence of Ar K_α satellite intensities from Ar^{4+} ions colliding with thin C foils whose thicknesses were 2–100 $\mu g/cm^2$ was measured. For $Ar^{6+,12+,13+}$, the thickness dependence was measured over the region 2–20 $\mu g/cm^2$ where the L-shell nonequilibrium region is contained, and for Ar^{11+} only one (2.6 $\mu g/cm^2$) target was examined. The experimental setup and methods have been already reported.[2]

The results obtained with Ar^{4+} and Ar^{12+} are shown in Fig. 1. The vertical scale, $\sigma_x(n)$, is the mean X-ray production cross section for each satellite, *i.e.*, the X-ray yield divided by integrated ion current and target thickness (in arbitrary units). In the thickness region below ~ 10 $\mu g/cm^2$ quite different thickness dependence is observed between the results for Ar^{4+} and for Ar^{12+}. This difference is caused by the difference in the projectile L-shell configuration and in the course of the equilibration process of the L shell. Furthermore, we may conclude that the mean K-vacancy formation cross section itself changes with the depth through the change in Ar-ion distribution over the initial L-vacancy number as follows. For thin targets we may neglect the collisional quenching of the K vacancy (or electron capture from a target atom into the projectile K vacancy). Thus the K-vacancy formation cross section, averaged over the initial no K-vacancy, n L-vacancy states with the weights of their populations in solid, can be estimated by

$$\bar{\sigma}_v = \sum_n \bar{\sigma}_x(n)/\omega(n) \quad \text{(for thin limit)}$$

where $\omega(n)$ is the fluorescence yield for the n-th satellite. The value of the left-hand side of the above equation is calculated using a theoretical fluorescence yield for each defect configuration[3] and our data, and plotted against the C thickness in Fig. 2. If the collisional quenching is taken into account, the change in $\bar{\sigma}_v$ may be further enhanced.

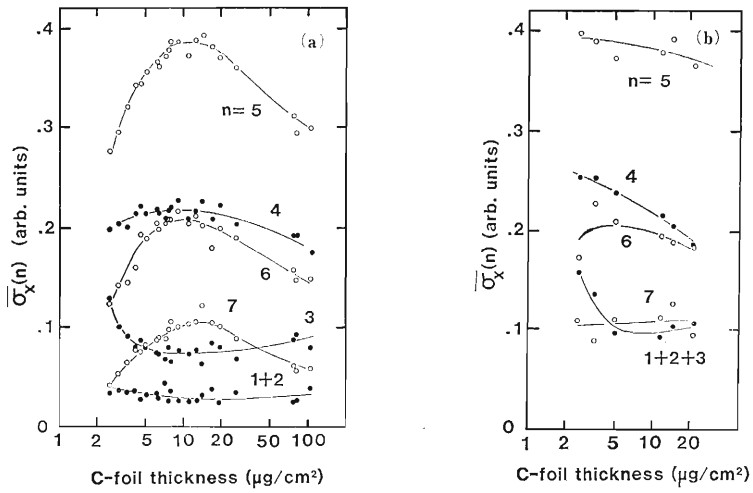

Fig. 1. (a), Mean Ar K_α X-ray production cross section for each satellite as a function of C-foil thickness. The projectile is Ar^{4+}. Solid lines are only for eye-guide; (b), Same as (a) except that the projectile is Ar^{12+}.

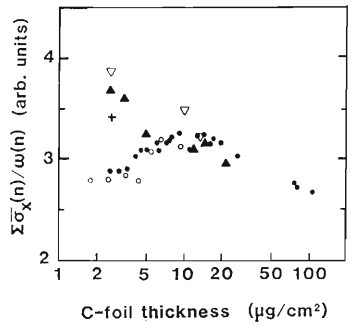

Fig. 2. $\sum_n \bar{\sigma}_x(n)/\omega(n)$ as a function of C-foil thickness. Closed circle, Ar^{4+}; open circle, Ar^{6+}; cross, Ar^{11+}; closed triangle, Ar^{12+}; open triangle, Ar^{13+}.

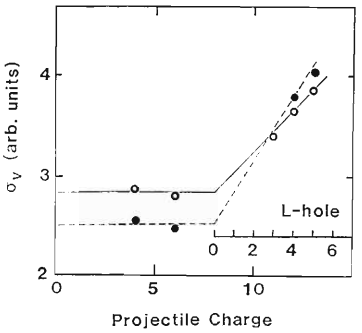

Fig. 3. Estimate for the K-vacancy production cross section. Horizontal scale is projectile charge state. Initial L-vacancy number is indicated at the bottom-right corner. Open circle, thinnest target (~2.6 μg/cm²); closed circle, extrapolated value to zero-thickness. Solid and dotted lines are drawn only for eye-guide.

In Fig. 3 the value at a thickness of ~ 2.6 μg/cm² and that extrapolated to zero-thickness are plotted as functions of the projectile charge state. The values for A^{4+} and Ar^{6+} are approximately equal, whereas $\bar{\sigma}_v$ for Ar^{11+}, Ar^{12+}, and Ar^{13+} seem to increase linearly with the charge. The onset of the increase is at 9+, where an L vacancy comes to exist. This increased part of $\bar{\sigma}_v$ can be attributed to the K-to-L excitation cross section, which is approximately 13 × (number of L vacancies) % of the background part (attributed to ionization cross section) in the zero-thickness limit.

In Fig. 4 $\bar{\sigma}_x(n)/\omega(n)$ extrapolated to the zero-thickness limit for Ar^{4+}, Ar^{12+}, and Ar^{13+} are plotted. This distribution is interpreted as the distribution over the L-shell configuration resulting from a single collision in which K and L electrons are ionized simultaneously, provided (1) the extrapolation is correct, (2) electron capture to L shell simultaneous with a K-vacancy formation collision is negligible, and (3) excitation from the K to L shell is negligible

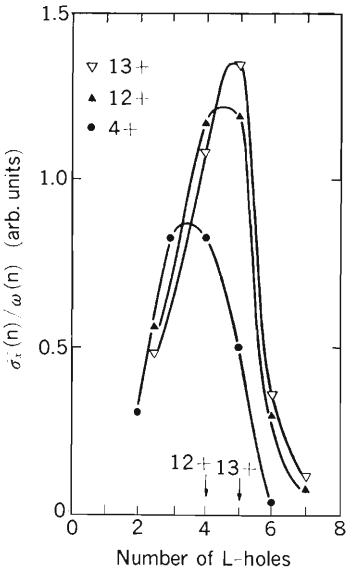

Fig. 4. Estimated cross sections for simultaneous formation of a K vacancy and n L vacancies. Projectile: Ar^{4+} (closed circle), Ar^{12+} (closed triangle), Ar^{13+} (open triangle). Initial L-vacancy number for each projectile charge is indicated by an arrow. The lines are drawn for eye-guide.

compared with K-shell ionization. In such a case it is curious, as seen in Fig. 4, that there are considerable intensities of $\bar{\sigma}_x(3)/\omega(3)$ for Ar^{12+} and $\bar{\sigma}_x(4)/\omega(4)$ for Ar^{13+}, of which the L-vacancy numbers (3 and 4) are less than those of the projections (4 and 5) by one. This fact may be another indication of the significance of the K-to-L excitation, for the assumptions (1) and (2) are considered to be not so bad.

for different projectile charge states diminishes, and most of them tend to decrease with the thickness.

Above ~ 20 μg/cm² the difference between $\bar{\sigma}_x(n)$ This decrease is caused by electron capture from a target atom to K vacancy of a projectile and the energy loss of the projectile. The data in this region could possibly be analyzed by some generalized version of 2- or 3-component model.[1] However, such an analysis seems to need too many adjustable parameters and uncertain assumptions. To enable us more straightforward approach, a series of subsidiary measurements are in progress.

References

1) See for example, H.-D. Betz, F. Bell, H. Panke, G. Kalkoffen, M. Welz, and D. Evers: *Phys. Rev. Lett.*, **33**, 807 (1974).
2) T. Mizogawa, Y. Awaya, T. Kambara, Y. Kanai, M. Kase, H. Kumagai, M. Mostafa Ismail, and K. Shima: *RIKEN Accel. Prog. Rep.*, **19**, 68 (1985).
3) C. P. Bhalla: *Phys. Rev. A*, **8**, 2877 (1973).

RIKEN Accel. Prog. Rep. 20 (1986)

III-2-13. Measurement of Impact Parameter Dependent Probabilities for K-Shell Ionization in Ar-Ca Collisions

R. Schuch,* Y. Awaya, T. Kambara, T. Mizogawa,
H. Kumagai, Y. Kanai, K. Shima, and H. Shibata

Impact parameter (b) dependence of target and projectile K-shell ionization probabilities ($P_k(b)$) were measured for collision system with Ar ions incident on a Ca target.

The measurement system was described previously.[1] An Ar beam of 40.6 MeV from the linac was collimated to 1 mm × 1 mm with a divergence of 0.02°. The target material of Ca was evaporated on a 2.5 μg/cm^2 C foil and positioned at 45° relative to the beam axis. The chickness of Ca ranged from 2 to 30 μg/cm^2. The characteristic X-rays from the projectile and target were detected by a 25.6 mm^2 Si(Li) detector placed at 90° to the beam direction at a distance of 16.5 mm. In the forward scattering direction scattered particles are counted by a parallel plate avalanche counter (PPAC) which covered the laboratory angles from 0.13° to 1.4°. The anode of the PPAC was devided into 16 rings for different scattering angles with an angular resolution of $\Delta\theta/\theta=0.05$. A coincidence circuit between the PPAC and Si(Li) allowed to measure K X-rays coincident with scattered particles. The total number of particles per ring of the PPAC was also measured and served as normalization for getting absolute K X-ray production probability $P_K(b)$. The purpose of the experiment was the investigation of solid effects on the $P_K(b)$.[2] For this, the absolute K-shell ionizaiton cross section was determined simultaneously by measuring Ar ions from elastic scattering at 20° to the beam with a surface barrier detector covered by a slit aperture.

The K-shell ionization probabilities for the target and projectile were obtained from the K X-ray production probability using fluorescence yields for neutral atoms and efficiency of the Si(Li) detector. The impact parameter b was obtained from the scattering angle calculated using a Bohr screened Coulomb potential.

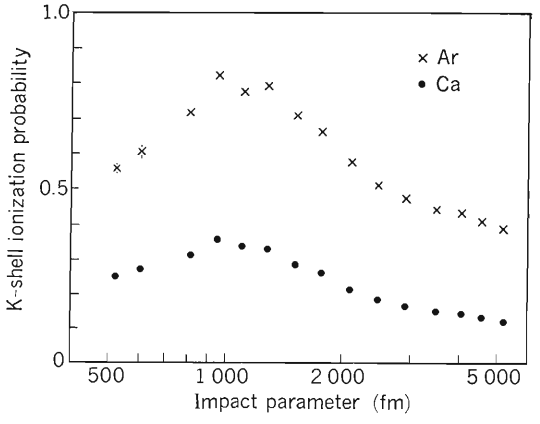

Fig. 1. Impact parameter dependence of the K-vacancy production probability ($P_K(b)$) for a 30 μg/cm^2 Ca target on a 2.5 μg/cm^2 carbon foil.

In Fig. 1 the values of $P_K(b)$ are shown for a Ca target with a thickness of 30 μg/cm^2. The error bars are from statistical errors only and the effect of the carbon backing is not corrected.

References

1) R. Schuch, Y. Awaya, T. Kambara, T. Mizogawa, Y. Kanai, H. Shibata, and K. Shima: *Z. Phys. D At. Mol. Clusters*, **4**, 339 (1987).
2) R. Schuch, G. Nolte, and H. Schmidt-Böcking: *Phys. Rev. A*, **22**, 1447 (1980).

* Department of Physics, Heidelberg University.

RIKEN Accel. Prog. Rep. 20 (1986)

III-2-14. Charge-State Distribution of Cr-Ions after Passage through a Carbon Foil

Y. Kanai, Y. Awaya, T. Kambara, M. Kase,
H. Kumagai, T. Mizogawa, and K. Shima

We started the present study on the charge-state distribution of heavy ions after collisions to investigate the heavy ions-target atom violent collisions. At the first stage, we measured the charge-state distributions of Cr-ions after passage through carbon foils with various thicknesses and at various scattering angles. The Cr^{5+}-ions were accelerated with RILAC to 1.23 MeV/amu and the charge state was analyzed with a beam analyzing magnet. The experimental setup is shown in Fig. 1. A projectile beam was collimated with two sets of four jaws slits. Scattering angles were determined by use of a movable aperture (1 mm in diameter) in front of a magnetic charge analyzer (AM magnet).[1] The distance between the target and the movable aperture was 870 mm. The charge-state distribution was measured with a parallel plate avalanche counter (PPAC) at the rear of the AM magnet.

Typical experimental results are shown in Fig. 2. With relatively thin targets (0.5 μg/cm^2 and 4 μg/cm^2), the charge state of the 0.33° scattered Cr-ions (broken lines in Fig. 2) is higher than that of the 0° scattered Cr-ions (solid lines). This result is consistent with an idea that a single violent collision (or a small impact-parameter collision, in which an impact parameter is as small as the K-shell radius of projectile ions) with a target atom increases the mean charge state of the ions almost to its equilibrium value in a thick target foil.[2] With a thick target (40 μg/cm^2), the charge state of the 0.33° scattered Cr-ions was determined from multiple large impact-parameter collisions after a single violent collision and the mean charge value of the 0.33° scattered Cr-ions was equal to that of the 0° scattered Cr-ions.

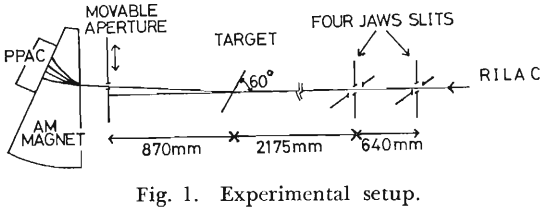

Fig. 1. Experimental setup.

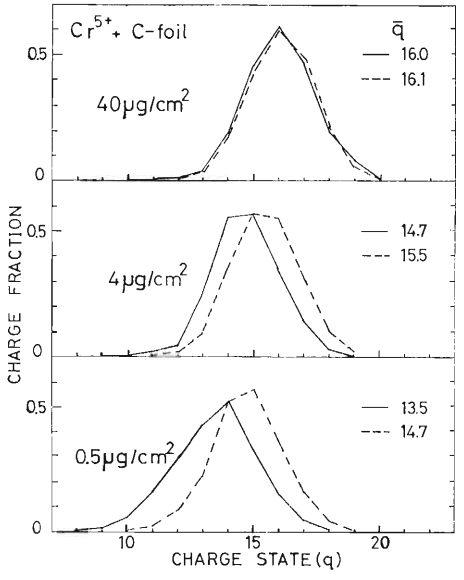

Fig. 2. Typical charge state distributions of Cr after passage through several thickness carbon foils. Solid lines are for the scattering angle 0°±0.06°, broken lines for the scattered angle 0.33°±0.06°. Mean charge ($\bar{q}$) of each condition is shown.

In a single violent collision, the probability of K-shell vacancy production accompanied with simultaneous multiple L-shall vacancy production must be large. For the study of the single violent collision, an experiment is necessary to be carried out by using a gas target, which is in preparation.

References

1) Y. Awaya, M. Kase, T. Kambara, H. Kumagai, Y. Kanai, T. Mizogawa, K. Shima, and T. Chiba: p. 132 in this report.
2) D. Maor, P. H. Mokler, D. Schull, and Z. Stachura: *Nucl. Instrum. Methods*, **194**, 377 (1982).

RIKEN Accel. Prog. Rep. 20 (1986)

III-2-15. Multiply-Charged Ions from SF_6 Produced by 1.05 MeV/amu Ar^{12+}-Ion Impact

H. Shibata, T. Tonuma, K. Baba,* S. H. Be, H. Kumagai, M. Kase, T. Kambara, I. Kohno, and H. Tawara

In previous Progress Reports, we presented some results on the observation of multiply-charged secondary ions produced from molecular gas targets, such as N_2, CH_4, and C_2H_2, by energetic Ar^{12+}-ion impact.[1,2] In these experiments, we found that the multiple ionization of target atoms is enhanced significantly and the peak positions in the mass-charge spectra of multiply-charged atomic ions resulting from molecular targets shift toward the high-energy side except for CH_4. This energy shift was attributed to the Coulomb potential of the multiply-charged molecular ions which were produced initially *via* charge transfer and inner-shell ionization and dissociated immediately into multiply-charged atomic ions. In this report, we present the result of the investigation for a much more complex molecular target, SF_6, in the collision with energetic Ar^{12+}-ions.

In order to understand the production mechanisms of multiply-charged atomic and molecular ions from molecular targets, we have used a mass-spectroscopic technique to separate various ions produced from SF_6 molecules with 1.05 MeV/amu Ar^{12+}-ions obtained from the linear accelerator (RILAC). The secondary ions produced are extracted under the influence of a relatively weak electric field (40 V/cm), accelerated up to 1,000 V, and then mass-charge analyzed with a double focusing magnet. A typical mass-charge spectrum of the ions from the SF_6 molecular target is shown in Fig. 1, which indicates the formation of singly- and multiply-charged sulfur (S^{i+}, up to $i=8$) and fluorine (F^{i+}, up to $i=5$) ions, in addition to dominant singly- (SF_n^+, $n=1$–6) and doubly-charged molecular ions (SF_n^{2+}, $n=1$–6). In Table 1 is shown a comparison of relative intensities of these atomic and molecular ions resulting from SF_6 molecules by Ar^{12+} impact with those by 500 eV electron impact obtained by Stanski and Adamczyk.[3]

From Fig. 1 and Table 1, we find the following features.

1) The relative production ratios of dissociated molecular and atomic ions are found to be enhanced in energetic heavy-ion impact, compared with those in electron impact. In particular, parent molecular ions (SF_6^+) are observed in heavy-ion impact, whereas their intensity was neglibibly small in electron impact. This singly-charged parent ion, therefore, is regarded as a metastable-state one.

2) In the case of singly-charged molecular ions (SF_n^+), the intensities of ions having odd numbers of n are stronger than those having even numbers. On the other hand, for doubly-charged molecular ions (SF_n^{2+}) the situation is opposite. This result

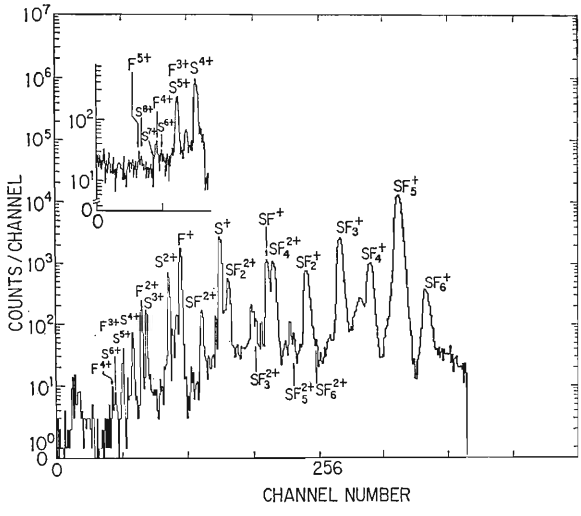

Fig. 1. A typical mass-charge spectrum of ions produced from SF_6 molecules in 1.05 MeV/amu Ar^{12+}-ion impact.

Table 1. Relative production ratios for various ions from SF_6 molecules in different charged-particle impacts.

Ion	Present study	500 eV e^- [3]	Ion	Present study	500 eV e^- [3]
SF_6^+	2.9 (−2)	small	S^+	2.1 (−1)	1.5 (−1)
SF_5^+	1.0	1.0	S^{2+}	5.4 (−2)	
SF_4^+	8.1 (−2)	1.1 (−1)	S^{3+}	1.4 (−2)	
SF_3^+	2.1 (−1)	3.4 (−1)	S^{4+}	5.9 (−3)	
SF_2^+	6.0 (−2)	7.3 (−2)	$S^{5+}+F^{3+}$	3.2 (−3)	
SF^+	9.0 (−2)	1.4 (−1)	S^{6+}	6.2 (−4)	
SF_6^{2+}	?		S^{7+}	small	
SF_5^{2+}	5.6 (−3)		S^{8+}	small	
SF_4^{2+}	8.4 (−2)	5.4 (−2)	F^+	1.4 (−1)	2.1 (−1)
SF_3^{2+}	9.7 (−3)		F^{2+}	1.9 (−2)	
SF_2^{2+}	4.4 (−2)	5.3 (−2)	F^{4+}	6.2 (−4)	
SF^{2+}	1.3 (−2)		F^{5+}	small	

* ULVAC Corporation.

is the same as that in the electron impact and seems to be due to the electronic structure of molecular ions. Further analysis is in progress.

References

1) H. Tawara, T. Tonuma, S. H. Be, H. Shibata, H. Kumagai, M. Kase, T. Kambara, and I. Kohno: *RIKEN Accel. Prog. Rep.*, **18**, 82 (1984).
2) H. Shibata, T. Tonuma, K. Baba, S. H. Be, H. Kumagai, M. Kase, T. Kambara, I. Kohno, and H. Tawara: *RIKEN Accel. Prog. Rep.*, **19**, 77 (1985).
3) T. Stanski and B. Adamczyk: *Int. J. Mass Spectrom. Ion Phys.*, **46**, 31 (1983).

RIKEN Accel. Prog. Rep. 20 (1986)

III-2-16. Production of Multiple-Charged Ions from CO and CO_2 Molecules in Energetic Heavy-Ion Impact

T. Matsuo, T. Tonuma, M. Kase, T. Kambara,
H. Kumagai, I. Kohno, and H. Tawara

We have conducted systematic investigations on the production of multiple-charged ions from molecular gas targets by energetic heavy-ion impact. In a previous measurement for an N_2 target, it was found that the peak positions of multiple-charged N^{i+}-ions in mass/charge (m/q) spectra shift toward a high-energy side, compared with corresponding Ar^{i+} peak positions from an Ar target, and additionally, this peak shift increases with increasing charge state of ions produced.[1] These findings strongly suggest that such initial kinetic energies of recoil ions are provided through the Coulomb potential of multiple-charged molecular ions produced first in collision. Peak shifts in m/q spectra have also been observed for other molecular targets such as NO, N_2O, and NO_2.

To obtain further insight into the mechanisms and systematics of the production of multiple-charged ions from molecular targets, we have used a mass-spectroscopic technique to separate various ions from CO and CO_2 molecules produced in Ar^{12+} impact. The projectile Ar^{12+}-ions were accelerated to 1.05 MeV/amu by the linear accelerator (RILAC).

Figure 1 shows m/q spectra of multiple-charged atomic ions produced from CO and CO_2 targets, together with those from Ar and CH_4 targets for comparison. It should be noted that the peaks observed with CO and CO_2 targets are shifted in position and broadened, compared with those with Ar and CH_4 targets. As reported previously,[2] the peaks of C^{i+}-ions from CH_4 show neither shift in position nor broadening compared with those of corresponding Ar^{i+}-ions which gain only a small amount of recoil energy.

In Fig. 2 are shown the observed energy shifts

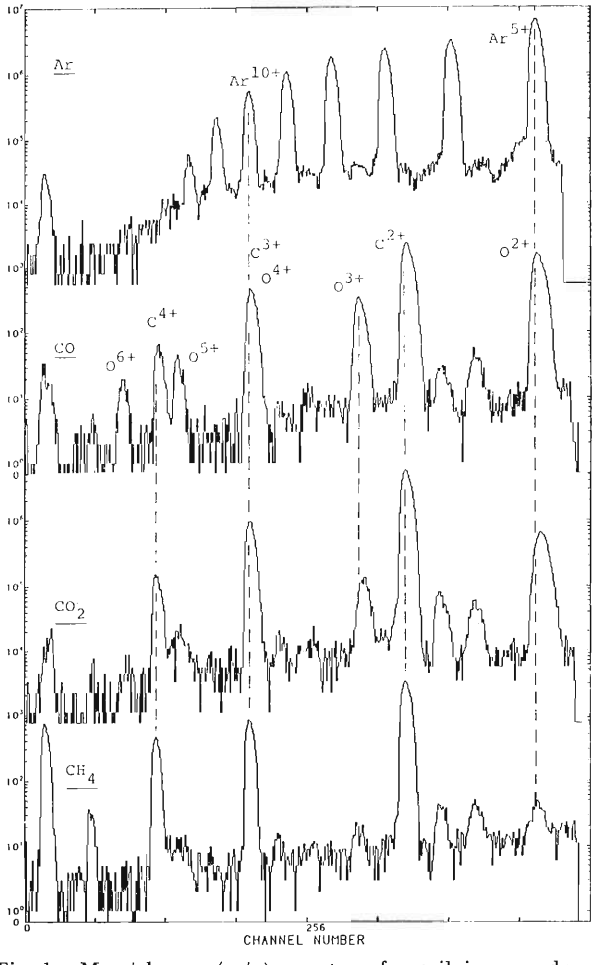

Fig. 1. Mass/charge (m/q) spectra of recoil ions produced from molecular targets CO and CO_2 by 1.05 MeV/amu Ar^{12+} ion impact. Vertical dashed-lines are drawn to show the shift of peak positions of the multiple-charged ions from CO and CO_2 targets with respect to those from Ar and CH_4 targets.

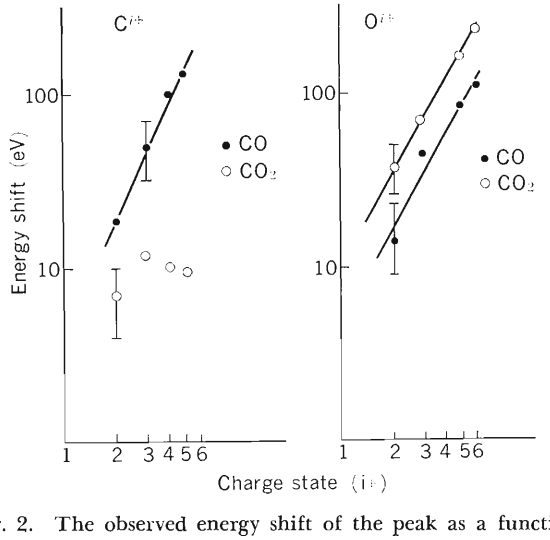

Fig. 2. The observed energy shift of the peak as a function of the charge state of recoil ions produced.

of multiple-charged atomic ions produced from CO and CO_2 targets. It is to be noted that the energy shift of C^{i+}- and O^{i+}-ions increases roughly as the square of the charge of ions in both CO and CO_2 molecules. This suggests that such kinetic energies are provided through the Coulomb explosion of highly ionized molecular ions produced first in the impact. With a CO molecule, the intensities of O^{i+}- and C^{i+}-ions ($i=1$–3) are nearly equal, and the energy shift are also roughly equal for C^{i+}- and O^{i+}-ions with the same charge within the limits of the present energy resolution. These results are well explained from the consideration that the dissociation of multiple-charged CO^{i+} molecular ions plays a dominant role in production of multiple-charged atomic ions. With a CO_2 molecule, the energy shift and peak broadening of C^{i+}-ion are very small; those of O^{i+}-ions are considerably greater than with a CO molecule. These results can also be explained by assuming that the multiple-charged atomic ions originate in multiple-charged molecular ions CO_2^{i+} which dissociate immediately after their production through the process:

$$CO_2^{i+} \longrightarrow O^{k+} + C^{m+} + O^{n+} \qquad (1)$$

In this dissociation, the oxygen ions receive strong Coulomb repulsion, whereas the carbon ion, located at the center of two dissociating oxygen ions, can obtain practically no kinetic energy. Thus, the present results show the importance of the atomic configuration of parent molecules in the dissociation of multiple-charged molecular ions produced by energetic heavy-ion impact. This finding is expected from the dynamic property of collisions; the collision time ($\sim 10^{-17}$ s) and electron rearrangement time ($\sim 10^{-16}$–10^{-17} s) are much shorter than the dissociation time of molecules ($\sim 10^{-14}$ s).

The recoiled molecular ion spectroscopy (REMIS) in heavy-ion impact is found powerful in studying the dynamic and structure of highly charged molecular ions.

References

1) H. Tawara, T. Tonuma, H. Shibata, M. Kase, T. Kambara, S. H. Be, H. Kumagai, and I. Kohno: *Phys. Rev. A*, **33**, 1385 (1986).
2) H. Tawara, T. Tonuma, H. Shibata, S. H. Be, H. Kumagai, M. Kase, T. Kambara, and I. Kohno: *Z. Phys. D, At. Mol. Clus.*, **2**, 239 (1986).

RIKEN Accel. Prog. Rep. 20 (1986)

III-2-17. Energy Spectra of Secondary Electrons Emitted from Al by Heavy-Ion Impact

A. Koyama, O. Benka, Y. Sasa, and M. Uda

Energy distributions of secondary electrons (SEs) emitted backward from thick Al target were measured in the SE energy region below 170 eV for the impact of He^{2+}, N^{6+}, Ne^{8+}, and Ar^{12+} which were selected with a magnetic analyser. These ions had the same velocities corresponding to 1.1 MeV/amu. The experimental setout was the same as described in a previous report.[1]

The ratios of SE yields for these heavy-ion impacts to those for He^{2+} impacts, $R(E)$, are shown in Fig. 1, which indicates that 1) above the energy of the Al L-VV Auger electrons, 65 eV, the SE yields for the N^{6+}, Ne^{8+}, and Ar^{12+} impacts are given by q^2-scaling, 2) the SE yields decrease from the values given by the q^2-scaling to those given by the stopping power scaling in the energy region from 20 to 60 eV, and 3) the SE yields become much smaller than those expected from the stopping power scaling in the energy region below 20 eV, where such a decrease is more pronounced when SE energies become lower and electric charges of projectiles becomes higher; for example, $R_{Ar,He}(E) \cong 5$, $R_{Ne,He}(E) \cong 4$, and $R_{N,He}(E) \cong 2.4$ at low energies near 0 eV. The ratios of these values, 5 : 4 : 2.4, are nearly equal to those of the respective charges of these projectiles, 12 : 8 : 6. Thus at low energies, the yields of SEs for heavy projectiles with equilibrium charges are approximately given by q^1-scaling.

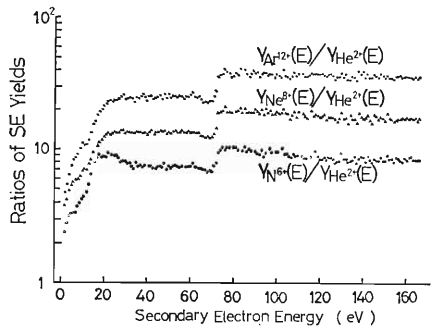

Fig. 1. Ratios of yields of secondary electrons emitted from Al by heavy-ion impacts to those induced by He^{2+} impacts, $R_{Ar,He}(E) = Y_{Ar^{12+}}(E)/Y_{He^{2+}}(E)$; $R_{Ne,He}(E) = Y_{Ne^{8+}}(E)/Y_{He^{2+}}(E)$; $R_{N,He}(E) = Y_{N^{6+}}(E)/Y_{He^{2+}}(E)$.

The electric charges selected here are nearly equal to the respective equilibrium ones at this velocity. Therefore, their charges after having penetrated a thin surface layer whose thickness is comparable to the SE escaping depth (~50 Å) will be the same as their original charges. Thus, such pronounced decrease in the yields of low energy SEs for projectiles with high charges compared with those expected from q^2-scaling is not considered to be due to the decrease in their charges after penetrating a target. The decrease can be explained in terms that for distant collisions the screening of the charge of projectiles due to the polarization of target electrons becomes effective.[2]

References

1) A. Koyama, Y. Sasa, and M. Uda: *RIKEN Accel. Prog. Rep.*, **18**, 86 (1984).
2) A. Koyama, O. Benka, Y. Sasa, and M. Uda: *Phys. Rev. B*, **34**, 8150 (1986).

RIKEN Accel. Prog. Rep. 20 (1986)

III-2-18. Z_2-Dependence of Energy of Loss-Electrons Backscattered from Metal Targets

A. Koyama, O. Benka, H. Ishikawa, Y. Sasa, and M. Uda

It is known that for gas targets, the energy of loss-electrons is equal to that of electrons having a velocity the same as that of projectiles from which the loss-electrons are stripped. Therefore, the energy of the peak of loss-electrons is independent of elements of gas targets.

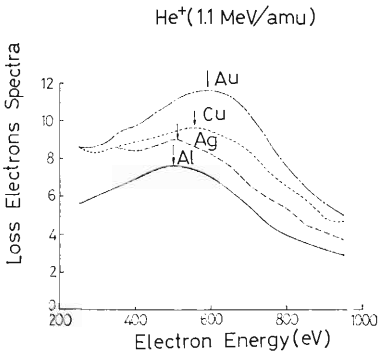

Fig. 1. Spectra of backscattered loss-electrons stripped from He^+-ions. Energy of He^+-ions is 4.4 MeV. The incident angle of the beam is 53° relative to the normal to the surface of a target. Only electrons emitted normal to the surface were energy-analyzed and detected.

On the contrary, for metal targets, target dependence was found for the energy of backscattered loss-electrons. The apparatus was described elsewhere.[1] He^+-ion beam was incident on a target with an angle of 53° relative to the normal to the target. Only those electrons backscattered normal to the surface of the target were energy analyzed and detected. Figure 1 shows the energy spectra of loss-electrons for the targets of Au, Ag, Cu, and Al. The energy of the He^+-ions was kept to be 4.4 MeV throughout the measurements. From this energy spectra it is concluded that the shorter the mean free-path for electron-loss, the higher the energy of loss-electrons. This implies that the Z_2-dependence of the energy of loss-electrons backscattered from metal targets comes from the Z_2-dependence of energy loss of these electrons inside the target before their escape from the surface.

Reference

1) A. Koyama, O. Benka, Y. Sasa, and M. Uda: *Nucl. Instrum. Methods B*, **13**, 637 (1986).

RIKEN Accel. Prog. Rep. 20 (1986)

III-2-19. Towards Production of Low Energy Pions and Muons Using Heavy-Ion Reactions

K. Ishida, T. Matsuzaki, and K. Nagamine

It has been known that nucleus-nucleus collisions can produce pions with the energy per nucleon significantly lower than the nucleon-nucleon threshold (280 MeV).

Pions and muons are very useful for the materials research. Positive pions and muons are considered to be light isotopes of hydrogen. Using μSR (muon spin rotation, relaxation and resonance) and channeling techniques, their states in matters, their diffusion properties, and the local magnetic field at the muon site have been extensively studied. Negative pions and muons can be considered to be heavy electrons which form mesonic atoms and molecules. Negative pions and muons are used for the hyperfine studies of the mesonic atoms, and their energy shifts have been used to determine nuclear charge radii. The negative muon also behaves as a catalyst for d-t fusion by forming a $(dt\mu)$ mesonic molecule. Here, we are going to estimate the production rate of low-energy pions and muons using the heavy-ion beams available at RIKEN Ring Cyclotron and their possible applications to material sciences.

In the pion/muon experiments mentioned above, the requirement of low energy muons has increased for the study of small samples and low density gases. For this purpose, positive surface muons have been extensively used so far. The surface muons are produced as follows. At first, positive pions are produced by nuclear collisions; some of the pions lose their energy and stop in the target and decay into muons with an energy of 4.12 MeV. The muons lose their energy in the target, but some fraction of them can emerge from the surface of the target.

Much lower-energy muons are required for the study of surface physics, and for the study of elementary particle physics in which muons or muoniums are stopped in vacuum. Recently, one of us and his collaborators succeeded in producing thermal energy muoniums by stopping muons in a hot tungsten foil;[1] they are now trying to ionize the muoniums by a three-photon laser resonance to produce thermal muons. In this report, we propose an alternative method to obtain low-energy muon beams directly by using heavy-ion reactions.

There are several meson factories in the world, which can produce very intense beams of pions or muons (typically 10^7 muons/s). All the factories use proton beams of high intensities (more than 100 μA) and energies above 500 MeV. Those high yields of pions and muons cannot be usually exceeded by using accelerators that deliver relatively low-current and low-energy heavy-ions.

Let us compare the case of a heavy-ion beam of 135 MeV/nucleon with that of a proton beam of 590 MeV on a carbon target.

		Range (g/cm^2)	Cross section (μb)	Typical intensity (particle μA)
135 MeV/u	^{12}C	6	0.2	<1
590 MeV	p	200	10	100

The cross sections were estimated from the literature.[2-4] Since the range of the proton is much larger than that of the heavy ion, the total pion production rate for a thick target becomes very large. A total yield is not essential, however, for the production of low-energy particles, since the pions and muons produced mainly near the surface can contribute to the low-energy component. An important factor is the yield of pion and muon per unit length, which is determined by the product of a cross section and a beam intensity. Even so the high intensity proton beam remains advantageous by three to four orders.

We will mention two points where the heavy-ion collisions may have an advantage over the proton-nucleus reactions. First, the negative pion production is enhanced by n-n interaction. Secondly, the yield of pions and muons is large at low energy; the pion energy distribution obtained by the heavy-ion reaction shows a peak around 10 MeV,[2] while the proton-induced reaction has a peak around 50 MeV. The low-energy pions produced are stopped more easily in a target than high-energy pions and decay near the surface to produce surface muons. Thus the conversion efficiency from pion to surface muon may be increased.

We show the Monte-Carlo calculation on the 135 MeV/u carbon nucleus injected into a carbon target of 1,000 mg/cm^2 in thickness. The normal of the target was 60° to the incident beam. The parameters used were:

Range energy relation for ^{12}C	$0.8E^{1.77}$
Total pion cross section	610 $(E/50)^{6.5}$ μb
Pion angular distribution	almost isotropic in C.M. system
Pion energy distribution (C.M. system)	
(^{12}C)	$P(E_\pi)=0.04\exp(-E_\pi/25)$
(proton, 0–50 MeV)	$P(E_\pi)=E_\pi/2,500$
Energy range relation for pion	$R=12E_\pi^{1.77}$
Range energy relation for muon	$R=15E_\mu^{1.77}$

where energies are expressed in MeV or MeV/u, and the ranges are in mg/cm^2. The efficiency of each step was

	^{12}C	Proton
Pion production	1.0×10^{-5}	5×10^{-4}
Pion stops in the target	0.39	0.09
Muon come out from the target	0.04	0.04

Figure 1 shows the depth distribution of the position calculated for the pion production and the pion stopping. The pion production decreases with depth owing to the energy loss of the projectile. The distribution of pion stopping positions is a little inhomogeneous, indicating the effect of low-energy pions with short ranges, but not so large as to compensate the low cross section. Thus, we might say that we cannot match the meson factories by a usual way. In Fig. 2 are shown the calculated position, angle, and energy distribution of muons emerging the target. The number of the muons increases almost linearly with muon's energy as expected from almost homogeneous pion stopping.

We have two choices in collecting and transporting a muon beam to a sample. One is a conventional magnetic beam transport line which can deliver both surface muons and pions. If the angular acceptance of 10^{-3} and momentum acceptance of $\pm 5\%$ are assumed, the number of muons will be 100/s, which surely depends on the beam intensity.

Another is an electric beam transport, which can handle muon beams with energies up to 100 keV with high efficiency. No one has tried so far to produce such a low-energy muon beam by this method. Since the fraction of muons below 10 keV will be 6×10^{-6}, the muon yield is calculated to be 1/s if we assume the angular acceptance of 0.1. This yield is not too low, since 10^4 muons would be enough to determine the muon polarization in a sample to a statistical level of 5%. The muons with these energy ranges may be useful for the studies of the layers near the surface. By selecting the energy of muons with a step of 10 keV, we can probe the surface layers with a resolution of 0.01 mg/cm^2.

The latter beam transport system may also be used to transport the secondary radioactive nuclei produced in heavy-ion reactions. We may have a chance to study a sample using both the muon probes and the other nuclear probes by hyperfine interaction techniques.

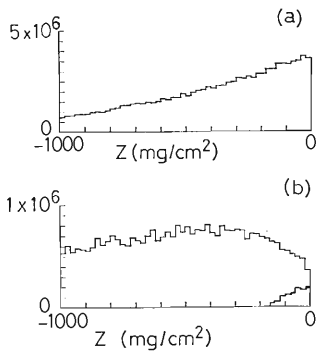

Fig. 1. Calculated depth distribution of the position for pion production (a) and pion stopping (b) for 135 MeV/u ^{12}C in a carbon target. The fraction of pions producing surface muons are also shown with a lower line in Fig. (b). Vertical scales are in pions/s per bin for a primary 1 μA beam.

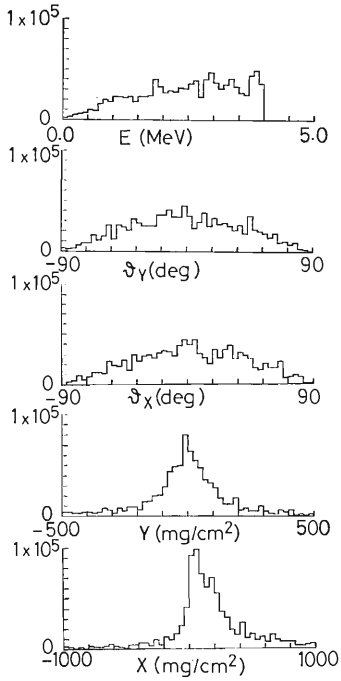

Fig. 2. Calculated position (X, Y), angle (θ_x, θ_y), and energy distribution of the muons emerging the target. Vertical scales are in muons/s per bin for a primary 1 μA beam.

References

1) A. P. Mills, Jr., J. Imazato, S. Saitoh, A. Uedono, Y. Kawashima, and K. Nagamine: *Phys. Rev. Lett.*, **56**, 1463 (1986); K. Nagamine and A. P. Mills, Jr.: *Sci. Papers I.P.C.R.*, **80**, 67 (1986).
2) J. Stachel, P. Braun-Munzinger, R. H. Freifelder, P. Paul, S. Sen, P. DeYoung, P. H. Zhang, T. C. Awes, F. E. Obenshain, F. Plasil, G. R. Young, P. Fox, and R. Ronningen: *Phys. Rev. C*, **33**, 1420 (1986).
3) C. Guet and M. Prakash: *Nucl. Phys. A*, **428**, 119c (1984).
4) J. F. Crawford, M. Daum, G. H. Eaton, R. Forsch, J. Garzon, H. Hirschmann, P.-R. Kettle, J. W. McCulloch, and E. Steiner: *Helv. Phys. Acta*, **53**, 497 (1980).

RIKEN Accel. Prog. Rep. 20 (1986)

III-2-20. Coulomb-Excitation ^{73}Ge Mössbauer Study Using a New-Type Piezoelectric Transducer

N. Sakai, F. Ambe, and K. Asai

This note reports the preliminary result on a Coulomb-excitation Mössbauer spectrum studied with the $^{40}Ar^{4+}$ beam of RILAC.

The ^{73}Ge nucleus is one of the less-used Mössbauer nuclei because of the following reasons: (1) The 13.3 keV first excited state has a large internal conversion coefficient in the order of 1,000, and a long lifetime (2.95 μs) which results in an extremely narrow Mössbauer line. (2) As shown in Fig. 1, the Mössbauer transition between the 66.7 keV state and the ground state does not occur because of the long lifetime (0.5 s) of this excited state. (3) The 68.7 keV state is not populated in the electron capture of ^{73}As, and only populated to a small extent in the β^- decay of ^{73}Ga. Thus, it is advantageous to study the ^{73}Ge Mössbauer effect by using the Coulomb-excitation method which can excite the 68.7 keV state.

A fixed natural Ge-metal target was exposed to a beam of 50 MeV $^{40}Ar^{4+}$ ions with a beam current of around 150 nA. The Coulomb-excited Ge nuclei were scattered and stopped in the Ge-metal target itself. The absorber used was powdered GeO_2 with a hexagonal structure. Both target and absorber were cooled with liquid N_2. A NaI(Tl) scintillation counter was used to detect 68.7 keV γ-rays.

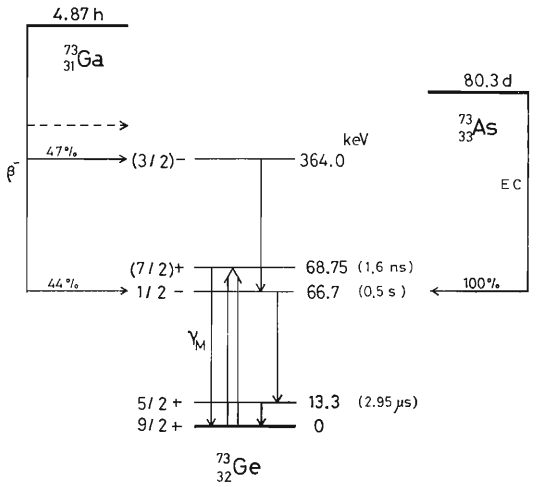

Fig. 1. Energy level scheme for the ^{73}Ge nucleus.

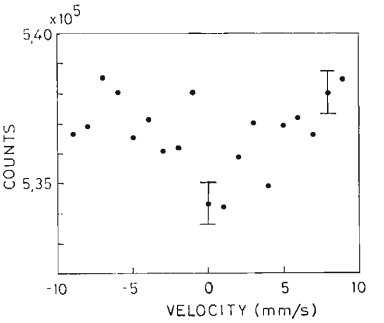

Fig. 2. Mössbauer spectrum of an GeO_2 absorber with a Ge-metal target. Both are cooled with liquid N_2.

The Mössbauer transducer employed was composed of a pair of piezoelectric bimorph actuators. This new-type transducer was proposed previously[1] and developed by one of the authors (N.S.). It was found that the actuators were useful not only at room temperature but also below 80 K.

The observed Mössbauer spectrum is shown in Fig. 2. A single absorption dip was observed. The full-width at half maximum is about 5 mm/s, and the depth of the absorption peak is only about 0.5% of the counts of off-resonance. These observations are consistent with the values reported in Ref. 2. A much better Mössbauer spectrum will be obtained by using a target of enriched ^{73}Ge on Cr-metal and an absorber of GeO_2 with a tetragonal structure. These materials are known[2] to induce a larger recoil-free fraction than the present case. Such improvements are now in progress together with an application of the piezoelectric actuators at liquid He temperature.

References

1) N. Sakai, F. Ambe, and K. Asai: *RIKEN Accel. Prog. Rep.*, **19**, 159 (1985).
2) G. Czjzek, J. L. C. Ford, Jr., J. C. Love, F. E. Obenshain, and H. H. F. Wegener: *Phys. Rev.*, **174**, 331 (1968).

RIKEN Accel. Prog. Rep. 20 (1986)

III-2-21. TDPAC Study on (^{111}In→) ^{111}Cd Ions in Silver Phosphate

S. Ambe, K. Asai, T. Okada, and F. Ambe

In non-conducting materials, the after-effects associated with the EC decay of ^{111}In are usually so large that the amplitudes of the time differential perturbed angular correlation (TDPAC) of ^{111}Cd γ-rays are attenuated strongly at low temperature. We showed that such spectra can be interpreted, in some cases, on the basis of after-effects-free spectra obtained at high temperature.[1-3] This report describes a study on the after-effects of the ^{111}In→ ^{111}Cd decay in silver phosphate (Ag_3PO_4).

Silver phosphate was prepared by neutralization of a dilute nitric acid solution of silver nitrate-sodium dihydrogen phosphate with sodium hydroxide. The X-ray powder pattern of the product showed no additional peaks due to impurities or other phases. About 65 mg of silver phosphate powder was developed over an area of 2 cm^2 on an aluminum plate and covered with an aluminum foil of 80 μm in thickness. The target assembly was irradiated with 30 MeV α-particles accelerated by the cyclotron, the back of the aluminum plate being cooled with water. The silver phosphate sample was blackened during irradiation due to radiation effects of the α-particles. Annealing at 800°C for 1.5 h in air recovered the intrinsic orange-yellow color of the compound. The TDPAC spectra of the annealed sample were recorded at various temperatures with NaI scintillation counters connected to a conventional fast-slow coincidence circuit.

Typical TDPAC spectra obtained are shown in Fig. 1. The spectra above 510°C showed little attenuation, indicating that ^{111}Cd ions are in nearly cubic environments in this temperature region. Between 300 and 450°C, no reproducible results were obtained. In some cases, TDPAC patterns characteristic of relaxation were recorded. In another, a periodic oscillation due to an electric quadrupolar interaction was observed superposed on a relaxation pattern. The results obtained at room temperature and at liquid nitrogen temperature suggest distributed static quadrupolar interactions as is usual for ^{111}In in insulators.

The crystal structure of silver phosphate at room temperature is cubic; each silver atom has four oxygen atoms as nearest neighbors and two silver atoms form a pair in the structure. The site symmetry of silver atoms is not cubic; silver phosphate

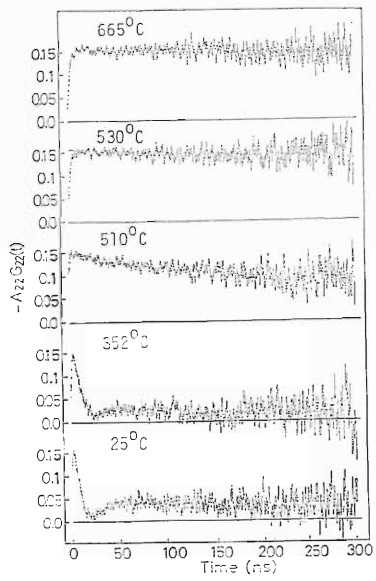

Fig. 1. Time-differential perturbed angular correlation of (^{111}In →) ^{111}Cd in silver phosphate.

undergoes phase transition at 520°C. The high-temperature form is also cubic, but its structure has not yet been determined.

It is interesting to note that the ^{111}Cd ions arising from ^{111}In in silver phosphate are in nearly cubic environments at 510°C, though the site symmetry of silver atoms in the matrix is not cubic at this temperature. The observation indicates that the (^{111}In→)^{111}Cd atoms do not simply occupy the sites of silver atoms. One possibility is that $^{111}Cd^{2+}$ ions replace pair of Ag^+ ions in the structure. The poor reproducibility of the TDPAC spectra in the temperature region 300–450°C suggests that diluted impurities or imperfections produced in the samples during TDPAC measurement play an important role in relaxation process. Further work is in progress to improve the reproducibility of the TDPAC spectra.

References

1) K. Asai, F. Ambe, S. Ambe, and H. Sekizawa: *J. Phys. Soc. Jpn.*, **53**, 4109 (1984).
2) F. Ambe, K. Asai, S. Ambe, T. Okada, and H. Sekizawa: *Hyp. Int.*, **29**, 1197 (1986).
3) K. Asai, F. Ambe, S. Ambe, T. Okada, and H. Sekizawa: *Hyp. Int.*, **34**, in press.

RIKEN Accel. Prog. Rep. 20 (1986)

III-2-22. An Investigation on the After-Effects of $^{111}In(\rightarrow {}^{111}Cd)$ EC Decay in α-Fe_2O_3

K. Asai, F. Ambe, S. Ambe, T. Okada, and H. Sekizawa

In our previous papers,[1,2] we reported studies on the after-effects of $^{111}In(\rightarrow {}^{111}Cd)$ EC decay in α-Fe_2O_3 above room temperature. This year, we measured the time differential perturbed angular correlation (TDPAC) in the same system far below room temperature, intending to deduce the hyperfine parameters for the electronic excited states produced by EC decay and their lifetimes. Sample preparation and experimental set-up were the same as described in Refs. 1 and 2.

The TDPAC spectrum $A_{22}\cdot G_{22}(t)$ observed at 85 K is shown in Fig. 1. If there were no disturbance around ^{111}Cd such as the after-effects of the EC decay, it would be reasonably assumed on the basis of the crystal and magnetic structure of α-Fe_2O_3[3] that the hyperfine interaction is unique, the EFG is axially symmetric, and the angle θ between the directions of H_{hf} and the principal axis of EFG is 0°.

First, we analyzed the spectrum on these assumptions. The values of the Larmor angular frequency ω_L and the quadrupolar angular frequency ω_Q were obtained by the least-squares fitting of the experimental data with a semi-empirical formula

$$A_{22}\cdot G_{22}(t) = C_1 \times G_{22}(t)_{uniq} + C_2$$

in the region $t \geqq 50$ ns, where C_1 and C_2 were adjustable parameters and $G_{22}(t)_{uniq}$ is the perturbation factor for an ensemble of randomly oriented microcrystals with a unique static interaction.[4] If the above assumptions hold exactly, C_1 is equal to A_{22}, C_2 vanishes, and the observed spectrum is reproduced in the whole time-range. The best fitted

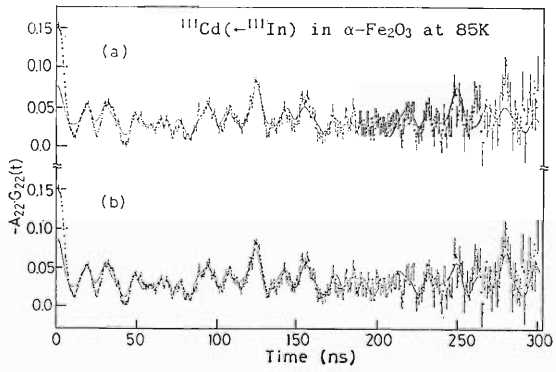

Fig. 1. TDPAC coefficient $A_{22}\cdot G_{22}(t)$ of the $^{111}Cd(\leftarrow {}^{111}In)$ γ-γ correlation in α-Fe_2O_3 at 85 K. The solid curves represent the fitted values of $C_1 \times G_{22}(t)_{uniq} + C_2$ (a): with the assumption of axially symmetric EFG with the principal axis parallel to the direction of H_{hf}, and (b): without the assumption in (a).

parameters and the χ^2-factors are tabulated in Table 1, and the fitted curves are shown in Fig. 1(a). As can be seen from Table 1 and in Fig. 1(a), the spectrum is reproduced rather well in the region $t > 50$ ns, but the absolute value of the amplitude, C_1, of $G_{22}(t)_{uniq}$ is considerably smaller than that of $A_{22}(\fallingdotseq -0.15)$, and the spectrum is not reproduced well in the region with small t.

Next, we analyzed the spectrum by the same procedure without restrictions on the angle θ and the asymmetry parameter, η, of EFG. The results are shown in Table 1 and Fig. 1(b). Compared with the analysis described above (Fig. 1(a)), the fitting for $t > 50$ ns is improved to some extent. On the

Table 1. Fitted parameters obtained on the assumptions described in the text. The parameters at 293 K[a] are tabulated for comparison.

Temperature (K)	$\omega_L \times 10^{-7}$ (rad/s)	$\omega_Q \times 10^{-7}$ (rad/s)	η	θ (deg.)	$-C_1$	$-C_2$	χ^2 [b]	Assumption
85	10.0	2.52	0.0	0.	0.051	0.024	1.63	A
85	9.9	2.54	0.05	6.	0.064	0.020	1.35	B
293	10.7	2.54[c]	0.0	90.	0.134	0.002	1.39	C
293	10.7	2.54	0.0	90.	0.111	0.009	1.32	D

a) taken from /1/. b) in a time-region $t \geqq 50$ ns. c) value of ω_{Q0}.
A, a unique static interaction with an axially symmetric EFG along <111>; B, a unique static interaction without the restriction in A; C, a Gaussian distribution of ω_Q with a width $\Delta\omega_Q/\omega_{Q0}=8\%$; D, a Gaussian distribution of θ with a width $\Delta\theta=6°$.

contrary, the misfit for $t < 50$ ns is not improved essentially. The value of ω_L is a little smaller than the one above the Morin temperature T_M, due to the difference in the contributions of the dipolar magnetic fields between the temperatures below and above T_M. On the other hand, the value of ω_Q agrees well with those at temperatures above T_M.

In the previous works,[1,2] we were able to reproduce the spectra at and above room temperature in the whole time-range by assuming a Gaussian distribution in one of the hyperfine parameters: θ around 90°, or ω_Q around ω_{Q0}. We tried to analyze the present spectrum below T_M by the same procedure, but were unable to obtain any satisfactory results.

The present results of analyses show that the TDPAC spectrum at 85 K has two distinctive features ascribed to the after-effects of $^{111}In(\rightarrow {}^{111}Cd)$ EC decay. (1) A strong decay is observed in the amplitude of the perturbation factor $G_{22}(t)$ in an initial period of about 50 ns. (2) The perturbation factor $G_{22}(t)$ could be analyzed fairly well by assuming a unique static interaction after that period, though the hyperfine parameters are slightly but definitely different from those expected from the crystal symmetry.

The ^{111}Cd ions arising from ^{111}In are in highly excited electronic states as a result of the Auger process following the EC decay. The excited states relax to the ground states through many electronic intermediate states with lifetimes spreading over a wide time range. It is proposed that there are two dominant groups in the intermediate states affecting the TDPAC spectrum, corresponding to the two features mentioned above. One group is the states populated in an early stage of the electronic relaxation with relatively high energy. The other group is some low-lying electronic excited states populated in the last stage of the electronic relaxation. A more detailed discussion and a likely model for ions in these low-lying excited states will be described elsewhere.[5]

References

1) K. Asai, F. Ambe, S. Ambe, and H. Sekizawa: *J. Phys. Soc. Jpn.*, **53**, 4109 (1984).
2) F. Ambe, K. Asai, S. Ambe, T. Okada, and H. Sekizawa: *Hyp. Int.*, **29**, 1197 (1986).
3) R. Lefever: Landolt-Börnstein New Series III, Vol. 12b, Springer-Verlag, Berlin-Heidelberg-New York, p. 7 (1980).
4) H. Frauenfelder and R. M. Steffen: Alpha-, Beta- and Gamma-Ray Spectroscopy (ed. K. Siegbahn), Vol. 2, North-Holland, Amsterdam, p. 1111 (1964).
5) K. Asai, F. Ambe, S. Ambe, T. Okada, and H. Sekizawa: *Hyp. Int.*, **34**, in press.

RIKEN Accel. Prog. Rep. 20 (1986)

III-2-23. Supertransferred Hyperfine Magnetic Fields at ^{111}Cd($\leftarrow{}^{111}$In) in Ferrimagnetic Oxides with Spinel Structure

K. Asai, T. Okada, and H. Sekizawa

We have been systematically investigating H_{STHF} at Cd^{2+} in ferrimagnetic oxides with the spinel structure by means of the time differential perturbed angular correlation (TDPAC) of 171–245 keV cascade γ-rays emitted from ^{111}Cd($\leftarrow{}^{111}$In). In spinel oxides, the parent nuclei ^{111}In occupy the A (tetrahedral) sites (denoted by ^{111}In(A)) and the daughter ^{111}Cd(A) feel H_{STHF} transferred from the magnetic ions on the nearest neighbor B (octahedral) sites. In a previous study on Fe_3O_4,[1] we obtained an average of the contributions of Fe^{3+}(B) and Fe^{2+}(B) ions to H_{STHF} at ^{111}Cd(A), but could not separate out each contribution. This year, we measured H_{STHF} at ^{111}Cd(A) in solid solutions $Fe_{3-x}M_xO_4$ (M=Ni or Co), where M^{2+} ions occupy the B sites. The purpose of this study is to elucidate the contributions of individual B site magnetic ions to the observed H_{STHF}.

Sample preparation, experimental set-up, and the definition of the directional anisotropy, $R(t)$, of the angular correlation were the same as described previously.[1] Representative spectra of the anisotropies, $R(t)$, for the specimens $Fe_{3-x}Ni_xO_4$ are shown in Fig. 1. The frequency spectra of these $R(t)$ give the distribution of $2\omega_L$ including its sign. From the sign of ω_L, the direction of $H_\perp$ was found to be parallel to the externally applied magnetic field H_{ext}. The distributions of H_{STHF}, corrected for H_{ext} (small compared with H_{STHF}), are shown in Fig. 2.

In magnetic oxides with the spinel structure, H_{STHF}

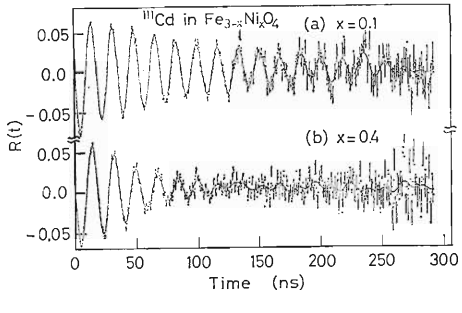

Fig. 1. Directional anisotropies, $R(t)$, of the coincident counts in $Fe_{3-x}Ni_xO_4$ at room temperature. The solid curves are fitted ones with the distributions of H_{STHF} shown in Fig. 2.

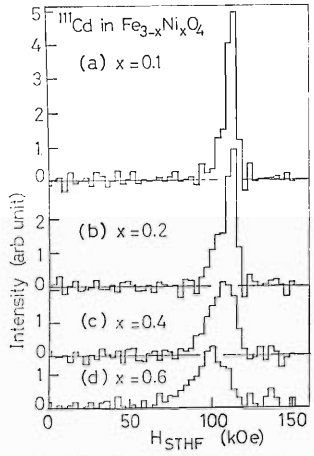

Fig. 2. Distributions of H_{STHF} at $^{111}Cd^{2+}$(A) in $Fe_{3-x}Ni_xO_4$.

at a nucleus on the A site can be regarded as the sum of the contributions of twelve magnetic ions on the nearest neighbor B sites. In the present paper, we denote the field from the j-th ion N_j(B) by $h(\leftarrow N_j)$. The composition dependence of H_{STHF} shown in Fig. 2 indicates that the field $h(\leftarrow Ni^{2+})$ is fairly smaller than $h(\leftarrow Fe^{2+})$. The overall shapes of the distributions of H_{STHF} were reproduced successfully by assuming binomial distributions of Ni and Fe ions on the nearest neighbor B sites, *i.e.*,

$$P(H_{STHF};\, x) \propto \sum_{\xi=1}^{12} {}_{12}C_\xi (1-x/2)^{12-\xi}(x/2)^\xi \cdot \delta(H_{STHF}-H_\xi)$$

$$H_\xi = (12-\xi)\cdot h(\leftarrow Fe) + \xi \cdot h(\leftarrow Ni^{2+})$$

where, ξ is the occupation number of Ni^{2+} ions on the nearest neighbor B sites, ${}_{12}C_\xi$ the binomial coefficient, $x/2$ the ratio of Ni^{2+} ions to the total magnetic ions on the B sites, and H_ξ the hyperfine magnetic field at ^{111}Cd when the occupation number of Ni^{2+} is ξ. The field $h(\leftarrow Fe)$ is an average of $h(\leftarrow Fe^{3+})$ and $h(\leftarrow Fe_3^{+})$ and will be a function of Ni^{2+} content, x. Similar analyses were performed also on the data in the system $Fe_{3-x}Co_xO_4$.

Figure 3(a) shows the $h(\leftarrow Fe)$ in both the systems, and Fig. 3(b) shows $h(\leftarrow Ni^{2+})$ and $h(\leftarrow Co^{2+})$, as functions of the composition. The abscissa of Fig. 3(a) is scaled linear in the ratio, $\mathcal{R}$, of Fe^{3+}(B) to the total Fe ions on the B sites. The ratio

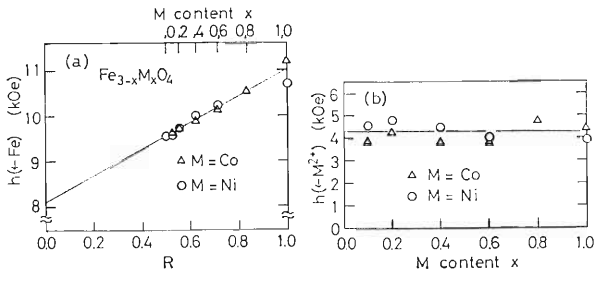

Fig. 3. Composition dependence of the hyperfine magnetic fields, $h(\leftarrow N_j)$, at Cd^{2+}(A) transferred from the individual magnetic ions, N_j(B), in $Fe_{3-x}M_xO_4$ with M=Co or Ni: (a) N_j=Fe. The quantity $\mathcal{R}$ is the ratio of F^{3+}(B) ions to the total Fe ions on the B sites, (b) N_j=Co, and =Ni.

$\mathcal{R}$ is related to the Ni content, x, as $\mathcal{R}=1/(2-x)$. It can be seen in Fig. 3(a) that $h(\leftarrow Fe)$ increases linearly with $\mathcal{R}$; this means that $h(\leftarrow Fe)$ is the weighted average of $h(\leftarrow Fe^{2+})$ and $h(\leftarrow Fe^{3+})$, *i.e.*,

$$h(\leftarrow Fe)=(1-\mathcal{R})\cdot h(\leftarrow Fe^{2+})+\mathcal{R}\cdot h(\leftarrow Fe^{3+})$$

The derived values of $h(\leftarrow Fe^{2+})$, $h(\leftarrow Fe^{3+})$, $h(\leftarrow Ni^{2+})$, and $h(\leftarrow Co^{2+})$ are 8, 11, 4, and 4 kOe, respectively; it should be noted that they are almost independent of the composition.

The above analyses are allowed only when Fe^{2+} and Fe^{3+} ions are undistinguishable due to the fast electron hopping among them as realized in the cases with small x. Even if the above condition does not hold, these analyses are justified as an approximation because the difference between $h(\leftarrow Fe^{2+})$ and $h(\leftarrow Fe^{3+})$ is considerably smaller than that between $h(\leftarrow Fe)$ and $h(\leftarrow M^{2+})$.

Detailed discussion on the values of h's obtained in the present study will be given elsewhere. Two brief comments are given on these values in comparison with previous works.[2,3]

The H_{STHF} at $Cd^{2+}(\leftarrow {}^{111m}Cd)$ in rocksalt-type oxides, CoO and NiO, were measured at 4.2 K.[2] The values of $h(\leftarrow Co^{2+})$ and $h(\leftarrow Ni^{2+})$ in these oxides calculated from their data are 29 and 32 kOe, respectively, which are 7 or 8 times as large as the present values in spinel-type oxides. These differences suggest a strong dependence of H_{STHF} on the angles of Cd^{2+}–O–M^{2+} (M=Co or Ni) bonds; they are $\fallingdotseq$120° in spinels and $\fallingdotseq$180° in rocksalts. The angle 120° is not favorable as compared with 180° for the spin transfer from the magnetic ions to the Cd ions *via* the $2p_\sigma$ orbitals of the oxygen ions. This transfer is one of the dominant mechanisms to produce H_{STHF}.

The second comment is about the comparison of H_{STHF} at Cd^{2+} and at In^{3+}. Both ions nominally have the same electronic configuration. From NMR results on H_{STHF} at In^{3+}(A) in $NiFe_2O_4$, the values of $h(In^{3+}\leftarrow Fe^{3+})$ and $h(In^{3+}\leftarrow Ni^{2+})$ were estimated to be 16 and 7.3 kOe, respectively.[3] These values are a few tens of percents larger than the present ones of $h(Cd^{2+}\leftarrow Fe^{3+})$ or $h(Cd^{2+}\leftarrow Ni^{2+})$. This fact shows that In^{3+}–O^{2-} bond is more covalent than Cd^{2+}–O^{2-} bond in this oxide, *i.e.*, the amount of the transfer of oxygen valence electrons, which are partially polarized by the B site magnetic ions, is larger in the former than in the latter. The same tendency that the covalency increases with the valence states of the cations is also observed between Sn^{4+}–O^{2-} and Cd^{2+}–O^{2-} bonds in α-Fe_2O_3.[4]

References

1) K. Asai, T. Okada, and H. Sekizawa: *J. Phys. Soc. Jpn.*, **54**, 4325 (1985).
2) H. H. Rinneberg and D. A. Shirley: *Phys. Rev. B*, **13**, 2138 (1976).
3) Y. Miyahara and S. Iida: *J. Phys. Soc. Jpn.*, **37**, 1248 (1974).
4) F. Ambe, K. Asai, S. Ambe, T. Okada, and H. Sekizawa: *Hyp. Int.*, **29**, 1197 (1986).

RIKEN Accel. Prog. Rep. 20 (1986)

III-2-24. Simulation Experiment on Carbon Coating of the First Wall of a Fusion Machine

Y. Sakamoto, H. Amemiya, Y. Ishibe, S. Kato, K. Okazaki,
H. Oyama, K. Yano, K. Akaishi,* N. Noda,* S. Amemiya,**
H. Minagawa,*** T. Hino,*** T. Yamashina, and S. Matsumoto****

Metal impurities in Tokamak plasma have satisfactorily been decreased by first wall carbon coating which the TEXTOR group has systematically developed.[1-4] The carbon coating is carried out by glow (FR-glow) discharge in hydrocarbon/hydrogen gas mixture. This needs a complicated treatment to decrease hydrogen recycling and change over hydrogen isotopes.

We constructed a plasma device (RIKEN ECR-2), which enable us to simulate a carbon coating process in fusion machines or to develop new methods for producing carbon films by creating various coating conditions on the base of ECR plasma.

Figure 1 shows a schematic diagram of the ECR-2 device.[5] A stainless steel tube with a diameter of 10 cm and a length of 1 m is placed in electromagnetic coils (EM) which provide an ECR magnetic field corresponding to 2.45 GHz microwave supplied from a magnetron source (MS). Three turbomolecular pumping systems (TMP + RP) evacuate a discharge tube, an Auger electron spectroanalysing system (AES) and a quadrupole mass analyzer with an orifice (QMA). We use a mixed gas of CH_4 and H_2, which are introduced through mass flow controllers. In most cases samples are fixed on a sample holder (SH) isolated electrically from the discharge chamber and can be applied direct current (DC) or radiofrequency (RF) voltage. The sample temperature can be raised with a heater (H) and is monitored with a thermocouple (TC). IG is an ionization gauge. The AES is used when *in situ* observation is necessary.

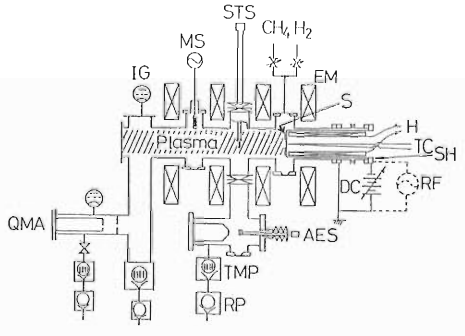

Fig. 1. Schematic diagram of RIKEN ECR-2: Carbon coating simulation device.

Plasma electrons with temperature of several eV collide with and dissociate gas molecules, for example,

$$2CH_4 + e \rightarrow 2CH_3 + H_2 + e$$

We can observe by use of the QMA system an increase in hydrogen partial pressure and a decrease in that of methane due to plasma. An example is given in Fig. 2, where the initial partial pressures are set identical (2×10^{-2} Pa) for hydrogen and methane. As we know each gas flow rate, simple calculations based on the mass conservation law give us the average H/C ratio in a deposited film. This estimation on the average H/C ratio is useful, because we can know the *in situ* dependence of the H/C ratio on the parameters of discharge. As an example we show the dependence of the H/C ratio on the microwave power in Fig. 3, where the total gas pressure is 6×10^{-2} Pa and the methane concentration is 25%.

Important characteristics obtained are shown in Table 1. We obtained the accurate H/C value from analysis using nuclear reactions ($^1H(^{15}N, \alpha\gamma)^{12}C$) and ($^{12}C(d, p)^{13}C$).

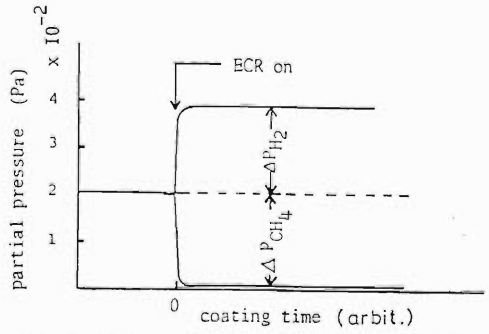

Fig. 2. Typical change in partial pressures of CH_4 and H_2 due to plasma production.

* PPL, Kyoto University.
** Faculty of Engineering, Nagoya University.
*** Faculty of Engineering, Hokkaido University.
**** National Institute for Research in Inorganic Materials.

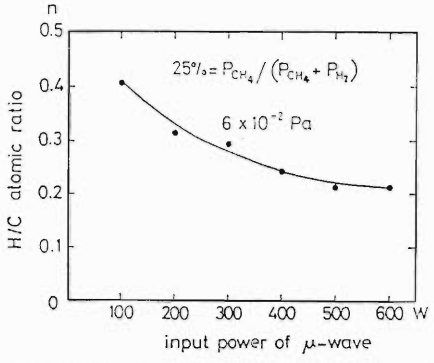

Fig. 3. An example of dependence of the mean H/C ratio in carbon film obtained from CH_4 and H_2 partial pressure measurements.

Table 1. Characteristics of carbon films.

Item	Condition	Estimation
Structure	$CH_4/H_2=1/1$	RHEED amorphous
	$p_{total}=0.01$-0.1 Pa	FTIR amorphous
	$P_{micro}=200$ W	
	$V_{bias}=0$-100 V	
Hardness	$V_{bias}=0$ V	870 kg/mm^2
Specific weight		3.0 g/cm^3
Hydrogen Concentration	$V_{bias}=0$ V ($V_{space}=+30$ V)	NRA 0.26
	$V_{bias}=-100$ V_{dc}	NRA 0.22
	$V_{bias}=-150$ V_{dc}	NRA 0.19
	$V_{bias}=175$ V_{rf} (amplitude)	NRA 0.16

Summarizing the items in Table 1, we can say (1) carbon films formed are high density, amorphous, and comparatively hard ones and (2), to decrease the hydrogen concentration, high energy ion bombardment is effective. By the way, a typical value of H/C in TEXTOR RG carbonization is about 0.4.[1)]

Carbonization has a possibility to deposit harmful

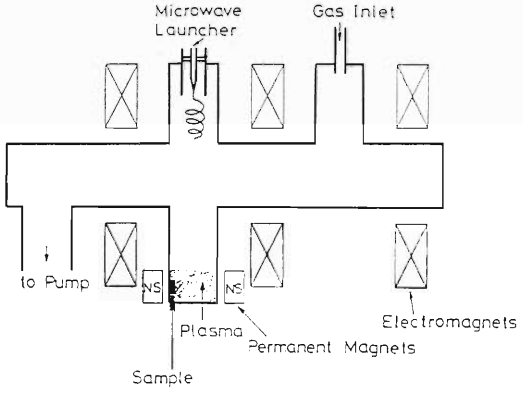

Fig. 4. Creation of local cleaning ECR plasma in a magnetic field by permanent magnets.

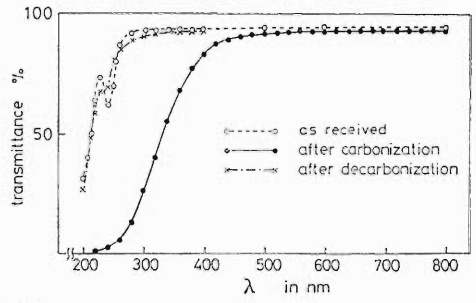

Fig. 5. Change in light transmittance of a quartz plate by carbonization and decarbonization.

films, for example, on observation windows, rf heating windows or high-voltage insulators. We succeeded in removing a carbon film (amorphours, on a substrate of quartz) by pure hydrogen ECR plasma produced locally in a magnetic field by the use of permanent magnets.[6)] Figure 4 shows the local plasma production in a branch of the discharge tube shown in Fig. 1. Figure 5 shows the results of light transmittance measurements on quartz samples "as received," "after carbonization" and "after decarbonization." The data show that we can utilize a local pure hydrogen plasma to remove a local harmful carbon film.

References

1) J. Winter: Invited paper presented at the 7th Int. Conf. PSI, May 5–9, 1986, Princeton, USA, *J. Nucl. Mater.*, **145/147** (1987) (in press).
2) N. Noda, Y. Ogawa, K. Masai, I. Ogawa, R. Ando, S. Hirokura, E. Kato, Y. Taniguchi, T. Akiyama, Y. Kawasumi, K. Kawahata, K. Toi, T. Watari, S. Tanahashi, K. Matsuoka, and Y. Hamada: *Jpn. J. Appl. Phys.*, **25**, L397 (1986).
3) W. P. Poschenrieder, G. Fußmann, G. v. Gierke, F. Mast, H. Niedermeyer, J. Roth, F. Söldner, K. Steinmetz, H. Verbeek, F. Wagner, G. Becker, H. S. Bosch, H. Brocken, K. Büchel, A. Eberhagen, D. Eckhartt, O. Gehre, J. Gernhardt, E. Glock, O. Gruber, G. Haas, J. Hofmann, A. Izvozchikov, G. Janeschitz, M. Kaufmann, F. Karger, M. Keilhacker, O. Klüber, M. Kornherr, K. Lackner, R. S. Lang, M. Lenoci, F. Leuterer, G. Lisitano, H. M. Mayer, K. McCormick, D. Meisel, V. Mertens, H. Murmann, J. N. Noterdaeme, A. Pietrzyk, H. Rapp, H. Riedler, H. Röhr, F. Ryter, W. Sandmann, F. Schneider, C. Setzensack, G. Siller, P. Smeulders, E. Speth, K.-H. Steuer, O. Vollmer, F. Wesner, and D. Zasche: Proc. 13th Eur. Conf. Controlled Fusion and Plasma Heating, Schliersec, April 14–18 (1986).
4) J. P. Coad, K. Behringer, and K. J. Dietz: *J. Nucl. Mater.*, **145/147** (1987) (in press).
5) Y. Ishibe, H. Ogawa, K. Okazaki, K. Yano, Y. Sakamoto, N. Noda, and Y. Hori: *Shinku*, **29**, 385 (1986) (in Japanese).
6) Y. Sakamoto, Y. Ishibe, K. Okazaki, and H. Oyama: *Jpn. J. Appl. Phys.*, **25**, 764 (1986).

RIKEN Accel. Prog. Rep. 20 (1986)

III-2-25. Measurement of Hydrogen Isotope in Carbon Films Produced by ECR Plasmas

K. Yano, H. Oyama, Y. Sakamoto, M. Yanokura,
I. Kohno, and K. Sugiyama

In thermonuclear fusion carbon coating of the first wall, which is in contact with high temperature plasmas, has attracted special interest, because metal impurities in plasmas are drastically decreased by this technique. Since a low content of hydrogen in the carbon film is required, we carried out carbonization experiments using an ECR plasma device (RIKEN ECR-2)[1] to simulate *in-situ* carbon coating of large fusion devices. The amount of hydrogen isotope in carbon films deposited was investigated mainly by an ERD (elastic recoil detection) method.

A gas mixture ($CH_4 + H_2$ or D_2) was used as a source gas. A microwave power of 200 W was usually launched through a helical antenna for production of plasmas. The electron density and electron temperature of a typical plasma were $\sim 10^{10}$ cm^3 and ~ 5 eV, respectively.

The amount of hydrogen isotope was measured by the ERD method using an Ar^{4+} beam of 50 MeV obtained from RILAC facilities.[2] The thickness

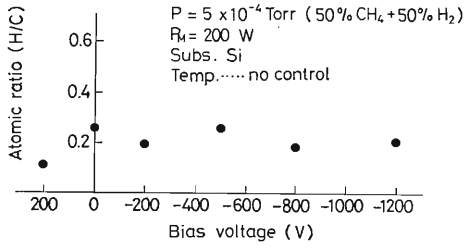

Fig. 1. Dependence of impinging hydrocarbon ions on the atomic ratio H/C.

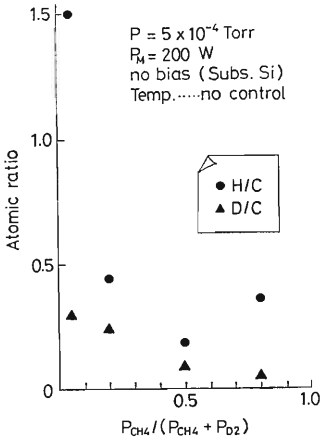

Fig. 2. Atomic ratios, H/C and D/C in carbon films deposited in CH_4+D_2 plasmas.

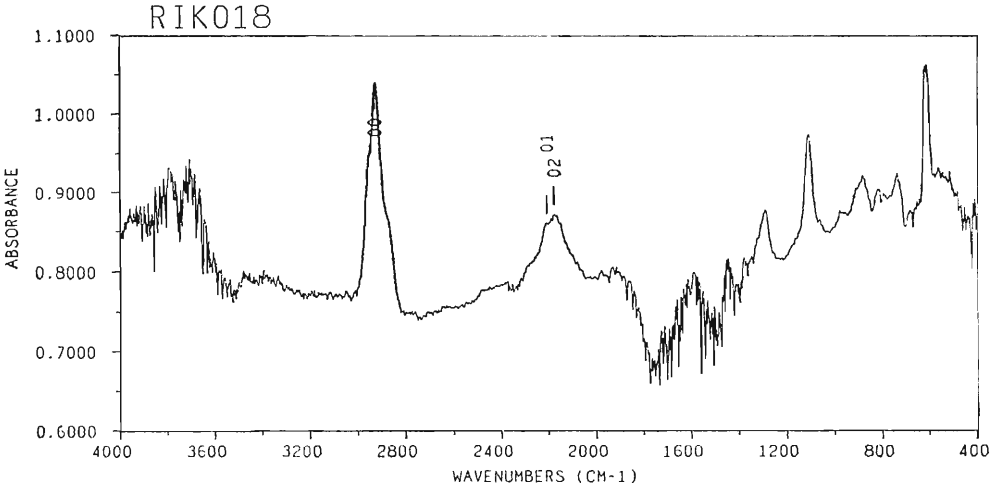

Fig. 3. Infrared absorption spectrum of carbon films deposited in CH_4+D_2 plasmas ($P_{D_2}/P_{CH_4}=1.0$).

of the films was also estimated by this technique. The atomic ratios of H/C and D/C were measured instead of absolute measurements of the amount of H, D, and C atoms. Figure 1 shows the atomic ratio, H/C, against bias voltage, which is applied to the substrates of a Si wafer (see Fig. 1 of a preceding paper). In this case, the gas mixture was composed of 50% CH_4 and 50% H_2. It becomes evident that the H/C is independent of the energies of impinging hydrocarbon ions and keeps the value of ~0.2. On the other hand, hydrocarbon ions are reflected and only neutral species take part in forming carbon films, when bias voltage is 200 V.

To examine the effect of H_2 added to the gas mixture, D_2 was used instead of H_2. The atomic ratios, H/C and D/C, are plotted as a function of $R=P_{CH_4}/(P_{CH_4}+P_{D_2})$ in Fig. 2. When $R=0.5$, the carbon films were 200 nm in thickness. For $R=0.05$ it was found from their ERD spectra that the carbon films were too thin to permit us to estimate the films thickness; therefore, it is still open to question whether or not D is contained in the carbon film. Figure 3 shows an infrared absorption spectrum for the carbon film ($R=0.5$). This spectrum closely resembles that of a dense amorphous carbon film.[3] The peak 00 is ascribed to a C–H bond; the peaks 01 and 02 are to a C–D bond. The result leads to the conclusion that the added D_2 are dissociated in plasmas and then D atoms combine with C atoms.

References

1) Y. Sakamoto, H. Amemiya, Y. Ishibe, S. Kato, K. Okazaki, H. Oyama, K. Yano, K. Akaishi, N. Noda, S. Amemiya, H. Minagawa, T. Hino, T. Yamashina, and S. Matsumoto: p. 71 in this report.
2) Y. Sakamoto, Y. Ishibe, K. Okazaki, H. Oyama, K. Yano, M. Yanokura, and I. Kohno: *RIKEN Accel. Prog. Rep.*, **19**, 98 (1985).
3) E. Vietzke: private communication.

RIKEN Accel. Prog. Rep. 20 (1986)

III-2-26. Hydrogen Trapping by Substitutional Impurity in $NbMo_{0.03}$ Alloys

E. Yagi, T. Kobayashi, F. Kano, S. Nakamura,
K. Watanabe,* Y. Fukai,* and T. Matsumoto**

It has been known that the addition of Mo to Nb increases the terminal solubility of hydrogen in an α-phase of the Nb-H system. For elucidation of its mechanism, the lattice location of hydrogen in Nb-Mo alloys was investigated by the channeling method utilizing a nuclear reaction $^{1}H(^{11}B, \alpha)\alpha\alpha$.[1]

Specimens were single crystals of $NbMo_{0.03}H_{0.02}$ and $NbMo_{0.03}H_{0.05}$, which were in the α-phase at room temperature. Hydrogen was doped in the gas phase. Channeling experiments were carried out with a 2.03 MeV $^{11}B^{2+}$ beam, which had 1.0 mm in diameter with a current of 1 nA. The collimation of the beam was better than 0.076°. The specimen was mounted on a holder of a three axis goniometer, with which the crystal orientation was set within the accuracy of $\pm$ 0.004°. Backscattered ^{11}B and emitted α-particles were detected with two solid state detectors at a scattering angle of 150° and 90°, respectively. In front of the detector for α-particles, a 4 μm Mylar foil was placed in order to stop scattered ^{11}B-particles. The vacuum in the scattering chamber produced by a turbomolecular pump was 4×10^{-7} Torr and a cold trap was equipped so as to surround the specimen and the detectors. More details of the exprimental setup have been described in previous papers.[1-5] In the present experiments, the channeling angular scans were made for <1 0 0> and <1 1 0> axes, and a {1 0 0} plane.

Figure 1 shows our example of the angular profiles of backscattered ^{11}B and emitted α-particles for the {1 0 0} planar channel in $NbMo_{0.03}H_{0.02}$ ((a)) and $NbMo_{0.03}H_{0.05}$ ((b) and (c)). Figure 1(a) and (b) were obtained at room temperature, and (c) at 100°C on the same specimen used in (b). The α-angular profile exhibited a narrow dip in $NbMo_{0.03}H_{0.02}$, whereas the dip became broader and a small central peak came to be observed in $NbMo_{0.03}H_{0.05}$ at room temperature. By heating the specimen up to 100°C, this profile changed drastically to a dip superposed with a central peak. In a previous paper[2] we concluded that hydrogen atoms in an α-phase of the Nb-H system are located at tetrahedral sites. For

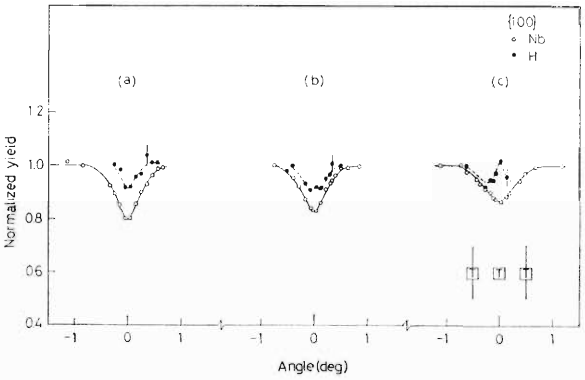

Fig. 1. Angular profiles of ^{11}B- and α-yields in (a) $NbMo_{0.03}H_{0.02}$ at room temperature, (b) $NbMo_{0.03}H_{0.05}$ at room temperature, and (c) $NbMo_{0.03}H_{0.05}$ at 100°C. The inset indicates the projection of T-sites onto the plane perpendicular to the {1 0 0} planar channel. The lines represent the projections of atomic planes, and the squares the projected positions of T-sites.

tetrahedral site occupancy, the {1 0 0} angular profile gives a dip superposed with a small central peak as shown in Fig. 1(c).

These results are interpreted to be that hydrogen atoms are located at sites different from the tetrahedral sites in $NbMo_{0.03}H_{0.02}$ and, at 100°C, they are located at the tetrahedral sites: at room temperature hydrogen atoms are trapped by Mo atoms and at 100°C they are detrapped. This interpretation is also supported by the results on the <1 0 0> and <1 1 0> channels. The α-angular profile in Fig. 1 (b), where the hydrogen concentration is higher than that of Mo, has both features of 1(a) and (c). This result indicates that some fraction of hydrogen atoms are located at the trapped sites and the remainder at the tetrahedral sites. The trapping efficiency was estimated from the comparison of α-angular profiles in $NbMo_{0.03}H_{0.05}$ observed at room temperature with those calculated by assuming that all hydrogen atoms are located at the trapped sites in $NbMo_{0.03}H_{0.02}$ and at the tetrahedral sites in $NbMo_{0.03}H_{0.05}$ at 100°. According to this estimation, each Mo atom trapps aproximately one hydrogen atom. Therefore, in $NbMo_{0.03}H_{0.05}$ about 60% of hydrogen atoms are located at the trapped sites and 40% at the tetra-

* Faculty of Science, Chuo University.
** National Research Institute for Metals.

hedral sites at room temperature. Analysis on the trapped sites in progress.

References

1) E. Yagi, T. Kobayashi, S. Nakamura, Y. Fukai, and K. Watanabe: *J. Phys. Soc. Jpn.*, **52**, 3441 (1983).
2) E. Yagi, S. Nakamura, T. Kobayashi, K. Watanabe, and Y. Fukai: *J. Phys. Soc. Jpn.*, **54**, 1855 (1985).
3) E. Yagi, T. Kobayashi, S. Nakamura, Y. Fukai, and K. Watanabe: *Phys. Rev. B*, **31**, 1640 (1985).
4) E. Yagi, T. Kobayashi, S. Nakamura, F. Kano, K. Watanabe, Y. Fukai, and S. Koike: *Phys. Rev. B*, **33**, 5121 (1986).
5) E. Yagi, S. Nakamura, T. Kobayashi, F. Kano, K. Watanabe, Y. Fukai, and T. Osaka: *J. Phys. Soc. Jpn.*, **55**, 2671 (1986).

RIKEN Accel. Prog. Rep. 20 (1986)

III-2-27. Study of Krypton Bubbles in Kr-Implanted Al by Means of Electron Diffraction

I. Hashimoto,* H. Yamaguchi,* E. Yagi, and M. Iwaki

In a previous work, the experiments on the thermal extraction of Kr atoms from Kr-implanted Al specimens have been carried out by using a mass spectrometer and diffusion coefficients were estimated to be of the order of 10^{-19}–10^{-18} m^2/s in the temperature range from 713 to 813 K.[1] These values are about seven orders of magnitude smaller than those obtained in the tracer diffusion experiment using ^{85}Kr.[2] With the help of electron microscopic observation, such a large difference was attributed to that, in the Kr-implanted specimens, Kr atoms exist in the form of Kr bubbles, whereas, in the specimens used in the tracer diffusion experiments, Kr atoms exist probably as isolated atoms; such small diffusion coefficients were considered to be those for the Kr bubbles.[1] Furthermore, we also found that the amount of extraction increased rapidly above 540 K with increasing temperature.[1] This fact suggests that the structure change takes place above 540 K. If such a structure change would be caused by the change in the state of Kr bubbles near the specimen surface, some changes would be reflected in electron diffraction patterns. Up to the present, however, an anomalous contrast of the diffraction pattern has not been observed. In the present work, the behavior of Kr bubbles in Kr-implanted Al for thermal annealing was studied in detail by means of electron diffraction and transmission electron microscopy (TEM).

Thin Al specimens (99.99% in purity) suitable for electron microscopy were prepared by conventional chemical- and electrolytical-polishing. Kr atoms were implanted at 50 keV to a dose of 10^{20}/m^2. The implanted specimens were examined with an H-800 electron microscope with a heating stage operating at 100 kV.

The electron diffraction patterns indicated the presence of double diffraction spots. It is known that a double diffraction effect is prominent when two crystalline phases coexist in a specimen.[3] Figure 1(a) shows an example of the selected area 110 electron diffraction pattern taken at room temperature on as-implanted specimens from the region in which Kr bubbles and Al matrix coexist. The illustration

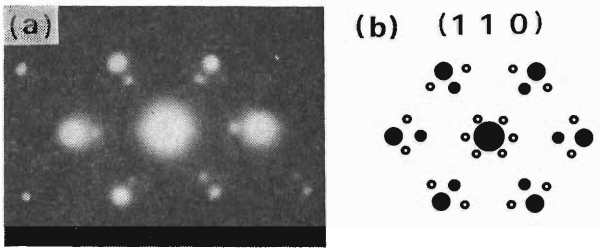

Fig. 1. An electron diffraction pattern taken at room temperature on a Kr-implanted specimen. (a), 110 selected area diffraction pattern from Al containing Kr bubbles; (b), Illustration of the diffraction pattern. Large spots represent reflections from an Al matrix, small spots are those from a solid Kr and open circles are due to double reflections.

in Fig. 1(b) was made up of only the relatively strong double diffraction spots. Most of the spots were observed experimentally. This result suggests that the Kr bubbles are in the solid phase. To reveal the origin of the double diffraction spots, we carried out the observation using the electron microscope in the same area as shown in Fig. 1. The results are shown in Fig. 2(a), (b), and (c); (a) shows a bright field image, (b) is a dark field one taken by the 200 reflection of Al, and (c) is a dark field one with the 200 reflection of Kr. The image of Kr bubbles in Fig. 2(c) are isolated better than those in Fig. 2 (a) and (b). Therefore, the double diffraction is considered to be due to the presence of both phases of the well-isolated solid Kr bubbles and the Al matrix. From the diffraction patterns, the lattice pa-

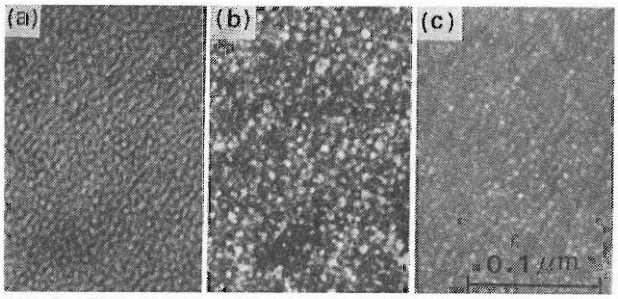

Fig. 2. Transmission electron micrographs of the same area taken under different diffraction conditions at room temperature. (a), the bright field image; (b), the dark field one taken by a 200 reflection of Al; (c), the dark field one taken by a 200 reflection of Kr.

* Faculty of Science, Science University of Tokyo.

rameter, the packing density, and the molar volume of solid Kr were estimated to be 0.534 ± 0.003 nm, 2.63×10^{28} atoms/m^3, and 22.92 cm^3/mol, respectively. The mean diameter of the Kr bubbles and the number in unit area were estimated to be 1.6 nm and 5.9×10^{16}/m^2, respectively.

Figure 3 shows examples of diffraction pattern during annealing; (a), (b), (c), and (d) represent those observed at 483, 618, 668, and 743 K using the heating stage, respectively. The double diffraction disappeared below 483 K, while diffraction reflections from the solid Kr remained up to 618 K. When the annealing temperature was 618 K, a diffuse ring corresponding to the "amorphous" Kr was observed as shown in Fig. 3(b). The diameter of the ring coincided with that of the 111 reflection of solid Kr and the intensity became maximum around 618 K. The ring disappeared just above 618 K; this indicates that the melting of Kr bubbles occurs through the "amorphous" state at temperatures about 620 K.

Furthermore, streaks were observed above 618 K as shown in Fig. 3(b), (c), and (d). To reveal their origin, we carried out TEM observation at room temperature on the same specimen after annealing at 823 K for 10 min. In this case, the streaks also remained in the diffraction pattern. From Fig. 4, it is to be noted that the mean diameter of the bubbles is 6.7 nm and the number of the bubbles in unit area is 7.5×10^{15}/m^2. The former is about four times and the latter is about 1/8 of those observed in as-implanted specimens as described above. This means that the bubbles grow by coalescence during annealing. In addition, a large and irregular shaped white contrast indicated with a circle in Fig. 4 observed in the micrograph is considered to be a microcrack formed during annealing. The mean diameter of the microcracks was 69 nm and their number in unit area was 1.3×10^{15}/m^2. From these results, the streaks are considered to be closely related to the existence of microcracks. The experiments with a scanning electron microscope is in progress.

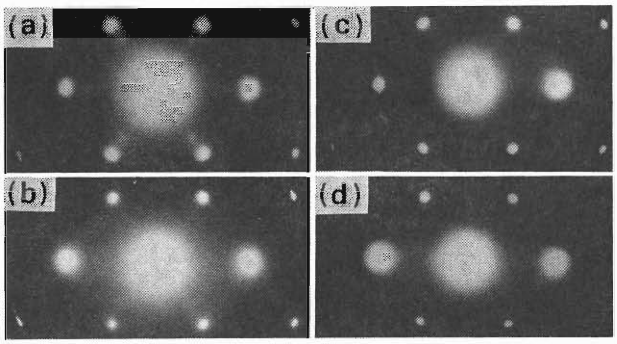

Fig. 3. Selected area diffraction patterns during annealing for the (1 1 0) orientation at (a) 483 K, (b) 618 K, (c) 668 K, and (d) 743 K.

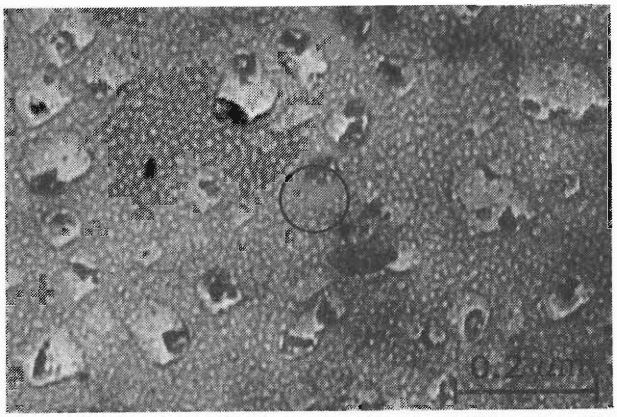

Fig. 4. Typical electron micrograph of the same specimen as shown in Fig. 3 after annealing at 823 K for 10 min. The irregular shaped white contrast is indicated by a circle.

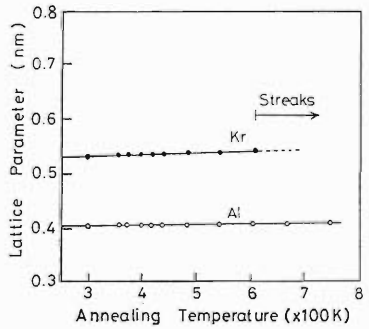

Fig. 5. Lattice parameter changes for solid Kr and Al during annealing.

The changes in the lattice parameters of Al and Kr during annealing obtained by the microdensitometric traces of diffraction spots are shown in Fig. 5. The apparent linear thermal expansion coefficients were estimated to be 2.7×10^{-5}/deg for Al and 3.5×10^{-5}/deg for Kr. The value for Al is coincident with that given in a handbook.[4] The detailed description is given in Ref. 5.

References

1) K. Takaishi, T. Kikuchi, K. Furuya, I. Hashimoto, H. Yamaguchi, E. Yagi, and M. Iwaki: *Phys. Status Solidi*, **95**, 135 (1986).
2) M. E. Gurevich, L. N. Larikov, V. M. Tyshkevich, and V. M. Falchenko: *Uhr. Fiz. Zh.*, **T24**, 658 (1979).
3) P. B. Hirsch, A. Howie, R. B. Nicholson, D. W. Pashley, and M. J. Whelan: Electron Microscopy of Thin Crystals, Butterworths, London, p. 148 (1965).
4) E. W. Washburn: International Critical Tables, Vol. 1, McGraw-Hill, New York and London, p. 103 (1926).
5) I. Hashimoto, H. Yorikawa, H. Mitsuya, H. Yamaguchi, K. Takaishi, T. Kikuchi, K. Furuya, E. Yagi, and M. Iwaki: *J. Nucl. Mater.*, **149** (1987) (in press).

RIKEN Accel. Prog. Rep. 20 (1986)

III-2-28. Eu-Ion Implantation in CaF_2 (II)

K. Aono, M. Iwaki, and S. Namba

In our previous report,[1] we have described the radiation damage and depth profiles of Eu in Eu-implanted CaF_2 investigated by means of a He^+ backscattering-channeling technique using the TANDETRON.

A study is carried out on the technique using the CaF_2 during Eu-implantation. Calcium fluoride specimens are colorless, transparent single crystal wafers grown by the Bridgman-technique. Their largest faces are parallel to the (1 1 1) cleavage plane. All wafers were mechanically mirror-polished and chemically etched. The Eu-implantation in CaF_2 was performed at room temperature to doses of 10^{13}–10^{16} cm^{-2} at 100 keV in a random direction at a low dose rate of about 0.2 μAcm^{-2}.

By implantation the surface was significantly darkened owing to dense lattice damage as GaP. However, no coloration of CaF_2 owing to the damage by 100 keV Eu-implantation was observed in the visible region. A <1 1 1> channeling measurement was carried out by using 1.5 MeV. He^+, and backscattered particles were detected at an angle of 150°.

Figure 1 shows a random and a <1 1 1> aligned spectra observed for CaF_2 implanted with 1×10^{16} and 1×10^{14} Eu^+cm^{-2}. The Eu depth profiles in the random and the <1 1 1> aligned spectra of a specimen implanted with 1×10^{16} cm^{-2} are of a Gaussian-type. A difference is exhibited between the random and the aligned Eu-spectra for the as-implanted specimen: for the implantation with 1×10^{16} cm^{-2} the scattering yield of the aligned Eu-spectrum shows a strong reduction in comparison with that of the random spectrum. These results suggest that most of Eu atoms will occupy substitutional lattice sites. The random spectra obtained from CaF_2 give the same

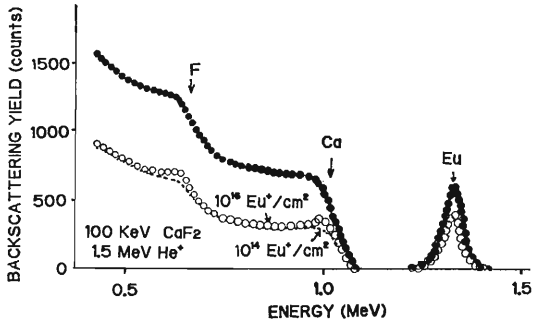

Fig. 1. Random and <1 1 1> aligned spectra observed for CaF_2 and Eu for Eu-implantation.

shape by implantation with 10^{16} and 10^{14} Eu^+cm^{-2}, indicating that no outdiffusion of Ca and F atoms occurs through the surface. In general, the random spectra for CaF_2 have two shoulders, which correspond to the energies of backscattered particles from Ca and F atoms on the surface. The radiation damage in Eu-implanted layers was investigated with the spectra obtained from Ca in CaF_2, because the spectra for Ca showed no overlap with those for F in the high energy region. The aligned spectrum for the specimen implanted with 10^{16} Eu^+cm^{-2} shows a little damage near the surface. The dose for the implantation with 1×10^{16} Eu^+cm^{-2} is in good agreement with about 0.9×10^{16} Eu^+cm^{-2} calculated from the spectra of Eu shown in Fig. 1.

The result shows that CaF_2 was implanted by ion at 100 keV without producing radiation damage.

Reference

1) K. Aono, M. Iwaki, and S. Namba: *RIKEN Accel. Prog. Rep.*, **19**, 93 (1985).

RIKEN Accel. Prog. Rep. 20 (1986)

III-2-29. Defect-Impurity Interaction in Ni-Implanted Aluminum

E. Yagi, F. Kano, S. Nakamura, M. Iwaki, and T. Osaka*

The ion-implantation is a useful technique of introducing impurity atoms to modify the surface layer of materials. This method, however, introduces not only impurity atoms but also lattice defects simultaneously, and the behavior of implanted atoms is affected by such defects. Therefore, in order to elucidate the mechanism for material modification, we have to study the impurity-defect interaction. In the present paper, the lattice locations of the Ni atoms implanted in Al crystals are studied by using a channeling method, and the results are discussed from the view point of the impurity-defect interaction in comparison with the results of Sn atoms implanted in Al; analysis of channeling angular profiles on Sn atoms was described in a previous paper.[1)]

Slices of about 1 mm in thickness were spark-cut from a single crystal rod of 99.999% purity. After chemical polishing, the slices were annealed in a vacuum of 10^{-6} Torr at 823 K for 7 h. The Ni^+ implantation was carried out at room temperature at 180 kV to three different doses $5 \times 10^{13}/cm^2$, $5 \times 10^{14}/cm^2$, and $5 \times 10^{15}/cm^2$. The axial channeling effect was investigated on the specimens implanted to latter two doses for <1 0 0>, <1 1 0>, and <1 1 1> axes at room temperature by means of backscattering with 1.5 MeV He^+ ions. The beam was collimated to give a divergence of less than 0.076°. The specimen was mounted on a three-axis goniometer whose angles were set to an accuracy of ± 0.004°. The irradiated area was 0.78 mm^2 and the beam current was 0.7–1.5 nA. The backscattered He^+ ions were detected with a surface-barrier solid state detector at a scattering angle of about 150°. Transmission electron microscopic observation was made on polycrystalline Al specimens with a 200 kV electron microscope.

The channeling angular profiles on a 5×10^{14} Ni/cm^2 implanted specimen (an average concentration: ~0.06 at%) are shown in Fig. 1. The angular profile of He ions backscattered by Ni atoms (Ni-profile) exhibits a shallow dip with a depth of about 50% of that of an Al-profile in all cases of <1 0 0>, <1 1 0>, and <1 1 1> channels. These Ni-dips are composed of two components: a narrow dip and a broad dip. No large peaks were observed in the region of a small incident angle ψ with respect to the channel axis. These results suggest that about a half of Ni atoms implanted are located at random sites (R-sites), and the remaining half are at slightly

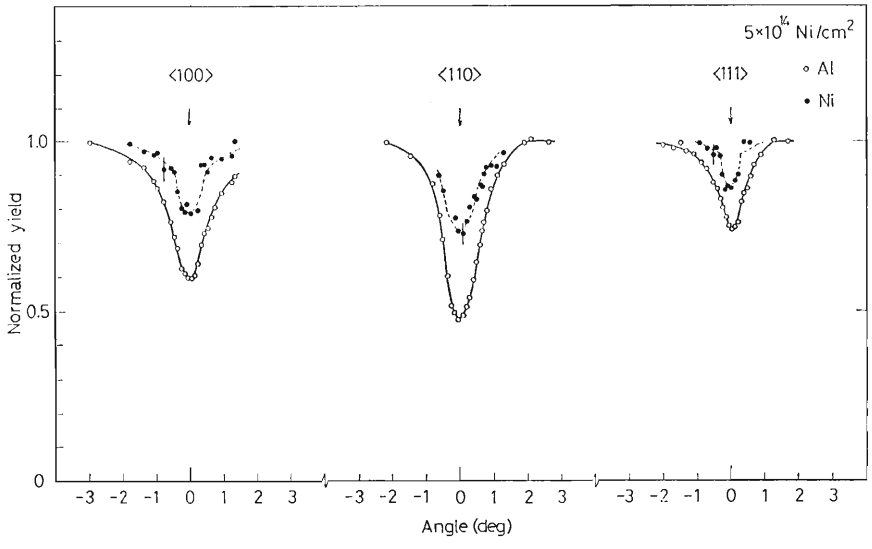

Fig. 1. Channeling angular profiles on the 5×10^{14}Ni/cm^2 implanted Al. Dotted curves represent the calculated profiles.

* The School of Science and Engineering, Waseda University.

displaced interstitial positions (I-sites), or at both I-sites and substitutional sites (S-sites). The location of Ni atoms can be examined in more detail by comparing the observed Ni-angular profiles with calculated ones. The calculation was performed using a multi-string model by assuming that the Ni atoms located at sites shadowed by the host Al atoms under the channeling conditions give the same angular profile as an Al-profile.

The observed profiles fitted well within the experimental error with the calculated ones for the distribution with 49% of the Ni atoms at the R-sites and 51% at the I-sites displaced in the <1 1 0> direction by 0.24 Å from a lattice point. The calculated results are shown in Fig. 1 by dotted curves. When the magnitude of displacement is small, other possibilities on the direction of displacement cannot be ruled out; however, the magnitude is not so sensitive to the direction. With increasing implantation dose to 5×10^{15}/cm^2, the Ni-profiles showed no drastical change as observed for Sn, as will be described below, but only became shallower. This indicates that the Ni atoms do not drastically change their location.

The electron micrographs are shown in Fig. 2. A number of dislocation loops and black dotts were observed. With increasing dose, the dislocation loops tangled to each other; no extra diffraction spots were observed.

For comparison, the distribution of Sn atoms over various sites, obtained from similar experiments on Sn-implanted Al,[1] is shown in Fig. 3. Most of the Sn atoms were located at the R-sites. In the 1×10^{14} Sn/cm^2 implantation, the remainder were located at the S-sites and the I-sites displaced in the <1 1 2> or <1 1 4> direction by 0.68 Å. As the dose was increased to 4×10^{14} Sn/cm^2, the fraction of the S- and I-site occupancies decreased, whereas the tetrahedral (T) and octahedral (O) site occupancies came to be observed. The T- and O-site occupancies were also observed in the channeling experiments by Swanson *et al.*, after annealing of low-temperature irradiated Al-0.03 at%Sn alloys above 220 K.[2] Several experiments have suggested that the Sn atoms in Al strongly interact with vacancies.[3-5] Therefore, the occupancies of Sn atoms at various sites are interpreted as follows by taking account of such interaction.[1] (1) The R-site occupancy results from the Sn atoms which are in the form of precipitates. Actually the precipitates were observed by electron microscopy. (2) The occupancy of the <1 1 2>- or <1 1 4>-displaced I-sites is due to the relaxation of an Sn atom induced by trapping a divacancy. The displacement of 0.68 Å is about 17% of the lattice constant. (3) The T- and O-site occupancies result from trapping more than two vacancies by an Sn atom. An Sn atom is displaced to the T-site by trapping three vacancies to take a configuration similar to a trivacancy or to the O-site by trapping five vacancies to take a configuration similar to a pentavacancy. These results indicate that with increasing dose much more vacancies are introduced during implantation, and they are trapped by Sn atoms to form larger clusters.

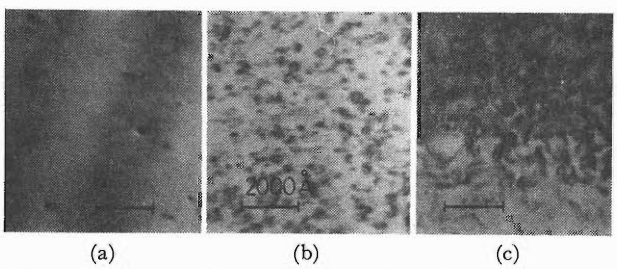

Fig. 2. Electron micrographs of Al specimens implanted with (a) 5×10^{13}Ni/cm^2, (b) 5×10^{14}Ni/cm^2, and (c) 5×10^{15}Ni/cm^2.

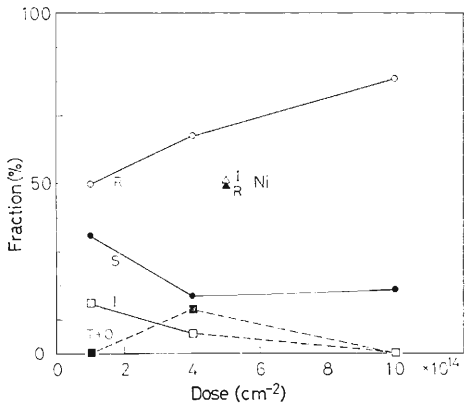

Fig. 3. Dose dependence of distribution of Sn atoms over various sites. A result on Ni is also plotted.

For Ni, the behavior is different. For 5×10^{14} Ni/cm^2 implantation, most of the Ni atoms are located at the R-sites. The R-site occupancy is also considered to result from the Ni atoms in the precipitates because the solubility of Ni in Al is small, less than 0.03 at% at 640°C.[6] The remainder are at the <1 1 0>-displaced I-sites. But the magnitude of displacement is much smaller than that of Sn atoms in spite of nearly the same dose as in the Sn-implantation, 0.24 Å, which is about 6% of the lattice constant. From the comparison with the calculation on relaxation around a vacancy,[7] the <1 1 0>-displaced I-site occupancy is considered to be due to the relaxation of an Ni atom induced by trapping a single vacancy. On increasing the implantation dose by a factor 10, no T- or O-site occupancy was observed; therefore, no multiple trapping of vacancies occurs. From these results, we conclude that the interaction of Ni atoms with vacan-

cies in Al is not so strong as that of Sn atoms. More detailed description is given in Ref. 8.

References

1) E. Yagi, A. Koyama, S. Nakamura, H. Sakairi, and R. R. Hasiguti: *Jpn. J. Appl. Phys.*, **24**, 137 (1985).
2) M. L. Swanson, L. M. Howe, and A. F. Quenneville: *Phys. Rev. B*, **22**, 2213 (1980).
3) H. Kimura and R. R. Hasiguti: *J. Phys. Soc. Jpn.*, **18**, Suppl., 73 (1963).
4) A. J. Perry and K. M. Entwistle: *J. Inst. Met.*, **96**, 344 (1968).
5) S. Ceresara and T. Federighi: *Philos. Mag.*, **10**, 893 (1964).
6) M. Hansen: Constitution of Binary Alloys, McGraw-Hill, New York (1958).
7) M. Doyama and R. M. J. Cotterill: Lattice Defects and Their Interactions (ed., R. R. Hasiguti), Gorden and Breach, New York, p. 79 (1967).
8) E. Yagi, F. Kano, S. Nakamura, M. Iwaki, and T. Osaka: *Mater. Forum*, **15-18**, 605 (1987).

RIKEN Accel. Prog. Rep. 20 (1986)

III-2-30. Isochronal Annealing of Proton- or α-Irradiated Cu_3Au at Low Temperatures

E. Yagi, H. Sakairi, A. Koyama, and R. R. Hasiguti*

The investigation of irradiation effects in Cu_3Au has long been made since the beginning of radiation effects research. Such an ordered alloy is a most appropriate system to study replacement collision in damage production and migration of vacancies, because their effects are observed as a large change in the ordered state. Therefore, the detailed study on ordered alloys will give important information on the damage production process and the behavior of defects. For understanding of damage structures and of behavior of irradiation induced defects, the annealing experiments at low temperatures are required. In the present study isochronal annealing experiments have been made up to 100 K by electrical resistivity measurement on Cu, ordered and disordered Cu_3Au irradiated with protons or α-particles below 30 K.

The Cu_3Au alloys were prepared by melting Cu and Au both of 99.999% purity in a quartz capsule. The Au concentration in this alloy was 25.8 at%. They were processed to foils of 30 μm in thickness. The electrical resistivities of ordered and disordered Cu_3Au were 2.3–2.8 $\mu\Omega$ cm and 12 $\mu\Omega$ cm at liquid-helium temperature, respectively. Irradiation was carried out with about 4.7 MeV protons or about 17.8 MeV α-particles below 30 K under the condition that incident ions penetrate the specimens. After irradiation, an isochronal annealing experiment of electrical resistivity was performed up to 100 K in 5 min pulse. Resistivity was measured at liquid-helium temperature. Irradiation was carried out to the doses which gave approximately the same increase in resistivity for both proton and α-particle irradiations.

Figure 1 shows the results on Cu irradiated with 4.8 MeV protons and 17.7 MeV α-particles below 15 K. As in the case of stage I recovery in electron irradiation, five substages I_a to I_e were observed below 60 K.

Figure 2 shows the results for the ordered Cu_3Au. For the specimens irradiated with protons or with low-dose α-particles (specimens #7-1, #7-4, #6-22, and #7-5), several substages were observed below 90 K: a small resistivity increase below 40 K and five substages between 40 and 90 K. These five substages are tentatively labeled I_A, I_B, I_C, I_D, and I_E in order of increasing temperature. Although a central temperature of each recovery stage seems to be slightly different between proton and α-irradiations, they are as follows. I_A, ~45 K; I_B, ~50 K;

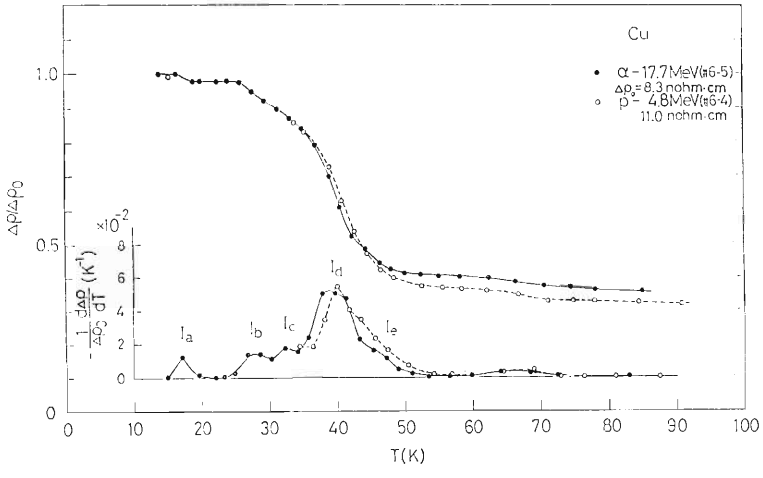

Fig. 1. Isochronal recovery curves of the electrical resistivity for p-4.8 MeV or α-17.7 MeV irradiated Cu. Resistivity increases $\Delta\rho_0$ are 11.0 nΩ cm for specimen #6-4 and 8.3 nΩ cm for specimen #6-5.

* Faculty of Engineering, Science University of Tokyo.

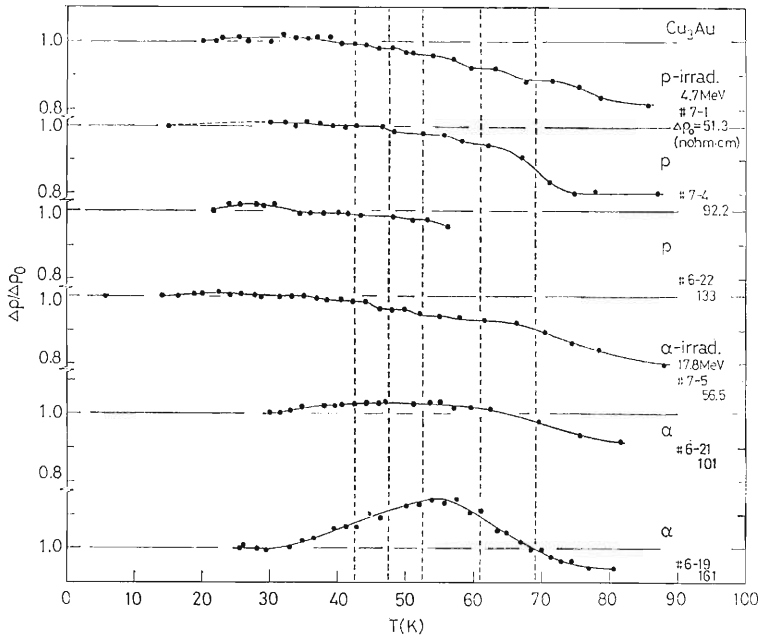

Fig. 2. Isochronal recovery curves of the electrical resistivity for p-4.7 MeV or α-17.8 MeV irradiated ordered Cu_3Au. Fraction not-annealed $\Delta\rho/\Delta\rho_0$ is obtained by normalizing the resistivity increase $\Delta\rho$ to the irradiation induced resistivity increase $\Delta\rho_0$(O–Cu_3Au).

I_C, ~58 K; I_D, ~65 K, and I_E, > 70 K. From the temperature derivatives obtained from the recovery curves shown in Fig. 2, it can be said that the peak temperatures of stages I_A, I_B, I_C, and I_D are independent of irradiation dose, and that of stage I_E is dependent on dose and shifts to lower temperatures with increasing dose. This behavior is similar to that of stages I_a to I_e in Cu. In Fig. 2, the fractional resistivity recovery (fraction not-annealed $\Delta\rho/\Delta\rho_0$) is normalized to the irradiation-induced resistivity increase $\Delta\rho_0$(O–Cu_3Au), which is composed of two contributions: a resistivity increase due to decrease in long-range ordering originating in the replacement between Cu and Au atoms and that due to Frenkel pairs. The latter component $\Delta\rho_{0,FP}$(O–Cu_3Au) was estimated to be $\Delta\rho_0$(O–Cu_3Au)/3.84 from previous papers.[1,2] Therefore, the fraction of the recovery of Frenkel pairs can be estimated by renormalizing the recovered resistivity to $\Delta\rho_{0,FP}$(O–Cu_3Au) instead of $\Delta\rho_0$(O–Cu_3Au). The result is shown in Fig. 3. There is a close similarity between substages below 90 K in ordered Cu_3Au and those of stage I in Cu in (1) the dose dependence of central temperatures of recovery stages and (2) the total fraction of recovery of Frenkel pairs.

It has been considered that the migration of interstitials produce no ordering in Cu_3Au.[3,4] A large resistivity recovery has been observed around 240 K in electron irradiated ordered Cu_3Au and the resistivity decreased to a value lower than the pre-irradiation ones.[5] This suggests the occurrence of the recovery of ordering. The recovery of this stage is attributed to the long-range migration of vacancies. Therefore, the recovery stages below 90 K are considered to be related to the interstitial migration. It seems to be very difficult for Au interstitials to make long-range migration retaining their configuration, because in ordered Cu_3Au all 12 nearest neighbor sites of an Au atom are occupied by Cu atoms, whereas it is possible for Cu interstitials to make long-range migration, because a half of {100} planes are occupied by only Cu atoms. Therefore, the stages I_A to I_E are assigned to those associated with Cu interstitials similarly to stages I_a to I_e in irradiated Cu. The stage I_E recovery is attributed to the long-range migration of Cu interstitials.

The small recovery of disordered Cu_3Au, different from the recovery of Cu and ordered Cu_3Au, may result from the suppressed long-range migration of interstitials below 90 K as seen from Fig. 3.

Large reverse annealing was observed above 30 K only in the α-irradiation (specimens #6-21 and #6-19) and is peculiar to the ordered state. It became more conspicuous with increasing dose. These results suggest that the spatial distribution of defects is different between proton and α-irradiations. The temperature range of the reverse annealing corresponds to that of I_A to I_C. Therefore, this reverse annealing is closely related to such spatial distribution, especially, to the interaction of closely located

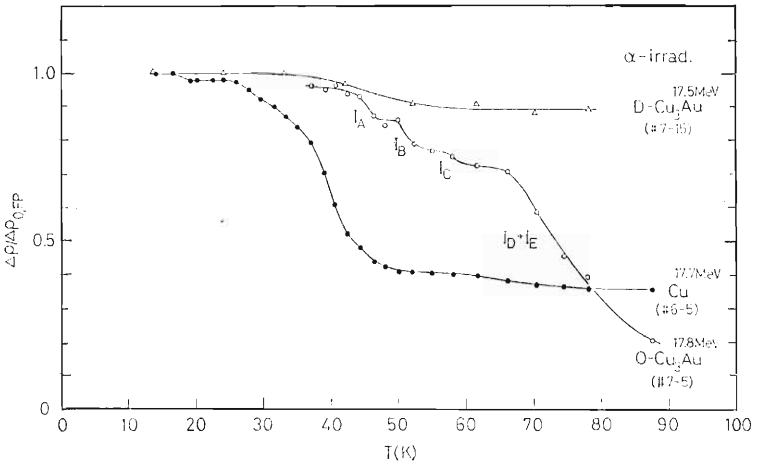

Fig. 3. Isochronal recovery curves of the electrical resistivity for α-irradiated disordered Cu_3Au, ordered Cu_3Au, and Cu. The fraction not-annealed is renormalized to the resistivity increase due to Frenkel pairs $\Delta\rho_{0,FP}$.

defects.

References

1) H. Sakairi, E. Yagi, A. Koyama, T. Karasawa, and R. R. Hasiguti: *J. Phys. Soc. Jpn.*, **43**, 999 (1977).
2) H. Sakairi, E. Yagi, A. Koyama, and R. R. Hasiguti: *J. Phys. Soc. Jpn.*, **50**, 3023 (1981).
3) J. A. Brinkman, C. E. Dixon, and C. J. Meechan: *Acta Met.*, **2**, 38 (1954).
4) S. Takamura and S. Okuda: *Rad. Eff.*, **17**, 151 (1973).
5) J. Gilbert, H. Herman, and A. C. Damask: *Rad. Eff.*, **20**, 37 (1973).

RIKEN Accel. Prog. Rep. 20 (1986)

III-3. Radiochemistry and Nuclear Chemistry

1. Production of Radioisotopes and Preparation of Labeled Compounds

T. Nozaki, M. Iwamoto, Y. Ohkubo, M. Suehiro,
F. Yokoi, and M. K. Kubo

In this period the following studies were undertaken: (1) production of ^{57}Ni as nickel tracer for the study of adsorption on silicon surface from an alkaline solution containing H_2O_2 and of absorption by plants; (2) synthesis of radiobromine-labeled bromoperidol and bromospiperone for neuro-receptor study; and (3) synthesis of $^{11}CH_3CH_2CO_2H$ (propionic acid) by the malonic ester synthesis.

Very clean washing of silicon wafers is indispensable in the production of silicon semiconductor devices. In this washing ultra-minute amounst of impurities are sometimes adsorbed on the silicon wafer to result in the deterioration of the device property. For the measurement of the adsorption of nickel, there are no suitable reactor-made radiotracer nuclides; they are of limited specific activity. Nickel-57 (36.0 h) was produced by the ^{56}Fe(^{3}He, 2n)^{57}Ni reaction and used for this purpose and for the investigation of the absorption of a minute amount of nickel by plants. In order to obtain ^{57}Ni in high specific activity, the target iron should be made free from nickel. Nickel was removed from iron by the following process: ether extraction of iron from 8 N HCl solution, washing of the extract with 8 N HCl, back-extraction of iron into water, and precipitation of ferric hydroxide. The precipitate was collected, dried, and reduced into metal powder by heating to 700°C in H_2 stream.

The iron powder was pressed into a disk and bombarded with 35 MeV ^{3}He particles. The target was dissolved in conc. HCl with occasional addition of Br_2. Iron was extracted twice into isopropyl ether from the solution, which was then passed through an ion exchange resin column (Dowex 1 × 8) for the removal of radio-cobalt and radio-manganese formed as by-products. The effluent was found to contain no radionuclides other than ^{57}Ni and a weak activity of ^{56}Ni (6.1 d).

Nickel was proved to be scarcely adsorbable on silicon from alkaline solutions containing H_2O_2 and ammonia or choline. The measurement of ^{57}Ni absorption by cucumber plants from the root gave results suggesting that nickel, different from titanium and germanium,[1] is absorbed by an active transport.

The study of ^{77,76,75}Br-labeled bromoperidol and bromospiperone has been continued in order to make them useful in practical diagnosis.[2] The safety in their intravenous injection was proved by the pyrogen test and by repeated injection of non-radioactive replica into volunteers. In the preparation of labeled bromoperidol by the Sandmeyer reaction, the product was found to be accompanied with a notable amount of haloperidol, which behaved competitively with bromoperidol *in vivo*. The reason for this was examined by neutron activation analysis of the reagents used in this synthesis, and was found to be the presence of a noticeable amount of chlorine in aminoperidol, the starting reagent, probably as hydrochloride. By purification of aminoperidol, the contamination to the radioactive bromoperidol was reduced significantly. For bromospiperone the contaimantion with chlorine was found to be much less notable, when the bromination was carried out under controlled conditions. By the PET (positron emission tomography) measurement of ^{76,75}Br-bromospiperone injected into a monkey (about 10 kg in weight), the striatum which is rich in dopamine receptor was clearly visualized. The striatum visualization was also possible by ^{76,75}Br-bromoperidol, for which nonspecific binding in the brain was of considerable degree.

By the use of $^{11}CH_3I$ obtained from the automatic synthesizer, propionic acid labeled with ^{11}C at the β-site ($^{11}CH_3CH_2CO_2H$) was prepared by the malonic-ester synthesis:

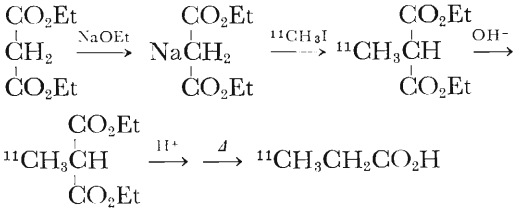

This compound is expected to show different *in-*

vivo behavior from that of $CH_3CH_2{}^{11}CO_2H$ and is probably useful for some diagnostic purposes. By the malonic ester synthesis with $^{11}CH_3I$, the preparation of various α-^{11}C-methyl fatty acids is under way, and the examination of their various possible uses, *e.g.*, the use of for heart diagnosis, is planned.

References

1) M. K. Kubo, Y. Minai, T. Nozaki, and T. Tominaga: *RIKEN Accel. Prog. Rep.*, **19**, 110 (1985).
2) T. Nozaki, S. Ambe, M. Iwamoto, E. Gotoh, T. Kitsunai, H. Nakatani, Z. Huang, Y. Minai, I. Arai, M. K. Kubo, M. Suehiro, and F. Yokoi: *RIKEN Accel. Prog. Rep.*, **19**, 106 (1985).

RIKEN Accel. Prog. Rep. 20 (1986)

III-3-2. Charged Particle Activation Analysis

T. Nozaki, Y. Itoh, M. Iwamoto, Y. Ohkubo,
T. Kimura, and H. Fukushima

In this period we have undertaken the following studies, most of which are of continuation from the last period:[1] (1) determination of the calibration curve for IR spectrophotometry of carbon in semiconductor silicon, (2) measurement of surface oxygen under various ambient air pressure, (3) analysis of carbon in aluminium and magnesium, (4) carbon in gallium arsenide, and (5) in-diffusion of nitrogen in silicon by the use of ^{15}N as activable tracer. Also, various samples, about 240 in all, were analyzed for carbon or oxygen in the trust analysis system by the Japan Chemical Analysis Center.[2] Details of the studies (3), (4), and (5) are described in succeeding pages of this volume.

The provisional calibration curve for IR spectrophotometry of C in Si given in the last volume has been elaborated by the correction for the difference in counting efficiency between the separated $Li_2{}^{11}CO_3$ and the graphite activation standard and for the interference of oxygen by way of the $^{16}O(^3He,2\alpha)^{11}C$ reaction.[1] Various careful measurements were carried out in order for the determination of the correction factors. The final result is shown in Fig. 1, together with the results of SIMS (secondary ion mass spectrometry) measured by a member laboratory of the committee organized for the determination of the calibration curve in JEIDA (Japan Electronic Industry Development Association). The SIMS workers have drawn a straight line parallel to the activation analysis line, regarding the difference between the two lines as the background in SIMS.

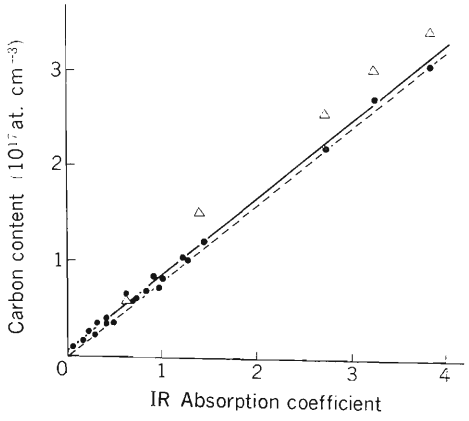

Fig. 1. Calibration curve for IR spectrophotometry of C in Si (605 cm^{-1}, at room temperature). Solid line, before correction for C in IR reference; Si (C concentration, 4.3×10^{15} at. cm^{-3}); broken line, after the correction; △, results of SIMS.

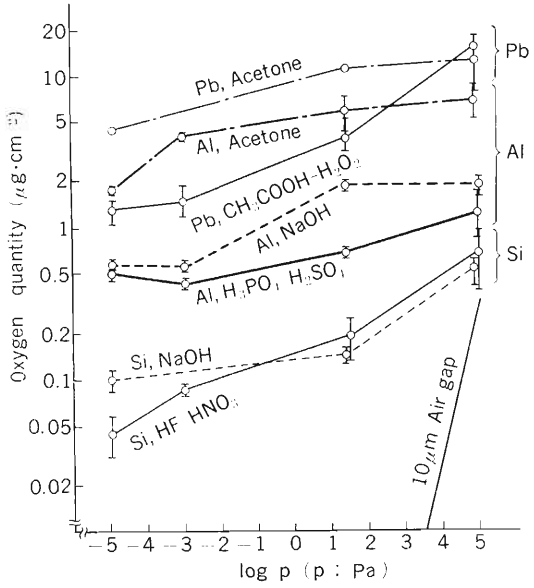

Fig. 2. Surface oxygen quantity at various ambient air pressures. Error bar indicates standard deviations for repeated runs.

The present result is expressed as

[C concentration] = 8.2×10^{16} at. cm^{-3} [IR absorption coefficient at the 607 cm^{-1} absorption peak (at room temperature)].

This calibration factor agrees very closely with our previous value,[3] and we are highly confident of it.

We continued the measurement of surface oxygen for many years and have finished the determination of oxygen on Si, Al, and Pb for various surface cleaning and for various pressures of ambient air. Our method is characterized by the sample arrangement in the charged particle bombardment.[4] Under this arrangement, oxygen on the surface can be determined under any atmospheric conditions. The results are summarized in Fig. 2, where oxygen quantity in an air gap of 10 μm is also given in relation to air pressure.

References

1) T. Nozaki, Y. Itoh, M. Iwamoto, Y. Ohkubo, T. Kimura, and H. Fukushima: *RIKEN Accel. Prog. Rep.*, **19**, 112 (1985).
2) T. Nozaki, Y. Itoh, M. Iwamoto, H. Shinyashiki, K. Nomura, T. Kimura, and H. Fukushima: *RIKEN Accel. Prog. Rep.*, **17**, 96 (1983).
3) Y. Endo, Y. Yatsurugi, N. Akiyama, and T. Nozaki: *Anal. Chem.*, **44**, 2258 (1972).
4) T. Nozaki and M. Iwamoto: *IPCR Cyclotron Prog. Rep.*, **11**, 116 (1977).

RIKEN Accel. Prog. Rep. 20 (1986)

III-3-3. Analysis of Carbon in Aluminium and Magnesium by Deuteron Activation

T. Nozaki, K. Sato, I. Izumi, H. Yoshikawa, and H. Nakahara

Precise determination of impurities, especially hydrogen, carbon and oxygen, in various high-purity metals are becoming more and more important with the progress of their fine uses. Aluminum belongs to these metals. It is produced by electrolytic reduction from fused salts by the use of graphite electrodes and is thus suspected to contain a notable amount of carbon. A highly reliable method of analysis is thus required for carbon in aluminium in order to make clear its behavior in the industrial production processes and its effect on the properties of aluminium. Usually the carbon is analyzed by conversion into CH_4, but the reliability of this method needs to be further ascertained by some more reliable and sensitive method.

We intend to first establish reliable procedure for determining trace amounts of carbon in aluminium by charged particle activation with the $^{12}C(d, n)^{13}N$ reaction and to then analyze aluminium of various post-treatments. We already reported the outline of the analytical procedure in the last volume.[1] Here we describe in more detail the procedure which we have established for routine use: (1) Sample plate (2 cm × 2 cm × 1 mm) is bombarded with deuterons (8.5 MeV, 3 μA, 10 min) and taken out immediately by the use of a target holder assembly specially designed for a quick operation under the supression of the worker's radiation exposure; (2) the surface of the bombarded sample (20 μm in thickness) was removed by etching with a diluted NaOH solution for elimination of surface contamination; (3) the sample is dissolved in concentrated HCl (15 ml) containing NH_4Cl (1.0 mmol) as carrier and $CuSO_4$ (1.5 g); (4) the solution is transferred to a small separatory funnel and dripped onto solid NaOH (10 g) in a distillation flask, which is then heated to distill $^{13}NH_3$ into a solution of sodium tetraphenylboron, $NaB(C_6H_5)_4$ (0.05 mol/l, 30 ml); and (5) the precipitate of $NH_4B(C_6H_5)_4$ thus formed is collected by filtration and its positron activity is measured by a well-type NaI scintillator or a pair of BGO scintillators operated in coincidence. The carrier recovery is determined by weighing. Graphite plates are used as the activation monitor.

The ^{13}N in the bombarded aluminium is thought to be converted quantitatively into $^{13}NH_4Cl$ in Step 3 from analogy with the behavior of nitrogen in the Kjeldahl method which has been used popularly for a century. The above entire process is completed within 30 min, and the radiochemical purity of the $^{13}NH_4B(C_6H_5)_4$ has proved completely satisfactory. Down to several ppb of carbon in aluminium can thus be determined reliably. The results of activation analysis in general have shown fairly good agreement with those of the conventional analysis by way of CH_4 generation.

We have analyzed aluminium samples prepared by the following methods for the following purposes: (1) rapid solidification of melts presumably saturated with carbon at several temperatures in order to obtain the solubility-temperature curve for carbon in liquid aluminium; (2) very slow solidification of the melt saturated with carbon in order to obtain the solubility of carbon in solid aluminium at the melting point (660°C); (3) mixing of the melt with AlF_3 in order to prove the reduction of carbon content by this treatment; and (4) remelting in order to examine its effect on carbon content.

Some results are shown in Fig. 1 and Table 1. From Fig. 1 the heat (ΔH) and entropy (ΔS) of

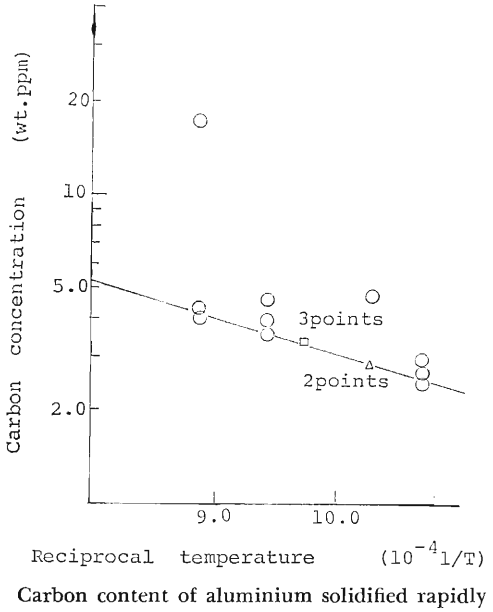

Fig. 1. Carbon content of aluminium solidified rapidly from the melt presumably saturated with carbon at various temperatures.

Table 1. Change of carbon content of aluminium by AlF_3 treatment of the melt.

Sample	Results of analysis (ppm wt)
Before treatment	5.13, 5.64
After treatment	1.76, 2.24
After repeated treatment	1.12, 2.95, 1.07, 1.34

solution for carbon in liquid aluminium seem to be obtained. However, ΔH thus obtained is only 18 kJ/mol, which is unreasonably small. The aluminium melts are thus suspected not to have been saturated with carbon. We are preparing samples for more reliable measurement of the ΔH and ΔS. The solid solubility of carbon in aluminium was obtained to be about 0.2 ppm at the melting point. As is seen in Table 1, the AlF_3 treatment has been proved to lower the carbon content, but its repetition seems not to have any notable further effect. As for the effect of remelting, aluminium containing 4.3 ppm of carbon was remelted and sampled at 748°C to give the carbon content of 0.97, 0.99, and 1.03 ppm for three repetition of the analysis. Samples taken from the same melt at 719°C gave results of 0.88, 0.87, and 0.85 ppm. The remelting is thus shown to reduce the carbon content.

Carbon in magnesium can also be determined by the same procedure. In the ^{14}C dating, accelerator mass spectrometry is much superior to radioactivity measurement for the lowering of the detection limit of ^{14}C for a limited amount of carbon sample. As the sample for the mass spectrometry, carbon in CO_2 is usually reduced to elemental carbon by the reaction with magnesium at about 950°C to be set in an ionization chamber. Impurity carbon in this magnesium is modern carbon and causes underestimation in the dating. High purity magnesium samples of two different origins were analyzed and have been shown to contain considerable quantities of carbon (over 10 ppm). These carbon levels gave serious errors in the dating for samples older than 10^4 y. Most part of the carbon is guessed to be present on the surface, with the quantity being reduced by suitable washing. More detailed study is needed concerning the origin of carbon in magnesium and especially for the reduction of its content.

Reference

1) T. Nozaki, Y. Itoh, M. Iwamoto, Y. Ohkubo, T. Kimura, and H. Fukushima: *RIKEN Accel. Prog. Rep.*, **19**, 113 (1985).

RIKEN Accel. Prog. Rep. 20 (1986)

III-3-4. Studies on Carbon in Gallium Arsenide

Y. Itoh, T. Nozaki, Y. Ohkubo, T. Kimura,
H. Fukushima, Y. Kadota,* and K. Sakai*

Carbo nin gallium arsenide is an electronically active impurity. The carbon concentration has been obtained mostly by infrared spectrophotometry at the local vibrational mode (LVM) between 582.25 cm^{-1} and 582.74 cm^{-1}.[1] This method is simple and non-destructive, but requires a calibration curve or a reference sample to determine absolute carbon contents. We have examined the method[2] for simultaneous determination of carbon and boron in gallium arsenide for its further improvement by activation with the $^{12}C(d,n)^{13}N$ and $^{nat}B(d,xn)^{11}C$ reactions. In our previous method, Molecular Sieve 5A cooled with liquid nitrogen was used to trap ^{13}N. However, some migration of ^{13}N in the Molecular Sieve trap often caused a serious problem in the activity measurement; counting efficiency changed during the measurement. We tried to use titanium sponge with which ^{13}N readily combines at an elevated temperature. For quantitative separation of ^{13}N and ^{11}C in pure states, we examined the recovery under different experimental conditions. First we changed a flow rate of hellium gas, which carried ^{13}N and ^{11}C. Since the recovery was found to be constant at flow rates between 40 and 200 ml min^{-1}, we fixed the flow rate to be 100 ml min^{-1} in the present experiments. The fusion temperature has been set at 1500°C, because a constant recovery was obtained at 900–1500°C. The length and diameter of a titanium-sponge column have been chosen to be 1.5 cm and 0.6 cm, respectively, because no difference was observed in the recovery for the column length between 1 and 6.5 cm. The temperature of the titanium sponge has been decided to be 830°C, the most suitable after testing in a range from 600 to 830°C. At a still higher temperature, the sponge is likely to bind to the inner surface of the quartz tube.

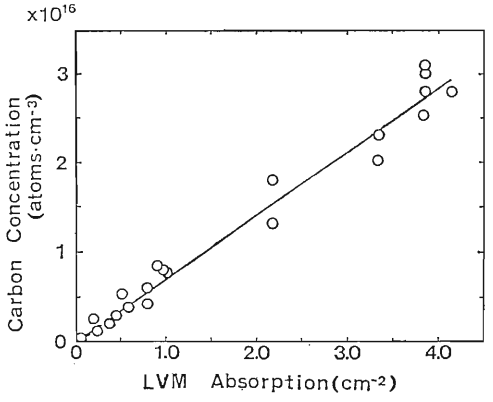

Fig. 1. Infrared absorption *vs.* carbon concentration. For a solid line, a proportionality constant is 7×10^{15} atoms·cm^{-3} per cm^{-2}.

Liquid-encapsulated (LEC) semi-insulating GaAs with different carbon levels were used for the determination of the calibration curve in IR spectrophotometry. Figure 1 shows a relationship between IR absorption (area of the absorption peak in the IR absorption spectrum) and carbon concentrations determined by actiavtion analysis. We can see linear dependence of the IR absorption on carbon concentration from 3×10^{14} to 3×10^{16} atoms·cm^{-3}. The proportionality constant is $(7 \pm 1) \times 10^{15}$ atoms·cm^{-3} for the absorption of 1 cm^{-2}. This value is about one third of the value of Brozel *et al.* (2.4×10^{16} atoms·cm^{-3} for cm^{-2}.[1]

References

1) M. R. Brozel, J. B. Clegg, and R. C. Newman: *J. Phys. D*, **53**, 5771 (1978).
2) T. Nozaki, Y. Itoh, Y. Ohkubo, T. Kimura, and F. Fukushima: *Jpn. J. Appl. Phys.*, **24**, L801 (1985).

* Central Research Laboratory, Sumitomo Metal Mining Co., Ltd.

RIKEN Accel. Prog. Rep. 20 (1986)

III-3-5. Diffusion of Nitrogen into Silicon

Y. Itoh, T. Nozaki, Y. Ohkubo, and Y. Mochizuki

Nitrogen is often suspected as one of the most interesting residual impurities in semiconductor materials. However, the determination of a trace amount of nitrogen in high-purity substances and the study of its behavior are difficult owing to the surface contamination and to the lack of a suitable nitrogen radio-tracer. We previously reported the possibility of using ^{15}N as an activable tracer for this study.[1] In order to measure the diffusion of nitrogen into silicon, we employed a ^{15}N tracer together with the method of activating it by the $^{15}N(\alpha, n)^{18}F$ reaction ($E=20$ MeV) with an equal probability along the depth by rotating a set of aluminium absorbers of suitably selected thicknesses and widths in the α-particle beam path.[2]

The depth profile of nitrogen diffused into silicon at various temperatures was obtained by this activation and repeated fine etching with $HF-HNO_3$. The ^{15}N in-diffused samples were prepared at Hitachi, Ltd. Silicon wafers were covered with ^{15}N-nitride films formed by epitaxy from $^{15}NH_3$ and SiH_4 and heated in argon containing 1.5% of $^{15}N_2$ at 1275, 1300, or 1350°C for 73 to 163 h. Silicon without nitride film was also heated for the same periods. Films of $Na^{15}NO_2$ (30% enrichment) were used as an activation standard for ^{15}N. They were precipitated on a 13-μm Al foil to 4–13 mg·cm^{-2} in thickness from a suspension in aceton. Kapton films (2% nitrogen) were used to check the uniformity of activation along the depth. Figure 1 shows the activation probability along the depth under the experimental conditions. The depth profiles of ^{15}N in silicon treated at two different temperatures are shown in Fig. 2. Pavlov's group estimated the diffusion constant of nitrogen in silicon using an indirect method on some assumptions.[3] The curves calculated from their results are also given in Fig. 2 for comparison. We continue the study for more reliable diffusion constant and solubility of nitrogen in silicon using the direct method described in this report.

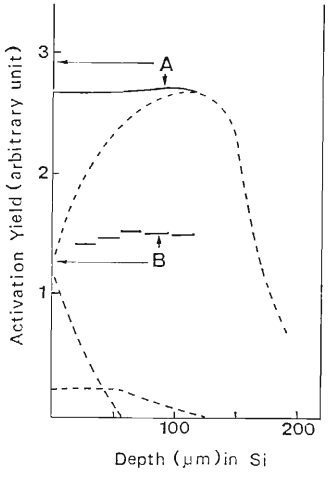

Fig. 1. Activation with an equal probability along the depth. Solid line (A), calculated relative activation yield consisting of three components (dashed lines) corresponding to the thickness of the aluminium absorber through which the 20 MeV α-particle passes; Solid line (B), relative activation yield.

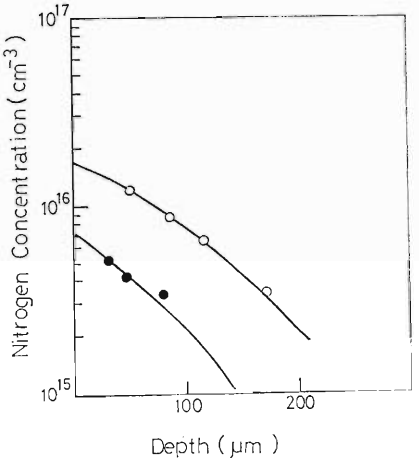

Fig. 2. In-diffusion profile of ^{15}N in silicon treated at 1350°C for 73 h (○) and at 1275°C for 163 h (●). The solid lines represent the curve calculated from Pavlov's data.

References

1) T. Nozaki, Y. Itoh, and Q. Qiu: Collected Papers for 7th MTAA, Ris, Natl. Lab., Copenhagen, p. 47 (1986).
2) Y. Itoh and T. Nozaki: *J. Radioanal. Chem.*, **70**, 329 (1982).
3) P. V. Pavlov, E. I. Zorin, D. I. Tetelbaum, and A. F. Khokhlov: *Phys. Status Solidi*, **35**, 11 (1976).

RIKEN Accel. Prog. Rep. 20 (1986)

III-3-6. Utilization of the D(^{3}He, p)^{4}He Reaction for High-Sensitivity Quantitative Analysis of Deuterium in Solids

Q. Qiu, T. Kobayashi, M. Yanokura, T. Nozaki,
M. Imai, and Y. Yatsurugi

Deuterium is used as an activable tracer free from the interference with environmental contamination which usually occurs in measurement of hydrogen in solids. We have already reported a quantitative analysis of deuterium using measurement of the solubility of hydrogen in single crystal silicon.[1] Samples for this measurement were prepared in Komatsu Electronic Metals Co., Ltd. by the following methods: (1) heating of high purity silicon in D_2 (100%) gas at 400, 700, 1,000, and 1,200°C for 10, 10, 8, and 5 h, respectively; (2) float zone-melting (FZ) of silicon in a slow stream of D_2–Ar in various mixing ratios (1, 10, 20, and 40% D_2) followed by sudden cut off of the heating power for rapid solidification of liquid silicon saturated with D_2 under a given partial pressure; and (3) pretreatment of the samples in heated trichloro-ethylene gas or by covering them with evaporated films of titanium or palladium and succeeding heating in D_2 gas at 1,200°C for 5 h. The pretreatment in (3) was expected to suppress the effect of surface oxide layer.

Deuterium contents in these samples were then measured. Often after measurement, the sample surface was washed with hydrofluoric acid or etched with HF–HNO_3 (5 to 200 μm etching) and the measurement was repeated. All silicon samples heated in 100% D_2 gas were found to contain about 2×10^{16} atm/cm^3 deuterium in the depth over 0.2 μm, regardless of the heating conditions. This value of deuterium concentration is nearly the detection limit of this method. Float zone-melting in 1% and 10% D_2 gas gave 2×10^{16} and 4.5×10^{16} atm/cm^3 D contents, respectively; but the zone-melting in 20% and 40% D_2 resulted in gas bubble formation in the silicon. The depth profile are shown in Fig. 1 for samples covered with surface layer of a-SiC, Ti, Pd, and SiO_2. The depth profile varied with the surface conditions of the samples. Surface oxide layer seems to suppress the in-diffusion rate noticeably. In order to obtain reliable solid solubility of hydrogen in silicon, we are making further efforts for preparing meaningful samples. Measurement for other materials are also under planning.

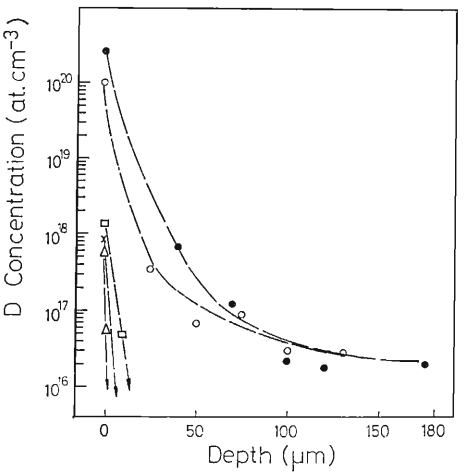

Fig. 1. Depth profile of deuterium in silicon heated in D_2 gas at 1,200°C for 5 h after various pretreatments. ●: Trichloro-ethylene treatment (heavy deposition of carbon), ○: Trichloro-ethylene treatment (light deposition of carbon), □: Without any pretreatment, △: Titanium evaporated film covering, ×: Palladium evaporated film covering.

Reference

1) Q. Qiu, T. Kobayashi, M. Yanokura, M. Imai, Y. Yatsurugi, and T. Nozaki: *RIKEN Accel. Prog. Rep.*, **19**, 129 (1985).

RIKEN Accel. Prog. Rep. 20 (1986)

III-3-7. Application of PIXE to Medical and Environmental Science

K. Maeda, Y. Sasa, H. Kusuyama, M. Maeda,*
H. Ishikawa, Y. Yokode, and M. Uda

PIXE (particle induced X-ray emission) spectroscopy is one of the most advanced, extremely sensitive and multielemental analyses. We have continued a study on the application of PIXE to medical and environmental science.[1-3] We report here the experiments recently made on human calculi and suspended particulates in sea water.

(1) Urinary stones

The study of calculus compositions is of prime importance to elucidate the mechanism of stone formation in human body. We have applied PIXE to the analysis of human urinary stones. Samples were surgically taken from patients of vesical (bladder, 3 cases), ureteral (8 cases), and renal (kidney, 1 case) stone diseases. Preliminary data obtained with some of these samples were reported previously.[4] The samples were irradiated with an 8 MeV He^+ beam of 0.5 mm in diameter. X-rays generated from the targets were detected with a Si(Li) detector through an X-ray absorber made of 1 μm polypropylene or 1.8 mm polyethylene film. The details of the data processing procedure were described elsewhere.[5]

Results of PIXE analysis are summarized in Table 1, where integrated peak intensities of Lα (for Pb) and Kα (for other elements) were normalized by use of Kα peak intensities of Ca which is a main component common to all of the samples. The stone types were determined by the X-ray diffraction method and/or IR spectrometry. The phosphate and oxalate stones coexist with each other but not with the urate stones. Magnesium is a main component of the phosphate stones and contained as much as Ca; whereas, much less amount of Mg is included in the oxalate and urate stones. The phosphate stones are characterized with high K and Sr contents in comparison to other stones. The Zn content changes drastically from sample to other and is extremely low in the urate stones (KI and TN). The vesical (bladder) stones seem to have a Na concentration higher than the others.

(2) Distribution of elements in calculus

To investigate the elemental distribution in calculi, scanning analysis of PIXE was carried out for large urinary stones. A crosssectional view of a vesical stone (KY in Table 1) is illustrated in Fig. 1. The stone is composed of layered outer shells (A) like an annual ring, a porous middle part (B), and a dense center part (C) including nuclei. The positions analyzed with PIXE are shown in Fig. 1 with △, ○, and ● for A, B, and C, respectively. Mean values of integrated intensities of Kα for each ele-

Table 1. Results of PIXE analyses on urinary stones: peak intensities of Lα (for Pb) and Kα (for other elements) normalized to CaKα=100.

Organ	Stone type	Patient	n_1	n_2	Absorber: 1 μm polypropylene							Absorber: 1.8 mm polyethylene				
					Na	Mg	P	S	Cl	K	Ca	Fe	Cu	Zn	Sr	Pb
Bladder	Phosphate	KY	12	12	0.74	41	182	<0.1	0.41	1.3	100	0.16	<0.28	7.8	0.90	<0.13
		KS	5	4	1.29	22	146	<0.1	0.61	2.3	100	0.43	<0.19	2.4	0.61	<0.17
		SO	1	1	1.16	24	144	0.9	1.9	1.8	100	1.5	<0.14	15.8	0.66	<0.07
Ureter	Phosphate	TK	1	1	0.22	17	143	0.4	0.28	2.4	100	0.80	<0.11	2.2	0.95	<0.07
		TO	1	1	0.67	8.9	104	0.5	0.48	1.2	100	<0.15	0.19	4.1	0.48	<0.08
	Phosphate	ES	3	1	0.45	0.6	39	1.3	0.80	0.55	100	1.8	0.31	4.8	0.30	0.26
	+Oxalate	YS	1	1	0.32	1.0	58	0.4	0.40	0.63	100	0.57	0.12	9.1	0.23	0.12
		MU	1	1	0.07	0.4	31	2.8	1.03	0.73	100	2.5	<0.17	12.9	0.26	0.11
	Oxalate	CN	2	0	0.19	0.2	9.3	0.5	0.42	0.42	100					
	Urate	KI	2	2	0.22	<0.1	0.4	0.3	0.61	0.43	100	3.4	0.16	0.5	0.13	<0.10
		TN	1	1	0.34	0.2	0.6	0.6	0.72	0.18	100	0.8	<0.17	0.5	0.12	<0.09
Kidney		TH	1	2	0.10	0.2	18.6	0.3	1.09	0.58	100	0.96	0.09	11.0	0.15	<0.08

n_1 and n_2 are number of analyzed points with a 1 μm polypropylene absorber and a 1.8 mm polyethylene absorber, respectively. Mean values are adopted for the targets of $n>1$.

* Tokyo University of Fisheries.

Table 2. Elemental distribution in a vesical stone (KY): peak intensities of Kα normalized to CaKα=100. SD: standard deviation.

Position	Absorber: 1 μm polypropylene					1.8 mm polyethylene			
	Na	Mg	P	Cl	K	Ca	Fe	Zn	Sr
Outside (outermost shell)	0.60	40	179	1.3	1.7	100	1.4	5.2	0.83
Inside (outermost shell)	0.55	34	172	0.5	0.5	100	<0.2	5.1	0.73
Outer part	0.80	27	151	0.5	1.0	100	<0.2	9.3	0.77
(SD, n=4)	(0.30)	(8)	(19)	(0.2)	(0.4)			(1.6)	(0.06)
Middle part	0.79	41	177	0.3	1.2	100	<0.3	8.8	0.97
(SD, n=4)	(0.18)	(22)	(55)	(0.2)	(0.4)			(1.5)	(0.13)
Center point	0.62	57	219	0.4	1.6	100	0.3	5.3	0.96
(SD, n=4)	(0.07)	(5)	(9)	(0.1)	(0.2)		(0.1)	(1.1)	(0.08)

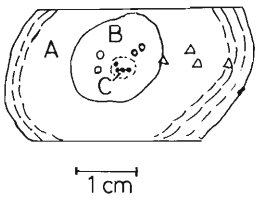

Fig. 1. Cross section of a vesical stone (KY in Table 1).

ment normalized to those of CaKα are given in Table 2, together with standard deviations (SD). High concentrations of Cl and Fe found outside the outermost shell may come from fluid surrounding the stone. Sodium and strontium seem to distribute almost homogeneously. Difference in Zn contents at the center part, and the middle and outer parts are beyond the standard deviations.

(3) Suspended particulates in water of the Antarctic Ocean

Suspended particulates act as main transport media for chemical species in hydrosphere. We have already reported the result of PIXE analysis on suspended particulates in the urban river water.[3,6] This year we have used PIXE to analyze suspended particulates in the water of the Antarctic Ocean where pollution caused by human activities is not so serious. Samplings were made in January and February 1984 at the stations located at (65°04′S, 116°09′E) and (60°56′S, 149°47′E). The sample waters were collected at the depths of 0, 100, 300, 500, 1,000, and 1,500 m at each station and filtered through 1 mg/cm² thick nuclepore filters of 0.80 μm in pore size. The filters loaded with the suspended particulates were washed with an ammonium carbonate solution and kept frozen until analysis. The concentration of Ca was rather high in the deep regions; however, some of the samples collected in the upper regions contained Ca in high concentration. In these samples the concentration of P was also high. Iron was enriched in the particulates collected in the deep regions. Aluminum seems to move in company with Fe.

References

1) K. Maeda, Y. Yokode, Y. Sasa, H. Kusuyama, and M. Uda: *Nucl. Instrum. Methods B*, **22**, 188 (1987).
2) M. Uda, K. Maeda, Y. Sasa, H. Kusuyama, and Y. Yokode: *Nucl. Instrum. Methods B*, **22**, 184 (1987).
3) K. Maeda, Y. Sasa, M. Maeda, and M. Uda: *Nucl. Instrum. Methods B*, **22**, 456 (1987).
4) K. Maeda, H. Kusuyama, Y. Sasa, Y. Yokode, and M. Uda: *RIKEN Accel. Prog. Rep.*, **19**, 118 (1985).
5) Y. Sasa, K. Maeda, and M. Uda: *Nucl. Instrum. Methods B*, **22**, 426 (1987).
6) K. Maeda, Y. Sasa, M. Maeda, S. Noriki, and M. Uda: *RIKEN Accel. Prog. Rep.*, **18**, 126 (1984).

RIKEN Accel. Prog. Rep. 20 (1986)

III-3-8. Application of PIXE and Diffraction Analysis to Ancient Remains

Y. Sasa, K. Maeda, and M. Uda

For the analysis of ancient remains, non-destructive and highly sensitive measuring methods are indispensable. PIXE is one of the most effective methods to gain our ends in view of elemental analyses. PIXE has advantages over other methods, *i.e.*, high sensitivity, simultaneous multielemental analysis, short data acquisition time, easy sample handling without pretreatment, limited amounts of samples and so on. Then several PIXE data have been reported on ancient potsherd.[1-6] Crystallographic analyses also bring us highly reliable information on structures and chemical constituents of archaeological samples.

In this report we will describe chemical and crystallographic surveys of ceramic products of different districts and ages. Concentrations of minor constituent elements in these ancient remains will give us keys to understand exchange or diffusion of cultures. These data will also contribute to elucidate technological backgrounds in ancient periods.

The samples analysed in this study were potsherds of different districts and ages: 1) three pieces of Majiayao category (B.C. 3000~4000) potsherds at the Yanshao stage of China from Qin'an Gansu China (referred to as Yanshao-1, 2, and 3, respectively), 2) three glazed sherds with brown-yellow, green, and blue color obtained from the Banbohr ruin in Pakistan dated back to 0–7th centuries (referred to as Banbohr-Brown-yellow, -Green, and -Blue), 3) three types of Japanese glazed porcelains named Kakiemon, Tsutsue, and UFSS11 (17th century). Target materials were irradiated with 8 MeV He^+ ions. The size of an ion beam focused on the target was 0.5×0.5 mm^2 and the beam intensity was selected as 0.2 or 20 nA on the targets for the case without or with an X-ray absorber. X-rays generated from the targets were detected with a Si(Li) detector through a 7.5 μm Be window. Measurements of trace amounts of elements which emit high energy X-rays were made through a thick polyethylene absorber (93 mg/cm^2) inserted between the target and the detector in order to depress the pile-up phenomenon in the detector. An electron shower was applied to the targets to reduce the charging effect. X-ray diffraction data were taken with use of an automated X-ray diffractometer equipped with a Cu radiation source, a graphite monochromator, and a NaI scintillation counter. A goniometer was scanned at a speed of $(2\theta^c/\text{min}) = 2$ and with time constant $= 1$ s.

Results of the PIXE analyses of the Chinese potsherds are summarized in Table 1, where integrated peak intensities for Kα were normalized by use of Si Kα peak intensities. The sherds have been painted with brown color agents for making simple and old fashioned patterns. PIXE analyses were carried out on both areas characterized with colored and non-colored. Mn, Fe, and S were concentrated on the brown colored parts for every Yanshao sample, suggesting that the color originated in compounds made from, at least, these three elements. The Yanshao-2 sherd had a high Al content on both colored and non-colored parts. This means that the sherd was produced by use of a type of raw material different from those of the other two sherds. X-ray diffraction analyses showed that α-quartz and orthoclase were main constituents in the three kinds of Yanshao samples. Mn_3O_4 or $(Mn, Fe)_3O_4$ was also detected from the colored parts. However, we found a muscovite, *i.e.*, a clay mineral including OH radi-

Table 1. Results of PIXE Analyses on Chinese potsherds.

	Na	Mg	Al	Si	P	S	Cl	K	Ca	Ti	Cr	Mn	Fe
Yanshao-1N*	1.1	4.3	28.9	100.0	4.2	0.73	0.73	13.1	22.8	0.47	0.07	0.11	2.1
Yanshao-1B*	0.68	3.0	24.9	100.0	4.5	2.1	0.51	13.3	12.0	1.1	0.11	7.70	4.7
Yanshao-2N	1.0	4.6	33.8	100.0	3.7	0.40	0.37	11.6	17.9	0.74	0.06	0.14	3.7
Yanshao-2B	0.96	4.2	36.2	100.0	3.9	0.79	0.20	12.9	19.4	0.92	0.05	5.1	5.9
Yanshao-3N	0.87	3.8	26.4	100.0	3.6	1.2	0.48	8.8	15.7	0.61	0.03	0.18	2.7
Yanshao-3B	0.76	2.5	25.8	100.0	4.4	4.1	0.98	11.7	18.2	0.89	0.07	7.4	7.9

* N and B represent non-colored and brown colored parts, respectively.
Each Kα intensity is normalized to Si Kα=100.0.

cals, from the X-ray pattern only for the Yanshao-2 sample. This suggests that the sherd was fired at lower temperature than those for the Yanshao-1 and Yanshao-3. Combining the results from PIXE and diffraction analyses we imagine that the Yanshao-2 sherd was produced at a place different from the other two or in earlier age than that for the others, and/or both. This assumption is also supported, at least in part, by the fact that the sound from tapping the sherd is characterized by a low-pitched tone for the Yanshao-2 but by a high-pitched one for the other two.

Surfaces of the Pakistan potsherds have been glazed and showed diffraction patterns characteristic of amorphous materials for all the samples examined in this study. However, the back and side faces of the potsherd were free from glazed materials and composed mainly of α-quartz and orthoclase together with small amounts of aluminosilicates. Crystallographically these main components are the same as those for Yanshao potsherds. It was confirmed from the PIXE analyses that the colors of the glazes are characterized by Pb and Fe (Pb Lα/Si Kα= ~0.03 and Fe Kα/Si Kα=~0.05) for the brown-yellow sherd as shown in Fig. 1, by Cu and Fe (Cu Kα/Si Kα=~0.006 and Fe Kα/Si Kα= ~0.006) for the green one, and Fe and Co (Fe Kα/Si Kα=~0.004 and Co Kα/Si Kα=~0.002) for blue one. In the latter two sherds high contents

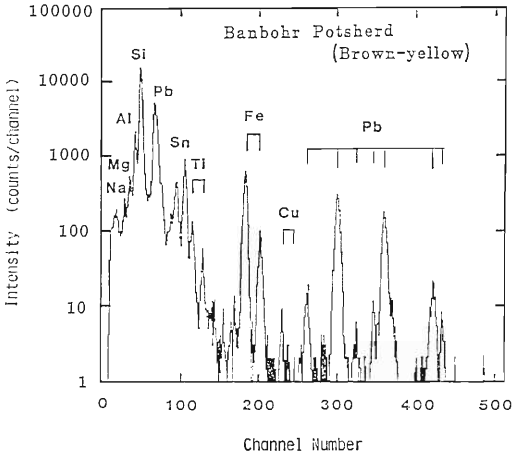

Fig. 1. PIXE spectrum from the Banbohr-Brown-yellow Potsherd dated back to 0–7th centuries.

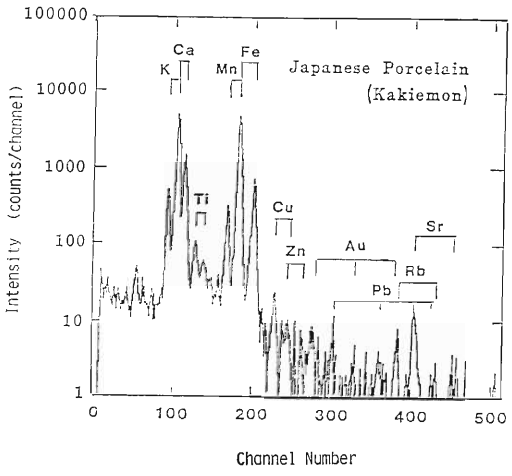

Fig. 2. PIXE spectrum from the Japanese porcelain, Kakiemon dated back to 17th century: a 1,000 μm polyethylene absorber was used.

of Na and K were found, which might make the glazes glassy.

Three kinds of Japanese green-blue procelains were also analyzed by PIXE. Impurities detected from glazed surfaces of Kakiemon were very low in contents, as shown in Fig. 2, compared with those from the ancient Chinese and Pakistan potsherds. Pale color was given by a small amount of Fe together with very small amounts of Ti, Mn, Cu, Zn, Au, and Pb. Such a tendency is, more or less, the same for the other two. This indicates that clay minerals and agents as raw materials were carefully chosen for porcelain production and glazing. The X-ray diffraction data also supported these results, *i.e.*, α-quartz was only one main constituent for the matrices.

References

1) G. Lagarde, I. Brissaud, J. Cailleret, P. Fontes, and Ch. Heitz: *Nucl. Instrum. Methods B*, **1**, 45 (1984).
2) Proc. PIXE Conf., in *Nucl. Instrum. Methods*, Heidelberg, Vol. 3 (1984).
3) I. Brissaud, A. Houdayer, C. Jehanno, and A. Sabir: *J. Radioanal. Nucl. Chem. Articles*, **89**, 473 (1985).
4) S. R. Ryan, H. J. Fischbeck, and K. Chesnut: *Nucl. Instrum. Methods B*, **10-11**, 645 (1985).
5) Proc. Int. Workshop on IBA in the Arts and Archaeology, in *Nucl. Instrum. Methods*, Pont-á-Mouson, Vol. B14 (1986).
6) Y. Sasa, K. Maeda, and M. Uda: *Nucl. Instrum. Methods B*, **22**, 426 (1987).

RIKEN Accel. Prog. Rep. 20 (1986)

III-3-9. Behavior of Light Elements in Hydrothermal Treatment of Glass Surface as Studied by Heavy-Ion Rutherford Forward Recoil Measurement

M. Aratani, Yanokura, Q. Qiu,* K. Sato, B. G. Yu,* and T. Nozaki

Weathering of minerals are regarded as fundamental recations on the surface of the earth. In the present study, a hydrothermal reaction of soda-lime glass was taken for a simple model of the early stage of the weathering, and its surface hydrothermally treated under various conditions are subjected to the Rutherford forward recoil measurement[1] with heavy ions from RILAC.

Pieces (9 mm × 19 mm) of S-1214 microslide glass (Matsunami Glass Ind., Ltd.) were boiled in water in a flask equipped with a reflux condenser for a few hours to several tens of hours. The samples were mounted on a target holder capable of supporting nine samples, and the target holder was placed at the center of a scattering chamber (1 m in diameter). Quantities and depth profiles of hydrogen in the surface layers of the samples were examined by using 50 MeV Ar^{4+} ion beam (2 mm × 2 mm), which was restricted around 25 nA after trial bombardment with high-intensity current, carried out to see irradiation effects on obtained spectra. The samples were slanted by an angle of 30° to the incident Ar^{4+} ion beam, and surface-barrier silicon detectors at the angles of 37° and 47° to measure recoiled light elements and to monitor argon scattered from the samples, respectively. In front of the 37° detector was located an aluminum foil of 20 μm, 13 μm, or 10 μm in thicknesses as an absorber for heavy recoils. SiO_2 films of 200 Å, 500 Å, and 1,000 Å in thicknesses on high-purity crystalline silicon and films of oxygen-containing amorphous silicon were employed for reference samples.

The energy spectra of forward recoil hydrogen are shown in Fig. 1. The spectrum for the untreated sample is regarded as being due to background hydrogen on the surface. The spectrum for the sample treated for 28 h is shown in Fig. 2 in comparison with the background hydrogen. The background hydrogen level is around 5×10^{15} atoms/cm^2 in every case. This value is the same as those for the surfaces of various kinds of substances observed by using this method.[2] Peak widths at half height of hydrogen were almost constant for all the samples independent of their treating times. The peak height increased with the treatment time and appeared to reach a saturated value in ten hours or so; this may be attributed to depth resolution estimated to be 500 Å under the present experimental conditions.

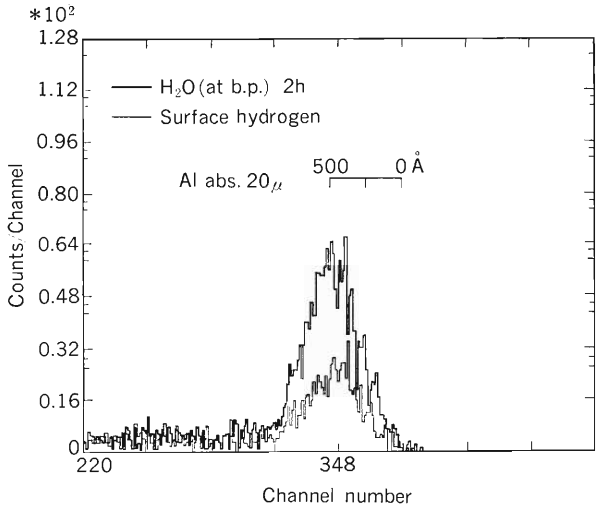

Fig. 1. Energy spectra of forward recoil hydrogen for the sample treated for 2 h and that without treatment.

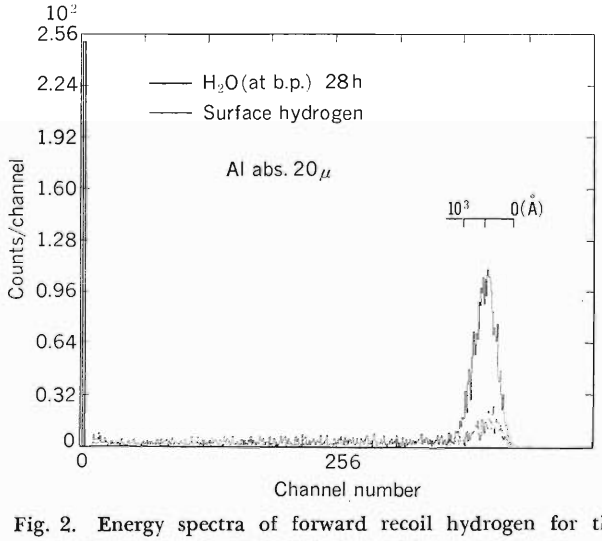

Fig. 2. Energy spectra of forward recoil hydrogen for the sample treated for 28 h and that without treatment.

* Research Laboratory for Nuclear Reactors, Tokyo Institute of Technology.

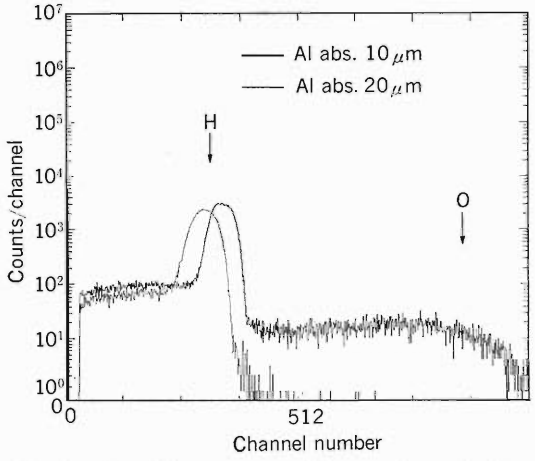

Fig. 3. Spectra with oxygen continuum through 10 μm Al foil and without it through 20μm Al foil (Oxygen containing a-Si).

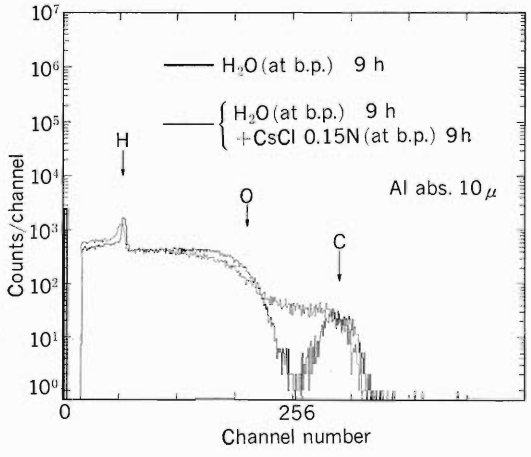

Fig. 4. Spectra for the samples with and without 0.15 M CsCl treatment for 9 h after hydrothermal treatment for 9 h.

Time required to obtain above spectra was a quarter hour or so. The irradiation effect on the heavy-ion bombardment was negligibly small under this condition, because slight tailing of hydrogen peak due to diffusion was recognized 4 h after irradiation. These spectra were obtained by using a 20 μm Al absorber.

The spectrum demonstrating oxygen continuum through 10 μm Al foil is shown in Fig. 3, in which a shift of the hydrogen peak is observed because of the difference in thicknesses between two foils. The spectrum for the sample boiled with a 0.15 M CsCl solution for 9 h after hydrothermal treatment for 9 h is shown in Fig. 4, in comparison with that for the sample treated only hydrothermally for 9 h. It is seen that decrease in surface oxygen and increase in surface carbon resulted from the CsCl treatment; this may be attributed to CO_3^{2-} or HCO_3^{2-} covering the fresh Cs glass surface.

Very recently, the hydrothermal reaction of glass came to attract attention in view not only of the fundamental processes in the hydrosphere but also of urgent problems related to disposal of radioactive waste. Rutherford scattering analysis comes to show its general usefulness for various problems.

References

1) H. Nagai, M. Aratani, T. Nozaki, M. Yanokura, I. Kohno, O. Kuboi, and Y. Yatsurugi: *RIKEN Accel. Prog. Rep.*, **16**, 125 (1982); H. Nagai, M. Aratani, S. Hayashi, T. Nozaki, M. Yanokura, I. Kohno, O. Kuboi, and Y. Yatsurugi: *RIKEN Accel. Prog. Rep.*, **17**, 102 (1983).
2) M. Aratani, H. Nagai, S. Hayashi, M. Yanokura, O. Kuboi, Y. Yatsurugi, I. Kohno, and T. Nozaki: *RIKEN Accel. Prog. Rep.*, **17**, 104 (1983).

RIKEN Accel. Prog. Rep. 20 (1986)

III-3-10. Substitution of Positive Ions in Glass Surface Layer Studied by Heavy-Ion Rutherford Scattering Analysis

B. G. Yu, M. Aratani, M. Yanokura, T. Nozaki, and E. Arai*

The ERDA (Elastic recoil detection analysis) technique in conjunction with RBS (Rutherford back scattering) has been used successfully in the analysis of positive ion substitution near the surface of soda-lime glass.[1] Soda-lime glass was boiled with H_2O for 24 h and then boiled with CsBr or $BaBr_2$ solution (0.1 N) for 3, 6, and 46 h. We expected the substitution of H^+ for Na^+ in the H_2O treatment and that of Cs^+ or Ba^{++} for H^+ in the succeeding treatment. The experiments were carried out using with 25 nA 49.65 MeV $^{40}Ar^{4+}$ from RILAC. The detector angles were 35° for detection of hydrogen by ERDA, 45° for the detection of Cs or Ba by RFS, and 165° for the detection of Cs or Ba by RBS. The target angle was 30° to the incident beam, and the beam spot was 1.5 × 1.5 mm² on the target.

The ERDA spectra are shown in Fig. 1 and RBS spectra in Fig. 3. Figure 2 shows spectra of RFS (Rutherford forward scattering) from Cs and of ERDA for light elements. The ERDA spectra in Fig. 1 obtained for the sample treated for 46 h in the CsBr solution show much less hydrogen than for the samples treated for 6 or 3 h. For these samples, an increase in Cs amount was observed

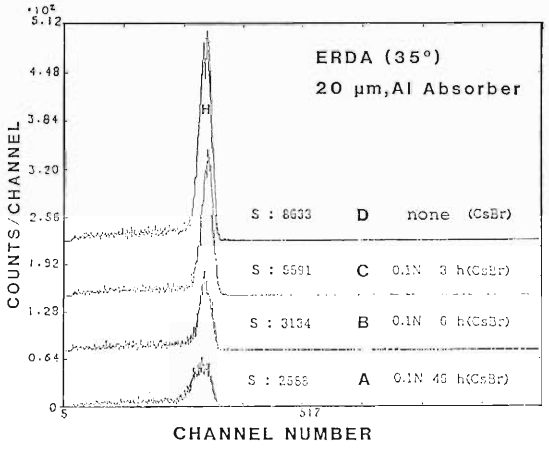

Fig. 1. ERDA spectra of H recoiled by Ar ions from the soda-lime glass boiled with water (24 h) followed by boiling with 0.1 N CsBr solution. Time of CsBr solution treatment: A, 46 h; B, 6 h; C, 3 h; D, no treatment. S indicates a hydrogen peak area.

* Research Laboratory for Nuclear Reactors, Tokyo Institute of Technology.

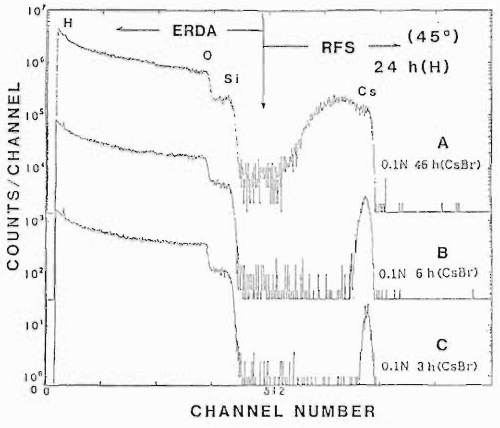

Fig. 2. ERDA spectra of H, O, and Si recoiled by Ar ions, and RFS spectra of Cs obtained with Ar ions.

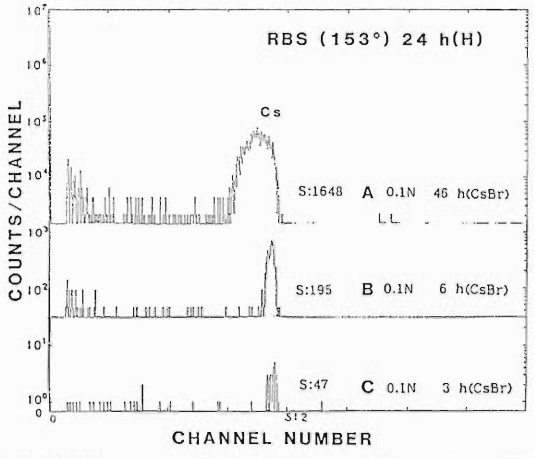

Fig. 3. RBS spectra of Cs obtained with Ar ions. S indicates a Cs peak area.

with decreasing H amount in the RFS spectra in Fig. 2 and RBS spectra in Fig. 3. For the sample treated for 46 h, the peak in the spectrum indicates that Cs is not located on the surface but inside the surface. The ERDA technique in conjunction with RBS has proved to be highly useful in tracing the movement of light and heavy elements simultaneously as exemplified by the substitution of positive ions in the glass surface layer.

Reference

1) B. G. Yu, M. Aratani, M. Yanokura, T. Nozaki, and E. Arai: Extended Abstracts, 47th Fall Meeting Jpn. Soc. Appl. Phys., p. 356 (1986).

RIKEN Accel. Prog. Rep. 20 (1986)

III-3-11. Elastic Recoil Analysis of Implanted H_2^+ Ions in Magnetic Bubble Garnets

R. Imura, R. Suzuki, M. Aratani, M. Yanokura, and T. Nozaki

Ion-implanted magnetic bubble memory devices are capable of very high-density storage.[1] These devices use the change in magnetic anisotropy of magnetic garnet films caused by internal stress due to ion implantation. High dose H_2^+ ions are usually implanted into the garnets to induce large anisotropy field changes. In the development of these devices, precise depth-profile analysis of the implanted H_2^+ ions has been requested to investigate the implantation and annealing effects of the H_2^+-implanted layer. We studied these effects by measuring the depth profiles of H_2^+ ions and the strain induced by implantation in bubble garnet films.

Elastic recoil detection analysis (ERDA) was used successfully for the depth-profile analysis of H_2^+ ions implanted in garnets. Using 50 MeV Ar^{++} ions generated by RILAC, we detected forward recoiled H^+ ions at a total scattering angle of 43° for the sample tilted at 33° with respect to the beam axis. Strain depth profiles were determined precisely from the X-ray rocking curve analysis based on the dynamical theory of X-ray diffraction.[2] Along with these measurements, H_2^+ ions bonding state was also investigated by means of Fourier transformed-infrared spectroscopy (FT-IR) analysis with attenuated total reflection method.[3]

Accuracy of the H_2^+ depth-profile analysis and the detection limit of H_2^+ ions in garnets in elastic recoil detection analysis method were checked by changing acceleration energy and ion dose in H_2^+ implantation. Figure 1 shows typical energy spectra for H_2^+-implanted garnet samples. The depth of the main peak in the H_2^+ ions profile became deep with increasing energy for implantation. A small peak which is found at the surface is attributed to absorbed hydrogen. The depth of the main peak agreed with the value calculated from the LSS (Lindhard, Scharff, and Schiott) theory. This depth-profile analysis indicates that the H_2^+ ions implanted in garnets can be measured with accuracy of 0.06 to 0.08 μm in depth resolution. The total H_2^+ ions content which is obtained from the integration of the profile is proportional to the implantation dose. The accuracy of H_2^+ ions content is within 10%. Considering the error of measurements and the background energy spectrum, detection limit of the H_2^+ ions implanted in garnets is found to be approximately $1 \times 10^{16}/cm^2$.

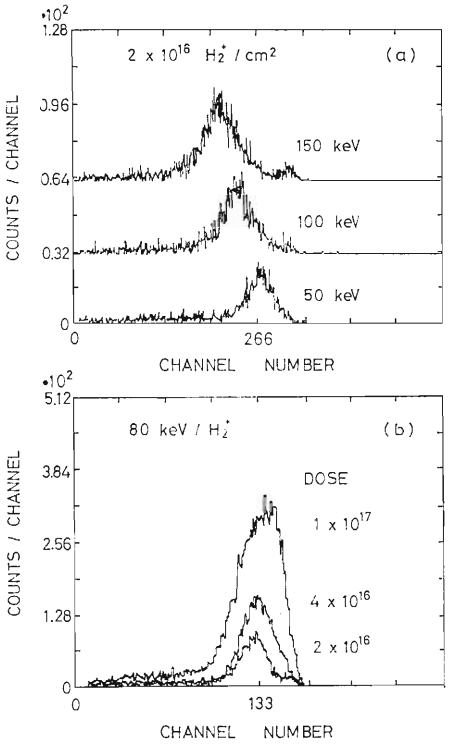

Fig. 1. Energy spectra for H_2^+ ions implanted in bubble garnets. (a), Dependence of H_2^+ implantation energy; (b), Dependence of H_2^+ implantation dose.

Depth profiles of H_2^+ ions and strain are shown in Fig. 2 for an as-implanted sample (180 keV, $4 \times 10^{16}/cm^2$) and the samples annealed at 150 and 200°C. As expected from the LSS theory, the depth of the main peak in the H_2^+ ions profile immediately after implantation is found deeper than that of the main peak in the strain profile. It should be noted that H_2^+ ions diffuse toward the surface by annealing and their distribution overlapped with the strain distribution after annealing at 150°C.

Figure 3 shows FT-IR spectra observed in the same samples as those shown in Fig. 2. There is no absorption related to the implanted H_2^+ ions in the spectrum before annealing; however, a strong absorption occurs at a wavenumbers of about 3,400 cm^{-1} in the spectrum of the sample annealed

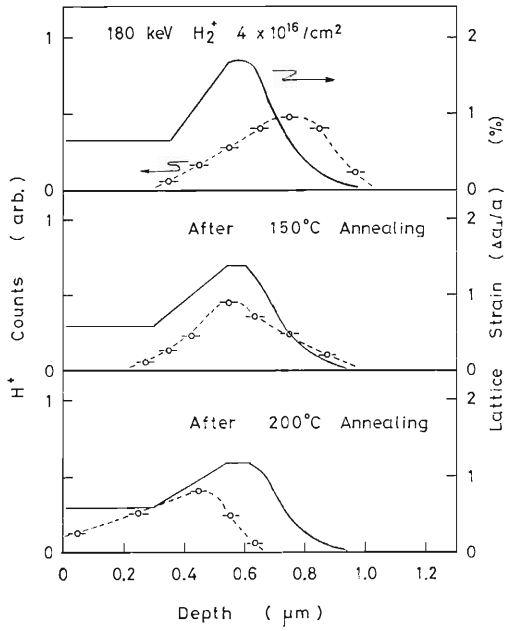

Fig. 2. Depth profiles of H_2^+ ions and strain for an as-implanted sample (180 keV, 4×10^{16}/cm²) and samples after annealing at 150 and 200°C.

at 150°C. This strong absorption indicates the existence of OH-bonding. It should be noticed that the H_2^+ ions implanted in garnets are combined with oxygen by annealing and the OH absorption becomes strong when the H_2^+ ions distribution overlapped with the strain distribution. Since the annealing temperature which gives the overlapping of distribution in H_2^+ ions and distribution in strain corresponds to temperature which induces the OH-bonding, the formation of the OH-bonding is considered to be due to the combination of diffused H_2^+ ions and free oxygen which are present in the region damaged by implantation.

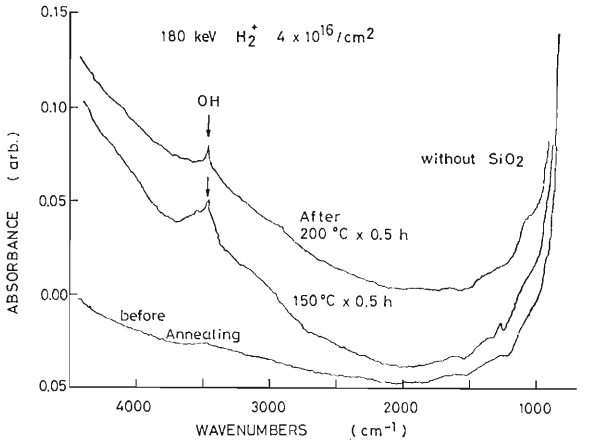

Fig. 3. FT-IR spectra observed for the same samples as those in Fig. 2.

Using elastic recoil detection analysis, X-ray analysis, and FT-IR spectroscopy, we examined the formation process of the OH-bonding in H_2^+-implanted garnets. Elastic recoil detection analysis is very useful method for the study of annealing behavior of H_2^+ ions implanted in bubble garnets.

References

1) Y. Sugita, R. Suzuki, T. Ikeda, T. Takeuchi, N. Kodama, M. Takeshita, R. Imura, T. Satoh, H. Umezaki, and N. Koyama: *IEEE Trans. Magn.*, **MAG-22**, 239 (1986).
2) T. Takeuchi, N. Ohta, Y. Sugita, and A. Fukuhara: *J. Appl. Phys.*, **54**, 715 (1983).
3) R. Imura and Y. Sugita: *J. Appl. Phys.*, **60**, 3269 (1986).

RIKEN Accel. Prog. Rep. 20 (1986)

III-3-12. Behavior of Releasing Agents Coated on Heated Substrates as Studied by Heavy-Ion Rutherford Scattering

I. Sugai, H. Kato, M. Aratani, M. Yanokura, and T. Nozaki

Heavy-ion Rutherford scattering was used for the study of the behavior of $NiCl_2$, which is used as a releasing agent in the preparation of a self-supporting carbon foil and is known to improve the lifetimes of the foils deposited on a substrate at high temperatures.[1,2] The releasing agent coated between the substrate and deposited layer plays important roles when the layer is separated in liquids, for example, water. Three kinds of measurements were performed: 1) dependence of the substrate temperature on the lifetime of the carbon foil; 2) substrate temperature effects on the behavior of $NiCl_2$; and 3) characterization on $NiCl_2$ coated on a heated substrate.

The samples were prepared by coating $NiCl_2$ to about 20 $\mu g/cm^2$ on a slide-glass plate pre-cleaned (Matsunami glass) and outgassed by heating them at 250°C for 15 min. The temperature of the substrates was controlled by a thermo-meter to within $\pm$ 5°C. The heating system for the radiation heating is composed of Kantal tantalum alloy heater wires, which was set inside the double stainless-steel roof for thermal shielding. The substrates coated with a releasing agent was kept at various temperatures from 25 to about 500°C during the DC arc-discharge deposition, and the effect of the temperature on the lifetime of the foils was investigated.

The results obtained are shown in Fig. 1. No clear improvement of the lifetime was observed. No measurement was carried out above 430°C, at which the substrate did not release the deposited carbon layer by immersion in water; the carbon layer could not be removed from the substrate by rubbing with a finger. In order to study the reason for this in releasing, we carried out following experiment. The substrate coated with $NiCl_2$ to about 100 $\mu g/cm^2$ at room temperature was heated to 460°C, and the weight changes of $NiCl_2$ was determined; the results are listed in Table 1.

During the heating at 400°C, the glass substrate changed its color to pale brown, and the surface was removed with a finger more easily than that without heating treatment. This result suggests that the $NiCl_2$ deposited at 460°C.

The results listed in Table 1 shows that most of $NiCl_2$ sublimated above 460°C. The glass substrates heated to temperatures lower than about 350°C were transparent. However, when the substrates heated at 350°C were exposed to the atmosphere, their surfaces changed to opaque due to the deliquescence of $NiCl_2$. The carbon layer deposited on the deliquescent $NiCl_2$ can not be lifted off from the substrate in water. Hence carbon should be deposited on the $NiCl_2$ later in the vacuum; the carbon layer thus prepared can be easily removed in water.

We applied the heavy-ion Rutherford scattering method both to backward (so-called Rutherford backscattering; RBS) and to forward angles to study

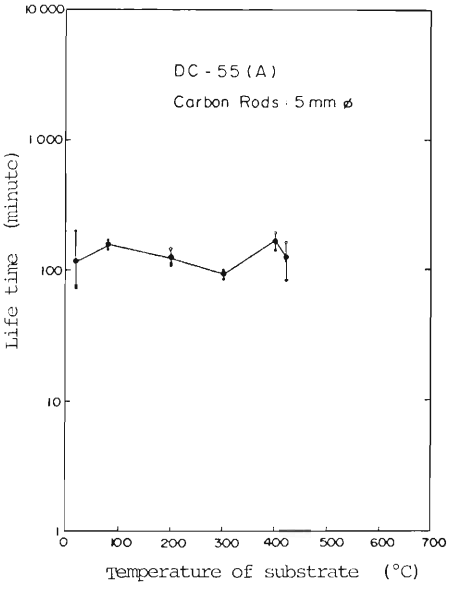

Fig. 1. Dependence of the substrate temperature on the lifetime of carbon foils.

Table 1. Effect of heat treatment on the decrease in the thickness of the $NiCl_2$ releasing agent.

Sample No.	Thickness of $NiCl_2$ before heating ($\mu g/cm^2$)	Thickness after heating at 460°C ($\mu g/cm^2$)	Decreased amount ($\mu g/cm^2$)
1	100	10	90
2	90	7	83
3	100	8	92
4	100	30	70

Samples #1, 2, and 3 coated on slide glasses and #4 coated on 4 μm Al thin foil.

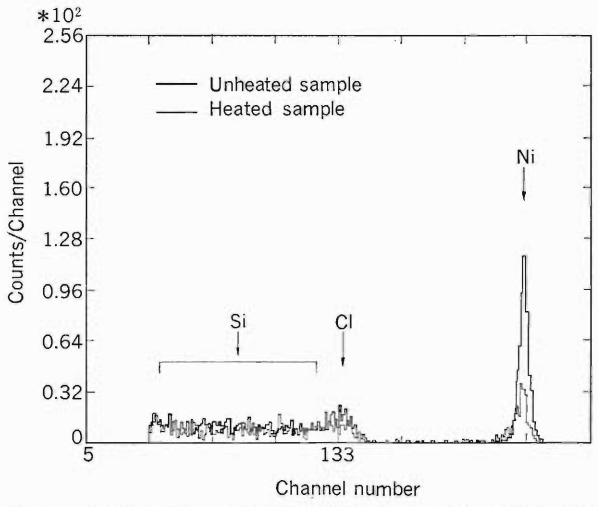

Fig. 2. Spectra of particles observed at backward angle (165°) for unheated and heated samples.

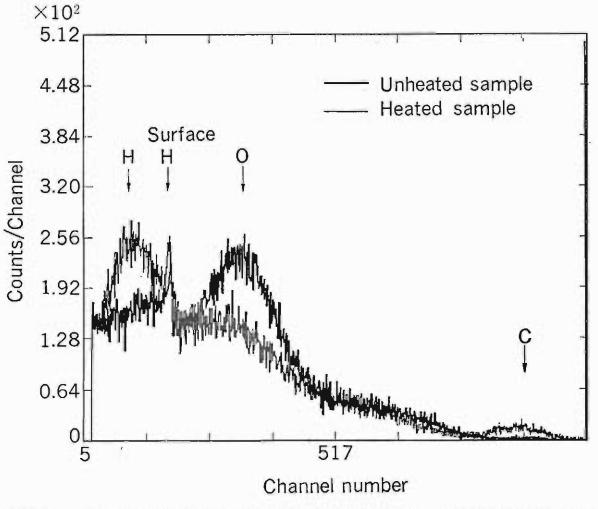

Fig. 3. Spectra of recoiled particles at forward angles (35°) for unheated and heated samples.

the behavior of $NiCl_2$ in the heating treatment. An ion beam of 50 MeV Ar^{4+} with 20 nA delivered from RILAC was used. Spectra of argon particles at backward angles and recoiled particles at forward angles are shown in Figs. 2 and 3, respectively, where a heated and unheated samples are compared.

Figure 2 clearly shows that the amount of the Ni layer on the substrate was decreased more pronouncedly than that on the unheated substrate. Figure 3 shows the spectra of light elements oxygen, carbon, and hydrogen. The amounts of hydrogen in the internal layer and on the surface were significantly reduced by heat treatment as well as those of carbon.

Oxygen, on the other hand, was increased by heat treatment, indicating that a chemical reaction occurred in the slide-glass substrate in the heating treatment. Further experiments are in progress.

References

1) S. Takeuchi, C. Kobayashi, Y. Satoh, T. Yoshida, E. Takekoshi, and M. Maruyama: *Nucl. Instrum. Methods*, **158**, 333 (1979).
2) J. Jaklovsky, ed.: Preparation of Nuclear Target for Particle Accelerators, Plenum Press, New York and London, pp. 17, 65 (1981).

RIKEN Accel. Prog. Rep. 20 (1986)

III-3-13. Evaluation of W/GaAs Interface Diffusion by the Rutherford Back Scattering (RBS)

K. Saito, K. Suzuki,* M. Yanokura, M. Aratani,
K. Sato, and T. Nozaki

A tungsten film is a promising gate electrode for a GaAs field effect transistor (FET). Since the electrical properties of FET is affected by the reaction or the diffusion at the interface of the tungsten film and the GaAs substrate, evaluation of these phenomena is indispensable for development of FET. The interface diffusion or reaction has been generally evaluated by Auger Electron Spectrometry (AES) or Secondary Ion Mass Spectrometry (SIMS) in which elemental depth profiles are obtained by sputtering the specimen with accelerated ions. In the W/GaAs systems, however, the depth resolution of an elemental profile is lowered by non-uniform sputtering and an accurate profile of a very thin interface layer can not be obtained in these methods. The RBS method is expected to be suitable this for purpose compared with other methods.

In order to obtain the high resolution for elemental depth profiles, high-energy heavy ions (Ar^{4+}, 50 MeV) from RIKEN RILAC were used and the analytical conditions were investigated. As a preliminary experiment, RBS measurements were performed with the most commonly used geometrical arrangement and an incident beam angle of 90°. Back scattered ions were measured at high angles.

The measured samples were non-annealed and annealed W(1,000 Å)/GaAs system. The RBS spectra, obtained by setting the angle of back scattered ions to be 157°, are shown in Fig. 1. Peaks in the high energy part of the profiles represent tungsten films and in the low energy part, a GaAs substrate. The separation between the peaks for the tungsten film and the GaAs substrate is fairly well, but the depth resolution, *i.e.* the sharpness of the shoulder of these peaks, is not satisfactory. A lower energy parts of the tungsten profile for the annealed sample is somewhat deformed. This deformation is considered to indicate the formation of a tungsten compound at the surface by annealing, though it cannot be identified in this experiment. In order to improve

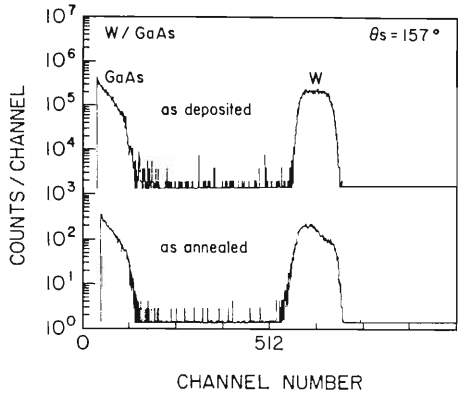

Fig. 1. RBS spectra of W (1,000Å)/GaAs system with and without annealing at 800°C for 30 min in nitrogen atmosphere. The depth resolution is 150Å.

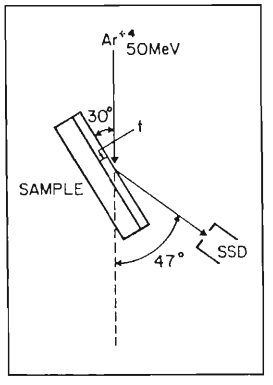

Fig. 2. Geometrical arrangement for high resolution depth analysis. Depth resolution is improved by tilting the sample and setting the detector at a smaller scattering angle.

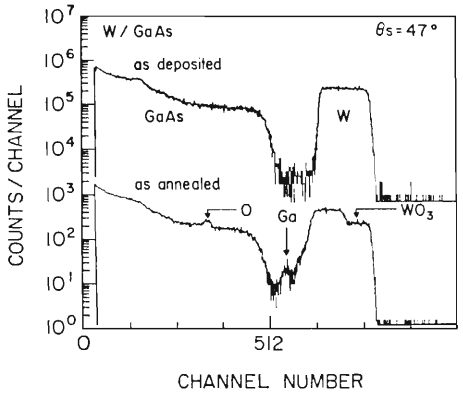

Fig. 3. RBS spectra for W (1,000Å)/GaAs systems obtained with the geometrical arrangement shown in Fig. 2. Depth resolution was improved remarkably to be less than 100Å.

* R&D Center, Toshiba Corp.

the depth resolution, measurements were performed with a lower incident-beam angle (30°) and a lower detection angle (47°) as shown in Fig. 2. The results of the RBS measurements with the same samples are shown in Fig. 3. The depth resolution was improved remarkably and was estimated to be less than 100 Å from the sharpness of the shoulder of the tungsten profile in the non-annealed sample. Interface diffusion of tungsten and gallium or arsenide, which is not clear in Fig. 1, was clearly observed in the annealed sample. Substrate atoms were found to diffuse deeply into tungsten films. Another merit of this geometry is to permit detection of recoiled atoms. The peak at a channel number 300 appearing on the profile of the GaAs substrate was identified with oxygen on tungsten film surface, which suggested the formation to tungsten oxide by annealing. In Fig. 4, the RBS spectra of annealed W/GaAs and WN_x/GaAs systems are shown.

Interface diffusion is not observed in the WN_x/GaAs system. The addition of nitrogen was found to improve the heat resistance of tungsten films.

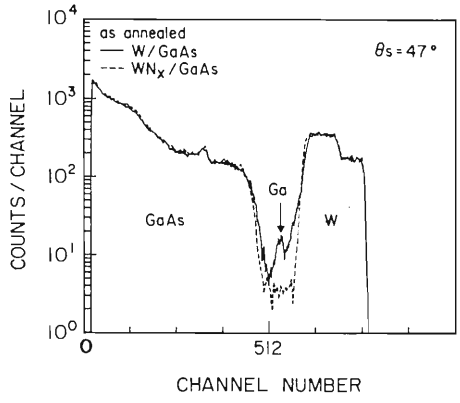

Fig. 4. RBS spectra for W (1,000Å) /GaAs and WN_x (1,000Å) / GaAs systems after annealing at 800°C for 30 min in nitrogen. No diffusion was observed at the interface in WN_x/GaAs system as compared with W/GaAs system, in which a large number of substrate atmos diffuse into a W-film.

RIKEN Accel. Prog. Rep. 20 (1986)

III-3-14. *In Situ* Emission Mössbauer Study on $^{119}Sb^{5+}$ ($\rightarrow ^{119}Sn$) and $^{57}Co^{2+}$ ($\rightarrow ^{57}Fe$) Ions at α-Fe_2O_3-Aqueous Solution Interface

S. Ambe, T. Okada, and F. Ambe

We previously reported Mössbauer spectroscopic investigations on the chemical states of no-carrier-added $^{119}Sb^{5+}$ and $^{57}Co^{2+}$ adsorbed on α-Fe_2O_3.[1-1)] In this period, *in situ* emission Mössbauer measurement was made on $^{119}Sb^{5+}$ ions adsorbed on α-Fe_2O_3 together with non-radioactive Sb^{5+} carrier ions. The effect of Sb^{5+} ions on the adsorption state of $^{57}Co^{2+}$ on α-Fe_2O_3 was also studied.

The $^{119}Sb^{5+}$ ions were adsorbed on 30 mg α-F_2O_3 powder from a 10 cm^3 0.25 mol/dm^3 KCl solution containing about 1 mg Sb^{5+}. About 0.3 mg Sb^{5+} was adsorbed at pH 2.5 and 4.0. The amounts of Sb adsorbed are less than that required to cover all the α-Fe_2O_3 surfaces monomolecularly. The experimental set up of the *in situ* emission Mössbauer measurement was described elsewhere.[2)]

The emission Mössbauer spectra obtained are shown in Fig. 1. It is seen from Fig. 1 that the width of the emission Mössbauer spectrum at pH 2.5 is much smaller than that of the no-carrier-added $^{119}Sb^{5+}$ ions,[2,5)] while essentially no effect of carrier Sb^{5+} ions is observed at pH 4.0. The observation at pH 2.5 is indicative of high energy bonding at low coverages, *i.e.*, in the absence of carrier Sb, the sites forming strong chemical bonds are occupied preferentially by $^{119}Sb^{5+}$. These interactions of $^{119}Sb^{5+}$ with strong bonding site are diluted out in the presence of carrier Sb leading to the small line width and weak average bonding.

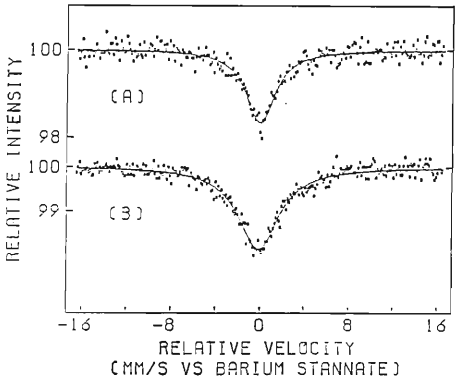

Fig. 1. *In situ* emission Mössbauer spectra of $^{119}Sb^{5+}$ ($\rightarrow ^{119}Sn$) ions adsorbed on α-Fe_2O_3 with Sb^{5+} carrier from 0.25 mol/dm^3 KCl solution: (A) pH 4.0 and (B) 2.5.

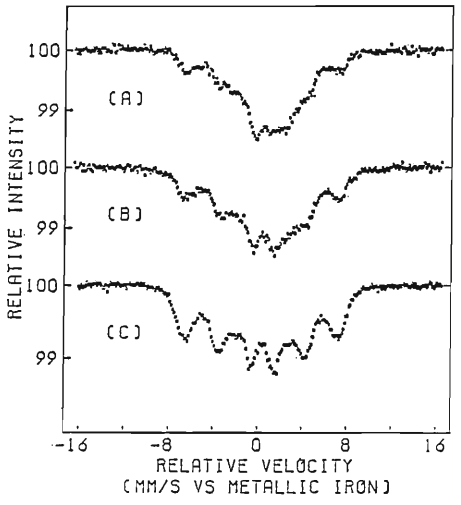

Fig. 2. *In situ* emission Mössbauer spectra of $^{57}Co^{2+}$ ($\rightarrow ^{57}Fe$) ions absorbed on α-Fe_2O_3 with Sb^{5+} ions from 0.1 mol/dm^3 KCl solution at pH (A) 5.5 and (B) 9.2 and from (C) 0.3 M KOH.

When bivalent $^{57}Co^{2+}$ ions were adsorbed on α-Fe_2O_3 together with Sb^{5+} ions, an increase in adsorption in the weakly acidic region was observed. For example, when 30 mg α-Fe_2O_3 was shaken with 10 cm^3 0.1 mol dm^{3-} KCl solution at pH 5.5 containing no-carrier-added $^{57}Co^{2+}$ and about 1 mg Sb^{5+} ions, 95% of $^{57}Co^{2+}$ and about 30% of Sb ions were adsorbed. The $[Sb(OH)_6]^-$ anions are considered to facilitate adsorption of bivalent $^{57}Co^{2+}$ ions on the positively charged surfaces of α-Fe_2O_3.

The emission spectra of the bivalent $^{57}Co^{2+}$ ions adsorbed under these conditions are shown in Fig. 2 along with the results obtained under different conditions. The *in situ* spectra of bivalent $^{57}Co^{2+}$ coadsorbed with Sb^{5+} ions are very different from those of $^{57}Co^{2+}$ adsorbed alone,[5)] showing a marked effect of the coadsorbed Sb^{5+} ions on the chemical structure of adsorbed $^{57}Co^{2+}$. The emission Mössbauer spectra are complex and their analysis is unfinished. It is evidents from the spectra, however, that the ^{57}Fe ions produced by EC decay of $^{57}Co^{2+}$ interact magnetically with the ordered ferric ions of the substrate; this means that $^{57}Co^{2+}$ are not adsorbed on the surface Sb^{5+} ions, but directly on the surface of α-Fe_2O_3.

References

1) T. Okada, S. Ambe, F. Ambe, and H. Sekizawa: *J. Phys. Chem.*, **86**, 4726 (1982).
2) F. Ambe, S. Ambe, T. Okada, and H. Sekizawa: *RIKEN Accel. Prog. Rep.*, **17**, 109 (1983).
3) F. Ambe, T. Okada, S. Ambe, and H. Sekizawa: *J. Phys. Chem.*, **88**, 3015 (1984).
4) F. Ambe, S. Ambe, T. Okada, and H. Sekizawa: *RIKEN Accel. Prog. Rep.*, **18**, 141 (1984).
5) F. Ambe, S. Ambe, T. Okada, and H. Sekizawa: Geochemical Processes at Mineral Surfaces (eds. J. A. Davis and K. F. Hayes), Amer. Chem. Soc., Washington, DC, p. 403 (1986).

RIKEN Accel. Prog. Rep. 20 (1986)

III-3-15. Emission Mössbauer Studies of No-Carrier-Added Sb-119 Electrodeposited on Gold

S. Ambe, F. Ambe, T. Okada, I. Tanaka,*
S. Nasu,* and F. E. Fujita*

In electrolysis of small amounts of antimony, it has been pointed out that the yield of electrodeposition is low and that the electrodeposited material is partly redissolved by washing with water.[1,2] The redissolution of electrodeposit by washing is a serious and general problem in preparation of thin radioactive sources. In relation to this problem it is not only important but also interesting to clarify the chemical states of deposits.

The present paper reports electrodeposition of no-carrier-added ^{119}Sb(V) (Mössbauer source nuclide of ^{119}Sn) from a Li_2SO_4 solution and the chemical states of electrodeposited ^{119}Sb on foil by *in situ* and *ex situ* emission Mössbauer spectroscopy.

No-carrier-added ^{119}Sb(V) was electrodeposited at about 10 V on an Au foil cathod (10 μm in thickness, 18 mm in diameter) from about 30-cm^3 0.12-mol dm^{-3} Li_2SO_4 solution at pH 1–12 using a spiral Pt wire anode at 50–60°C.

Emission Mössbauer measurement on (^{119}Sb→)^{119}Sn was performed on convensional Mössbauer spectrometers (Austin S-600 and Ranger 700 series) using ^{119}Sb on Au foil as a source and $BaSnO_3$ (0.9 mg ^{119}Sn cm^{-2}) as a standard absorber. The isomer shifts are presented relative to $BaSnO_3$ at room temperature.

Although no appreciable electrodeposition of ^{119}Sb was observed from weak alkaline and neutral solutions within 1 h, ^{119}Sb was efficiently electrodeposited at pH 1–2. In the present study electrolysis was carried out with a 0.12-mol dm^{-3} Li_2SO_4 solution at pH 1.5. Typical yield curves of electrodeposition are shown in Fig. 1. The dotted line shows that interruption of electrolysis for sampling an aliquot from the electrolyte resulted in redissolution of the deposited ^{119}Sb. The other points in Fig. 1 were obtained by sampling aliquots under applied voltage. Although the experimental conditions were essentially the same, the yield varied greatly from a run to another.

A typical *in situ* emission Mössbauer spectrum of ^{119}Sb on Au is shown in Fig. 2(a). It consists of two singlets with isomer shifts of 1.66 and 2.72 mm s^{-1}.

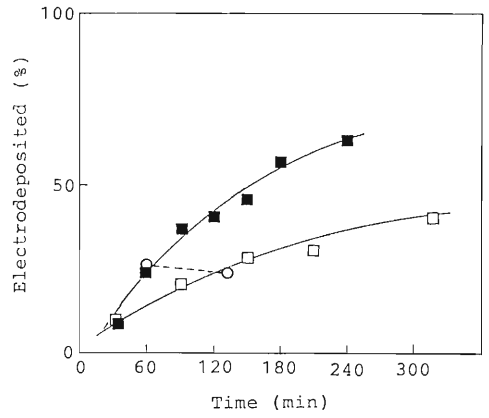

Fig. 1. Yield of electrodeposition of ^{119}Sb (V) on a gold foil.

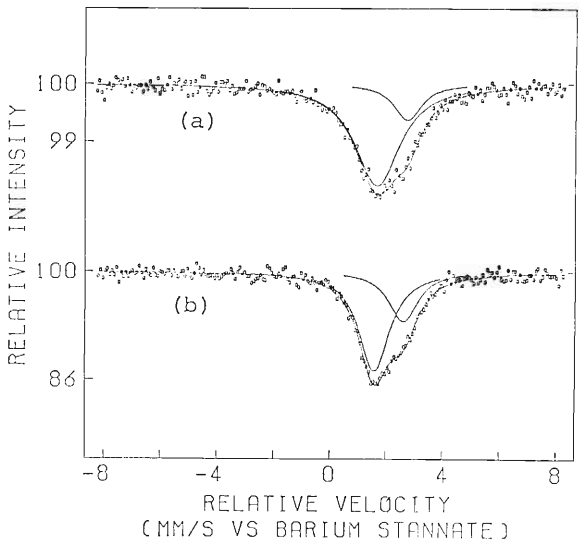

Fig. 2. *In situ* (a) and *ex situ* (b) emission Mössbauer spectra of ^{119}Sb on gold foils.

We reported previously that the substitutional ^{119}Sb atoms in an Au matrix give a single line of an isomer shift of 1.83 mm s^{-1} at 78 K.[3] The emission spectrum of ^{119}Sb in antimony metal consists of a single line with an isomer shift of 2.68 mm s^{-1} at 78 K.[4] We ascribe the component in the *in situ* spectrum with an isomer shift of 1.66 mm s^{-1} to ^{119}Sb atoms on the surface of gold foil and the other with that of 2.72 mm s^{-1} to ^{119}Sb in antimony metal. The amount

* Faculty of Engineering Sciences, Osaka University.

of antimony in the electrolyte (<300 ng) is estimated to have been smaller than the calculated value for a monolayer deposition on the foil. The ^{119}Sb observed in antimony metal suggests that antimony atoms form aggregates of metal instead of depositing homogeneously.

A spectrum of ^{119}Sb on the gold washed with ethanol and dried after electrodeposition is shown in Fig. 2(b). The spectrum also consists of two singlets having almost the same isomer shifts as those of the *in situ* spectrum. This result suggests that washing and drying cause no appreciable change in the chemical states of electrodeposited ^{119}Sb.

References

1) M. Bellemare and J.C. Roy: *Nucl. Instrum. Methods*, **97**, 131 (1971).
2) W. Parker, M. Croës, and K. Sevier: *Nucl. Instrum. Methods*, **7**, 22 (1960).
3) I. Tanaka, S. Nasu, F.E. Fujita, F. Ambe, S. Ambe, and T. Okada: *J. Phys. F*, **16**, L151 (1986).
4) F. Ambe, S. Ambe, H. Shoji, and N. Saito: *J. Chem. Phys.*, **60**, 3773 (1974).

RIKEN Accel. Prog. Rep. 20 (1986)

III-3-16. Mössbauer Spectroscopic Studies of Ruthenium Compounds

Y. Kobayashi, M. Katada, H. Sano,* T. Okada, K. Asai,
S. Ambe, and F. Ambe

Ruthenium belongs to the secondary transition elements and displays ten oxidation states from − 2, 0 to + 8.[1] Consequently, studies of the valence state and electronic configuration in ruthenium compounds have attracted much attention of many investigators. However, chemical applications of the Mössbauer effect in ^{99}Ru and ^{101}Ru have been limited by the experimental difficulties: both the source and absorber must be kept at liquid-helium temperature, a thick absorber must be used because of a low recoil-free fraction and both ^{99}Ru and ^{101}Ru have only short-lived source nuclides. In this period, a Mössbauer absorption spectroscopic investigation was started by using an absorber of ruthenium powder metal, in order to obtain useful information on the chemical environment around the ruthenium nuclei in ruthenium compounds.

The source nuclide ^{99}Rh was produced by the ^{99}Ru(p,n)^{99}Rh reaction (Fig. 1) on ruthenium metal with 13 MeV protons in the cyclotron. This method for source preparation was essentially similar to that given by Kistner[2,3] and Mössbauer *et al.*[4] Natural ruthenium metal of purity 99.9% (216 mg/cm^2) was packed in a source holder (Fig. 2) made of aluminium and covered with aluminium foil; the diameter of the source holder was 30 mm. During bombardment, cooling water was circulated on the back side of the holder. Three days after bombardment, the γ-ray spectrum of the irradiated ruthenium metal in the holder was measured with LEPS (Low-Energy Photon Spectrometry) to determine produced nuclides. The results are shown in Fig. 3. Although not only 90 keV Mössbauer transition γ-rays of ^{99}Rh but γ-rays of ^{100}Rh ($T_{1/2}$ = 20.8 h) from ^{100}Ru and $^{101+101m}$Rh ($T_{1/2}$ = 4.3 d) from ^{101}Ru were observed because natural ruthenium metal was bombarded, the radioactivities of non-Mössbauer nuclides decayed more rapidly than ^{99}Rh and the signal-to-noise ratio was improved after 10 d. The source was used for the Mössbauer spectroscopic measurements over 2 months after preparation.

It is necessary to obtain a Mössbauer spectrum at very low temperature because the Mössbauer transition energy is very high (Fig. 1) and the Debye-Waller factors for most ruthenium compounds are significantly lower than that of ruthenium metal. A Dewar bottle, Model HD-700 (Ranger Inc.), was used after slight improvement for cooling both source and absorber to liquid-helium temperature. The capacities for liquid helium and liquid nitrogen of the Dewar were 5 and 2 dm^3, respectively, with a helium consumption rate of 0.11–0.12 dm^3/h.

Absorption spectra were recorded on a multi-chan-

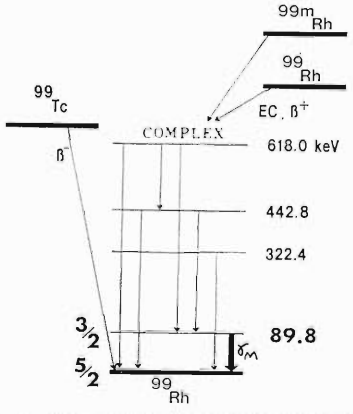

Fig. 1. Energy level diagram for ^{99}Ru.

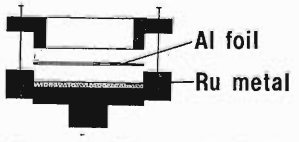

Fig. 2. Source holder made of aluminium.

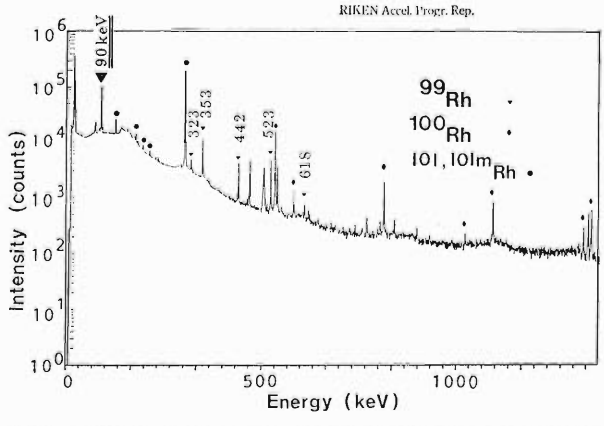

Fig. 3. γ-Ray spectrum of proton-irradiated natural ruthenium metallic powder.

* Department of Chemistry, Faculty of Sciences, Tokyo Metropolitan University.

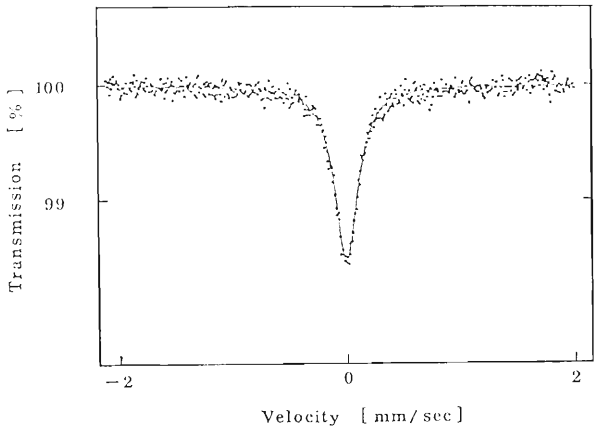

Fig. 4. Mössbauer spectrum of ruthenium metallic powder (223 mg/cm^2) at liquid helium temperature.

nel analyzer, Model ECON-2 (Northern Inc.), connected with a driving unit, Model VT-200 (Ranger Inc.), and a scintillation detector with a 2-mm thick NaI(Tl) crystal. Velocity calibration for ruthenium spectroscopy was accomplished by measuring the spectrum of ^{57}Fe in pure iron foil.

A Mössbauer spectrum obtained with an absorber of ruthenium metallic powder is shown in Fig. 4. The line width of the singlet line in our work was 0.25 ± 0.01 ml/s, which was slightly narrower than those given in other reports.[2-4] The absorption was $1.56 \pm 0.05\%$, almost in good agreement with the reported results.[2-4]

References

1) S. E. Livingstone: Comprehensive Inorganic Chemistry, Vol. 3 (eds. J. C. Bailar, Jr., H. J. Emeléus, Sir R. Nyholm, and A. F. Trotman-Dickenson), Pergamon Press, Oxford, Chap. 43, p. 1190 (1975).
2) O. C. Kistner, S. Monaro, and R. Segnan: *Phys. Lett.*, **5**, 299 (1963).
3) O. C. Kistner: *Phys. Rev.*, **144**, 1022 (1966).
4) G. Kaindl, W. Potzel, F. Wagner, U. Zahn, and R. L. Mössbauer: *Z. Physik*, **226**, 103 (1969).

RIKEN Accel. Prog. Rep. 20 (1986)

III-4. Radiation Chemistry and Radiation Biology

1. High-Density Excitation by Heavy Ion: Techniques of Subnanosec Measurement of Emission Decay and a Track-Scope Using Optical Fibers

K. Kimura, A. Fundoh, T. Nishina, K. Kanai,
T. Ueno, and M. Kataoka

One of the most characteristic irradiation-effects of heavy ion is the high-density excitation of electrons in an outermost shell. All high energy states such as ions, excited states of inner-shell electrons, and high Rydberg states are converted into lower excited states of an outermost shell through ion-electron recombination, Auger effects, and internal conversions.

We have been concerned with direct observation of the high-density effect using techniques of measuring emission spectra and its decay. This report describes two new techniques to elucidate dynamics of excited states formed at high density and to observe emission spectra along the path of ion-tracks, in other words, track-depth-resolved emission spectra.

(1) Emission-decay measurement with 100 ps resolution

Most of lower excited molecules decay in a few ns in FWHM in the isolated system. In the high density excitation by heavy ion, excited states interact with each other to shorten their lifetimes or sometime to convert other excited states or to produce clusters of excited states as shown by our previous studies.[1,2]

The observation of such processes requires a measurement technique with a resolution shorter than ns. If this is possible, one may expect to observe some of the second order processes such as the case mentioned above. We have already reported a technique with 1 ns time-resolution.[3] In this system, a single-ion hitting and single-photon counting technique was developed along with a coincidence technique. A timing pulse to inform the timing of ion hitting was generated by a photomultiplier which detects photons emitted from a thin scintillator foil penetrated by an ion. The limiting step of this system is the time-resolution of photomultiplier and the lifetime of emission from the scintillator-film. Resultant resolution was therefore limited to about 1 ns. This system is, however, characterized by the merit of an infinitesimally short pulse-width of ion because of single-ion hitting. Therefore, the faster detector can be developed, the better time-resolution can be obtained. Now, we adopted an MCP (micro channel plate) to obtain a fast timing pulse of the ion hitting and constructed a measuring system shown in Fig. 1. An ion passes through an assembly of two coaxial copper-cylinders before, hitting a target. These two cylinders are isolated electrically and have entrance orifices of 1.5 mm in diameter and exit orifices of 2 mm in diameter. An MCP (Hamamatsu Photonics, a tandem of type F1551-21) is mounted behind a copper plate (with an orifices of 1 mm in diameter) placed at the bottom of the inner cylinder. A thin carbon film of 50 $\mu g/cm^2$ is attached on the entrance orifice of the outer cylinder. This assembly is placed in a static magnetic field which is adjustable in intensity. Secondary electrons emitted by penetration of ion through the carbon film are accelerated to 2 keV between the outer and inner cylinders and bended by the magnetic field toward the copper plate at the bottom of the inner cylinder and eliminated by the orifice. Thus, only secondary electrons which have the same kinetic energy and an orbit with a definite curvature and path length can attain MCP; thus MCP can generate a precise fast timing pulse. One may expect at least 100 ps time-resolution for the timing of ion hitting, since the rise-time of MCP is known to be below 100 ps. To amplify such a fast pulse, a fast preamp was developed, which was composed of micro

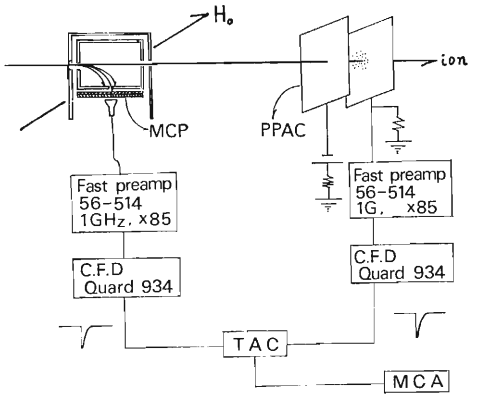

Fig. 1. Block diagram of detectors and the circuit.

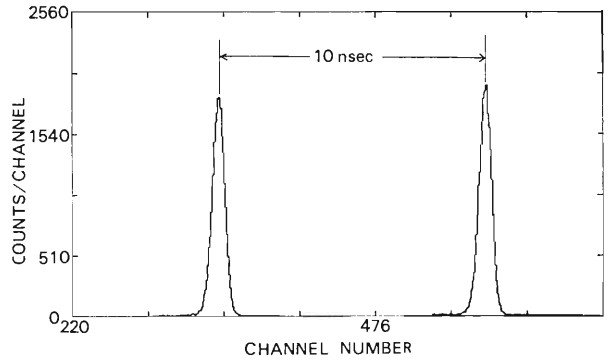

Fig. 2. Resolution of the detector, measured using a system shown Fig. 1 and 1.32 MeV/amu Ar^{4+} ions.

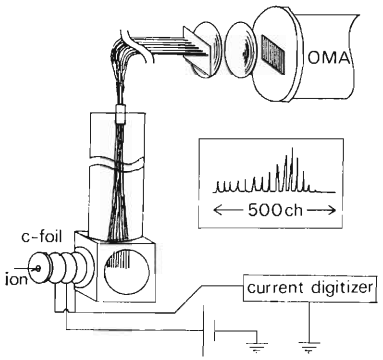

Fig. 3. Track-scope for measurement of track-depth-resolved emission-intensity.

PC 1652G by NEC, resulting in a specification of 38 db at 1 GHz. The time-resolution of this assembly was measured by a coincidence technique shown in Fig. 1 using TAC whose start pulse was given from the above assembly and whose stop pulse was given by PPAC (Parallel Plate Avalanche Counter) developed by one of present authors.[4] The resolution of PPAC was ascertained using 1.3 MeV/amu Ar ions from RILAC to be 199 ps in FWHM. Using the same projectile, the time-resolution of the present assembly was estimated to be 481 ps from Fig. 2 which displays pulse counts *vs.* channel number (44.2 ps/channel). Although this resolution is as low as 1/5 of the expected one, the time profile given in Fig. 2 shows a fairly good symmetric structure; this suggests that the time-jitter is not due to the time-retardation caused by miss matching of the detector system. The value of 481 ps is 1.9 of the flight time of Ar ions from the carbon foil to PPAC. The former may be considerably improved by narrowing beam slits and the latter can be reduced by using a thinner foil (a few $\mu g/cm^2$). Actual measurement of emission decay will be facilitated by using a MCP-mounted photomultiplier (Hamamatsu, R1564) whose lifetime is below 100 ps.

(2) Track-depth-resolved emission spectra

Excitation processes by ions, *e.g.* knock on collision, glancing collision, and charge exchange, are dependent on ion energy. The effect of secondary electrons, sort and population of excited states, and charge number of ions produced are also energy-dependent. In condensed matter, a large density effect is added to the above ones, and also all events occur in a microscopic range. If these events and their dynamics can be observed directly along the path of ion track, this must be a goal of the subject of eluciation of radiation effect. However, it is too difficult to measure the track by separating it into sections as small as sub μm. Then, we have made measurements on high-density He gas, in which a track length becomes 11 mm for 5 MeV/amu N ions; these experiments have been previously reported.[1,2] A result shows that emission efficiencies for most peaks, dL/dE, increase with increasing penetration depth, and the increase continues still to the region where the stopping power tends to decrease from its maximum value. This was explained to be caused by the decreasing of track-radius, increase in probability of direct excitation, and charge exchange, based on another result that helium excimer-excimer collisions doesn't lead to nonradiative processes, in contrast with usual scintillators and molecular photochemical processes. Furthermore, existence of the pumping cycle from nonradiative state *i.e.*, ^3a to higher radiative states seems to suggest an increase in the lowest state, ^1A, the emission from which is at 800 Å and considered most intense. We developed a new simple track-scope for precise observation of UV- and VUV-emission intensities particularly in a region of decreasing stopping power after passing through its maximum value by using samples at high-density. The scope is composed of a linear array of quartz fibers as shown in Fig. 3. A terminal of the array was coated with sodium salicylate to convert VUV light to UV with a peak at 420 nm and was set close and laterally to the tracks. Light from another terminal was focused on a photoplate of an OMA (Optical Multichannel Analyzer by Princeton Applied Research) to count photons from each fiber simultaneously. Thus, this scope enable us simultaneously to measure the track-image of UV- and VUV-emission with a resolution of 50 μm. Namely, the measurement can be done independently of instability of ion current. Calibration of photosensitivity having been finished, measurement will be made in the next beam time.

References

1) K. Kimura: *J. Chem. Phys.*, **84**, 2002 (1986).
2) K. Kimura: *J. Chem. Phys.*, **84**, 2010 (1986).
3) K. Kimura, K. Mochizuki, T. Fujisawa, and M. Imamura: *Phys. Lett. A*, **78**, 108 (1980).
4) H. Kumagai, S. H. Be, M. Ishihara, Y. Ikegami, M. Fuse, and E. Gotoh: *RIKEN Accel. Prog. Rep.*, **18**, 164 (1984).

RIKEN Accel. Prog. Rep. 20 (1986)

III-4-2. Modification of α-Particle-Induced Cell Killing and Non-Repairable DNA Lesion by Hypertonic Treatment

T. Kosaka, I. Kaneko, K. Eguchi-Kasai, K. Nakano, and A. Maruhashi

The cell killing effect by low linear-energy-transfer (LET) radiation is enhanced by exposing the cells to an anisotonic solution.[1,2] The hypertonic treatment carried out immediately after γ-radiation inhibited the rejoining of DNA double strand breaks (dsb); this results suggested that the low LET radiation-induced cell damage sensitized by hypertonic solution is closely related to non-repairable DNA lesion.[3]

The present report describes that the hypertonic treatment enhances the cell killing caused by α-particles (22 MeV) possibly owing to the inhibition of the rejoining of DNA dsb induced by α-particles.

Chinese hamster HA-1 cells were used throughout the experiment. Cell survival is assayed by a colony formation technique, and DNA dsb by a neutral filter elution technique.[4]

The survival curve of HA-1 cells irradiated with γ-rays or α-particles are shown in Fig. 1. The cell survival after irradiation with γ-rays or α-particles was reduced by the hypertonic treatment. The survival curve obtained with γ-rays has two components: an initial shoulder region followed by a linear-response region. The hypertonic treatment carried out immediately after γ-irradiation strongly reduced survival. The survival curve with α-particles is found to be linear against absorbed dose. The hypertonic treatment followed by α-particles irradiation slightly enhanced the cell killing.

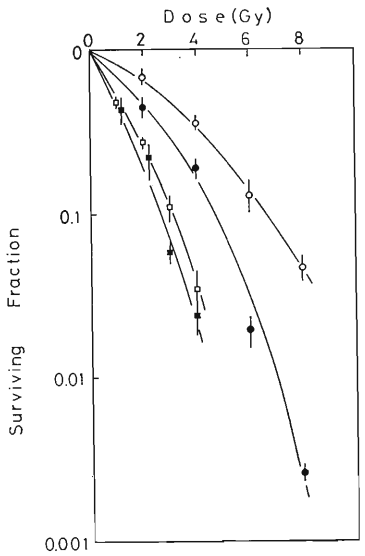

Fig. 1. Dose survival curves for HA-1 cells. Cells irradiated with γ-rays (○) and α-particles (□), γ-rays followed by hypertonic treatment (●) and α-particles followed by hypertonic treatment (■).

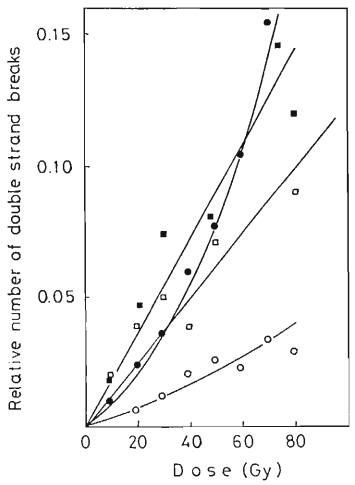

Fig. 2. Dose-response curve for non-repairable DNA lesion in HA-1 cells. Relative number of double strand break in DNA of cells irradiated with γ-rays (○). α-particles (□), γ-rays followed by hypertonic treatment (●) and α-particles followed by hypertonic treatment (■).

The dose-response curve for non-repairable DNA lesion caused by γ-rays or α-particles after incubation at 37°C for 14 h are shown in Fig. 2. The non-repairable DNA lesions increase with an increase in absorbed dose of γ-rays or α-particles. The dose response curve of the non-repairable DNA lesion caused by γ-irradiation has also two components: an initial shoulder region followed by a linear response region. The hypertonic treatment after γ-irradiation enhances the non-repairable DNA lesion and affected the shape of the shoulder and the linear-response region of the non-repairable DNA lesion. The dose-response curve obtained by α-irradiation is found to be linear against absorbed dose as described. The hypertonic treatment after irrradiation slightly enhanced the non-repairable DNA lesion. These dose-response curves were found to be a mirror image of the survival curves obtained with α-particles and γ-rays. The relative number of dsb

(RN) was calculated from minus logarithm of the fraction retained on the filter at 15 ml of fraction. The values of D_{37} are obtained from equivalent doses of 37% cell survivor. RNs at D_{37} for γ-irradiation alone, for γ-irradiation followed by the hypertonic treatment, for α-irradiation alone, and for α-irradiation followed by the hypertonic treatment are 0.0016, 0.0019, 0.0016, and 0.0024, respectively. These cell damage caused by α-particles as well as that caused by γ-rays, and cell killing caused by ionizing radiation relates to the amount of the non-repairable DNA lesion.

References

1) H. Utsumi and E. E. Elkind: *Radiat. Res.*, **77**, 346 (1979).
2) G. Raaphorst and W. C. Dewey: *Int. J. Radiat. Biol.*, **49**, 383 (1979).
3) T. Kosaka, I. Kaneko, and H. Koide: Unpublished data.
4) M. O. Bradley and K. W. Kohn: *Nucleic Acids Res.*, **7**, 793 (1979).

RIKEN Accel. Prog. Rep. 20 (1986)

III-4-3. Oxygen Effect on DNA Double Strand Breaks in Human Melanoma Cells Induced by α-Particle Beam

K. Eguchi-Kasai, I. Kaneko, A. Maruhashi, T. Kosaka,
T. Takahashi, and K. Nakano

Reduction in the oxygen enhancement ratio (OER) in cell inactivation is one of the major features of high-LET radiation.[1] The reason for the small OER value in comparison with those for low-LET radiation has not been entirely understood. We have made a special apparatus to irradiate cultured cells with an α-particle beam from the cyclotron under hypoxic conditions and have examined the OER effect on inactivation of human melanoma cells (NMV-I).[2] Here, we describe the oxygen effect on DNA double strand breaks (DNA dsb) induced by α-particles in HMV-1 cells.

Procedures for gas replacement and irradiation have been described previously.[2] Oxygen concentration in the culture medium surrounding cells was less than 2.5 ppm. Linear energy transfer (LET) of α-particles in the cell was 77 keV/μm. DNA dsb was detected by a neutral elution method, by which DNA dsb can be sensitively detected with a low detection limit of 3 Gy.[3] Relative number of DNA dsb was shown on the ordinates in Figs. 1 and 2 in arbitrary units (minus log F). The curves in these figures were fitted to a linear-quadratic relationship by linear regression analysis.

Total DNA dsb induced by ^{60}Co γ-rays increased quadratically with dose under both hypoxic and aerobic conditions (Fig. 1). Much enhanced DNA dsb was induced under the aerobic conditions than under the hypoxic conditions. The OER value for the DNA dsb was 1.6 at a 300-DNA dsb level. Total DNA dsb can be divided into two classes: repairable and non-repairable dsb. About 3/4 of the total DNA dsb induced with γ-rays was rejoined during post-irradiation-incubation at 37°C. The repairable DNA dsb might not play a important role in the cell inactivation. The DNA dsb remaining after incubation is considered to be non-repairable. The non-repairable DNA dsb also quadratically increased with dose and was much more induced under the aerobic conditions than under the hypoxic conditions (Fig. 2a). The OER value for the non-repairable DNA dsb was 1.6 and the same as that

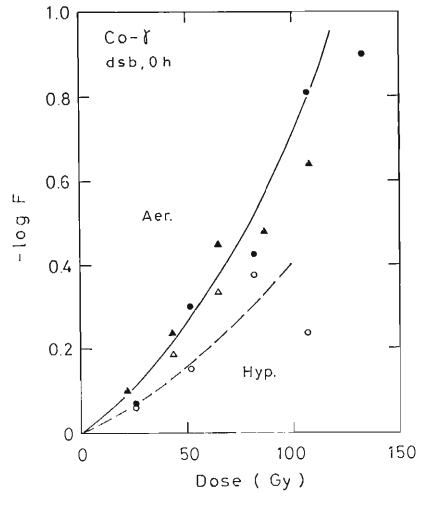

Fig. 1. Oxygen effect on DNA dsb induced by ^{60}Co γ-ray in human melanoma cells (HMV-I).

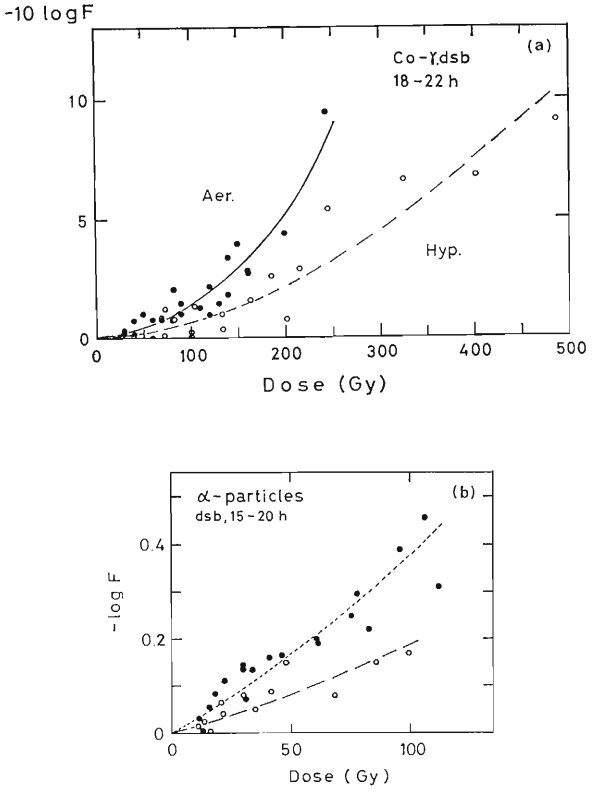

Fig. 2. Oxygen effect on non-repairable DNA dsb in human melanoma cells (HMV-I). a, ^{60}Co γ-ray; b, α-particle.

for the total DNA dsb. This result suggests that oxygen has no effects on the repair of DNA dsb induced with γ-rays. Thus, only non-repairable DNA dsb was detected after irradiation with α-particles. Non-repairable DNA dsb induced by α-particles increased almost linearly with dose and was induced much more under the aerobic conditions than under the hypoxic conditions (Fig. 2b). The OER value for the non-repairable DNA dsb was 1.9.

The OER value of α-particles cannot be directly compared with those of γ-rays, because of the difference in the shapes of the curves. Thus the numbers of non-repairable DNA dsb per cell at 37% survivor were calculated from every fitting curve. They were almost constant among 4 curves in spite of the differences in radiation quality and irradiation conditions. This result indicates that the non-repairable dsb closely relates to cell inactivation induced by radiations.

References

1) E. A. Blakely, C. A. Tobias, T. C. H. Yang, K. C. Smith, and J. T. Lyman: *Radiat. Res.*, **80**, 122 (1979).
2) K. Eguchi, I. Kaneko, T. Kosaka, T. Takahashi, and K. Nakano: *RIKEN Accel. Prog. Rep.*, **19**, 136 (1985).
3) M. O. Bladley and K. W. Kohn: *Nucleic Acid Res.*, **7**, 793 (1979).

RIKEN Accel. Prog. Rep. 20 (1986)

III-4-4. Calculation of Dose around the Path of an Ion and Microdosimetric Considerations of the Effects of Heavy Ions on Microorganisms

T. Takahashi, F. Yatagai, S. Konno, T. Katayama, K. Izumo, and T. Tabata*

Reliable evaluation of the dose around the trajectory of an ion is essential for interpretation of the inactivation cross sections of microorganisms. Recently, Hansen and Olsen[1] reported that a modified Katz's energy deposition formula, to which they introduced a parameter α,[2] successfully explains the response of a radiochromic dye film dosimeter to high LET radiations when α was chosen to be 1.67. This parameter appears in the range energy relation of electrons, $R=kw^{\alpha}$, where R and w are the range and energy of electrons, respectively, and k is a constant. As to our data on inactivation cross section of *E. coli*, however, a lower value of α, very close to unity, seems appropriate. To overcome such difficulty, we have calculated the dose around the path of an ion by using Tabata and Ito's energy deposition algorithm for electrons.[3] This algorithm is an improved version of that used by Kobetich and Katz,[4] and gives a better fit to data over a wider range of electron energy.

(1) Calculation of the dose D_T around the path of an ion

As a first step, secondary electrons were assumed to be ejected perpendicular to the path of an ion.[5] The number of the secondary electrons with energies between w_i and $w_i+(\Delta w)_i$ generated per unit path length of a heavy ion is given by

$$(\Delta n)_i=CZ^{*2}\beta^{-2}w_i^{-2}(\Delta w)_i \qquad (1)$$

Here, C is a constant ($C=0.85$ keV/100 μm for water), the effective charge Z^*e is given by $Z^*e=Ze\,[1-\exp(-125\beta Z^{-2/3})]$ (Ze is the nuclear charge of an ion,) and β is the ratio of the velocity of the ion to that of light.

Electrons are taken to be initially free[5] (though very weakly bound to a water molecule) and secondary electrons having energies more than 1 eV were taken into account. Energy deposition D_j was calculated in the jth shell, which is located between radii $x=x_j$ and $x=x_j+(\Delta x)_j$ from the trajectory of an ion:

$$D_j=\sum_i (\Delta n)_i E_{ij}(\Delta x)_j \qquad (2)$$

where E_{ij} is the effective stopping power at $x=x_j$ for an electron with energy w_i and is given by Tabata and Ito to be $E_{ij}=y'(x_j)$ and $y'(x)=-\frac{d}{dx}[\eta(x)\,T(x)]$. Here, $\eta(x)$ is the transmission coefficient, *i.e.*, the fraction of the number of incident electrons at the depths $\geqq x$ and $T(x)$ is the ratio of the total kinetic energy deposited at the depths $\geqq x$ to the number of electrons deposited at the same region of depth. $T(x)$ and $\eta(x)$ are analytically given in Ref. 3 for a semi-infinite half-space $\geqq x$, and the calculated values for $\eta(x)$ and $T(x)$ were assumed to be applicable approximately to the present situation. The effective atomic number and atomic weight of water were calculated to be 7.22 and 13, respectively, according to Ref. 3. Since the range-energy relation of electrons plays an important role in these calculations, Tabata and Ito's extrapolated range R_{ex} is compared below with the ranges given by other authors. It is larger than Booz and Smith's R_{95} for T. E. gas[6] or R_{csda} in water given in ICRU 16,[7] but smaller than Butts and Katz's range R_{BK} for water below about 1.5 keV. From about 3 keV to about 10 keV, R_{ex} is larger than R_{BK} but a little smaller than R_{csda} given in Ref. 7. The density of energy delivery (erg/cm^3) $D_T(x_j)$ at the distance x_j from the trajectory of an ion is easily found to be

$$D_T(x_j)=\sum_i (\Delta n)_i E_{ij}/(2\pi x_j) \qquad (3)$$

and is compared with Butts and Katz's dose $D_{KZ}(x)$,[5] where the constant α was taken to be unity and the transmission coefficient was not taken into consideration (Fig. 1). $D_T(x_j)$ was calculated from 1 Å to R_{ex} with appropriate intervals, and the results were stored as "tables" in a computer disk.

(2) Normalization of D_{KZ} and D_T to LET_∞

Both $D_{KZ}(x)$ and $D_T(x)$ mentioned above are essentially doses due to close collisions. In a previous paper,[2] D_{KZ} added by D_p, which includes dose due to distant collisions, was denoted by D_{KA}, and

* Radiation Center of Osaka Prefecture.

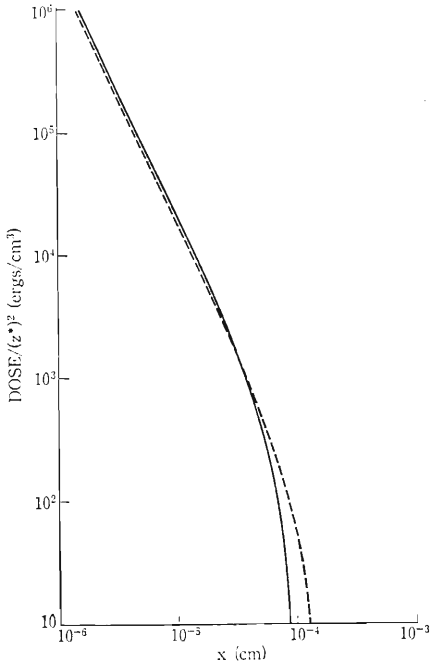

Fig. 1. Comparison of $D_{KZ}(x)$ (solid line) and $D_T(x)$ (dotted line) for ions with 4 MeV/u. $D_{KN}(x)$ is equal to $D_{KZ}(x)$ and $D_{TN}(x)$ is equal to $D_T(x)$ in the region $x>$ 1 Å from the path of an ion.

$2\pi\int_{1\text{Å}}^{\infty} xD_{KA}(x)\,dx$ was found to be nearly equal to LET_∞.[7] Therefore it seems reasonable to normalize D_{KZ} and D_T to LET_∞, as in the case of Chatterjee and Schaefer's dose. The normalization of the dose in water was made by the use of following equations:

$$D_{KN}(x)=D(x_1) \qquad x\leqq x_1 \tag{4}$$

$$D_{KN}(x)=D_{KZ}(x) \qquad x>x_1 \tag{5}$$

Here, D_{KN} is Butts and Katz's dose normalized to LET_∞. In the present paper, x_1 was chosen to be 1 Å and $D(x_1)$ was determined so as to fulfil the following equation:

$$\pi x_1^2 D(x_1)+2\pi\int_{x_1}^{\infty} xD_{KZ}(x)\,dx=LET_\infty \tag{6}$$

No difference in the calculation of inactivation cross sections was found when x_1 was chosen to be 10 Å or 20 Å. Since the situation was the same for D_T, it was also normalized by Eq. (6) when D_{KZ} was substituted by D_T. The normalized D_T is denoted by D_{TN}, hereafter. The second term on the left-hand side of Eq. (6) is about 80% of LET_∞ for D_{KZ} and about 85% for D_T (for $x_1=1$ Å) in case of N, C, and He ions of several MeV/u.

(3) Mean dose absorbed with a sensitive element

If a sensitive element is a short cylinder of radius a whose axis is parallel to and at distance r from the path of an ion, the mean absorbed dose $\bar{D}(r)$ is calculated from Eqs. (7) and (8) in Ref. 8 for D_{KN} and D_{TN}. The core radius x_1 is assumed to be ~1 Å as a constant but this rough approximation does not cause any erroneous effect on $\bar{D}(r)$ if x_1 is chosen to be sufficiently small.

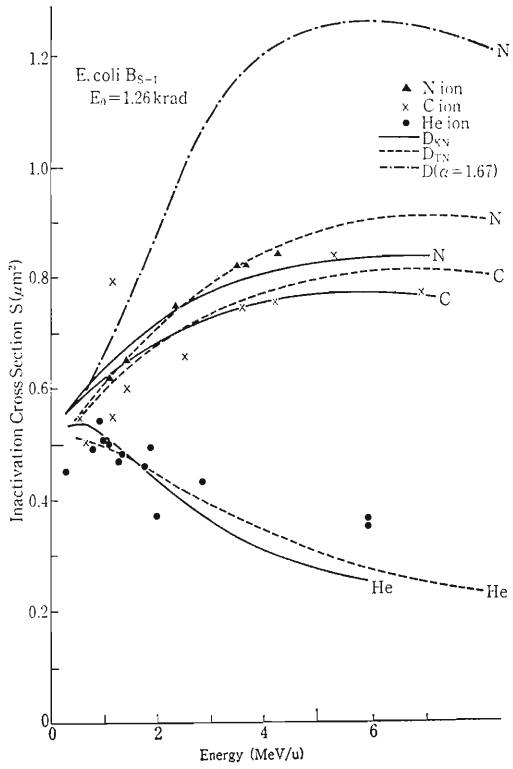

Fig. 2. Inactivation cross section S as a function of energy of ions for *E. coli* B_{s-1}. Solid lines are calculated using D_{KN} and dotted lines using D_{TN}; dot-dashed line is calculated by modified Katz's dose $D(\alpha=1.67)$.

(4) Analysis of inactivation cross section by D_{KN} and D_{TN}

The inactivation cross section of *E. coli* B_{s-1} was analyzed by use of D_{KN} and D_{TN} by the same procedure as in Ref. 2. From least squares analysis, by the use of D_{KN}, the area of the sensitive element was found to be $\pi a^2=0.50\ \mu m^2$ for *E. coli* B_{s-1}. The experimental inactivation cross sections were also well explained by use of D_{TN}, as shown in Fig. 2, but deviation is obvious for the modified Katz's dose ($\alpha=1.67$)[1] as mentioned above. When Hansen and Olsen's constants $\alpha=1.67$ and $k=5.11\times10^{-11}$ in the equation $R=kw^\alpha$ are chosen, the range of electrons of energy 10 keV is close to that given in ICRU 37,[7] but only about 60% of electrons are transmitted to the region $x>R_{ex}/2$, according to the calculation based on Ref. 3. Therefore the modified Katz's dose ($\alpha=1.67$),[1] in which the transmission coefficient is not taken into account, seems to overestimate the dose at least at the region $r>R_{max}/2$, where R_{max} is the range of δ-electrons with maximum kinetic energy. The authors have also analyzed inactivation cross sections for vegetative cells of *E. coli* B/r and of *B. subtilis* spores to heavy ions with

the same procedure as in Ref. 2; details will be published.[9]

References

1) J. W. Hansen and K. J. Olsen: *Radiat. Res.*, **97**, 1 (1984).
2) T. Takahashi, F. Yatagai, K. Izumo, S. Konno, and T. Katayama: *RIKEN Accel. Prog. Rep.*, **19**, 138 (1985).
3) T. Tabata and R. Ito: *Nucl. Sci. Eng.*, **53**, 226 (1974); T. Tabata and R. Ito: *Jpn. J. Appl. Phys.*, **20**, 249 (1981).
4) E. J. Kobetich and R. Katz: *Nucl. Instrum. Methods*, **71**, 226 (1969).
5) J. J. Butts and R. Katz: *Radiat. Res.*, **30**, 855 (1967).
6) B. G. R. Smith and J. Booz: 6th Symp. Microdosimetry (eds. J. Booz and H. G. Ebert), Vol. 2, Harwood Academic Publishers, Ltd., London, p. 759 (1978).
7) ICRU Report 16, Linear energy transfer, International Commission on Radiation Units and Measurements (1970); ICRU Report 37, Stopping power for electrons and positrons (1984).
8) T. Takahashi, F. Yatagai, and S. Kitayama: *Adv. Space Res.*, **3**, No. 8, 95 (1983).
9) T. Takahashi, F. Yatagai, S. Konno, T. Katayama, and I. Kaneko: *Adv. Space Res.*, **5** (in press).

RIKEN Accel. Prog. Rep. 20 (1986)

III-5. Instrumentation

1. Calibration Test of Si-Detector Telescopes with Large Geometric Factors for Isotope Identification in the Heavy Cosmic Ray Particles

T. Doke, N. Hasebe,*1 T. Imai, J. Kikuchi,*2 T. Kohno, K. Nagata,*3
A. Nakamoto,*4 H. Murakami,*4 S. Yanagita,*5 and T. Yanagimachi*4

In the GEOTALL mission,[1] which will be launched in 1992, ΔE–E silicon detector telescopes with large geometric factors are planned to be used for observing the isotopic abundance of heavy solar flare or galactic cosmic ray particles. Recently, the first models of position sensitive ΔE silicon detectors (ΔE-PSDs) to be used in the ΔE–E detector telescopes were made by the Hamamatsu Photonics Co. and the thickness uniformity, the energy resolution, and the position resolution of them have been investigated by using heavy-ion beams from RIKEN Ring cyclotron.

In the experiment, two ΔE-PSDs (No. 312 and 313) of 26 mm × 26 mm in size and ~30 μm in thickness and one ΔE-PSD (No. 317) of 50 mm × 50 mm in size and ~250 μm in thickness were tested for helium ion beams of 10 MeV/n and nitrogen ion beams of 5.7 or 6.0 MeV/n. The thin ΔE-PSDs are the models of ΔE-detectors to be used in the HEP-MI sensor in the GEOTALL mission and the thick ΔE-PSD for the HEP-HI sensor.[1] The thickness, the energy resolution, and the position resolution in these detectors depend on the incident position of the beam. To simultaneously measure them, a copper plate of 0.6 mm in thickness, in which 81 holes of 0.5 mm in diameter are drilled in the matrix of 9 × 9 with the equal interval of 5 mm, was placed 21 cm apart from a target, made of gold foil of 2.32 mg/cm^2 in thickness, at the angle of 30° to the beam direction, and then a ΔE-PSD to be investigated was set just behind the copper plate used as a collimeter. If ΔE-PSD has a linear response on position, its output should show a pattern with square geometry.

Thus obtained 2-dimensional pattern in thick ΔE-PSD No. 317 is symmetric, but remarkably deformed compared with the original pattern of square geometry as shown in Fig. 1 (a) and (b). Here, (a) was obtained for nitrogen ions of 6 MeV/n and (b) for helium ions of 10 MeV/n. In both cases, the central part is expanded and the side part compressed. To remove such deformation, ΔE-PSD with a new readout electrode system,[2] which is expected to have a good linear response, is being developed. Nitrogen ions bombarded stop inside the detector, while helium ions penetrate the detector. The deposited energy in the former, therefore, is remarkably large compared with that in the latter, an excellent position resolution is expected for a nitrogen ion beam. Thus,

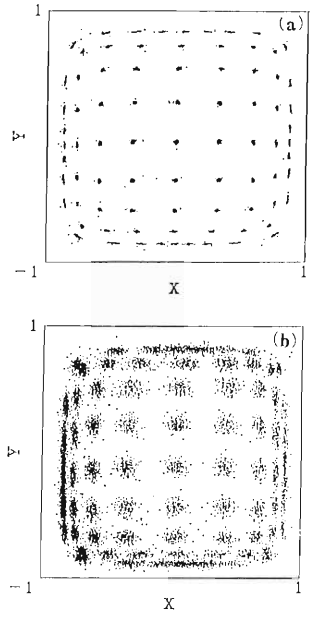

Fig. 1. Two dimensional patterns obtained by thick ΔE-PSD (No. 317). (a), for nitrogen ion beam of 6 MeV/n; (b), for helium ion beam of 10 MeV/n.

*1 Faculty of General Education, Ehime University.
*2 Science and Engineering Research Laboratory, Waseda University.
*3 Faculty of Engineering, Tamagawa University.
*4 Faculty of Science, Rikkyo University.
*5 Department of Earth Science, Ibaraki University.

(a)

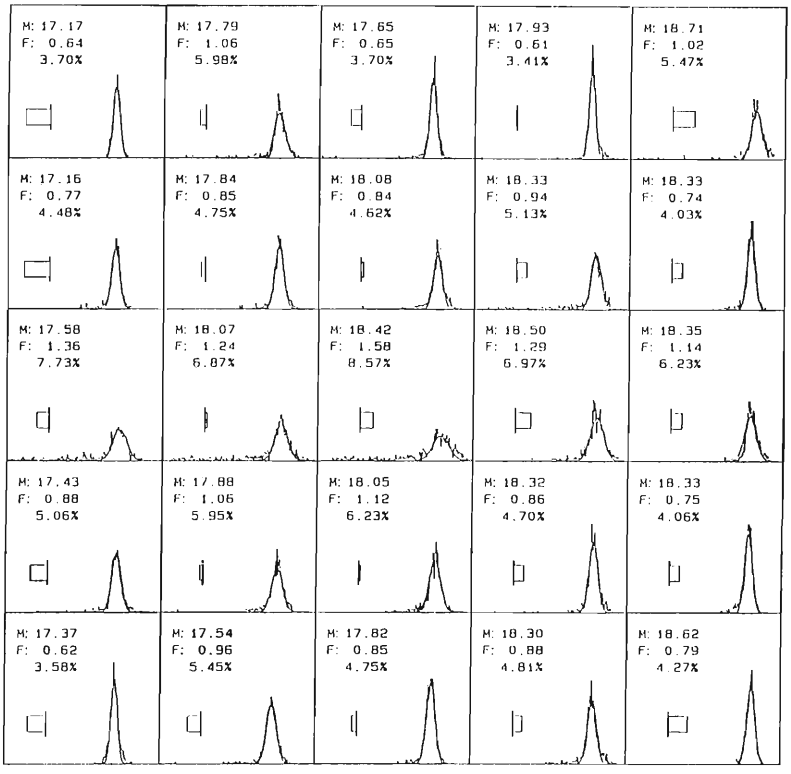

ΔE Spectra

(b)

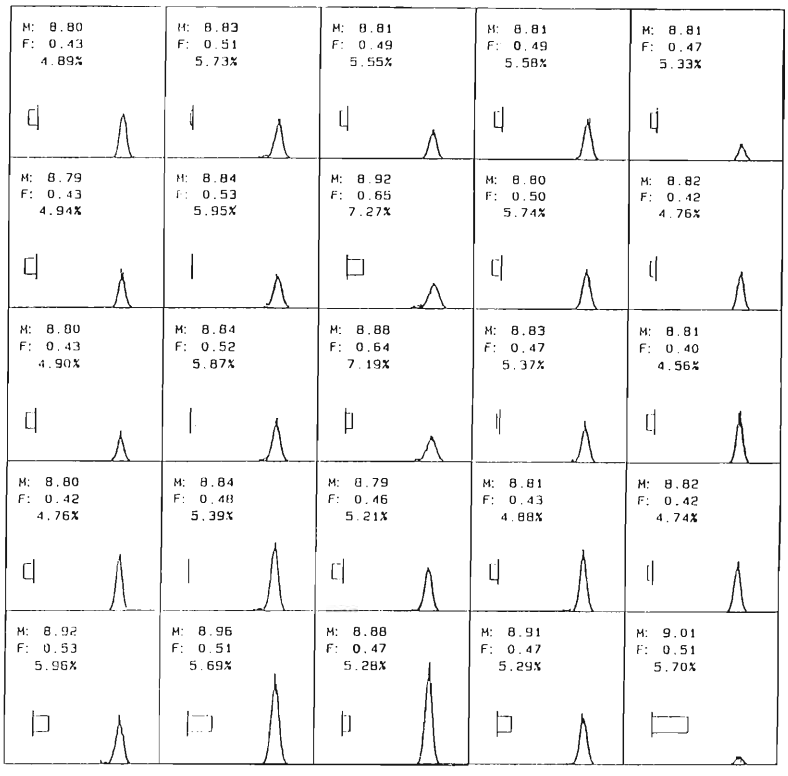

ΔE Spectra

Fig. 2. Energy loss distribution obtained by using thin ΔE-PSD (No. 312) and thick ΔE-PSD (No. 317). (a) Data of No. 312 for nitrogen ion beam of 6 MeV/n; (b) data of No. 317 for helium ion beam of 10 MeV/n. Each energy loss distribution in (a) or (b) corresponds to that obtained at each hole in the matrix holes of 5×5 taken with the equal interval of 5 mm in the collimeter plate.

the position resolution in (a) is simply limited by the size of the collimeter holes. For the helium ion beam, the position resolution roughly agrees with that estimated from an electronic noise level. On the other hand, the data obtained by thin ΔE-PSDs show non-symmetric patterns as well as the remarkable deformation as in that for thick ΔE-PSD. The reason why such non-symmetric patterns were obtained is under investigation.

Figures 2 (a) and (b) show the energy distributions measured at 25 holes ($=5 \times 5$ matrix) taken with an equal interval of 5 mm in the collimeter plate for thin ΔE-PSD No. 312 and for thick ΔE-PSD No. 317, respectively. The energy distribution (a) was obtained for a nitrogen ion beam of 6 MeV/n and (b) for a helium ion beam of 10 MeV/n. In both cases, the width of the energy loss distribution at the central part is the worst. This may be explained by taking the so-called "channeling effect" into consideration. For both cases, the time constant of the amplifier was long enough to collect all the produced charges to the collector. In the thick ΔE-PSD, the FWHM of the energy loss distribution for helium ions of 10 MeV/n except for the central region agrees roughly with that estimated theoretically ($\sim$4.6%). In thin ΔE-PSDs, however, the FWHMs of the distributions range from 1.2 to 2.5 times larger than the theoretical one ($\sim$3%) except for the central part. These worse resolutions are considered to be due mainly to the microscopic non-uniformity in detector thickness.

The local fluctuation of thickness in ΔE-PSD was investigated by measuring the mean values of the energy loss distributions for charged particles passing through collimeter holes except for the central region. The fluctuation of thickness in thick ΔE-PSD No. 317 was $\pm$ 0.6%, which is uniform enough to identify the adjacent isotopes around Fe. In thin ΔE-PSDs, on the other hand, the fluctuations are $\pm$ 2.4% for No. 312 and $\pm$4.5% for No. 313, which includes the systematic variation of detector thickness. If such a systematic variation can be removed, thin ΔE-PSD with non-uniformity of $\sim$ $\pm$0.5% would be realized.

References

1) T. Doke, N. Hasebe, J. Kikuchi, T. Kohno, A. Nakamoto, A. Nishida, K. Maezawa, H. Murakami, T. Terasawa, B. Wilken, S. Yanagita, and T. Yanagimachi: Report of Sci. and Eng. Res. Lab., Waseda University, No. 85–4, 22 July (1985).
2) T. Doke: Report of Sci. and Eng. Res. Lab., Waseda University No. 86–7, 22 September (1986).

RIKEN Accel. Prog. Rep. 20 (1986)

III-5-2. ^{2}He Spectrometer

T. Motobayashi, S. Satoh,* H. Murakami,* H. Sakai,** and M. Ishihara

The (d, ^{2}He) reaction is a useful tool in investigating spin-flip isovector excitation of nuclei because of its selectivity of $\Delta S=1$, $\Delta T_z=+1$.[1] It is difficult, however, to obtain experimental data with high statistics because the product of the (d, ^{2}He) reaction is an unbound di-proton system, which must be identified by measuring two protons in coincidence. The beam intensity is restricted to maintain the counting rate of each detector low enough so that the ratio of accidental coincidence events to the true events is reasonably small and the pulses from the detectors are not deteriorated.

One means to obtain good counting statistics of ^{2}He is to use detectors with large solid angles. It can be achieved by setting the detectors at a small distance from a target. However this does not work properly by using standard detectors of thick casing. These two detectors should be set close to each other because the two protons are emitted at a small relative angle (around 10° for $E_{^2\mathrm{He}}=60$ MeV). To overcome this difficulty we developed Si-solid-state-detectors (SSD's) specially designed for the ^{2}He detection. They have a large effective area compared with the size of the casing.

Another way to improve counting efficiency is to set many counters around a target. This can increase a total solid angle without increasing the counting rate for each detector. We developed an SSD counter array with 4-telescopes in a geometry of 2 × 2 matrix. In actual measurement we employed two arrays. This makes an increase in detection efficiency by about 50 times compared with the case of using only two telescopes consisting of commercially available SSD's.

We also developed compact pre-amplifiers and shaping amplifiers to treat many signals from the counter array. The whole system was used in the measurements of the ^{90}Zr(d, ^{2}He) reaction at $E_d=70$ MeV at Research Center for Nuclear Physics, Osaka University.

Figure 1 shows a schematic view of the SSD counter array for ^{2}He detection. Each telescope consists of one ΔE- and two E-counters. The ΔE counters are 150–400 μm thick surface barrier detectors

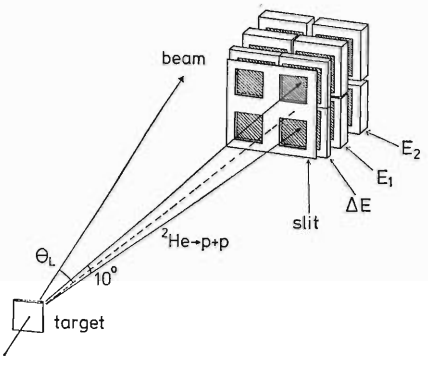

Fig. 1. Schematic view of the ^{2}He spectrometer.

and E-counters are 4.7–5.5 mm thick Li-drifted Si detectors. Each detector is mounted in a casing of 27 × 27 mm^2 made of plastic. The active area of the detectors are about 20 × 20 mm^2. Protons originating in ^{2}He are detected by the ΔE- and first E-counters, and the second ones are used as veto counters to reject unwanted events arrising from high energy protons and deuterons. In actual measurement, the slits of 15 × 15 mm^2 are set in front of the detectors. The distance of the counter array from the target is 130 mm. This geometry gives the solid angle of 13 msr for each telescope. The detection angle of one telescope is 10° apart from that of the neighboring telescope. The effective solid angle for detecting ^{2}He by a pair of telescope is about 3 msr for 60 MeV ^{2}He.

The pre-amplifier system, which consists of hybrid amplifier tips as main components, is set inside a detector housing. Six shaping amplifier tips are set in a one-span standard NIM module. Four such modules are necessary to treat 24 signals from the two counter arrays. They are set near a scattering chamber. The pre-amplifier system and the shaping amplifier are electrically connected with parallel twist-pair cables through multi-connectors.

* Department of Physics, Rikkyo University.
** Research Center for Nuclear Physics, Osaka University.

Reference

1) D. P. Stahel, R. Jahn, G. J. Wozniak, and J. Cerny: *Phys. Rev. C*, **20**, 1680 (1979); T. Motobayashi, H. Sakai, N. Matsuoka, T. Saito, K. Hosono, A. Okihana, M. Ishihara, S. Shimoura, and A. Sakaguchi: *Phys. Rev. C*, **34**, 2365 (1986).

RIKEN Accel. Prog. Rep. 20 (1986)

III-5-3. Parallel Plate Avalanche Counter —Application in the Coulomb Excitation Study—

H. Kumagai, M. Fuse, E. Gotoh, M. Ohshima,*
A. Hashizume, and T. Inamura

Multiple Coulomb excitation by heavy ions provides a useful means to obtain accurate transition moments for up to high spin states ($J \simeq 20\hbar$ or even larger) in atomic nuclei model-independently.[1,2] A standard method used is to detect deexciting γ-rays in coincidence with scattered particles recorded with a large solid angle; particles have to be detected with a position sensitive counter array in order to make a kinematical correction for observed γ-rays. Here we report a particle counter system designed for this purpose.

The parallel plate avalanche counter (PPAC)[3] affords a large-size position-sensitive area for heavy ions, has an excellent time resolution and high-counting rate capability, and is thus best suited to the present application. We have so far constructed several different types of PPAC and investigated their fundamental characteristics,[4] aiming at establishing basic techniques required for use in experiments at the RIKEN Accelerators. Some of these counters have already been used in atomic physics experiments.[5]

For application to Coulomb excitation experiments we have recently started to construct a new system consisting of a scattering chamber and four built-in modules of PPAC, as shown in Fig. 1. The counters are arranged to cover a large solid angle for the particle detection. Thin walls (1 mm thick) of the scattering chamber facilitate the detection of γ-rays using Ge(Li) detectors placed outside the chamber. The gas volume for the PPACs is separated from the vacuum region with four windows each of which is made of an aluminized Mylar film (2.5 μm in thickness, 75 mm × 81 mm in area). Each PPAC module consists of three planer electrodes; an X-position sensitive cathode (cathode-X), an anode, and a Y-position sensitive cathode (cathode-Y). They are placed in parallel 3 mm apart from one another. Cathode-X consists of 20 strips of a thin (40 μg/cm^2) gold layer evaporated on 2 μm thick Mylar film. The strips are 4.5 mm wide and 110 mm long and are spaced 0.5 mm apart. The anode is a 2 μm thick Mylar film, on both sides of which a

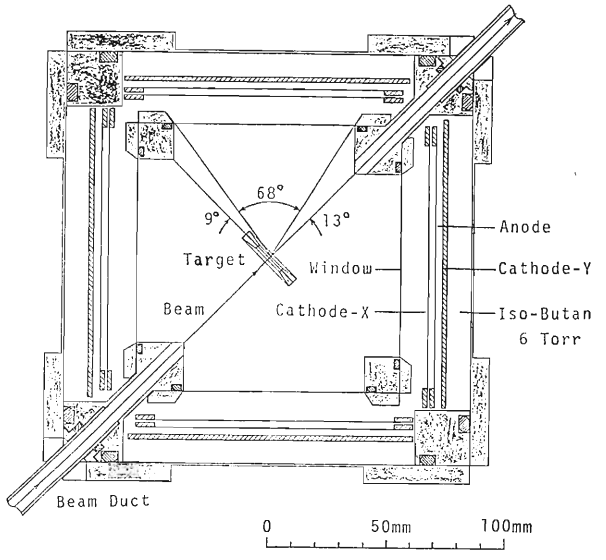

Fig. 1. Schematic view of the PPAC system designed for the Coulomb excitation study.

40 μg/cm^2 gold layer (100 mm × 100 mm in area) is evaporated. Cathode-Y, made from a printed circuit board, has 20 strips of a copper layer 4.8 mm wide and 110 mm long with 0.2 mm inter-strip spacing. All the contiguous strips in the cathodes are connected to each other with resisters of 25 Ω. The position detection is accomplished by using the charge division technique for the charges induced on the cathode strips by avalanche.

In processing the cathode signals, we have adopted a new method which uses no charge sensitive amplifier: Signals from the counters are amplified in low-noise, wide-band amplifiers without any shaping of signal pulses, and then fed to a charge-to-digital converter (QDC). Position information is derived from the digitalized data using a computer. Since the shape of the pulse from PPAC is sharp, a short pulse (~60 ns duration) can be used to gate the QDC input. This enables the position detection of the incident particles even at counting rates as high as some hundreds of kilo counts per second. This is in contrast to the conventional method involving pulse shaping time of typically 0.5 μs, which suffers from the pile-up effect when the counting rate ex-

* Japan Atomic Energy Research Institute, Tokai.

ceeds 10^4 counts per second.

Figure 2 shows the position spectrum obtained by detecting alpha particles from a ^{241}Am source passing through 16 holes (2 mm in diameter, 25 mm apart from one another) made on a screen placed in front of the counter. Full-width-at-half-maximum (FWHM) values for the peaks ranged from 2.5 mm to 3.3 mm in position. The present values are about three times larger than the values typical for the conventional method, but good enough for the present application in view of the required position resolution of 5 mm to 10 mm. Normalized numbers

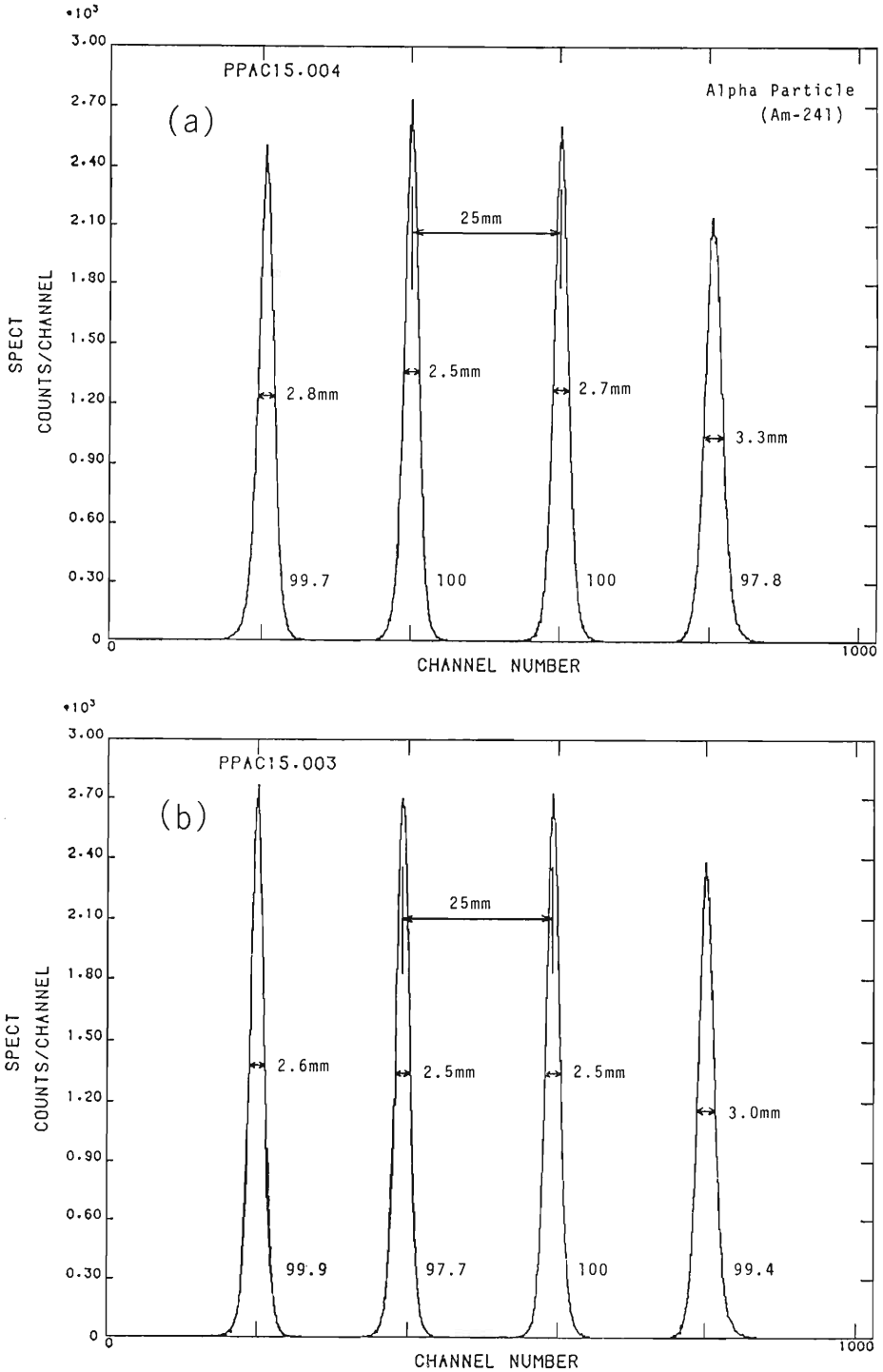

Fig. 2. Position spectra obtained for (a) *X*-axis and (b) *Y*-axis, using wide-band amplifiers and QDC. Figures appearing at the bottom of the peaks represent normalized total numbers of counts for the respective peaks.

of counts for respective peaks, given in the bottom of the peaks in Fig. 2, indicate that the uniformity of detection efficiency better than $\pm 1\%$ is obtained.

References

1) B. Katalinski, A. Baecklin, D. Cline, C.Y. Wu, R.M. Diamond, A. Macchiavalli, and M.A. Stephens: Proc. of the 16th Mikolajki Summer School on Nuclear Physics, Poland, p. 2 (1984).
2) D. Cline: Nuclear Structure 1985, Elsevier Science Publishers, B.V., Amsterdam, p. 313 (1985).
3) H. Stelzer: *Nucl. Instrum. Methods*, **133**, 409 (1976).
4) H. Kumagai, S. Sasagase, and T. Wada: *Reports I.P.C.R.*, **62**, 114 (1986) (in Japanese).
5) Y. Kanai, Y. Itoh, T. Koizumi, H. Shibata, T. Matsuo, H. Kumagai, T. Kambara, M. Kase, T. Mizogawa, and Y. Awaya: *RIKEN Accel. Prog. Rep.*, **19**, 146 (1985).

RIKEN Accel. Prog. Rep. 20 (1986)

III-5-4. Construction of a Two-Dimensional Multiwire Drift Chamber

H. Shimizu,* J. Iimura,* H. Ohnuma,* and M. Ishihara

A two-dimensional Multiwire Drift Chamber (MWDC) has been developed as a multi-purpose position detector to be used in the RIKEN Ring Cyclotron facility. It is also a test chamber for a focal plane detector in a magnetic spectrograph.[1]

In spite of very attractive properties of MWDC's, such as good position accuracy, a large detection area, and simple operation,[2] they have not been extensively used in nuclear experiments, where the effect of multiple scattering in the chambers is serious. This effect prevents one from using so called a "double chamber method"[3] to reduce left-right ambiguity when MWDC's are used in low energy experiments. In RIKEN Ring Cyclotron energy region, however, the effect is not serious unless further position measurements are made far downstream. Thus the following requirements are taken into consideration in the design of the RIKEN MWDC:

(1) The chamber should be as thin as possible.

(2) Left-right ambiguity should be resolved without another chamber.

(3) The chamber should have simple structure (for simple operation and low cost).

We have constructed, bearing these conditions in mind, two identical MWDC's. Each chamber consists of a 230×230 mm^2 duralumin frame, 16.8 mm in thickness, for a wire plane and two 1.6 mm thick brass frames for grounded cathode planes. The inner windows of the cathode frames are covered with a gold-evaporated Mylar foil, 6 μm in thickness (condition 1). One of the cathode planes can be replaced with a multi-strip cathode plane as an option for two-dimensional read-out. The basic cell geometry is shown in Fig. 1. The square geometry has been chosen so that the cathode planes need not to have graded fields (condition 3). The wire plane consists of 8 sense wires and 8 field-shaping wires. These wires are soldered to gold-plated brass pins insulated with Delrin sheaths. The field-shaping wire to sense wire distance (drift length) is 10.00 ± 0.01 mm. The distance between the wire plane and the cathode plane is 10 mm. The sense wires and field-shaping wires are gold-plated tungsten, 20 μm in diameter and gold-plated molybdenum, 80 μm in diameter, respectively. The wire tension was measured to be 37.5 ± 2.5 g for sense wires and 182.1 ± 4.0 g for field-shaping wires, respectively, by searching for resonance frequency of current put on the individual wire in a magnetic field. The left-right information can be obtained from induced signals on neighboring field-shaping wires (condition 2).

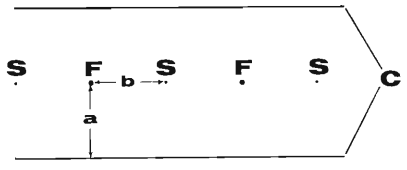

Fig. 1. Geometry of drift cell. S, sense wires (+HV); F, field shaping wires (grounded); C, cathode planes (grounded); $a = b = 10$ mm.

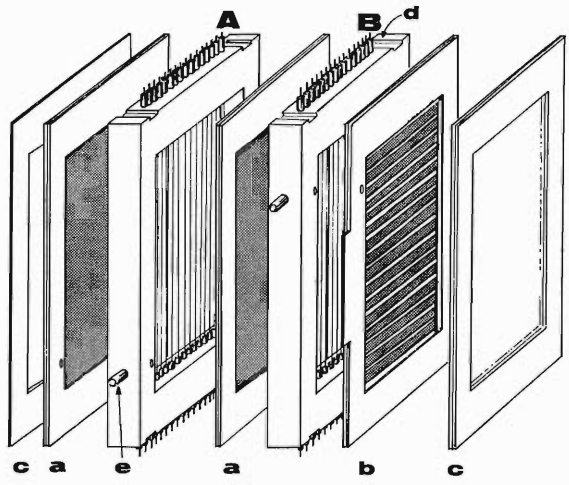

Fig. 2. Exploded view of MWDC assembly. A and B, wire frames; a, cathode frames; b, cathode strips; c, Mylar frames; d, alignment slots; e, gas inlet, outlet.

Several units of the MWDC's can be combined to make various kinds of chamber assemblies. An exploded view of a standard chamber-assembly is shown in Fig. 2. It consists of two MWDC's, A and B, which are identical but with B staggered by one-half wire spacing with respect to A. The alignment of the two chambers is achieved by means of rectangular metal pieces and the mating slots machined precisely with respect to the first wire of a given chamber. In this assembly left-right ambiguity can be resolved by using sense wire signals from the two chambers.

* Department of Physics, Tokyo Institute of Technology.

As performance test of the MWDC's is underway with a ^{106}Ru β-source. Further tests will be conducted with a proton beam.

References

1) H. Ohnuma, T. Ichihara, K. Ieki, M. Ishihara, S. Kato, T. Kubo, K. Maeda, T. Motobayashi, H. Orihara, and H. Shimizu: p. 134 in this report.
2) F. Sauli: CERN Rep., 77–09 (1977).
3) J. Heintze and A. H. Walenta: *Nucl. Instrum. Methods*, **111**, 461 (1973); D. C. Cheng, W. A. Kozanecki, R. L. Piccioni, C. Rubbia, R. L. Sulak, H. J. Weedon, and J. Wittaker: *Nucl. Instrum. Methods*, **117**, 157 (1974).

RIKEN Accel. Prog. Rep. 20 (1986)

III-5-5. Test of Electron-Ion Merging Beam Experiment

Y. Kanai, Y. Awaya, Y. Itoh, T. Kambara, H. Kumagai, T. Koizumi, T. Mizogawa, S. Ohtani, K. Okuno, H. Shibata, S. Takagi, and S. Tsurubuchi

We rebuilt an EBIS apparatus, called "Proto-NICE," in order to study collisional processes of electrons and heavy ions by a merged electron-ion beom method and reported the test data of the Proto-NICE as an EBIS-type ion source.[1,2]

In the present stage, the Proto-NICE has been set on a RILAC beam line (B1) and the tests of the electron-ion merging beam experiment are being carried out. The argon ions (Ar^{4+}, 1.24 MeV/u) from RILAC enter the interaction region through an axial, 2 mm-diameter hole in the cathode of the electron gun of the Proto-NICE. The charge state distribution of argon ions at the down stream of the Proto-NICE are measured by a charge state analyzer using a magnet and a Parallel Plate Avalanche Counter (PPAC).[3] Electron-ion collision energy is changed by varying electron energy. The acceleration voltage of electrons of the Proto-NICE is modulated at 141 Hz as shown in Fig. 1. The data on the charge state of the ions merged with electrons (abbreviated as "on state") and the data without electrons ("off state") are measured and accumulated by using respective memories. These two sets of data normalized with integrated Ar^{4+} ions beam currents, which are measured with a Faraday cup in front of the PPAC, can be compared with each other. The ratio Ar^{3+}/Ar^{4+} of "on state" is as same as that of "off state," 3×10^{-6}, because this value is determined from Ar^{4+}-residual gas (10^{-7} Torr $\times$ 6 m) collisions. The change in the ratio Ar^{3+}/Ar^{4+} by the electron-ion collisions in the Proto-NICE, which is expected to be of the order of 10^{-8}, is small compared with the overall ratio Ar^{3+}/Ar^{4+}. We have to make efforts to reduce the amount of residual gas (10^{-8} Torr or less) in the beam ducts and charge analyzer to measure this change.

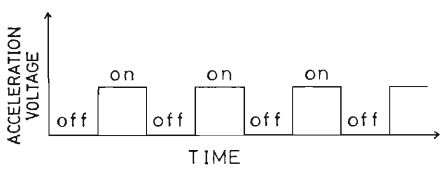

Fig. 1. Electron acceleration voltage modulation.

Table 1. Width of the Gaussian fitted to the data. Values are normalized to the broadest width (condition (e)).

Ar^{4+} Energy	Electron energy (Acceleration voltage)	Electron currents	Width of Ar^{4+}
(a) 1.24 MeV/u	630 eV	16 mA	0.78
(b) 1.24	0	0	0.99
(c) 1.24	630*	0*	0.97
(d) 1.24	0*	0*	1.00
(e) 1.24	0**	0**	1.00

* Off the filament currents of the electron gun of the Proto-NICE.

** Stop the operation of the Proto-NICE (used as a beam duct).

We measured the profiles of Ar^{4+} ion beams with the PPAC at the down stream of the Proto-NICE. The width, which is the width of the Gaussian fitted to the data and normalized to the broadest case, and the conditions for each profile for typical cases are listed in Table 1. The profile of Ar^{4+} for "on state" (Table 1(a)) is narrower than that for "off state" (Table 1(b)). The acceleration voltage modulation without electrons does not affect the width (Table 1(c) and (d)). The existence of electrons affects the width. This means that the argon ion beam and the electron beam are merged in the Photo-NICE and the interactions between them make the ion beam focussed.

References

1) S. Ohtani, Y. Awaya, Y. Itoh, T. Kambara, Y. Kanai, T. Koizumi, T. Mizogawa, K. Okuno, H. Shibata, S. Takagi, and S. Tsurubuchi: *RIKEN Accel. Prog. Rep.*, **19**, 144 (1985).

2) T. Mizogawa, Y. Awaya, Y. Itoh, T. Kambara, Y. Kanai, T. Koizumi, S. Ohtani, K. Okuno, H. Shibata, S. Takagi, and S. Tsurubuchi: *Mass Spectrosc.*, **35**, 1 (1987).

3) Y. Awaya, M. Kase, T. Kambara, H. Kumagai, Y. Kanai, T. Mizogawa, K. Shima, and T. Chiba: p. 132 in this report.

RIKEN Accel. Prog. Rep. 20 (1986)

III-5-6. A Broad-Range Magnetic Charge Analyzer

Y. Awaya, M. Kase, T. Kambara, H. Kumagai,
Y. Kanai, T. Mizogawa, K. Shima, and T. Chiba

A magnet for analyzing the charge state of heavy ions with incident energies of up to about 1.5 MeV/amu has been constructed. This magnetic analyzer has been designed to analyze and detect heavy ions with different charge states simultaneously and to be capable of resolving ions with charge of qe from those of $(q \pm 1)e$ at $q \approx 20$ by adopting a position sensitive parallel plate avalanche counter (PPAC) as a detector.

The specification of the magnet are as follows:

radius	150 cm
maximum magnetic field	1.5 Wb/m^2
angle of deflection	25°
gap of pole pieces	3 cm
aperture of vacuum chamber	2.3 cm × 10 cm
total weight	about 3 tons

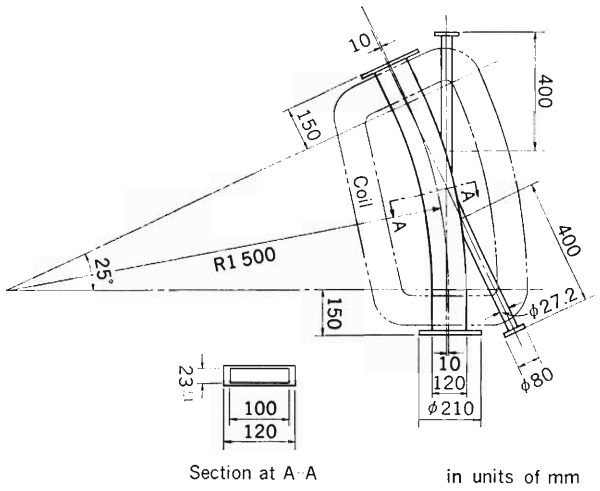

Fig. 1. A plane figure of the magnet and the vacuum chamber of the analyzer.

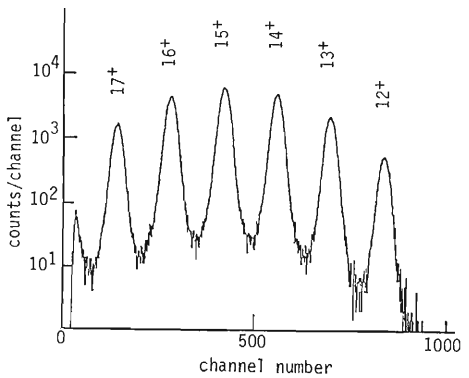

Fig. 2. The charge spectrum of 1.3 MeV/amu Ti^{15+} ions after passing through a 10 μg/cm^2 C foil.

A plane figure of the magnet and the vacuum chamber is shown in Fig. 1. A PPAC[1] is placed at the distance of about 5 cm from the exit port of the magnet in order to detect the heavy ions with different charges in the range from qe to 0.6 qe. The size of the entrance window of the PPAC is 10 cm ×

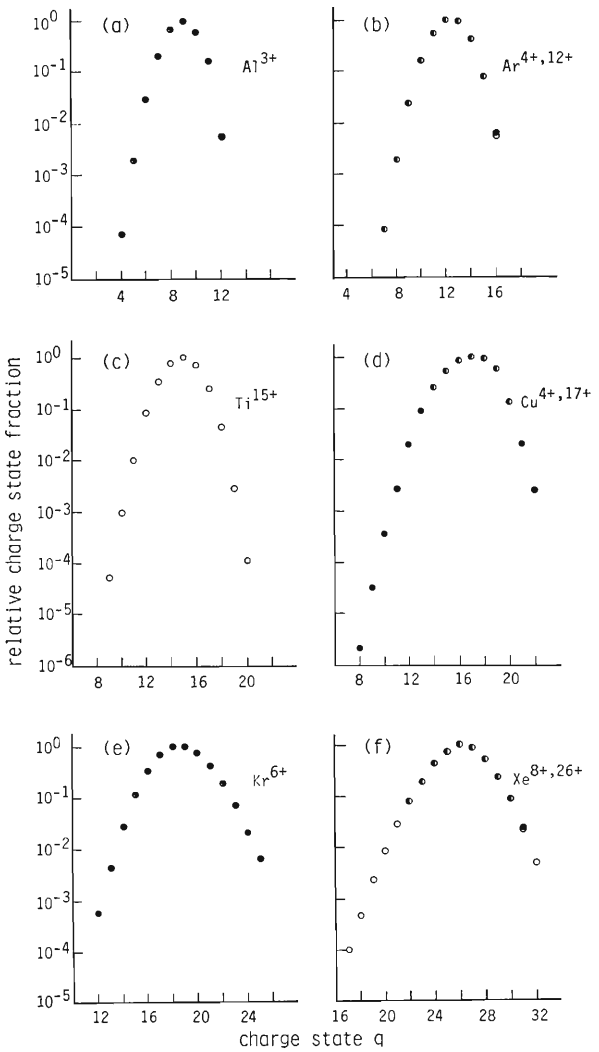

Fig. 3. Relative charge state fractions of various heavy ions after passing through a 10 μg/cm^2 C foil. (a), 0.83 MeV/amu Al^{3+} ions; (b), 1.3 MeV/amu Ar^{4+} and Ar^{12+} ions; (c), 1.3 MeV/amu Ti^{15+} ions; (d), 0.83 MeV/amu Cu^{4+} and Cu^{17+} ions; (e), 0.83 MeV/amu Kr^{6+} ions; and (f), 0.83 MeV/amu Xe^{8+} and Xe^{26+} ions. Dots show the values for lower charge ions, circles those for higher ones, and the half blackened circles mean the overlap of dots and circles.

2 cm and is covered with an aluminum-evaporated 2.5 μm Mylar foil. Isobuthane gas is flowed in the PPAC at a pressure of about 6 Torr. The position of incident ions is determined by the charge division method using signals from the cathode. A timing signal is obtained from the anode when required.

Measurements of charge distributions of some species of heavy ions after passing through a 10 $\mu g/cm^2$ carbon foil were carried out not only to test the equipments but also to obtain new data in the region of the mass and energy of heavy ions where there are scarce reports. Figure 2 shows an example of the charge distribution spectrum obtained at one measurement with 1.3 MeV/amu Ti^{15+} ions passing through the carbon foil.

The relative charge state fraction for 1.3 MeV/amu Ar^{4+}, Ar^{12+}, and Ti^{15+}, 0.83 MeV/amu Al^{3+}, Cu^{4+}, Cu^{17+}, Kr^{6+}, Xe^{8+}, and Xe^{26+} ions after passing through the carbon foil are shown in Fig. 3(a)–(f). The Al^{3+}, Ar^{4+}, Cu^{4+}, Kr^{6+}, and Xe^{8+} ions were obtained directly from RILAC and Ar^{12+}, Ti^{15+}, Cu^{17+}, and Xe^{26+} ions were obtained by making the beams pass through a charge stripper. The initial charge state of Ti ions was 4+. The momentum of all the ions were analyzed by using a beam analyzing magnet.

There are no difference between the distribution of the charge fraction for Ar^{4+} and that for Ar^{12+} ions (Fig. 3(b)), between Cu^{4+} and Cu^{17+} ions (Fig. 3(d)), and that between Xe^{8+} and Xe^{26+} ions. This means the thickness of carbon foil of 10 $\mu g/cm^2$ is enough to make 1.3 MeV/amu Ar ions, 0.83 MeV/amu Cu and Xe ions equilibrate in charge. On the basis of this result, the charge fractions obtained for Al and Kr indicate that these ions are in charge equilibrium and the charge fraction for Ti indicates that it is in or nearly in equilibrium.

This magnetic analyzer, which is named "AM magnet," will be used for the measurements of charge distribution of heavy ions scattered not only at zero degree but also at small angles, coincidence measurements between X-rays and scattered ions and merging beam experiments between heavy ions and electrons.

Reference

1) H. Kumagai, T. Kubo, M. Ishihara, M. Fuse, and E. Gotoh: *RIKEN Accel. Prog. Rep.*, **19**, 148 (1985).

RIKEN Accel. Prog. Rep. 20 (1986)

III-5-7. Design Study of Experimental Facilities for Light and Light-Heavy Ion-Induced Reactions

H. Ohnuma,* T. Ichihara, K. Ieki, M. Ishihara, S. Kato,**
T. Kubo, K. Maeda,*** T. Motobayashi, H. Orihara,**** and H. Shimizu

Medium-energy light and light-heavy ion beams will become available from RIKEN Ring Cyclotron at the installation of an injector AVF cyclotron.[1] Design study of a detection system is in progress to facilitate particle measurements in experiments with those beams.

The basic idea of the layout of the system as shown in Fig. 1 is to use a beam swinger magnet along with a cascade-type magnetic spectrometer for charged-particles and with a time-of-flight (TOF) spectrometer for neutrons.

Since the incident beam direction will be rotated by a swinger, there is no need to rotate the magnetic spectrometer in angular distribution measurements. This makes the design of a magnetic spectrometer free from many restrictions imposed otherwise and makes a construction of cascade-type spectrometer possible. A proposed spectrometer consists of three quadrupoles and two dipoles (QQDQD) with two focal planes, one after the first dipole and the other after the second dipole. The first three elements (QQD) with the first focal plane will serve as a low-resolution, large-solid-angle spectrometer. The second focal plane will be used when higher resolution is required. The third quadrupole and the second dipole magnifies the image on the first focal plane in this latter case, hence the name of cascade-type spectrometer. Design characteristics of the proposed spectrometer are given in Table 1.

The beam swinger consists of a quadrupole triplet and two dipoles, and similar in its basic form to that at CYRIC.[2] It is designed not only for beam direction rotation but also for momentum dispersion of the incident beam. Dispersion matching is much easier to realize in the present system than in an ordinary system without a swinger, since the beam

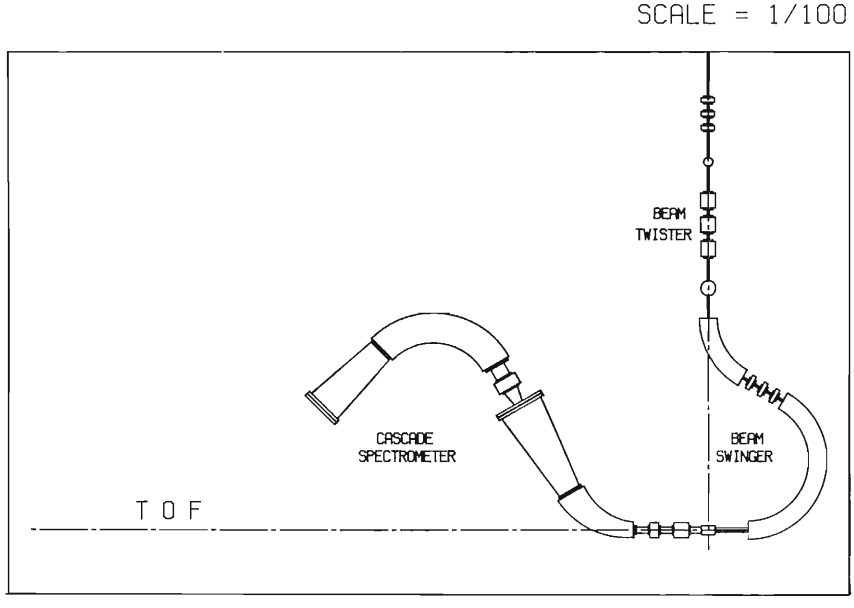

Fig. 1. Layout of the proposed system consisting of the beam swinger, magnetic spectrometer, and neutron flight path.

* Department of Physics, Tokyo Institute of Technology.
** Faculty of Liberal Arts, Yamagata University.
*** College of General Education, Tohoku University.
**** Cyclotron and Radioisotope Center, Tohoku University.

Table 1. Design characteristics of the spectrometer.

Configuration	Q-Q-D (first stage) Q-D (second stage)*
Number of focal planes	2
First order resolving power	5,000 (first stage) 13,000 (second stage)*
Momentum byte $(\rho_{(max)})/(\rho_{(min)})$	1.41 (first stage) 1.04 (second stage)
Aperture	200 mr (in the reaction plane) 100 mr (vertical to the reaction plane)*
Maximum solid angle	20 msr*
Mean orbit radius	2.4 m
Maximum magnetic field	1.5 T
Gap of dipole magnets	20 cm (D1) 10 cm (D2)
Angular resolution	3 mr
Angle of measurements	−10 to +10 deg. (zero deg. mode) +10 to +30 deg. (forward mode) +30 to +140 deg. (backward mode)*

* Tentative

will be dispersed along the rotation axis of the spectrometer.

The flight path for the neutron TOF measurement will be 20–40 m at the beginning with future extension expected. Large volume liquid scintillation counters will be used for neutron detection.

The present system allows simultaneous measurements of charged particles and neutrons emitted in the same direction. This and the large solid angle of the magnetic spectrometer should enable us to detect various kinds of unbound particles, such as $\bar{d}$, ^{2}He, α^{*}, and ^{8}Be, broadening hopefully the scope of the nuclear reaction and structure studies.

The production of a medium-energy neutron beam is also under discussion. Design studies of other related equipments, *e.g.* spin rotators and polarimeters, are in progress. Construction of thin two-dimensional multiwire drift chambers is also underway.

References

1) H. Kamitsubo: *RIKEN Accel. Prog. Rep.*, **15**, 149 (1981).
2) H. Orihara and T. Murakami: *Nucl. Instrum. Methods*, **188**, 15 (1981).

RIKEN Accel. Prog. Rep. 20 (1986)

III-5-8. Projectile Fragments Separator for RIKEN Ring Cyclotron

T. Kubo, K. Asahi, T. Ichihara, T. Matsuzaki, M. Fukuda,
K. Nagamine, I. Tanihata, and M. Ishihara

Recently much attention is being paid to unstable nuclides far from the stability line of the nuclear chart. In order to perform research on such nuclides, an on-line separator for projectile fragments, named RIPS (RIken Projectile fragments Separator), has been proposed at RIKEN Ring Cyclotron Facility. The use of projectile fragmentation in heavy-ion reactions is of great advantage to provide the unstable nuclides. A large number of nuclides far from the stability line are produced as projectile fragments. The fragmentation yields are concentrated around zero degree with a small angular spread. Besides, the fragmentation conserves a velocity of projectile although fragments have small spreading of velocity. These features enable efficient collection and separation.

The RIPS system is an achromatic spectrometer with an intermediate focal plane. Figure 1 shows the layout of the system. It consists of two dipole (D1 and D2), seven quadrupole (Q1, Q2, Q3, Q4, Q5, Q6, and Q7), and two sextupole (SX1 and SX2) magnets. The intermediate focal plane (F1) after the Q3 magnet is dispersive with respect to magnetic rigidity ($B\rho$). The Q3 magnet is used to adjust the dispersion at F1 arising from the D1 magnet. The focusing at F1 is achieved by using the Q1 and Q2 magnets. The SX1 magnet corrects chromatic aberrations at F1. The D1 magnet has a curved entrance boundary, by which a sextupole component is introduced, to correct non-chromatic aberrations at F1. The final focal plane (F2) at the end of the system is achromatic with respect to $B\rho$. The Q4 and Q5 magnets are used to obtain the achromatism at the exit of D2 magnet. The focusing at F2 is achieved by using the Q6 and Q7 magnets. The roles of the SX2 magnet and a curved exit boundary of the D2 magnet are similar to those of the sextupole components for F1.

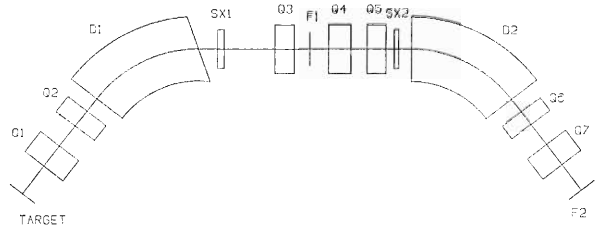

Fig. 1. Layout of the RIPS system.

Table 1. Design characteristics of the RIPS system.

Configuration	Q-Q-D-SX-Q-Q-Q-SX-D-Q-Q
Number of focal planes	2, dispersive and achromatic
Aperture	±30 mr (horizontal) ±40 mr (vertical)
Maximum solid angle	4.8 msr
Maximum $B\rho$	6 T·m
$B\rho$ acceptance	±3%
First order resolution at F1 ($P/\Delta P$)	~2,000

The isotope separation with the RIPS system will be made by using the following two methods simultaneously:

1) separation by selection of a $B\rho$ value,
2) separation by a thick $B\rho$-degrader set at the F1 focal plane.

The first method corresponds to the separation by A/Z of fragments. The $B\rho$ values of fragments are proportional to their A/Z, because the projectile fragmentation approximately conserves a projectile velocity. The second method utilizes the isotope dependence of the $B\rho$ loss in the degrader, which can be expressed as $\Delta(B\rho)/x\,\alpha-(A^3/Z^2)\,(B\rho)^{-3}$. When the degrader is used, the focusing position moves on the F2 plane according to A^3/Z^2 of fragments. The use of a slit enables the separation by A^3/Z^2 of fragments. A wedge-shaped degrader,[1] which does not change the dispersion at F1, will be used so as not to break the achromatism. The design goal of mass resolution ($A/\Delta A$) is more than 100.

The design characteristics of RIPS system are given in Table 1. The solid angle and the $B\rho$ acceptance are determined considering spreads of fragmentation spectra. The solid angle is about five times large compared with the similar spectrometer LISE[2] at GANIL. Large part of fragmentation yields can be collected with the RIPS system although the collection efficiency depends on a projectile energy and a combination of projectile and fragment. The maximum $B\rho$ is about 1.7 times larger than that of RIKEN Ring Cyclotron. This is advantageous for the collection of neutron-rich nuclides far from the stability line, because the use of a

higher projectile energy becomes possible.

The RIPS system has a beam swinger just before a target to collect fragments produced at backward angles. This makes the production of polarized nuclei possible.

The detailed design of the system is now in progress.

References

1) J. P. Dufour, R. Del Moral, H. Emmermann, F. Hubert, D. Jean, C. Poinot, M. S. Pravikoff, A. Fleury, H. Delagrange, and K. H. Schmidt: *Nucl. Instrum. Methods A*, **248**, 267 (1986).
2) R. Anne and C. Signarbieux: GANIL Report, RA/NJ 278 (1982).

RIKEN Accel. Prog. Rep. 20 (1986)

III-5-9. Beam Plasma Effects in Operating with an Ion-Guide Isotope Separator On-Line

K. Morita, T. Inamura, T. Nomura, J. Tanaka, H. Miyatake, M. Fujioka, T. Shinozuka, M. Yoshii,* H. Hama,* K. Taguchi,* K. Sueki, Y. Hatsukawa, K. Furuno, and H. Kudo

An ion-guide isotope separator on-line (IGISOL) has been first constructed at University of Jyväskylä. The IGISOL has a prominent advantage that it works almost independently of chemical and physical properties of elements and therefore can be applied to all elements equally well. The IGISOL has been successfully tested mainly using light-ion induced reactions and proven to work very stably for a long period of time.[1)]

We have constructed an IGISOL at INS (the Institute for Nuclear Study) and have been testing its performance. The present report is concerned with an effort to extend the application of the IGISOL to heavy-ion induced reactions. In doing so, an important problem is the plasma effect which should be significant in such reactions: The dense plasma formed by collision between beam particles and helium atoms along a beam path may induce quick neutralization of charged reaction products and therefore reduce the fraction of useful 1+ ions. This effect is probable since reaction products are mostly recoiled out in the beam direction. The density of the plasma formed by heavy-ion beams is proportional to the energy loss of the beam in gas, the number of beam particles, and the gas pressure inside a target chamber. We have detected the effect of the plasma on the extraction efficiency of reaction products by changing the density under the identical experimental conditions.

Relative efficiencies were measured by using reactions ^{27}Al(α, 2 pn)^{28}Al at 33 MeV, ^{19}F(^{12}C, 2 pn)-^{28}Al at 38 MeV, and ^{12}C(^{19}F, 2 pn)^{28}Al at 60 MeV as a function of beam intensity. Incident energies were chosen to give the same excitation energy of the compound nucleus produced in these reactions.

A 6 μm Al foil was used for the target for the ^{27}Al(α, 2 pn) reaction, LiF of about 2 mg/cm^2 in thickness evaporated onto a thin Al foil was used for the ^{19}F(^{12}C, 2 pn) reaction, and a 3 mg/cm^2 self-supporting natural carbon foil was used for the ^{12}C-(^{19}F, 2 pn) reaction. All the measurements were performed by detecting the 1.78-MeV γ-rays following the β-decay ($t_{1/2}$ = 2.2 min) of ^{28}Al with a 80 cm^3 pure Ge counter at the tape transport position. The pressure of the target chamber was set at 60 mbar. Other parameters were fixed throughout the measurements.

The results are shown in Fig. 1. For the α-induced reaction the efficiencies are nearly constant when the

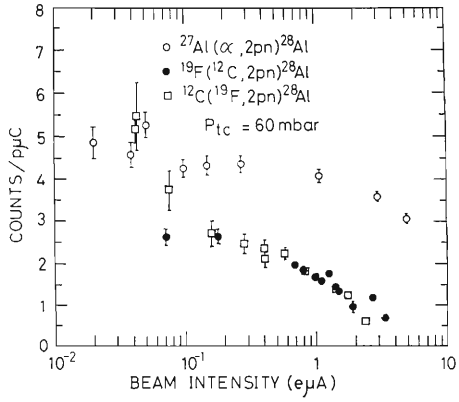

Fig. 1. Yields of 1.78 MeV γ-rays normalized by the integrated beam current versus average beam intensities in the ^{27}Al(α, 2pn)^{28}Al, ^{19}F(^{12}C, 2pn)^{28}Al, and ^{12}C(^{19}F, 2pn)-^{28}Al reactions.

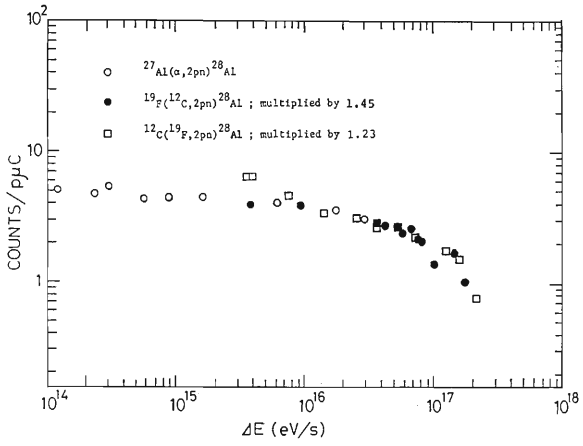

Fig. 2. The same as in Fig. 2, but plotted against ΔE, the product of beam intensity and estimated energy loss of beam particles in helium gas of 60 mbar under the present experimental conditions. ΔE=Energy loss in He×number of beam particles.

* Faculty of Science, Tohoku University.

beam intensity (I_b) is less than 1 μA, but decrease with the beam intensity in the range of $I_b > 1$ μA. This decrease in the efficiency becomes prominent even at low intensities for the ^{12}C- and ^{19}F-induced reactions. In Fig. 2, the same normalized yields are plotted as a function of the product of the beam intensity and energy loss of beam particles in helium gas of 60 mbar. It is clearly seen that all the experimental points lie on a smooth curve. This indicates that the observed change in the relative efficiency is primarily due to the change in plasma density formed along the path of a beam, which should be proportional to the quantity taken as the abscissa.

The present results provide the first clear evidence that the efficiency of the IGISOL is strongly affected by the plasma formed by beam particles in buffer gas when the plasma density becomes high. This indicates that the rate of the neutralization of recoil ions is enhanced by the dense plasma.[2)]

References

1) J. Ärje, J. Äystö, H. Hyvönen, P. Taskinen, V. Koponen, J. Honkanen, K. Valli, A. Hautojarvi, and K. Vierinen: *Nucl. Instrum. Methods A*, **247**, 431 (1986).

2) K. Morita, T. Inamura, T. Nomura, J. Tanaka, H. Miyatake, M. Fujioka, T. Shinozuka, M. Yoshii, H. Hama, K. Taguchi, K. Sueki, Y. Hatsukawa, K. Furuno, and H. Kudo: Proc. 11th Int. Conf. Electromagnetic Isotope Separators and Techniques Related to Their Applications (EMIS-11), Los Alamos, Aug. (1986).

RIKEN Accel. Prog. Rep. 20 (1986)

III-5-10. INS Gas-Filled Recoil Separator

H. Miyatake, T. Nomura, H. Kawakami,* J. Tanaka, M. Oyaizu,*
K. Morita, T. Shinozuka, H. Kudo, K. Sueki, and Y. Iwata**

A gas-filled recoil isotope separator (GARIS) has been constructed at INS.[1] The present GARIS mainly aims at efficient collection of reaction products by separating them from beam particles for the study of short-lived nuclei.

Reaction products recoiled otu of a target have broad distributions both in charge and momentum. When they enter a dipole magnetic field with gas of low pressure, they follow an average trajectory corresponding to their momenta and average charges ($\bar{q}$) defined by their multiple collision with gas atoms. Because the average charge is roughly proportional to momentum, the average trajectory is almost independent of the initial distributions of momentum and charge states, and depends only on their mass (A) and atomic number (Z).[2] Main characteristics of this kind of separator are relatively high efficiency (order of 10%) and its short separation time (1 μs).

The present GARIS consists of Q-Q-D-Q-Q configuration as schematically shown in Fig. 1. The maximum magnetic rigidity of the dipole magnet and dispersion of this system are 2.4 T·m and 7.14 mm for 1% of $\Delta B\rho/B\rho$, respectively. A region filled by helium gas is separated from the vacuum region by a thin nickel foil of 1.77 mg/cm^2 and 16 mm in diameter, located just before the target position upstream. The pressure of helium gas is measured by a capacitance manometer at the detector chamber and is controlled remotely with a solenoid-type gas-inlet valve at the target chamber. The vertical and horizontal acceptance angle are usually 70 mr and 50 mr, respectively.

The present GARIS has been tested first by using ^{16}O and ^{40}Ar beams which pass through the Ni-window and have thus significant momentum spread. Later we have also tested it by using the reaction ^{58}Ni(^{12}C, pn)^{68}As at 44 MeV, in which the Ni-window is used as a target. The various experimental parameters such as beam enegies and momentum spreads are listed in Table 1.

The efficiency of the GARIS is defined as a ratio of the amount of radio-activity of interest collected at the focal plane and that recoiled out of the target. We obtained the efficiency for ^{68}As from the measurement of the yields with 1,016 keV γ-rays decaying from this nucleus. This value slowly decreased from 12.3 to 8.0% when the pressure of helium increased from 0.27 to 1.01 Torr. We also measured the resolution, $\Delta B\rho/B\rho$, for various beams to compare calcu-

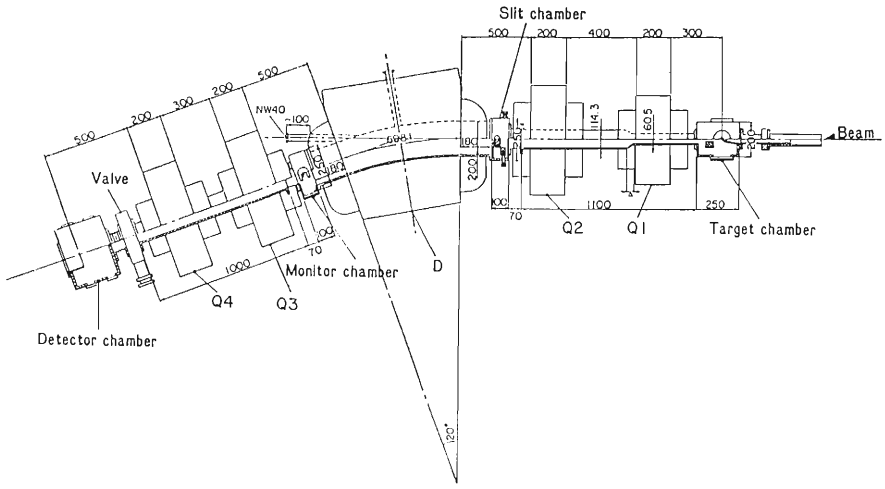

Fig. 1. A schematic drawing of the present GARIS. Q1, Q2, Q3, and Q4 are quadrupole magnets and D is a dipole magnet.

* Institute for Nuclear Study, University of Tokyo.
** Faculty of Science, Hiroshima University.

Table 1. Experimental parameters and results. $\bar{E}$ and Δp are the mean energy and the momentum spread, respectively, after passing through the Ni-foil. The $\bar{v}/v_0$ is the average ionic velocity in unit of v_0 at the midpoint of the dipole magnet after correction of the energy loss by helium gas. The given average charge is the one at the He pressure (p_{He}) which corresponds to the minimum resolution.

Ion (Beam energy)	Ni-foil thickness (mg/cm²)	$\bar{E}$ (MeV)	$\bar{v}/v_0$	$\Delta p/\bar{p}$ (%)	p_{He} (Torr)	$\bar{q}$ (e)
^{16}O (33 MeV)	2.21	22.89	6.81	3.87	13.0	6.61±0.52
^{16}O (26 MeV)	2.21	15.06	5.53	6.50	6.0	5.67±0.41
^{40}Ar (38 MeV)	1.77	17.90	3.85	18.3	3.0	6.11±0.34
^{68}As	1.77	3.60	1.35	111.0	0.75	2.72±0.31

lated values with experimental ones. It is well known that the resolution is mainly determined by statistics of charge-changing collision, multiple scattering, velocity dispersion, and beam optics. We estimated these effects in the same way as described in Ref. 2. The effects of energy loss of ions in helium gas was also taken into count. Figure 2 shows the pressure dependence of the resolution for ^{40}Ar in which experimental values are measured by Faraday cup set at the focal plane. The calculated values are shown by solid curve in Fig. 2. It is noted that a value of an effective charge-changing cross section, which is needed to estimate the contribution from the charge-changing collision, is chosen to be 7.7% of that calculated by using a unified empirical formula for a single electron capture[3] in order to obtain the best fit. The above values is consistent with the one given in Ref. 2. We also fitted calculated values to experimental ones for ^{68}As and ^{16}O.

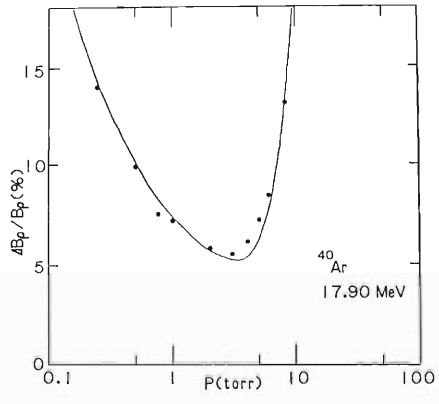

Fig. 2. The measured dependence of the resolution $\Delta B\rho/B\rho$ on helium pressure for ^{40}Ar ions at 17.9 MeV. The other experimental parameters are given in Table 1. The experimental errors are about 10% for all points. A solid curve shows the calculated values explained in the text.

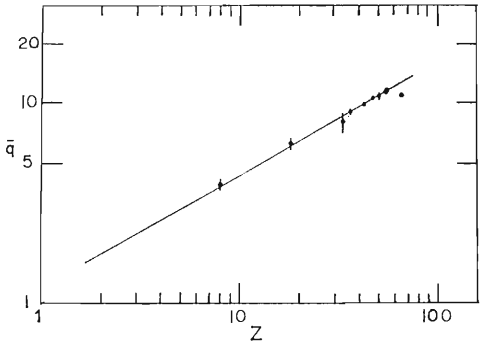

Fig. 3. The measured average charges obtained in helium gas of low pressure as a function of atomic numbers. Experimental values of ^{16}O, ^{40}Ar, ^{68}As, ^{84}Kr, ^{90}Mo, ^{103}Ag, ^{110}Sn, ^{132}Xe, ^{125}Cs, and ^{149}Tb are plotted. The values from ^{84}Kr to ^{149}Tb are taken from Ref. 4. All the experimental points are normalized to those of the ionic velocity of $v=4v_0$ ($v_0=c/137$). A solid line shows $\bar{q} \propto Z^{0.57}$ dependence.

The minimum resolution was obtained to be 5% for ^{40}Ar at the He pressure of 3 Torr in this test experiment.

Finally we measured average charge ($\bar{q}$) at the helium pressure corresponding to the minimum resolution as shown in the last column of Table 1. Petrov *et al.*[4] have shown that $\bar{q}$ of ion moving in helium gas with relatively low velocities of $v/v_0=4$, in which v_0 is the Bohr velocity ($v_0=c/137$), is proportional to $Z^{0.57}$ for $36 \leq Z \leq 54$. In order to see whether this holds for smaller Z values, the present data are plotted together with the results of Ref. 4 in Fig. 3. It is clear that the $Z^{0.57}$ dependence of $\bar{q}$ holds well down to $Z=8$.

At present a study of α-decays from unknown nuclei, whose half-lives are expected to be the order of μs, is in progress with the GARIS.

References

1) H. Miyatake, T. Nomura, H. Kawakami, J. Tanaka, M. Oyaizu, K. Morita, T. Shinozuka, H. Kudo, K. Sueki, and Y. Iwata: Proc. 11th Int. Conf. Electromagnetic Isotope Separators and Techniques Related to Their Applications (EMIS-11), Los Alamos National Laboratory, USA, Aug. 18–20 (1986); *Nucl. Instrum. Methods B*, **26**, 309 (1987).
2) P. Armbruster, J. Eidens, J. W. Gruter, H. Lawin, E. Rockl, and K. Sistemich: *Nucl. Instrum. Methods*, **91**, 499 (1971).
3) H. Knudsen, H. K. Haugen, and P. Hvelplund: *Phys. Rev. A*, **23**, 597 (1981).
4) L. A. Petrov, V. A. Karnaukov, and D. D. Bogdanov: *Sov. Phys. JETP*, **32**, 1042 (1971).

RIKEN Accel. Prog. Rep. 20 (1986)

III-5-11. The Experimental Beamline for the First Beam from RIKEN Ring Cyclotron

M. Fukuda, T. Kubo, I. Tanihata, K. Asahi,
M. Ishihara, and H. Taketani*

An experimental beamline named "20-degrees course" has been designed for the experiments using first beams from RIKEN Ring Cyclotron (Fig. 1). A main purpose of this line is to perform the experiments easily on exotic nuclei produced by projectile fragmentation.[1,2] Figure 1 shows that a primary beam and reaction products coming out from a target are separated by making them pass through a dipole magnet of 350 mmϕ in radius. In this situation, the radius of curvature of the central ray ρ is $\sim$2 m and maximum $B\rho$ is about 3 T·m.

As the central ray is bent by 20°, the dispersion becomes 0.342·l cm per 100% rigidity difference (l: the distance from the center of the magnet). Because the typical interval between the primary beam and the central ray becomes several cm at Slit-2, the primary beam can be stopped here.

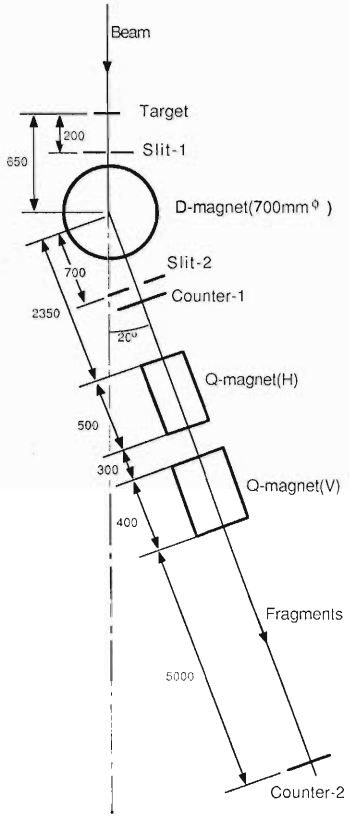

Fig. 1. Schematic drawing of "20-degrees course." Length in cm.

* Department of Applied Physics, Tokyo Institute of Technology.

Table 1. Counting rates of objective nuclide and most frequent contaminants at Counter-1.

^{18}O beam		^{40}Ar beam	
Object: ^{14}Be	15 cps	Object: ^{33}Al	110 cps
^{7}Li	49	^{20}F	4.8×10^{5}
^{8}Li	2,600	^{21}F	5.1×10^{5}
^{11}Be	450	^{23}Ne	6.5×10^{5}
^{12}Be	1,100	^{25}Na	5.9×10^{5}
^{13}Be	350	^{27}Mg	4.7×10^{5}

It is not possible, however, to separate a specific nuclide completely from a large number of nuclides produced by fragmentation by use of such a simple magnet. In Table 1, we exemplified the counting rates of each nuclide after Slit-2, assuming that ob-

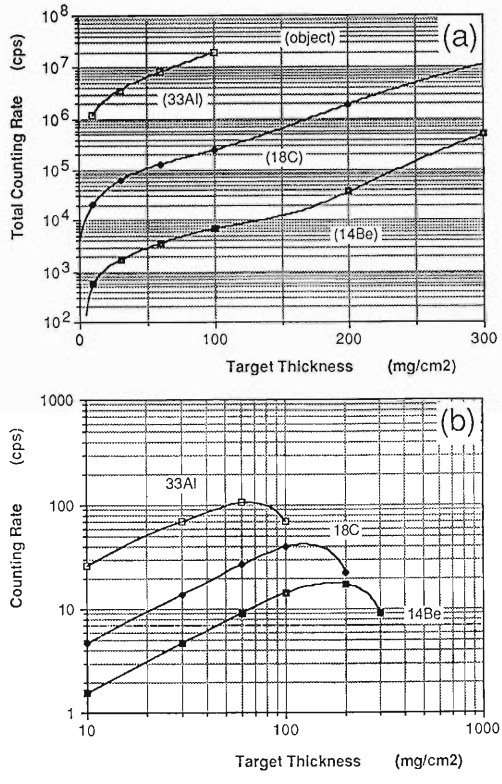

Fig. 2. (a) Total counting rates at Counter-1 and (b) counting rates of objective nuclides. The target is ^{9}Be. The better S/N, the thinner the target.

Table 2. Transmission from the target to Counter-2 for three combinations of a beam and a fragment.

Fragment (Beam)	Transmission
^{14}Be (^{18}O)	1.0%
^{18}C (^{22}Ne)	2.0%
^{33}Al (^{40}Ar)	3.9%

jective fragments are ^{14}Be and ^{33}Al from ^{18}O and ^{40}Ar beams, and targets are 100 and 60 mg/cm^2 ^{9}Be. In this calculation, the angular and momentum spreading of fragments by reaction and the energy distribution by energy loss in the target were taken into account. The values of cross sections for projectile fragmentation were taken from GANIL's data.[2] Slit-1 and -2 were set to improve S/N. The width of the slits were assumed to be 3 mm (S1) and 2 cm (S2). The above estimates indicate that these slits improve S/N at Counter-1 by 20–300 times.

Spreading of fragments after passing through the magnet is very sensitive to the target thickness. Figure 2 (a) and (b) shows counting rates calculated for whole nuclides and an objective after Slit-2 as a function of target thickness for a few combinations of a beam and an object. The yields of the objects become maximum around 100 mg/cm^2. The decrease in yields for thicker target is ascribed to the broadening of energy distribution of fragments owing to a distributed production depth in the target and the difference in energy loss between the beam and the fragments. In comparison with this effect, multiple scattering contributes little to the decrease in the yields. The mean scattering angle $\Delta\theta_{sc}$ in these situation is $\sim 10^{-3}$ rad, which is $\sim$10 times as small as the above effect.

In order to investigate the transmission of the system and the distribution of objective fragments at the focal point, we carried out Monte-Carlo simulation. Some of the results are shown in Table 2 and Fig. 3. From this calculation, we found that, at Counter-2, S/N becomes a few times better than that at Counter-1.

At this line, experiments on neutron rich exotic nuclei, *e.g.*, the search for new isotopes or lifetime measurements using the rotating catcher,[3] are being planned.

References

1) M. Langevin, E. Quiniou, M. Bernas, J. Galin, J. C. Jacmart, F. Naulin, F. Pougheon, R. Anne, C. Detraz, D. Guerreau, D. Guillemaud-Mueller, and A. C. Mueller: *Phys. Lett. B*, **150**, 71 (1985).
2) D. Guerreau: Proc. Int. Conf. Heavy Ion Nuclear Collisions in the Fermi Energy Domain, C4–155 (1986).
3) M. Fukuda, T. Kubo, K. Asahi, I. Tanihata, M. Ishihara, H. Kumagai, Y. Oikawa, T. Abe, and H. Taketani: p. 146 in this report.

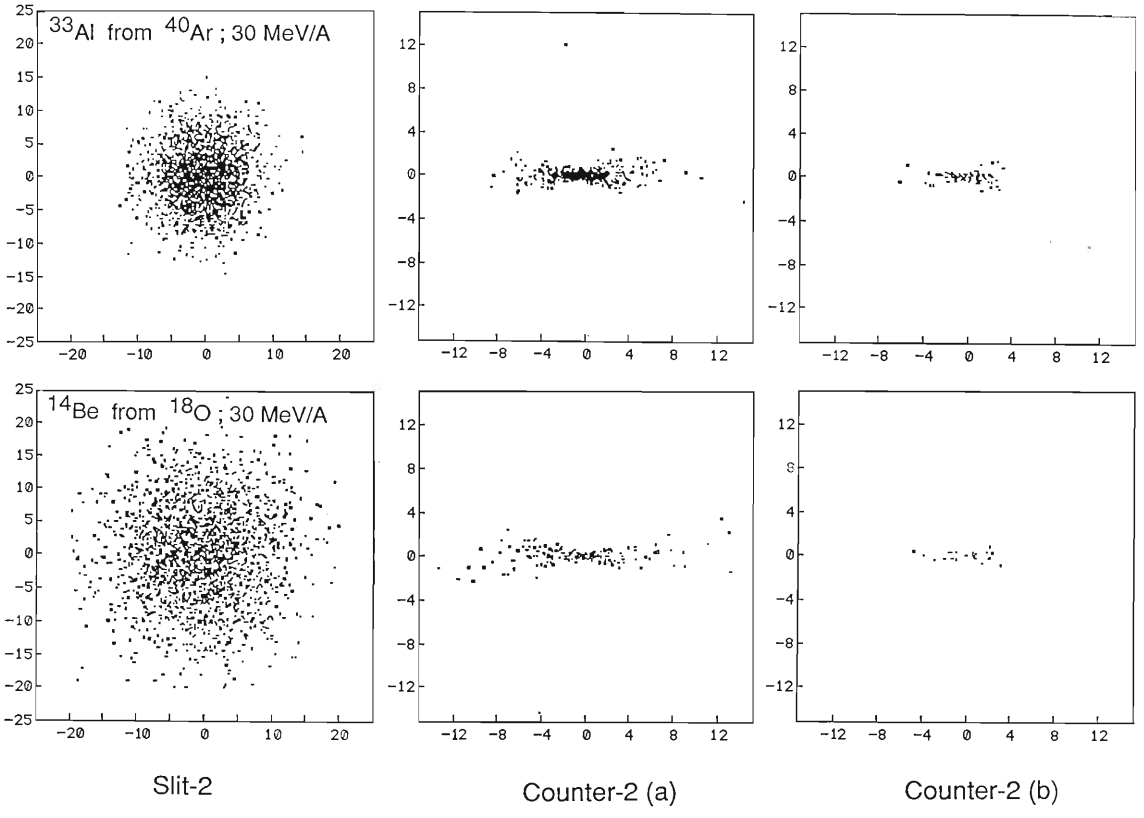

Fig. 3. Position distributions of objective nuclide at Slit-2 and Counter-2 by Monte-Carlo simulation. Two cases for different combinations of a beam and an object are shown (upper and lower). The targets are 60 and 100 mg/cm^2 ^{9}Be. Counter-2 (a) and (b) indicate the cases without and with the slits, respectively. The unit is cm.

RIKEN Accel. Prog. Rep. 20 (1986)

III-5-12. Sensitivity Test of Resonance Ionization Spectroscopy

H. Katsuragawa, T. Minowa, M. Shimazu, K. Nishiyama,* and T. Inamura

We have tested the sensitivity of resonance ionization spectroscopy (RIS) using an apparatus constructed last year.[1)]

Figure 1 shows the block diagram of the experimental setup. The Tl atoms are excited and photoionized by a single frequency two-step resonant process with a tunable dye laser (peak power 10 kW) pumped by a nitrogen laser (peak power 200 kW, repetition rate 10 Hz). The wavelength of the output beam of the dye laser was tuned to 377.6 nm which corresponded to that of the $7^2S_{1/2}$–$6^2P_{1/2}$ transition of thallium. Pairs of ion and electron generated by resonance ionization were detected with a pair of CERATRON detectors (ceramic electron multiplier, MURATA EMW-6081B). They were set opposite to each other and the distance between the two was 5 cm. The observed time-of-flight (TOF) of a thallium ion was 1.3 μs. This agrees well with the estimated value of 1 μs from the electric field (4.5 kV applied) and geometrical arrangement of the CERATRON detectors. The FWHM of the Tl peak on the TOF spectrum was about 100 ns. The time resolution of the detecting system itself was 17 ns. The signal-to-noise ratio has been improved by the order of 10^2 compared with the single detection of electrons or ions. The TOF spectrum is presented in Fig. 2. A small peak on the right-hand side is considered due to diffusion-pump oil molecules.

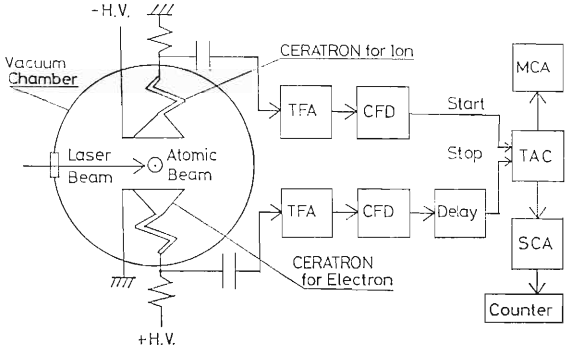

Fig. 1. A block diagram of experimental system. The meanings of the abbreviations in the figure are as follows: TFA, timing filter amplifier; CFD, constant fraction discriminator; TAC, time-to-amplitude converter. MCA, multichannel analyzer; SCA, single-channel analyzer; H.V., high voltage.

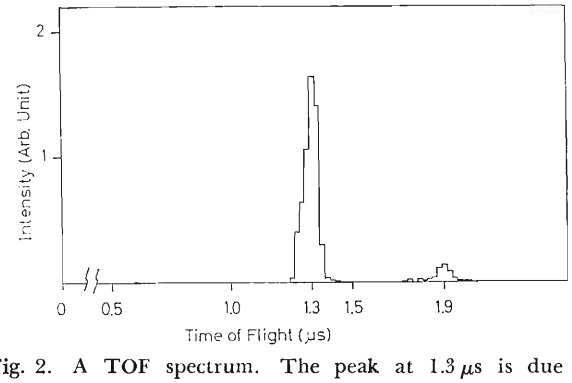

Fig. 2. A TOF spectrum. The peak at 1.3 μs is due to Tl and the small peak at 1.9 μs is considered due to molecules of the diffusion-pump oil.

We measured average counts per laser pulse at various temperatures of the thallium sample. Figure 3 presents the experimental results. The average counts (I) per laser pulse are plotted against $1/T$, where T is the temperature of the Tl sample in Kelvin. We assumed that the intensity of a Tl beam was proportional to the saturated vapor pressure at the surface of the Tl sample. The solid line in Fig. 3 was obtained from the least-squares fit of the data to the form

$$\log I = -A/T + B$$

where $A = 12{,}300$ (15) and $B = 20.5$ (3).

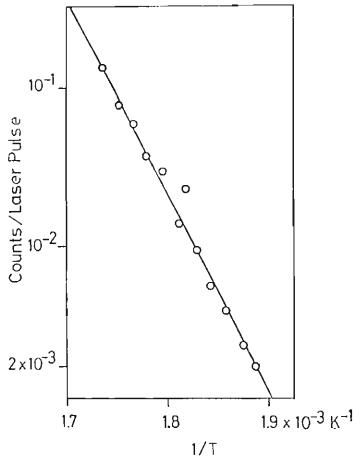

Fig. 3. Average counts per laser pulse are plotted against $1/T$, where T is the temperature of the Tl sample in Kelvin.

* Faculty of Science, Toho University.

In the present work, it is assumed that almost 100% resonance ionization of Tl atoms took place in the irradiation area, based on experimental results of RIS of Tl atoms using the same dye laser of the same power in a previous work.[2] From the average counts per laser pulse in the irradiation area (10^{-4} cm^{-3}) at 592 K, it is concluded that the sensitivity of this method reached the thallium density of 20 atoms/cm^3, which is by the order of 10^4 better than the proportional counter cell method.[3] The sensitivity will be further improved when an Einzel lens system is used to converge ions.

References

1) T. Inamura, K. Morita, K. Ando, H. Katsuragawa, T. Minowa, and M. Shimazu: *RIKEN Accel. Prog. Rep.*, **19**, 157 (1985).
2) T. Minowa, H. Katsuragawa, A. Kawamura, and M. Shimazu: *Opt. Commun.*, **60**, 37 (1986).
3) H. Katsuragawa, T. Minowa, M. Shimazu, and T. Inamura: Contributed to the EMIS-11 Conference, Los Alamos, N.M., 18–22 August (1986), and to be published in *Nucl. Instrum. Methods.*

RIKEN Accel. Prog. Rep. 20 (1986)

III-5-13. A Rotating Catcher System for Projectile Fragments

M. Fukuda, T. Kubo, K. Asahi, I. Tanihata, M. Ishihara,
H. Kumagai, Y. Oikawa, T. Abe, and H. Taketani*

A rotating catcher system has been disigned for lifetime measurements of exotic nuclei produced by projectile fragmentation with a beam from RIKEN Ring Cyclotron. A schematic drawing of the rotating catcher system is shown in Fig. 1. On the first stage, secondary particles separated from the primary beam are particle-identified by a combination of time-of-flight and dE/dX measurements. Two silicon ΔE-counters are set in front of the catcher with an energy absorber between them. The absorber is for particle identification. The last ΔE-counter is position sensitive to record the landing position on the catcher. The catcher is a rotating Al plate of about 1 mm in thickness (peripheral part) and 350 mm in radius. The angular velocity of the catcher is variable in the range of 0.1–10 rps in order to match the rotating velocity to the life of an objective nuclide.

Emitted β-rays from fragments on the rotating catcher are detected by position sensitive plastic strip counters and E_β-counters placed behind the strip counters. Each strip is a plastic scintillator of 1 mm in thickness, 2 mm in width, and 27 mm in length. One hundred chips of the strip are set along the pass of rotation. The minimum distance between the catcher plate and them is about 1 mm. E_β-counters are consisted of six plastic scintillators of about 80 × 80 × 150 mm in size and set at a distance of 10–15 cm from the catcher.

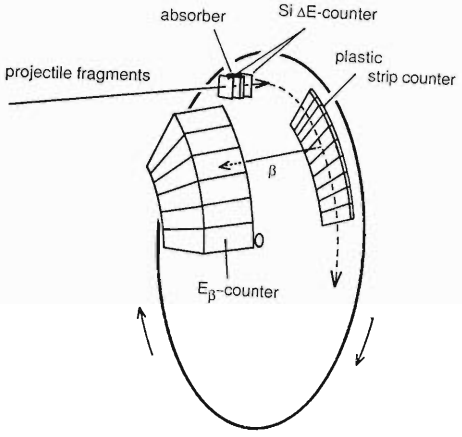

Fig. 1. A schematic drawing of the rotating catcher system.

Position information is used to connect a β-ray and a particle identification signals *via* angular velocity of the catcher. Therefore, energy and time information of β-rays can be recorded on a magnetic tape with information on the corresponding parent nuclide.

The width of the strip counter and the distance between the counters and the rotating catcher have a large influence on the position resolution Δx. If there is an isotropic point source at a distance d from the counters, position distribution becomes a Lorentzian type of FWHM $= 2d$. The width of the strip counter, therefore, is desirable to be $2d$. The condition of suppressing the probability that there are more than two stopped fragments in a width Δx on the catcher is given by

$$\frac{\Delta x}{v} \cdot N \lesssim 1$$

where v is the velocity of rotation and N is the stopping rate of fragments on the catcher. From this equation, the maximum counting rate becomes $N_{max} = v/\Delta x = 10^2$–$10^4$ cps depending on the life of an objective nuclide, when $\Delta x = 2$ mm.

This system will be used at 20-degree course[1] as one of the first experiments at RIKEN Ring Cyclotron.

Reference

1) M. Fukuda, T. Kubo, I. Tanihata, K. Asahi, M. Ishihara, and H. Taketani: p. 142 in this report.

* Department of Applied Physics, Tokyo Institute of Technology.

RIKEN Accel. Prog. Rep. 20 (1986)

III-5-14. Radiation-Detected NMR Measuring System for Short-Lived Radioactive Isotopes

H. Kumagai, K. Asahi, and M. Ishihara

Projectile fragmentations at intermediate energies provide a means to produce a wide variety of unstable nuclei which have been difficult to access so far. Spin-polarized unstable nuclei become available if these reactions are combined with a polarizing method such as those using laser optical pumping, tilted-foil, or ultra-low temperature techniques. Furthermore a simple model consideration of the fragmentation process[1] suggests that these product nuclei are spin-oriented even without any polarizing technique. These expectations motivate a number of interesting experiment[2,3] involving the nuclear magnetic resonance (NMR) detected through a change in the angular distribution of nuclear radiations. We here report a system we have recently developed for such measurements.

Block diagram of the system is shown in Fig. 1. The essential part of the present system consists of five electronics modules designed for the present purpose. A programmed sequence generator (PSG) provides signals to control the procedures of the measurement including beam bombardment, detection of radiations emitted from product nuclei, and application of the radio frequency (RF) field, according to the prearranged sequence stored in the memory. Figure 2 illustrates the procedures taken in a typical experiment. More detailed description of PSG is given elsewhere.[4] A two-channel digital-to-analog converter (DAC) feeds analog voltages to an RF oscillator to control the frequency and amplitude of the RF field. Any functional form can be chosen for the time variation in the frequency and amplitude, by loading properly programmed voltage steps to the PSG memory. At every event, the signal from the counter electronics, non-stop time-to-digital converter (TDC) registers the time elapsed after the end of beam bombardment. The clock in non-stop TDC starts at the end of beam bombardment and continues to run upon accepting an event signal. This feature is very useful when β decay process is

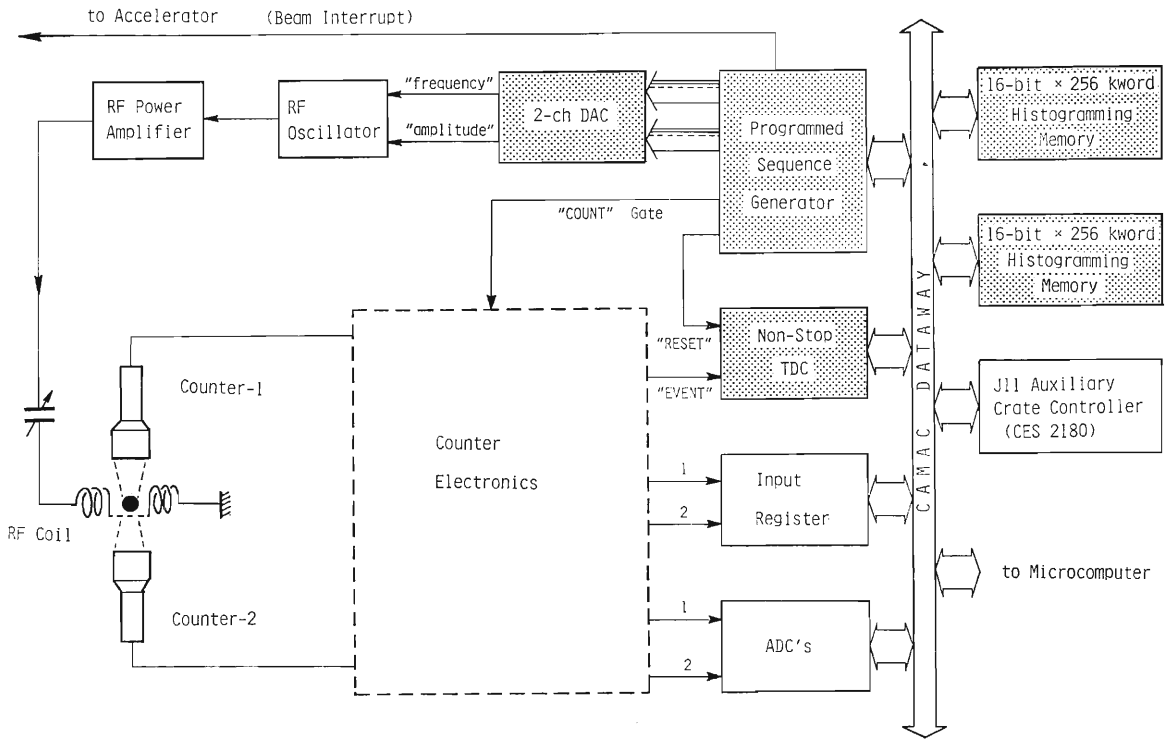

Fig. 1. Block diagram of the control system for radiation-detected NMR measurement. Shaded boxes represent the modules developed in this study.

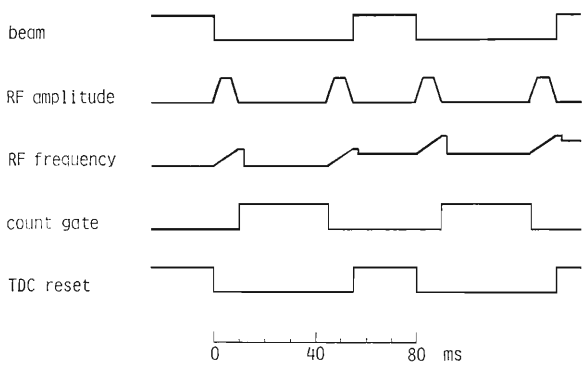

Fig. 2. Typical time chart for the procedures taken in the experiment.

involved, since more than one events per beam-intervening period (usually chosen to be of the same order as the decay lifetime) are needed to attain a required statistics in a limited length of the beam time. The data obtained from non-stop TDC, PSG, and other CAMAC standard modules such as ADC and input register are processed in auxiliary crate controller, and the resulting multi-dimensional histograms are constructed in two modules of 16 bit × 256 kword histogramming memory (HM). Sixteen chips of 256 kbit memory are installed in each HM module. They are backed up with batteries so that the data may hold at an accidental power failure.

The presently developed modules constitute a compact and flexible system, for which a small-size microcomputer can be employed for on-line monitoring and final recording of the data on a floppy disk.

References

1) K. Asahi and M. Ishihara: p. 21 in this report.
2) K. H. Tanaka, Y. Nojiri, T. Minamisono, K. Asahi, and N. Takahashi: *Phys. Rev. C*, **34**, 580 (1986).
3) K. Asahi, M. Ishihara, T. Shimoda, T. Fukuda, N. Takahashi, K. Katori, S. Shimoura, N. Ikeda, C. Konno, K. Hanakawa, A. Nakamura, T. Itahashi, Y. Nojiri, and T. Minamisono: *J. Phys. Soc. Jpn.*, **55**, Suppl., 1032 (1986).
4) H. Kumagai, K. Asahi, and M. Ishihara: p. 149 in this report.

RIKEN Accel. Prog. Rep. 20 (1986)

III-5-15. Programed Sequence Generator

H. Kumagai, K. Asahi, and M. Ishihara

Measurement of the decay of short-lived isotopes produced with medium-energy heavy-ion beams obtained from RIKEN Ring Cyclotron will provide useful information for the studies of β decay, nuclear structures, and solid-state physics. Such studies essentially use a periodically repeated sequence of procedures, such as target bombardment with a pulsed beam and subsequent manipulation of external conditions followed by detection of decay as a function of time;[1] therefore, a versatile control system for these procedures is needed for the experiment to be carried out efficiently. We have made a small-size electronics module which provides several control signals to the experimental devices following a prearranged sequence stored in memory. Use of such a dedicated module facilitates accurate timing control and largely simplifies software consideration for the data acquisition system, compared with relying on the help of a computer which concurrently handles the data acquisition.

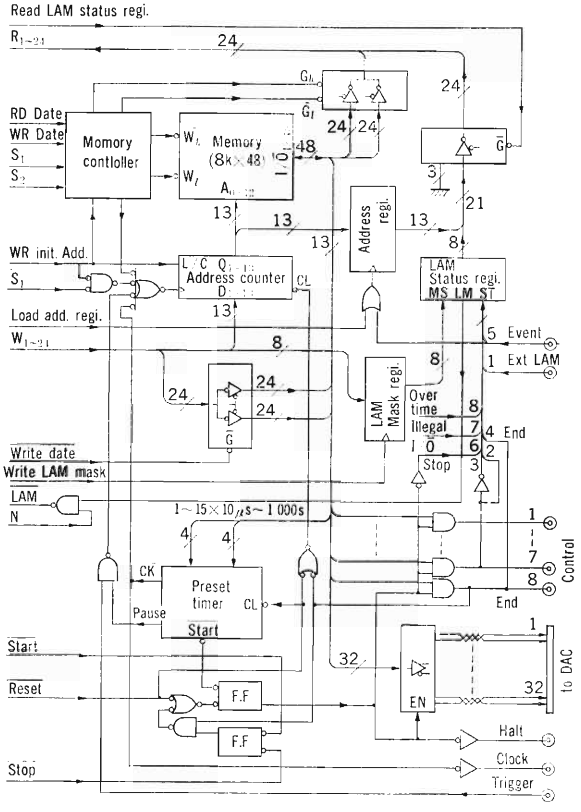

Fig. 1. Block diagram of the programmed sequence generator. Circuits for the CAMAC function decoder are not shown.

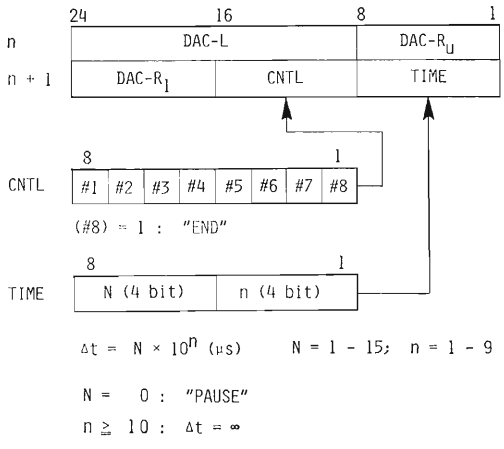

Fig. 2. Format of 48 bit data stored in the memory.

The block diagram of the module is shown in Fig. 1. A 48 bit, 8 kword static random access memory (SRAM) contains a programed sequence of operation loaded from a computer. Each word corresponds to an individual step of the sequence, and has a structure illustrated in Fig. 2. It consists of a 40 bit code (composed of 16 bit DAC-R, 16 bit DAC-L, and 8 bit CNTL) representing the output states of the control signals, and an 8 bit code (TIME) specifying the time duration for these output states to be maintained. At the end of the duration the address counter is incremented to initiate a subsequent step of the sequence. The data stored in DAC-L and DAC-R are fed through a differential line driver to two 52-pin connectors on the front panel. These signals are normally used as inputs for a 2-channel 16 bit digital-to-analog converter (DAC), which provides the analog signals to control the experimental conditions such as the frequency of the radio frequency (RF) field for NMR. The 8 bit data in CNTL are buffered by 50 Ω line drivers and fed to output coaxial terminals. These logic signals are typically used to start and stop a beam, to gate counter signals, and to trigger external devices. The address counter is cleared when END code (represented by "1" state in CNTL#8) is encountered, thus enabling the repetition of the sequence by restarting at address 0. PAUSE code is

also available, which stops the sequence and brings the module into the waiting state for an input signal to restart. The module accepts eight external signals which interrupt or modify the operation.

The present functions are installed in a double-width CAMAC standard module and controlled *via* the CAMAC data bus.

Reference

1) K. Asahi, M. Ishihara, T. Shimoda, T. Fukuda, N. Takahashi, K. Katori, S. Shimoura, N. Ikeda, C. Konno, K. Hanakawa, A. Nakamura, T. Itahashi, Y. Nojiri, and T. Minamisono: *J. Phys. Soc. Jpn.*, **55**, Suppl. 1032 (1986).

RIKEN Accel. Prog. Rep. 20 (1986)

III-5-16. Test-Bench System for On-Line Data Acquisitions System of RIKEN Ring Cyclotron Facility

T. Ichihara, T. Inamura, K. Asahi, and M. Ishihara

A prototype data acquisition system based on Micro VAX-II for the test and development of the new data-acquisition system for RIKEN Ring Cyclotron facility was installed last year. We have developed software of this system for special-purpose experiments such as the experiments at the GANIL (under Japan-France collaboration program) carried out successfully in May 1986.

This year we have improved the system as follows:

(1) Main memory size of the Micro VAX-II computer was increased from 2 MB to 6 MB.
(2) 1600 BPI, a 75 IPS magnetic tape driver was installed.
(3) A new 270 MB Disk driver was installed.
(4) A laser beam graphic printer (CANON LBP-8/A2) was installed.
(5) A Tektronix 4205 intelligent color graphic display and a 4696 color hard copy (ink jet methods) unit were installed.
(6) Serial terminal lines (RS-232C) were increased from 5-lines to 9-lines.
(7) The maximum user number of the Micro VMS system (software license) was increased from 2 to 8.
(8) A 9600 bps 4-ch optical modem was installed.
(9) Three 9600 bps base line 2-wire modems were installed.
(10) Connection to the NTT DDX-P and KDD VENUS-P public network system (X.25) at 9600 bps is in progress.
(11) A local area network (LAN) system based on the Ethernet hardware (10 Mbps) and the Decnet software is in progress.

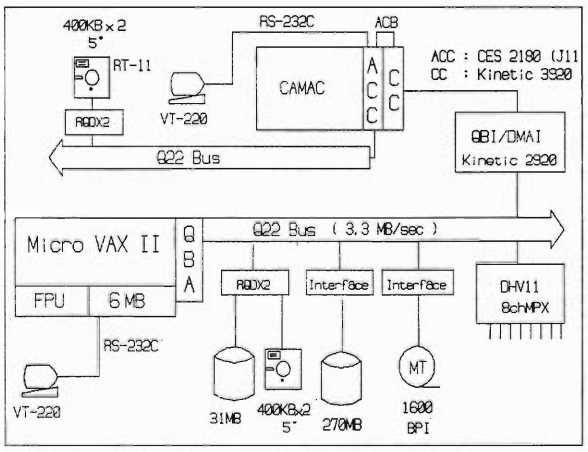

Fig. 1. A block diagram of the Micro VAX-II and CES 2180 ACC (J-11) data acquisition system for the GANIL experiments and for test and development of RIKEN Ring Cyclotron data acquisition system.

The new configuration is shown in Fig. 1. We have developed the device driver software for the Kinetic 2920–3920 crate controller which is capable of block-mode DMA data transfer. The maximum data transfer rate is 500 kB/s. We are now preparing to connect our computer system to a public network system (NTT DDX-P and KDD VENUS-P) with X.25 protocols.

The experiments with RIKEN Ring Cyclotron will be started in April 1987. To match this schedule we are preparing the final design of the whole data acquisition system for RIKEN Ring Cyclotron. In 1987, some part of this new data acquisition system will be installed in RIKEN Ring Cyclotron facility.

RIKEN Accel. Prog. Rep. 20 (1986)

IV. NUCLEAR DATA

1. Status Report of the Nuclear Data Group

A. Hashizume, Y. Tendow, Y. Ohkubo, T. Nozaki, and K. Kitao

In this period efforts were focused on the three following items. The first is related to the operation and application of programs related to EXFOR systems. The second is the compilation of new EXFOR, files of nuclear reaction cross sections. The third is the mass-chain evaluation work of nuclear structure for the implement of Evaluated Nuclear Structure Data File (ENSDF) and compilation of reference files originated in Japan.

(1) The programs presented by the courtesy of IAEA were implemented and have been operated successfully. They are Check Entry Run, Extract from Master Run, Prepare Edited Exfor Listing Run, and Prepair Author Proof Listing Run. The functions of these programs were explained in Ref. 1. As the Check Entry Run is very usefull for the error check of first edited files, this program has been distributed to the EXFOR compilers. The center host computer M-380 has been replaced with M-780; a microcomputer of PC9801 has been effectively used.

By utilizing a graphic display (No. 084) and its supporting program, a flexible graph describing program has been completed. This program can make graphs using the data filed in EXFOR. When many experimental results are expressed in a graphic form, it is very convenient to know the present status of the results. We are now editing these graphs of excitation curves.

(2) The reactions in which we mainly interested are those whose products are utilized in mediobiological applications. The cross sections of the reactions which produce the following isotopes have been compiled in the EXFOR file. The isotopes are ^{11}C, ^{13}N, ^{15}O, ^{18}F, ^{28}Mg, ^{52}Fe, ^{67}Ge, ^{74}As, ^{77}Br, ^{82}Br, ^{77}Kr, ^{81}Rb, ^{82m}Rb, ^{111}In, ^{123}Xe, ^{127}Xe, ^{123}I, ^{124}I, and ^{125}I nuclei.[1] We have also compiled the reaction cross sections for various combinations of incident particles and target nuclei described in the same reports.

Furthermore, since the last meeting of the nuclear data center held in October 1985,[2] we begun compilation of the integrated nuclear reaction cross section data originated in Japan in the EXFOR files. The main sources of recent data are annual reports published by universities and institutes having accelerator facilities.

In collecting the excitation functions of reactions which produce the radioisotopes for medical use, we have found some discrepancies between the experimental results.[3,4] In view of these discrepancies, we realized the importance of the standard or monitor reactions. In the foil activation method by which the cross sections are measured, a target consists of a stack of two kinds of foils, one is for investigation and the other for monitoring. The ^{12}C(p, pn)^{11}C reaction can be used as a primary standard for proton-induced reactions. In particular, the absolute cross sections of this reaction have been measured in a wide range of incident energies. For other than ^{12}C(p, pn) reaction, ^{27}Al(p, 3np)^{24}Na, ^{63}Cu(p, 2n)-^{62}Zn, ^{65}Cu(p, n)^{65}Zn, and ^{65}Cu(p, pn)^{64}Cu reactions are used for monitoring. For deuteron, the ^{27}Al(d, x)-^{24}Na reaction is used. For alpha induced reactions, an an aluminum target is also used to induce ^{27}Al(α, x)-^{24}Na. Typical errors of measured cross sections of the ^{12}C(p, pn)^{11}C reaction are within 3 to 5% in the energy range between 20 MeV and 28 GeV. The data of these reaction cross sections were compiled and compaired. The errors of these monitor reactions are scattered between 3 to about 10%, depending on the kind of reactions and incident energies.

(3) The recent reference files published periodically by Brookhaven National Laboratory (BNL) should cover all references in the field of nuclear physics, but the reports published in Japan were not completely filed. Upon the request, the references of annual reports and quartary reports published in Japan were compiled and were sent to the BNL Data Center. In connection with this work, all reference files of Nuclear Data Sheets were received from the Japan Atomic Energy Research Institute. In these files, BNL uses an extended EBCDIC code and, for the printing out, the change of the code was required. The code change program from the extended EBCDIC code to the ATF (Advanced Text Formation for science) system in FACOM and a search program of intended references were made. By applying these program, a reference book of γ-ray induced reactions is nearly completed. This reference book is motivated by the evaluation of activities induced by γ-ray irradiation of foods.

(4) For the mass chain evaluation of nuclear structure data, we have started to evaluate the nuclear structure of the $A=177$ mass chain. This mass chain is different from the mass region in which our Japanese group owes, but this evaluation work is started in advance the schedule of evaluation on nuclear structure data in world-wide network.

References

1) A. Hashizume, Y. Tendow, Y. Ohkubo, and T. Nozaki: *RIKEN Accel. Prog. Rep.*, **19**, 162 (1985).
2) Report on the 8th IAEA Consultants' Meeting of the Nuclear Reaction Data Centers, INDC (NDS)-178 Oct. (1985).
3) A. Hashizume and Y. Tendow: *RIKEN Accel. Prog. Rep.*, **19**, 163 (1985).
4) K. Kitao, A. Hashizume, Y. Tendow, and Y. Ohkubo: p. 156 in this report.

RIKEN Accel. Prog. Rep. 20 (1986)

IV-2. Nuclear Reaction Data for ^{52}Fe Production

Y. Tendow, A. Hashizume, Y. Ohkubo, and K. Kitao

As a part of the compilation of nuclear reaction data concerning radioisotope production for medical applications, the excitation functions and production yields for ^{52}Fe appeared so far in publications were reviewed.

The positron-emitting ^{52}Fe ($T_{1/2}$ 8.3 h) has been recognized as a useful agent for bone marrow imaging in studying the erythropoietic tissue or other metabolic processes. Other iron isotopes such as ^{55}Fe and ^{59}Fe are not suitable for this purpose because their half-lives are too long and the energies of accompanying γ-rays are too high or low. They act as harmful or interfering impurities for patients as well as for measurements. It is, therefore, necessary to establish a ^{52}Fe production method which is free from other iron impurities as less as possible.

^{52}Fe is also used as the parent nuclide for a ^{52}Fe–^{52m}Mn generator system which separates ^{52m}Mn ($T_{1/2}$ 21.1 m). Radiomanganese has shown its usefulness as an imaging agent in myocardial diagnosis. ^{52}Fe containing other radioiron impurities can be used for the generator system because the iron impurities result in no interfering manganese daughters. In this case, ^{52}Fe producing reactions which would be accompanied with significant production of other radioiron become usable.

Experimental excitation functions for the ^{52}Fe producing reactions, fundamental data to evaluate production yields, have not sufficiently been accumulated. It appears that we are not in the stage to make an evaluation of ^{52}Fe production cross sections for recommendation. Table 1 shows the experimental excitation functions, and Table 2 the production yields measured both appeared in publications to date.

Table 1. Excitation functions for ^{52}Fe.

Reaction	Energy{peak} (MeV)	σ_{max} (mb)	Target	Ref.
^{55}Mn(p, 4n)	40-73{54}	1.4	Mn metal	1
^{54}Fe(p, p2n)	33-44{45}	1.4	Fe metal	2
^{54}Fe(p, t)	18-23	0.3	Fe metal	3
^{54}Fe(p, dn)	33-60{45}	4	Fe metal	4
^{59}Co(p, spall)	59-98{77}	0.44	Co metal	5
^{58}Ni(p, αp2n)	42-56	1.8	Ni metal	6
^{52}Cr(^{3}He, 3n)	23-44{35}	5	Cr metal	7
^{59}Co(α, 3p8n)	113-170	0.26	Co metal	8
^{54}Fe(α, α2n)	38-40	0.34	Fe metal	9
^{54}Fe(^{6}Li, X)	55-94	4.8	^{54}Fe	10

Table 2. Production yields for ^{52}Fe.

Reaction	Energy (MeV)	Production yield (μCi/μAh)	Target	Ref.
^{55}Mn(p, 4n)	65	160	MnO_2	11
^{55}Mn(p, 4n)	70-50	200	Mn metal	12
^{55}Mn(p, 4n)	70	98	Mn metal	13
^{55}Mn(p, 4n)	73-39	670	Mn metal	1
	60-39	380		
^{55}Mn(p, 4n)	70	110	Mn metal	14
^{58}Ni(p, spall)	193.0	50	Ni metal	13
Cu(p, spall)	590	0.25 mb	Cu metal	15
Fe(p, spall)	590	0.80 mb	Fe metal	
Cu(p, spall)	590	0.27 mb	Cu metal	16
Fe(p, spall)	590	0.675 mb	Fe metal	
Ni(p, spall)	588	700	Ni metal	17
Ni(p, spall)	200	67	Ni metal	14
Ni(p, spall)	800	3,300	Ni metal	14
Ni(p, spall)	800	138	Ni metal	18
^{52}Cr(^{3}He, 3n)	45.5	50	Cr metal	7
^{52}Cr(^{3}He, 3n)	23	0.7	Cr metal	19
^{52}Cr(^{3}He, 3n)	40	50	Cr metal	20
^{52}Cr(^{3}He, 3n)	33	20	Cr metal	21
^{52}Cr(^{3}He, 3n)	45-30	22.5	Cr metal	22
^{50}Cr(α, 2n)	65	8/gm	Cr metal	23
^{50}Cr(α, 2n)	30	3.3	Cr metal	24
^{50}Cr(α, 2n)	30	0.5	Ce metal	25
Cu(^{12}C, spall)	1,032	0.35 mb	Cu metal	26

Although there are a variety of production methods available, a rather limited number of schemes have been conveniently utilized in practices for nuclear medical applications so far. In practical point of view, noticeable reactions among those are (^{3}He,3n), (α, 2n), (p, 4n), and (p, spallation).

The ^{nat}Cr(^{3}He, 3n)^{52}Fe reaction seems the most suitable to produce the ^{52}Fe almost free from impurities. The reaction is feasible with a relatively low energy cyclotron.

The ^{nat}Cr(α, 2n)^{52}Fe reaction also produces a small amount of ^{55}Fe impurities. Though not a pure ^{52}Fe, the product is adequately usable for a generator system.

The ^{nat}Mn(p, 4n)^{52}Fe reaction provides ^{52}Fe in relatively high yields, but produces also iron impurities as in the (α, 2n) reaction. This reaction seems to be convenient when proton beams of about 60 MeV are available.

The (p, spallation) reaction which requires a high energy facility of larger scale has been reported to

give the highest yields for ^{52}Fe. This reaction is considered advantageous for the carrier free separation of ^{52m}Mn in the Fe-Mn generator system because the reaction employs targets other than manganese.

Generally speaking, the data for ^{52}Fe production reactions are still insufficient and further experiments are needed.

References

1) K. Suzuki: *Radioisotopes*, **34**, 537 (1985) (in Japanese).
2) R. Michel, G. Brinkmann, H. Weigel, and W. Herr: *Nucl. Phys. A*, **322**, 40 (1979).
3) B. L. Cohen and T. H Handley: *Phys. Rev.*, **93**, 514 (1954).
4) I. R. Williams and C. B. Fulmer: *Phys. Rev.*, **162**, 1055 (1967).
5) R. A. Sharp, R. M. Diamond, and G. Wilkinson: *Phys. Rev.*, **101**, 1943 (1956).
6) S. Tanaka, M. Furukawa, and M. Chiba: *J. Inorg. Nucl. Chem.*, **34**, 2419 (1972).
7) M. W. Greene, E. Lebowitz, P. Richards, and M. Hillman: *Int. J. Appl. Radiat. Isot.*, **21**, 719 (1970).
8) R. Michel and G. Brinkmann: *Nucl. Phys. A*, **338**, 167 (1980).
9) S. Tanaka, M. Furukawa, S. Iwata, M. Yagi, H. Amano, and T. Mikumo: *J. Phys. Soc. Jpn.*, **15**, 1547 (1960).
10) J. Jastrzebski: *Phys. Rev. C*, **19**, 724 (1979).
11) G. B. Saha and P. A. Farrer: *Int. J. Appl. Radiat. Isot.*, **22**, 495 (1971).
12) T. H. Ku, P. Richards, L. G. Stang, Jr., and T. Prach: *Radiology*, **132**, 475 (1979).
13) L. Mausner, T. Prach, and P. Richards: *Am. Chem. Soc. Symp. Ser.*, No. 241, 77 (1984).
14) R. W. Atcher, A. M. Friedman, and J. R. Huizenga: *Int. J. Nucl. Med. Biol.*, **7**, 75 (1980).
15) J. E. Cline and E. B. Nieschmidt: *Nucl. Phys. A*, **169**, 437 (1971).
16) C. J. Orth, H. A. O'Brien, Jr., M. E. Schillaci, B. J. Dropesky, J. E. Cline, E. B. Nieschmidt, and R. L. Brodzinski: *J. Inorg. Nucl. Chem.*, **38**, 13 (1976).
17) V. J. Sodd, K. L. Scholz, and J. W. Blue: *Med. Phys.*, **1**, 25 (1974).
18) F. J. Steinkruger, G. E. Bentley, H. A. O'Brien, Jr., M. A. Ott, F. H. Seurer, W. A. Taylor, and J. W. Barnes: *Am. Chem. Soc. Symp. Ser.*, No. 241, 179 (1984).
19) J. R. Dahl and R. S. Tilbury: *Int. J. Appl. Radiat. Isoto.*, **23**, 431 (1972).
20) Y. Murakami, F. Akiba, and O. Ezawa: Proc. Symp. New Development in Radiopharmaceuticals and Labelled Compounds, IAEA, Vienna, Vol. 1, p. 257 (1973).
21) G. V. S. Rayudu, S. P. H. Shirazi, E. W. Fordham, and A. M. Friedman: *Int. J. Appl. Radiat. Isot.*, **24**, 451 (1973).
22) R. Bett, J. G. Cuninghame, J. A. B. Goodall, J. I. S. Hill, H. E. Sims, H. H. Willis, and A. L. Nichols: *U.K. At. Energy Auth.*, AERE-R 9453 (1979).
23) Y. Yano and H. O. Anger: *Int. J. Appl. Radiat. Isot.*, **16**, 153 (1965).
24) M. L. Thakur, A. D. Nunn, and S. L. Waters: *Int. J. Appl. Radiat. Isot.*, **22**, 481 (1971).
25) D. J. Silvester and J. Sugden: *Nature*, **210**, 1282 (1966).
26) T. Lund, D. Molzahn, B. Bergersen, E. Hagebo, I. R. Haldorsen, and C. Richard-Serre: *Z. Phys. A*, **304**, 43 (1982).

RIKEN Accel. Prog. Rep. 20 (1986)

IV-3. On Nuclear Data for Production of ^{77}Br

K. Kitao, A. Hashizume, Y. Tendow, and Y. Ohkubo

A survey on the published nuclear reaction data for the production of ^{77}Br by charged particles and the entry work of these data to a data library, maintained by Nuclear Data Section, International Atomic Energy Agency, was performed, and the compilation of these data including thick target yields has been also continued.

Radioactive isotopes of bromine have been considered to be suitable agents to prepare labeled radiopharmaceuticals. Because the compounds labeled with bromine are more stable than those with other elements owing to the stronger bond to carbon as compared with that to iodine. Among radioisotopes of bromine, ^{77}Br is most favorable because of its rather longer half-life ($T_{1/2}=57$ h) and lower-energy γ-rays of 239 keV (abundance 23.9%) and 521 keV (23.6%).

^{77}Br is produced directly with charged-particle reactions or is obtained as decay products of ^{77}Kr ($T_{1/2}=77.4$ min). Since the method of production of ^{77}Br with the α-particle-induced reaction on arsenic was developed by Helus,[1] following reactions have been proposed, and the cross sections or the thick-target yields were measured:

^{75}As(α, 2n)	$E=14.2$ MeV
^{77}Se(p, n)$^{+}$	$E=2.2$ MeV
^{78}Se(p, 2n)$^{+}$	$E=12.8$ MeV
^{79}Br(p, p2n)$^{+}$	$E=19.2$ MeV
^{81}Br(p, p4n)$^{+}$	$E=29.3$ MeV
^{79}Br(d, p3n)	$E=21.7$ MeV
^{81}Br(d, p5n)	$E=35.4$ MeV
^{79}Br(p, 3n)^{77}Kr	$E=23.0$ MeV
^{81}Br(p, 5n)^{77}Kr	$E=41.3$ MeV
^{79}Br(d, 4n)^{77}Kr	$E=25.6$ MeV
^{81}Br(d, 6n)^{77}Kr	$E=36.2$ MeV
^{76}Se(^{3}He, 2n)^{77}Kr^{+}	$E=6.5$ MeV
^{77}Se(^{3}He, 3n)^{77}Kr^{+}	$E=14.2$ MeV
^{78}Se(^{3}He, 4n)^{77}Kr	$E=25.1$ MeV
^{76}Se(α, 3n)^{77}Kr	$E=28.2$ MeV
Mo(p, spallation)^{77}Br	

E: threshold energy

$^{+}$: enriched target was used

As mentioned above, few data have been obtained with the enriched target, while practical data such as thick-target yields have been given in almost published papers. It is reported that the errors in the measurement of cross sections were estimated to be 10–25%. Figure 1 shows large discrepancies between excitation functions measured for Br+p reactions. **Dikšić *et al.*[2]** compared the experimental excitation function with the theoretical prediction by intranuclear cascade and two pre-equilibrium models followed by equilibrium evaporation on the ^{79}Br(p, 3n) and (p, p2n), and ^{81}Br(p, 5n) and (p, p4n) reactions (Fig. 2).

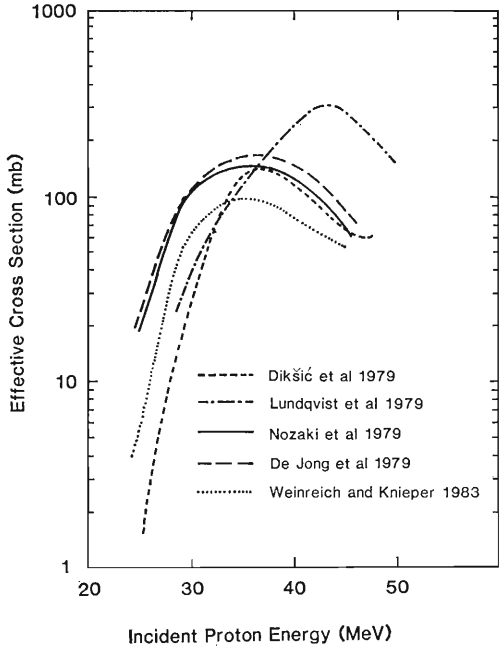

Fig. 1. Cross sections measured for the proton-induced reaction with bromine of the natural isotopic composition.

The ^{77}As(α, 2n)^{77}Br (^{75}As has 100% natural abundance) is most widely used for production of ^{77}Br with bombarding energy of 28–30 MeV. Selenium consists of many isotopes. Both ^{77}Se(p, n) and ^{78}Se(p, 2n)^{77}Br reactions are also used practically, but enriched targets should be used to prevent contamination with other isotopes. The production of ^{77}Br by the spallation process allows the preparation of a batch with larger activities. The cross sections for the spallation of Mo with 800 MeV protons were measured. The Se(^{3}He, xn)^{77}Kr reactions have resulted in considerably lower yield.

Measurements of cross sections and thick-target yields were carried out by using stacked foil techniques, with following reactions as monitor: ^{27}Al(p, 3pn)^{24}Na, ^{63}Cu(p, p2n)^{61}Cu, ^{63}Cu(p, 2n)^{62}Zn, ^{63}Cu-

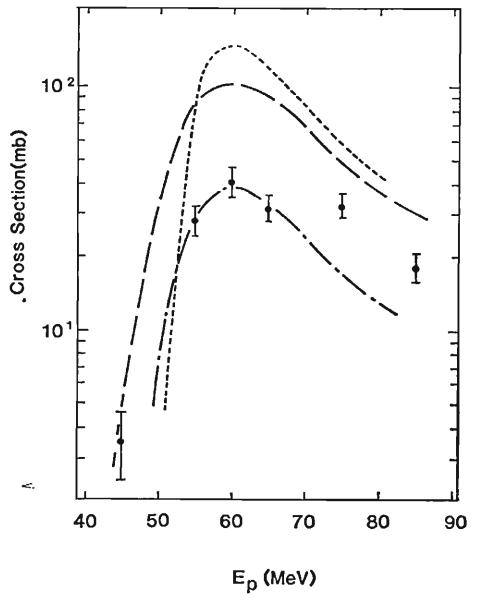

Fig. 2. Comparison of theoretical and experimental cross sections for ^{79}Br (p,3n). Experimental values are from Dikšić *et al.*[2] ---, Internucleon cascade-evaporation model; -·-, Gadioli's excitation model; ——, pre-equilibrium geometry-dependent hybrid model.

(p, n)^{63}Zn, ^{27}Al(d, 3p2n)^{24}Na, ^{63}Cu(^{3}He, p3n)^{62}Zn, and ^{65}Cu(^{3}He, 2n)^{66}Ga.

For the cross sections of ^{27}Al(p, 3pn)^{24}Na reaction, the values of 6–8% were cited as errors. It is reported that the results of integrated beam currents monitored by using the ^{65}Cu(^{3}He, p3n)^{62}Zn and ^{65}Cu(^{3}He, 2n)^{66}Ga reactions agreed within 10%. The errors in the cross sections for the ^{63}Cu(p, n)-^{63}Zn reaction with proton of higher than 30 MeV and the ^{63}Cu(p, 2n)^{62}Zn reaction with proton of higher than 40 MeV were estimated to be 15% for a natural copper target owing to the contributions from the ^{65}Cu(p, 3n)^{63}Zn and the ^{63}Cu(p, 4n)^{62}Zn reactions, respectively. Generally speaking, however, definite information on the reliability of these monitor reactions is still lacking. Thus, the critical evaluation for these monitoring reactions is essential in the compilation of cross sections for the production reactions.

References

1) F. Helus: *Radiochem. Radioanal. Lett.*, **3**, 45 (1970).
2) M. Dikšić, J.-L. Galinier, H. Marshall, and L. Yaffe: *Phys. Rev. C*, **19**, 1753 (1979).

RIKEN Accel. Prog. Rep. 20 (1986)

IV-4. On ^{124}I Production Cross Section

A. Hashizume, Y. Tendow, K. Kitao, and Y. Ohkubo

^{124}I is often produced as a by-product of ^{123}I which is one of the most useful radionuclides for nuclear medical studies using computed tomography. Because ^{124}I has a half-life (4.8 d) longer than that of ^{123}I (13.2 h) and emits many higher energy γ-rays, the former becomes undesirable impurity *in vivo* studies. It is important, therefore, to learn the production yield of ^{124}I relative to that of ^{123}I.

The excitation functions obtained for the ^{127}I(p, 5n)^{123}I reaction were compiled previously in Ref. 1. The ^{127}I(p, x, y) type reactions have been studied by Dikšić and Yaffe[2] in the energy range from 20 to 85 MeV. Though the starting point of excitation function as well as the cross sections of ^{127}I(p, p3n)-^{124}I show a small difference from those of ^{127}I(p, 5n), the peak of excitation function of the (p, p3n) reaction is more broad than that of the (p, 5n) reaction as shown in Fig. 1. In the region of higher incident energies, Kuznetsova *et al.*[3] investigated the cross sections between 100 and 680 MeV and Landenbauer *et al.*[4] studied the cross sections in the energy range from 250 MeV to 1 GeV where the cross sections decrease to 1.8 mb.

Above authors also compared the experimental cross sections with calculated ones based on a Monte

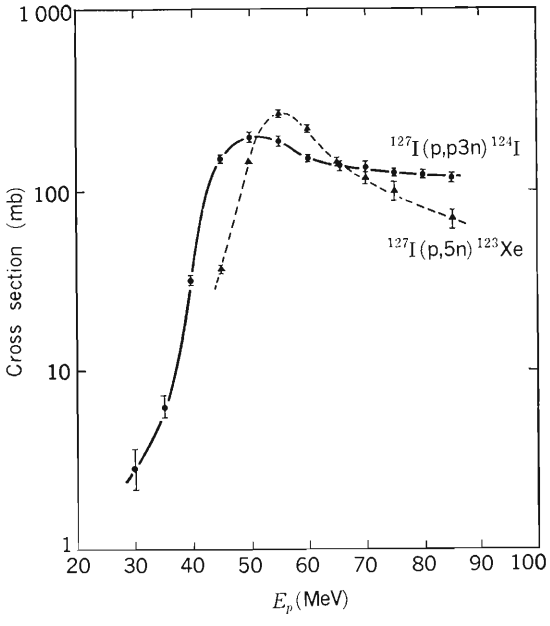

Fig. 1. Excitation functions of ^{127}I(p, p3n)^{124}I and ^{127}I(p, 5n)^{123}Xe.

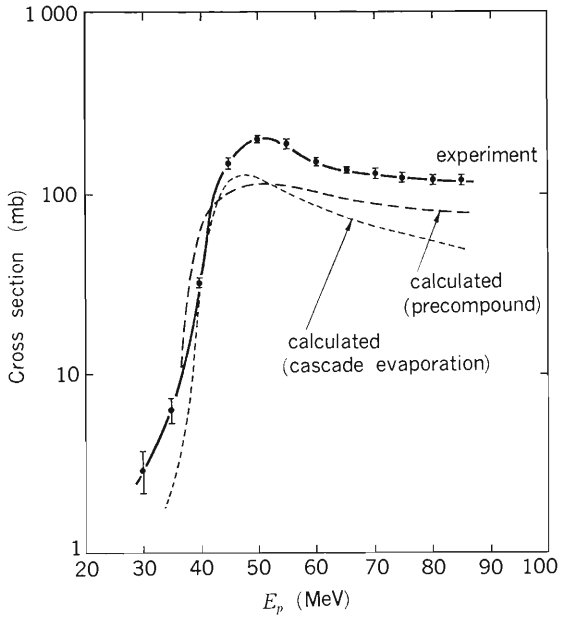

Fig. 2. Comparison of experimental and calculated excitation functions for ^{127}I(p, p3n)^{124}I reaction.

Carlo internuclear cascade evaporation model and also based on a preequilibrium model. However, the agreement is not satisfactory. The experimental values are larger than calculated ones by a factor of about 2 (Fig. 2).

Reuland and Caretto[5] investigated the cross sections of (p, n) and (p, 2n) reactions for several targets at an incident energy of 400 MeV. They revealed that the ^{124}Te(p, n)^{124}I reaction has a cross section of 1.3 mb and ^{124}Te(p, 2n) 3.6 mb. If one compares the ratio of these cross sections to those of other targets such as ^{52}Cr, ^{63}Cu, the high (p, 2n)/(p, n) ratio is obtained for the ^{124}Te target. These differences were attributed by these authors to the differences in the ratios of excitation energy and neutron separation energy.

Though the excitation curves for (p, 5n) and (p, 3np) are close to each other in the same energy region, ^{123}Xe, a rare gas, can be easily purified by chemical methods. If an appropriate purification method is employed, one hardly finds ^{124}I in ^{123}Xe. Thus, the importance of chemical separation techniques should be stressed.

The practical yields of ^{124}I and ^{123}I in the Te + p

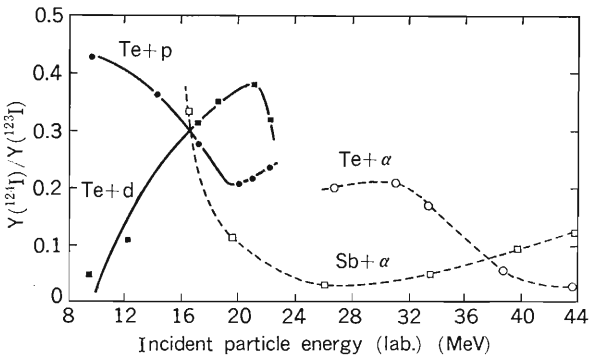

Fig. 3. The yield ratios of ^{124}I and ^{123}I for thick targets as a function of incident particle energies.

reaction have been investigated by Dmitriev *et al.*[6] On the basis of their experimental data, the yield ratios of ^{124}I to ^{123}I are shown in Fig. 3 as a function of proton energy, where the yield ratios for other reaction types were also shown. In these reactions, the ratios of ^{124}I to ^{123}I of induced reactions with a Te or an Sb target show low minimum values compared with those of proton or deuteron induced reactions.

Yu *et al.*[7] examined the Xe isotope yields by bombarding ^{238}U with 11.5 GeV protons. The independent yields of Xe isotopes show mass dependency, and, in the neutron deficient sides, ^{124}Xe and ^{135}Xe show maximum yields of 3.0 and 3.1 mb, respectively. The recoil ranges of Xe isotopes in this reaction were also measured and, for the neutron-deficient products, their ranges were by a factor of more than 2 shorter than those of neutron-richer ones, suggesting some different mechanism is involved for the neutron-deficient productions.

Fissions of the ^{209}Bi + ^{12}C system were investigated by Branquinho and Robinson[8] at Manchester University. When the compound nucleus' excitation energy was 66 MeV, the fission yields were 1.63×10^{-3}, 3.73×10^{-3}, 3.84×10^{-3}, and 0.706×10^{-4} for ^{124}I, ^{126}I, ^{128}I, and ^{131}I, respectively. Iodine fission yields were also examined in the ^{40}Ar + ^{238}U system by de Saint-Simon *et al.*[9] The independent yield cross sections for ^{124}I were 0.683 mb for 240 MeV of ^{40}Ar and 2.64 mb for 340 MeV. The fission yields are discussed from the view point of complete fusion and quasielastic-transfer-induced fission.

References

1) A. Hashizume and Y. Tendow: *RIKEN Accel. Prog. Rep.*, **19**, 163 (1985).
2) M. Dikšić and L. Yaffe: *J. Inorg. Nucl. Chem.*, **39**, 1299 (1977).
3) M. Ia. Kuznetsova, V. N. Mekhedov, and V. A. Khalkin: *Sov. Phys. JETP*, **34** (7), 759 (1958).
4) I.-M. Landenbauer and L. Winsberg: *Phys. Rev.*, **119**, 1306 (1960).
5) D. J. Reuland and A. A. Caretto, Jr: *J. Inorg. Chem.*, **31**, 1915 (1969).
6) P. P. Dmitriev, M. V. Panarin, and Z. P. Dmitrieva: *At. Energy*, **49**, 329 (1978).
7) Y. W. Yu, N. T. Porile, R. Warasila, and O. A. Schaeffer: *Phys. Rev. C*, **8**, 1091 (1973).
8) C. L. Branquinho and V. J. Robinson: *J. Inorg. Nucl. Chem.*, **39**, 921 (1977).
9) M. de Saint-Simon, R. J. Otto, and G. T. Seaborg: *Phys. Rev. C*, **18**, 1651 (1978).

RIKEN Accel. Prog. Rep. 20 (1986)

V. ACCELERATOR DEVELOPMENT

1. Status of RIKEN Ring Cyclotron Project in 1986 —Commissioning of RIKEN Ring Cyclotron—

H. Kamitsubo

An Ar^{12+} beam accelerated to 21 MeV/u was successfully extracted from RIKEN Ring Cyclotron (RRC) at 15:34 on December 16. A beam accelerated at RILAC up to 1.28 MeV/u was injected into RRC. The frequency of the RF systems was 28 MHz for both accelerators. As the oscillator of the 6th RF amplifier of RILAC was disassembled for improvement, we were obliged to accelerate ions with other five acceleration resonators, therefore, the final energy was lower than the expected value. For this reason a harmonic number of 10 was adopted instead of the designed number of 9.

We started coupled operation of RILAC and RRC on November 28. It took several days to adjust the beam diagnostic devices and the buncher installed in the beam transport line from RILAC to RRC by using the beam and to bring the beam to the first injection bending magnet of RRC.

We succeeded in injection of the beam to the first acceleration orbit of RRC on December 3, and the beam reached the outermost radius on December 10. Then we succeeded in making a complete isochronous field with a help of the radial phase probe on December 16 to extract the beam with ease. On December 20 the beam was transported to the E1 experimental hall.

The assembly of magnet vacuum chambers was started in January and completed in April. They were assembled one by one and examined carefully that air leakage was less than the specified value for each chamber. Beam diagnostic devices such as radial probes were built in the chambers and tested in August and September.

The first resonator of the RF system was assembled in July and the second one in August. After careful vacuum tests, measurements of the static characteristics of the resonators were pursued in August and September. At the same time the assembly of an amplifier system was continued.

The beam transport line between RILAC and RRC was installed in July and August. Field distributions were measured for all the bending magnets and the Q-magnets before they were installed in the beam line. Pipes and chambers for the beam diagnostic devices are made of aluminum. The injection elements such as bending magnets in the central region, magnetic inflection channels, and an electric inflection channel were built in the positions in July and August. Extraction elements and a beam transport line to the E1 experimental hall was installed in September. The vacuum test and stability measurements of the power supplies were performed after their installation.

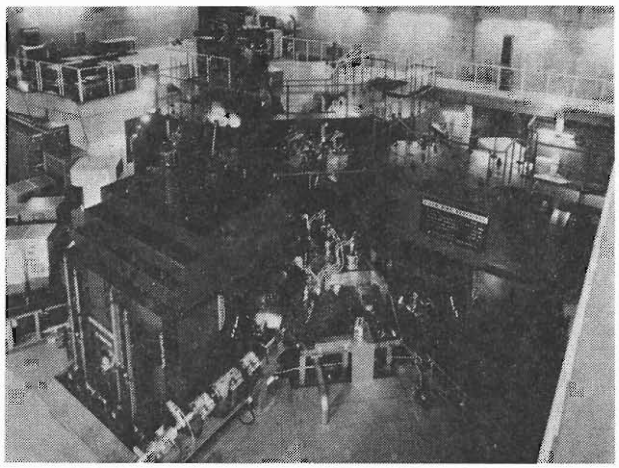

Fig. 1. Photograph of RIKEN Ring Cyclotron.

Soft-ware development for the control system was continued throughout 1986. Those for CAMAC modules named CIM and DIM, which locally control the power supplies and the beam diagnostic devices, were mainly written in assembler language and developed by ourselves. All the programs for the main control computers are written in UNIX and FORTRAN and developed also by us.

The construction of RRC was completed in September, 1986. Figure 1 shows a photograph of RRC taken from the south-east corner of the cyclotron vault. The beam is injected to the other side of RRC and extracted at this side. Two bending magnets and the beam transport line to the experimental halls are shown in the foreground.

We continued power tests of the RF systems dur-

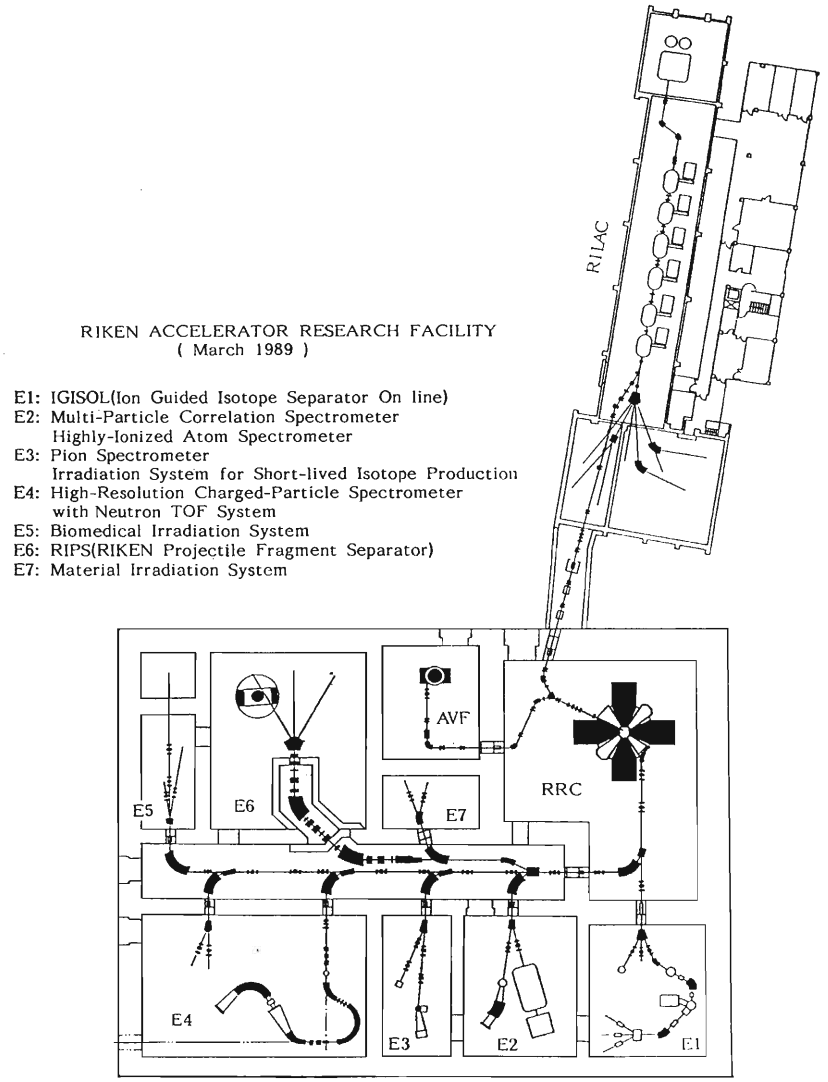

Fig. 2. Plan view of the RIKEN Accelerator Research Facilities.

ing October and November. The vacuum of the whole system was very good and pressure inside the chambers reached 2×10^{-6} Pa. After the first acceleration trial, the vacuum in the resonators became poor; small leakages were found at welded parts of the cooling pipes inside the resonators. The first overhaul of RRC is scheduled in February, when they will be repaired. Some other repairs and improvements will also be made. RRC will be open to the test experiments from April in 1987.

The construction of the second injector, an AVF cyclotron with $K=70$ MeV, and the beam transport lines to the experimental halls will be started. Extension of the building to the west will also start in next year and will be completed in 1988. Three experimental halls, which will be used for studies of nuclear reactions and structure and for biological studies, will be available by the end of 1988. Figure 2 shows a full layout of the building together with the accelerators, the beam transport lines, and the main research facilities.

RIKEN Accel. Prog. Rep. 20 (1986)

V-2. First Trial of Beam Acceleration in RRC

S. Motonaga, Y. Yano, A. Goto, M. Kase, K. Hatanaka,
T. Wada, H. Takebe, and H. Kamitsubo

At 15 : 34 on December 16, 1986, we succeeded in extraction of a 21 MeV/u 12^{+} argon beam from RIKEN Ring Cyclotron (RRC). An argon beam of 1.28 MeV/u from RILAC was injected into RRC. Acceleration was performed with a harmonic number of 10 instead of 9 (normal operation). This number was adopted because RILAC was operated with five resonators except the last one (sixth), the amplifier of which had been disassembled for improvement.

The whole components were assembled during the period from January to September, 1986. In the vacuum chamber equipped with ten 10,000 l/s cryopumps and four 5,000 l/s cryopanels, a pressure of 3×10^{-8} Torr was achieved at early October. The resonators were operated at a dee voltage of 140 kV, which exceeds the dee voltage required for acceleration of an argon beam at 28 MHz. The isochronous field of the sector magnets could be arranged with an accuracy of few parts in 10^{-4} by the field setting program. The progress in the first operational trials for RRC is as follows.

Sept. '86 The whole components were assembled. The vacuum system was tested and found to be satisfactory. Transportation of a beam from RILAC to RRC was tried.

19 Sept. '86 All of work related to radioactive isotopes and accelerators had to be stopped intermittently until the end of November because of a radiation hazard accident outbroken in another section of the institute.

Oct. '86 The RF system was tested. (The 11th Cyclotron conference, '86-Tokyo, was held.)

28 Nov.–3 Dec. The beam injection system was adjusted.

29 Nov. The first trial of beam injection was made.

3 Dec. The beam injection to RRC was achieved. The beam was accelerated up to the radius $R =$ 2.87 m. (Note: the extraction radius $R = 3.45$ m)

5 Dec.–10 Dec. Adjustment of beam injection, initial acceleration, beam centering and beam

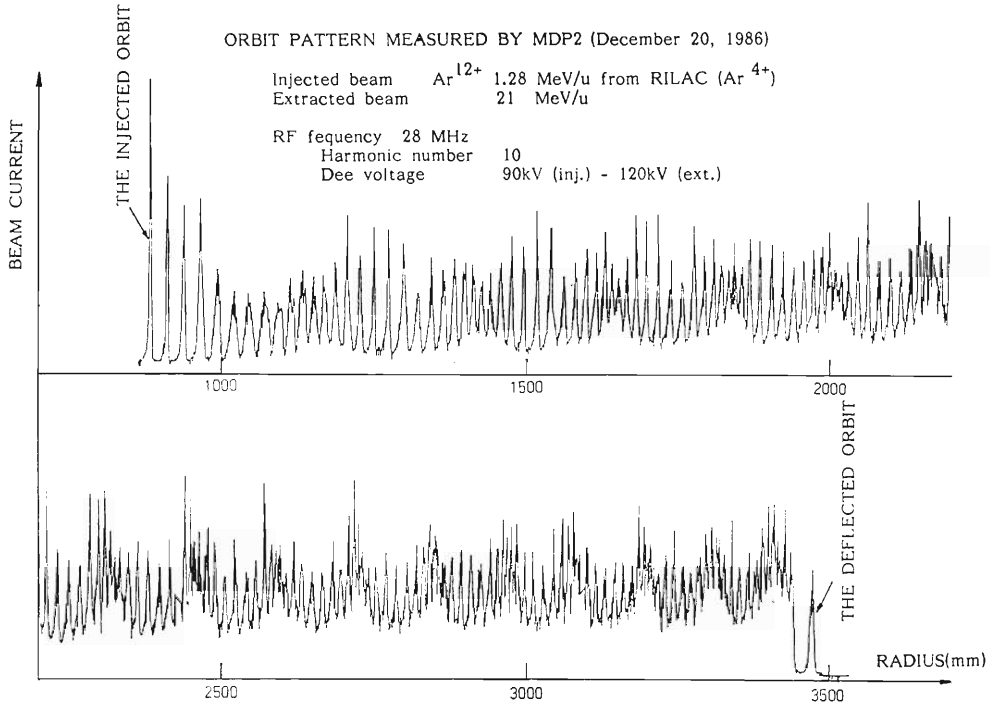

Fig. 1. Beam patterns in RRC measured with the radial probe. The abscissa is the distance in mm from the machine center. The ordinate is the measured beam current in arbitrary units. The peak around the radius of 3,470 mm is the Ar beam accelerated to 21 MeV/u.

acceleration were tested. The beam was accelerated up to the extraction radius, but could not be extracted.

11 Dec.–16 Dec. The trial for beam extraction was carried out, and we succeeded in extracting the beam at 15:34 on December 16. During this period, the beam phase probes installed in the S-valley chamber were completed, and beam phase was measured using them.

20 Dec. The beam was accelerated successfully and transferred to the experimental hall E1 for an inspection according to the radiation-safety regulation by the government.

Thus, the first injection of a beam took only 6 d and its first extraction 15 d, after the first operation of the whole system of RRC. During this trial RRC operated with enough reliability and good reproducibility. Figure 1 shows an orbit pattern measured with the radial probe MDPI.

After these initial operations, we have carried out repair of the vacuum system of the RF resonator from the end of January, 1987. The period is scheduled until the end of March, and we will start the operation again at the beginning of April.

RIKEN Accel. Prog. Rep. 20 (1986)

V-3. Present Status of RF Resonator for RIKEN Ring Cyclotron

K. Ogiwara, T. Fujisawa, S. Kohara, Y. Oikawa, and I. Takeshita

The design of radio-frequency (RF) system for RIKEN Ring Cyclotron ($K=540$) has been already described.[1]

Two RF resonators have been installed at the site in September 1986; Fig. 1 is their picture. Their electrical characteristics are measured on low-level signals from a frequency synthesizer. The results are compared with the calculation based on a one-dimensional transmission line approximation.[2] Measured resonant frequencies of the fundamental mode and the higher-order ones are shown by dots in Fig. 2. The solid line shows the calculated frequency of the fundamental mode and the broken lines show the multiples of measured ones. The broken lines cross the higher-order mode frequencies at several points, where an undesirable mode is possibly excited by a higher harmonic component in the RF power. In such a case, the relation between the undesirable mode and the fundamental mode has to be changed by moving a capacitive tuner and movable boxes.

In Fig. 3, the shunt impedances (R_s) defined at the extraction radius and Q-values (Q) are shown together with calculations. The Q-value was deduced from the width of the resonance curve which was measured by two capacitive coupler coupled very weakly to the resonator. The shunt impedance was measured by perturbation method using a dielectric ceramic ball to avoid the effect of RF magnetic field. The fundamental frequency in Fig. 2 and

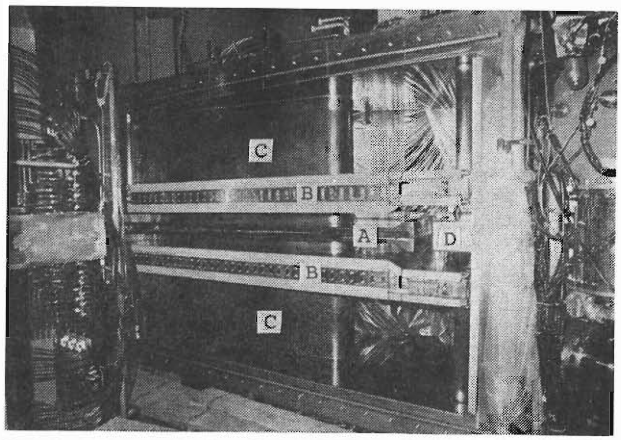

Fig. 1. Picture of the RF resonator. A, Dee; B, Movable box; C, Stem; D, Capacitive tuner.

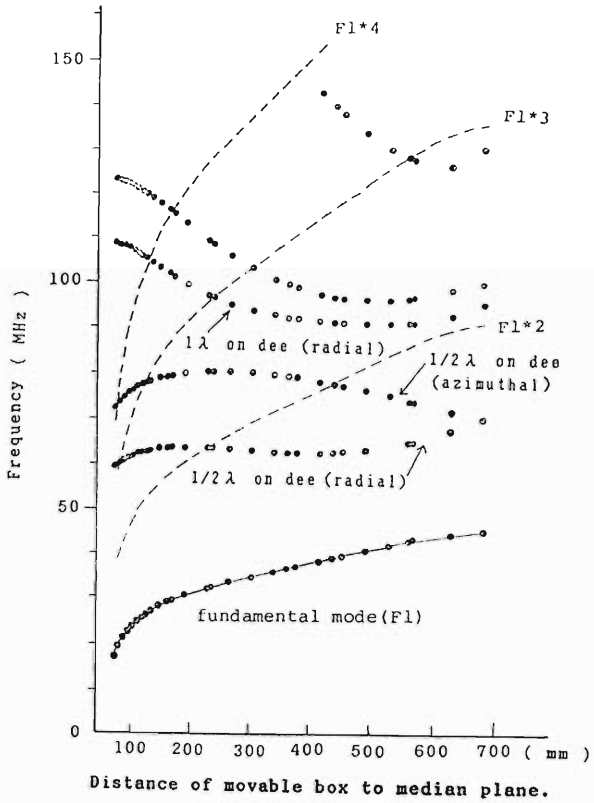

Fig. 2. Resonant frequencies of fundamental and higher-order modes.

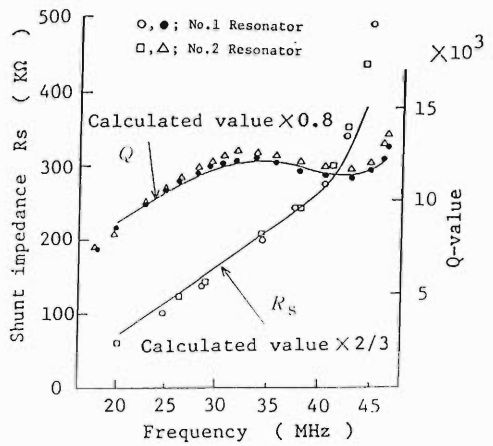

Fig. 3. Q-values and shunt impedance. The lines show calculations.

frequency dependences of Q and R_s are well reproduced by the calculations, while measured Q is about 4/5 of the calculated one, and measured R_s is about 2/3. Such disagreement is due to the fact that the structure of the resonator is too complex for one-dimensional transmission line approximation and resistances of many contacts are not taken into account.

Relative distributions of RF electric field along the dee gap were measured in the same way for the shunt impedance. The results are shown in Fig. 4, where the dee voltages are normalized near the beam injection radius. The radially increasing voltage distribution are obtained. The dee voltages at the injection and extraction radii for the input power of 220 kW are calculated from the shunt impedances and the radial voltage distributions; these are shown in Fig. 5. The input power of 220 kW is enough to generate the dee voltage required for beam acceleration. Although designed mechanically in up-down symmetry, the resonator has asymmetry due to fabrication errors to cause the RF electric field inside the dee. This field is undesirable for beam acceleration. Furthermore, it might disturb beam diagnostic systems or give rise to local heating of the structure. The field (vertical component) was measured with the pickup in the dee as shown in Fig. 6(b). Figure 6(a) shows the ratio of the electric

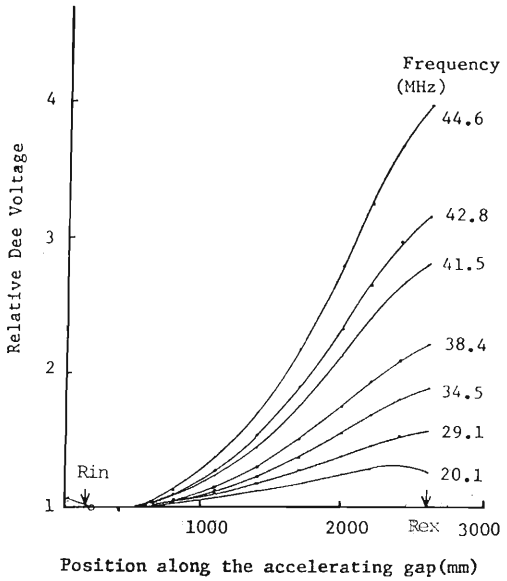

Fig. 4. Relative distributions of RF electric field along the dee gap.

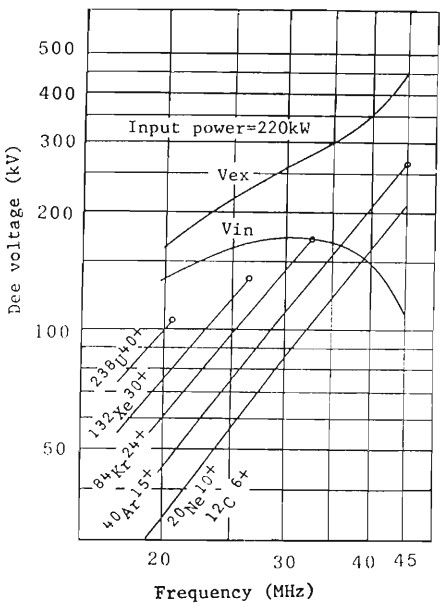

Fig. 5. Dee voltage estimated by low-level test for the input power of 220 kW. V_{ex} and V_{in} are voltages at the extraction and injection radii, respectively. The voltage at the extraction radius required to accelerate various ions are also shown.

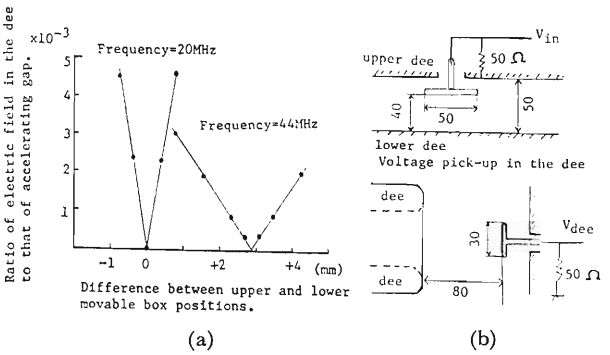

Fig. 6. (a), Ratio of RF electric field inside the dee to that of the accelerating gap. The lines are drawn to guide the eye; (b), Dee voltage pickups for low-level test.

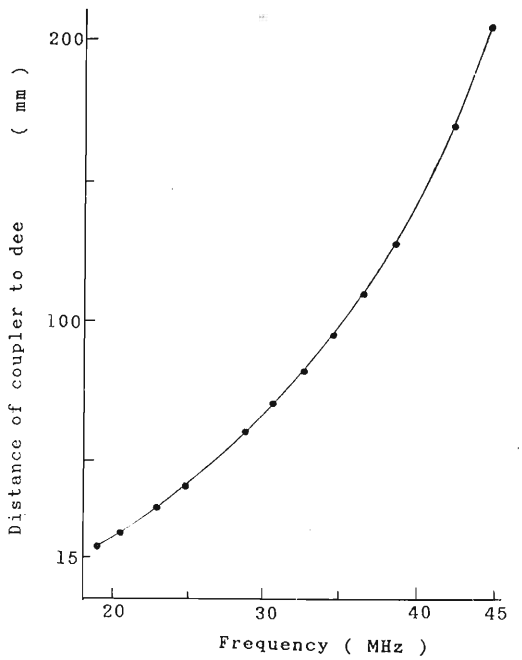

Fig. 7. Position of the coupler for good impedance matching.

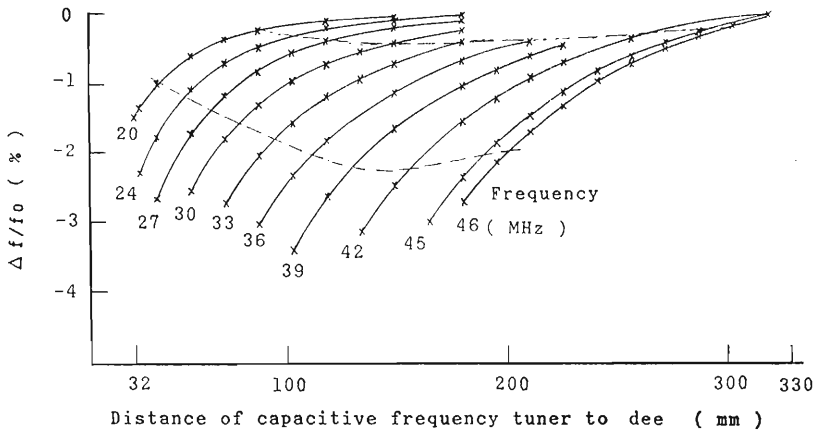

Fig. 8. Dependence of the resonant frequency on the capacitive tuner.

field inside the dee to the accelerating field against difference between positions of the movable boxes. As we can see, the inner field can be canceled by setting the boxes in asymmetry.

The RF power is fed into the resonator through a 50 Ω coaxial feeder line which is coupled with the resonator by a capacitive coupler. Its positions satisfying the impedance matching are realized within its stroke of 20 cm through the frequency range as shown in Fig. 7.

Fine tuning of the resonant frequency is made by moving a capacitive tuner. Dependence of the resonant frequency on the capacitive tuner was measured and shown in Fig. 8. The region between two broken lines shows practically useful position of the tuner.

At the first power test in 28 MHz, a multipactoring arose at the dee voltage of about 300 V and was easily overridden after pulse excitation with input power of about 60 kW. We obtained the dee voltage of 140 kV with the input power of 55 kW; it is consistent with the shunt impedance measured.

References

1) H. Kamitsubo: Proc. 10th Int. Conf. Cyclotron Appl., East Lansing, USA, pp. 257–262 (1984).
2) K. Ogiwara, M. Hara, and T. Fujisawa: *Reports I.P.C.R.*, **57**, 222 (1981) (in Japanese).

RIKEN Accel. Prog. Rep. 20 (1986)

V-4. Performance of Power Amplifier of RIKEN Ring Cyclotron

T. Fujisawa, K. Ogiwara, S. Kohara, I. Yokoyama,
M. Nagase, Y. Chiba, and Y. Kumata*

The radio-frequency system of RIKEN Ring Cyclotron has been described.[1] The main parts of the amplifier were fabricated last year[2] and have been tested and improved this year. Figure 1 shows the latest scheme of the final and driver amplifiers, in which the pair of all-pass networks in previous design[1] is replaced with a cascade of a transformer and an all-pass network, and several electrical constants of the components are changed. The whole system was installed in the cyclotron vault in August 1986 and its performance was studied.[3] Figure 2 shows tuning characteristics of the plate circuit and Fig. 3 matching condition of the output capacitor. The measurement was carried out on low level signals from a synthesizer where the output port was terminated by a dummy load of 50 Ω as shown in the inset of Fig. 3 and the plate load resistance was kept at 180 Ω. In Fig. 4, the input impedance and tuning characteristics of the cathode circuit are shown. The parameters are cathode resistances simulating driving powers for the tube. Figure 5 shows the voltage gain and the input impedance of the all-pass network. The performance of each element is consistent with the design.

In a power test, a parasitic oscillation with a

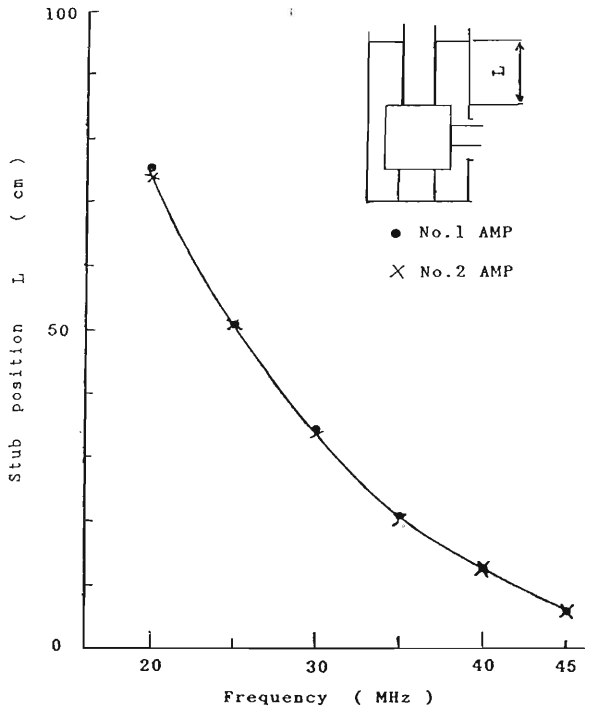

Fig. 2. Tuning characteristics of the plate circuit of the final amplifier.

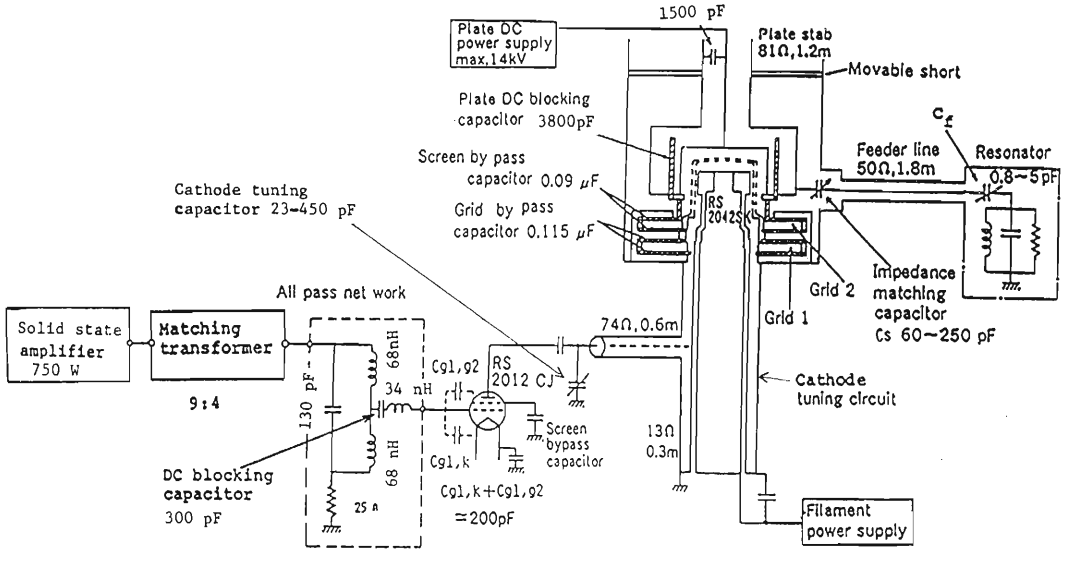

Fig. 1. Schematic drawing of the final and driver amplifiers.

* Sumitomo Heavy Industries, Ltd.

frequency of 650 MHz was detected at the output port independently of tuning frequency. This parasitic mode was suppressed by mounting dumping resistors on the plate tuning circuit as shown in Fig. 6. Table 1 shows typical operating conditions of the amplifier system. The performance is satisfactory for most of frequencies, but maximum output powers of the final amplifier are reduced to 160 kW at the frequency around 40 MHz and to 225 kW around 27 MHz. These reductions of the output power are caused by the 80 MHz resonance between screen and control grids, as explained in Fig. 7(a), which is excited by higher harmonic component of tuning frequencies of 40 or 27 MHz. In order to avoid the effect of this resonance, we will shift the resonant frequency higher than 90 MHz by improving

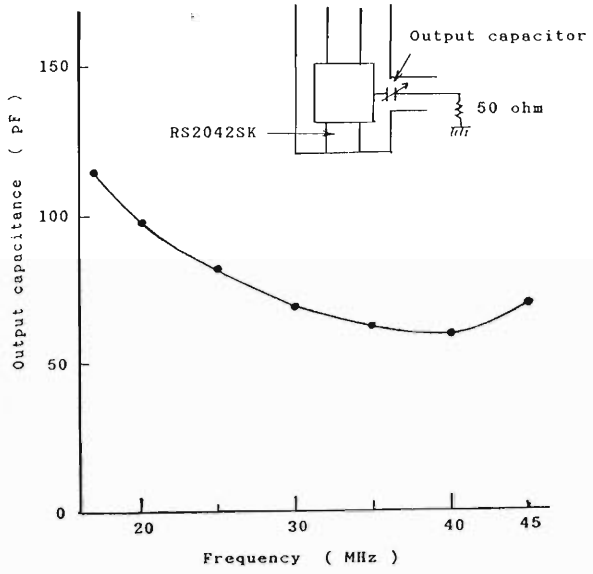

Fig. 3. Matching condition of the output capacitor.

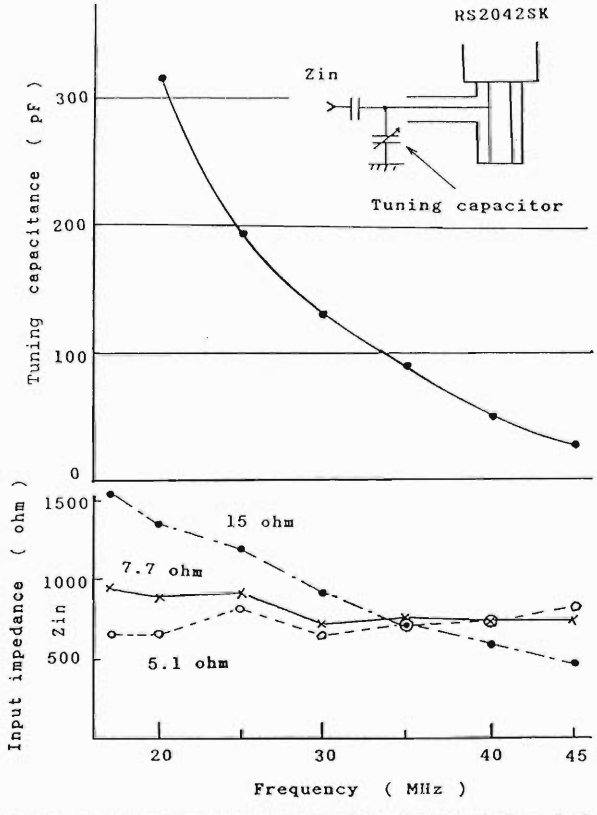

Fig. 4. Input impedance and tuning characteristics of the cathode circuit.

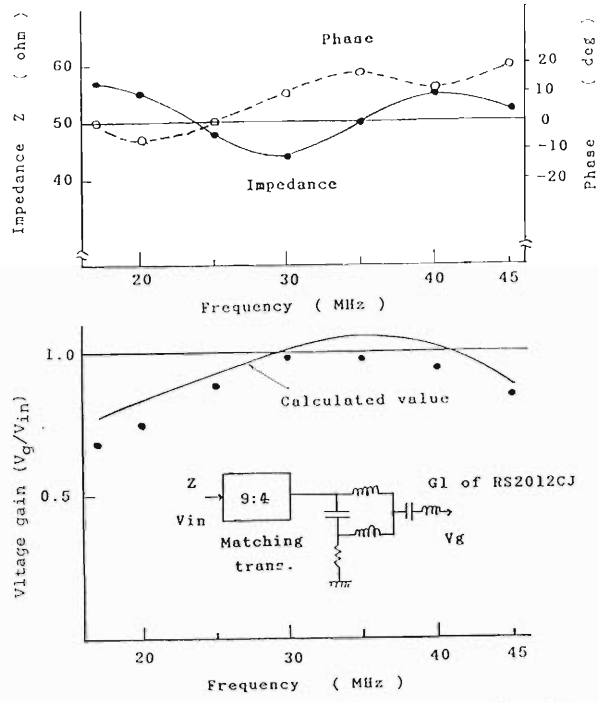

Fig. 5. Voltage gain and input impedance of the all-pass network.

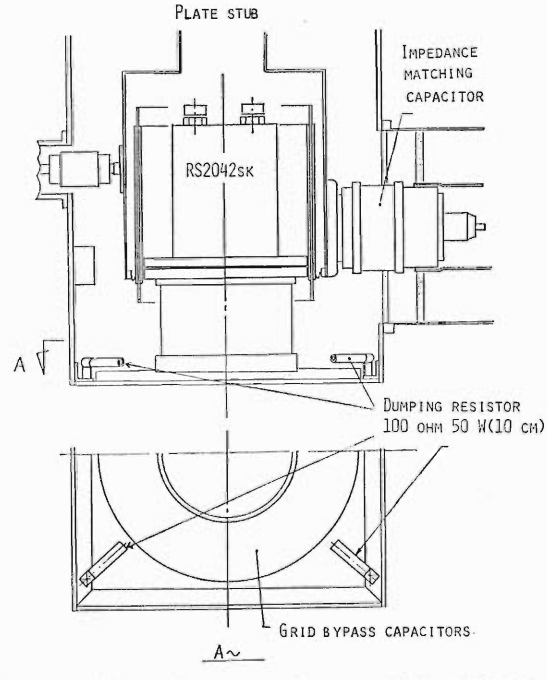

Fig. 6. Resistors for suppressing parasitic oscillation at 650 MHz.

Table 1. Typical operating condition of final and driver amplifier.

Frequency (MHz)	Pre-Amp. output power (W)	Driver amplifier (V_p=6.8 kV, V_{g1}=−125 V, V_{g2}=800 V)					Final amplifier (V_p=12.5 kV, V_{g1}=−340 V, V_{g2}=1,100 V)				
		Electrode current			RF amplitude		Electrode current			RF amplitude	Output power (kW)
		G1 (mA)	G2 (mA)	Plate (A)	Eg(peak) (V)	Ep(peak) (kV)	G1 (A)	G2 (A)	Plate (A)	Ep(peak) (kV)	
17	450	−40	200	3.1	135	5.2	−0.74	1.2	36	9.6	300
20	350	−30	200	3	160	5.8	−0.6	1.2	39	10	300
25	600	−70	100	3.6	150	5	−0.7	1.2	40	11	300
27	660	−50	50	3.0	150	4.7	−1.2	1.2	30	8.6	225
30	480	−130	60	3.9	160	3.8	−0.6	1.5	37	10.8	324
35	640	−180	60	4.6	160	4	−1.0	1.3	40	10.7	300
40	640	−80	50	3	140	3.7	−1.2	0.6	24	7.0	160
45	800	−10	80	3.4	150	4.7	−1.0	1.0	35	7.8	290

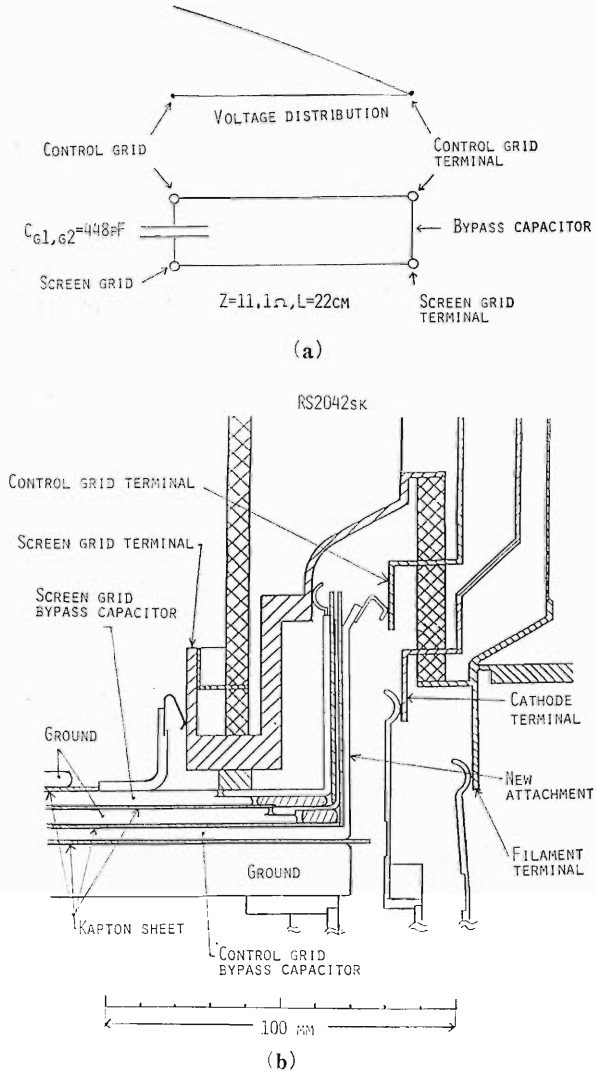

Fig. 7. Equivalent circuit between screen and control grids (a) and improvement of connections of control and screen grids (b).

the connection of the tube as shown in Fig. 7(b).

We started beam acceleration test using Ar^{12+} ions at the frequency of 28 MHz in November 1986. The resonators were powered at the vacuum pressure of about 1×10^{-6} Torr. Multipactoring arose at the dee voltage of about 300 V, but it was easily overcome after pulse excitation with input power of about 60 kW. We obtained the dee voltage of 140 kV with the input power of 55 kW. The automatic frequency tuning system, the dee voltage stabilizer, and the phase stabilizer were working well. The dee voltage stability is within $\pm1.5\times10^{-4}$ and the phase stability is better than $\pm0.2°$. In the near future we will make power test of the RF system throughout the frequency range designed.

References

1) T. Fujisawa, K. Ogiwara, S. Kohara, Y. Oikawa, I. Yokoyama, M. Hara, I. Takeshita, and Y. Chiba: Proc. 10th Int. Conf. Cyclotron and Appl., East Lansing, USA, p. 311 (1984); T. Fujisawa, K. Ogiwara, S. Kohara, Y. Oikawa, I. Yokoyama, I. Takeshita, Y. Chiba, and Y. Kumata: *Sci. Papers I.P.C.R.*, **79**, 12 (1985); T. Fujisawa, K. Ogiwara, S. Kohara, Y. Oikawa, I. Yokoyama, I. Takeshita, Y. Chiba, and Y. Kumata: Proc. 1985 Particle Accelerator Conf., Vancouver, Canada, p. 2897 (1985).

2) T. Fujisawa, S. Kohara, K. Ogiwara, I. Yokoyama, M. Nagase, and Y. Chiba: *RIKEN Accel. Prog. Rep.*, **19**, 170 (1985).

3) T. Fujisawa, K. Ogiwara, S. Kohara, Y. Oikawa, I. Yokoyama, M. Nagase, I. Takeshita, Y. Chiba, and Y. Kumata: Proc. 11th Int. Conf. Cyclotron and Appl., Tokyo, Japan (1986).

RIKEN Accel. Prog. Rep. 20 (1986)

V-5. Control System of RIKEN Ring Cyclotron

T. Wada, H. Takebe, J. Fujita, T. Kambara, and H. Kamitsubo

RIKEN Ring Cyclotron system is controlled by means of three mini-computers, which are linked with one another through optical fiber loops.[1] Figure 1 shows a block diagram of the control system. Computer 1 stores the field mapping data of magnets. At a request from any control computer (computer 2 or 3), time consuming tasks such as orbit calculations and transport calculations are performed by computer 1 using these mapping data, and the results are sent back to the control computer. Computer 1 is equipped with a CAMAC SHD and can be used as a back-up computer for the control computers. Computer 1 is also linked with the central computer of the institute (FACOM M-780). Computer 2 controles RILAC through GP-IB using optical fiber links. Computer 3 controls the ring cyclotron through the CAMAC bit serial loop. The console devices are linked with computer 3 without a CAMAC system. This computer is also linked with a computer (MITSUBISHI MX-3000) of the radiation safety control system.[2] For radiation safety, MX-3000 has the highest priority in accelerator operation. Before starting operation, an operator should ask MX-3000 for permission. If any erratic conditions occur in the safety system during operation, MX-3000 sends back a beam-stop command.

Six CAMAC crates are distributed in four power supply rooms. One is installed in an operators' console. These CAMAC crates are linked by a bit serial CAMAC loop of optical fiber cables. A disadvantage of this optical loop is that it has no bypass function when any crate is powered off.

Two types of intelligent module are used for the interface between controlled devices and the CAMAC system.[3] CIM is a CAMAC module and DIM is an interface module to each controlled device and installed closely to the device. CIM executes message transfer between the control computer and DIM. Information is transferred between CIM and DIM through plastic optical fiber cables. The maximum length of this cable is limited to 30 m. DIM executes local sequence control, local surveillance, function generation, and testing. Each DIM has several digital input/output (DI/DO) ports and sixteen analog input (AI) ports. The DI/DO ports of DIM for power supply are of a 12 V opto-coupled type.

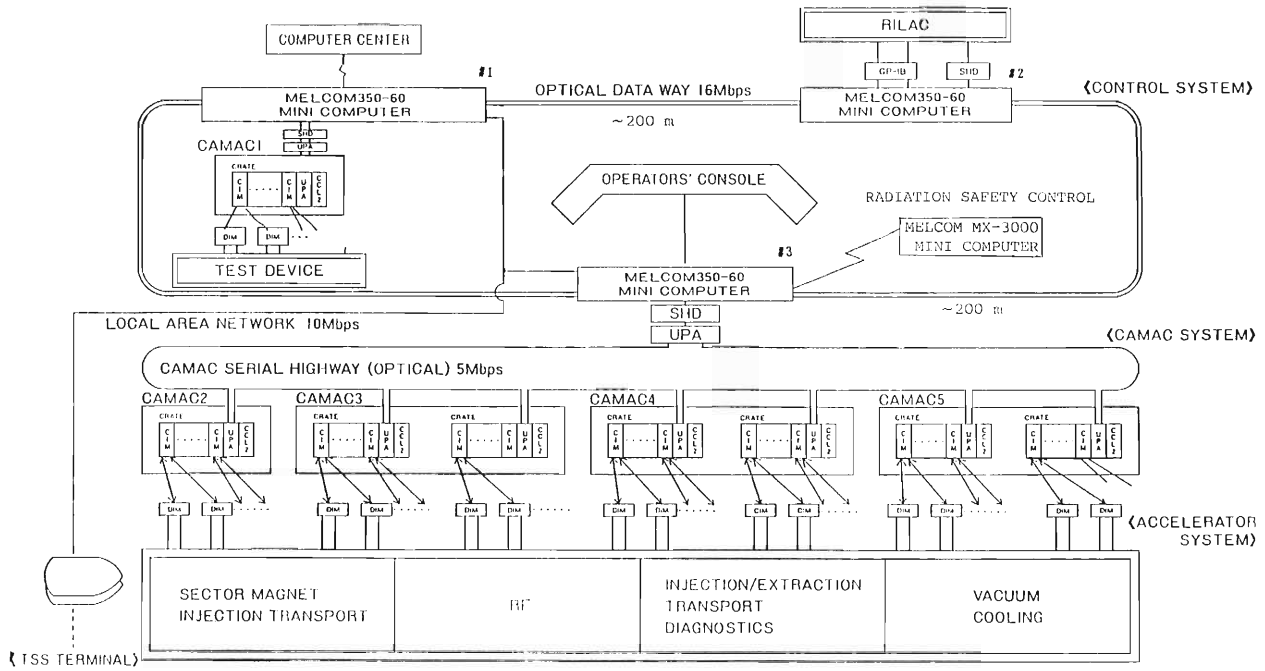

Fig. 1. Block diagram of control system. SHD, serial highway driver; UPA, U-Port Adapter; CCL2, Serial crate controller.

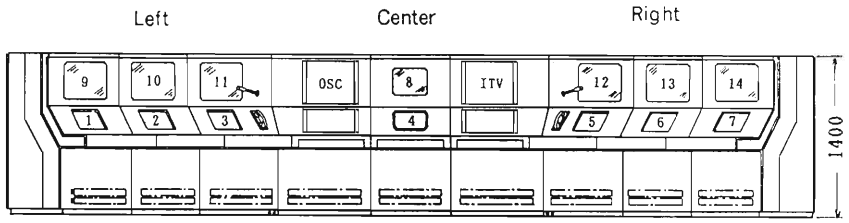

Fig. 2. Operators' console.

DIM for beam diagnostics has TTL level DI/DO ports in order to carry on such high speed exchange of data as that from a beam profile monitor or an emittance measuring system. For control of main differential probes (MDP), DIM are linked to a dedicated microprocessor. Since high speed control is performed for the RF system by programable controllers (PC), the main jobs of DIM are start/stop and monitoring. Status and analog values are sent to the control computer. A vacuum control system also uses PC. Almost all interlocks and sequence control are performed by PC. Vacuum gauges and the temperatures of cryopumps are read by DIM. A residual gas analyzer (QMA) is controlled by a dedicated microcomputer, and the data are transferred directly to the control computer through optical RS232C line. For a cooling system, DIM only reads the status. The total numbers of CIM and DIM are 30 and 170, respectively.

Diagnostics of controlled devices is carried out conveniently by verifying the response of the devices. For this local diagnostics, an local area network (Ethernet[4]) with a transmission rate of 10 Mbps is used. Four interface terminals (TIA) are prepared; two are placed closely to computer 1 and 3, and the other two are closely to the CAMAC stations. Diagnosis is carried out by plugging a TSS terminal unit into a port of a nearest TIA. These ports are also used for displaying machine status in an operator room or counting rooms by selecting a desired part of the machine on a keyboard. Since this network links two computers (computer 1 and 3), an operator is accessible to each computer.

Figure 2 shows an operators' console, which consists of three parts (center, left, and right parts); the left and right parts are made equivalent to each other. The console devices are linked directly to computer 3 without CAMAC interface. The center part is prepared for devices such as a ITV, a scope, and error message output CRT. CRT's, #1–#7, are model VT241 of DEC with touch pannels (TP) on the screens. CRT #8 is VT241 without TP. CRT's #9 and #14 are low-speed full graphic displays, #10 and #13 are high-speed full graphic CRT's, and #11 and #12 are character displays. Almost all man-machine interactions are performed by TP's and information is displayed on CRT's, #9–#13. The first assignment of the role to each TP is done at the center TP (#4).

The operating system OS60/UMX is a combination of a real time and UNIX system. The application programs are first developed in the UNIX system and later executed in the real time system for high-speed response. The application programs are written in FORTRAN 77 language. These programs are composed of several tens of thousands of steps. The data base about accelerator devices are almost completed. The required memory is about 20 kB. In our computer, different tasks occupy independent logical memory space in order to avoid addressing overlaps. These tasks exchange information through the common area, to which other computers are accessible through a data way.

Many kinds of programs have been developed for the man-machine interface with TP. We can use TP conveniently and flexibly, and lay out various types and colors of push buttons on it. The programs for DIM of power supply are extensively improved to carry on high-speed execution.

References

1) T. Wada, H. Takebe, J. Fujita, T. Kambara, and H. Kamitsubo: 11th Int. Conf. Cyclotron and Their Applications, Tokyo, Japan, Oct. (1986).
2) I. Sakamoto, S. Fujita, T. Wada, and H. Takebe: p. 206 in this report.
3) N. Nagase, H. Takebe, T. Wada, and K. Shimizu: 11th Int. Conf. Cyclotron and Their Applications, Tokyo, Japan, Oct. (1986).
4) Digital Equipment Corporation: Introduction to Local Area Network, USA (1982).

RIKEN Accel. Prog. Rep. 20 (1986)

V-6. Sector Magnet

H. Takebe, T. Wada, M. Nagase, S. Motonaga, and A. Goto

A final field measurement was made in July 1986 along the hill center line of the sector magnet installed with a vacuum chamber. The cycling[1] process of the sector magnet excitation was slightly changed, as can be seen from Fig. 1, because the multiple (DACs) current set routine was possible by means of a CIM-DIM*,[2] micro-program. Figure 2 shows the effects of the excitation histories preceding

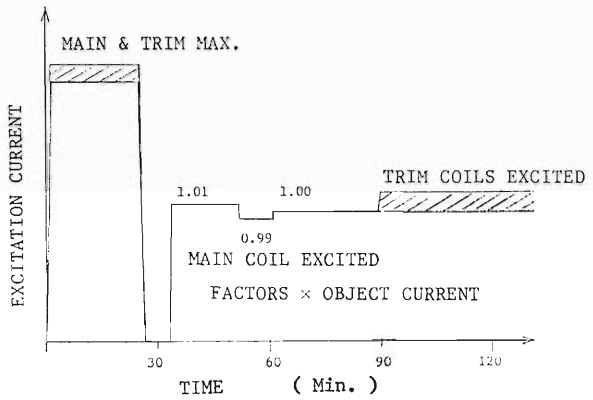

Fig. 1. Time chart of the cycling process for the sector magnet.

* CIM-DIM: Communication Interface Module and Device Interface Module.

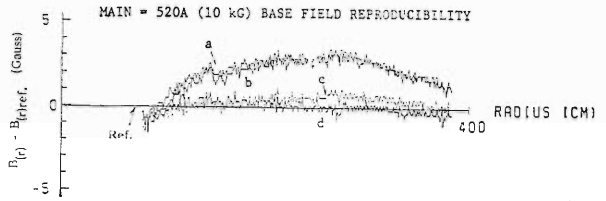

Fig. 2. Reproducibility of the magnetic field distributions measured at field level of 10 kG (main coil=520 A, the trim coils excited), after the cycling process. The field level before the cycling were a: 0 A; 6 kG (3 h), b: 300 A; 6 kG (12 h), c: 520 A; 10 kG (3 h), d: 520 A; 10 kG (3 h), and Ref: 520 A; 10 kG (3 h). The trim coils were excited at all the level except the case 'a.'

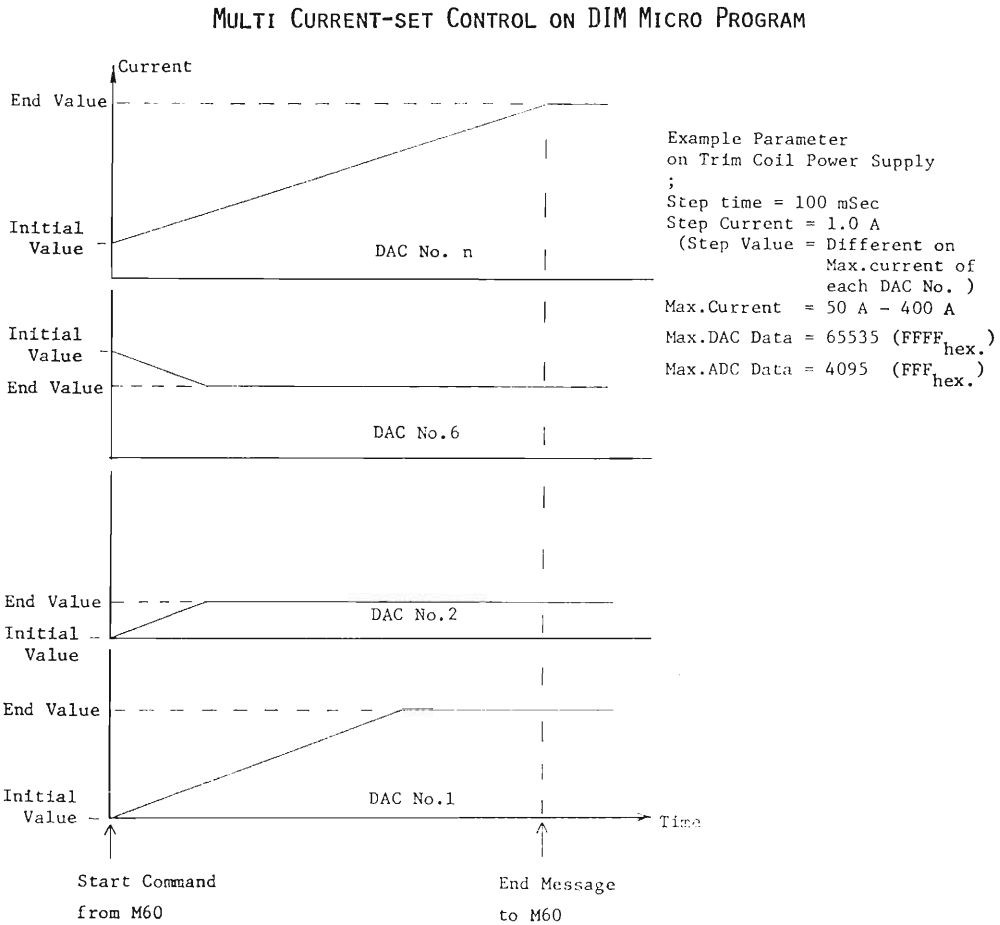

Fig. 3. Time chart of a multiple current set control by the DIM micro task.

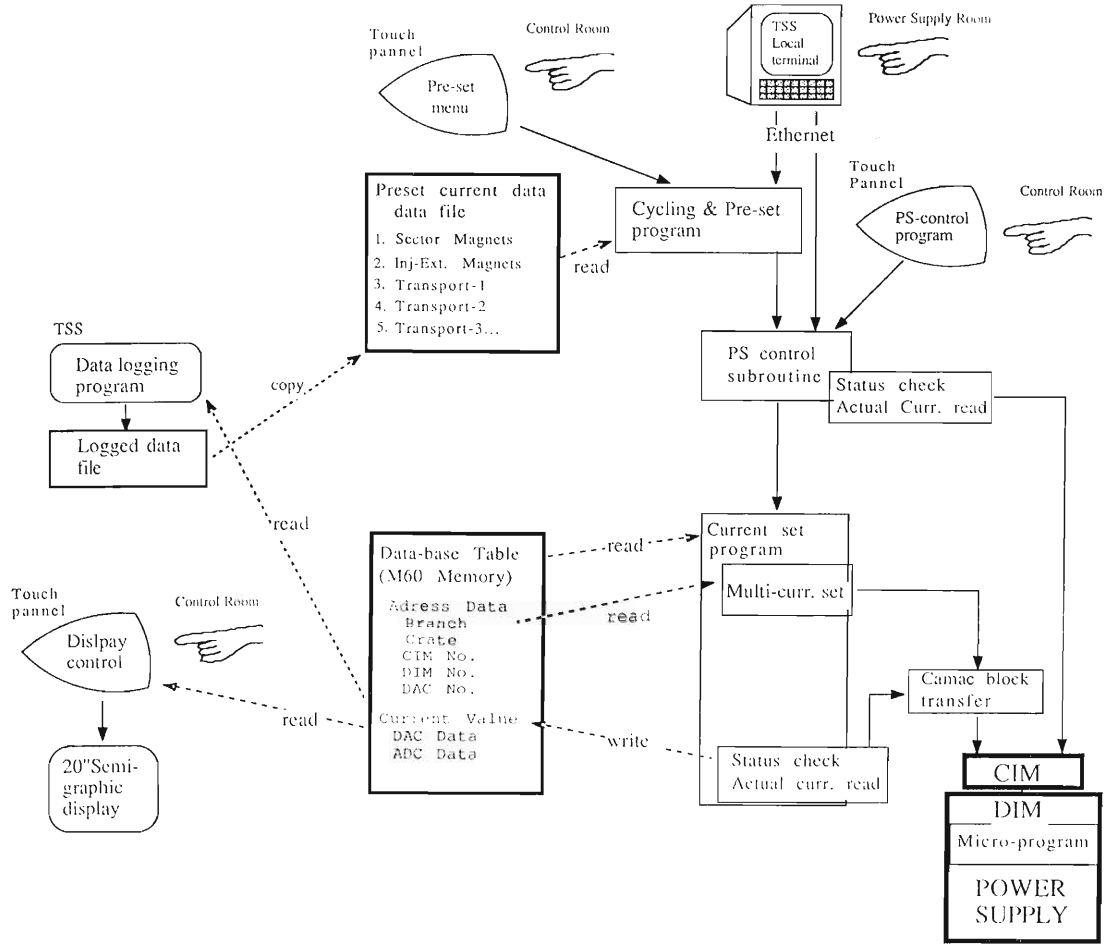

Fig. 4. Flow diagram of the magnets power supplies control sequence.

the cycling on the field distributions along the sector center line at the same excitation currents (520 A, 10 kG). The reproducibility of the field distributions was less than 1 G when the excitation level, just before the cycling process, was the same as that of the case c and d, and less than 3 G even when the excitation levels before the cycling process were different between the case a (0 G), b (6 kG) and the reference (10 kG). Magnetic field stability measured by an NMR gaussmeter, whose probe is located near the back side gap spacer (outer radius) of the sector magnet, is less than 1 G in 5 h after the cycling. Because of a small drift appeared in one or two days, a magnetic field feed back loop program was created in the M-60 software using the NMR gaussmeter and an M2 power supply.

At this time, magnet current control programs were modified using a new CIM-DIM micro tasks. The current set process of the DIM micro task is similar to the M-60 FORTRAN program at the last field measurement.[1] Figure 3 shows a time chart of this multiple set process in one DIM. The maximum DAC number is 15, the step time 100 ms, and the step current 1.0 A in the case of the sector magnet power supply. The M-60 computer only sends parameter data to all DACs of each power supply using a CAMAC block transfer routine, and a start command to the DIM, so that, a start up routine of the huge number of trim and main coils becomes faster.[2] This program is also used for the beam transport system's and injection/extraction system's power supplies.

Since the maximum current values against the full bit of the DAC and ADC, step current value, CAMAC crate number, station number, DIM number, and the coil name are stored in an M-60's memory and a table file, the user application (touch panel controling, etc.) program calls a semi-basic subroutine with only a power supply name and current values. The current preset program (FORTRAN) and those data files for the beam accelerations are stored and developed in an UNIX operating system. And some of control programs are transferred and run on a real time operating system (Fig. 4). A power supply check and a program test are performed by using local TSS terminals through a Local Area Network (Ethernet).

References

1) H. Takebe, S. Motonaga, and T. Wada: *RIKEN Accel. Prog. Rep.*, **19**, 174 (1985).
2) M. Nagase, H. Takebe, T. Wada, and K. Shimizu: Proc. 10th Int. Conf. Cyclotrons and Their Application (1986).

RIKEN Accel. Prog. Rep. 20 (1986)

V-7. Beam Transport System for RIKEN Ring Cyclotron

K. Hatanaka, T. Inamura, Y. Yano, A. Goto, M. Kase, and H. Kamitsubo

The beam transport system for RIKEN Ring Cyclotron consists of lines from injectors to the cyclotron and those from the cyclotron to experimental halls. One of the injectors is the heavy-ion linac (RILAC) which was completed in 1980, and the other an AVF cyclotron which will be constructed in two years. We have installed a beam transfer line from RILAC and a beam channel to an experimental hall. The remaining lines will be constructed in two years. The beam transfer line from RILAC is about 64 m long. The installed line to the experimental hall is a straight one with four quadrupole triplets.

Figure 1 shows the perspective view of the line from RILAC. The beam transfer line consists of eight dipole magnets, fourteen quadrupole doublets, thirteen quadrupole singlets, and thirteen steering magnets in both the horizontal and the vertical directions. The beam from RILAC passes a charge stripper (a thin carbon foil) and is deflected with a dipole magnet DAL0 by an angle of 100 mrad. This magnet, made of laminations of 0.35 mm thick silicon steel, can be excited by pulsed current to make possible time-sharing of the beam between RIKEN Ring Cyclotron and RILAC experimental halls.

The spatial dispersion at the slit SLL10 after the magnet DML1 is calculated to be 0.46 m. In taking account of the beam size at this position, the momentum resolving power is about 20 and a single charge state is selected with the slit for light ions. The system from DAL0 to DML2 is a beam shifting section, where an achromatic beam from RILAC is again achromatic at the exit of DML2. Four quadrupole singlets QSJ24–QSJ27 are introduced to obtain the erect ellipses at SLJ27 in the transverse phase space. The slit position SLJ27 is the object point for the succeeding momentum analyzing system from QDJ28 to QSJ31. The line after the slit SLJ27 is described in detail in Ref. 1.

The magnetic field was measured in the midplane for all the dipole magnets except for DAL0 by means of a carriage of three hall probes driven

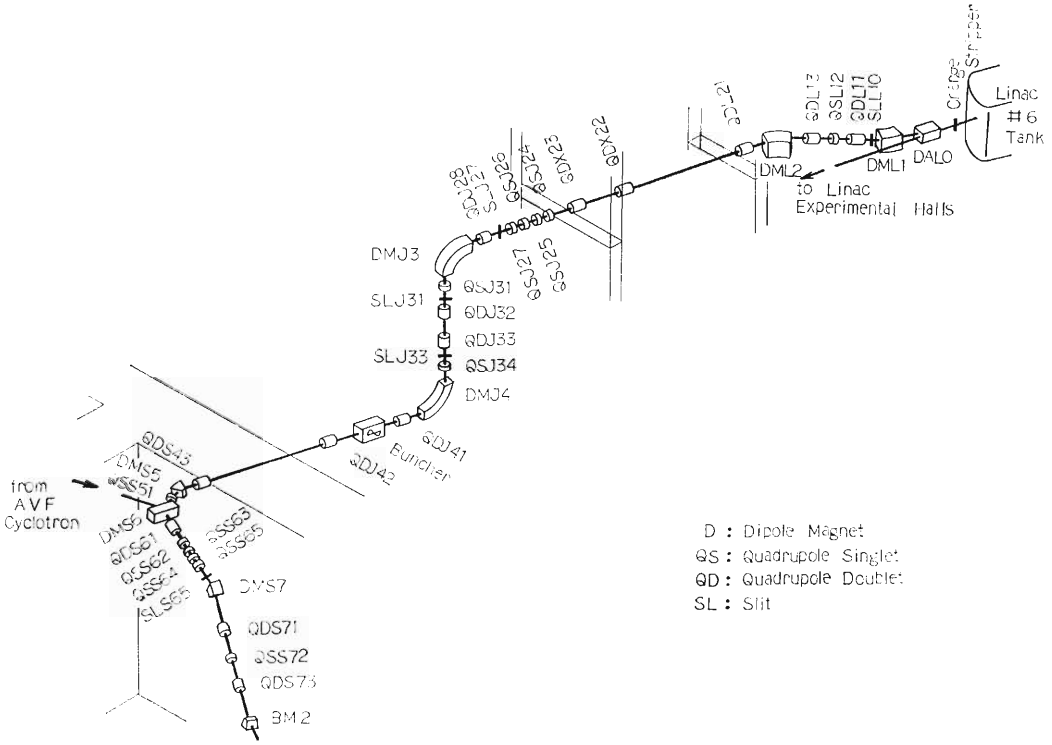

Fig. 1. Perspective view of the beam transfer line from RILAC. The vertical distance between DMJ3 and DMJ4 is 7.8 m and that between DMS7 to BM2 is 4.0 m.

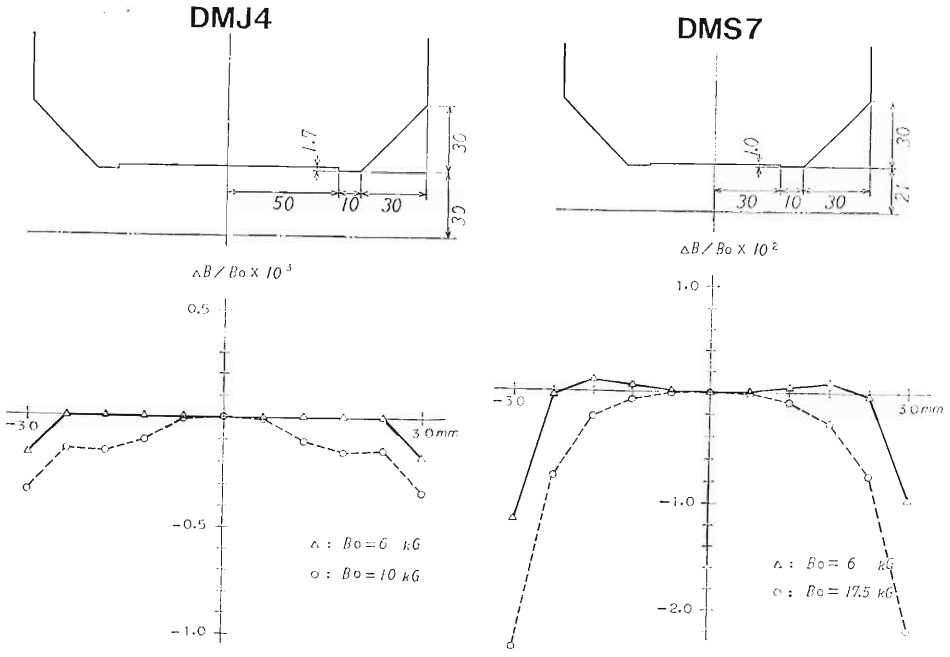

Fig. 2. Cross sectional view of the pole of dipole magnets and the radial distributions of the magnetic field.

Table 1. Parameters of the quadrupole magnets.

Type	Q170	Q220	Q420
Aperture (mm)	70.0	70.0	70.0
Max. gradient (T/m)	15.0	15.0	15.0
Max. current (A)	260.0	260.0	260.0
Max. voltage (V)	15.5	18.0	28.0
Length (mm)	170.0	220.0	420.0
Effective length (mm)	200.0 ±0.3	249.7 ±0.5	450.7 ±0.5

by a step motor. Examples of the measured radial distributions of the magnetic field are shown in Fig. 2. The deviation of the field $\Delta B/B$ is less than $1\cdot10^{-3}$ for DMS7 in the required region which is estimated to be less than 20 mm in full width from an ion-optical calculation; for other magnets the deviation is less than $2\cdot10^{-4}$ in a much wider region. The deviation of the effective field length at different excitations is less than 1 mm for all the magnets.

Quadrupole magnets are of three types. Their parameters are summarized in Table 1. The magnets of the type Q170 are used in the beam transfer line from RILAC. A quadrupole triplet in the line to the experimental hall consists of two Q220 and one Q420 magnets. The pole of hyperbolic profile has a 70 mm base width. A yoke has a square structure. In order to obtain the wide flat region of the effective length, the optimum end-cut shape was determined by referring the experimental results obtained at KEK and INS.[2] The field distributions in the midplane were measured for two magnets of each type at three exciting currents of 100, 200, and 260 A. The deviation of the effective length is less than 1 mm for all magnets and for all excitations within the radial region of ±30 mm. Azimuthal distributions of the field were measured at the center of the magnets and at a radius of 30 mm. The measured data were analyzed to give the strength of multipole components. The values of the multipole components relative to the quadrupole one are $7\cdot10^{-4}$, $2\cdot10^{-3}$, and $3\cdot10^{-4}$ for the 3rd, 5th, and 7th multipoles, respectively.

References

1) N. Kishida and Y. Yano: *Sci. Papers I.P.C.R.*, **75**, 214 (1981).
2) M. Kumada, H. Someya, I. Sakai, and H. Sasaki: Proc. 2nd Symp. Accel. Sci. Tech., 75 (1978).

RIKEN Accel. Prog. Rep. 20 (1986)

V-8. Beam Buncher for RIKEN Ring Cyclotron

A. Goto, T. Fujisawa, I. Takeshita, T. Urai,
Y. Ikegami, and Y. Yamada

A beam buncher has been completed and set up in the course of the beam transport line from the injector RILAC to RIKEN Ring Cyclotron. It worked successfully during the first operation of RIKEN Ring Cyclotron, and the beam bunching was obtained at the entrance of the cyclotron. Specifications of the beam buncher and its model study were reported elsewhere.[1,2]

Figure 1 shows a cut-away view of the buncher. The vacuum chamber which contains the drift tubes is made of alminum alloy. The parting disk between this vacuum chamber and the coaxial stub at atmospheric pressure is made of ceramics (Al_2O_3). Figure 2 gives the results of measurement of resonant frequencies, Q values, and shunt impedances together with the calculations based on the transmission line approximation. The resonant frequencies

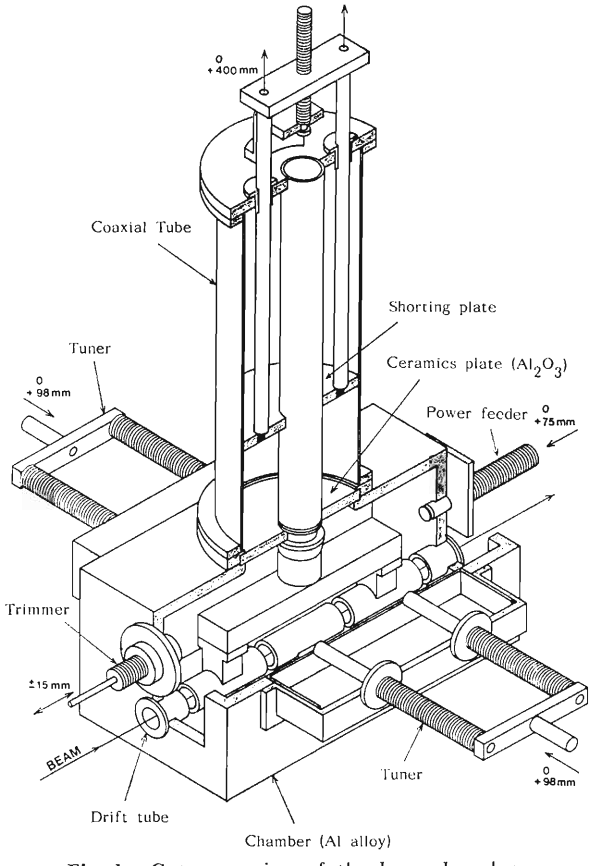

Fig. 1. Cut-away view of the beam buncher.

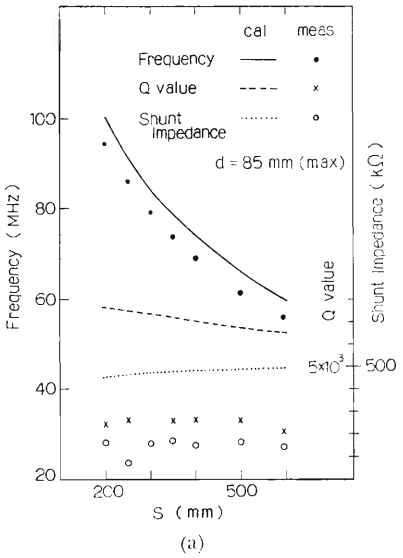

(a)

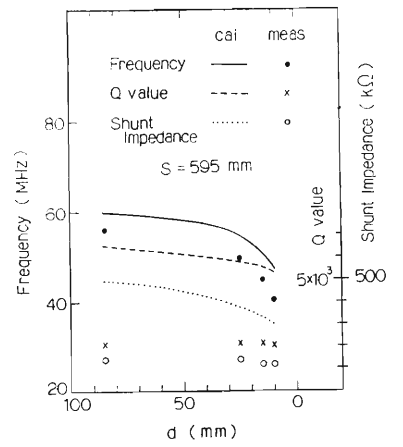

(b)

Fig. 2. (a) Measurements of resonant frequencies, Q values, and shunt impedances against the position of the movable shorting plate (s) for the distance between the frequency tuner and the drift tubes being maximum (d=85 mm). The calculations using the transmission line approximation are also shown for comparison. (b) The same as Fig. 2 (a) against the position of the frequency tuner (d) for s being nearly maximum (s=595 mm).

cover the required frequency range (40–90 MHz). The Q values and shunt impedances were found to be about a third of the design values. This results from the fact that the dielectric loss of the ceramics

disk is larger than expected. We will replace this ceramics disk with a thinner one having smaller dielectric loss. The beam buncher, however, could produce enough voltage for the first beam (the injection energy of Ar^{12+} is 1.28 MeV/u; the voltage required is about 7 kV at RF frequency of 56 MHz). In Fig. 3 is shown a photograph of the buncher at the due place. Figure 4 shows a block diagram of the RF amplifier system. The RF signal is fed from the signal generator of RILAC. The frequency of this signal is doubled with a frequency doubler. The drift-tube voltage and its phase are automatically stabilized by comparing the pickup signal from the resonator with a reference signal. The resonant frequency of the resonator is automatically tuned by monitoring the incident and reflected power on the feeder line. The system can be remotely operated with the help of a computer control system. The bunch signal of the beam obtained just before the entrance of the cyclotron is shown in Fig. 5.

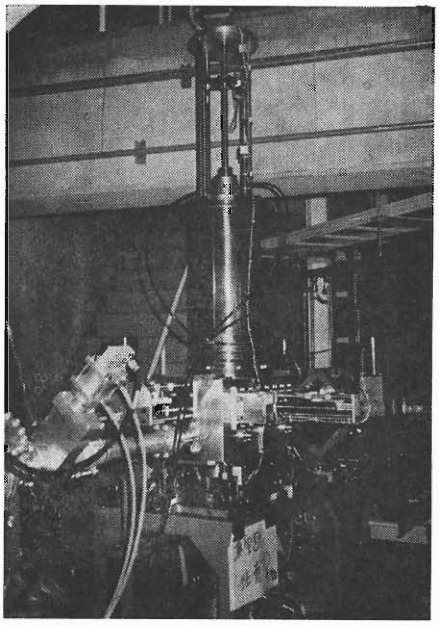

Fig. 3. Photograph of the beam buncher.

References

1) A. Goto, T. Fujisawa, and I. Takeshita: *RIKEN Accel. Prog. Rep.*, **18**, 184 (1984).
2) A. Goto, T. Fujisawa, I. Takeshita, and K. Ogiwara: *RIKEN Accel. Prog. Rep.*, **19**, 184 (1985).

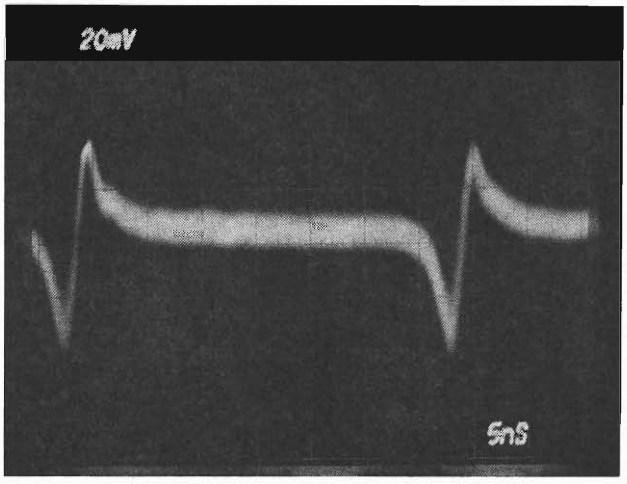

Fig. 5. Bunch signal picked up just before the entrance of the cyclotron.

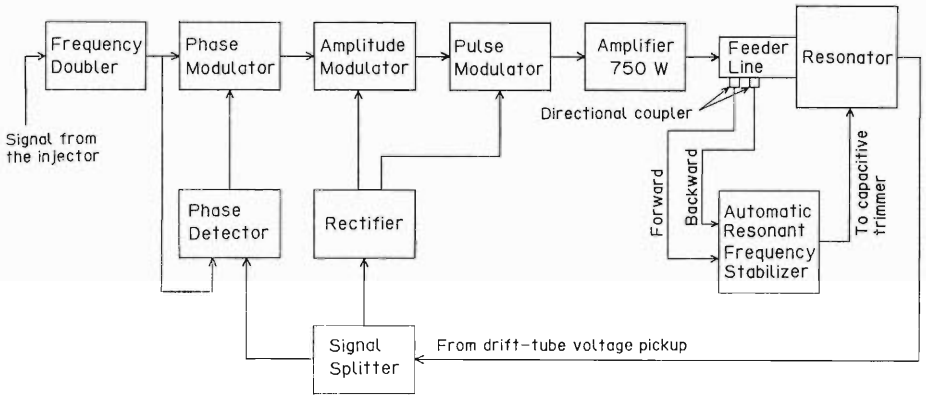

Fig. 4. Block diagram of the RF amplifier system.

RIKEN Accel. Prog. Rep. 20 (1986)

V-9. Beam Diagnostic Equipment in the Beam Transport Line between RILAC and RIKEN Ring Cyclotron

M. Kase, I. Takeshita, I. Yokoyama, Y. Oikawa, and M. Saito

Figure 1 illustrates the layout of the beam diagnostic equipment along the beam transport line between RILAC (RIKEN linac) and RIKEN Ring Cyclotron. Since the beam line is as long as 65 m, beam handling along the beam line requires a number of beam diagnostic probes such as beam profile monitors (denoted as PF in Fig. 1), Faraday cups (FC), capacitive phase probes (PP), emittance monitors (EM), and slit systems (SL), some of which are shown in Fig. 2.

Every diagnostic probe and its actuator have been built on a stainless-steel flange (NW100 type for an emittance monitor, and CF152 for other probes). They are normally mounted on a diagnostic chamber. Several types of diagnostic chambers, having different numbers of ports, have been installed at each position depending on local requirements. These chambers as well as beam pipes were made of aluminum alloy, because of its low out-gassing rate and low cost.

A beam profile monitor is used for the measurement of beam intensity distribution in three directions on the plane perpendicular to the beam axis. The principle of the measurement is the wire scanning method.[1] In addition to two cross wires diagonal to the driving axis, the third wire has been strung perpendicular to it. A pneumatic driver moves the probe head in linear action by a stroke of 75 mm at a rate of around 75 mm/s. The sensitive region is inside a circle of 50 mm in diameter around the beam axis. The positions of the probe head are detected precisely by two photo switches near the both ends of the stroke. The relative position from these absolute positions is detected by a rotary encoder which is rotated by a probe shaft *via* rack and pinion gears; the position resolution is 0.08 mm. When the profile monitor is mounted on the diagnostic chamber at 45° to the vertical axis, the beam intensity distributions in the horizontal, vertical and 45° directions can be obtained. These data permit a tomographical display of a beam on a computer CRT.

As shown in Fig. 1, in every straight beam line, there is at least one Faraday cup, which will aid to estimate beam transmission along the beam line. Some of them also works as a beam stopper under controls of the radiation safety system for men and the protection system for instruments. A rough but

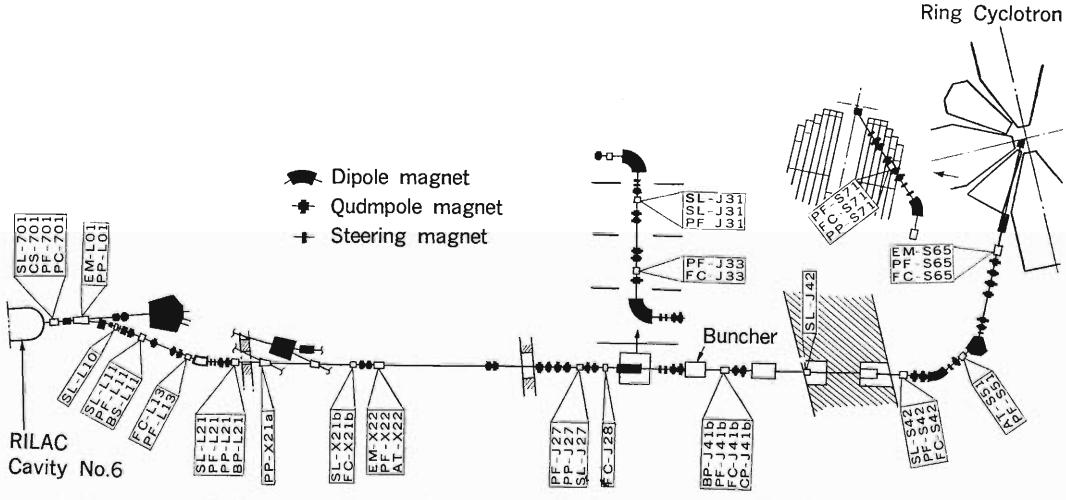

Fig. 1. Layout of the beam diagnostic system in the beam transport line between RILAC and RIKEN Ring Cyclotron. Open rectangles on the line indicate the diagnostic chambers. The devices mounted there are shown nearby using symbols. First two letters of them show the device name. PF, profile monitor; SL, slit system; FC, Faraday cup; PP, phase probe; EM, emittance monitor; CS, charge stripper; AT, beam attenuator; BP, bunch probe (coaxial Faraday cup).

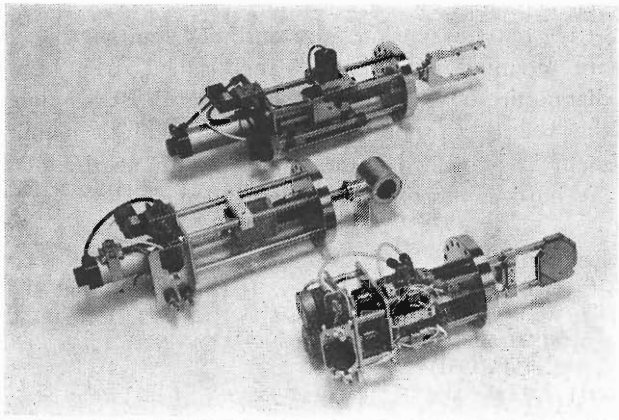

Fig. 2. Photograph of diagnostic equipment used in the beam transport line. The upper one is a profile monitor, the middle a Faraday cup, and the lower a slit system.

easy estimation of the beam transmission along the beam transport lines can be made with a non-destructive intensity monitor. It is using the ionization of residual gas in a beam pipe.[2)]

Beam phases with respect to an RF accelerating system are measured with five capacitive phase probes. PP-L21, PP-X21a, and PP-J27 are used for precise measurement of the energy of a beam from RILAC, while PP-S71 and PP-J41b are for tuning of the buncher RF voltage and phase. The time structure of beam bunch can be measured with a coaxial Faraday cups (BP-L21 and BP-J41b in Fig. 1). It also works as a phase probe, when a beam is as weak as less than 10 nA. Signals from these probes are transferred *via* coaxial cables to the control console of RIKEN Ring Cyclotron and displayed on an oscilloscope.

Electronics for the beam diagnostic equipment are shown in Fig. 3. The beam diagnostic devices, like other devices such as magnet power supplys, are connected through DIM-CIM modules[3)] to a CAMAC loop under the control of computers in RIKEN Ring Cyclotron control system.[4)] In the

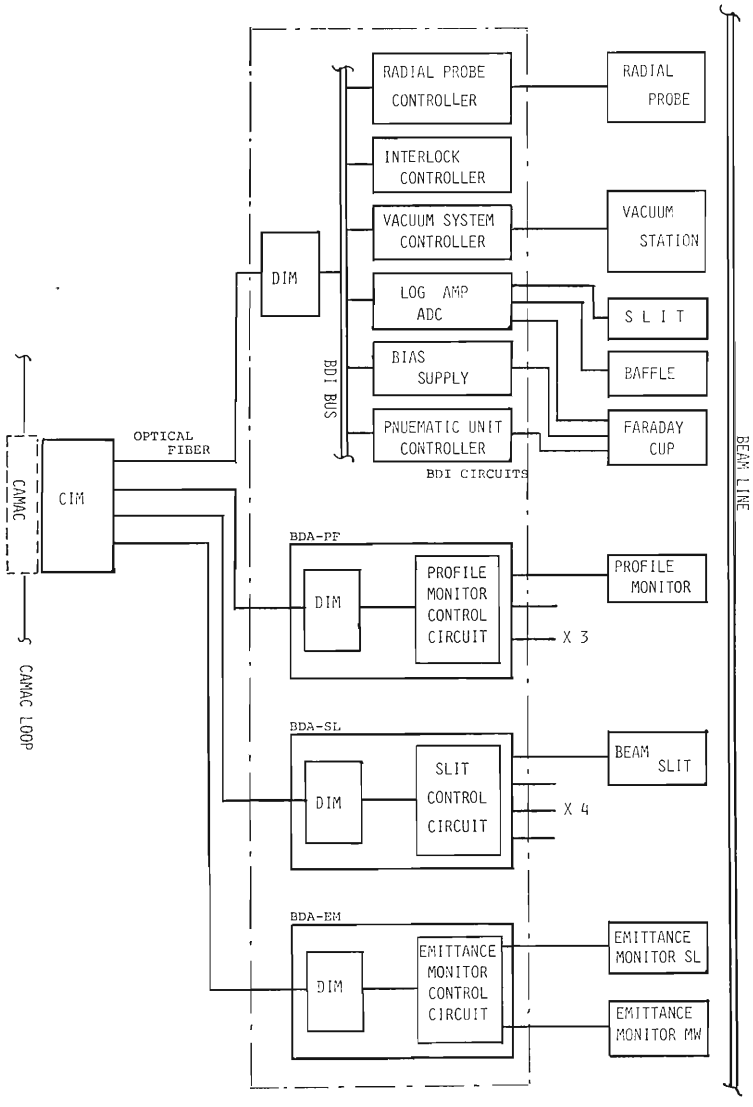

Fig. 3. Block diagram of the circuits for the beam diagnostic system.

beam diagnostic system, however, additional circuits connecting the diagnostic equipment and DIM modules are needed. These circuits can be divided into two groups, BDI and BDA.

The BDI-circuits, which are built in the plug-in modules (according with DIN 41494), use DIM digital input/output as a common bus line. A variety of circuits (up to 64) can be connected to one DIM module *via* the bus; they include a pneumatic driver controller, a bias supply, a vacuum system controller, and an interlock circuit. Analog signals as beam currents from a Faraday cup or slit system are fed into a log-amplifier and converted into digital signals in one of the BDI-circuits.

A beam profile monitor, a slit system, and an emittance monitor are controlled with the BDA-circuits. These circuits have two boards inside. One is a DIM board and the other a control circuit for each device. The latter board has a counter for rotary encoder, a driver for stepping motors, and so on.

The circuits enclosed by dash-dot lines in Fig. 3 are mounted inside a 19″ rack called as a beam diagnostic station (BDS). There are six BDS's along the beam transport line. Every diagnostic equipment is connected with the circuits in nearby BDS *via* hard cables of shorter than 10 m.

References

1) O. B. van Dyck, A. Harvey, H. H. Howard, and D. I. Roeder: *IEEE Trans. Nucl. Sci.*, **NS-22**, 1570 (1975); M. Hemmi and I. Yokoyama: *RIKEN Accel. Prog. Rep.*, **15**, 146 (1981).
2) M. Kase and E. Ikezawa: *RIKEN Accel. Prog. Rep.*, **19**, 210 (1985).
3) K. Shimizu, T. Wada, J. Fujita, and I. Yokoyama: 10th Int. Conf. Cyclotron and Their Applications, East Lansing, Michigan, USA, April (1984).
4) T. Wada, J. Fujita, I. Yokoyama, T. Kambara, and H. Kamitsubo: *Sci. Papers I.P.C.R.*, **79**, 28 (1985).

RIKEN Accel. Prog. Rep. 20 (1986)

V-10. Replacement of Computer for the Control System of RILAC

T. Kambara, E. Ikezawa, and T. Wada

A new computer network system has been introduced to control the accelerator complex (RILAC and RIKEN Ring Cyclotron).[1] The network consists of three MELCOM 350-60/500 computers of Mitsubishi Electric Corp. (M-60). One of them is dedicated to control RILAC in place of a HP-1000

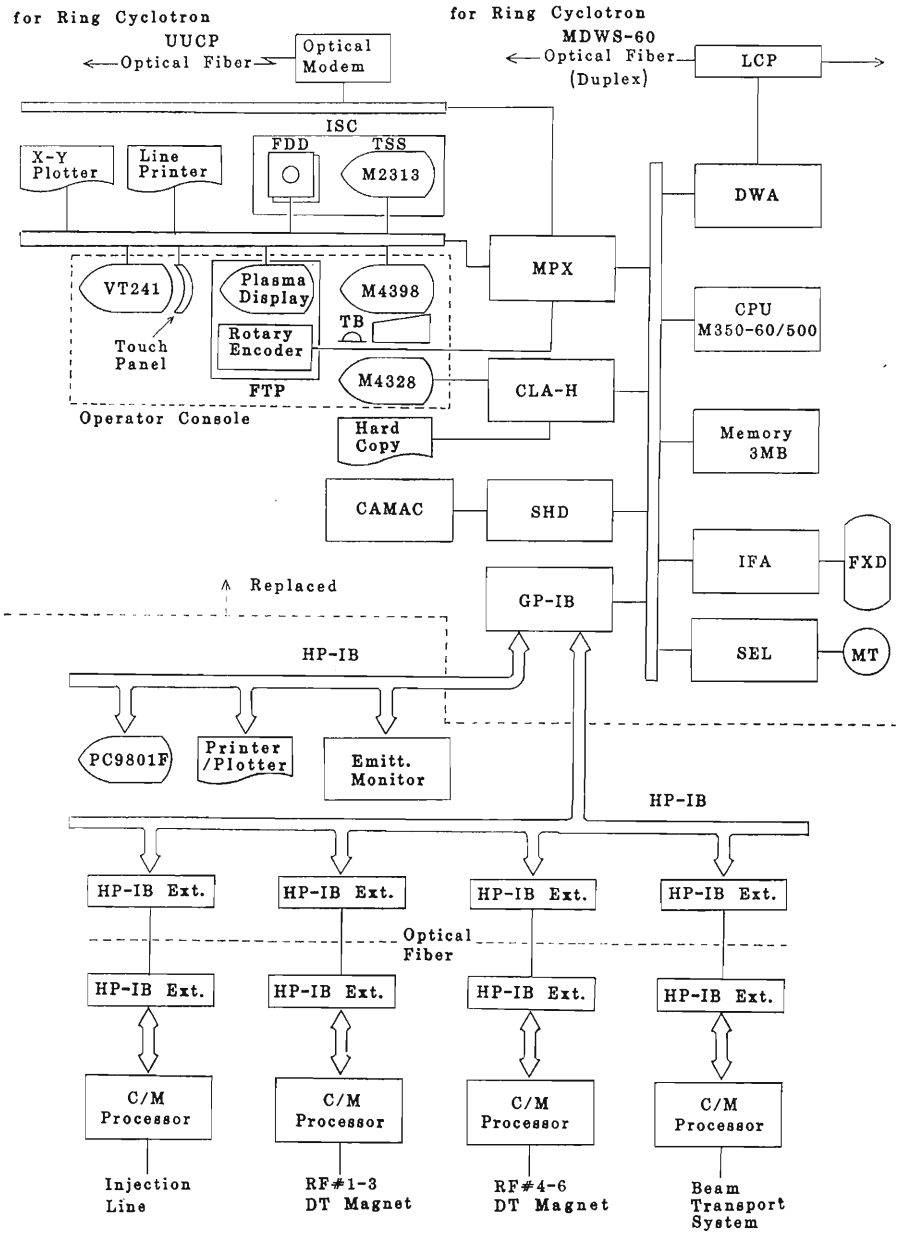

Fig. 1. Block diagram of the new computer system. LCP, loop coupler; DWA, dataway adapter; IFA, intergrated file adapter; SEL, selector channel; MPX, multiplexer channel, CLA-H, computer linkage adapter—high speed type; SHD, CAMAC bit serial highway driver; MDWS, Mitsubishi Dataway System; UUCP, UNIX-UNIX Copy network; ISC, intelligent system console; C/M, control and measurement; FTP, fine tuning panel; TB, track bowl.

Table 1. Configuration of the computer.

Computer	MELCOM 350-60/500
Memory	3 MB
Fixed disc	202 MB
Magnetic tape	1 (1,600/800 bpi)
Floppy disc	2 (8″)
Line printer	1 (390 lpm)
Plotter	1 (10 pens)
20″ Color character display	1
20″ Color graphic display	1
Touch panel (VT241)	1
Fine tuning panel	1
HP-IB	2 (575 kB/s)
CAMAC SHD	1 (5 MB/s)

computer of Yokogawa-Hewlett-Packard Ltd. (YHP), which had been used since November 1979.[2] The computer system with mass storage and peripheral devices were totally replaced, but control and measurement processors (HP2240A/2241A supplied by YHP) were preserved to be used for signal input/output with RILAC devices in the old system. These processors are interfaced to the new system with HP-IB. The new devices are listed in Table 1. A block diagram of the new system is shown in Fig. 1.

There are four devices on the operator console in the new system: a color character CRT terminal (M4398), a color graphic CRT terminal (M4328), a fine tuning panel, and a VT241 CRT terminal. The M4398 CRT displays the status and parameters of the devices in selectable tables and also can receive the commands from operators *via* a keyboard. The M4328 CRT displays the general status of RILAC in graphic form. The fine tuning panel has a plasma display, 4 rotary encoders, and 16 push buttons with lamps and is used for the fine tuning of magnet currents. The VT241 CRT has a touch panel and is used for the fine tuning of RF voltages.

Eight-inch floppy discs are used for storage of RILAC parameters during operation in place of casette tapes in the old system. A CAMAC system is used for beam diagnostic devices installed newly in RILAC beam lines. The operating status of RIKEN Ring Cyclotron can be transferred through the computer network (MDWS-60) and displayed on the M4328 CRT. The source programs and messages are transferred through the UNIX-UNIX Copy network (UUCP).

The new computer was installed in November 1985 in the computer room of RILAC building. After installation and initial adjustments, the development of application programs was continued till July 1986. The programs which had been developed on the HP-1000 computer were transferred to the M-60. In the transfer, FORTRAN source files on the HP-1000 disc were written on magnetic tapes in ASCII format and copied to the M-60 UNIX file. They were then modified to involve the real time and display functions specific to the new computer. Some programs have been newly developed for the new console devices like the touch panel and the rotary encoders. During the program development, RILAC was operated with the HP-1000 computer. In August 1986, the operator console was modified for new console devices. The new computer has been used for operation since September without critical troubles.

References

1) T. Wada, J. Fujita, K. Shimizu, I. Yokoyama, T. Kambara, and H. Kamitsubo: *IEEE Trans. Nucl. Sci.*, **NS-32**, 2095 (1985).
2) T. Kambara: *Reports I.P.C.R.*, **62**, 88 (1986) (in Japanese).

RIKEN Accel. Prog. Rep. 20 (1986)

V-11. Present Status of the Vacuum System for RIKEN Ring Cyclotron

K. Ikegami, S. Nakajima, and S. H. Be

The vacuum chamber[1] for RIKEN Ring Cyclotron consisting of four magnet vacuum chambers, two valley vacuum chambers, and two RF resonator chambers was completed at the end of September, 1986, and evacuated with ten cryopumps of pumping speed of 1×10^4 l/s and four panel-type cryopumps of 5×10^3 l/s. Early October, we achieved a pressure less than 5×10^{-6} Pa, which is sufficiently low for heavy-ion acceleration.

After each chamber was fabricated at a factory, we applied chemical cleaning to the inner surface of the chamber. The chemical cleaning was carried out as follows:

1) Machine oil was removed with a Freon (DIFLON SOLVENT-S_3) jet.

2) Animal and vegetable oils were removed with an alkali solution (NEOS-K) jet.

3) Welding scales and oxided layers were removed with a water jet (at room temperature) 1 h after suffusing on the surface with an acid solvent (NEOS-CM 305FA) including a surfactant and an inhibitor. The acid solvent was simultaneously washed out with a water jet.

4) Acid residues were removed with a neutralizer (NEOS-CM 308).

5) Finally, the surface was sprayed with a water jet.

After chemical cleaning, leak detection was performed with a helium detector connected with the forepump side of a turbomolecular pump, and mass spectrum of residual gases was monitored on a quadrupole mass analyzer. To estimate the leak rate of a chamber indirectly, we also used a pressure build-up method occasionally. The total leak rate of the chamber was suppressed to less than 10^{-7} Pa · m^3/s.

From February to May in 1986, four magnet vacuum chambers brought in our institute were assembled between the magnet poles and subjected separately to leakage check. Figure 1 shows a photograph of the magnet vacuum chamber after chemical cleaning. The N-sector magnet vacuum chamber under assembling is shown in Fig. 2.

The RF resonator chamber has an intricate structure with a large volume, and a dee, a stems, a moving boxes, *etc.* are inserted into the chamber. After checking leakage of the chamber, we assembled the insertion parts and checked leakage again. From July to August, two RF resonators and two valley chambers were set in the cyclotron vault.

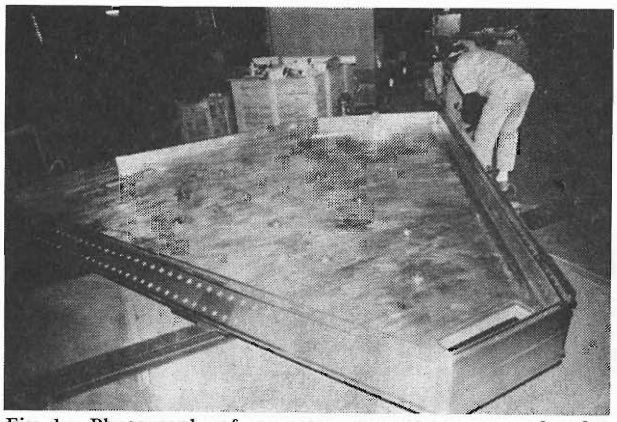

Fig. 1. Photograph of a sector magnet vacuum chamber after chemical cleaning.

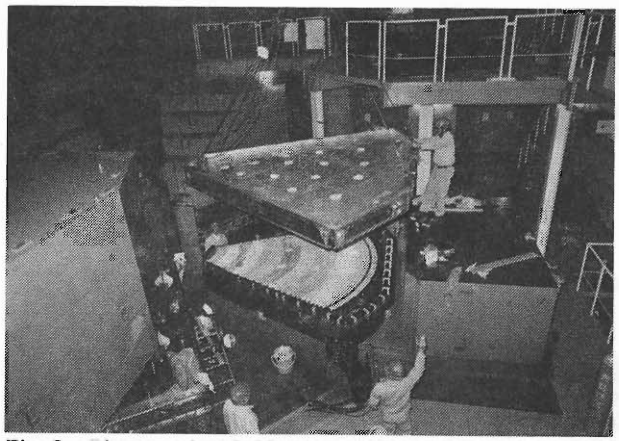

Fig. 2. Photograph of N-sector magnet vacuum chamber under assembling between the magnet poles in the cyclotron vault. Trim coils covered a flash-coated thin ceramic insulator is shown under the chamber.

Early September, we carried out preliminary experiments for the discharge cleaning with the 3/8 sections (two magnet chambers and one valley chamber) of the whole chamber to reduce has gas load from inner surfaces of the chamber. Electron cyclotron resonance discharge cleaning (ECR-DC)[2] was applied to the magnet chambers, and radio frequency assisted glow discharge cleaning (RFAG-DC) was applied to the valley chamber. Dominant contaminations of the inner surface, namely hydrocarbon which

was left from the manufacturing process, were removed by the discharge cleaning. The detail for the RFAG-DC will be reported by us in this report.[3]

After integrating eight chambers into one, we checked leakage. Then ten cryopumps and four panel type cryopumps[4] were installed at the chamber, because charcoal in a cryopump becomes a source of outgassing even at room temperature and a small leakage is very difficult to detect. A photograph of RIKEN Ring Cyclotron installed with the vacuum chamber is shown in Fig. 3, which also shows the cryopumps installed with the valley chamber. Figure 4 is a photograph of seven compressors of cryopumps.

The pumping system is controlled by a programming controller[5] set in the cyclotron vault, and its graphic panel for local operation is shown in Fig. 5. Remote operation is conducted with a computer control system of RIKEN Ring Cyclotron through the CIM-DIM interface.[6] At the end of September, the pumping system was completed and evacuation of the chamber was started. The pump down time from atmospheric pressure to 10 Pa by using mechanical booster pumps of 2,600 m^3/h with a rotary pump of 4,700 l/min was about 13 min. After evacuation to 10^{-3} Pa with four turbomolecular pumps of 5×10^3 l/s, the chamber was evacuated with ten cryopumps of 10^4 l/s and four panel type of cryopumps of 5×10^3 l/s. After continued evacuation for one week, we achieved the pressure of the order of 10^{-6} Pa that is sufficient to accelerate heavy ions.

Fig. 3. Photograph of RIKEN Ring Cyclotron assembled with the vacuum chamber. Three cryopumps installed at the valley chamber is shown.

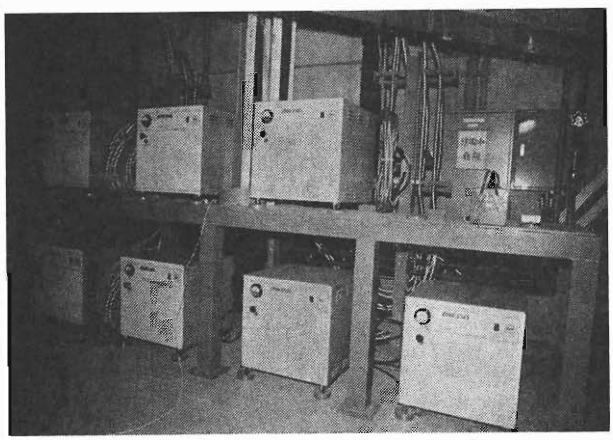

Fig. 4. Photograph of seven compressors of cryopumps.

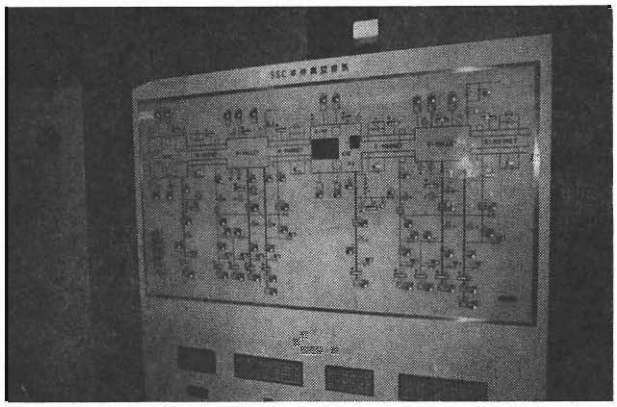

Fig. 5. Photograph of the graphic local control panel set in the cyclotron vault.

References

1) K. Ikegami, S. Nakajima, S. H. Be, I. Takeshita, Y. Oikawa, and S. Motonaga: *RIKEN Accel. Prog. Rep.*, **18**, 172 (1984).
2) K. Ikegami, S. Nakajima, Y. Oikawa, Y. Ishibe, H. Ohyama, Y. Sakamoto, S. Motonaga, and H. Kamitsubo: *Sci. Papers I.P.C.R.*, **77**, 78 (1982).
3) K. Ikegami, S. Nakajima, and S. H. Be: p. 185 in this report.
4) N. Ohsako, K. Morimoto, T. Kikuchi, K. Ikegami, S. Nakajima, Y. Oikawa, and S. H. Be: *RIKEN Accel. Prog. Rep.*, **19**, 191 (1985).
5) K. Ikegami, S. Nakajima, Y. Oikawa, and S. H. Be: *RIKEN Accel. Prog. Rep.*, **18**, 189 (1984).
6) T. Wada, J. Fujita, K. Shimizu, I. Yokoyama, and T. Kambara: *RIKEN Accel. Prog. Rep.*, **17**, 138 (1983).

RIKEN Accel. Prog. Rep. 20 (1986)

V-12. Application of the RF Assisted DC Glow Discharge Cleaning to the Valley Chamber for RIKEN Ring Cyclotron

K. Ikegami, S. Nakajima, and S. H. Be

The vacuum chamber[1] of RIKEN Ring Cyclotron has a large volume and a large inner surface area; moreover, baking is impossible because of the intricate structure. We applied a radio-frequency assisted glow-discharge cleaning (RFA-GDC) to its valley-chamber to reduce the gas load from the inner wall surface. Preliminary experiments were performed to investigate the discharge cleaning effect.

The volume of the valley chamber is 1.5 m^3 with an inner surface area of 25 m^2. A turbomolecular pump of 5,000 l/s was used to evacuate the chamber. For detection of residual gases during the discharge cleaning, a quadrupole mass analyzer was set at another chamber separated from the valley chamber with an oriffice of 10 l/s for N_2 gas and evacuated with a turbomolecular pump of 300 l/s.

The RFA-GDC head inserted near the center of the chamber supplies RF and DC voltages simultaneously. It consists of a central tube for introducing hydrogen gas to the chamber and an anode coil made of a hollow stainless-steel tube of 6 mm in diameter allowing water cooling. The coil (1.2 μH) has 6 windings of 50 mm in diameter and 100 mm in length. The RF voltage was supplied with a 13.56 MHz RF generator with a maximum power of 300 W. This RF electrode system was coupled to a DC power supply (0–1 kV, 5 A at maximum) through an LC network. Figure 1 shows a schematic diagram of the RF and DC coupling network for the anode coil; the gas puffing tube is also indicated.

To measure the pressure P_I at which the discharge ignites and the pressure P_Q at which the discharge is quenched, we applied a constant DC voltage of 900 V to the chamber for introducing hydrogen gas. Figure 2 shows variation in the pressures P_I and P_Q as a function of the RF power. The minimum pressures, P_I and P_Q, were 3.5×10^{-1} Pa and 1.5×10^{-2} Pa, respectively. A small RF power of 15 W, which will be described later, suffices to maintain the discharge at pressures as low as 10^{-2} Pa in the chamber. The quenching pressure P_Q of the RF-assisted glow discharge was a factor of 10 lower than that of a conventional glow discharge. The discharge at pressures as low as 10^{-2} Pa decreases read sorption of gases released by the discharge. Ignition of the discharge was easily achieved by gas-puffing near the RF antenna. To estimate the ion-current arriving at the chamber wall, we set two ion-current probes having the surface area of 3 cm^2. One was set near the RF antenna anode and the other at 1 m separated from the antenna anode. The current density per unit wall surface area as a function of discharge current is shown in Fig. 3. The average ion-current density at the discharge current of 1.0 A was approximately 12 μA/cm^2, which corresponds to the ion-flux density of 7.2×10^{13} ions/$cm^2 \cdot$ s. Figure 4 shows a photograph of the RF glow discharge cleaning. The discharge voltage and current were 330 V and 1.0 A, respectively.

Figure 5 shows a typical discharge voltage as a function of the discharge current under the condi-

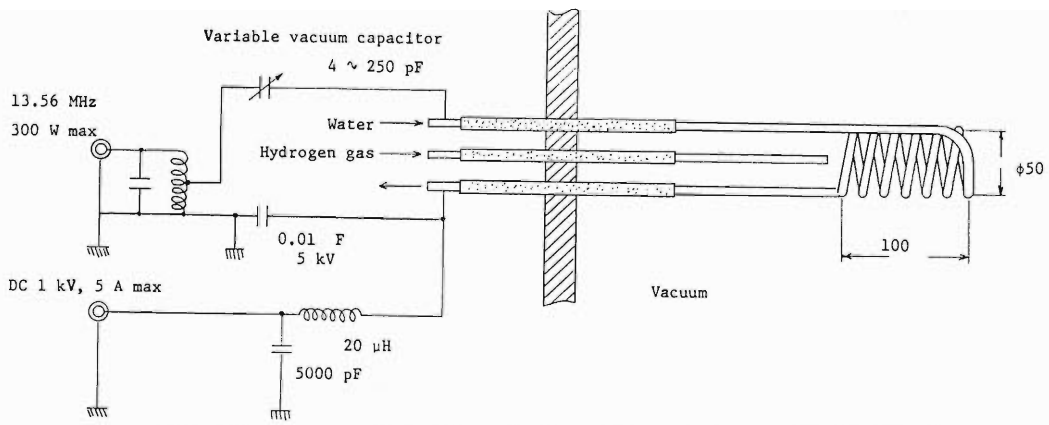

Fig. 1. Schematic diagram of the RF and DC coupling network for RFA-GDC head.

tions of a constant DC voltage of 900 V and constant RF power as the working pressures decrease from the igniting pressure P_I to the quenching pressure P_Q. Figure 5 shows that the discharge voltage decreased with an increase in the discharge current, and that the operating points at relatively stable discharge for any working pressure and RF power fall nicely on a straight line. A discharge voltage as a function of discharge current at two operating

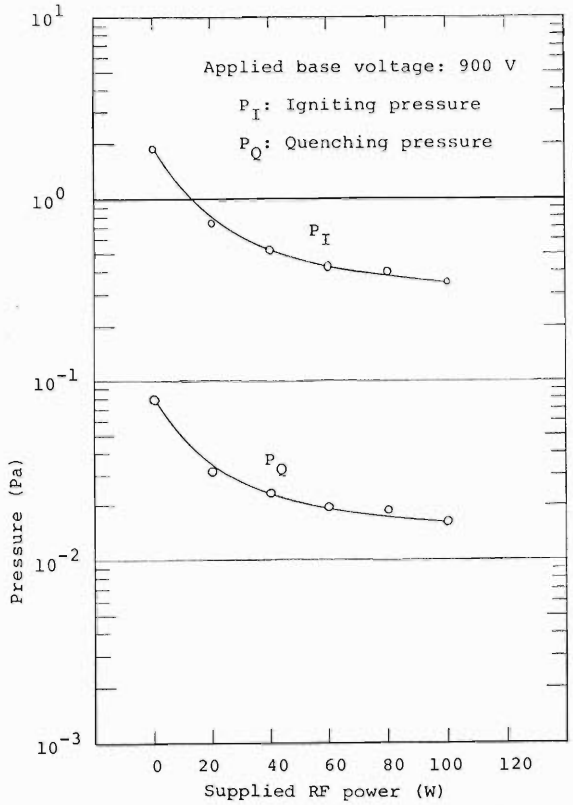

Fig. 2. Variation in ignition (P_I) and quenching (P_Q) pressures for discharges as a function of the RF power.

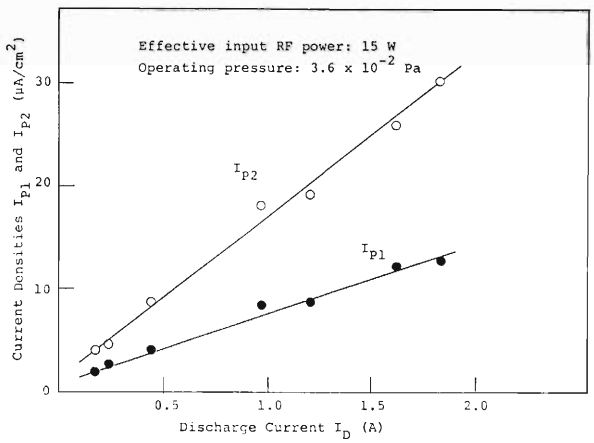

Fig. 3. Current density measured by two ion current probes as a function of the discharge current.

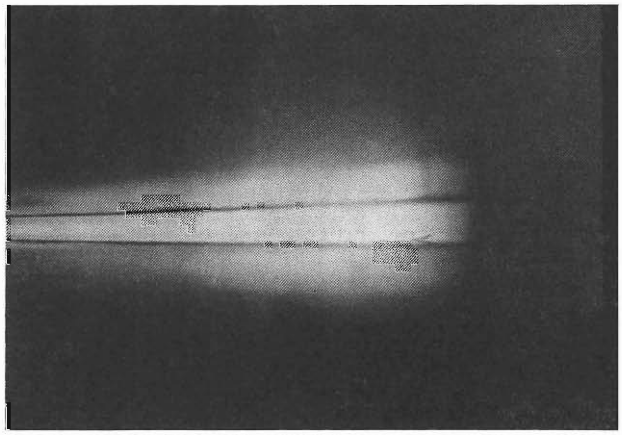

Fig. 4. Photograph of a glow discharge when discharge voltage and current are 330 V and 1.0 A, respectively.

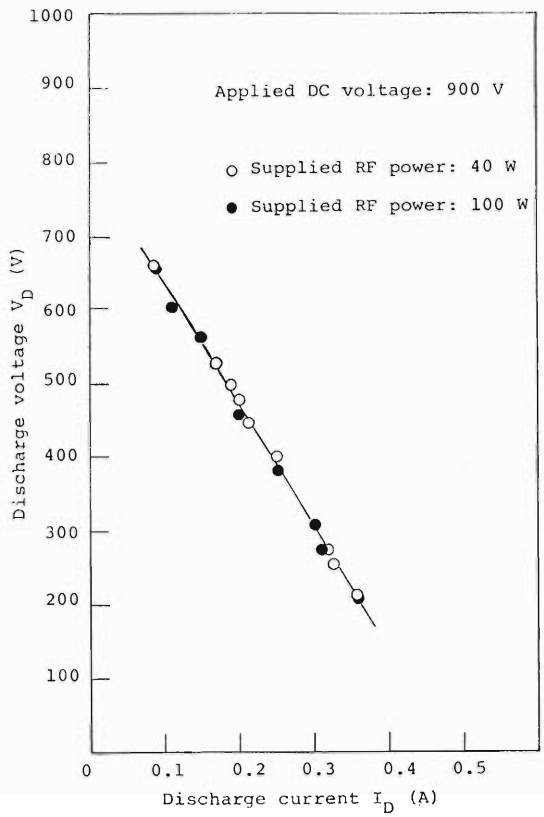

Fig. 5. Discharge voltage curve as a function of discharge current when constant voltage of 900 V was applied.

pressures is shown in Fig. 6, from which we can find that the discharge voltage V_D increases rapidly with a slight increase in the I_D to 0.5 A, and that in the region of more than 0.5 A, V_D keeps a constant value with increasing discharge current V_D. This constant region of V_D corresponds to a normal glow discharge region. Thus we can maintain the normal glow discharge ignited at a lower pressure. The ignition at the lower pressure makes the evacuation after the

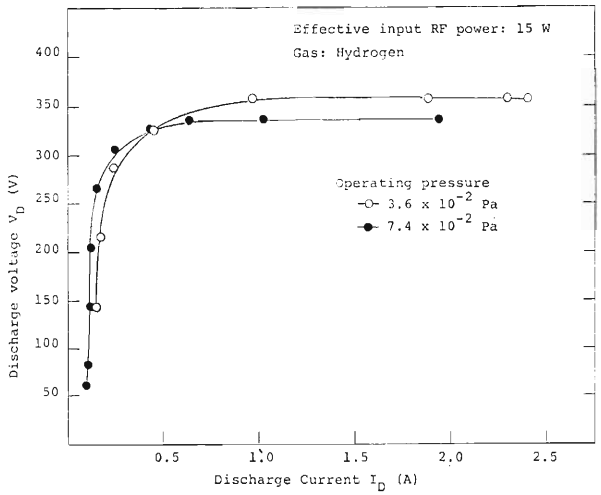

Fig. 6. Discharge voltage curve as a function of discharge current at two operating pressures.

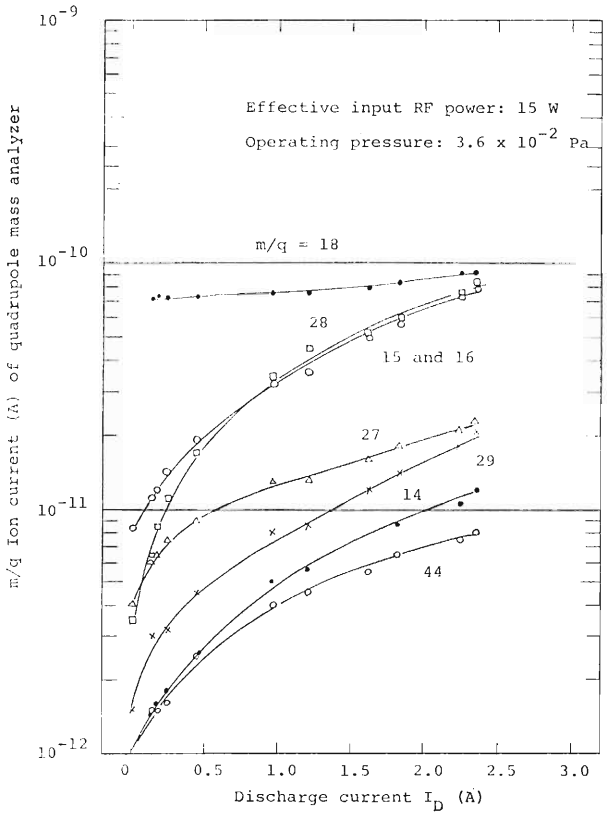

Fig. 7. Variation in partial pressures as a function of discharge current.

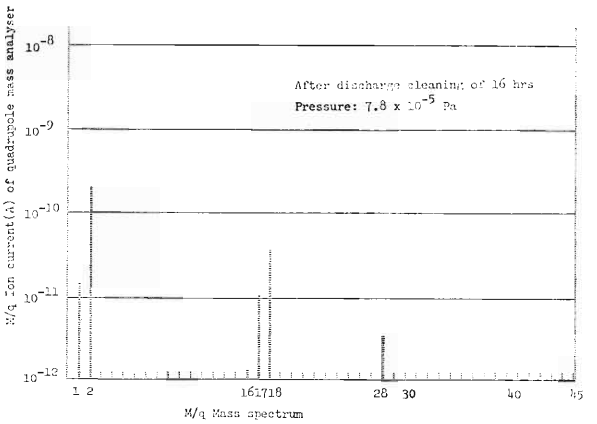

Fig. 8. Mass spectrum of residual gases after discharge cleaning for 16 h. The operating pressure was 3.5×10^{-2} Pa. The discharge voltage and current were 330 V and 1.0 A, respectively.

discharge cleaning easier.

Partial pressures (as the ion current of QMA) of gaseous impurities released by the RF-assisted glow discharge are shown in Fig. 7 as a function of the discharge current, which shows that the release of the impurities except water of $m/q=18$ increases rapidly with an increase in the discharge current. Further, the amount of the impurity released from the surface decreased with discharge cleaning time, though not shown. Figure 8 shows a mass spectrum of residual gases after the discharge cleaning for 16 h at the discharge voltage of 330 V and current of 1.0 A. Figure 8 also shows that the dominant contaminants of the inner surface, *i.e.*, hydrocarbons resulting from manufacturing processes, were removed by glow discharge. Thus we conclude that the RF glow discharge cleaning is effective in removing the contaminants from the inner surface of the chamber.

Reference

1) K. Ikegami, S. Nakajima, S. H. Be, I. Takeshita, Y. Oikawa, and S. Motonaga: *RIKEN Accel. Prog. Rep.*, **18**, 172 (1984).

RIKEN Accel. Prog. Rep. 20 (1986)

V-13. Injection System for an Injector Cyclotron

N. Nakanishi and T. Kageyama

An AVF cyclotron as an injector for RIKEN Ring Cyclotron has been designed.[1] In order to accelerate various types of ions, the cyclotron must be adaptable for external ion sources. An ECR-source, by which we can obtained highly charged ions, is scheduled to be equipped with a cyclotron. Other kinds of ion sources will be also equipped from now on. For this purpose, beam transport lines between ion sources to the cyclotron and a beam inflection system to the median plane of the cyclotron have been designed. The brief description will be given here on the beam line and the inflection system. The beam line must have functions not only to guide beams to the cyclotron but also to be capable of adjusting optical properties of the beam.

A preliminary beam line, as shown in Fig. 1, consists of 4 sections. A quadrupole triplet immediately after the source focuses the beam to a double waist at the object point of the following charge state analysing section. It is also considered to use electric quadrupoles in place of the magnetic ones for this purpose. The charge state analysing section is of mirror symmetry having the configuration of a telescopic cell of quadrupole doublet + dipole + quadrupole doublet in the half system. In this case we can achieve the charge resolution of $dQ/Q = 1/40$. A phase space matching section composed of 4 quadrupoles is installed subsequently. The system makes the beam which the focusing conditions at the exit of an inflector. In the axial hole of the

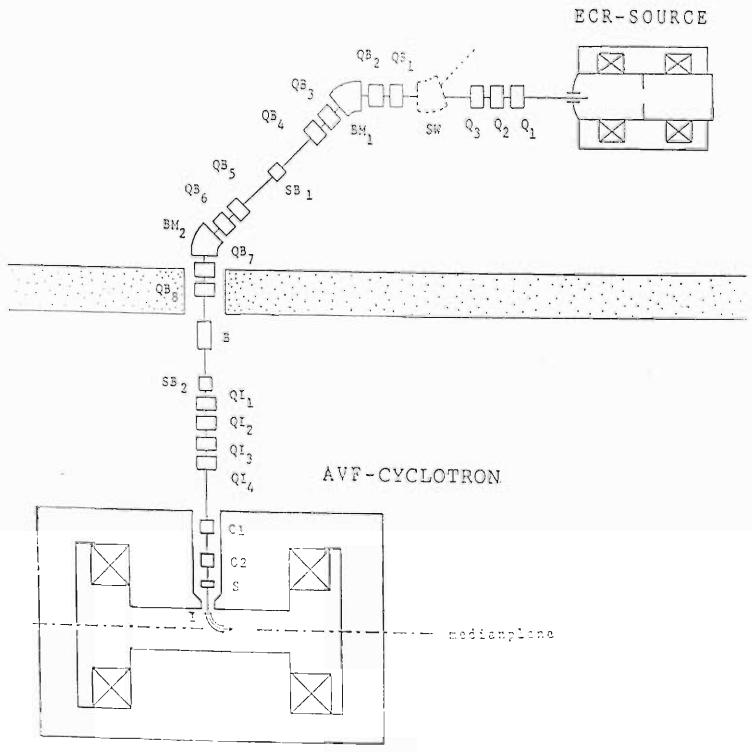

Fig. 1. A preliminary beam line from an ECR source to the cyclotron.

cyclotron, the beam receives focusing and rotating actions due to the stray field. In order to correct the unwanted rotation of the optical axis, a beam

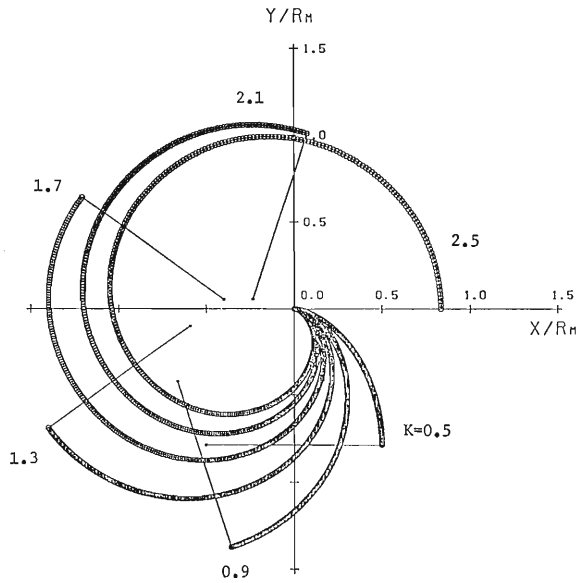

Fig. 2. Beam orbits projected on the median plane, and the rotation centers at the exit of the spiral inflector. The coordinates are normalized by the magnetic radius of R_m.

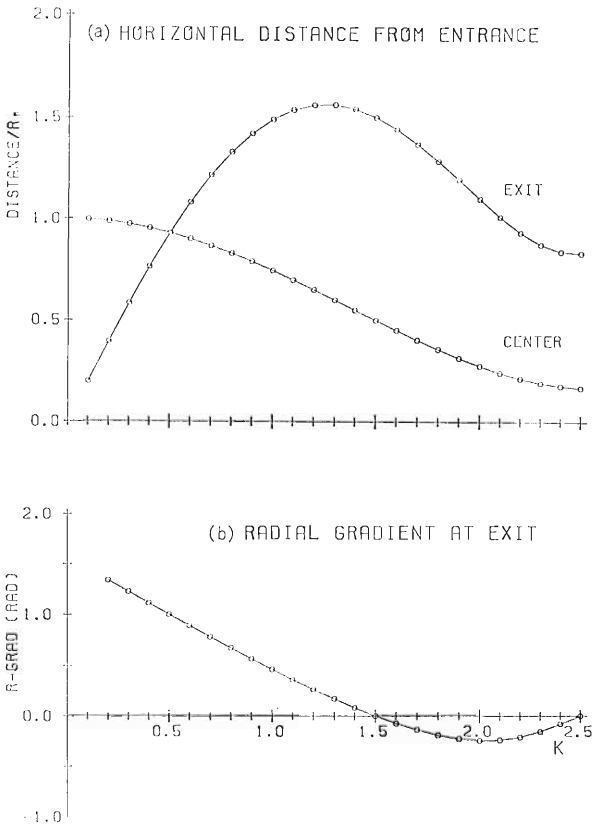

Fig. 3. K dependence of the distances from the entrance of the inflector to its exit and the rotation center at the exit (top), and the radial gradient of the beam at the exit *versus* K (bottom).

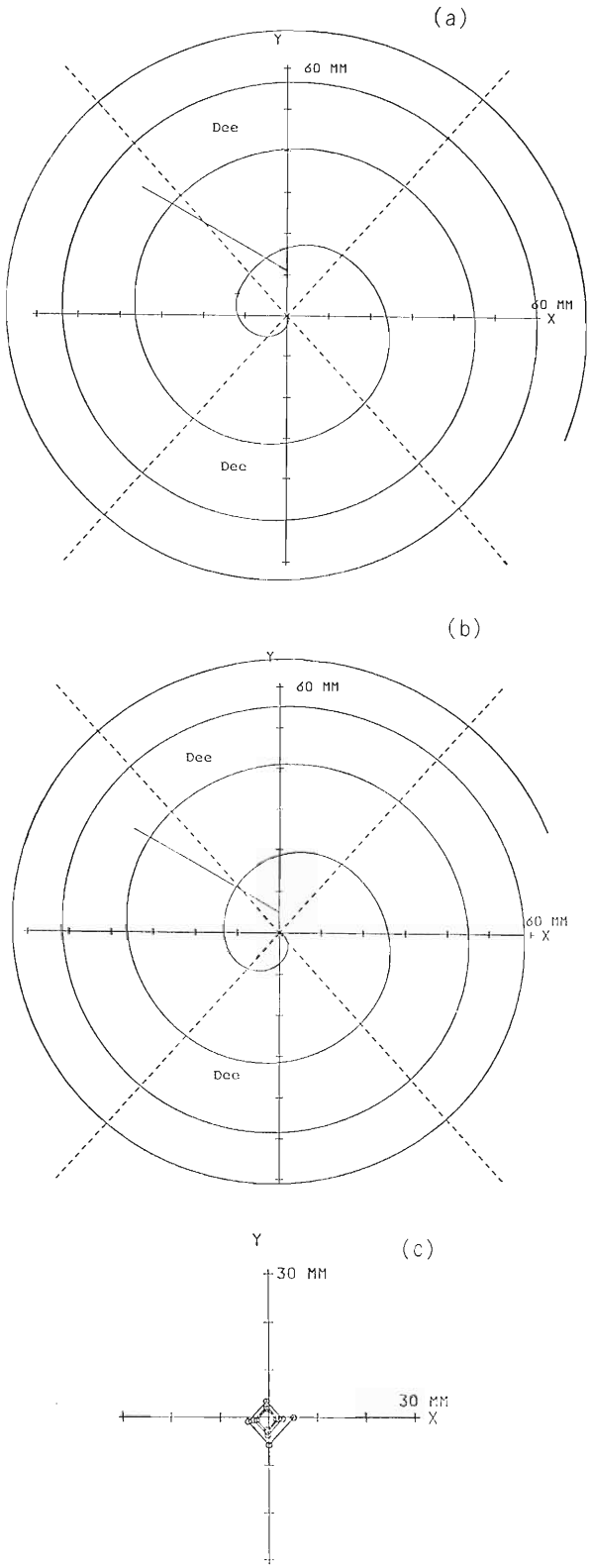

Fig. 4. Typical beam orbits in the central region of the cyclotron. Broken lines show the central lines of accelerating gaps, and a thick line a front of the puller. (a), C^{4+} beam is injected with 20.4 keV and accelerated up to 7 MeV/u in a mode of $h=2$; (b), Proton beam is injected with 6.4 keV and accelerated up to 50 MeV in a mode of $h=1$; (c), Behavior of the instantaneous rotation center for the case of the C^{4+} beam.

rotating system has to be provided. For the matching and rotating sections, we have not yet examined their specifications for the lack of magnetic field data in this area.

It is well known that there are three types of beam inflectors from the axial beam line to the magnet median plane: an electrostatic mirror, a hyperboloid inflector, and a spiral inflector. Because of its flexibility, small volume, and low electric power, we employ the spiral inflector. Its shape projected on the median plane is determined from a value of $K = R_e/2R_m$, where R_e and R_m are the electric and magnetic radii at the exit of the inflector, respectively.[2] In Fig. 2 are shown beam orbits projected on the median plane, and rotation centers corresponding to each beam orbit. Figure 3(a) also shows the K dependences of the distances from the entrance of the inflector to its exit and the rotation center at the exit, and Fig. 3(b) the radial gradient of the beam at the exist *vs.* K. Calculation has been performed for on-axis beams in an assumed magnetic field in order to optimize the inflector parameters and examine optical properties of beams in the central region of the cyclotron. Particles will be accelerated on constant orbits for harmonic numbers of $h = 1$, 2, and the orbit center must converge to the machine center after a certain number of rotation. Typical examples are shown in Figs. 4(a), (b), (c) for the each acceleration mode. A tentative result has been obtained of $K = 1.38$, $R_e = 2.3$ cm, and $R_m = 0.83$ cm. For different acceleration modes, optimization of the acceleration condition has to be made by movement of the puller and the rotation of the inflector with respect to the machine axis.

References

1) N. Nakanishi and T. Kageyama: *RIKEN Accel. Prog. Rep.*, **19**, 197 (1985).
2) J. L. Belmont and J. L. Pabot: *IEEE Trans. Nucl. Sci.*, **NS-13**, 191 (1966).

RIKEN Accel. Prog. Rep. 20 (1986)

V-14. Focusing Magnetic Channel of the Baby Cyclotron

T. Karasawa

An electrostatic deflector pulls ion beams out of their circulating orbits, and then the beams pass through the fringing field of the main magnet. The gradient of this field gives radial defocusing effects to the beams. A magnetic channel that has a field of inverse radial gradient against the fringing field reduces radial divergence of the beam at an extraction window on an acceleration chamber.

On the Baby Cyclotron, an entrance of the magnetic channel is positioned 75 degrees downstream from an exit of the deflector; its expanding in angle is 26 degrees. A beam probe follows near an exit of the magnetic channel. In Fig. 1, a layout of the deflector and the magnetic channel with the acceleration chamber is shown.

The magnetic channel consists of three iron bars, the cross section of which is shown in Fig. 2A. This type of the magnetic channel was invented by Odera *et al.*[1] In a uniform external field, the magnetic induction inside an iron bar is twice as much as the external field induction. Magnetic induction outside of the iron bar is represented by

$$B_z = R^2\{(z^2-y^2)/(z^2+y^2)\}B_0$$

For notations see Fig. 2B. This equation means that the outer field is proportional to external field as long as the iron is not magnetically saturated. When the iron is saturated, the outer induction is nearly constant independently of the external field.

In the magnetic channel of the BC-1710 type cyclotron, the iron bars of cross sectional radius of 2.5 mm are placed with an aperture of 18 mm. The carbon content of the iron bars is below 0.01%. When the induction inside the iron is below the saturation, a relative magnetic field gradient on the median plane is calculated and the results at the center (the middle point between the inner bar and the outer bars) are shown in Fig. 3, as a function of the gap between the iron bars.

High magnetic fields are used in the Baby Cyclo-

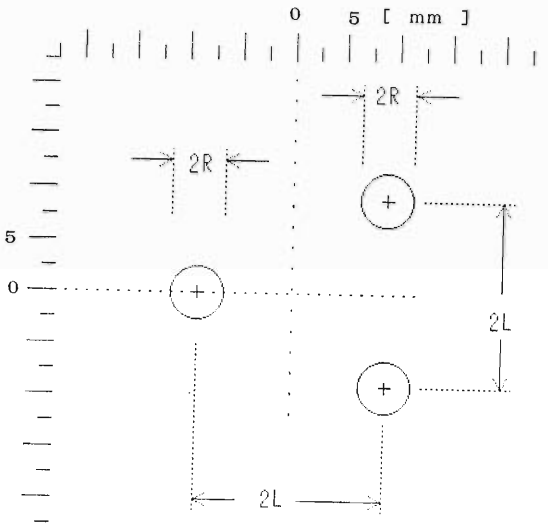

Fig. 2A. Cross section of magnetic channel.

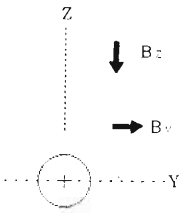

Fig. 2B. Notation of coordinate.

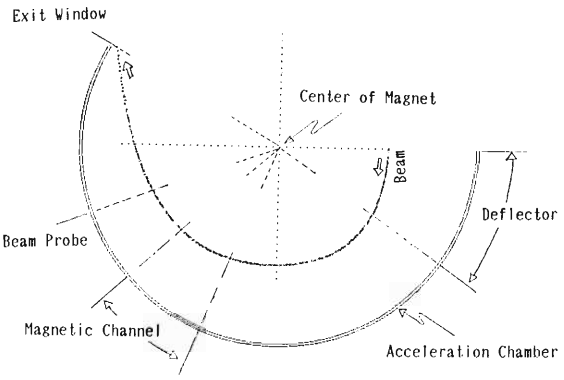

Fig. 1. A layout of deflector, magnetic channel, beam probe and exit window on acceleration chamber.

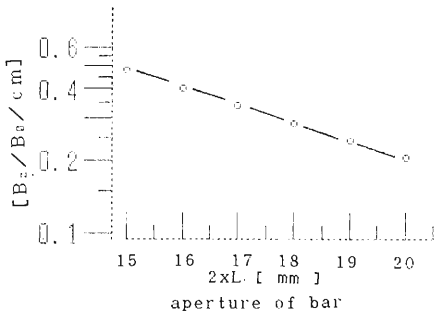

Fig. 3. Field gradient of the magnetic channel *vs.* aperture between iron bars (at the middle point between the iron bars on the median plane).

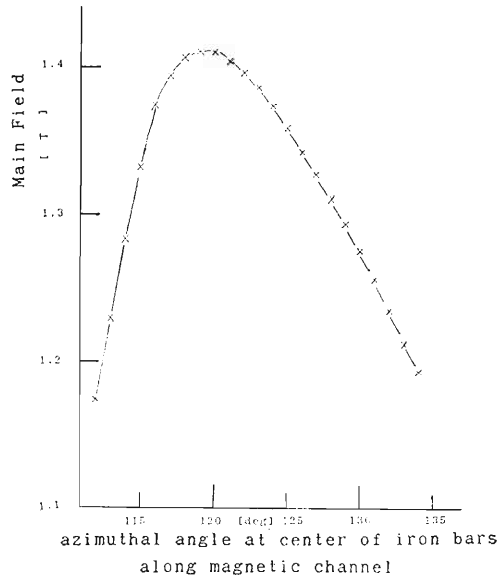

Fig. 4. Field by main magnet along the center of the magnetic channel.

tron, and the magnitude of the main field at the position where the magnetic channel is placed is higher than 1.0 T. The magnetic fields along the center line of the magnetic channel for proton acceleration are shown in Fig. 4. In this case, the iron bars of the magnetic channel are fully saturated. We suppose that the field gradient produced by the magnetic channel is constant along the beam path independently of the main field. The gradients are calculated to be 0.31 and 0.34 T/cm for saturation inductions of 2.2 and 2.4 T in the iron, respectively.

We have studied an effect of the magnetic channel on the deflected beam by numerical calculations of radial orbits. Firstly, a reference ray is determined so that a reference particle arrives at the center of the exit window on the acceleration chamber without the magnetic channel. Secondly, the magnetic channel is so placed that the reference ray is not affected by the magnetic channel field. The calculation starts at the entrance of the deflector. Seven particles on a phase space around the reference ray (two different radius and two different radial momentum) are calculated. These seven particles have the same total momentum. In Fig. 5, the phase space at the entrance of the deflector is shown. Trajectories of the radial motions are calculated as far as the exit window on the acceleration chamber and a radial spacing of a pair of particles are discussed. The #2 and #5 particles are parallel beams with respect to the reference ray at the entrance of the deflector. As the field gradient of the channel increases from zero, the radial spacing of #5–#2 reduces at the exit window. When the gradient is zero, the radial spacing is 62 mm, and when the gradient is about 0.23 T/cm, the radial

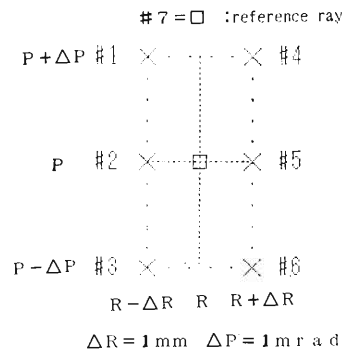

Fig. 5. Phase space at the entrance of the deflector (start point).

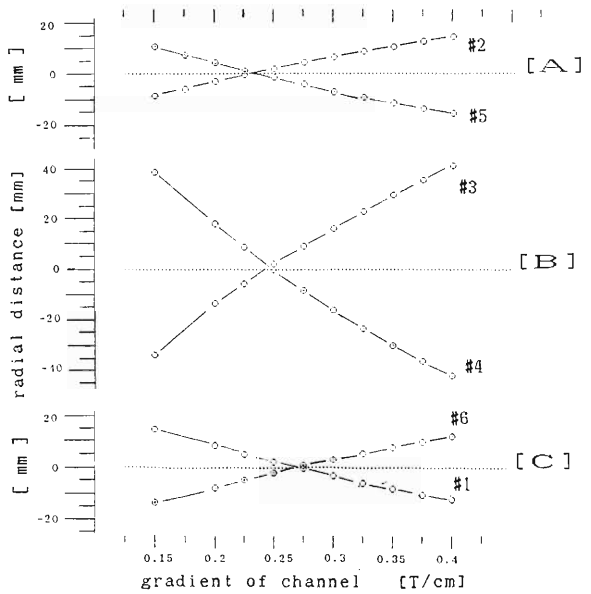

Fig. 6. A: Radial distance of #2 and #5 particles, B: Radial distance of #3 and #4 particles, C: Radial distance of #1 and #6 particles (at the exit window on the acceleration chamber).

spacing is nearly zero, which means focused beam. When the gradient increases furthermore, the radial spacing increases, which means over focused beam. The displacements of #2 and #5 particles from the reference ray at the exit window *versus* the gradient are shown in Fig. 6A. The displacements of #2 and #5 particles are nearly the same except its sign, and we have so selected a pair of particles as to satisfy this condition: #1 with #6 and #3 with #4.

The #3 and #4 particles are diverging beams, but the #1 and #6 particles are converging beams at the entrance of the deflector. At the entrance of the magnetic channel, the radius of #1 particles is already larger than that of #6 particles. The displacements of the pair of #3 and #4 particles and the pair of #1 and #6 particles from the reference ray *versus* the gradient are shown in Fig. 6B and 6C, respectively. In Table 1, the focusing gradient for each pair are shown. For parallel beams,

Table 1. Focusing gradient.

Pair of particles	Focusing gradient (T/cm)
#2-#5	0.23
#3-#4	0.24
#1-#6	0.27

Each pair of the particles is focused at the exit window on the acceleration chamber

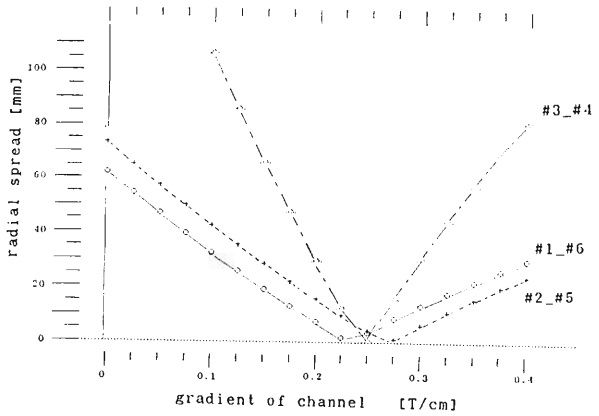

Fig. 7. Radial spread *vs.* the gradient of magnetic channel (at the exit window on the acceleration chamber).

Table 2. Radial spread for zero gradient, upper and lower gradient for narrow radial spread at the exit window.

Pair of particles	Radial spread* (cm)	Upper gradient (T/cm)	Lower gradient (T/cm)
#2-#5	6.2	0.29	0.18
#3-#4	19.5	0.31	0.19
#1-#6	7.4	0.31	0.20

* for zero gradient at the exit window

it is weekest. When a source point may be assigned for each pair, the source point gets nearer to the magnetic channel and the gradient becomes stronger.

For each pair, we define the radial spread at the exit window as the distance between the inner and outer particles. In Fig. 7, the radial spread *versus* the gradient of the channel is shown. At a given gradient, the radial spreads vary according to the initial condition of the pair, but the focusing gradients are not so widely changed.

Beams, which we practically handle are a mixture of particles having different radii and radial momentums within a some extent. For practical use of the magnetic channel, the radial spread of the deflected beam must be reduced below the width of the extraction window on the acceleration chamber. In rough estimation, we try to reduce the radial spread for each pair to less than 1/5 of the spread at zero gradient. For each pair, the spread at zero gradient and the gradient at which the spread is reduced to 1/5 are shown in Table 2. The gradi-

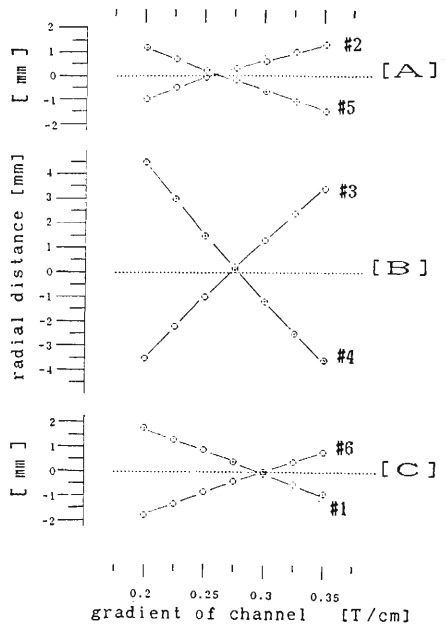

Fig. 8. A: Radial distance of #2 and #5 particles, B: Radial distance of #3 and #4 particles, C: Radial distance of #1 and #6 particles (at the beam probe).

Table 3. Limiting gradients for reversed beam profile.

Pair of particles	Focusing gradient	
	At beam probe (T/cm)	At exit window (T/cm)
#2-#5	0.26	0.23
#3-#4	0.27	0.24
#1-#6	0.30	0.27

ents have two values: the upper gradient is above focusing gradient and the lower is below it. For practical use, we are able to fix the gradient of the channel at a value between the lower and the upper values.

During the beam test at the factory, reversed beam profiles between the beam probe and the exit window on the acceleration chamber have been observed. When the beam focuses between them, this phenomenon may occur. The displacement from the reference ray to the particles of each pair at the beam probe near the focusing gradient are shown in Fig. 8A, B, and C. By comparing Fig. 8 with Fig. 6, we can estimate the gradient for the reversed beam for each pair. These are listed in Table 3. If we can determine a phase plot representing the real beam, we can estimate the gradient of the channel within narrow values; however we have no experimental results to determine which pair among three pairs described above is good approximation to the real beam. Hence the gradient of the channel is estimated within relatively wide values above 0.23 and below 0.30 T/cm. When the effective cross-sectional radius of the iron bar is reduced from

2.5 mm to 2.25 mm, the calculated value of the gradient is 0.25 T/cm for saturation induction of 2.2 T inside the iron.

We have made an interpretation about the effect of the magnetic channel in high field from the experimental observation of the reversed beam and computation of particle trajectory on a simple assumption of the phase plot.

Reference

1) M. Odera, Y. Miyazawa, T. Tonuma, M. Henmi, and O. Terajima: *Nucl. Instrum. Methods*, **65**, 247 (1968).

RIKEN Accel. Prog. Rep. 20 (1986)

V-15. Sputter PIG Source for RILAC

Y. Miyazawa, M. Hemmi, T. Chiba, and M. Kase

A new sputter PIG source of indirectly-heated-cathode type has been developed for RILAC. The production of multicharged ions of solid elements have been measured on its test bench.[1] Figure 1 shows a cross sectional view of the sputter PIG source. The anode consists of three parts, and the middle part of them having the ion exit slit and two anode holders is built interchangeably. Such construction allowed easy mechanical fitting of the anode geometry. This middle part is made of stainless steel and milled away by a section of 16×26 mm^2 from the rear-side of the anode. We made a sputtering

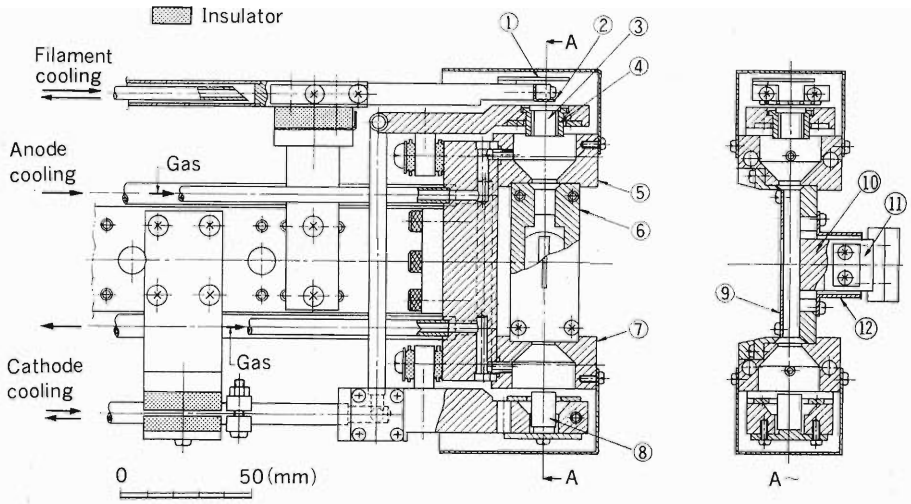

Fig. 1. Cross sectional view of the sputter PIG source. 1, electron shield (Mo); 2, filament (0.8, W); 3, cathode (W); 4, cathode heat shield (Mo); 5, anode holder (copper); 6, anode (stainless steel); 7, anode holder; 8, anti-cathode (W); 9, beam slit (Mo); 10, sputtering electrode; 11, clamp of the sputtering electrode (copper); 12, shield of the clamp (stainless steel).

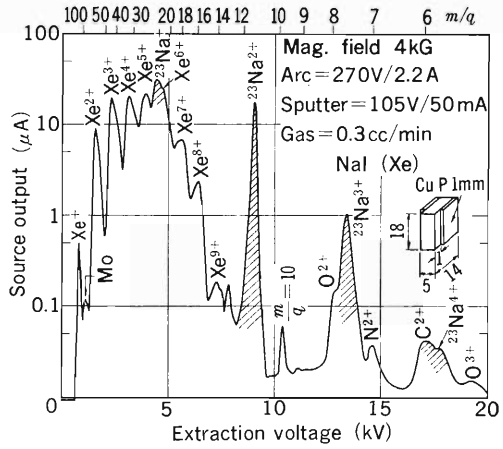

Fig. 2. M/q spectrum of NaI sputtered in a xenon discharge.

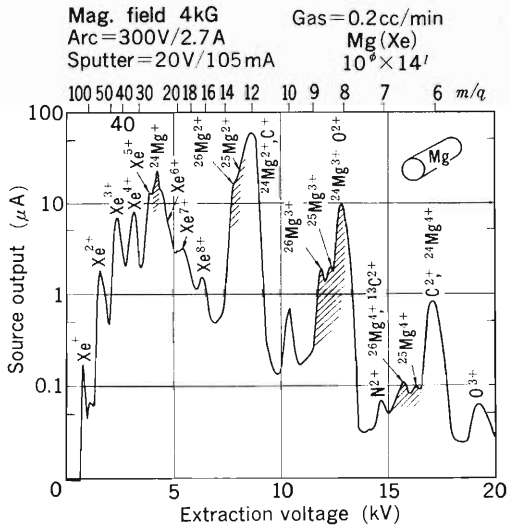

Fig. 3. M/q spectrum of Mg sputtered in a xenon discharge.

electrode with a surface area of 80 to 140 mm^2. To prevent the electrode from melting, it was supported with a water-cooled clamp fitted into the shield of the clamp with a gap of 1 mm. Typical sizes of the sputtering materials were a $5\times18\times14$ mm^3 block and a $\phi10\times14$ mm^3 column. An observed M/q spectrum of ions of solid elements are shown in Figs. 2–11. For operation of this source Ar or Xe gas was used to support the arc discharge. Table 1 gives the output currents obtained by the ion source. Ions of solid elements, Na^{4+}, Mg^{4+}, Al^{4+}, Si^{5+}, Ti^{6+}, Cr^{7+}, Fe^{6+}, Ni^{7+}, Cu^{7+}, and Ge^{8+} have been obtained.

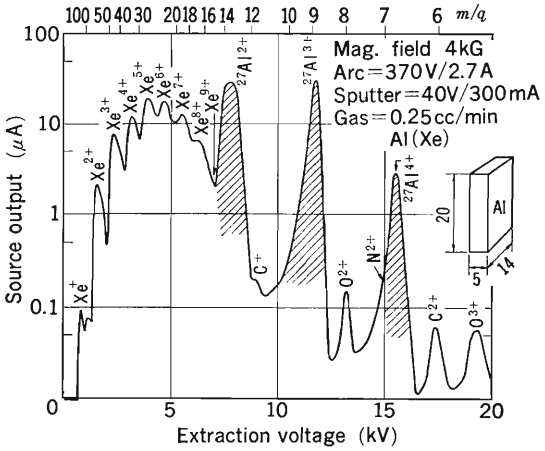

Fig. 4. M/q spectrum of Al sputtered in a xenon discharge.

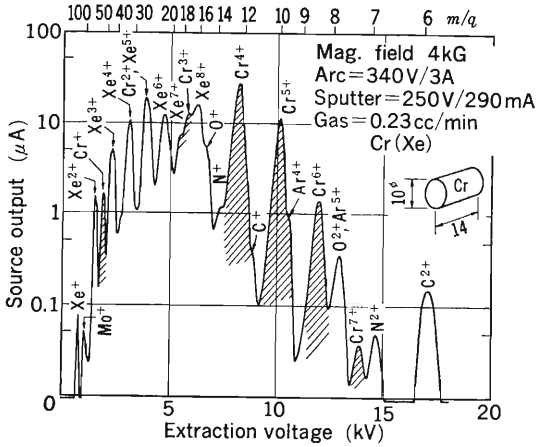

Fig. 7. M/q spectrum of Cr sputtered in a xenon discharge.

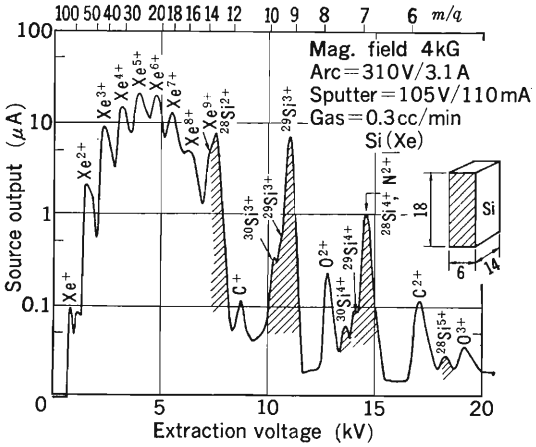

Fig. 5. M/q spectrum of Si sputtered in a xenon discharge.

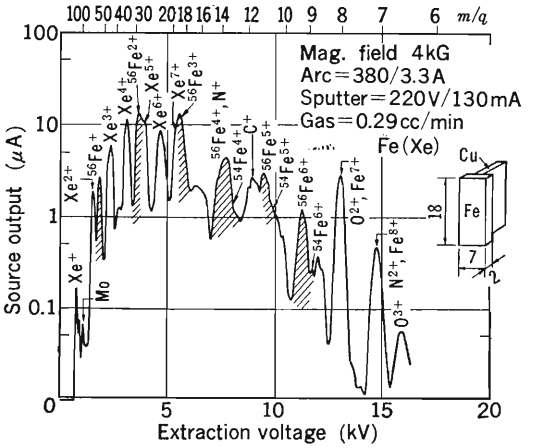

Fig. 8. M/q spectrum of Fe sputtered in a xenon discharge.

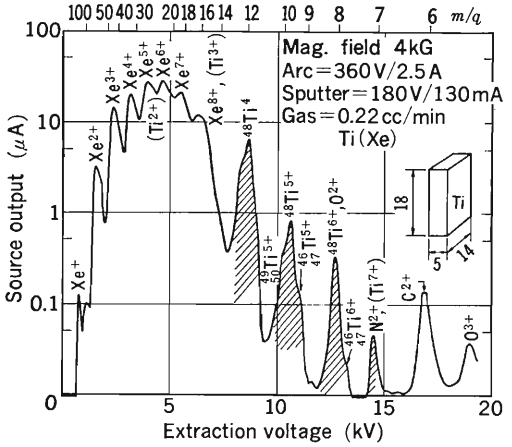

Fig. 6. M/q spectrum of Ti sputtered in a xenon discharge.

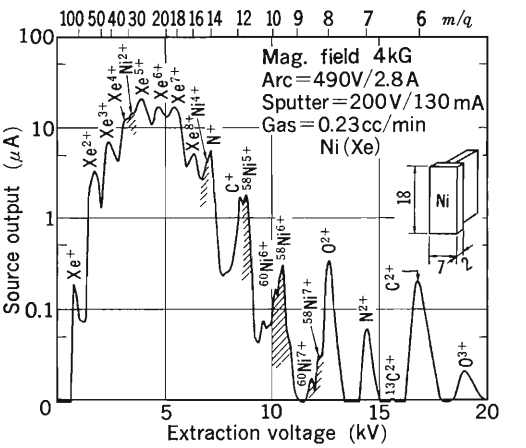

Fig. 9. M/q spectrum of Ni sputtered in a xenon discharge.

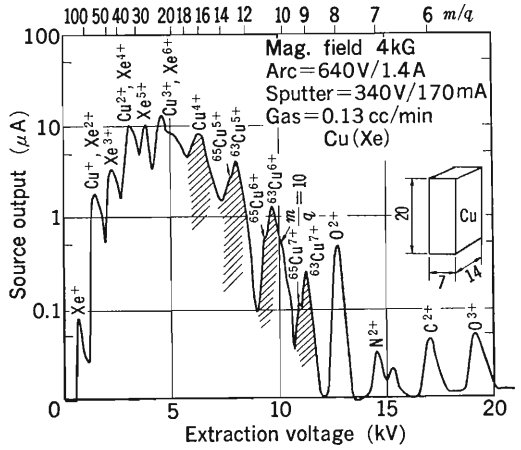

Fig. 10. M/q spectrum of Cu sputtered in a xenon discharge.

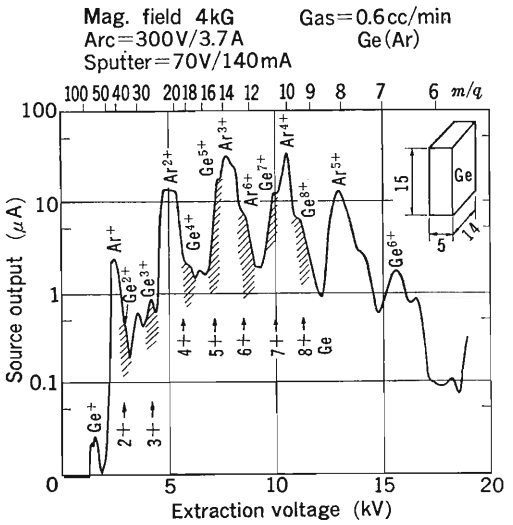

Fig. 11. M/q spectrum of Ge in an argon discharge.

Table 1. The output currents of RILAC ion source.

	1+	2+	3+	4+	5+	6+	7+	8+	9+	10+	11+	12+
										Sputtering materials		
Na (Ar)	5.5	4.3	0.6							NaI crystal		
(Xe)	—	17	1.1	0.02						//	//	
Mg (Ar)	4	23	5	0.25						Mg block		
(Xe)	—	60	7	0.2						//	//	
Al (Ar)	13	—	70	—						Al block		
(Xe)	—	30	30	2.8						//	//	
Si (Ar)	2.5	—	12	2.5						Si crystal		
(Xe)	—	8	7	1	0.02					//	//	
Ti (Ar)	1	8	8	11	—	—				Ti block		
(Xe)	—	—	—	7	0.8	—				//	//	
Cr (Ar)	1.2	9	15	—	—	2	0.1			Cr block		
(Xe)	1.5	—	—	27	11	1.4	0.03			//	//	
Fe (Ar)	2	10	10	—	5.5	0.8	—			Fe block		
(Xe)	2.8	—	—	4.5	3	1.2	—			//	//	
Ni (Ar)										Ni block		
(Xe)	—	—	—	—	1.8	0.3	0.02			//	//	
Cu (Ar)	1	6	—	12	—	—	0.3			Cu block		
(Xe)	—	—	—	8.5	4	1.3	0.25			//	//	
Ge (Ar)	—	—	0.9	2	6	6	5	2		Ge crystal		
(Xe)	—	—	—	—	—	—	0.05	0.07		//	//	

Ions, Mg^{3+}, Al^{3+}, Si^{3+}, Ti^{5+}, Ni^{6+}, and Cu^{6+}, were accelerated by RILAC and delivered to various target stations. Gases indicated in the parentheses were used to support arc discharge. The dashed line shows the lower limit of the charge-to-mass ratios of ions which can be accelerated by RILAC.

Reference

1) Y. Miyazawa, M. Hemmi, T. Chiba, and M. Kase: *RIKEN Accel. Prog. Rep.*, **19**, 184 (1985).

RIKEN Accel. Prog. Rep. **20** (1986)

V-16. Performance of ECR2

M. Yanokura, S. Ishii, and H. Nonaka

The performance of ECR2[1] (RIKEN Electron Cyclotron Resonance type-ion source) has been improved since January 1986. An extracted beam current of Ar 1+ ion was about 1 μA when reported last year. This value is not satisfactory for RILAC. The purpose of the present improvement is to increase beam currents.

Improvements were made on a few points. One is a reform of the 1st cavity. A quartz tube of 400 mm in length and 21 mm in diameter was inserted into the 1st cavity, and gas was admitted by using a slow leak valve into the quartz tube. Since conductance of the tube was very small, a pressure difference arose between inner and outer sides of the quartz tube; the calculated pressure difference was of about 2 order of magnitude. During operation of the ion source, ECR plasma was formed only inside the tube. The pressure in the quartz tube was around 10^{-4} Torr. Produced ions collide the inner wall of the quartz tube, but ion loss is rather small because the charge exchange cross section at the surface of the quartz tube is smaller than those at other materials. Thus, the pressure at the RF injection port was reduced, and no RF discharge took place at this position.

The second improvement is made on an extraction system. Before improvement, the bore diameter of the first electrode faced to the plasma surface was 10 mm. The bore diameter of acceleration electrode was equal to that of the first electrode; the acceleration gap was about 4 mm. The extraction system was improved by referring to a LBL ECR ion source.[2] The parameters of the new extraction system are as follows:

1) the bore diameter of the 1st electrode is 8 mm;

2) the bore diameter of the acceleration electrode is 10 mm; and

3) the acceleration gap width is 21 mm.

The beam-current loss at the extraction system was decreased by this improvement. The load of an extraction power supply was also decreased.

Figure 1 shows two types of charge distribution of an extracted Ar beam after improvement. The vacuum pressure under each condition is also shown in Fig. 1. Open circles show high-intensity but poor charge distribution data; triangles show low-intensity but better charge distribution data. Matching between microwave and plasma for high-pressure operation is better than that for low-pressure operation. Beam currents of both data are higher than those of the last year and Ar 1+ current are 20 times larger than those reported last year; however, we need more intense beams of high charge-states for RILAC.

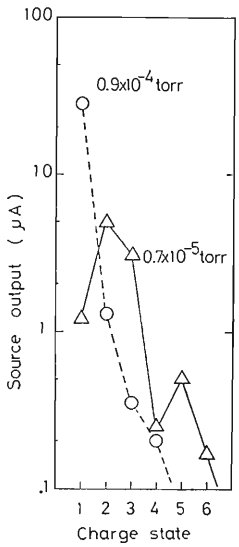

Fig. 1. Charge distribution of the extracted Ar beam.

We now plan further modifications; they are

1) installation of an additional coil to decrease an axial magnetic field gradient at the ECR point;

2) increase in pumping speed, which lowers the operating pressure at the 2nd stage to lower than 10^{-6} Torr;

3) modifications for increasing the RF electric field in the cavity; and

4) installation of an electrode adjust mechanism and a beam converging element such as a solenoid coil.

References

1) M. Yanokura, S. Ishii, and Y. Sakamoto: *RIKEN Accel. Prog. Rep.*, **19**, 214 (1985).

2) C. M. Lyneis: Proc. 7th Int. ECR Ion Source Workshop, Jülich Nuclear Centre Publ., p. 1 (1986).

RIKEN Accel. Prog. Rep. 20 (1986)

V-17. Three Dimensional Analysis of RF Electromagnetic Field by the Finite Element Method

M. Hara, T. Wada, K. Mitomori, and F. Kikuchi

Calculation of an electromagnetic field is very important in designing accelerators. We have already developed some computer codes[1,2] to calculate an electromagnetic field in cavity resonators, based on the finite element method. Everything goes quite well in a two-dimensional or axi-symmetric case. Three-dimensional calculation, however, had difficulty in imposing a divergence free condition. We have tried a finite element formulation where divergence free condition is treated by a penalty method; however, the results were not fully satisfactory.

We have developed special finite element models with "exotic" nodal configurations for two and three dimensional elements.[3] In these models, the tangential component of the electric field at each side of each element is taken to be an unknown variable which is constant on the side and continuous along the interelement boundaries. Some mixed finite element models are presented with numerical results for two- and three-dimensional problems. Satisfactory results have been obtained for simple problems.

1) Basic Equations

We deal with a time-harmonic electric field in vacuum of bounded region surrounded by a perfect conductor. It is described by Maxwell's equations, which are reduced to

$$\text{div } \boldsymbol{E}=0 \tag{1}$$

and

$$\text{rot rot } \boldsymbol{E}=\lambda \boldsymbol{E} \tag{2}$$

where $\lambda=\omega^2/c^2$.

The boundary condition is

$$\boldsymbol{n}\times\boldsymbol{E}=0 \text{ on the surface} \tag{3}$$

where $\boldsymbol{n}$ is a unit vector normal to the surface.

In Eq. (2),

for $\lambda\neq 0$, div $\boldsymbol{E}=1/\lambda$ div (rot rot $\boldsymbol{E}$) $=0$, and

$\lambda=0$, rot $\boldsymbol{E}=0$, but not div $\boldsymbol{E}=0$.

We must treat an eigenvalue problem for a real vector-valued function. A difficulty of this problem is in dealing with the divergence-free condition (1).

2) New Type of Finite Element Models

These models have quite different node configurations from usual finite element ones because unknown variables are taken not on nodal points but on the sides of the element. We call these models exotic models. Detailed formulation of these models are presented in Ref. 4 and here we only summarize the results. In Ref. 4 weak formulations for Maxwell's equations are presented based on the mixed and penalty methods. Mixed formulation is based on the Lagrange multiplier.

Characteristics of these models are:

(1) Tangential components of the electric field on the sides of the element are adopted as unknown variables, which are constant on the sides;

(2) The divergence-free condition is fully satisfied in each element;

(3) The electric field is not strictly continuous, but only tangential component is continuous along the interelement boundaries;

(4) The handling of the boundary condition is easy;

(5) Only five types of elements are in practical use.

In Fig. 1, five types of mixed finite element models with exotic nodal configurations are shown. In these elements, the triangular element for the two-dimensional and axi-symmetric case and tetrahedral element for the three dimensional case are important for practical use.

In the finite element model of the two dimensional case, we take the following approximation of $\boldsymbol{E}$ in an element:

(1) linear polynomial approximation;

(2) rot $\boldsymbol{E}=$constant;

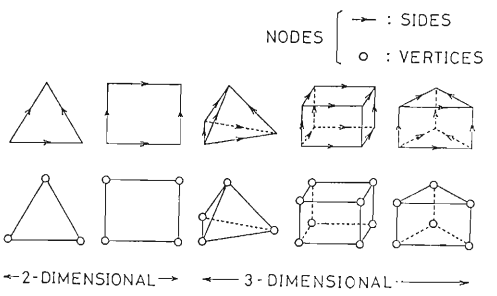

Fig. 1. Types of exotic element models. Only these five types can be used for our new types of finite element models. Upper and lower rows show the sides and nodes of the elements, respectively.

(3) div $\boldsymbol{E}=0$;

(4) The tangential component is constant on each side of the element;

The electric field $\boldsymbol{E}=(E_x, E_z)$, in this element, is written as

$$E_x=\alpha_1+\alpha_2 y$$
$$E_y=\alpha_3-\alpha_2 x$$

In these equations, the coefficient of y in E_x and that of x in E_y have the same absolute value and opposite signs due to the above condition (4). Then,

$$\text{rot } \boldsymbol{E}=\frac{\partial E_y}{\partial x}-\frac{\partial E_x}{\partial y}=-2\alpha_2$$

and

$$\text{div } \boldsymbol{E}=\frac{\partial E_x}{\partial x}+\frac{\partial E_y}{\partial y}=0$$

In this element model, shape functions are given as

$$E_x=\sum_{i=1}^{3}\frac{-l_i(y-y_i)}{2A}E_{s,i+3}S_i$$

and

$$E_y=\sum_{i=1}^{3}\frac{l_i(x-x_i)}{2A}E_{s,i+3}S_i$$

where s indicates the side of $i+3$ in Fig. 2, l_i is the length of the side of $i+3$, and S_i indicates the sign of l_i.

From this expressions, the element stiffness matrix M_s and element mass matrix M_m are given by

$$\boldsymbol{M}_s(i,j)=(1/A)[l_i l_j S_i S_j]$$

and

$$\begin{aligned}\boldsymbol{M}_m(i,j)&=(1/4A^2)[S_iS_jl_il_j\iint\{(x-x_i)(x-x_j)\\&\quad+(y-y_i)(y-y_j)\}\,dx\,dy\\&=(1/A)[S_iS_jl_il_j\{x_i^*x_j^*+y_i^*y_j^*\\&\quad-(1/6)(x_1^*x_2^*+x_2^*x_3^*+x_3^*x_1^*\\&\quad+y_1^*y_2^*+y_2^*y_3^*+y_3^*y_1^*)\}]\end{aligned}$$

where A is the area of the element and $x_1^*=x_1-x_M$ with x_M being the center of gravity.

In the finite element model of the three-dimensional case, regions of arbitrary three-dimensional shapes can be divided into tetrahedral elements with quite good approximation. In the same manner as the two-dimensional triangular element, following conditions are required for this finite element model.

(1) linear polynomial approximation;

(2) rot $\boldsymbol{E}=$constant;

(3) div $\boldsymbol{E}=0$;

(4) Tangential components are constant on each side of the element.

The electric field $\boldsymbol{E}=(E_x, E_y, E_z)$, in this element is written as

$$E_x=\alpha_1+\alpha_2 y+\alpha_3 z$$
$$E_y=\alpha_4-\alpha_2 x+\alpha_5 z$$
$$E_z=\alpha_6-\alpha_3 x-\alpha_5 y$$

The element stiffness and mass matrices for the tetrahedral case are also given through the procedure as the case of two dimensional, but the explicit expression is too complicate to write down.

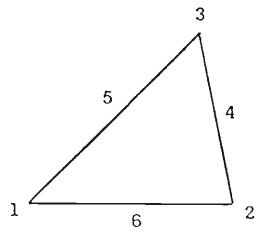

Fig. 2. Triangular element. Figures 1–3 indicate nodal points and Figs. 4–6 indicate sides. The tangential component of electric field on each side is constant and continuous, but normal component is not continuous at the interface of elements.

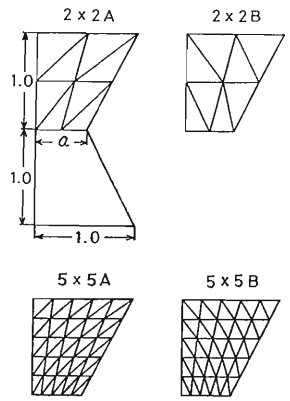

Fig. 3 (a). Two-dimensional mesh.

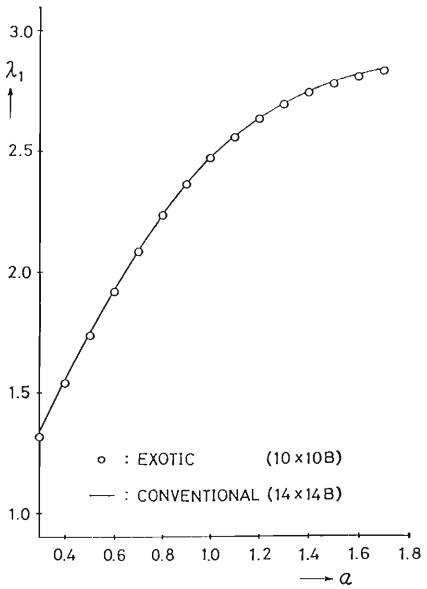

Fig. 3 (b). Calculated eigenvalue. Notch depth dependence on eigenvalue is shown. The results show good agreement with the calculation with a conventional finite element model.

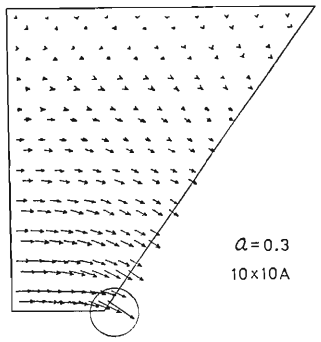

Fig. 3 (c). Electric fields calculated at the center of mass of each triangular element.

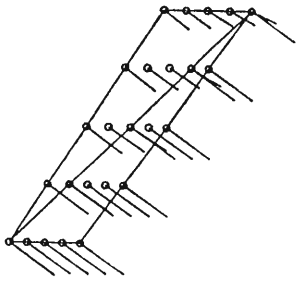

Fig. 3 (d). Electric fields in two triangular elements at the edge indicated by the circle in Fig. 3 (c). In these figures, eigenvalue and eigenvectors are calculated on the sides of elements and, from these values, the electric fields at arbitrary points are calculated.

3) Numerical Results

We made some calculations for several simple problems to check the validity of our approach.

Figure 3 shows the calculations of a two-dimensional problem. We calculated the field in a rectangular domain with a notch of depth a. Figure 3(a) shows two types of meshes. We calculated the lowest eigenvalue using a triangular element. Using symmetric properties of the fields, only an upper half area is divided and calculated. The notch dependence(a) of the lowest eigenvalue for 10×10B meshes is shown in Fig. 3(b), in which the solid line indicates the results obtained with the conventional method.[1] The calculated eigenvalues show good agreement with a conventional method and the eigenvalue dependence on a is consistent with the perturbation theory. Figure 3(c) shows the field distribution calculated at the center of mass of each triangular element. In Fig. 3(d), the field in two triangular elements at the edge are shown. Bars indicate the magnitude and direction of the electric fields. The electric fields at element interfaces have different values which depend on the element. In this model, only tangential components are continuous. For the same reason, the exact electric fields should have no normal component on the symmetry plane, but the calculated ones have a small amount as such. This kind of errors is inherent in this method.

For a three-dimensional problem, we calculated a deformed parallelepiped cavity. Figure 4 shows the lowest eigenvalues with deformation x. This variation of the eigenvalue consists with the perturbation theory. That is, when the volume where electric

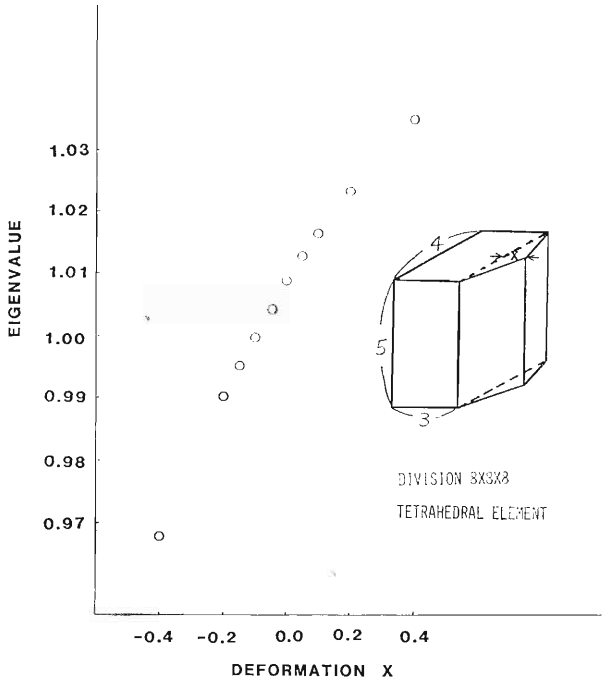

Fig. 4. Variation in eigenvalue with deformation.

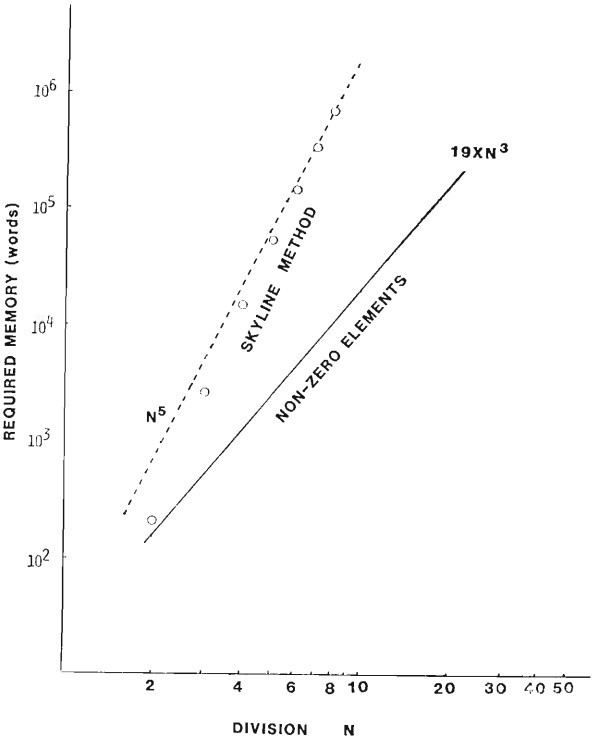

Fig. 5. Required memory *vs* division N.

field is strong is reduced, the eigenvalue should be reduced. It is well known that in the three-dimensional calculations a large size of computer memory is required. Figure 5 shows the required memory size estimated *vs* division number N that the required memory has N^5 dependence. It is because the skyline scheme is adopted for the solver. When the division is N, the order of matrix is nearly proportional to N^3. In the skyline scheme, the bandwidth is nearly proportional to N^2 and the required memory size is approximately proportional to N^5. According to our mesh generator program, the maximum nonzero components of one column or row is expected to be 19 considering the symmetry of the matrix; therefore, the minimum size of memory to store the matrix is about $19 \times N^3$, which line is also indicated in this figure. At present, we are developing a computer code based on some iteration methods which can take advantage of this storage property.[5]

References

1) M. Hara, T. Wada, A. Toyama, and F. Kikuchi: *Sci. Papers I.P.C.R.*, **75**, 143 (1981).
2) M. Hara, T. Wada, T. Fukasawa, and F. Kikuchi: *IEEE Trans. Mag.*, **19**, 2417 (1983).
3) M. Hara, T. Wada, K. Mitomori, and F. Kikuchi: Proc. 11th Int. Conf. Cyclotrons and Their Applications, Tokyo, Oct. (1986).
4) F. Kikuchi: "A finite element method for 3-D analysis of cavity resonators," in preparation.
5) Y. Iwashita: private communications.

RIKEN Accel. Prog. Rep. 20 (1986)

VI. RADIATION MONITORING

1. Calculation of Neutron Skyshine over the Area around RIKEN Ring Cyclotron Facility

T. Shikata, N. Nakanishi, S. Fujita, H. Kamitsubo, and T. Kosako*

We have previously estimated the dose rate due to skyshine.[1,2] Recently, importance functions for neutron skyshine have been calculated by Hayashi and Nakamura[3] and Alsmiller[4] for a point source location at 15 m in height and by Hayashi and Nakamura[5] at 0 m in height, for energies up to 400 MeV and various source-to-field point distances. In these calculations the importance functions are presented for several $\cos\theta_s$ intervals in the upper hemisphere; the emission angle, θ_s, is shown in Fig. 1, and the source is assumed to be independent of the azimuthal angle. This report describes more precise recalculation using the importance functions of the neutron dose due to the skyshine over the area around RIKEN Ring Cyclotron facilities. We calculated the source neutron fluxes traversing through a roof using the one-dimensional discrete ordinate code ANISN and the neutronphoton multigroup cross section library DLC87/HILO for neutron energies from thermal to 400 MeV and photon energies from 10 keV to 14 MeV.

RIKEN Ring Cyclotron facilities are built on the slope: the level of the air-ground interface lies above the roof of the experimental hall at one side of the vault and below the roof at the other side. Thus, we have calculated the dose rates for both source locations at 15 m and 0 m in height. Neutrons emitted by reactions ^{12}C(135 MeV/u, $6\cdot10^{12}$ pps) and ^{12}C(75 MeV/u, $6\cdot10^{12}$ pps) on a ^{56}Fe thick target were selected as sources; the spectrum of the former is given in Ref. 1, and that of the latter is in Ref. 6. Energies of carbon ions of 135 MeV/u and 75 MeV/u correspond to the highest ones, when carbon ions are accelerated with the future AVF cyclotron and with RILAC as injectors, respectively. These spectra show many energetic neutrons not only in the forward direction to the beam direction but in the sideward direction compared with other available spectra calculated in nuclear reactions with light projectiles.[7,8]

In the calculation, neutrons ejected from the target into a cone having a half apex angle of 60 degree were taken as an original source, and a given effective thickness of the roof was assumed. Next we made following simplifications in calculating the dose rate: the neutrons escaped from the whole surface of the roof were replaced by those emitted isotropically from a point source giving an equivalent integral flux; importance functions for any θ_s were substituted by those for a cosine interval, $0.2 < \cos\theta_s < 0.4$. According to the calculated results

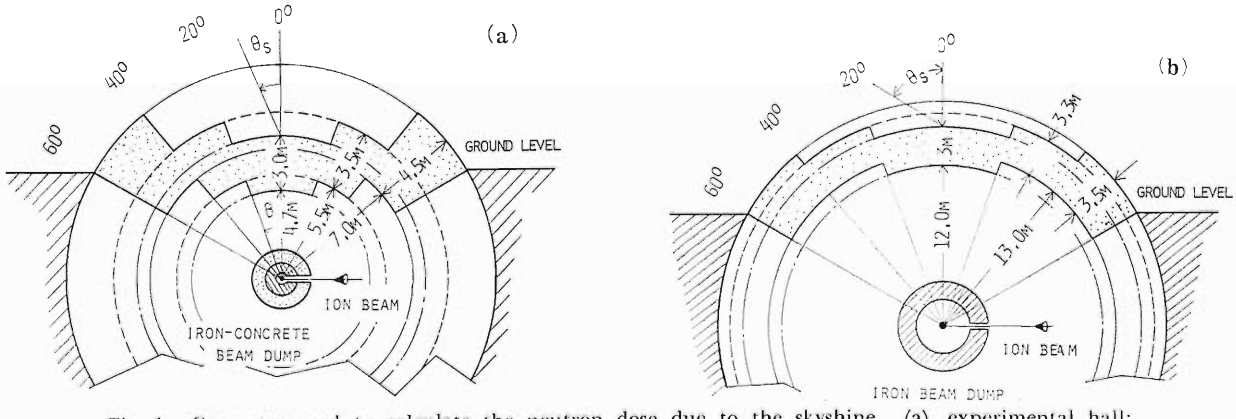

Fig. 1. Geometry used to calculate the neutron dose due to the skyshine. (a) experimental hall; (b) the cyclotron vault.

* Research Center for Nuclear Science and Technology, The University of Tokyo.

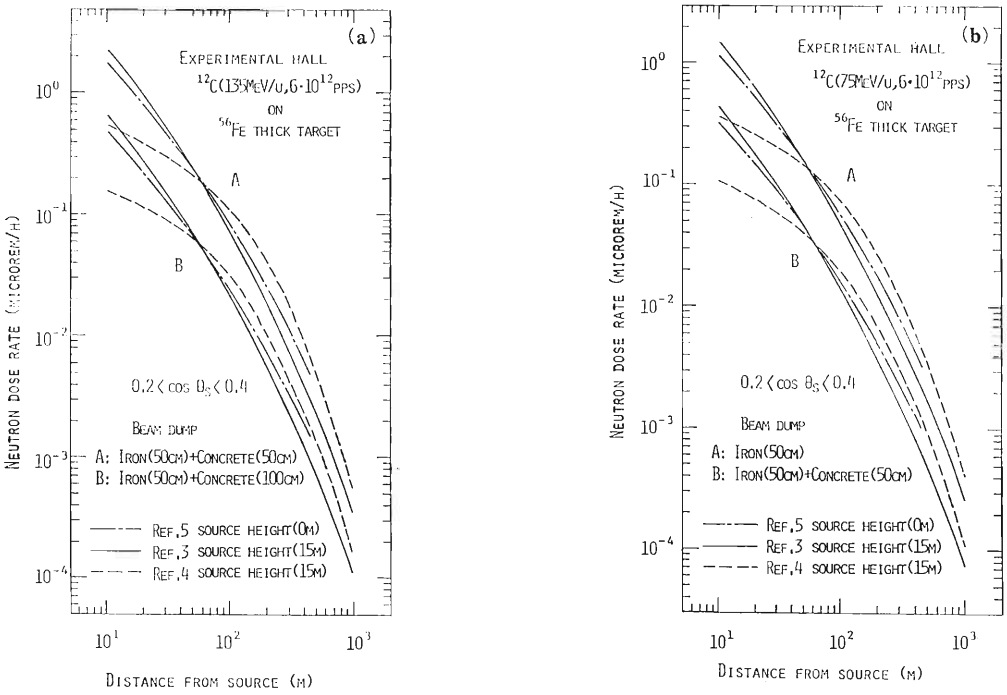

Fig. 2. Dose rate due to the neutron skyshine over the area around an experimental hall. (a) ^{12}C (135 MeV/u, 6·10^{12} pps) on a ^{56}Fe thick target; (b) ^{12}C (75 MeV/u, 6·10^{12} pps) on a ^{56}Fe thick target.

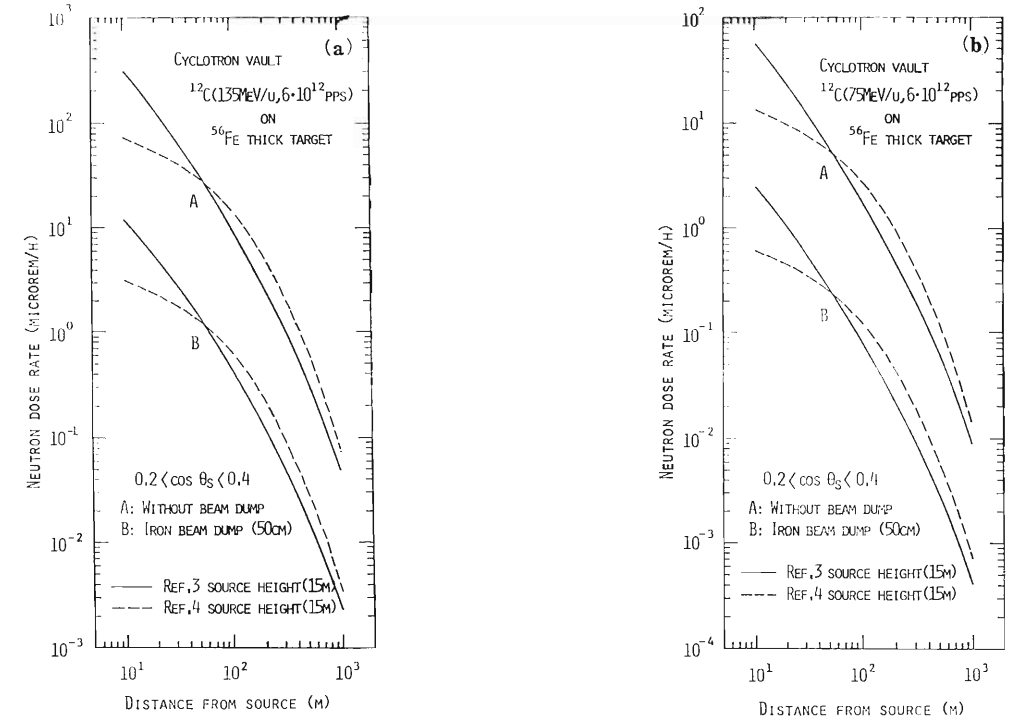

Fig. 3. Dose rate due to the neutron skyshine over the area around the cyclotron vault. (a) ^{12}C (135 MeV/u, 6·10^{12} pps) on a ^{56}Fe thick target; (b) ^{12}C (75 MeV/u, 6·10^{12} pps) on a ^{56}Fe thick target.

given in Refs. 3, 4, and 5, the importance functions at a given distance not very far from the source increases with θ_s. The functions for the above interval are somewhat larger than those averaged over all cosine intervals. Thus the dose rates obtained will be of safety side. The geometry for the calculation and the results are shown in Figs. 1, 2, and 3. Figures 2 and 3 indicate that the source height

dependency of the calculated doses is rather small and may be applied to other vertical source locations not markedly different from those used here. Finally, it should be emphasized that the beam loss in the cyclotron vault will be about one tenth of the total beam, and ions will not always be accelerated with full power of the accelerators.

References

1) S. Fujita, S. Yamaji, and T. Shikata: *I.P.C.R. Cyclotron Prog. Rep.*, **14**, 203 (1980).
2) T. Shikata, T. Kosako, S. Fujita, S. Yamaji, and H. Kamitsubo: *Sci. Papers I.P.C.R.*, **77**, 99 (1983).
3) K. Hayashi and T. Nakamura: *Nucl. Sci. Eng.*, **91**, 332 (1985).
4) R. G. Alsmiller, Jr., J. Barish, and R. L. Childs: ORNL/TM-7512 (1980).
5) K. Hayashi and T. Nakamura: Private communication.
6) T. Nakamura: INS-NUMA-5 (1977).
7) T. A. Gabriel, R. T. Santro, H. W. Bertini, and N. M. Larson: ORNL-TM-4334 (1973).
8) R. G. Alsmiller: Cited in the report of H. A. Smith, Jr. (*IUCF Internal Rep.*, No. 74–6).

RIKEN Accel. Prog. Rep. 20 (1986)

VI-2. Radiation Safety Control System for RIKEN Ring Cyclotron

I. Sakamoto, S. Fujita, T. Wada, and H. Takebe

A Radiation Safety Control System (RSCS) consists of a radiation monitoring system and a radiation protection control system. Figure 1 shows a block diagram of the RSCS. A large number of devices for the RSCS are distributed in RIKEN Ring Cyclotron building. Since there are more than two hundred parameters and intricated control sequences for operating the RSCS, a computer control system is introduced: the host computer is a MITSUBISHI MX-3000.

(1) Radiation monitoring system

Four monitoring posts at the boundary of the Accelerator Facility and one in the control room have been installed to measure the leakage-radiation during operation of RIKEN Ring Cyclotron. A NaI(Tl) scintillation detector and a helium-3 counter are placed in each post to detect environmental γ-rays and neutrons, respectively, besides, eleven ionization chambers and eight BF_3 counters are used to measure the radiation level at RIKEN Ring Cyclotron vault and the experimental rooms.

In order to measure the radioactivity in drain water and in the air of the experimental rooms and at the exit of the exhaust duct, three activity monitoring stations have been built in RIKEN Ring Cyclotron building. The radioactivity in the drain water is measured with a NaI(Tl) and plastic scintillation detector. The radioactivity in the air (gases and airborne dust) is measured with a NaI(Tl), ZnS(Ag), and plastic scintillation detector. All the data coming from monitors are logged periodically by the MX-3000 and stored in diskfiles; the MX-3000 can draw a graph by using those data.

We succeeded in extracting a 21 MeV/u 12^+ argon beam from RIKEN Ring Cyclotron on December 16, 1986, and transported the beam on the target at the E1 experimental room on December 20. The beam intensity was 30–100 nA.

Leakage-radiation during operation of RIKEN Ring Cyclotron has been measured inside and outside RIKEN Ring Cyclotron building. Figure 2 shows an example of the intensity increase when the Ar beam was accelerated. No leakage γ-rays and neutrons from RIKEN Ring Cyclotron building was detected.

(2) Radiation protection control system

The radiation protection control system consists of card-operated gate-bars, safety keys, operation status lamps, radiation level indicators, shield doors, hand-foot-clothes monitors, and rotary shutters.

The entrance to and exit from the controlled area are checked very strictly by a personal card. At the entrance of each experimental room the radiation level inside the room is displayed on the radiation

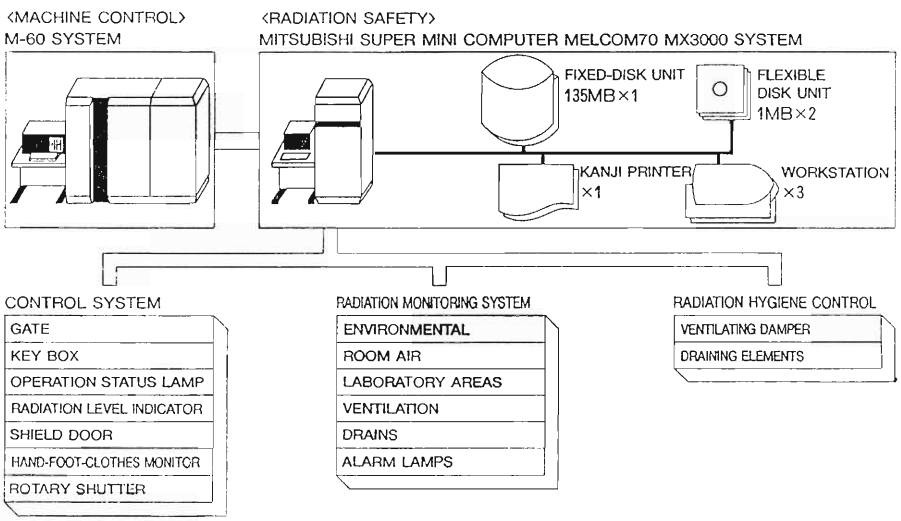

Fig. 1. Block diagram of the Radiation safety control system for RIKEN Ring Cyclotron.

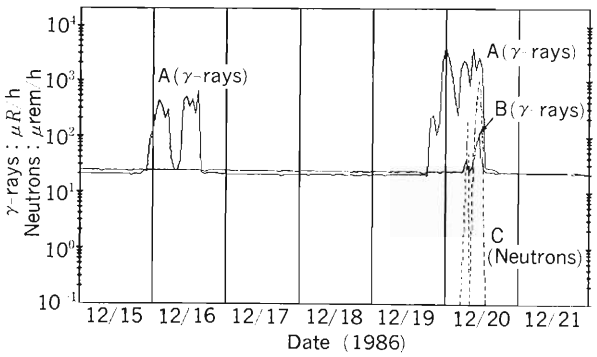

Fig. 2. Comparison of day variations of the radiation level measured with radiation monitors in RIKEN Ring Cyclotron vault and the E1 experimental room. A, an ionization chamber in the ring cyclotron vault; B, an ionization chamber in the E1 experimental room; and C, a BF_3 counter in the E1 experimental room.

level indicators, by indicating each level with Green, Yellow, or Red. The operation conditions of RILAC, the AVF cyclotron, and RIKEN Ring Cyclotron are also displayed on the operation status lamps.

RIKEN Ring Cyclotron is controlled with a computer system,[1] consisting of a MITSUBISHI M-60, which is linked with the MX-3000 of the RSCS. For radiation safety, the MX-3000 has the highest priority in accelerator operation. Before starting operation, an operator should ask the MX-3000 for permission. If any erratic conditions occur in the RSCS during operation, the MX-3000 sends a beam-stop command.

The MX-3000 permits RIKEN Ring Cyclotron operation, when

(a) No person is in RIKEN Ring Cyclotron vault and experimental room where beams will be used;

(b) The shield doors are closed in RIKEN Ring Cyclotron vault and in the experimental room where beams will be used;

(c) The rotary shutters are open in the beam course where the beam will be used; But other rotary shutters are closed.

Persons are not permitted to enter the relevant vault or rooms, when

(d) RIKEN Ring Cyclotron is in operation;

(e) Beams are being handled in the experimental room;

(f) The radiation level of the experimental room is Red level, or the radioactivity in the air of the room is at high level.

(3) Display on CRT terminal

The radiation level of each experimental room is also indicated with color, Green, Yellow, or Red, which is displayed on three Cathode Ray Tube (CRT) terminals together with the number of persons working in this area. The status of safety keys, RILAC operation, AVF cyclotron operation, RIKEN Ring Cyclotron operation, shield doors, rotary shutters, and ventilating damper are also displayed on these CRT terminals, which are placed on the RSCS control desk, RIKEN Ring Cyclotron operation desk, and the underground passage.

Reference

1) T. Wada, H. Takebe, J. Fujita, T. Kambara, and H. Kamitsubo: p. 170 in this report.

RIKEN Accel. Prog. Rep. 20 (1986)

VI-3. Routine Monitoring of RIKEN Accelerators

I. Sakamoto, S. Fujita, M. Yanokura, T. Kobayashi, O. Kurihara, and I. Kohno

The present report describes the results of routine radiation monitoring carried out for the cyclotron, RILAC, and TANDETRON from April 1985 to March 1986. Aspects of the leakage radiation from the cyclotron are described in a succeeding report.

(1) Residual activities of the cyclotron

In January 1986 the dose rates due to residual activities of the machine were measured 17 days after shutdown. The results are shown in Table 1.

The external exposure doses for two workers during replacement of the septum were 6 and 10 mrem.

(2) Surface and air contaminations in the cyclotron building

The surface contamination has been kept below 10^{-5} μCi/cm^2 on the floors of the cyclotron vault, the underground passage, and the experimental areas, and below 10^{-4} μCi/cm^2 on the floors of the hot laboratory and chemical laboratories. The radioactive nuclides found by γ-ray spectrometry were ^{65}Zn and ^{58}Co in the cyclotron vault and the experimental areas, and ^{137}Cs and ^{210}Pb in the hot laboratory and chemical laboratories. The contamination was wiped off twice a year and immediately after this decontamination; thus, the activities on the floor of the most of above places were reduced below 10^{-7} μCi/cm^2.

Table 1. Dose rates of residual activities.

Location	Dose rate (mR/h)
ca. 25 cm apart from septum (before replacement of septum)	100
ca. 20 cm apart from septum holder (after replacement of septum)	100

When radioactive substances were handled in the hot laboratory and chemical laboratories, the air in the draft chamber was activated. The air in the draft chamber was exhausted; the radioactivity in the exit was below 10^{-12} μCi/cm^3.

(3) Drainage

The radioactivities in drain water from the cyclotron and the linac building were found to be of the order of 10^{-8}–10^{-5} μCi/cm^3. The total activity in aqueous effluents was about 200 μCi, and the nuclides found by γ-ray spectrometry were ^{75}Se, ^{77}Br, and ^{137}Cs.

(4) Radiation monitoring for RILAC and TANDETRON

The leakage radiation during operation of the RILAC was measured in the circumference of the linac building every month. No leakage of γ-rays and neutrons from the linac building was detected. No contamination of the surface and air due to residual activities was found in the control area in

Table 2. Annual exposure doses received by RIKEN accelerator workers from April 1985 to March 1986.

Workers	Number of persons				Collective dose (man-mrem)
	Dose undetectable	10–100 (mrem)	>100 (mrem)	Total	
Cyclotron operation and maintenance group	8	0	0	8	0
Linac operation and maintenance group	10	0	0	10	0
Nuclear physicists	9	1	0	10	10
Accelerator physicists	11	1	0	12	50
Physicists in other fields	26	1	0	27	100
Nuclear chemists	2	6	1	9	780
Radiation chemists	2	0	0	2	0
Biological chemists	5	1	0	6	10
TANDETRON workers	9	0	0	9	0
Health physicists	6	0	0	6	0
Total	88	10	1	99	950

Average annual dose per person: 9.6 mrem
Maximum individual annual dose: 370 mrem

the linac building.

X-ray monitoring was carried out for the TANDETRON when boron ions were accelerated. When a vanadium target was bombarded with 2.0 MeV B^{2+} ions at 1 nA, the maximum irradiation dose rates measured around TANDETRON was 0.7 mR/h. No leakage X-rays was detected around the target chamber and outside the TANDETRON room.

(5) Personnel monitoring

The external exposure doses to personnel were measured by using γ-ray and neutron film badges. The doses received by accelerator workers during the present period are shown in Table 2. The collective γ-rays dose to all workers was 950 man-mrem, while the collective dose owing to thermal and fast neutron exposures was too small to be detected. The collective dose to the workers was about 52% of the value in the preceding period.

In this period the average annual dose per person was 9.6 mrem, and the maximum individual annual dose was 370 mrem.

RIKEN Accel. Prog. Rep. 20 (1986)

VI-4. Leakage-Radiation Measurement in the Cyclotron Building

I. Sakamoto, S. Fujita, and I. Kohno

In May 1985 the leakage radiation was measured at various points in the cyclotron building, when a tin target placed in the beam course No. 2 was bombarded with helium ions at a beam intensity of 12–14 μA.

The γ-ray dose rate was measured with an ionization chamber survey meter, and the dose equivalent rate for fast neutron and slow neutron was measured with a "rem meter."* The results are shown in Fig. 1.

The leakage dose measured from April 1985 to March 1986 with γ-ray and neutron film badges placed at two positions on the underground passage (points A and B in Fig. 1) are shown in Table 1.

Of the dose values at point A measured every month, the maximum total dose of 1,120 mrem was observed in May, when the values for γ-rays and thermal neutron and fast neutrons were 580, 70, and 470 mrem, respectively.

The fast neutron doses observed at point A in May and June, 470 mrem and 310 mrem, were larger than those in other months. These results let us to conclude that the increase in the neutron dose was mainly due to activation analysis and radioisotope production.

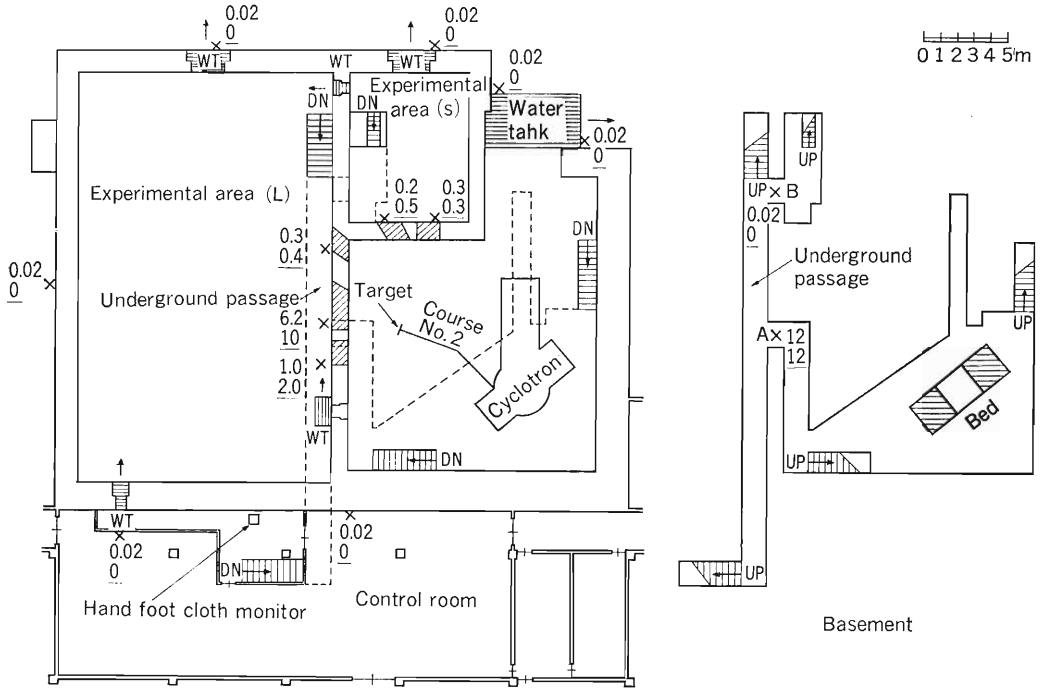

Fig. 1. Leakage-radiation (neutrons and γ-rays) in the cyclotron building.

Operating conditions		Dose unit	
E_α	: 40 MeV	γ-ray	: mR/h
Beam course	: No. 2	Neutron	: mrem/h (under line)
Target	: Sn		

Those data include 0.02 mR/h background radiation; Measured on May 1985.

* A Neutron Dose Rate Meter 2202, manufactured by AB Atomenergi, Sweden.

Table 1. Leakage-radiation dose (in mrem) in the underground passage of the cyclotron building from April 1985 to March 1986.

Month	Point A*				Point B*			
	γ-Rays (mrem)	Thermal neutrons (mrem)	Fast neutrons (mrem)	Total (mrem)	γ-Rays (mrem)	Thermal neutrons (mrem)	Fast neutrons (mrem)	Total (mrem)
4,85'	380	30	140	550	10	0	20	30
5	580	70	470	1,120	10	0	30	40
6	540	70	310	920	0	0	10	10
7	110	10	20	140	0	0	0	0
8	0	0	0	0	0	0	0	0
9	60	10	20	90	0	0	10	10
10	190	10	70	270	0	0	0	0
11	250	30	150	430	0	0	20	20
12	120	10	70	200	0	0	10	10
1,86'	0	0	0	0	0	0	0	0
2	200	30	80	310	0	0	20	20
3	210	20	160	390	0	0	0	0
Total	2,640	290	1,490	4,420	20	0	120	140

* See Fig. 1.

RIKEN Accel. Prog. Rep. 20 (1986)

VI-5. Calculation for the Design of an Iron Beam Dump for Shielding of Neutrons

N. Nakanishi, T. Shikata, S. Fujita, and T. Kosako*

Among radiations produced by the accelerator in a few hundreds of million electron volts per nucleon energy range, the most penetrating component is the high-energy neutron flux. In this energy range, the effect of capture-γ-rays generated in the shield on the dose equivalent is relatively small. Therefore, we have primarily focused our study on the neutron shielding.

We have previously obtained a design chart for determination of the thickness of shielding materials based on a two-layer slab model.[1] This chart enables us to determine the thicknesses of a concrete wall of the building and a local shield simultaneously and easily, at any arbitrary thickness ratio.

In the present report, similar charts for designing an iron beam dump obtained by using a concentric spherical shell model are given. In the calculation of the neutron dose at a point on the surface of a concrete wall, say, point B shown in Fig. 1(a), this configuration was represented by a model consisting of concentric spheres radii of which were taken to be the distances from the point neutron source to the interfaces of media in a specified direction (point B) as illustrated in Fig. 1(b). The dose rates on the outer surface (point B) were then calculated as a function of the thickness of a concrete shell, with a radius of an iron sphere taken as a parameter.

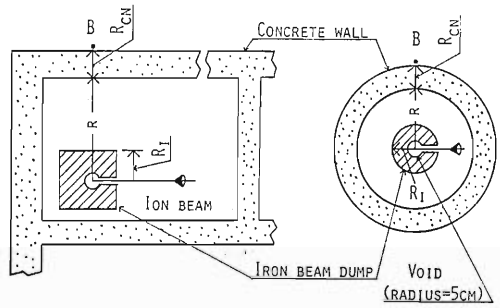

Fig. 1. Model for the calculation of doses.

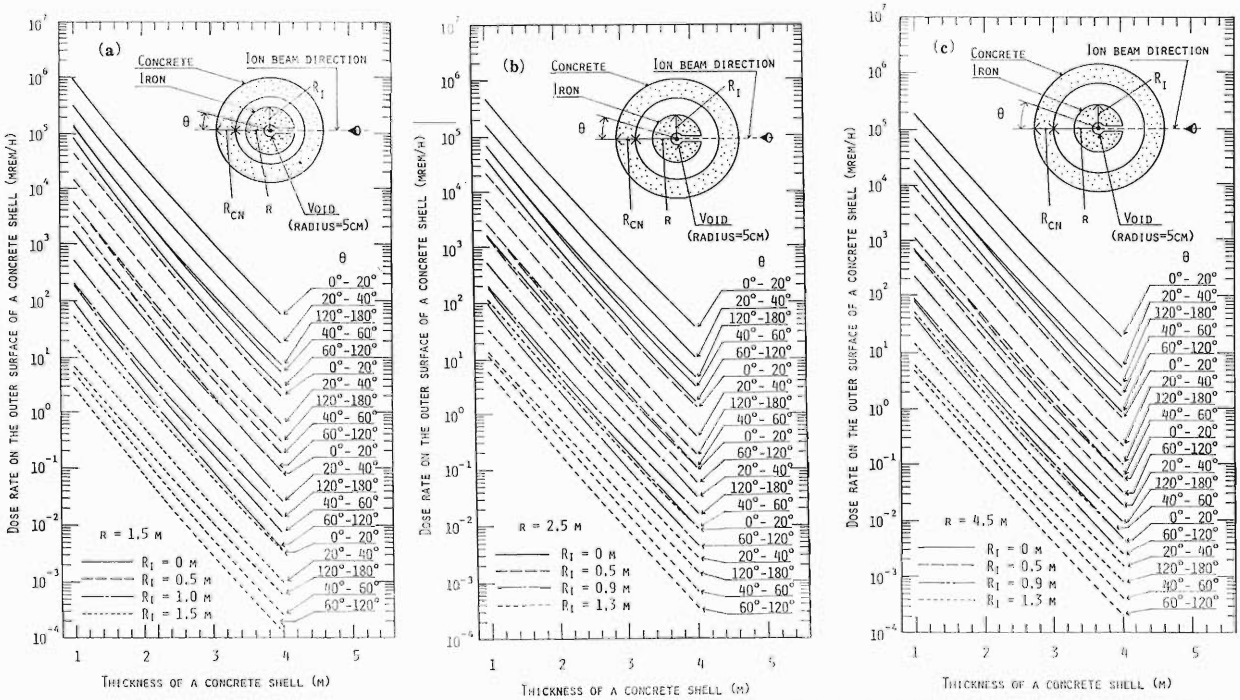

Fig. 2. Design charts. Dose rates on the outer surface of a concrete wall as a function of R_{CN}, with R_I taken as a parameter; θ stands for a specified angular interval of interest.

* Research Center for Nuclear Science and Technology, The University of Tokyo.

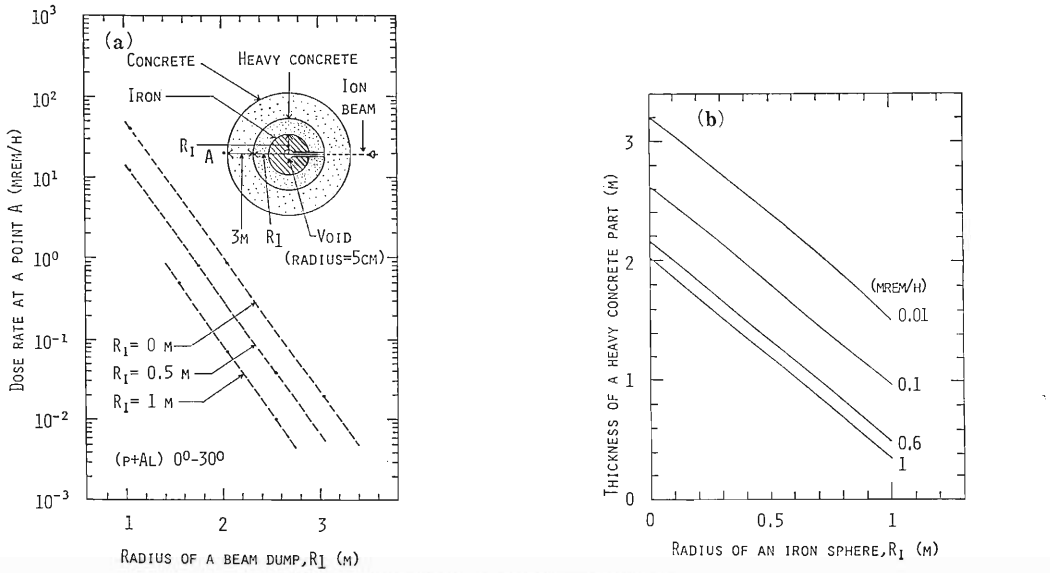

Fig. 3. The corrected Fig. 2 in Ref. 2.

The computer code and the cross section library used in the calculation are the one-dimensional discrete ordinate code ANISN and DLC-87/HILO, respectively. Neutrons were assumed to be emitted by a reaction of ^{12}C(135 MeV/u, $6 \cdot 10^{12}$ pps) on a ^{56}Fe thick target.[2] In the transport calculation using the ANISN code of the spherical geometry having the source neutron at the center, the source should be isotropic. In the present case, however, we applied the ANISN code to a source having angular dependence and, in order to calculate the approximate dose rate in θ direction to the incident ion beam, we used an isotropic source, which intensity per unit solid angle per a given energy interval was equal to that of the assumed source in the same θ direction. Results of the calculation for average dose rates on given θ intervals are shown in Fig. 2. We can simultaneously determine R_{CN} and R_I, which yield a tolerance dose rate at the surface of a concrete wall in a specified direction θ to the ion beam, at any arbitrary ratio (R_{CN}/R_I) at a given R from Fig. 2.

When the thickness of a wall is given, a similar chart can be obtained easily for a composit beam dump; for instance, an iron-heavy concrete one. In a previous report,[3] the design charts for this case were given; however, we found errors in Fig. 2 in Ref. 3 and gave the corrected one in the present report as Fig. 3.

References

1) T. Shikata, N. Nakanishi, S. Fujita, and T. Kosako: *RIKEN Accel. Prog. Rep.*, **19**, 218 (1985).
2) S. Fujita, S. Yamaji, and T. Shikata: *IPCR Cyclotron Prog. Rep.*, **14**, 203 (1980).
3) N. Nakanishi, T. Shikata, S. Fujita, and T. Kosako: *RIKEN Accel. Prog. Rep.*, **18**, 194 (1984).

VII. LIST OF PUBLICATIONS

1. Accelerator development and accelerator physics
   1) S. Ishii, H. Amemiya, and M. Yanokura: "An Optimum Condition of Multipole Field for an ECR-Type Ion Source," *Jpn. J. Appl. Phys.*, **25**, 712 (1986).
   2) F. Kikuchi: "An Isomorphic Property of two Hilbert Spaces Appearing in Electromagnetism: Analysis by the Mixed Formulation," *Jpn. J. Appl. Math.*, **3**, 53 (1986).
   3) S. Kaizu and F. Kikuchi: "An Imbedding Theorem for a Hilbert Space Appearing in Electromagnetics," *Sci. Pap. Coll. Arts Sci. Univ. Tokyo*, **36**, 81 (1986).

2. Nuclear physics and nuclear instrumentation
   1) N. Yoshinaga: "Intrinsic States in the sdg Interacting Boson Model," *Nucl. Phys. A*, **456**, 21 (1986).
   2) S. Kubono, K. Morita, M. H. Tanaka, A. Sakaguchi, and M. Sugitani: "Highly Excited High Spin States in ^{28}Si Populated through the ^{12}C(^{20}Ne) Reaction," *Nucl. Phys. A*, **457**, 461 (1986).
   3) Y. Gono, T. Kohno, M. Sugawara, Y. Ishikawa, and M. Fukuda: "Collective Vibrations in ^{218}Ra," *Nucl. Phys. A*, **459**, 427 (1986).
   4) S. Suzuki, T. Doke, A. Hitachi, A. Yunoki, K. Masuda, and T. Takahashi: "Photoionization Effect in Liquid Xenon Doped with Triethylamine (TEA) or Trimethylamine (TMA)," *Nucl. Instrum. Methods A*, **245**, 78 (1986).
   5) S. Kubono, M. H. Tanaka, H. Kawakami, K. Sueki, H. Miyatake, T. Nomura, K. Morita, M. Ishihara, S. Kato, C. Konno, and A. Sakaguchi: "High-Energy Gamma Ray Spectrometer for Heavy-Ion Induced Experiments," *Nucl. Instrum. Methods A*, **251**, 74 (1986).
   6) T. Murakami, J. Kasagi, H. Tachibanaki, K. Yoshida, Y. Shibata, T. Nakagawa, M. Ogihara, S. M. Lee, T. Kubo, and T. Motobayashi: "Properties of BaF_2 Scintillators in Charged Particle Detection," *Nucl. Instrum. Methods A*, **253**, 163 (1986).
   7) T. Otsuka and N. Yoshinaga: "Fermion-Boson Mapping for Deformed Nuclei," *Phys. Lett. B*, **168**, 1 (1986).
   8) A. Akiyama, K. Heyde, A. Arima, and N. Yoshinaga: "The Structure of the ^{168}Er Nucleus and the ^{160}Er(t, p)^{168}Er Reaction in Terms of the sdg Interacting Boson Model," *Phys. Lett. B*, **173**, 1 (1986).
   9) J. Kasagi, H. Harada, T. Murakami, K. Yoshida, H. Tachibanaki, and T. Inamura: "Enhanced E2 transitions between 9^- and 8^- States in ^{110}Sn and ^{112}Sn," *Phys. Lett. B*, **176**, 307 (1986).
   10) H. Sakai, N. Matsuoka, T. Saito, A. Shimizu, M. Tosaki, M. Ieiri, K. Imai, A. Sakaguchi, and T. Motobayashi: "Measurements of $K_y{}^y$ at 0° for the ^{2}H($\vec{p}$, $\vec{n}$)2p Reaction at 50, 65, and 80 MeV," *Phys. Lett. B*, **177**, 155 (1986).
   11) Y. Nagashima, J. Schimizu, T. Nakagawa, Y. Fukuchi, W. Yokota, K. Furuno, M. Yamanouchi, S. M. Lee, N. X. Dai, T. Mikumo, and T. Motobayashi: "Effects of Entrance Channel and Compound Nucleus in the Fusion Cross Sections for ^{28}Si+^{28}Si, ^{16}O+^{40}Ca, ^{32}S+^{30}Si, and ^{12}C+^{50}Cr," *Phys. Rev. C*, **33**, 176 (1986).
   12) T. Kohno, M. Adachi, S. Fukuda, M. Taya, M. Fukuda, H. Taketani, Y. Gono, M. Sugawara, and Y. Ishikawa: "Level Structure and Electromagnetic Properties in ^{212}Ra," *Phys. Rev. C*, **33**, 392 (1986).
   13) S. Kubono, K. Morita, M. H. Tanaka, A. Sakaguchi, and M. Sugitani: "$g_{9/2}$ Single Particle State in ^{28}Si," *Phys. Rev. C*, **33**, 1524 (1986).
   14) K. H. Tanaka, Y. Nojiri, T. Minamisono, K. Asahi, and N. Takahashi: "Polarization of ^{12}B Produced in ^{14}N-Induced Reactions," *Phys. Rev. C*, **34**, 580 (1986).
   15) T. Motobayashi, H. Sakai, N. Matsuoka, T. Saito, K. Hosono, A. Okihana, M. Ishihara, S. Shimoura, and A. Sakaguchi: "Analyzing Power Measurements of (d, ^{2}He) Reactions on Light Nuclei," *Phys. Rev. C*, **34**, 2365 (1986).
   16) A. Sakaguchi, K. Nagatani, M. Torikoshi, S. I. Hayakawa, T. Motobayashi, O. Satoh, T. Yamaya, M. Fujiwara, N. Matsuoka, and H. Sakai: "Spectroscopy with the Singlet-Deuteron Reaction ^{12}C(α, $d_{s=0}$)^{14}N at 50 MeV," *Phys. Rev. Lett.*, **56**, 1112 (1986).
   17) N. Yoshinaga, A. Akiyama, and A. Arima: "The sdg Interacting Boson Model Applied to ^{168}Er," *Phys. Rev. Lett.*, **56**, 1116 (1986).
   18) S. Kubota, T. Motobayashi, J. Ruan, F. Shiraishi, and Y. Takami: "A New Barium-Fluoride Plastic Scintillator," *IEEE Trans. Nucl. Sci.*, **33**, 370 (1986).

19) K. Ikeda, S. Yoshida, and S. Yamaji: "Application of Time-Dependent Mean-Field Theory to Heavy Ion Collisions: Simple Example of an S-Matrix Calculation for Elastic Scattering," *Z. Phys. A-Atomic Nuclei*, **323**, 285 (1986).
20) Y. Nojiri, K. Takeyama, K. Matsuta, K. Asahi, and T. Minamisono: "Nuclear Polarization Production by the Tilted Foil Technique and Its Application," *J. Phys. Soc. Jpn.*, **55**, Suppl., 391 (1986).
21) K. H. Tanaka, Y. Nojiri, T. Minamisono, K. Asahi, and N. Takahashi: "Study of ^{12}B Polarization in ^{14}N-Induced Reactions," *J. Phys. Soc. Jpn.*, **55**, Suppl., 790 (1986).
22) K. Asahi, M. Ishihara, T. Shimoda, T. Fukuda, N. Takahashi, K. Katori, S. Shimoura, N. Ikeda, C. Konno, H. Hanakawa, A. Nakamura, T. Itahashi, Y. Nojiri, and T. Minamisono: "Beta Decay of Polarized Nucleus ^{15}C Produced in Heavy-Ion Reaction," *J. Phys. Soc. Jpn.*, **55**, Suppl., 1032 (1986).
23) Y. Nojiri, K. Takeyama, K. Matsuta, K. Asahi, and T. Minamisono: "Nuclear Polarization of Short-Lived β Emitters ^{8}Li, ^{12}B, and ^{27}Si Created by the Tilted Foil Technique," *J. Phys. Soc. Jpn.*, **55**, Suppl., 1086 (1986).
24) H. Ohsumi, M. Ishihara, S. Kohmoto, K. Asahi, K. Sugimoto, T. Tanabe, T. Hattori, and K. Haga: "Nuclear Spin Polarization of ^{27}Al Produced by Tilted-Foil Method and Determination of the Polarization by Coulomb Excitation," *J. Phy. Soc. Jpn.*, **55**, Suppl., 1088 (1986).
25) T. Inamura: "Massive Transfer in Heavy Ion Reactions," Heavy Ions in Nuclear Physics, Hardwood Academic Publishers, New York, p. 1 (1986).
26) Y. Ishibe, H. Oyama, K. Okazaki, K. Yano, Y. Sakamoto, N. Noda, and Y. Hori: "Carbon Coating by ECR Plasma," *J. Vac. Soc. Jpn.* (in Japanese), **29**, 385 (1986).
27) A. Yunoki, K. Masuda, J. Kikuchi, T. Takahashi, and T. Doke: "Measurement of α-β Ratio in Scintillation from Liquid Argon," *Bull. Sci. Eng. Lab. Waseda Univ.*, **113**, 54 (1986).
28) H. Kumagai, T. Takahashi, T. Kubo, and M. Ishihara: "Parallel Plate Avalanche Counter for Heavy-Ion Dosimetry," *Hoshasen* (in Japanese), **12**, 38 (1986).
29) H. Kumagai, M. Sasagase, and T. Wada: "An On-Line Data Acquisition System at RILAC," *Reports I.P.C.R.* (in Japanese), **62**, 114 (1986).
30) K. Asahi: "On-Line Isotope Separator Project at RIKEN," *Genshikaku Kenkyu* (in Japanese), **31**, 69 (1986).

3. Atomic and solid-state physics

1) S. Hara, H. Sato, S. Ogata, and N. Tamba: "Vibrationally and Rotationally Resolved Cross Sections and Angular Distributions of Photoelectrons from H_2," *J. Phys. B: At. Mol. Phys.*, **19**, 1177 (1986).
2) S. H. Be, T. Tonuma, H. Kumagai, H. Shibata, M. Kase, T. Kambara, I. Kohno, and H. Tawara: "Net Ionization Cross Sections of Rare Gases by Collisions of Fast Highly Charged Heavy Particles," *J. Phys. B: At. Mol. Phys.*, **19**, 1771 (1986).
3) H. Sato and S. Hara: "Theoretical Study of Autoionizing States of Molecules: II The $^1\Sigma_u^+$ and $^1\Pi_g$ States of H_2," *J. Phys. B: At. Mol. Phys.*, **19**, 2611 (1986).
4) S. Hara and M. Nakamura: "Determination of the Photo-Ionization Asymmetry Parameter," *J. Phys. B: At. Mol. Phys.*, **19**, L467 (1986).
5) I. Tanaka, S. Nasu, F. E. Fujita, F. Ambe, S. Ambe, and T. Okada: "^{119}Sb Mössbauer Study on Quenched-in Vacancies in Gold," *J. Phys. F: Met. Phys.*, **16**, L151 (1986).
6) E. Yagi, S. Nakamura, T. Kobayashi, F. Kano, K. Watanabe, Y. Fukai, and T. Osaka: "Lattice Location Study on H in Ta by the Channeling Method," *J. Phys. Soc. Jpn.*, **55**, 2671 (1986).
7) S. Hara, T. Ishihara, and N. Toshima: "Variational Calculation for Muonic Molecules," *J. Phys. Soc. Jpn.*, **55**, 3293 (1986).
8) K. Nagamine: "Recent Topics in Muon Spin Polarization Phenomena and μSR Experiments," *J. Phys. Soc. Jpn.*, **55**, Suppl., 402 (1986).
9) M. Uda, A. Koyama, Y. Sasa, and O. Benka: "Chemical Effects on Augar Spectra Induced by Fast Ions," *Nucl. Instrum. Methods B*, **13**, 196 (1986).
10) A. Koyama, O. Benka, Y. Sasa, and M. Uda: "Energy Spectra of Secondary Electrons from Al Induced by High Speed He^{2+} and Ar^{12+} Impact," *Nucl. Instrum. Methods B*, **13**, 637 (1986).
11) K. Nakanishi, K. Iguchi, A. Ohsaki, and T. Watanabe: "Classical-Trajectory Monte Carlo Calculations for Coulomb-Interacting Three-Body Systems," Atomic Collision Res. in Japan-Prog. Rep., No. 12, p. 6 (1986).
12) Q. Ma, X. Zhang, Y. Liu, and T. Watanabe: "Total and Differential Cross Sections for $(\mu^+\mu^-)$ Formation by Collisions of μ^+ with

(μ^-p) including Excited States in First Born Approximation," Atomic Collision Res. in Japan-Prog. Rep., No. 12, p. 8 (1986).
13) M. Iwai, I. Shimamura, and T. Watanabe: "Extended Bethe Surface: Behavior of the Generalized Oscillator Strength along Isoelectronic Sequence," Atomic Collision Res. in Japan-Prog. Rep., No. 12, p. 17 (1986).
14) S. Karashima, T. Watanabe, X. Zhang, Q. Ma, and Y. Liu: "Electron Stripping Cross Section of Multiply Charged Ions by Neutral Atoms," Atomic Collision Res. in Japan-Prog. Rep., No. 12, p. 32 (1986).
15) T. Mizogawa, Y. Awaya, T. Kambara, Y. Kanai, M. Kase, H. Kumagai, P. H. Mokler, and K. Shima: "Effect of L-Hole Population on K-Hole Formation Cross Section for Argon Ion Passing through thin Carbon Foil," Atomic Collision Res. in Japan-Prog. Rep., No. 12, p. 45 (1986).
16) Y. Awaya, T. Kambara, M. Kase, H. Kumagai, T. Mizogawa, Y. Kanai, and K. Shima: "A Broad Range Magnetic Charge Analyzer," Atomic Collision Res. in Japan-Prog. Rep., No. 12, p. 57 (1986).
17) K. Fujima, T. Watanabe, and K. Mima: "X-Ray Spectra Emitted from High Density and High Temperature Si," Atomic Collision Res. in Japan-Prog. Rep., No. 12, p. 126 (1986).
18) I. Shimamura and M. Iwai: "An R-Matrix Method for Wave Functions That Are Accurate Close to the Coordinate Origin," Atomic Collision Res. in Japan-Prog. Rep., No. 12, p. 151 (1986).
19) F. Ambe, K. Asai, S. Ambe, T. Okada, and H. Sekizawa: "Comparative Mössbauer and TDPAC Studies on the After-Effects of the EC Decays of ^{119}Sb and ^{111}In in α-Fe_2O_3," *Hyperfine Interact.*, **29**, 1197 (1986).
20) N. Sakai and H. Sekizawa: Observation of Mössbauer Spectrum without Utilizing Doppler Motion," *Hyperfine Interact.*, **29**, 1521 (1986).
21) M. Schmolz, K.-P. Döring, K. Fürderer, M. Gladisch, N. Haas, D. Herlach, G. Majer, J. Rosenkranz, W. Schäfer, L. Schimmele, W. Schwarz, A. Seeger, and E. Yagi: "Positive Muons in Iron: Dipolar Fields at Tetrahedral Sites and Jump Frequencies at Low Temperatures," *Hyperfine Interact.*, **31**, 199 (1986).
22) K. Nagamine and K. Ishida: "μSR in Polyacetylenes," *Hyperfine Interact.*, **32**, 535 (1986).
23) K. Nishiyama, K. Ishida, K. Nagamine, T. Matsuzaki, Y. Kuno, H. Shirakawa, R. Kiefl, and J. H. Brewer: "Precise Measurement of HFS Constant of the Muonium Substituted Radical in cis-Polyacetylene," *Hyperfine Interact.*, **32**, 551 (1986).
24) N. Toshima and T. Watanabe: "Simplified Distorted-Wave Treatment for Asymmetric Electron-Capture Processes," *Phys. Rev. A*, **33**, 1382 (1986).
25) H. Tawara, T. Tonuma, H. Shibata, M. Kase, T. Kambara, S. H. Be, H. Kumagai, and I. Kohno: "Production of Multiply Charged Molecular Ions (N_2^{12+}–N_2^{14+}) and Multiply Charged Atomic Ions (N^{6+}, N^{7+}) in Energetic, Heavy-Ion Impact on N_2 Molecules," *Phys. Rev. A*, **33**, 1385 (1986).
26) T. Tonuma, H. Shibata, S. H. Be, H. Kumagai, M. Kase, T. Kambara, I. Kohno, A. Ohsaki, and H. Tawara: "Production of Highly Charged Slow Ar Ions Recoiled in 1.05 MeV/amu Ne^{q+} (q=2, 7–10) and Ar^{q+} (q=4, 6, 10–14)-Ion Bombardment," *Phys. Rev. A*, **33**, 3047 (1986).
27) J. Kasagi, K. Yoshida, T. Murakami, and H. Harada: "Measurements of $K\alpha_2$ to $K\alpha_1$ Intensity Ratios for $62 \leqq Z \leqq 82$ by 3.5 MeV Proton Bombardment," *Phys. Rev. A*, **34**, 2480 (1986).
28) A. Koyama, O. Benka, Y. Sasa, and M. Uda: "Energy Spectra of Secondary Electrons from Al Induced by Heavy Ion Impact," *Phys. Rev. B*, **34**, 8150 (1986).
29) E. Yagi, T. Kobayashi, S. Nakamura, F. Kano, K. Watanabe, Y. Fukai, and S. Koike: "Direct Evidence of Stress-Induced Site Change of H in V Observed by the Channeling Method," *Phys. Rev. B*, **33**, 5121 (1986).
30) O. Benka and M. Uda: "Molecular-Orbital Model for the Chemical Effect on the *K*-X-Ray Spectrum of Fluorine," *Phys. Rev. Lett.*, **56**, 54 (1986).
31) A. P. Mills, Jr., J. Imazato, S. Saitoh, A. Uedono, Y. Kawashima, and K. Nagamine: "Generation of Thermal Muonium in Vacuum," *Phys. Rev. Lett.*, **56**, 1463 (1986).
32) O. Benka and M. Uda: "Resonant Electron-Transfer Relaxation Observed in Fluoring *K* Auger Spectra," *Phys. Rev. Lett.*, **56**, 1667 (1986).
33) Y. Awaya: "X-Ray Production in Heavy Ion-Atom Collisions," Proc. Symp. Region of Hybrid Studies and Nuclear Physics-RCNP-P-86, p. 126 (1986).
34) M. Uda: "Chemical Effects in Characteristic X-Rays Emitted from Multiply Ionized States," Atomic and Nuclear Heavy Ion Inter-

actions Brasov Int. School 1984, Central Institute of Physics Bucharest Romania, p. 293 (1986).
35) T. Minowa, H. Katsuragawa, A. Kawamura, and M. Shimazu: "Highly Sensitive Detection of Thallium Atoms Using Resonance Ionization," *Opt. Commun.*, **60**, 37 (1986).
36) H. Tawara, T. Tonuma, H. Shibata, S. H. Be, H. Kumagai, M. Kase, T. Kambara, and I. Kohno: "Multiply Charged Ions Produced from C_2H_2 and CH_4 Molecules in Energetic, Heavy Ion Impact," *Z. Phys. D, Atoms, Molecules and Clusters*, **2**, 239 (1986).
37) K. Takaishi, T. Kikuchi, K. Furuya, I. Hashimoto, H. Yamaguchi, E. Yagi, and M. Iwaki: "Thermal Extraction of Krypton in Aluminum Using Mass Spectrometer," *Phys. Status Solidi A*, **95**, 135 (1986).
38) T. Mizogawa, Y. Awaya, T. Kambara, Y. Kanai, M. Kase, H. Kumagai, P. H. Mokler, and K. Shima: "Target Thickness Dependence of Kα Satellite Intensities of Argon Ions Colliding with Thin Carbon Foils," Proc. Int. Semin. Dynamic Processes of Highly Charged Ions, p. 55 (1986).
39) A. Koyama: "Ion Induced Auger Electron Spectroscopy," Kotai Hyomen Biryo Bunseki (in Japanese), Keiei-Kaihatsu Center, Tokyo, p. 153 (1986).
40) M. Uda: "Fast Ion Induced X-Ray Spectroscopy," Kotai Hyomen Biryo Bunseki (in Japanese), Keiei Kaihatsu Center, Tokyo, p. 141 (1986).
41) K. Maeda: "PIXE (Ion Induced X-Ray Spectroscopy)," Kotai Hyomen Biryo Bunseki (in Japanese), Keiei Kaihatsu Center, Tokyo, p. 166 (1986).
42) A. Awaya: "Multiple Inner-Shell Ionization of Heavy Ions Passing through Foils," Atomic and Nuclear Heavy Ion Interactions (eds. Al. Berinde, I. A. Orobantu, and V. Zoran), Central Inst. Phys., Bucharest, Romania, Vol. 1, p. 241 (1986).
43) T. Watanabe: "Photo-Excitation, Photo-Ionization and Photo-Chemical Processes of Atoms and Molecules," Synchrotron Radiation (in Japanese), (ed. Phys. Soc. Jpn.), Baifu-kan Publish., Co., Tokyo, p. 183 (1986).
44) K. Nagamine: "New Movement of Solid State Physics Research Using Muons—Pulsed μSR—," *Kotaibuturi* (in Japanese), **21**, 125 (1986).
45) K. Nagamine and A. P. Mills, Jr.: "Thermal Muonium in Vacuum: Its Birth and Future," *Sci. Papers I.P.C.R.*, **80**, 67 (1986).
46) K. Nagamine and K. Ishida: "Material Synthesis and Nuclear/Muon Probes," *Sci. Papers I.P.C.R.*, **80**, 77 (1986).
47) A. Koyama, Y. Sasa, Y. Ishibe, A. Shiraishi, T. Shiga, H. Ohmori, M. Fuse, and M. Uda: "Construction of a UHV Apparatus for Spectroscopy of Ion-Induced Electrons from Solids," *Reports I.P.C.R.* (in Japanese), **62**, 218 (1986).
48) S. Karashima and T. Watanabe: "Stopping Power for Energetic Heavy Ions in a High Temperature Material," Proc. 2nd Int. Topical Symp. Inertial-Confinement Fusion Research by High Power Beams (ed. K. Yasui), Technol. Univ. Nagaoka, Nagaoka, p. 377 (1986).

4. Radiochemistry, radiation chemistry and radiation biology
1) K. Kimura: "Spectral Measurements along the Path of N Ions Impinged into Dense He Gas (400 Torr, 5.2 K). I. Emission Spectra and Decay Measurements," *J. Chem. Phys.*, **84**, 2002 (1986).
2) K. Kimura: "Spectral Measurements along the Path of N Ions Impinged into Dense Helium Gas (400 Torr and 5.2 K). II. Excimer Reactions Dependent on Stopping Power and Large Emission Yields near the Termination of the Track," *J. Chem. Phys.*, **84**, 2010 (1986).
3) K. Kimura: "Electronic Excitation at High-Density by Heavy-Ion Irradiation," *Radiat. Chem.* (in Japanese), **42**, 2 (1986).
4) T. Takahashi and S. Konno:: "W-Values and Fano Factors in Liquids and Gases—Mainly on Liquefied Rare Gases—," *Radiat. Chem.* (in Japanese), **42**, 21 (1986).
5) K. Kimura: "Clustering of Helium-Excimer under the High-Density Electronic Excitation by Heavy Ion Irradiation," *Ioniz. Radiat.* (in Japanese), **12**, No. 3, 32 (1986).
6) I. Kohno, M. Yanokura, S. Motonaga, H. Kamitsubo, M. Yatsuhashi, T. Suematsu, and H. Kobayashi: "Effects on the Fast Neutron Irradiation on Cable Materials," *IEEE Trans. Nucl. Sci.*, **NS-33**, Vol. 1, 77 (1986).
7) F. Ambe, S. Ambe, T. Okada, and H. Sekizawa: "*In Situ* Mössbauer Studies of Metal Oxide/Aqueous Solution Interfaces with Adsorbed Co-57 and Sb-119 Ions," Geochemical Processes at Mineral Surfaces, Am. Chem. Soc., Washington, D.C., p. 403 (1986).
8) T. Nozaki, Y. Itoh, T. Masui, and T. Abe: "Behavior of Oxygen in the Crystal Formation and Heat Treatment of Silicon Heavily Doped with Antimony," *Appl. Phys.*, **59**, 2562 (1986).

(Papers Presented at Meetings)

1. Accelerator development and accelerator physics
   1) F. Kikuchi: "Mixed and Penalty Formulation for an Eigenvalue Problem in Electromagnetics," Annu. Meeting Math. Soc. Jpn., Kyoto, Apr. (1986).
   2) F. Kikuchi: "Formulations and Finite Element Approximations for an Eigenvalue Problem in Electromagnetics," 15th Numerical Analysis Symp., Karuizawa, May (1986).
   3) S. Ishii, H. Amemiya, and M. Yanokura: "An Optimum Condition of Multipole Field for an ECR-Type Ion Source," 7th Workshop on ECR Ion Sources, Jülich, E. Germany, May (1986).
   4) F. Kikuchi, M. Hara, and T. Wada: "Weak Formulation for Finite Element Analysis of an Eigenvalue Problem in Electromagnetism," 10th Symp. Computational Methods in Structural Engineering and Related Fields, Tokyo, July (1986).
   5) F. Kikuchi: "Saddle Point Type Variational Principle and an Finite Element Approximations," Symp. Real Functions and Functional Analysis, Naruto, July (1986).
   6) F. Kikuchi, M. Hara, and T. Wada: "Mixed Finite Element Analysis of an Eigenvalue Problem in Electromagnetism," 7th Symp. Finite Element Methods in Flow Problems, Tokyo, Aug. (1986).
   7) M. Hara: "Principle of Synchrotron Radiation," Symp. Application of Synchrotron Radiation to Biology, Wako, Sept. (1980).
   8) F. Kikuchi: "Mixed and Penalty Formulations for Finite Element Analysis of an Eigenvalue Problem in Electromagnetism," 1st World Congr. Computational Mechanics, Austin, USA, Sept. (1986).
   9) T. Inamura: "RIKEN Accelerators and Their Experimental Programme," Int. School-Seminar on Nucl. Phys., Dubna, USSR, Sept. (1986).
   10) T. Fujisawa, K. Ogiwara, S. Kohara, Y. Oikawa, I. Yokoyama, M. Nagase, I. Takeshita, Y. Chiba, and Y. Kumata: "Radio Frequency System of the RIKEN Ring Cyclotron," 11th Int. Conf. Cyclotron and Their Applications, Tokyo, Oct. (1986).
   11) I. Kohno, K. Ogiwara, S. Fujita, K. Ikegami, T. Kageyama, S. Kohara, and H. Takebe, "RIKEN 160 cm Cyclotron," 11th Int. Conf. Cyclotron and Their Applications, Tokyo, Oct. (1986).
   12) N. Nakanishi, T. Kageyama, and H. Kamitsubo: "AVF-Cyclotron as an Injector for the RIKEN Ring Cyclotron," 11th Int. Conf. Cyclotron and Their Applications, Tokyo, Oct. (1986).
   13) T. Wada: "Control System of the RIKEN Ring Cyclotron," 11th Int. Conf. Cyclotron and Their Applications Tokyo, Oct. (1986).
   14) M. Kase, I. Yokoyama, I. Takeshita, Y. Oikawa, M. Saito, and Y. Yano: "Beam Diagnostic Equipments for RIKEN Ring Cyclotron and its Beam Lines," 11th Int. Conf. Cyclotron and Their Applications, Tokyo, Oct. (1986).
   15) A. Goto, H. Takebe, S. Motonaga, K. Hatanaka, Y. Yano, T. Wada, and N. Nakanishi: "Isochronous Fields for RIKEN Ring Cyclotron," 11th Int. Conf. Cyclotron and Their Applications, Tokyo, Oct. (1986).
   16) H. Kamitsubo: "Progress in RIKEN Ring Cyclotron Projects," 11th Int. Conf. Cyclotron and Their Applications, Tokyo, Oct. (1986).
   17) M. Hara, T. Wada, K. Mitomori, and F. Kikuchi: "Three Dimensional Analysis of RF Electromagnetic Field by the Finite Element Method," 11th Int. Conf. Cyclotron and Their Applications, Tokyo, Oct. (1986).
   18) M. Hara, T. Wada, K. Mitomori, and F. Kikuchi: "Three Dimensional Analysis of RF Electromagnetic Field by the Finite Element Method IV (Exotic Model)," Autumn Meeting Phys. Soc. Jpn., Kobe, Oct. (1986).
   19) F. Kikuchi: "Numerical Analysis of an Eigenvalue Problem in Electromagnetics by the Mixed Method," Applied Mathematics Symp., Kyoto, Dec. (1986).

2. Nuclear physics and nuclear instrumentation
   1) H. Hofmann and S. Yamaji: "Large Scale Nuclear Collective Motion," Int. Conf. on Quantum Chaos (Fourth International Colloquium on Statistical Nuclear Physics), Cuernavaca, Mexico, Jan. (1986).
   2) S. Yamaji and H. Hofmann: "Study of Transport Equation Based on Locally Harmonic Approximation," JAERI Symp. Heavy Ion Nuclear Physics and Chemistry in Tandem-Energy Region II, Tokai, Ibaraki, Jan. (1986).
   3) H. Kumagai, T. Takahashi, T. Kubo, and M. Ishihara: "Parallel Plate Avalanche Counter for Heavy-Ion Dosimetry," Radiation Detector and Dosimetry, Tsukuba, Jan. (1980).
   4) N. Yoshinaga and S. Yamaji: "Dipole Moment of ^{220}Ra (I)," 41th Annu. Meeting Phys. Soc. Jpn., Tokyo, Mar. (1986).
   5) K. Asahi: "On-Line Isotope Separator Project

at RIKEN," 41th Annu. Meeting Phys. Soc. Jpn., Tokyo, Mar. (1986).
6) T. Murakami, J. Kasagi, H. Harada, T. Tachibanaki, K. Yoshida, S. Kubono, M. Yasue, M. H. Tanaka, M. S. Lie, M. Ogiwara, H. Fujiwara, and S. C. Jeong: "High Energy γ Rays Emitted from Highly Excited States in the Continuum," 41th Annu. Meeting Phys. Soc. Jpn., Tokyo, Apr. (1986).
7) J. Kasagi, H. Harada, T. Murakami, K. Yoshida, H. Tachibanaki, and T. Inamura: "Large B(E2) Values Observed for $9^- \rightarrow 8^-$ Transitions in $^{110\text{-}112}$Sn," 41st Annu. Meeting Phys. Soc. Jpn., Tokyo, Apr. (1986).
8) H. Harada, T. Murakami, H. Tachibanaki, K. Yoshida, Y. Shibata, J. Kasagi, T. Kubo, and T. Inamura: "Shape Change Observed for Yrast High-Spin States in $^{110\text{-}112}$Sn," 41st Annu. Meeting Phys. Soc. Jpn., Tokyo, Apr. (1986).
9) Y. Shibata, K. Yoshida, H. Harada, T. Murakami, and J. Kasagi: "Radiation Damage Test of BaF_2 Scintillator," 41th Annu. Meeting Phys. Soc. Jpn., Tokyo, Apr. (1986).
10) A. Hitachi, S. Suzuki, A. Yunoki, J. Kikuchi, T. Doke, K. Masuda, and T. Takahashi: "Photoionization Phenomena in Liquid Argon Admixed with Impurities," 41th Annu. Meeting Phys. Soc. Jpn., Tokyo, Apr. (1986).
11) S. Suzuki, T. Sano, A. Yunoki, A. Hitachi, T. Takahashi, K. Masuda, and T. Doke: "Photoionization Phenomena in Liquid Xenon Admixed with TEA or TMA," 41th Annu. Meeting Phys. Soc. Jpn., Tokyo, Apr. (1986).
12) M. Fukuda, Y. Gono, T. Kohno, and M. Sugawara: "γ-Ray Spectroscopy of ^{220}Ac with BGOACS System," 41th Annu. Meeting Phys. Soc. Jpn., Tokyo, Apr. (1986).
13) K. Okazaki, H. Oyama, Y. Ishibe, S. Kato, Y. Sakamoto, S. Amemiya, T. Tsurita, Y. Hori, K. Akaishi, K. Kawahata, and N. Noda: "Influence of *in situ* Carbon Coating on Window Materials in Fusion Experimental Devices," 7th Int. Conf. Plasma Surface Interactions in Controlled Fusion Devices, Princeton, USA, May (1986).
14) S. Yamaji and N. Yoshinaga: "Dipole Moment of Ra Nuclei in the Two-Molecular Configulation," RCNP Symp. Nuclear Physics in High Spin States, Osaka, July (1986).
15) K. Morita, T. Inamura, T. Nomura, J. Tanaka, H. Miyatake, M. Fujioka, T. Shinozuka, M. Yoshii, H. Hama, K. Taguchi, K. Sueki, Y. Hatsukawa, K. Furuno, and H. Kudo: "An Ion-Guide Isotope Separator On-Line at INS," EMIS-11 (11th Int. Conf. Electromagnetic Isotope Separators and Techniques Related to Their Applications), Los Alamos, USA, Aug. (1986).
16) H. Miyatake, T. Nomura, H. Kawakami, J. Tanaka, M. Oyaizu, K. Morita, T. Shinozuka, H. Kudo, K. Sueki, and Y. Iwata: "INS Gas-Filled Recoil Isotope Separator," EMIS-11 (11th Int. Conf. Electromagnetic Isotope Separators and Techniques Related to Their Applications), Los Alamos, USA, Aug. (1986).
17) H. Harada, J. Kasagi, T. Murakami, K. Yoshida, T. Inamura, and T. Kubo: "Spherical and Deformed States in High-Spin Yrast Region of ^{110}Sn and ^{112}Sn," Int. Nucl. Phys. Conf., Harrogate, U.K., Aug. (1986).
18) Y. Sakamoto, H. Amemiya, Y. Ishibe, S. Kato, K. Okazaki, H. Oyama, K. Yano, K. Akaishi, N. Noda, S. Amemiya, H. Minagawa, T. Hino, T. Yamashina, and S. Matsumoto: "Simulation Experiment on Carbon Coating of First Wall of Fusion Machines," 14th Symp. Fusion Technology, Avignon, France, Sept. (1986).
19) K. Yano, H. Amemiya, Y. Ishibe, K. Okazaki, S. Kato, and Y. Sakamoto: "Production of Carbon Films by Means of ECR Plasma," 47th Meeting Jpn. Soc. Appl. Phys., Sapporo, Sept. (1986).
20) K. Asahi, M. Ishihara, T. Shimoda, T. Fukuda, N. Takahashi, K. Katori, S. Shimoura, N. Ikeda, A. Nakamura, K. Hanakawa, T. Itahashi, Y. Nojiri, and T. Minamisono: "Beta Decay of Polarized Nucleus ^{15}C and Magnetic Moment of the $1/2^+$ Ground State," 1986 Fall Meeting Phys. Soc. Jpn., Kobe, Oct. (1986).
21) K. Asahi, M. Ishihara, T. Ichihara, Y. Gono, J. Kasagi, A. C. Mueller, R. Anne, D. Bazin, D. G. Mueller, R. Bimbot, and W. D. Schmidt-Ott: "Spin Alignment in Projectile Fragmentation at Intermediate Energies," 1986 Fall Meeting Phys. Soc. Jpn., Kobe, Oct. (1986).
22) N. Yoshinaga and S. Yamaji: "Dipole Moment of ^{220}Ra (II)," 1986 Fall Meeting Phys. Soc. Jpn., Kobe, Oct. (1986).
23) K. Sueki, H. Nakahara, I. Kohno, and T. Matsuse, "Mass Division by Equilibrium Process and Nonequilibrium Process at Heavy Ion Nuclear Reaction," 1986 Fall Meeting Phys. Soc. Jpn., Kobe, Oct. (1986).
24) Y. Gono, T. Kohno, Ch. Briancon, F. A. Beck, and Château de Cristal Collaboration: "Study of ^{222}Th with BGOACS and 4π Crystal Ball," 1986 Fall Meeting Phys. Soc. Jpn., Kobe, Oct. (1986).
25) H. Harada, T. Murakami, K. Yoshida, K.

Takeuchi, M. Sakurai, J. Kasagi, T. Inamura, and T. Kubo: "B(E2) Values of the Rotational Band in ^{112}Sn," 1986 Fall Meeting Phys. Soc. Jpn., Kobe, Oct. (1986).

26) K. Yoshida, J. Kasagi, T. Murakami, H. Harada, T. Inamura, and T. Kubo: "Highly-Excited High-Spin States in ^{110,112}Sn," 1986 Fall Meeting Phys. Soc. Jpn., Kobe, Oct. (1986).

27) H. Miyatake, T. Nomura, H. Kawakami, J. Tanaka, M. Oyaizu, K. Morita, K. Sueki, H. Kudo, T. Shinozuka, and Y. Iwata: "INS Gas-Filled Recoil Isotope Separator," 1986 Fall Meeting Phys. Soc. Jpn., Kobe, Oct. (1986).

28) Y. Sakamoto, H. Amemiya, Y. Ishibe, S. Kato, K. Okazaki, H. Oyama, K. Yano, S. Amemiya, H. Minagawa, T. Hino, and T. Yamashina: "Simulation Experiment on Carbon Coating: RIKEN ECR-2," 3rd Fall Meeting Jpn. Soc. of Plasma Physics and Nuclear Fusion, Tokyo, Oct. (1986).

29) T. Yanagimachi: "Test of PSD's Resolutions with He and N Beams at the Cyclotron," RIKEN Symp. Heavy Ion Observation Techniques in Space and Laboratory, Wako, Nov. (1986).

30) T. Doke: "Improvement of 2-Dimensional Position Sensitive Silicon Detector," RIKEN Symp. Heavy Ion Observation Techniques in Space and Laboratory, Wako, Nov. (1986).

31) Y. Ishibe, H. Amemiya, S. Kato, K. Okazaki, H. Oyama, Y. Sakamoto, K. Yano, S. Amemiya, S. Matsumoto, H. Minagawa, T. Hino, and T. Yamashina: "Carbon Coating by ECR Plasma (II)," 27th Joint Meeting Vacuum, Osaka, Nov. (1986).

32) Y. Ishibe: "Evaluation of Carbon Films Coated by the RIKEN ECR-2 Device," RIKEN Symp. Plasma Vapour Deposition and Estimation of the Deposited Films, Wako, Nov. (1986).

33) S. Yamaji and H. Hofmann: "Transport Coefficients for Fission at High Excitations," RIKEN Symp. Non-Equilibrium Process in Fission and Fusion, Wako, Nov. (1986).

34) K. Asahi: "Beta Decay of Nuclei Far off the Stability Line," RIKEN Symp. Nuclear Structures and Nuclear Interactions in the Regions Far from the Stability Line, Wako, Dec. (1986).

35) K. Asahi: "Radioactive Beam Course at RIKEN and Future Experiments," RCNP Workshop on Physics Using Secondary Beams, Osaka, Dec. (1986).

3. Atomic and solid-state physics

1) E. Yagi: "Lattice Location Study on Hydrogen in Metals by Using Ion Beam," 2nd Meeting Interaction between Ion Beams and Solids, Yugawara, Jan. (1986).

2) T. Kambara, Y. Awaya, T. Watanabe, K. Ando, M. Kase, H. Kumagai, Y. Kanai, and K. Shima: "Studies of Charge State Distribution of Swift Heavy Ions Passing through Solid Target," 2nd Meeting Interaction between Ion Beams and Solids, Yugawara, Jan. (1986).

3) Y. Awaya: "X-Ray Production in Heavy Ion-Atom Collisions," Symp. Region of Hybrid Studies and Nuclear Physics, Osaka, Jan. (1986).

4) Y. Kanai, Y. Awaya, T. Watanabe, K. Ando, T. Kambara, M. Kase, H. Kumagai, and K. Shima: "Studies of Charge State Distribution of Swift Heavy Ions Passing through Solid Target," Symp. Interaction between Ion Beams and Solids, Tokyo, Feb. (1986).

5) T. Mizogawa, Y. Awaya, T. Kambara, Y. Kanai, and M. Kase: "Carbon-Foil Thickness Dependence of Ar K Satellite Lines in Ar Ion-C Foil Collisions," RIKEN Symp. 7th Meeting Atomic Collisions by Using Accelerators, Wako, Feb. (1986).

6) P. H. Mokler: "Experiments with Decelarated Highly Charged Heavy Ions," RIKEN Symp. 7th Meeting Atomic Collisions by Using Accelerators, Wako, Feb. (1986).

7) K. Asai, T. Okada, and H. Sekizawa: "TDPAC of γ-Rays Emitted from ^{111}Cd ($\leftarrow^{111}$In) in Magnetic Oxides," Application of Perturbed Angular Correlation Technique to Solid State Physics, Kumatori, Feb. (1986).

8) E. Yagi: "Researches in Materials Science Using Ion Beam in RIKEN Institute," Symp. Fundamental Problems and Application of Heavy Ions, Univ. Tokyo, Feb. (1986).

9) M. Iwai, I. Shimamura, and T. Watanabe: "Dependence of Minima in Generalized Oscillator Strengths on Excitation Cross Sections," 41th Annu. Meeting Phys. Soc. Jpn., Tokyo, Mar. (1986).

10) K. Fujima, K. Mima, and T. Watanabe: "X-Ray Spectrum Analysis of High Density Laser Plasma by DV-Xα Method," 41th Annu. Meeting Phys. Soc. Jpn., Tokyo, Mar. (1986).

11) S. Karashima, I. Kawada, T. Sato, and T. Watanabe: "Estimation of Stopping Power of High Temperature and High Density Substances for Heavy Ions," 41th Annu. Meeting Phys. Soc. Jpn., Tokyo, Mar. (1986).

12) F. Ambe, K. Asai, S. Ambe, and H. Seki-

zawa: "TDPAC of γ-Rays Emitted from ^{111}Cd($\leftarrow^{111}$In) in In_2O_3," 41th Annu. Meeting Phys. Soc. Jpn., Tokyo, Mar. (1986).
13) H. Sekizawa, K. Asai, and T. Okada: "An TDPAC Study on Ferrites with the Spinel Structure," 41th Annu. Meeting Phys. Soc. Jpn., Tokyo, Mar. (1986).
14) T. Mizogawa, Y. Awaya, T. Kambara, M. Kase, H. Kumagai, Y. Kanai, M. M. Ismail, and K. Shima: "Dependence of Kα Satellite Spectra of 50 MeV Ar Beams on the Thickness of Target Foils," 41th Annu. Meeting Phys. Soc. Jpn., Tokyo, Mar. (1986).
15) K. Shima, K. Umetani, Y. Awaya, T. Kambara, Y. Kanai, H. Kumagai, M. Kase, T. Mizogawa, and M. M. Ismail: "Excitation Process of Ions in Heavy Ion-Foil Collisions," 41th Annu. Meeting Phys. Soc. Jpn., Tokyo, Mar. (1986.)
16) E. Yagi, S. Nakamura, T. Kobayashi, F. Kano, K. Watanabe, Y. Fukai, and T. Osaka: "Lattice Location of Hydrogen in Tantalum," 41th Annu. Meeting Phys. Soc. Jpn., Tokyo, Mar. (1986).
17) K. Nishiyama, T. Matsuzaki, K. Nagamine, K. Ishida, and H. Shirakawa: "Measurement on Muonium Substituted Radical in cis-Polyacetylene," 41th Annu. Meeting Phys. Soc. Jpn., Tokyo, Apr. (1986).
18) K. Ishida, K. Nagamine, and H. Shirakawa: "Muon Spin Resonance Studies on Polyacetylene III," 41th Annu. Meeting Phys. Soc. Jpn., Tokyo, Apr. (1986).
19) I. Furutate, T. Kokubu, S. Satoh, Y. Ando, T. Motobayashi, and S. Shirato: "DWBA Analysis of Neutron Induced Reactions on ^{6}Li and ^{7}Li at 14 MeV," 41th Annu. Meeting Phys. Soc. Jpn., Tokyo, Apr. (1986).
20) H. Ohsumi, K. Hanakawa, M. Ishihara, Y. Nagai, T. Motobayashi, K. Katori, and H. Gotoh: "Strength of Highly Excited One-Particle States in ^{209}Bi Excited by ^{208}Pb(α, t) Reaction Studied by t-γ Coincidence Method," 41th Annu. Meeting Phys. Soc. Jpn., Tokyo, Apr. (1986).
21) P. H. Mokler: "Atomic Physics with Heavy Ions—The Past Ten Years at GSI and Future Developments," 41th Annu. Meeting Phys. Soc. Jpn., Tokyo, Apr. (1986).
22) I. Hashimoto, H. Yorikawa, H. Mitsuya, H. Yamaguchi, K. Takaishi, T. Kikuchi, K. Furuya, E. Yagi, and M. Iwaki: "Behavior of Kr Bubbles in Kr-Implanted Aluminum," 41th Annu. Meeting Phys. Soc. Jpn., Tokyo, Apr. (1986).
23) H. Kusuyama, T. Watanabe, K. Yoshida, M. Tomita, M. Hobo, S. Sakamoto, Y. Uchijima, K. Okada, K. Maeda, Y. Sasa, and M. Uda: "Elemental Analysis by Particle Induced X-Ray Emission (I) Urinary Stone Diseases," 74th Annu. Meeting Jpn. Urological Association, Hiroshima, Apr. (1986).
24) H. Katsuragawa, T. Minowa, K. Nishiyama, and T. Inamura: "Resonance Ionization Spectroscopy of Tl by Atomic Beam," 33rd Spring Meeting Jpn., Soc. Appl. Phys. and Related Societies, Funabashi, Apr. (1986).
25) Y. Fukai, K. Watanabe, and E. Yagi: "Nature and Some Consequences of Stress-Induced States of Hydrogen in BCC Metals," Int. Conf. Properties and Applications of Metal Hydrides, Maubuisson, May (1986).
26) E. Yagi, S. Nakamura, T. Kobayashi, F. Kano, K. Watanabe, Y. Fukai, and T. Osaka: "Lattice Location Study of H in Ta by Channeling Method," Int. Conf. Properties and Applications of Metal Hydrides, Maubuisson, May (1986).
27) S. Karashima and T. Watanabe: "Stopping Power for Energetic Heavy Ions in a Finite Temperature Material," 2nd Int. Topical Symp. ICF Research by High-Power Particle Beams, Nagaoka, June (1986).
28) M. Schmolz, K.-P. Döring, K. Fürderer, M. Gladisch, N. Haas, D. Herlach, G. Majer, J. Rosenkranz, W. Schäfer, L. Schimmele, W. Schwarz, A. Seeger, and E. Yagi: "Positive Muons in Iron: Dipolar Field at Tetrahedral Sites and Jump Frequencies at Low Temperatures," 4th Int. Conf. Muon Spin Rotation, Relaxation, and Resonance, Uppsala, Sweden, June (1986).
29) K. Nagamine: "μSR in Polyacetylenes," 4th Int. Conf. Muon Spin Rotation, Relaxation, and Resonance, Uppsala, Sweden, June (1986).
30) K. Nishiyama, K. Ishida, K. Nagamine, T. Matsuzaki, Y. Kuno, H. Shirakawa, R. Kiefl, and J. H. Brewer: "Precise Measurement of HFS Constant of the Muonium Substituted Radical in cis-Polyacetylene," 4th Int. Conf. Muon Spin Rotation, Relaxation, and Resonance, Uppsala, Sweden, June (1986).
31) M. Uda, O. Benka, K. Fuwa, K. Maeda, and Y. Sasa: "Chemical Effects in PIXE," 4th Int. Conf. PIXE and Its Application to Analytical Chemistry, Tallahassee, USA, June (1986).
32) M. Uda, K. Maeda, Y. Sasa, H. Kusuyama, and Y. Yokode: "Trial of Cancer Diagnosis by PIXE," 4th Int. Conf. PIXE and Its Application to Analytical Chemistry, Talla-

hassee, USA, June (1986).
33) Y. Sasa, K. Maeda, and M. Uda: "Application of PIXE and Diffraction Analysis to Ancient Remains," 4th Int. Conf. PIXE and Its Application to Analytical Chemistry, Tallahassee, USA, June (1986).
34) K. Maeda, Y. Yokode, Y. Sasa, H. Kusuyama, and M. Uda: "Multielemental Analysis of Human Thyroid Glands Using Particle Induced X-Ray Emission (PIXE)," 4th Int. Conf. PIXE and Its Application to Analytical Chemistry, Tallahassee, USA, June (1986).
35) K. Maeda, Y. Sasa, M. Maeda, and M. Uda: "Diagnosis of River Pollution by PIXE," 4th Int. Conf. PIXE and Its Application to Analytical Chemistry, Tallahassee, USA, June (1986).
36) K. Ishida, K. Nagamine, and H. Shirakawa: "Muon Spin Rotation and Relaxation Studies of Undoped and Iodine-doped Polyacetylene," Int. Conf. Science and Technology of Synthetic Metals (ICSM '86), Kyoto, June (1986).
37) T. Watanabe: "Laser Spectroscopy in Atomic Processes," Symp. Laser Spectroscopy in Fundamental Science, Chofu, July (1986).
38) T. Watanabe: "Theory of Hydrogen Nucleus Transfer Reaction," 4th Special Meeting μ-meson Catalyzed Nuclear Fusion, The Research Society for Atomic Energy, Tokyo, July (1986).
39) T. Watanabe: "Specificity of Highly Charged Ions," RIKEN Symp. Int. Semin. Dynamic Processes of Highly Charged Ions, Susono, Aug. (1986).
40) N. Shimakura, H. Sato, M. Kimura, and T. Watanabe: "Low Velocity Collision of O^{6+} with He by MO Base Treatment," RIKEN Symp. Int. Semin. Dynamic Processes of Highly Charged Ions, Susono, Aug. (1986).
41) M. Iwai, I. Shimamura, and T. Watanabe: "Manifestation of Minima in the Generalized Oscillator Strengths as Minima in the Integrated Cross Sections for Ion-Atom Collisions," RIKEN Symp. Int. Semin. Dynamic Processes of Highly Charged Ions, Susono, Aug. (1986).
42) K. Nakanishi, K. Iguchi, A. Ohsaki, and T. Watanabe: "Classical-Trajectory Monte Carlo Calculations for Coulomb-Interacting Three Body Systems," Int. Conf. Atom. Phys. and Few Body Systems (ICAP-X and Few Body XI), Tokyo, Aug. (1986).
43) S. Karashima, T. Watanabe, X. Zhang, Q. Ma, and Y. Liu: "Electron Stripping Cross Sections of Multiply Charged Ions by Neutral Atoms," Int. Conf. Atom. Phys. and Few Body Systems (ICAP-X and Few Body XI), Tokyo, Aug. (1986).
44) Q. Ma, X. Zhang, Y. Liu, and T. Watanabe: "Total and Differential Cross Sections for $(\mu^+\mu^-)$ Formation by μ^+ with (μ^-p) including Excited States in the First Born Approximation," Int. Conf. Atom. Phys. and Few Body Systems (ICAP-X and Few Body XI), Tokyo, Aug. (1986).
45) T. Tonuma, T. Matsuo, K. Baba, M. Kase, T. Kambara, S. H. Be, H. Kumagai, I. Kohno, and H. Tawara: "Multiply Charged C^{i+} and O^{i+} Ions from Molecular Targets by 1.05 MeV/amu Ar^{12+} Ion Impact," Int. Conf. Atom. Phys. and Few Body Systems (ICAP-X and Few Body XI), Tokyo, Aug. (1986).
46) K. Fujima, K. Mima, and T. Watanabe: "X-Ray Spectra Emitted from High Density and High Temperature Si," Int. Conf. Atom. Phys. and Few Body Systems (ICAP-X and Few Body XI), Tokyo, Aug. (1986).
47) S.-M. Zhou, X.-X. Zhang, Q.-C. Ma, J.-F. Cheng, Y.-Y. Liu, and T. Watanabe: "Calculation of Ionization Cross Sections for Multicharged Ions by Proton Impact with BEA and TFD Method," Int. Conf. Atom. Phys. and Few Body Systems (ICAP-X and Few Body XI), Tokyo, Aug. (1986).
48) X.-W. Liu, Q.-C. Ma, J.-F. Cheng, X.-X. Zhang, Y.-Y. Liu, and T. Watanabe: "Total and Differential Cross Sections for $(\mu^+\mu^-)$ Formation by Collisions of μ^+ with (μ^-p) in the Eikonal Approximation," Int. Conf. Atom. Phys. and Few Body Systems (ICAP-X and Few Body XI), Tokyo, Aug. (1986).
49) N. Shimakura, H. Sato, M. Kimura, and T. Watanabe: "Electron Capture in Pseudo-Two-Electron System O^{6+}+He: Molecular Basis Expansion Method," Int. Conf. Atom. Phys. and Few Body Systems (ICAP-X and Few Body XI), Tokyo, Aug. (1986).
50) I. Shimamura and M. Iwai: "An R-matrix Method for Wave Functions That Are Accurate Close to the Coordinate Origin," Int. Conf. Atom. Phys. and Few Body Systems (ICAP-X and Few Body XI), Tokyo, Aug. (1986).
51) M. Iwai, I. Shimamura, and T. Watanabe: "Extended Bethe Surface: Behavior of the Generalized Oscillator Strength along Isoelectronic Sequence," Int. Conf. Atom. Phys. and Few Body Systems (ICAP-X and Few Body XI), Tokyo, Aug. (1986).
52) K. Shima, K. Umetani, S. Fujioka, M. Yamaguchi, Y. Awaya, T. Kambara, T. Mizogawa, and Y. Kanai: "Evolution of Fast Heavy Ion Excitation in Solid Target-0.83–2.4 MeV/u

Br^{q+}, $Cu^{q+}+C$," Int. Conf. Atom. Phys. and Few Body Systems (ICAP-X and Few Body XI), Tokyo, Aug. (1986).
53) T. Mizogawa, Y. Awaya, T. Kambara, Y. Kanai, M. Kase, H. Kumagai, P. H. Mokler, and K. Shima: "Target Thickness Dependence of Kα Satellite Intensities of Ar Ions Colliding with Thin Carbon Foils," Int. Conf. Atom. Phys. and Few Body Systems (ICAP-X and Few Body XI), Tokyo, Aug. (1986).
54) K. Ando, Y. Awaya, S. Kohmoto, H. Kumagai, T. Tonuma, S. Tsurubuchi, and K. Sato: "Identification of Highly Ionized Aluminum in Beam-Foil Spectrum," Int. Conf. Atom. Phys. and Few Body Systems (ICAP-X and Few Body XI), Tokyo, Aug. (1986).
55) K. Nagamine: "Thermal Muonium and Muon Catalyzed Fusion with Pulsed Muon Experiments," Int. Conf. Atom. Phys. and Few Body Systems (ICAP-X and Few Body XI), Tokyo Aug. (1986).
56) S. Hara and M. Nakamura: "Determination of Photoionization Asymmetry Parameter," Int. Conf. Atom. Phys. and Few Body Systems (ICAP-X and Few Body XI), Tokyo, Aug. (1986).
57) T. Motobayashi: "Symmetries among the Proton and Neutron Induced Transfer Reactions on ^{6}Li and ^{7}Li," Int. Workshop on Few-Body Approach to Nuclear Reactions in Tandem and Cyclotron Energy Region, Tokyo, Aug. (1986).
58) H. Katsuragawa, T. Minowa, M. Shimazu, and T. Inamura: "Electron-Ion Coincidence Method for Ultra-Sensitive Detection of Atoms," 11th Int. Conf. Electromagnetic Isotope Separators and Techniques Related to Their Applications, Los Alamos, USA, Aug. (1986).
59) A. Ohsaki, T. Watanabe, K. Nakanishi, and K. Iguchi: "μ-Transfer Cross Sections from (μ^-d) or (μ^-t) to and α in High Velocity Region Using Classical Trajectory Monte Carlo Method," Int. Symp. Muon-Catalyzed Fusion μ-CF86, Tokyo, Sept. (1986).
60) S. Hara, T. Ishihara, and N. Toshima: "Variational Calculation for Muonic Molecules," Int. Symp. Muon-Catalyzed Fusion μ-CF86, Tokyo, Sept. (1986).
61) K. Nagamine: "Muonic X-Ray Measurement on the μ^- Sticking Probability in Muon-Catalyzed Fusion of Liquid d-t Mixture," Int. Symp. Muon-Catalyzed Fusion μ-CF86, Tokyo, Sept. (1986).
62) E. Yagi, F. Kano, S. Nakamura, M. Iwaki, and T. Osaka: "Defect-Impurity Interaction in Sn- or Ni-Implanted Aluminum," Int. Conf. Vacancies and Interstitials in Metals, West Berlin, F. R. Germany, Sept. (1986).
63) E. Yagi, A. Koyama, H. Sakairi, and R. R. Hasiguti: "Isochronal Annealing of Proton- and α-Irradiated Cu_3Au at Low Temperatures," Int. Conf. Vacancies and Interstitials in Metals, West Berlin, F. R. Germany, Sept. (1986).
64) H. Mitsuya, I. Hashimoto, H. Yorikawa, H. Yamaguchi, E. Yagi, and M. Iwaki: "Behavior of Kr Bubbles in Kr-Implanted Aluminum (II)," 1986 Fall Meeting Phys. Soc. Jpn., Nishinomiya, Sept. (1986).
65) E. Yagi, T. Kobayashi, S. Nakamura, F. Kano, K. Watanabe, Y. Fukai, and T. Matsumoto: "Lattice Location of Hydrogen in NbMo Alloys," 1986 Fall Meeting Phys. Soc. Jpn., Nishinomiya, Sept. (1986).
66) T. Okada, T. Yamadaya, and K. Asai: "^{111}Cd TDPAC Study on a Single Crystal $Li_{0.5}Fe_{2.5}O_4$," 1986 Fall Meeting Phys. Soc. Jpn., Nishinomiya, Sept. (1986).
67) K. Asai, F. Ambe, S. Ambe, T. Okada, and H. Sekizawa: "An Investigation on the After-Effects of ^{111}In($\rightarrow^{111}$Cd) EC Decay in α-Fe_2O_3," 1986 Fall Meeting Phys. Soc. Jpn., Nishinomiya, Sept. (1986).
68) K. Nagamine: "International Conference Report: International Symposium on Muon-Catalyzed Nuclear Fusion," 1986 Fall Meeting Phys. Soc. Jpn., Nishinomiya, Sept. (1986).
69) K. Ishida, T. Matsuzaki, Y. Hirata, and K. Nagamine: "Muon Transfer Reaction to Helium Impurity in Liquid Hydrogen," 1986 Fall Meeting Phys. Soc. Jpn., Nishinomiya, Sept. (1986).
70) A. Uedono, T. Emado, S. Tanigawa, and H. Sakairi: "The Study of Agglomeration and Release Process of Helium Implanted in Metals by Slow Position Beam," 1986 Fall Meeting Phys. Soc. Jpn., Nishinomiya, Sept. (1986).
71) K. Asai, S. Ambe, T. Okada, and F. Ambe: "TDPAC Study on (^{111}In$\rightarrow$)^{111}Cd Ions in Silver Phosphate," 7th Int. Conf. Hyperfine Interactions, Bangalore, India, Sept. (1986).
72) K. Asai, F. Ambe, S. Ambe, T. Okada, and H. Sekizawa: "An Investigation on the After-Effects of ^{111}In($\rightarrow^{111}$Cd) EC Decay in α-Fe_2O_3," 7th Int. Conf. Hyperfine Interactions, Bangalore, India, Sept. (1986).
73) K. Asai, T. Okada, and H. Sekizawa: "Super-transferred Hyperfine Magnetic Fields at ^{111}Cd($\leftarrow^{111}$In) in Ferrimagnetic Oxides with the Spinal Structure," 7th Int. Conf. Hyper-

fine Interactions, Bangalore, India, Sept. (1986).

74) K. Ishida, K. Nagamine, and H. Shirakawa: "μSR Studies on Polyacetylenes," 7th Int. Conf. Hyperfine Interactions, Bangalore, India, Sept. (1986).

75) K. Yano, H. Amemiya, Y. Ishibe, K. Okazaki, H. Oyama, S. Kato, and Y. Sakamoto: "Production of Carbon Film by ECR Plasma," 47th Fall Meeting Jpn. Soc. Appl. Phys., Sapporo, Sept. (1986).

76) M. Shimazu, T. Minowa, and H. Katsuragawa: "Monochromatic Image Observations of Flames of an Internal-Combustion Engine," 47th Fall Meeting Jpn. Soc. Appl. Phys., Sapporo, Sept. (1986).

77) T. Mizogawa: "Electron Configuration of Ar Ions Passing through Carbon Foils," Symp. Ion Excitation and Scattering, Tsukuba, Sept. (1986).

78) T. Watanabe: "New Fields by Using Extreme Intensive and High Bright Light Sources—From the View Point of Atomic and Molecular Physics," Symp. Overview on New Research Fields Using Extreme Intensive and High Bright Light Source in VUV and Soft X-Ray Region, Omachi, Oct. (1986).

79) A. Koyama, O. Benka, H. Ishikawa, Y. Sasa, and M. Uda: "Z_2-Dependence of the Energy of Backscattered Electrons Stripped from He^+," 1986 Fall Meeting Phys. Soc. Jpn., Kobe, Oct. (1986).

80) A. Koyama, O. Benka, H. Ishikawa, Y. Sasa, and M. Uda: "Secondary Electrons from Metal Surfaces Induced by Heavy Ion Impact," 1986 Fall Meeting Phys. Soc. Jpn., Kobe, Oct. (1986).

81) T. Motobayashi, S. Satoh, H. Sakai, N. Matsuoka, T. Saito, K. Hosono, M. Ishihara, S. Shimoura, S. Hatori, and A. Okihana: "^{90}Zr(d, ^{2}He) Reaction," 1986 Fall Meeting Phys. Soc. Jpn., Kobe, Oct. (1986).

82) S. Kubota, S. Shirato, T. Motobayashi, H. Murakami, Y. Ando, S. Satoh, T. Murakami, and J. Kasagi: "Neutron Detection by Plastic-BaF_2 Scintillator," 1986 Fall Meeting Phys. Soc. Jpn., Kobe, Oct. (1986).

83) H. Murakami, S. Kubota, S. Shirato, K. Gen, and T. Motobayashi: "n-γ Discrimination Circuit for Plastic-BaF_2 Scintillator," 1986 Fall Meeting Phys. Soc. Jpn., Kobe, Oct. (1986).

84) S. Satoh and T. Motobayashi: "SSD Spectrometer for ^{2}He Detection," 1986 Fall Meeting Phys. Soc. Jpn., Kobe, Oct. (1986).

85) T. Matsuzaki, K. Ishida, Y. Hirata, K. Nagamine, S. E. Jones, M. A. Paciotti, A. J. Caffrey, and H. R. Maltrud: "Basic Experiment on Muon Catalyzed Fusion I," 1986 Fall Meeting Phys. Soc. Jpn., Kobe, Oct. (1986).

86) T. Watanabe: "Problems in X-Ray Lasers Using Highly Charged Ions," Symp. Physical Processes in X-Ray Lasers, Nagoya, Nov. (1986).

87) K. Muraoka, S. Sasaki, I. Kohno, and J. Nishizawa: "Proton Irradiation into the SI Thyristor," 5th Symp. Ion Beam Technology, Hosei Univ., Tokyo, Dec. (1986).

4. Radiochemistry, radiation chemistry, and radiation biology

1) Q. Qiu, T. Kobayashi, M. Yanokura, M. Iwai, Y. Yatsurugi, and T. Nozaki: "Utilization of the D(^{3}He, p)^{4}He Reaction in High-Sensitivity Analysis of Deuterium in Solids," 4th Symp. Ion Beam Technology, Hosei Univ., Tokyo, Dec. (1985).

2) T. Takahashi, Y. Kameda, C. Shimakawa, Y. H. Kang, K. Eguchi, K. Nakano, T. Katayama, and I. Kaneko: "Application of Solid State Plastic Detector to Heavy Ion Dosimetry and Microdosimetry," 33rd Spring Meeting Jpn. Soc. Appl. Phys. and Related Societies, Funabashi, Apr. (1986).

3) K. Kimura: "Dynamics of Helium-Excimer Clusters," 41th Annu. Meeting Phys. Soc. Jpn., Tokyo, Apr. (1986).

4) Y. Kadota, K. Sakai, T. Nozaki, Y. Itoh, and Y. Ohkubo: "Determination of Carbon Concentration in the LEC GaAs Crystal," 4th Int. Conf. III-V Semi-Insulating Materials, Hakone, May (1986).

5) I. Kaneko: "DNA Strand Breaks in Mammalian Cells by Heavy Ion Particles," Symp. Prospects on Tritium Radiation Genetics, Mishima, June (1986).

6) Q. Qiu, T. Kobayashi, M. Yanokura, M. Iwai, Y. Yatsurugi, and T. Nozaki: "Utilization of the D(^{3}He, p)^{4}He Reaction in High-Sensitivity Analysis of Deuterium in Solids," 10th Symp. Ion Sources and Ion-Assisted Technology, Tokyo, June (1986).

7) T. Nozaki, Y. Itoh, S. Hayashi, and Q. Qiu: "Utilization of Deuterium and ^{15}N as Activable Tracers in Solid State Sciences," 7th Int. Conf. Modern Trends in Act. Anal., Copenhagen, Denmark, June (1986).

8) H. Fukushima, T. Kimura, H. Hamaguchi, T. Nozaki, Y. Itoh, and Y. Ohkubo: "Routine Determination of Light Elements by Charged Particle Activation Analysis," 7th Int. Conf. Modern Trends in Act. Anal., Copenhagen, Denmark, June (1986).

9) H. Sunaga, T. Uematsu, R. Tanaka, and I. Kohno: "Measurement of Distribution of Proton Beam Radiation Dose Using Cyclotron," 23rd Meeting Isotope Research in Science and Technology, Tokyo, July (1986).
10) T. Takahashi, S. Konno, and F. Yatagai: "Calculation of Dose around the Path of a Heavy Ion and Its Application," RIKEN Symp. Mechanism of Biological Effect of High LET Radiation, Tokyo, July (1986).
11) K. Eguchi-Kasai and I. Kaneko: "DNA Lesion in Mammalian Cells by Heavy Ion Particles," RIKEN Symp. Mechanisms of Biological Effects by High LET Radiation, Tokyo, July (1986).
12) T. Takahashi, T. Katayama, K. Takahashi, Y. Takayanagi, and I. Kaneko: "Inactivation of *B. Subtilis* Spores by a Single Heavy Ion," 3rd Spore Seminar, Tokyo, July (1986).
13) T. Takahashi, F. Yatagai, S. Konno, T. Katayama, and I. Kaneko: "Microdosimetric Considerations of Effects of Heavy Ions on Microorganisms," 26th Plenary Meeting Committee on Space Research, Toulouse, France, July (1986).
14) K. Kimura: "Possibility of Dimer and Clusters between Helium-Excimers Produced at High-Density by Irradiation of Heavy-Ion at Low Temperature," Int. Conf. Atom. Phys. and Few Body Systems (ICAP-X and Few Body XI), Tokyo, Aug. (1986).
15) T. Nozaki: "Accelerator Production of Radioisotopes and Their Utilization in Other Fields than Nuclear Medicine," Int. Conf. Nuclear and Radiochemistry, Beijing, China, Sept. (1986).
16) M. Iwamoto and T. Nozaki: "Charged Particle Activation Analysis for Surface Oxygen under Various Ambient Pressure," Int. Conf. Nuclear and Radiochemistry, Beijing, China, Sept. (1986).
17) K. Kimura and M. Kataoka: "An Ion-Track Scope Using Optical Fibers," 1986 Fall Meeting Phys. Soc. Jpn., Nishinomiya, Sept. (1986).
18) T. Takahashi, S. Konno, T. Tabata, and R. Ito: "Calculation of Dose around the Trajectory of an Heavy Ion and Its Application," 47th Fall Meeting Jpn. Soc. Appl. Phys., Sapporo, Sept. (1986).
19) Q. Qiu, T. Kobayashi, M. Yanokura, T. Nozaki, M. Iwai, and Y. Yatsurugi: "Utilization of the D(^{3}He, p)^{4}He Reaction in High-Sensitivity Analysis of Deuterium in Solids," 47th Fall Meeting Jpn. Soc. Appl. Phys., Sapporo, Sept. (1986).
20) Y. Itoh, T. Nozaki, Y. Ohkubo, T. Miura, Y. Kadota, K. Sakai, T. Kimura, and H. Fukushima: "Simultaneous Charged Particle Activation Analysis of Carbon and Boron in GaAs," 47th Fall Meeting Jpn. Soc. Appl. Phys., Sapporo, Sept. (1986).
21) B. G. Yu, M. Aratani, M. Yanokura, T. Nozaki, and E. Arai: "Substitution of Positive Ions in Glass Surface Layer Studied by Heavy-Ion Rutherford Scattering Analysis," 47th Meeting Jpn. Soc. Appl. Phys., Sapporo, Sept. (1986).
22) K. Asai, S. Ambe, T. Okada, and F. Ambe: "TDPAC of (^{111}In→)^{111}Cd in Silver Phosphate," 30th Symp. Radiochemistry, Sendai, Oct. (1986).
23) K. Asai, F. Ambe, S. Ambe, T. Okada, and H. Sekizawa: "Chemical Effects of the EC Decay of ^{111}In in α-Fe_2O_3 by TDPAC," 30th Symp. Radiochemistry, Sendai, Oct. (1986).
24) S. Ambe, F. Ambe, T. Okada, I. Tanaka, S. Nasu, and F. E. Fujita: "Emission Mössbauer Spectra of ^{119}Sb Electroplated on Au Surface," 30th Symp. Radiochemistry, Sendai, Oct. (1986).
25) M. Yanokura, K. Sato, M. Aratani, M. Nozaki, and K. Saito: "Study on Phase Transition in Heat Treatment of W/GaAs by Heavy Ion Scattering," 30th Symp. Radiochemistry, Sendai, Oct. (1986).
26) K. Sato, T. Nozaki, and I. Izumi: "Determination Carbon in Aluminium by Charged Particle Activation Analysis," 30th Symp. Radiochemistry, Sendai, Oct. (1986).
27) M. Aratani, M. Yanokura, Q. Qiu, K. Sato, B. G. Yu, and T. Nozaki: "Hydrogenated Surface Layers of Soda-Lime Glass Studied by the Forward Recoil Measurement with Heavy-Ions," 30th Symp. Radiochemistry, Sendai, Oct. (1986).
28) Y. Itoh, T. Nozaki, Y. Ohkubo, and T. Miura: "Diffusion of Nitrogen in Silicon Using ^{15}N as an Activable Tracer," 30th Symp. Radiochemistry, Sendai, Oct. (1986).
29) K. Kimura, M. Kataoka, and H. Kumagai: "A Technique for Subnanosecond Decay Measurement of Heavy-Ion Induced Photoemission," 29th Conf. Radiation Chemistry, Kyoto, Oct. (1986).
30) T. Nozaki: "Charged Particle Activation Analysis of Impurity Light Elements in Semiconductor Materials," 11th Int. Conf. Cyclotrons and Their Applications, Tokyo, Oct. (1986).
31) I. Kaneko, K. Eguchi-Kasai, T. Takahashi, T. Kosaka, and K. Nakano: "Beam Port and Irradiation Chamber of the RIKEN

Ring Cyclotron for Biological Samples," 11th Int. Conf. Cyclotron and Their Applications, Tokyo, Oct. (1986).
32) K. Eguchi-Kasai, T. Kosaka, I. Kaneko, A. Maruhashi, and K. Nakano: "Cell Death and DNA Lesions Caused by Accelerated Charged Particles," 11th Int. Conf. Cyclotron and Their Applications, Tokyo, Oct. (1986).
33) T. Takahashi, F. Yatagai, T. Katayama, S. Konno, K. Takahashi, Y. Takayanagi, K. Nakano, and I. Kaneko: "Calculation of Dose around the Trajectory of an Ion and Interpretation of Inactivation Cross Sections of Microorganisms," 29th Annu. Meeting Jpn. Radiat. Res. Soc., Kanazawa, Oct. (1986).
34) K. Eguchi-Kasai, T. Kosaka, K. Nakano, I. Kaneko, and A. Maruhashi: "Oxgen Effect on DNA Lesion in Mammalian Cells by α-Particle Beam," 29th Annu. Meeting Jpn. Radiat. Res. Soc., Kanazawa, Oct. (1986).
35) M. Suehiro, F. Yokoi, T. Nozaki, and M. Iwamoto: "Contamination from Nonradioactive Bromine and Chlorine in the Synthesis of Radiobromine-Labelled Butylophenone Derivatives for Neuro-Receptor Study," 26th Meeting Jpn. Soc. Nuclear Medicine, Kamogawa, Nov. (1986).
36) T. Takahashi, F. Yatagai, T. Katayama, T. Doke, and H. Ohashi: "Inactivation of Microorganisms by Different Heavy Ions," Int. Symp. Biological Science in Space, Nagoya, Nov. (1986).

VIII. LIST OF OUTSIDE USERS AND THEIR THEMES

(Jan.–Dec. 1986)

1)	S. Orito and S. Nakamura "Test of Sensibility of CR39 Track Detector for High Energy Proton"	Faculty of Science, Univ. Tokyo
2)	T. Kimura and H. Fukushima "Radiochemical Analysis of ^{16}O, ^{14}N and ^{12}C in Si Crystal and GaAs"	Japan Chemical Analysis Center
3)	H. Homareda "Production of ^{43}K"	Faculty of Medicine, Kyorin Univ.
4)	T. Hayashi and A. Ohnishi "Radiation Damage of Cover Glass for a Solar Cell"	Institute of Span and Astronautical Science
5)	K. Yamamoto and I. Yoshii "Study of Single Event Upset in Microprocessors by Bombarding ^{14}N and ^{40}Ar Particles"	Semiconductor R & D Lab., Toshiba Co., Ltd.
6)	M. Yatsuhashi and T. Suematsu "Effects of the Proton Irradiation on Cable Materials"	Fujikura, Ltd.
7)	H. Tanaka and Y. Kitamura "Study of Latch-up in Microprocessors by Bombarding ^{14}N and ^{42}Ar Particles"	NEC, Ltd.
8)	A. Mario "Study of Single Event Upset in Microprocessors by Bombarding ^{14}N and ^{20}Ne Particles"	Japan Trust Center for Electronic Parts
9)	K. Muraoka and S. Sasaki "Improvement of Static Induction Thyristors by Proton Irradiation"	Toyo Semicon Co., Ltd.
10)	M. Watanabe and K. Ueno "Improvement of Thyristors by Proton Irradiation"	Fuji Electric Corporate R & D, Ltd.
11)	T. Abe and K. Tomii "Improvement of Thyristors by Proton Irradiation"	Semiconductor R & D Lab., Matsushita Electric Work Co., Ltd.

IX. LIST OF SEMINARS

(Jan.–Dec. 1986)

1) M. Tohyama, Univ. Giessen (West Germany), 29 January
"Two-Body Collision Effects on Fusion Window"

2) T. Yukawa, KEK (Ibaraki), 12 February
"Statistics of Level"

3) Y. Mori, KEK (Ibaraki), 18 February
"International Workshop on Polarized Sources and Targets"

4) S. Midorikawa, INS (Tokyo), 26 February
"Heavy Ion Reaction and Axion"

5) T. Cheon, Michigan State Univ. (USA), 9 April
"Density Matrix Expansion for Optical Potential"

6) M.J.A. de Voigt KVI (Netherlands), 22 April
"Super Deformed High Spin States"

7) Y. Koike, Univ. Tokyo (Tokyo), 7 May
"Nucleon-Nucleon Interaction Based on the Flip-Flop Model"

8) G. Graw, Univ. Munich (West Germany), 14 May
"High Resolution Studies with Polarized Deuterons near 20 MeV"

9) R. Nagaoka, Univ. Tokyo (Tokyo), 20 May
"Pauli-Principle Effects in Pion Scattering from the Light Nuclei"

10) N. Takigawa, Tohoku Univ. (Miyagi), 26 May
"Report on ANL Symposium and Some Other Topics on Heavy Ion Collisions"

11) T. Kobayashi, KEK (Ibaraki), 6 June
"Gas Chamber for the Detection of Heavy Ions"

12) H. Sakamoto, Tsukuba Univ. (Ibaraki), 24 June
"Microscopic Analysis of Anharmonicities in Nuclear Quadrupole Collective Motions by Use of the Self-Consistent Effective Interaction"

13) M. Odera, Sumitomo Heavy Industries, Ltd. (Tokyo), 26 June
"ECR Ion Sources Meeting (Jülich) and Linac Meeting (Stanford)"

14) N. Tajima, Univ. Tokyo (Tokyo), 1 July
"The Unusual High Spin Isomer in ^{182}O and the Proton-Neutron Interaction"

15) W. Galster, Tsukuba Univ. (Ibaraki), 15 July
"Central Heavy Ion Collision at Intermediate Energy"

16) S. Ohta, KEK (Ibaraki), 29 July
"Forces between Quark Clusters"

17) R. J. Peterson, Univ. Colorado (USA), 9 September
"New Results on Isoscalar Giant Resonances"

18) Y. Iseri, Chiba-Keizai Junior College (Chiba), 30 October
"Break-up Effect of the Deuteron in the Polarized Deuteron Elastic Scattering"

19) R. C. Sethi, Bhabha Atomic Energy Institute (India), 30 October
"Design of Sectors for AVF Cyclotron"

20) R. K. Bhandari, Bhabha Atomic Energy Institute (India), 30 October
"Variable Energy Cyclotron Facility at Culcutta"

21) D. Heindy, RCNP (Osaka), 18 November
"Pre-scission Neutron Multiplicities and Fission Dynamics"

22) R. Anne, GANIL (France), 1 December
"LISE at GANIL Construction and Recent Results"

23) S. Nomachi, KEK (Ibaraki), 2 December
"Measurement of Antiproton-Proton Cross Sections at Low Antiproton Momenta"

24) T. Kamae, Univ. Tokyo (Tokyo), 9 December
"New Detection Method of γ-Ray and Its Application to Medical CT-Spectroscopy"

25) S. Takeuchi, Univ. Tokyo (Tokyo), 16 December
"Pauli-Blocking Effect of Quarks in Nuclei"

26) Y. Haneishi, Nihon Univ. (Tokyo), 16 December
"Backward Production of Proton in Proton-Nucleus Collisions at Low and Intermediate Energy"

27) M. Matsuo, Kyoto Univ. (Kyoto), 16 December
"Microscopic Description of Anharmonic Gamma-Vibrations by Means of the Self-Consistent-Collective-Coordinate Method"

28) T. Uchiyama, Tohoku Univ. (Miyagi), 24 December
"EMC Effect"

X. LIST OF PERSONNEL

Members of the Board

AWAYA Yohko 粟屋容子
HASHIZUME Akira 橋爪 朗
KAMITSUBO Hiromichi 上坪宏道
KATSUMATA Koichi 勝又紘一
KOHNO Isao 河野 功
MATSUOKA Masaru 松岡 勝
NOZAKI Tadashi 野崎 正
SAKAMOTO Yuichi 坂本雄一
UDA Masayuki 宇田応之
CHIBA Yoshiaki 千葉好明
ISHIHARA Masayasu 石原正泰
KANEKO Ichiro 金子一郎
KIRA Akira 吉良 爽
KURIHARA Osamu 栗原 修
NAGAMINE Kanetada 永嶺謙忠
SAKAIRI Hideo 坂入英雄
TANIHATA Isao 谷畑勇夫
WATANABE Tsutomu 渡部 力*

* chairman

Cyclotron Operation and Maintenance Group

FUJITA Shin 藤田 新
KAGEYAMA Tadashi 影山 正
KOHNO Isao 河野 功
TAKEBE Hideki 武部英樹
IKEGAMI Kumio 池上九三男
KOHARA Shigeo 小原重夫
OGIWARA Kiyoshi 荻原 清

Linac Operation and Maintenance Group

CHIBA Yosiaki 千葉好明
IKEZAWA Eiji 池沢英二
KAMBARA Tadashi 神原 正
KUBO Toshiyuki 久保敏幸
YANOKURA Minoru 矢野倉 実
HEMMI Masatake 逸見政武
INOUE Toshihiko 井上敏彦
KASE Masayuki 加瀬昌之
MIYAZAWA Yoshitoshi 宮沢佳敏

Scientific and Engineering Personnel

Cosmic Ray Laboratory

IMAI Takashi 今井 喬
KOHNO Tsuyoshi 河野 毅

Cyclotron Laboratory

BE Suck Hee 裵 碩喜
FUJITA Jiro 藤田二郎
HARA Masahiro 原 雅弘
INAMURA Takashi 稲村 卓
KARASAWA Takashi 唐沢 孝
MORITA Kosuke 森田浩介
FUJISAWA Takashi 藤沢高志
GOTO Akira 後藤 彰
HATANAKA Kichiji 畑中吉治
KAMITSUBO Hiromichi 上坪宏道
KOHNO Isao 河野 功
MOTONAGA Shoshichi 元永昭七

NAGASE Makoto 長瀬 誠
NAKANISHI Noriyoshi 中西紀喜
SAKAMOTO Ichiro 坂本一郎
SHIMIZU Kazuo 清水和男
TOYAMA Mitsuru 遠山 満
YAMAJI Shuhei 山路修平
YOKOYAMA Ichiro 横山一郎
NAKAJIMA Shunji 中島諄二
SAITO Motozo 斎藤始三
SHIKATA Takashi 四方隆史
TAKESHITA Isao 竹下勇夫
WADA Takeshi 和田 雄
YANO Yasushige 矢野安重
YOSHINAGA Naotaka 吉永尚孝

(Visitors)
ANNE Remy (GANIL, France)
CHABERT Andre (GANIL, France)
DOKE Tadayoshi 道家忠義* (Sci. Eng. Res. Lab., Waseda Univ.)
EGUCHI-KASAI Kiyomi 江口-笠井清美 (Inst. Basic Med. Sci., Univ. Tsukuba)
EJIRI Hiroyasu 江尻宏泰 (Dept. Phys., Osaka Univ.)
FUJIOKA Manabu 藤岡 学 (Cyclotron Radioisot. Cent., Tohoku Univ.)
FUKUMOTO Sadayoshi 福本貞義 (KEK)
FURUNO Kohei 古野興平 (Inst. Phys. Tandem Accel. Cent., Univ. Tsukuba)
HIRAKI Akio 平木昭夫 (Fac. Eng., Osaka Univ.)
IEKI Kazuo 家城和夫 (Dept. Phys., Tokyo Inst. Technol.)
IKEGAMI Hidetsugu 池上栄胤 (RCNP, Osaka Univ.)
INOUE Makoto 井上 信 (RCNP, Osaka Univ.)
ISOYA Akira 磯矢 彰 (Sch. Sci., Tokai Univ.)
IWASHITA Yoshihisa 岩下芳久 (Inst. Chem. Res., Kyoto Univ.)
KADOYA Shingo 角矢真吾 (Japan Gasoline Co.)
KANEKO Kumetaro 金子粂太郎 (Inst. Nucl. Study, Univ. Tokyo)
KASAGI Jirota 笠木治郎太 (Dept. Phys., Tokyo Inst. Technol.)
KATORI Kenji 鹿取謙二 (Dept. Phys., Osaka Univ.)
KATSURAGAWA Hidetsugu 桂川秀嗣 (Dept. Phys., Toho Univ.)
KIKUCHI Fumio 菊地文男 (Coll. Arts Sci., Univ. Tokyo)
KOBAYASHI Shinsaku 小林晨作 (Dept. Phys., Kyoto Univ.)
KOHMOTO Susumu 河本 進 (Univ. Electro-Commun.)
KONDO Michiya 近藤道也 (RCNP, Osaka Univ.)
KUDO Hisaaki 工藤久昭 (Dept. Chem., Niigata Univ.)
MALLIK Chaturanan (V.E.G. Cent., B.A.R.C., India)
MATSUKI Seishi 松木征史 (Inst. Chem. Res., Kyoto Univ.)
MINOWA Tatsuya 箕輪達哉 (Dept. Phys., Toho Univ.)
MIURA Iwao 三浦 岩 (RCNP, Osaka Univ.)
MIYATAKE Hiroari 宮武宇也 (Fac. Sci., Osaka Univ.)
MOTOBAYASHI Tohru 本林 透 (Fac. Sci., Rikkyo Univ.)
MURAKAMI Takeshi 村上 健 (Dept. Phys., Tokyo Inst. Technol.)
NAGAMIYA Shoji 永宮正治 (Dept. Phys., Univ. Tokyo)
NAKAHARA Hiromichi 中原弘道 (Dept. Chem., Tokyo Metropolitan Univ.)
NAKAI Koji 中井浩二 (KEK)
NOMURA Toru 野村 亨* (Inst. Nucl. Study, Univ. Tokyo)
NONAKA Hideki 野中英生 (Sumitomo Heavy Ind. Ltd.)
ODERA Masatoshi 小寺正俊* (Sci. Eng. Res. Lab., Waseda Univ.)
ONISHI Naoki 大西直毅 (Dept. Phys., Coll. Gen. Educ., Univ. Tokyo)
OTA Shigemi 太田滋生 (KEK)

QIAO Qingwen (Inst. Mod. Phys., Academia Sinica, China)
SAKURADA Yuzo 桜田勇三 (ULVAC Co.)
SATO Kenichi 佐藤憲一 (Div. Phys., Tohoku Coll. Pharm.)
SHIMAZU Mitsuyoshi 島津備愛 (Dept. Phys., Toho Univ.)
SHINOZUKA Tsutomu 篠塚 勉 (Cyclotron Radioisot. Cent., Tohoku Univ.)
SHIRAISHI Haruki 白石春樹 (Natl. Res. Inst. Metals)
SUEKI Keisuke 末木啓介 (Inst. Nucl. Study, Univ. Tokyo)
TAKEKOSHI Hidekuni 竹腰秀邦 (Inst. Chem. Res., Kyoto Univ.)
TAKEMASA Tadashi 武政尹士 (Dept. Phys., Saga Univ.)
TAKIGAWA Noboru 滝川 昇 (Dept. Phys., Tohoku Univ.)
TAMAGAKI Ryozo 玉垣良三 (Dept. Phys., Kyoto Univ.)
TANAKA Hitoshi 田中 均 (Japan Gasoline Co.)
TANAKA Jinichi 田中仁市 (Inst. Nucl. Study, Univ. Tokyo)
TANAKA Koki 田中幸基 (Nippon Steel Corp.)
TORIZUKA Kanji 鳥塚莞爾 (Fac. Med., Kyoto Univ.)
TSUNEMOTO Hiroshi 恒元 博 (Natl. Inst. Radiol. Sci.)
WANG Zhen (Inst. Mod. Phys., Academia Sinica, China)
YAMAZAKI Takashi 山崎 魏 (RCNP, Osaka Univ.)
YOSHIDA Nobuaki 吉田宣章 (Dept. Phys., Univ. Tokyo)
YOSHIDA Shiro 吉田思郎 (Dept. Phys., Tohoku Univ.)
YOSHINAGA Naotaka 吉永尚孝 (Comput. Cent., Univ. Tokyo)

* Visiting Professor

(Students)
HARADA Hideo 原田秀郎 (Dept. Phys., Tokyo Inst. Technol.)
HATSUKAWA Yuichi 初川雄一 (Dept. Chem., Tokyo Metropolitan Univ.)
KOIKE Yuji 小池裕司 (Dept. Phys., Univ. Tokyo)
MITOMORI Kuniharu 三戸森国東 (Coll. Hum. Sci., Nihon Univ.)
NAGAI Masahito 永井雅人 (Fac. Sci., Toho Univ.)
YAMAGUCHI Kazuhisa 山口和久 (Coll. Hum. Sci., Nihon Univ.)
YOSHIDA Koichi 吉田光一 (Dept. Phys., Tokyo Inst. Technol.)

Linac Laboratory

CHIBA Toshiya 千葉利哉
CHIBA Yoshiaki 千葉好明
GONO Yasuyuki 郷農靖之
HEMMI Masatake 逸見政武
INOUE Toshihiko 井上敏彦
KAMBARA Tadashi 神原 正
KASE Masayuki 加瀬昌之
KUBO Toshiyuki 久保敏幸
KUMAGAI Hidekazu 熊谷秀和
MIYAZAWA Yoshitoshi 宮沢佳敏
MIZOGAWA Tatsumi 溝川辰己
TANIHATA Isao 谷畑勇夫
TONUMA Tadao 戸沼正雄
YANOKURA Minoru 矢野倉 実

(Visitors)
FUJIWARA Ichiro 藤原一郎 (Inst. At. Energy, Kyoto Univ.)
ITO Noriaki 伊藤憲昭 (Dept. Cryst. Mater., Nagoya Univ.)
NONAKA Hideki 野中英生 (Sumitomo Heavy Ind., Ltd.)
SUGAWARA Masahiko 菅原昌彦 (Fund. Sci., Chiba Inst. Technol.)

(Student)
FUKUDA Mitsunori 福田光順 (Fac. Sci., Tokyo Inst. Technol.)

Radiation Laboratory

ASAHI Koichiro 旭 耕一郎
HASHIZUME Akira 橋爪 朗
ISHIHARA Masayasu 石原正泰
KOHNO Toshiyuki 河野俊之
OKANO Masaharu 岡野真治
TENDOW Yoshihiko 天道芳彦
GONO Yasuyuki 郷農靖之
ICHIHARA Takashi 市原 卓
IZUMO Koichi 出雲光一
KONNO Satoshi 金野 智
TAKAHASHI Tan 高橋 旦

(Visitors)
DOKE Tadayoshi 道家忠義 (Sci. Eng. Res. Lab., Waseda Univ.)
FUJIOKA Manabu 藤岡 学 (Dept. Phys., Tohoku Univ.)
HASEGAWA Takeo 長谷川武夫 (Inst. Nucl. Study, Univ. Tokyo)
HITACHI Akira 月出 章 (Sci. Eng. Res. Lab., Waseda Univ.)
IIO Masahiro 飯尾正広 (Fac. Med., Univ. Tokyo)
KITAO Kensuke 喜多尾憲助 (Natl. Inst. Radiol. Sci.)
KOBAYASHI Hisanobu 小林久信 (Fac. Eng., Saitama Univ.)
KUBOTA Shinzou 窪田信三 (Fac. Sci., Rikkyo Univ.)
KUSAKARI Hideshige 草刈英栄 (Fac. Educ., Chiba Univ.)
LEE Sang Mu 李 相茂 (Univ. Tsukuba)
MASUDA Kimiaki 増田公明 (Sch. Sci. Eng., Waseda Univ.)
MOTOBAYASHI Toru 本林 透 (Fac. Sci., Rikkyo Univ.)
MURAMATSU Hisakazu 村松久和 (Nat. Lab. High Energy Phys.)
OHSUMI Hideaki 大隅秀晃 (Fac. Sci., Osaka Univ.)
OHTSUKA Hideko 大塚秀子
ONAI Yoshio 尾内能夫 (Dept. Phys., Cancer Inst.)
SHIBAMURA Eido 柴村英道 (Saitama Coll. Health)
SHIMIZU Hajime 清水 肇 (Fac. Sci., Tokyo Inst. Technol.)

(Students)
IIMURA Jiro 飯村次郎 (Dept. Phys., Tokyo Inst. Technol.)
ONO Yoichi 小野陽一 (Fac. Educ., Chiba Univ.)
SHINOHARA Hideo 篠原秀雄 (Fac. Educ., Chiba Univ.)
SUZUKI Satoshi 鈴木 聡 (Sch. Sci. Eng., Waseda Univ.)

Atomic Processes Laboratory

ANDO Kozo 安藤剛三
IWAI Masahiro 岩井正博
KANAI Yasuyuki 金井保之
SHIMAMURA Isao 島村 勲
AWAYA Yohko 粟屋容子
KAMBARA Tadashi 神原 正
NISHIDA Masami 西田雅美
WATANABE Tsutomu 渡部 力

(Visitors)
FRITSH Wolfgang (Hahn-Meitner Inst. für Kernforschung)

FUJIMA Kazumi 藤間一美 (Dept. Phys., Chuo Univ.)
HARA Shunsuke 原 俊介 (Dept. Phys., Univ. Tsukuba)
HITACHI Akira 月出 章 (Inst. Sci. Technol., Waseda Univ.)
ISHII Keishi 石井慶之 (Dept. Eng. Sci., Kyoto Univ.)
ISMAIL M. Mostafa (Dept. Phys., Cairo Univ.)
ITOH Yoh 伊藤 陽 (Fac. Sci., Josai Univ.)
KARASHIMA Shosuke 唐島照介 (Dept. Electr. Eng., Tokyo Univ. Sci.)
KOBAYASHI Nobuo 小林信夫 (Dept. Phys., Tokyo Metropolitan Univ.)
KOIKE Fumihiro 小池文博 (Sch. Med., Kitasato Univ.)
KOIZUMI Tetsuo 小泉哲夫 (Dept. Phys., Rikkyo Univ.)
KOYAMA Naoto 小山直人 (Dept. Eng. Phys., Univ. Electro-Commun.)
LIN Chii-Dong 林 啓東 (Dept. Phys., Kansas State Univ.)
MATSUO Takashi 松尾 崇 (Dept. Pathol., Tokyo Med. Dent. Univ.)
MATSUZAWA Michio 松澤通生 (Dept. Eng. Phys., Univ. Electro-Commun.)
MIZOGAWA Tatsumi 溝川辰巳 (Fac. Sci., Saitama Univ.)
MOKLER H. Paul (Gesellschaft für Schwerionenforschung)
OHSAKI Akihiko 大崎明彦 (Inst. Mol. Sci.)
OHTANI Shunsuke 大谷俊介 (Inst. Plasma Phys., Nagoya Univ.)
OKUNO Kazuhiko 奥野和彦 (Dept. Phys., Tokyo Metropolitan Univ.)
SATO Hiroshi 佐藤浩史 (Dept. Phys., Ochanomizu Univ.)
SATO Kuninori 佐藤国憲 (Inst. Plasma Phys., Nagoya Univ.)
SATO Yo 佐藤 陽 (Fac. Sci., Josai Univ.)
SCHUCH Reinhold (Dept. Phys., Heidelberg Univ.)
SHIBATA Hiromi 柴田裕実 (Res. Cent. Nucl. Sci. Technol., Univ. Tokyo)
SHIMA Kunihiro 島 邦博 (Tandem Accel. Cent., Univ. Tsukuba)
SHIMAKURA Noriyuki 島倉紀之 (Gen. Educ. Dept., Niigata Univ.)
TAKAGI Shoji 高木祥示 (Dept. Phys., Toho Univ.)
TAWARA Hiroyuki 俵 博之 (Inst. Plasma Phys., Nagoya Univ.)
TOSHIMA Nobuyuki 戸嶋信幸 (Inst. Appl. Phys., Univ. Tsukuba)
TSURUBUCHI Seiji 鶴淵誠二 (Fac. Technol., Tokyo Univ. Agric. Technol.)
URAKAWA Junji 浦川順治 (Natl. Lab. High Energy Phys.)

(Students)
HINO Kenichi 日野健一 (Dept. Appl. Phys., Univ. Tokyo)
NAKANISHI Kiyotaka 中西清隆 (Dept. Chem., Waseda Univ.)

Metal Physics Laboratory

ISHIDA Katsuhiko 石田勝彦
MATSUZAKI Teiichiro 松崎禎市郎
SHIOTANI Nobuhiro 塩谷亘弘
KOYAMA Akio 小山昭雄
NAGAMINE Kanetada 永嶺謙忠
YAGI Eiichi 八木栄一

(Students)
KANO Fumihisa 鹿野文寿 (Sch. Sci. Eng., Waseda Univ.)
NAKAMURA Shiho 中村志保 (Sch. Sci. Eng., Waseda Univ.)

Magnetic Materials Laboratory

ASAI Kichizo 浅井吉蔵
SAKAI Nobuhiko 坂井信彦
OKADA Takuya 岡田卓也

Plasma Physics Laboratory

ISHIBE Yukio 石部行雄
OKAZAKI Kiyohiko 岡崎清比古
SAKAMOTO Yuichi 坂本雄一
ISHII Shigeyuki 石井成行
OYAMA Hitoshi 大山 等
YANO Katsuki 矢野勝喜

(Visitors)

SUGIYAMA Kazuo 杉山和夫 (Fac. Eng., Saitama Univ.)
YAMASHINA Toshiro 山科俊郎 (Fac. Eng., Hokkaido Univ.)

Semiconductors Laboratory

(Visitor)

AONO Keiko 青野桂子 (Coll. Lib. Arts, Kitasato Univ.)

Solid-State Chemistry Laboratory

KOBAYASHI Masayoshi 小林雅義
SASA Yoshihiko 佐々嘉彦
MAEDA Kuniko 前田邦子
UDA Masayuki 宇田応之

(Visitors)

BENKA Oswald (Johannes Kepler-Univ. Linz, Austria)
ISHII Keizō 石井慶造 (Cyclotron Radioisot. Cent., Tohoku Univ.)
KUSUYAMA Hiroyuki 楠山弘之 (Saitama Medical School)
MUKOUYAMA Takashi 向山 毅 (Inst. Chem. Res., Kyoto Univ.)
YOKODE Yutaka 横出 裕 (Sch. Med., Nihon Univ.)

(Student)

ISHIKAWA Hiroshi 石川 浩 (Dept. Phys., Sci. Univ. Tokyo)

Radiochemistry Laboratory

AMBE Fumitoshi 安部文敏
ARATANI Michi 荒谷美智
IWAMOTO Masako 岩本正子
NOZAKI Tadashi 野崎 正
AMBE Shizuko 安部静子
ITOH Yoshiko 伊東芳子
MIURA Taichi 三浦太一
OHKUBO Yoshitaka 大久保嘉高

(Visitors)

FUKUSHIMA Hiroto 福嶋浩人 (Japan Chemical Analysis Cent.)
HUANG Ziwei 黄 子蔚 (Inst. Biol. Pedol. Psamol. Res., China)
IMAI Masato 今井正人 (Komatsu Electronic Metals Co., Ltd.)
IMURA Ryo 井村 亮 (Cent. Res. Lab., Hitachi, Ltd.)
IZUMI Iwao 泉 巌 (Nippon Light Metal Co., Ltd.)

KATADA Motomi 片田元巳 (Dept. Chem., Fac. Sci., Tokyo Metropolitan Univ.)
KATO Hajime 加藤 一 (Fac. Educ., Yamanashi Univ.)
KIMURA Toshimasa 木村敏正 (Japan Chemical Analysis Cent.)
MINAI Yoshitaka 薬袋佳孝 (Fac. Sci., Univ. Tokyo)
MOCHIZUKI Yasuhiro 望月康弘 (Hitachi, Ltd.)
NASU Saburo 那須三郎 (Fac. Eng. Sci., Osaka Univ.)
OOHIRA Shigeo 大平重男 (Nikkei Techno Res. Co., Ltd.)
SAITO Kazuo 斎藤和雄 (Toshiba Corp., R & D Cent.)
SUEHIRO Makiko 末広牧子 (Tokyo Metropolitan Geriatric Hospital)
SUGAI Isao 菅井 勲 (Inst. Nucl. Study, Univ. Tokyo)
SUZUKI Ryo 鈴木 良 (Cent. Res. Lab., Hitachi, Ltd.)
YATSURUGI Yoshifumi 八剱吉文 (Komatsu Electronic Metals Co., Ltd.)
YOKOI Fuji 横井風児 (Ment. Muscular Disord., Natl. Cent. Nerv.)

(Students)
ARAI Iwao 新井五輪夫 (Fac. Pharm., Sci. Univ. Tokyo)
KOBAYASHI Yoshio 小林義男 (Fac. Sci., Tokyo Metropolitan Univ.)
KUBO Kenya 久保謙哉 (Fac. Sci., Univ. Tokyo)
QUI Qi 邱 齐 (Res. Lab., Nucl. React. Tokyo Inst. Technol.)
SATO Kazuhiro 佐藤和広 (Fac. Sci., Toho Univ.)
TANAKA Isao 田中 功 (Fac. Eng. Sci., Osaka Univ.)
YOSHIKAWA Hideki 吉川英樹 (Fac. Sci., Tokyo Metropolitan Univ.)
YU Byongon 俞 炳坤 (Res. Lab., Nucl. React., Tokyo Inst. Technol.)

Radiation Chemistry Laboratory
KIMURA Kazuie 木村一宇

(Visitor)
ITO Yasuo 伊藤泰男 (Res. Cent. Nucl. Sci. Technol., Univ. Tokyo)

(Students)
FUNDOH Atsushi 分銅淳至 (Dept. Phys., Chuo Univ.)
HARA Korehisa 原 是久 (Dept. Phys., Chuo Univ.)
IIDA Tsuyoshi 飯田 剛 (Dept. Phys., Chuo Univ.)
KANAI Koichi 金井浩一 (Dept. Phys., Chuo Univ.)
KATAOKA Masayoshi 片岡将克 (Dept. Phys., Chuo Univ.)
NISHINA Takuya 仁科卓也 (Dept. Phys., Chuo Univ.)
UENO Takao 上野貴男 (Dept. Phys., Chuo Univ.)

Radiobiology Laboratory
KANEKO Ichiro 金子一郎 NAKANO Kazushiro 中野和城

(Visitors)
EGUCHI-KASAI Kiyomi 江口-笠井清美 (Inst. Basic Med. Sci., Univ. Tsukuba)
MAJIMA Hideyuki 馬嶋秀行 (Fac. Med., Univ. Tokyo)

MARUHASHI Akira 丸橋　晃 (Inst. Clin. Med., Univ. Tsukuba)
OKADA Gensaku 岡田源作 (Tokyo Metropolitan Nurse Sch.)

(Student)
KOSAKA Toshiyuki 小坂俊之 (Dept. Vet. Radiol., Nihon Univ.)

Safety Control Affairs Office
KAGAYA Satoru 加賀屋　悟
KURIHARA Osamu 栗原　修
MIYAGAWA Makoto 宮川真言
SHINOHARA Shigemi 篠原茂己
USUBA Isao 薄葉　勲
KATOU Takeo 加藤武雄
MATSUZAWA Yasuhide 松沢安秀
SAKAMOTO Ichiro 坂本一郎
TAKI Kenro 滝　剣朗

Beam Analysis Center
IWAKI Masaya 岩木正哉
SAKAIRI Hideo 坂入英雄
KOBAYASHI Takane 小林　峰

AUTHOR INDEX

RIKEN Accelerator Progress Report

理化学研究所加速器年次報告　第20巻（1986）

印　刷　昭和62年（1987）8月25日
発　行　昭和62年（1987）8月31日
発行者　理化学研究所
代表者　宮　島　龍　興
〒351-01　埼玉県和光市広沢2番1号
電話（0484）62－1111
編集者　理化学研究所加速器運営委員会
製　作　財団法人　学会誌刊行センター
〒113　東京都文京区弥生2丁目4番16号
印刷所　有限会社　学　術　製　版
〒105　東京都港区東新橋2丁目9番11号

定価 5,000円

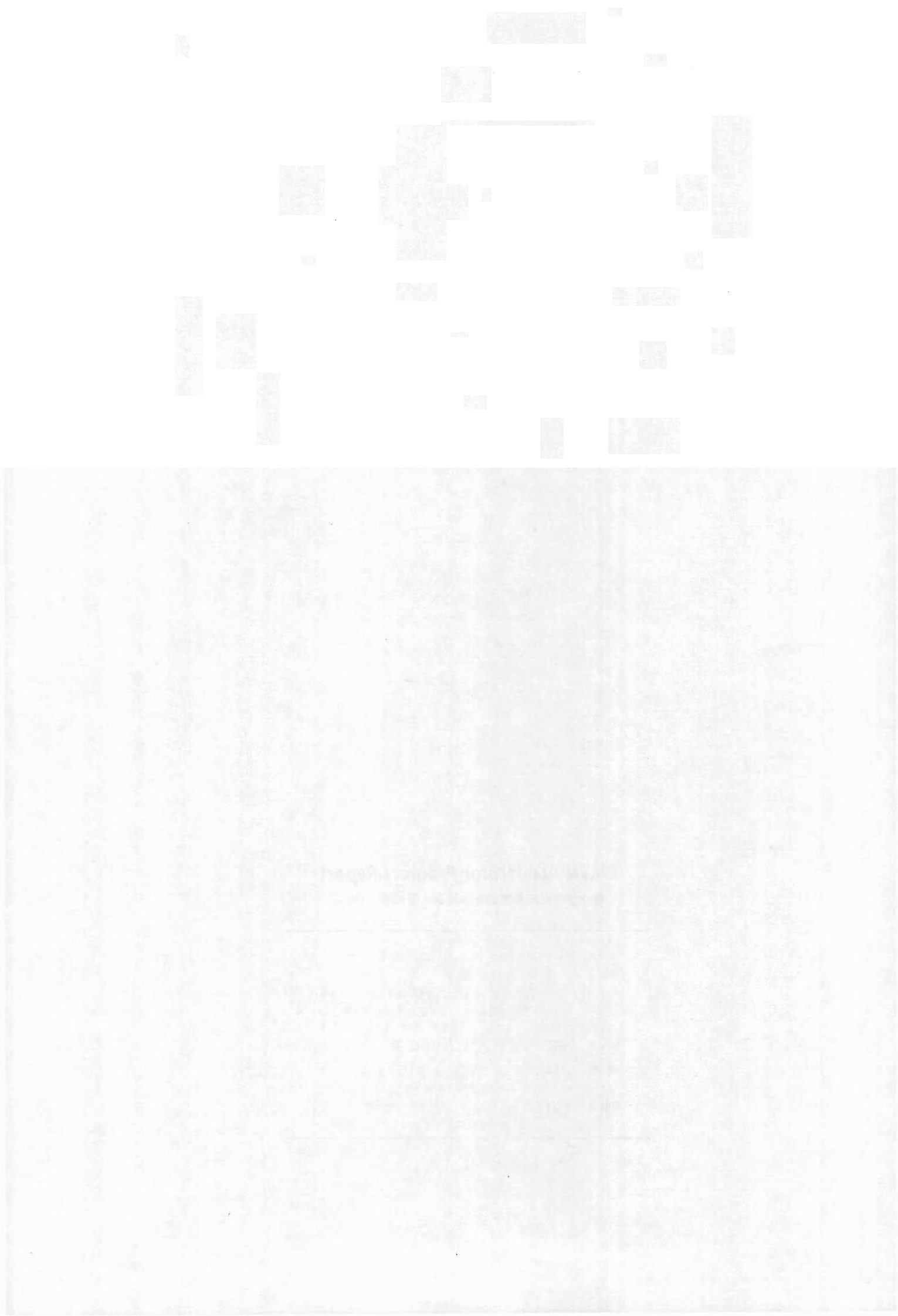

理化学研究所

埼玉県　和光市　広沢